419p

N63-14717
Code-1

Technical Report No. 32-77

Design Parameters for Ballistic Interplanetary Trajectories Part I. One-way Transfers to Mars and Venus

V. C. Clarke, Jr.
W. E. Bollman
R. Y. Roth
W. J. Scholey

OTS PRICE

XEROX $ 22.25

MICROFILM $ 12.77

JET PROPULSION LABORATORY
CALIFORNIA INSTITUTE OF TECHNOLOGY
PASADENA, CALIFORNIA

January 16, 1963

NATIONAL AERONAUTICS AND SPACE ADMINISTRATION
CONTRACT NO. NAS 7-100

Technical Report No. 32-77

Design Parameters for Ballistic Interplanetary Trajectories Part I. One-way Transfers to Mars and Venus

V. C. Clarke, Jr.
W. E. Bollman
R. Y. Roth
W. J. Scholey

T. W. Hamilton

T. W. Hamilton, Chief
Systems Analysis Section

JET PROPULSION LABORATORY
CALIFORNIA INSTITUTE OF TECHNOLOGY
PASADENA, CALIFORNIA

January 16, 1963

CONTENTS

CONTENTS (Cont'd)

TABLES

FIGURES

FIGURES (Cont'd)

FIGURES (Cont'd)

FIGURES (Cont'd)

FIGURES (Cont'd)

FIGURES (Cont'd)

FIGURES (Cont'd)

FIGURES (Cont'd)

FIGURES (Cont'd)

FIGURES (Cont'd)

FIGURES (Cont'd)

FIGURES (Cont'd)

FIGURES (Cont'd)

FIGURES (Cont'd)

FIGURES (Cont'd)

FIGURES (Cont'd)

FIGURES (Cont'd)

FOREWORD

This Report presents, in graphical form, the extensive results of studies of the characteristics of ballistic interplanetary trajectories to Venus (1962–1970) and Mars (1962–1977). Also included are a description of the physical model, development of the equations of the model, and a discussion of the properties of the trajectories.

Companion volumes (Refs. 1 and 2) present the same results in numerical form. This Report is intended to provide data in volume to trajectory and guidance analysts, so that they may perform preliminary design studies and conduct investigations of the properties of ballistic interplanetary trajectories.

ABSTRACT

The general characteristics of ballistic interplanetary trajectories are discussed, and detailed equations are developed for the analytical model. Extensive data are presented in graphical form for trajectories to Venus (1962–1970) and Mars (1962–1977). These 313 graphs include: (1) curves of *vis viva* geocentric energy vs launch date for minimum-energy trajectories, and (2) curves of 18 different trajectory parameters vs launch date for various *vis viva* geocentric energies. The trajectories were computed on the IBM 7090 digital computer by numerical evaluation of the analytical model, after which specific parameters of interest were automatically plotted, carefully checked, and analyzed. Procedures are outlined for use of these data by the trajectory engineer in the design and analysis of interplanetary trajectories.

I. INTRODUCTION. ANALYTICAL MODEL FOR INTERPLANETARY TRAJECTORIES

The analytical model used in the generation of Venus and Mars trajectory parameters consists of three distinct phases of two-body motion: (1) an escape hyperbola near the launch planet, (2) elliptical[1] motion under the attraction of the Sun, and (3) terminal hyperbolic motion near the target planet.

A. *Heliocentric Motion*

Solution of the heliocentric elliptic motion is obtained first under the following assumptions:

(1) The launch and target planets move in orbits about the Sun as given in the national ephemerides. Their velocity components are obtained by using two-body conic formulas, mean orbital elements, and their tabular positions, as listed in the ephemerides.

(2) The launch and target planets are massless. Thus, the only force acting on the probe is that of the Sun.

(3) The position of the probe at launch into the heliocentric orbit is the center of the massless launch planet. Its position at arrival on the heliocentric orbit is the center of the massless target planet.

[1]Hyperbolic heliocentric motion is not considered herein.

Thus, for solution of the heliocentric phase of motion, the attractions of the launch and target planets are temporarily disregarded. The primary result to be obtained from the solution of the heliocentric-transfer problem is determination of the hyperbolic-excess velocity vector relative to the launch planet.

1. Determination of Planar Orientation

Since the launch and arrival positions of the probe are assumed to be the centers of the launch and target planets, they can immediately be determined, given the launch and arrival[2] times, by consulting the ephemeris. Further, the orientation of the heliocentric transfer plane can immediately be found. Let $\mathbf{R}_L$ be the Sun–launch-planet position vector at launch time T_L, and let $\mathbf{R}_p$ be the Sun–target-planet position vector at arrival time T_a (Fig. 1-1). Planar orientation is then found from the unit normal $\mathbf{W}$ to the plane, as follows:

$$\mathbf{W} = \frac{\mathbf{R}_L \times \mathbf{R}_p}{R_L\, R_p \sin \Psi} \qquad (1\text{–}1)$$

where the angle Ψ is defined below. The inclination i to

[2]Or, for convenience, the launch date and flight time can be specified.

the ecliptic plane[3] can be found by

$$\cos i = \mathbf{W} \cdot \mathbf{K}' \qquad (1\text{–}2)$$

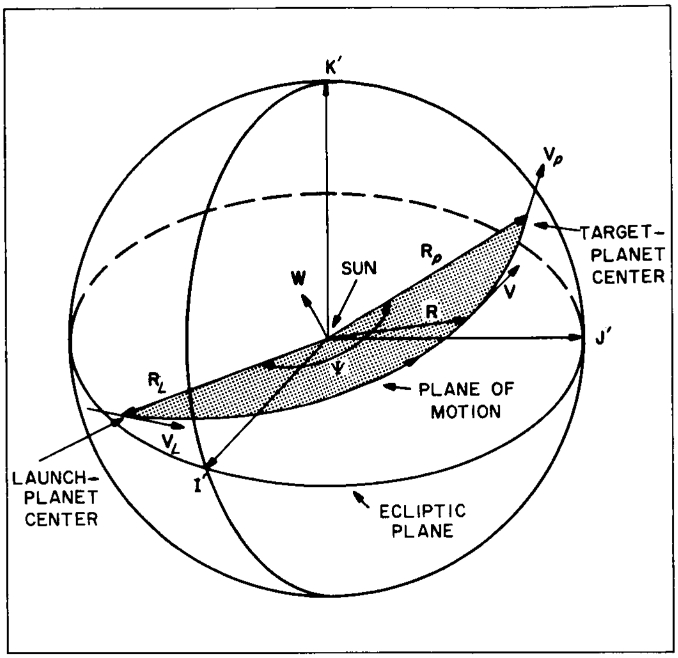

Fig. 1–1. Heliocentric-transfer geometry

where $\mathbf{K}'$ is a unit vector pointing in the direction of the ecliptic north pole.

2. In-Plane Relations

The heliocentric central angle Ψ (Fig. 1–1) is also readily determined by utilizing the positions of the launch and target planets. This angle may be obtained from

$$\cos \Psi = \frac{\mathbf{R}_L \cdot \mathbf{R}_p}{|\mathbf{R}_L|\,|\mathbf{R}_p|} \qquad (1\text{–}3)$$

$$\sin \Psi = \operatorname{sgn}\,[(\mathbf{R}_L \times \mathbf{R}_p) \cdot \mathbf{K}']\,(1 - \cos^2 \Psi)^{1/2} \qquad (1\text{–}4)$$

The velocity vector $\mathbf{V}$ of the spacecraft anywhere along its path may be obtained from

$$\mathbf{V} = \frac{V}{R}[(\mathbf{W} \times \mathbf{R}) \cos \Gamma + \mathbf{R} \sin \Gamma] \qquad (1\text{–}5)$$

Here, $\mathbf{R}$ is the heliocentric position vector, $R = |\mathbf{R}|$, and V is the heliocentric speed, obtained from

$$V = \sqrt{(GM_S)\left(\frac{2}{R} - \frac{1}{a}\right)} \qquad (1\text{–}6)$$

[3]In this Report, the interest is only in transfers which have the same rotational motion about the Sun as do the planets: thus, $0 \leq i \leq \pi/2$.

and the path angle Γ is found from

$$\sin \Gamma = \left[\sqrt{\frac{R}{(1 - e^2)(2a - R)}}\,\right] e \sin v \qquad (1\text{–}7)$$

In Eqs. 1–6 and 1–7, GM_S is the universal gravitational constant times the mass of the Sun ($= 2.959122083 \times 10^{-4}$ au^3/day^2); a and e are the semimajor axis and eccentricity of the transfer ellipse, respectively; and v is the true anomaly of the probe, given by

$$\cos v = \frac{a(1 - e^2) - R}{eR} \qquad (1\text{–}8)$$

3. Lambert's Theorem

Now, there are two unknowns in Eqs. 1–5 to 1–8 which prevent their immediate evaluation: the semimajor axis a and the eccentricity e. The determination of these quantities is the main problem. Battin (Ref. 3) has shown that the eccentricity is actually a function of the semimajor axis. Thus, it is first necessary to determine a. The semimajor axis is related to the time of flight T_F by Lambert's Theorem, which states: *The transfer time between any two points on an ellipse is a function of the sum of the distances of each point from the focus, the distance between the points, and the semimajor axis of of the ellipse.* Functionally, the theorem is stated as

$$T_F = T_F(R_L + R_p, C, a) \qquad (1\text{–}9)$$

where the distance C between the launch planet at launch time and the target planet at arrival time, as shown in Fig. 1–2, is obtained from

$$C = |\mathbf{R}_p - \mathbf{R}_L| \qquad (1\text{–}10)$$

Since the time of flight T_F and the launch and arrival positions R_L and R_p are known, only the semimajor axis remains to be found by iterative solution of Eq. 1–9. After the semimajor axis a is obtained, the heliocentric velocities of the probe at launch and arrival times $\mathbf{V}_L$

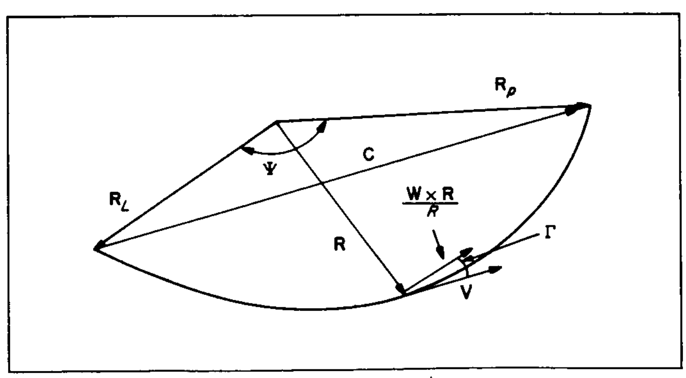

Fig. 1–2. In-plane–transfer geometry

and $\mathbf{V}_p$ may be evaluated from Eq. 1–5 under the conditions $R = R_L$ and $R = R_p$. The path angles Γ_L, Γ_p and true anomalies v_L, v_p at launch and arrival times[4] may also be evaluated from Eqs. 1–7 and 1–8 under the same conditions.

Finally, the desired end result, the hyperbolic-excess velocity $\mathbf{V}_{hL}$ relative to the launch planet, may be found (Fig. 1–3) by

$$\mathbf{V}_{hL} = \mathbf{V}_L - \mathbf{V}_1 \tag{1–11}$$

where $\mathbf{V}_1$ is the velocity of the launch planet at launch time.

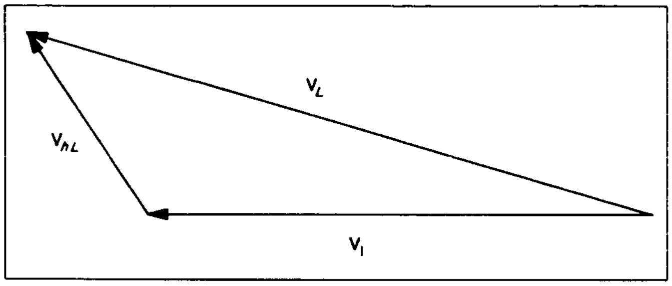

Fig. 1–3. Determination of hyperbolic-excess velocity vector

B. *Launch-Planet Escape Hyperbola*

The key result from the solution of heliocentric transfer is the hyperbolic-excess velocity vector $\mathbf{V}_{hL}$ at launch. The reason for the importance of this vector is that it tells the direction in which the probe must be traveling relative to the launch planet when on the point of leaving the planet's gravitational influence. There are an infinite number of escape trajectories (all hyperbolas) which can have the same hyperbolic-excess velocity vector. However, only a portion of these are practical for use when related to existing launch sites and boost-vehicle constraints. For example, it would be ridiculously costly in payload—and impractical—to shoot a vehicle straight up. Criteria for selection of a family of feasible escape trajectories are given below.

1. Assumptions

The solution of the escape phase of motion is obtained under the following assumptions: (1) The probe is acted on only by the gravitational force of the launch planet, and (2) the oblateness effects of the launch planet are neglected.

[4]The details of quadrant choice for these angles are found in Ref. 3.

The direction of the asymptote of the escape hyperbola is found by normalizing the hyperbolic-excess vector $\mathbf{V}_{hL}$. The injection energy C_3 of the escape hyperbola[5] is found by squaring the hyperbolic-excess speed, or

$$C_3 = V_{hL}^2 \tag{1–12}$$

Thus, in contrast to the heliocentric problem, the launch planet is now "massy," whereas the influence of the Sun is neglected. However, the hyperbolic-excess velocity vectors found by solving the heliocentric problem are used as a starting point to solve the escape problem.

2. Size and Shape of Escape Hyperbola

As previously stated, only some of the infinite number of escape trajectories are practical. Two of the practical aspects of a set of trajectories are the sizes and shapes of the hyperbolas.

Size is basically determined by the energy C_3, which, in turn, is a function of boost-vehicle capability. For boost vehicles in use at this writing (or shortly to be available), values of energy less than or equal to 25 km²/sec² are considered reasonable. The larger the value of energy that the booster is required to deliver, the smaller the payload and launch period over which the vehicle may be fired.

The shape of the hyperbola is determined by its eccentricity, which is a function of both the energy and the perifocal distance, according to

$$e = 1 + \frac{R_p C_3}{GM} \tag{1–13}$$

where R_p is the perifocal distance and GM is the universal gravitational constant times the mass of the launch planet. From Eq. 1–13, it can be seen that, for a fixed perifocal distance, the eccentricity increases linearly with the energy. The value of perifocal distance is not arbitrary, but depends strongly on the boost-vehicle trajectory. It has been shown (Ref. 4) that, in the great majority of cases, it is necessary and desirable to use a circular parking orbit as part of the preinjection phase of the escape trajectory. It is, further, an interesting fact that the altitude of the parking orbit determines the perifocal distance. If h is the parking-orbit altitude and R_0 is the launch planet's radius, then, to an extremely close degree of approximation,

$$R_p = R_0 + h \tag{1–14}$$

[5]C_3 is actually twice the total energy per unit mass; i.e., the *vis viva* integral.

or the perifocal distance is equal to the launch-planet-centered radius of the parking orbit. In Ref. 4, it also has been shown that the lowest possible parking orbit (80–100 nm) allows greatest payload capability. Thus, using 100 nm for the parking-orbit altitude, a practical value of perifocal distance is 6560 km. The perifocal distance will vary only slightly about this value for other parking-orbit altitudes, or even for direct-ascent-type preinjection trajectories. Therefore, *both* the size and shape are essentially determined by the energy alone, which is found from Eq. 1–12.

Given the size and shape of the escape hyperbola, its planar orientation must be determined. This can be done by considering two vectors: (1) the direction of the hyperbolic-excess vector, denoted by a unit vector **S**, and (2) a unit vector $\mathbf{R}_L^1$ directed from the center of the launch planet to the launch site. The vehicle's flight plane will essentially be determined by these two vectors, as shown in Fig. 1–4. A unit normal **W** to the launch-planet-centered flight plane is determined by

$$\mathbf{W} = \frac{\mathbf{R}_L^1 \times \mathbf{S}}{|\mathbf{R}_L^1 \times \mathbf{S}|} \qquad (1\text{–}15)$$

with the constraint that the Z component of **W** is always positive.

Since $\mathbf{R}_L^1$ is a function of time, according to the rotation rate of the launch planet, the planar orientation must continually change. In effect, this says that the launch azimuth is a continuous function of launch time.

A detailed description of the geometrical aspects of the launch-planet ascent trajectory is not given here, but may be found in Ref. 4.

C. *Calculation of Differential Corrections*

The calculation of differential corrections for interplanetary trajectories may be accomplished in several ways and depends on the choice of independent and dependent variables. In this Report, a numerical differencing scheme is used. Basically, the independent variables—the injection energy C_3, declination Φ_S, and right ascension Θ_S of the outgoing asymptote **S** of the escape hyperbola—are varied, one at a time, to produce variations in the dependent variables—the components of the impact parameter **B** and the time-of-flight T_F.

The impact parameter **B** is defined as a vector originating at the center of the target planet and directed perpendicular to the incoming asymptote of the target-centered approach hyperbola (Fig. 1–5). The impact parameter **B** is resolved into two components which lie in a plane normal to the incoming asymptote **S**. The orientations of the reference axes in this plane are arbitrary, but one is usually selected to lie in a fixed plane. Thus, define a unit vector **T**, lying in the *ecliptic* plane, according to

$$\mathbf{T} = \frac{\mathbf{S} \times \mathbf{K}'}{|\mathbf{S} \times \mathbf{K}'|} \qquad (1\text{–}16)$$

where **K′** is a unit vector normal to the ecliptic plane. The remaining axis is then given by a unit vector **R**, defined by

$$\mathbf{R} = \mathbf{S} \times \mathbf{T} \qquad (1\text{–}17)$$

Figure 1–6 illustrates the orientation of the **R**, **S**, **T** target coordinates.

The impact parameter **B** lies in the **R–T** plane and has miss components $\mathbf{B}\cdot\mathbf{T}$ and $\mathbf{B}\cdot\mathbf{R}$. The condition $\mathbf{B}\cdot\mathbf{T} = \mathbf{B}\cdot\mathbf{R} = 0$ denotes vertical impact on the target. Thus, $\mathbf{B}\cdot\mathbf{T}$, $\mathbf{B}\cdot\mathbf{R}$, and T_F are the three target dependent variables. If Q_i represents a set of generalized independent variables, such as injection position and velocity or other convenient variables, then the partial derivatives $\partial\mathbf{B}\cdot\mathbf{T}/\partial Q_i$, $\partial\mathbf{B}\cdot\mathbf{R}/\partial Q_i$, $\partial T_F/\partial Q_i$ are first-order differential corrections or error coefficients relating miss at the target and flight-time errors to the independent variables.

A convenient set of independent variables for interplanetary trajectories is the *vis viva* injection energy C_3, the declination Φ_S, and the right ascension Θ_S of the asymptote of the escape hyperbola. These variables essentially describe the launch hyperbolic-excess velocity vector $\mathbf{V}_{hL}$.

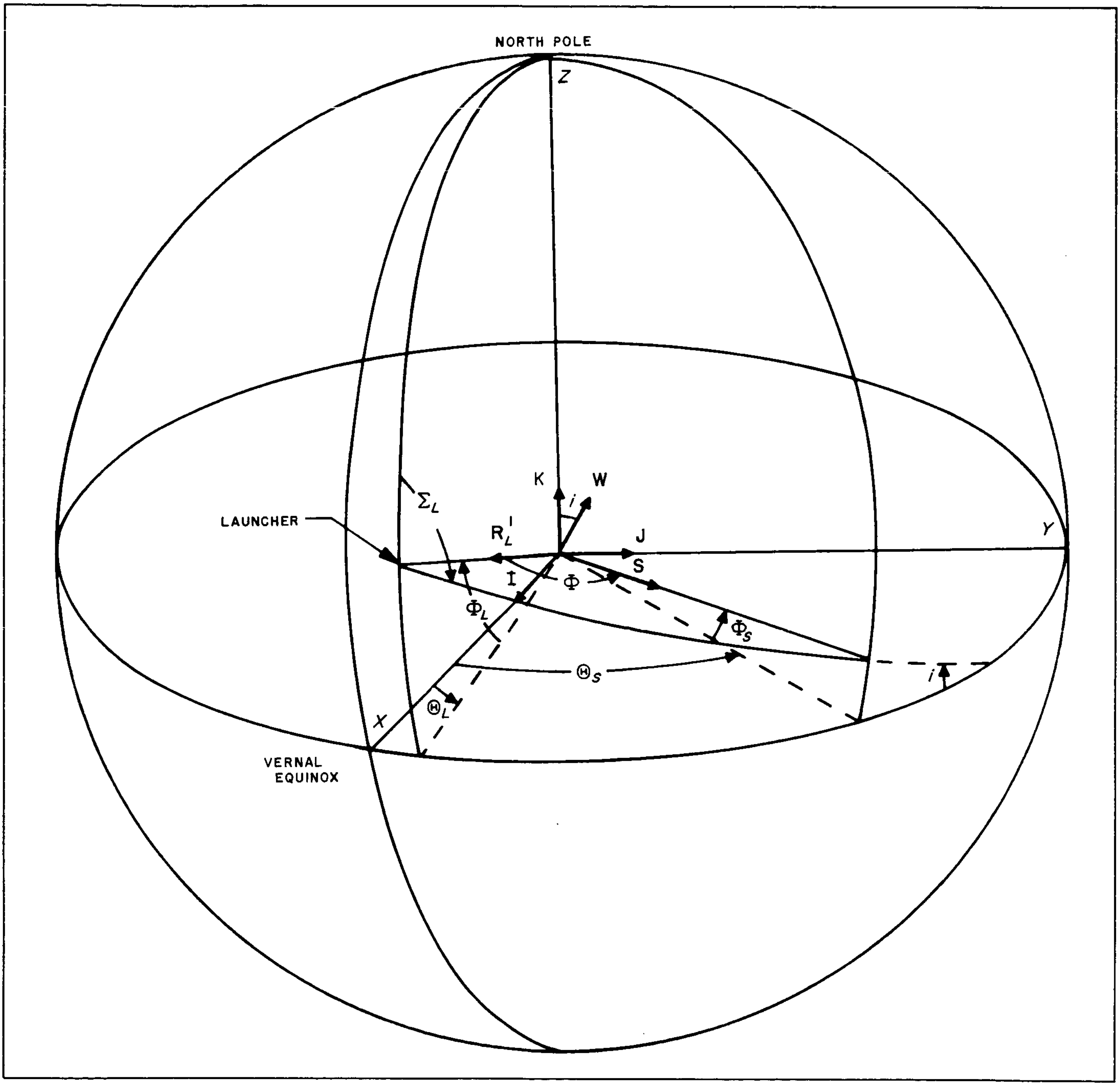

Fig. 1–4. Vehicle flight plane

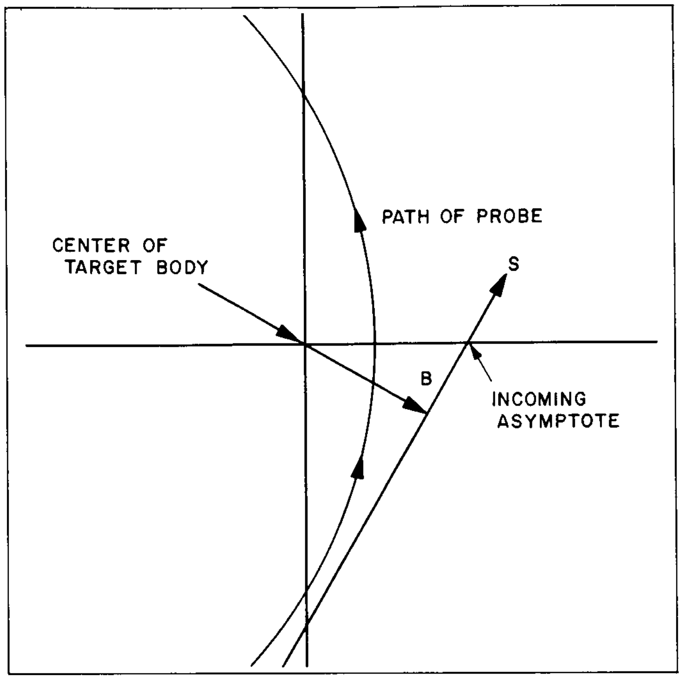

Fig. 1–5. Impact parameter

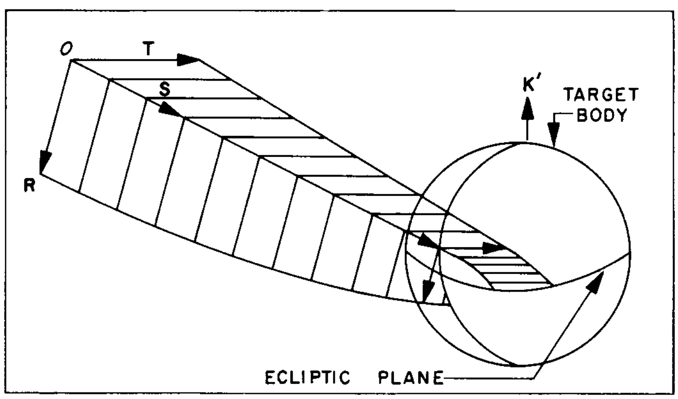

Fig. 1–6. The **R**, **S**, **T** target coordinate system

II. DETAILED EQUATIONS FOR TRAJECTORY COMPUTATIONS

In Section I, a summary was given of the physical model used to generate the parameters of Venus and Mars trajectories. The purpose of this Section is to present, in full detail, the equations of the Jet Propulsion Laboratory's Heliocentric Conic Trajectory Program[6], including the equations of Lambert's Theorem[7], which were developed for this investigation. The equations were coded for the Laboratory's IBM 7090 digital computer.

This program has proved very useful over the past few years in studying and analyzing interplanetary trajectories. Some of the results of these studies are presented graphically in Sections III to XVIII of this Report. The program has been devised for calculation of trajectories from any planet in the solar system to any other planet. In addition, by adding the appropriate orbital elements, trajectories to comets or to any body of known motion may be computed.

The Heliocentric Conic Trajectory Program is divided into four major sections:

(1) The heliocentric phase, in which basic computations are made for a unique conic trajectory, of given flight time, that passes through the center of two massless planets rotating around the Sun, as defined in the national ephemerides.

(2) The near-launch-planet phase, in which a launch-planet–centered conic is fitted to the heliocentric conic for a given launch azimuth and launch site.

(3) The near-target-planet phase, in which the parameters of the planetocentric conic at the target are calculated.

(4) Computation of partial derivatives which relate miss and time-of-flight errors at the target to variations in the hyperbolic-excess velocity vector of the escape hyperbola near the launch planet.

A. Heliocentric Phase

1. Determination of Position at Launch and Arrival

For any given time, the positions of the planets can be obtained from the ephemerides, referenced to a given coordinate system and epoch. For the present purposes, the heliocentric ephemerides of the planets, referenced to the mean equator and equinox of 1950.0, were selected.

From these ephemerides, one may find the position vector $\mathbf{R}'_L$ of the launch planet at launch time T_L, the position vector $\mathbf{R}'_p$ of the target planet at arrival time T_a, and the position vector $\mathbf{R}'_{LA}$ of the launch planet at arrival time. For practical and computational purposes, it is convenient to transform these coordinates to a heliocentric ecliptic, mean-of-*launch*-date system. Thus, two rotation matrices must be computed. First, a rotation is made from heliocentric equatorial coordinates, mean of 1950.0, to heliocentric equatorial, mean of *launch* date. This is accomplished by means of the matrix A, whose elements are given below (as obtained from Ref. 5):

$$\left.\begin{aligned}
a_{11} &= 1 - 0.000029697T^2 - 0.00000013T^3 \\
a_{12} &= -a_{21} = -0.02234988T - 0.00000676T^2 + 0.00000221T^3 \\
a_{13} &= -a_{31} = -0.00971711T + 0.00000207T^2 + 0.00000096T^3 \\
a_{22} &= 1 - 0.00024976T^2 - 0.00000015T^3 \\
a_{23} &= a_{32} = -0.00010859T^2 - 0.00000003T^3 \\
a_{33} &= 1 - 0.00004721T^2 + 0.00000002T^3
\end{aligned}\right\} \qquad (2\text{–}1)$$

where T is the number of Julian Centuries of 36,525 days past the epoch 1950.0.

The second rotation transforms the coordinates from heliocentric equatorial, mean of launch date, to heliocentric ecliptic, mean of launch date. This is accomplished by means of the matrix E:

$$E = \begin{bmatrix} 1 & 0 & 0 \\ 0 & \cos\epsilon & \sin\epsilon \\ 0 & -\sin\epsilon & \cos\epsilon \end{bmatrix} \qquad (2\text{–}2)$$

[6]Coded by W. J. Scholey and R. Y. Roth of the JPL Computer Applications and Data Systems Section.
[7]Developed by E. Dobies, formerly of JPL, and coded by C. A. Seafeldt, of the JPL Computer Applications and Data Systems Section.

where ϵ is the mean obliquity of the ecliptic on the launch date and $\sin \epsilon$ and $\cos \epsilon$ are approximated by the following equations from Ref. 6:

$$\left.\begin{aligned} \sin \epsilon &= \sin \epsilon_0 + P(T) \cos \epsilon_0 - \frac{1}{2} P^2(T) \sin \epsilon_0 \\ \cos \epsilon &= \cos \epsilon_0 - P(T) \sin \epsilon_0 - \frac{1}{2} P^2(T) \cos \epsilon_0 \end{aligned}\right\} \quad (2\text{–}3)$$

where

$$\begin{aligned} P(T) = &- 0.000227111T - 0.0000000286T^2 \\ &+ 0.00000000878T^3 \end{aligned} \quad (2\text{–}4)$$

and ϵ_0 is the mean obliquity of the ecliptic for 1950.0.

Now, in general, the components of the position vectors $\mathbf{R}_L$, $\mathbf{R}_{LA}$, and $\mathbf{R}_p$ are found in mean-equinox, ecliptic-of-launch-date coordinates by

$$\left.\begin{matrix} \mathbf{R}_L \\ \mathbf{R}_{LA} \\ \mathbf{R}_p \end{matrix}\right\} = EA \left\{\begin{matrix} \mathbf{R}'_L \\ \mathbf{R}'_{LA} \\ \mathbf{R}'_p \end{matrix}\right. \quad (2\text{–}5)$$

The unit vectors $\mathbf{R}^1_L$, $\mathbf{R}^1_p$ may then be found:

$$\mathbf{R}^1_L = \frac{\mathbf{R}_L}{R_L} \qquad \mathbf{R}^1_p = \frac{\mathbf{R}_p}{R_p} \quad (2\text{–}6)$$

where

$$R_L = |\mathbf{R}_L| \text{ and } R_p = |\mathbf{R}_p| \quad (2\text{–}7)$$

The heliocentric central angle Ψ, i. e., the angle between $\mathbf{R}_L$ and $\mathbf{R}_p$, is computed from

$$\left.\begin{aligned} \cos \Psi &= \frac{\mathbf{R}_L \cdot \mathbf{R}_p}{R_L\, R_p} \\ \sin \Psi &= \operatorname{sgn}\,[(\mathbf{R}_L \times \mathbf{R}_p) \cdot \mathbf{K}'] \,(1 - \cos^2 \Psi)^{1/2} \end{aligned}\right\} \quad (2\text{–}8)$$

where $\mathbf{K}'$ is the unit vector normal to the ecliptic plane in the direction of the ecliptic north pole.

The unit vector $\mathbf{W}$ normal to the probe's orbit plane, is found from the vector equation

$$\mathbf{W} = \frac{\mathbf{R}_L \times \mathbf{R}_p}{R_L\, R_p \sin \Psi} \quad (2\text{–}9)$$

Subsequently, the inclination of the orbit to the ecliptic plane i may be found from

$$\cos i = \mathbf{W} \cdot \mathbf{K}' \quad (2\text{–}10)$$

where $0 \leqq i \leqq \pi/2$ are the only cases of interest to this program.

Essentially, calculation of the $\mathbf{W}$ vector determines the planar orientation of the transfer conic.

2. Application of Lambert's Theorem

As shown in Section I, the semimajor axis a may be found, given the flight time T_F, $\mathbf{R}_L$, and $\mathbf{R}_p$. One uses Lambert's Theorem, which states:

> *The transfer time between any two points on an ellipse is a function of the sum of the distances of each point from the focus, the distance between the points, and the semimajor axis of the ellipse.*

Or, functionally,

$$T_F = T_F\,(R_L + R_p, C, a) \quad (2\text{–}11)$$

where C is the chord distance from $\mathbf{R}_L$ to $\mathbf{R}_p$, or

$$C = |\mathbf{R}_p - \mathbf{R}_L| \quad (2\text{–}12)$$

Now, since T_F, $\mathbf{R}_L$, $\mathbf{R}_p$, and C are known, Lambert's Theorem can be used to solve for a by an iterative process described below.

First, the transfer time T_m of the minimum-energy trajectory is computed from Eqs. 2–13 to 2–22.

The minimum semimajor axis a_m for an ellipse can be found from

$$a_m = (R_L + R_p + C)/4 \quad (2\text{–}13)$$

and e_m, the eccentricity of the orbit with a minimum semimajor axis, is expressed by

$$e_m = \sqrt{1 - \frac{p_m}{a_m}} \quad (2\text{–}14)$$

where p_m is the semilatus rectum obtained by

$$p_m = \frac{2(2a_m - R_L)\,(2a_m - R_p)}{C} \quad (2\text{–}15)$$

The true anomaly at launch v_{Lm} is found from Eqs. 2–16 and 2–17. First, compute the angle ϕ:

$$\cos \phi = \frac{R_L - a_m\,(1 - e^2_m)}{e_m\, R_L} \qquad 0 \leqq \phi \leqq \pi \quad (2\text{–}16)$$

where ϕ is an angle from the aphelion to R_L.

It can then be shown from the geometry of the minimum-energy ellipse (Fig. 2–1) that

$$\left.\begin{aligned} v_{Lm} &= \pi - \phi \\ v_{Lm} &= \pi + \phi \end{aligned}\right\} \begin{aligned} &0 < \Psi < \pi \\ &\pi < \Psi < 2\pi \end{aligned} \quad (2\text{–}17)$$

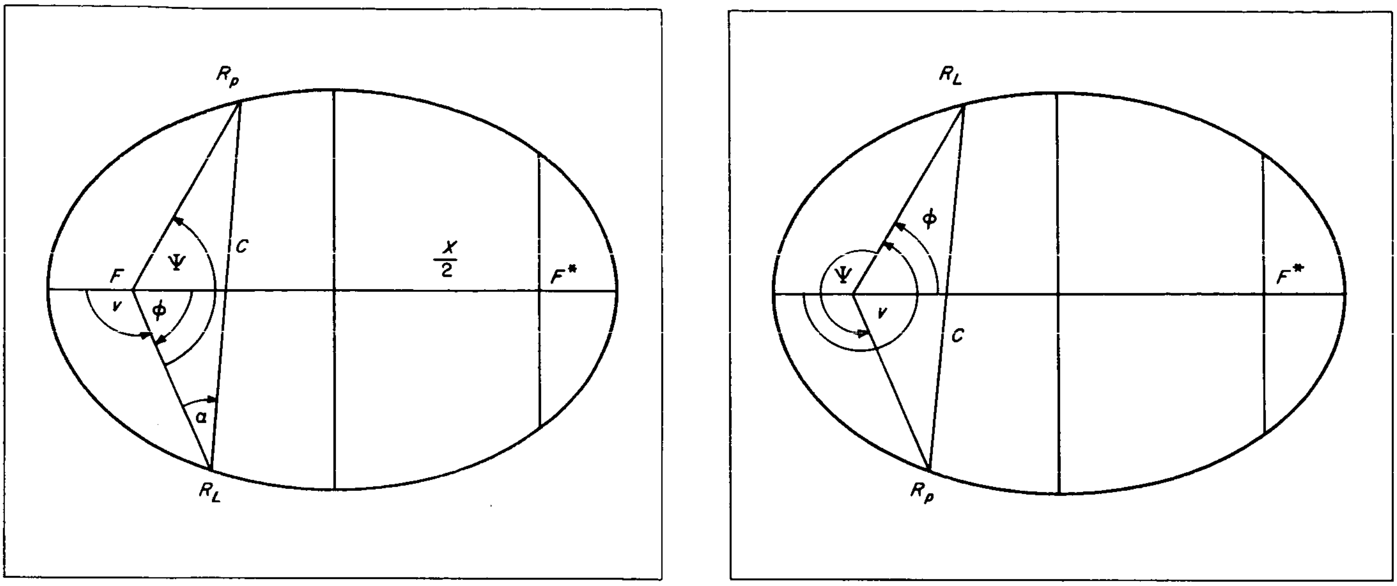

(a) Central angle less than 180 deg

(b) Central angle greater than 180 deg

Fig. 2–1. Geometrical configuration of heliocentric conic

The true anomaly at arrival on the minimum-energy ellipse v_{pm} can be found from

$$v_{pm} = v_{Lm} + \Psi \tag{2–18}$$

Now, the mean anomaly M_{Lm} at launch in the ellipse can be found from

$$M_{Lm} = E_{Lm} - e_m \sin E_{Lm} \tag{2–19}$$

where E_{Lm}, the eccentric anomaly, is given by the equations

$$\left.\begin{aligned} \cos E_{Lm} &= \frac{e_m + \cos v_{Lm}}{1 + e_m \cos v_{Lm}} \\ \text{and} \quad & \\ \sin E_{Lm} &= \frac{\sqrt{1 - e_m^2}\,\sin v_{Lm}}{1 + e_m \cos v_{Lm}} \end{aligned}\right\} \quad 0 \le E_{Lm} \le 2\pi \tag{2–20}$$

The mean anomaly at arrival M_{pm} can be obtained in a similar manner. Then, the mean-anomaly difference is

$$\Delta M_m = M_{pm} - M_{Lm} \tag{2–21}$$

By use of this difference, T_m, the time for a minimum-energy trajectory from launch to target, can be found from the equation

$$T_m = \frac{a_m^{3/2}\,\Delta M_m}{2\pi} \tag{2–22}$$

where the units are years and astronomical units (au).

Next, the semimajor axis a, corresponding to the given flight time T_F, is obtained. At this point, there can be two types of trajectories, $T_F > T_m$ or $T_F < T_m$.

For $T_F > T_M$, let $a_{i+1} = (i + 1)a_m$, until $T_F(a_{i+1}) > T_F$

For $T_F < T_M$, let $a_{i+1} = (i + 1)a_m$, until $T_F(a_{i+1}) < T_F$

where $i = 1, 2, \ldots n$, and $a_1 = a_m$. Note that $T_F(a_i)$ is the time of flight corresponding to a_i, and is calculated from Eqs. 2–24 to 2–29 and 2–19 to 2–22; here, however, the subscript i is used in place of m. When $T(a_i) < T_F < T(a_{i+1})$, then $a_i < a < a_{i+1}$, and a slope-intercept method is used to obtain an approximation on a. Using a_{i+1} for a first estimate on a_j, and using

$$\begin{aligned} a_j &= a_{j-1} - \Delta a \left[\frac{T_F - T(a_{j-1})}{T(a_i) - T_F}\right] \\ \Delta a &= (a_{j-1} - a_i) \end{aligned} \tag{2–23}$$

subscript $j = 1, 2, \ldots n$

for subsequent estimates, the value of a_j is used for a to calculate α and β.

$$\left.\begin{aligned} \beta &= \cos^{-1}\left[\frac{C^2 + R_L^2 - R_p^2 - 4a\,(R_p - R_L)}{2C(2a - R_L)}\right] \quad 0 < \beta < \pi \\ \alpha &= \cos^{-1}\left[\frac{R_L - R_p \cos \Psi}{C}\right] \quad 0 < \alpha < \pi \end{aligned}\right\} \tag{2–24}$$

Now, the linear eccentricity X can be found from

$$X^2 = 4a^2 - 2R_L\,(2a - R_L)\,\left[1 + \cos\left(|\alpha - \beta|\right)\right] \quad \text{(2–25a)}$$

$$X^2 = 4a^2 - 2R_L\,(2a - R_L)\,\left[1 + \cos\left(|\alpha + \beta|\right)\right] \quad \text{(2–25b)}$$

Equation 2–25a is used if $T_F > T_m$, and $\Psi > \pi$; or if $T_F < T_m$, and $\Psi < \pi$. However, Eq. 2–25b applies if $T_F > T_m$, and $\Psi < \pi$; or if $T_F < T_m$, and $\Psi > \pi$.

Then, the true anomaly at launch is found from

$v_L =$

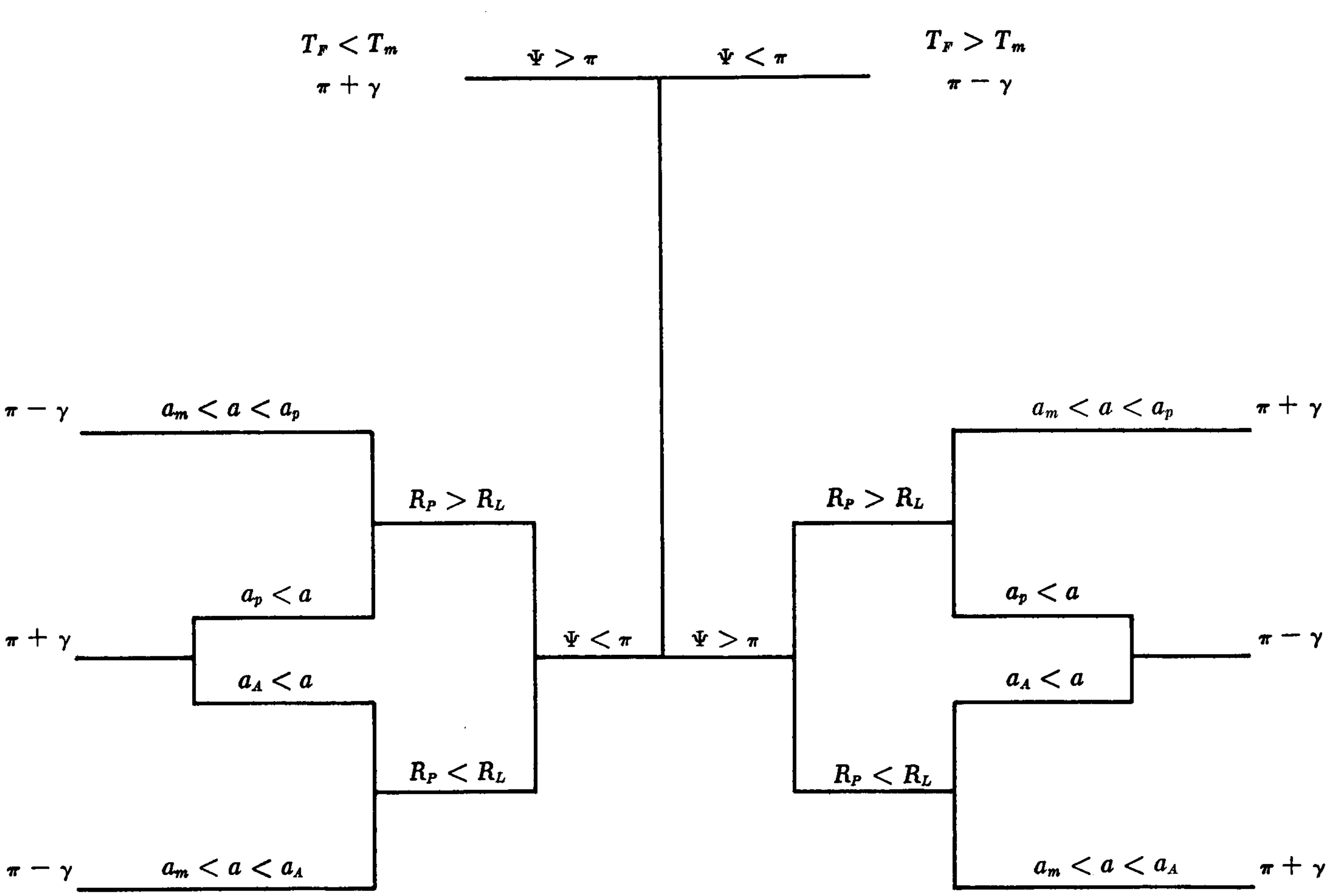

(2–26)

and γ is found from

$$\cos\gamma = \frac{X^2 + 4a\,R_L - 4a^2}{2\,X\,R_L} \qquad \text{(2–27)}$$

Also, a_A and a_p, the semimajor-axis limits, are found from

$$\left.\begin{aligned} a_A &= \frac{R_p}{1 + \dfrac{R_p - R_L}{R_p - R_L\cos\Psi}} \\ a_p &= \frac{R_L}{1 + \dfrac{R_L - R_p}{R_L - R_p\cos\Psi}} \end{aligned}\right\} R_p > R_L \qquad \text{(2–28)}$$

If $R_L > R_p$, a_A and a_p are interchanged. The true anomaly at arrival v_p is found from

$$v_p = v_L + \Psi \qquad 0 < v_p < 2\pi$$

and the eccentricity e is found from

$$e = \frac{X}{2a} \tag{2–29}$$

Then, $T(a_j)$ is recalculated using Eqs. 2–19 to 2–22.

When $|T_F - T(a_j)| < \epsilon$, a predetermined convergence criterion, the conic is considered to be the one desired, and $a(= a_n)$, e, v_L, v_p are the parameters of the heliocentric transfer orbit.

At this point, the transfer orbit is completely determined. Other key quantities are calculated as shown in the following paragraphs.

3. Calculation of Velocity Vectors for Probe and Planet

The heliocentric velocity of the probe $\mathbf{V}$ (with the subscript L for launch time or p for arrival time), can be calculated by using the equation

$$\mathbf{V} = \frac{V}{R}[(\mathbf{W} \times \mathbf{R}) \cos \Gamma + \mathbf{R} \sin \Gamma] \tag{2–30}$$

where

$$V = \sqrt{(GM_S)\left(\frac{2}{R} - \frac{1}{a}\right)} \tag{2–31}$$

The path angle Γ can be found by the expression

$$\sin \Gamma = \left[\sqrt{\frac{R}{(1 - e^2)(2a - R)}}\right] e \sin v \tag{2–32}$$

where

$$0 \leq \Gamma \leq \frac{\pi}{2} \quad \text{if} \quad 0 \leq v \leq \pi$$

$$-\frac{\pi}{2} \leq \Gamma \leq 0 \quad \text{if} \quad \pi \leq v \leq 2\pi$$

The velocity vectors $\mathbf{V}_1$ and $\mathbf{V}_2$ of the launch and target planets, respectively, are found in a similar manner. In this calculation, however, the semimajor axis a, the path angle Γ, and the eccentricity of the orbit e all refer to the respective planet's orbit around the Sun. The true anomaly v of the planet in its orbit at any time can be found from Eqs. 2–33 to 2–36.

The unit vector $\mathbf{W}$ normal to the planet's orbit plane is given by

$$\mathbf{W} = \sin \Omega \sin i, \cos \Omega \sin i, \cos i \tag{2–33}$$

where i is the inclination of the planet's orbital plane to the ecliptic and Ω is the longitude of the planet's ascending node.

The unit vector $\mathbf{P}$ directed toward the perihelion is expressed by

$$\left.\begin{aligned} P_X &= \cos \omega \cos \Omega - \sin \omega \sin \Omega \cos i \\ P_Y &= \cos \omega \sin \Omega + \sin \omega \cos \Omega \cos i \\ P_Z &= \sin \omega \sin i \end{aligned}\right\} \tag{2–34}$$

where ω is the argument of perihelion of the planet.

The unit vector $\mathbf{Q}$ right-handed to $\mathbf{P}$ and $\mathbf{W}$, is obtained from

$$\mathbf{Q} = \mathbf{W} \times \mathbf{P}$$

Then

$$\left.\begin{aligned} \cos v &= \mathbf{R}^1 \cdot \mathbf{P} \\ \sin v &= \mathbf{R}^1 \cdot \mathbf{Q} \end{aligned}\right\} \tag{2–35}$$

where, again, $\mathbf{R}^1$ is the Sun–planet unit vector.

Numerical values for the planet elements a, e, i, Ω, and ω (from Ref. 7) are presented in Table 2–1.

Finally, the hyperbolic-excess velocity vector at launch or arrival $\mathbf{V}_h$ can be found from

$$\mathbf{V}_h = \mathbf{V} - \mathbf{V}_{planet} \tag{2–36}$$

4. Calculation of Various Trajectory Parameters

To assist the trajectory engineer in selecting and designing interplanetary trajectories, various key trajectory parameters are computed. The formulas for these are given below.

The angle γ between the hyperbolic-excess velocity vector and the planet's orbital plane can be found at launch and arrival by

$$\sin \gamma = \frac{\mathbf{W} \cdot \mathbf{V}_h}{V_h} \qquad -\frac{\pi}{2} \leq \gamma \leq \frac{\pi}{2} \tag{2–37}$$

The right ascension Θ and the declination Φ of the asymptote (launch or arrival) can be found by use of the expressions

$$\sin \Phi = S_Z \qquad -\frac{\pi}{2} \leq \Phi \leq \frac{\pi}{2} \tag{2–38}$$

Table 2-1. Mean planet elements

Planet	Semimajor axis a, au	Eccentricity e	Inclination to ecliptic i, deg	Longitude of ascending node Ω, deg	Argument of perihelion ω, deg
Mercury	0.387098	0.205625+0.000020T[a]	7.003819+0.00175T	47.737778+1.18500T	28.937778+0.36944T
Venus	0.723331	0.006793−0.000050T	3.394264+0.00125T	76.236389+0.90556T	54.619305+0.50139T
Earth	1.000000	0.016729−0.000042T	0	0	102.078056+1.71667T
Mars	1.523679	0.093357+0.000094T	1.849986−0.000639T	49.173611+0.77389T	285.965000+1.06667T
Jupiter	5.2027	0.048417+0.000164T	1.305875−0.005694T	99.948611+1.01056T	273.577222+0.59944T
Saturn	9.546	0.055720−0.000345T	2.490583−0.003889T	113.226806+0.87306T	338.850694+1.08528T
Uranus	19.20	0.0471 +0.0002T	0.772792+0.000639T	73.726528+0.49861T	96.129028+1.11250T
Neptune	30.09	0.00872 +0.00004T	1.774486−0.00953T	131.230833+1.09889T	272.935934−0.43222T
Pluto	39.5	0.247	17.140000−0.00556T	109.633750+1.35806T	113.860694+0.03083T

[a]Measured in Julian Centuries from 1950.0

and

$$\left.\begin{aligned}\cos\Theta &= \frac{S_X}{\sqrt{S_X^2+S_Y^2}}\\ \sin\Theta &= \frac{S_Y}{\sqrt{S_X^2+S_Y^2}}\end{aligned}\right\} \quad 0 \le \Theta \le 2\pi \qquad (2\text{–}39)$$

where

$$\mathbf{S} = \frac{\mathbf{V}_h}{V_h} E^T = (S_X, S_Y, S_Z) \qquad (2\text{–}40)$$

Here, E is the rotation matrix given by Eq. 2–2; $\mathbf{S}$ is a unit vector in the direction of the outgoing asymptote when $\mathbf{V}_h$ is calculated at launch, and in the direction of the incoming asymptote when $\mathbf{V}_h$ is calculated at the target.

Other quantities which are of interest for the heliocentric phase are given in Eqs. 2–41 to 2–48, below.

The communication distance at arrival R_C is expressed by

$$\left.\begin{aligned}R_C &= |\mathbf{R}_C|\\ \mathbf{R}_C &= \mathbf{R}_p - \mathbf{R}_{LA}\end{aligned}\right\} \qquad (2\text{–}41)$$

The arrival (or departure) angle α is obtained from

$$\cos\alpha = \frac{\mathbf{V}_{planet}\cdot\mathbf{V}_h}{V_{planet}V_h} \quad 0 \le \alpha \le \pi \qquad (2\text{–}42)$$

The angle ζ_L between the launch hyperbolic-excess velocity and the Sun–launch–planet line at launch is defined by

$$\cos\zeta_L = \frac{\mathbf{V}_{hL}\cdot\mathbf{R}_L^1}{V_{hL}} \quad 0 \le \zeta_L \le \pi \qquad (2\text{–}43)$$

There are six other angles: ζ_p, the Sun–probe–target angle; ζ_E, the Sun–target–Earth angle; ζ_C, the probe-target–Canopus angle; η_S, the supplement of the angle between the projection of the target–Sun vector on the **R–T** plane and the **T** direction; η_E, the supplement of the angle between the projection of the target–Earth vector on the **R–T** plane and the **T** direction; η_C, the supplement of the angle between the projection of the target–Canopus vector on the **R–T** plane and the **T** direction. Here, **T** is a unit vector lying in the ecliptic plane, given by

$$\left.\begin{aligned}\mathbf{T} &= \frac{\mathbf{S}_p\times\mathbf{K}'}{|\mathbf{S}_p\times\mathbf{K}'|}\\ \mathbf{R} &= \mathbf{S}_p\times\mathbf{T}\end{aligned}\right\} \qquad (2\text{–}44)$$

and

$$\left.\begin{aligned}\cos\zeta_p &= -\mathbf{S}_p\cdot\mathbf{R}_p^1\\ \cos\zeta_E &= -\mathbf{S}_p\cdot\mathbf{R}_C^1\\ \cos\zeta_C &= \mathbf{S}_p\cdot\mathbf{C}\end{aligned}\right\} \quad 0 \le \zeta \le \pi \qquad (2\text{–}45)$$

where $\mathbf{C}$ is a unit vector to the star Canopus, and $\mathbf{R}_C^1$ is obtained by normalizing $\mathbf{R}_C$ from Eq. 2–41.

$$\left.\begin{aligned} \sin \eta_s &= \frac{\mathbf{R}\cdot\mathbf{R}_p^1}{\sin \zeta_p} \\ \cos \eta_s &= \frac{\mathbf{T}\cdot\mathbf{R}_p^1}{\sin \zeta_p} \\ \sin \eta_E &= \frac{\mathbf{R}\cdot\mathbf{R}_C^1}{\sin \zeta_E} \\ \cos \eta_E &= \frac{\mathbf{T}\cdot\mathbf{R}_C^1}{\sin \zeta_E} \\ \sin \eta_C &= -\frac{\mathbf{R}\cdot\mathbf{C}}{\sin \zeta_C} \\ \cos \eta_C &= -\frac{\mathbf{T}\cdot\mathbf{C}}{\sin \zeta_C} \end{aligned}\right\} \quad 0 \le \eta \le 2\pi \qquad (2\text{–}46)$$

The angle σ_p between the projection of the incoming asymptote on the target planet's orbital plane and the target-planet–Sun line at arrival time is defined by

$$\left.\begin{aligned} \cos \sigma_p &= -\mathbf{R}_p^1 \cdot \mathbf{S}_{pr} \\ \sin \sigma_p &= -\mathbf{S}_{pr}\cdot(\mathbf{W}_2 \times \mathbf{R}_p^1) \end{aligned}\right\} \quad -\pi \le \sigma_p \le \pi \qquad (2\text{–}47)$$

where $\mathbf{S}_{pr}$, the projection of $\mathbf{S}_p$ on the target planet's orbital plane, can be found by

$$\mathbf{S}_{pr} = \frac{\mathbf{S}_p - \mathbf{W}_2(\mathbf{S}_p\cdot\mathbf{W}_2)}{|\mathbf{S}_p - \mathbf{W}_2(\mathbf{S}_p\cdot\mathbf{W}_2)|} \qquad (2\text{–}48)$$

Here, $\mathbf{W}_2$ is a unit vector normal to the target planet's orbital plane.

B. *The Planetocentric-Conic Trajectories*

The trajectory near the launch planet is found by application of several conditions:

(1) The injection energy C_3 and the direction $\mathbf{S}$ of the outgoing asymptote of the escape hyperbola are obtained from the solution of the heliocentric-transfer problem as given in Section II–A above.

(2) The vehicle is launched from a given launch site, specified by its latitude and longitude, into a low-altitude circular parking orbit.

(3) After coasting in the parking orbit for a time t_c, as determined below, the final stage ignites and propels the spacecraft to the final injection energy.

(4) The parking-orbit altitude plus the launch planet's radius is equal to the perifocal distance of the escape hyperbola. This is a good practical approximation, since it is most efficient to inject the spacecraft into the escape hyperbola near the perifocus.

(5) The launch planet is assumed to be spherical in shape.

Given these conditions, the following formulae are used to compute the parameters of the near-launch-planet trajectory.

The eccentricity e of the launch-planet conic can be computed from

$$e = 1 + \frac{R_p C_3}{GM_L} \qquad (2\text{–}49)$$

where R_p is the perifocal distance of the near-launch-planet conic, and C_3 is the *vis viva* energy, defined as

$$C_3 = V_{hL}^2 \qquad (2\text{–}50)$$

and GM_L is the universal gravitational constant times the mass of the launch planet. The radius to injection R is found from

$$R = \frac{p}{1 + e\cos v} \qquad (2\text{–}51)$$

where v is the true anomaly of injection on the launch-planet escape hyperbola, and p is the semilatus rectum given by

$$p = \frac{-GM_L(1 - e^2)}{C_3} \qquad (2\text{–}52)$$

The path angle at injection Γ is found from

$$\cos \Gamma = \frac{\sqrt{p\,GM_L}}{VR} \qquad \begin{aligned} 0 \le \Gamma \le \frac{\pi}{2}, &\ \text{if } 0 \le v \le \pi \\ -\frac{\pi}{2} \le \Gamma \le 0, &\ \text{if } \pi \le v \le 2\pi \end{aligned} \qquad (2\text{–}53)$$

where V, the injection speed, is given by

$$V = \sqrt{C_3 + \frac{2GM_L}{R}} \qquad (2\text{–}54)$$

The vector $\mathbf{W}$, perpendicular to the plane of the conic, can be found by the solution of the two vector equations

$$\left.\begin{aligned} \mathbf{W}\cdot\mathbf{S} &= 0 \\ \mathbf{W}\cdot\mathbf{W} &= 1 \end{aligned}\right\} \quad \begin{aligned} W_X S_X + W_Y S_Y + W_Z S_Z &= 0 \\ W_X^2 + W_Y^2 + W_Z^2 &= 1 \end{aligned} \qquad (2\text{–}55)$$

where

$$W_X = \frac{-(W_Y S_Y + W_Z S_Z)}{S_X} \qquad (2\text{–}56)$$

and

$$W_Y = \frac{-W_Z S_Y S_Z}{S_X^2 + S_Y^2} \pm \frac{S_X}{S_X^2 + S_Y^2}\sqrt{1 - S_Z^2 - W_Z^2} \qquad (2\text{–}57)$$

It should be recalled that S is a unit vector in the direction of the outgoing asymptote of the escape hyperbola. Thus, a condition is set on W_Z:

$$W_Z^2 \leq 1 - S_Z^2 \qquad (2\text{–}58)$$

From the geometry (Fig. 2–2) of the launch azimuth Σ_L and the launch latitude Φ_L, it can be shown that

$$W_Z = \cos\Phi_L \sin\Sigma_L \qquad (2\text{–}59)$$

From Eqs. 2–58 and 2–59, the $W_Z{}^2$ restrictions can be calculated as a restriction on Σ_L, since Φ_L and S are fixed:

$$\sin^2\Sigma_L \leq \frac{1 - S_Z^2}{\cos^2\Phi_L} \qquad (2\text{–}60)$$

A vector **B**, orthogonal to S and **W**, is calculated:

$$\mathbf{B} = \mathbf{S} \times \mathbf{W} \qquad (2\text{–}61)$$

Now, let **P** be a unit vector in the direction of the perifocus as shown in Fig. 2–3:

$$\mathbf{P} = \mathbf{S}\cos v_s + \mathbf{B}\sin v_s \qquad (2\text{–}62)$$

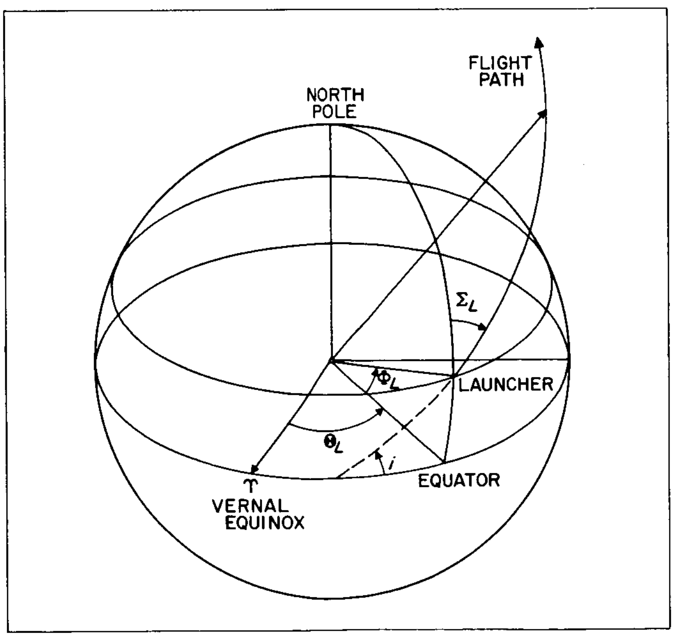

Fig. 2–2. Trajectory-plane–launch-site geometry

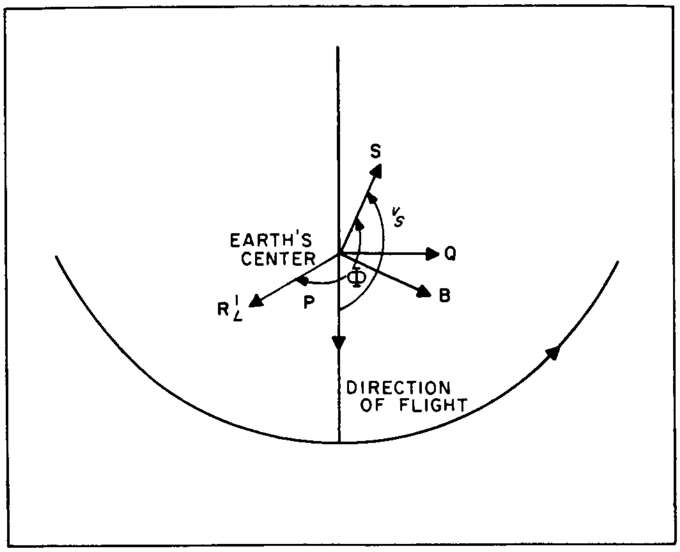

Fig. 2–3. Trajectory-plane geometry

Then **Q** is the unit vector at right angles to **P**:

$$\mathbf{Q} = \mathbf{S}\sin v_s - \mathbf{B}\cos v_s \qquad (2\text{–}63)$$

The true anomaly v_s of the outgoing asymptote S is given by

$$\cos v_s = -\frac{1}{e} \qquad 0 \leq v_s \leq \pi \qquad (2\text{–}64)$$

The right ascension Θ_L of the launcher can be found from

$$\left.\begin{aligned} \cos\Theta_L &= \frac{W_X \sin\Phi_L \sin\Sigma_L + W_Y \cos\Sigma_L}{W_Z^2 - 1} \\ \sin\Theta_L &= \frac{W_Y \sin\Phi_L \sin\Sigma_L - W_X \cos\Sigma_L}{W_Z^2 - 1} \end{aligned}\right\} \quad 0 \leq \Theta_L \leq 2\pi \qquad (2\text{–}65)$$

where Φ_L is the latitude of the launcher. A unit vector $\mathbf{R}_L^1$ in the direction of the launcher can be calculated in the vernal-equinox equatorial system by

$$\mathbf{R}_L^1 = \cos\Phi_L\cos\Theta_L, \cos\Phi_L\sin\Theta_L, \sin\Phi_L \qquad (2\text{–}66)$$

The angle Φ between the launcher and the perifocus of the conic is given by

$$\left.\begin{aligned} \cos\Phi &= \mathbf{R}_L^1 \cdot \mathbf{P} \\ \sin\Phi &= \mathbf{R}_L^1 \cdot \mathbf{Q} \end{aligned}\right\} \quad 0 \leq \Phi \leq 2\pi \qquad (2\text{–}67)$$

The angle between launch and injection Φ_I is defined by

$$\Phi_I = 2\pi - \Phi + v \qquad (2\text{–}68)$$

where, again, v is the true anomaly at injection into the escape hyperbola.

A unit vector $\mathbf{R}^1$ toward injection is seen in Fig. 2–4 to be

$$\mathbf{R}^1 = \mathbf{P}\cos v + \mathbf{Q}\sin v = (R_X, R_Y, R_Z) \qquad (2\text{–}69)$$

The injection latitude Φ is given by

$$\sin\Phi = R_Z \qquad -\frac{\pi}{2} \leq \Phi \leq \frac{\pi}{2} \qquad (2\text{–}70)$$

The right ascension of injection Θ can be found from

$$\left.\begin{aligned} \cos\Theta &= \frac{R_X}{\sqrt{R_X^2 + R_Y^2}} \\ \sin\Theta &= \frac{R_Y}{\sqrt{R_X^2 + R_Y^2}} \end{aligned}\right\} \quad 0 \leq \Theta \leq 2\pi \qquad (2\text{–}71)$$

The longitude of injection θ can be calculated from

$$\theta = \Theta - \Theta_L - \omega t_b + \theta_L \qquad 0 \leq \theta \leq 2\pi \qquad (2\text{–}72)$$

where

- θ_L is the longitude of the launcher
- ω is the rotational rate of the earth
- t_b is the time from launch to injection

Here,

$$t_b = t_1 + t_2 + [\Phi_I - (\Phi_1 + \Phi_2)]\, k_{\dot\phi} \qquad (2\text{–}73)$$

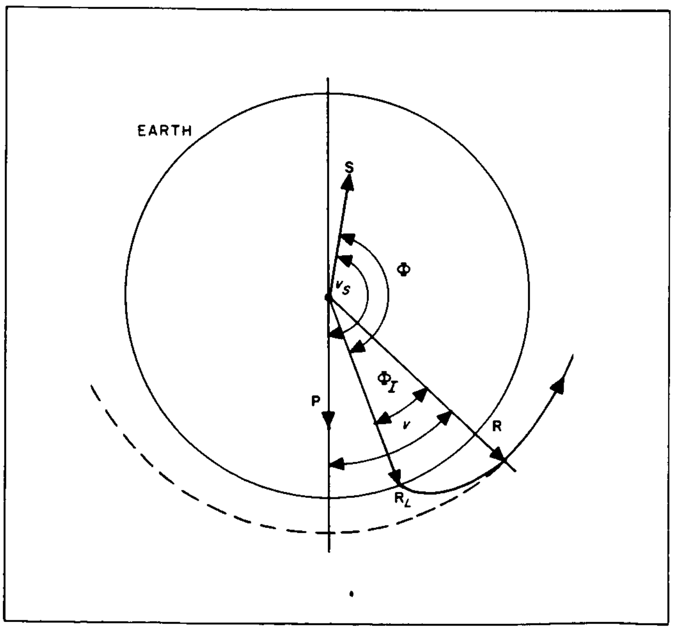

Fig. 2–4. Ascent-trajectory geometry

where

- t_1 is the time of first burn (into the parking orbit)
- t_2 is the time of second burn (into the escape hyperbola)
- Φ_1 is the angle of first burn
- Φ_2 is the angle of final burn
- $k_{\dot\phi}$ is the inverse parking-orbit rate = 14.689 sec/deg for a 100-nm Earth parking orbit

The time of coast t_c is given by

$$t_c = [\Phi_I - (\Phi_1 + \Phi_2)]\, k_{\dot\phi} \qquad (2\text{–}74)$$

The relations stated above are illustrated in Fig. 2–5.

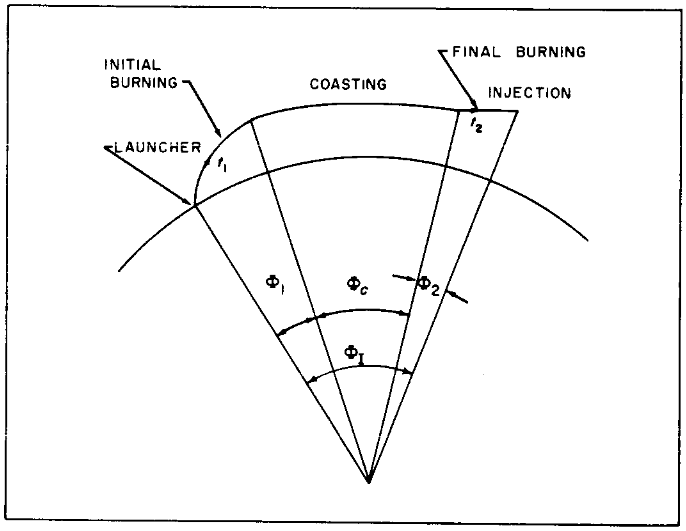

Fig. 2–5. Powered trajectory modified by coasting

The azimuth at injection Σ can be computed from

$$\cos\Sigma = \frac{S_Z - k_3\sin\Phi}{k_4\cos\Phi} \qquad 0 \leq \Sigma \leq \pi \qquad (2\text{–}75)$$

where

$$\left.\begin{aligned} k_3 &= \frac{\sqrt{e^2 - 1}}{e}\sin v - \frac{1}{e}\cos v \\ k_4 &= \frac{\sqrt{e^2 - 1}}{e}\cos v + \frac{1}{e}\sin v \end{aligned}\right\} \qquad (2\text{–}76)$$

The unit vector to final-stage ignition $\mathbf{R}_2^1$ can be found in a manner similar to that used for $\mathbf{R}$:

$$\mathbf{R}_2^1 = \mathbf{P}\cos(v - \Phi_2) + \mathbf{Q}\sin(v - \Phi_2) \qquad (2\text{–}77)$$

The latitude Φ_2 of final-stage ignition is computed from

$$\sin \Phi_2 = R_{Z2} \qquad -\frac{\pi}{2} \leq \Phi_2 \leq \frac{\pi}{2} \tag{2-78}$$

The right ascension Θ_2 of final-stage ignition is given by

$$\left.\begin{aligned} \cos \Theta_2 &= \frac{R_{X2}}{\sqrt{R_{X2}^2 + R_{Y2}^2}} \\ \sin \Theta_2 &= \frac{R_{Y2}}{\sqrt{R_{X2}^2 + R_{Y2}^2}} \end{aligned}\right\} \; 0 \leq \Theta_2 \leq 2\pi \tag{2-79}$$

and the longitude θ_2 of final stage ignition is defined by

$$\theta_2 = \theta + \Theta_2 - \Theta + \omega t_2 \tag{2-80}$$

The angle Δv between injection and the outgoing asymptote is expressed as

$$\Delta v = v_s - v$$

The launch time T_L can be found by

$$T_L = \frac{\Theta_L - \theta_L - GHA}{\omega} \qquad 0 \leq (\Theta_L - \theta_L - GHA) \leq 2\pi \tag{2-81}$$

where GHA is the Greenwich Hour Angle at 0^h UT of the launch day as shown in Fig. 2–6, and is obtained from

$$\begin{aligned} \text{GHA} = {} & 100^\circ.07554260 \\ & + 0^\circ.9856473460\, T_d \qquad 0 \leq GHA \leq 2\pi \\ & + 2^\circ.9015 \times 10^{-13}\, T_d^2 \end{aligned} \tag{2-82}$$

Here, T_d = days past 0^h January 1, 1950.

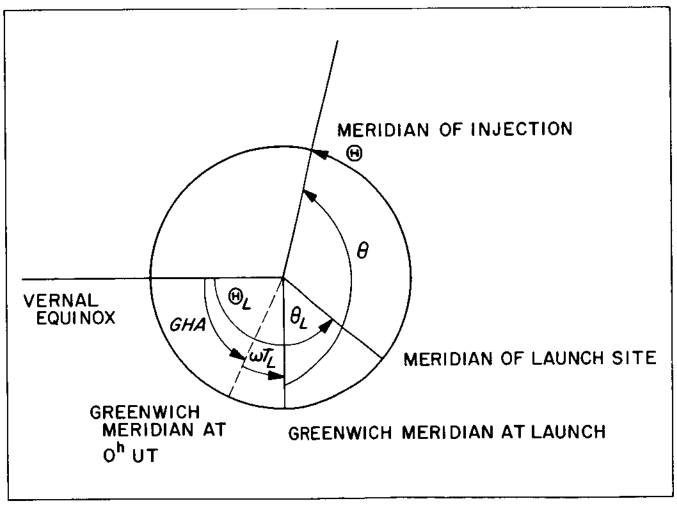

Fig. 2–6. Relation between longitude, right ascension, and time in equatorial plane

The injection time T is calculated from

$$T = T_L + t_b \tag{2-83}$$

C. *Differential Corrections*

As outlined in Section I–C, the calculation of differential corrections, or partial derivatives relating variations in the impact parameter **B** and flight time T_F to variations in the hyperbolic-excess velocity vector $\mathbf{V}_{hL}$ at launch, are performed by a numerical differencing technique.[8]

The basic idea in this technique is to compute a varied or perturbed trajectory and then difference it with the reference case. A small variation $\Delta\mathbf{V}_{hL}$ in the hyperbolic-excess velocity vector is equivalent to a small variation $\Delta\mathbf{V}_L$ in the launch heliocentric-velocity vector. Letting primed quantities denote variables on the perturbed trajectory, the launch heliocentric velocity on this trajectory is, then,

$$\mathbf{V}_L' = \mathbf{V}_L + \Delta\mathbf{V}_{hL} \tag{2-84}$$

where

$$\begin{aligned} \Delta\mathbf{V}_{hL} = {} & (C_3)^{1/2}\,\Delta\Phi_S\,[-\sin\Phi_S\cos\Theta_S, -\sin\Phi_S\sin\Theta_S, \cos\Phi_S], \\ & (C_3)^{1/2}\,\Delta\Theta_S\,[-\cos\Phi_S\sin\Theta_S, \cos\Phi_S\cos\Theta_S, 0], \\ & \frac{-\Delta C_3}{2\,(C_3)^{1/2}}\,[\cos\Phi_S\cos\Theta_S, \cos\Phi_S\sin\Theta_S, \sin\Phi_S] \end{aligned}$$

where $\Delta\Phi_S$, $\Delta\Theta_S$ are small angular variations (0.2 deg), and the energy variation is $\Delta C_3 = 0.005\, C_3$.

The semimajor axis a' is obtained from

$$a' = \frac{R_L}{2 - \dfrac{V_L'^2 R_L}{GM_S}} \tag{2-85}$$

The radial rate $\dot{R}_L'$ is given by

$$\dot{R}_L' = \frac{\mathbf{V}_L' \cdot \mathbf{R}_L}{R_L} \tag{2-86}$$

The semilatus rectum p' and eccentricity e' are computed from

$$p' = \frac{R_L^2\,(V_L'^2 - \dot{R}_L'^2)}{GM_S} \tag{2-87}$$

$$e' = \left(1 - \frac{p'}{a'}\right)^{1/2} \tag{2-88}$$

[8]This method was developed by William Kizner, Research Specialist, Systems Analysis Section, Jet Propulsion Laboratory.

The eccentric anomaly at launch E'_L is expressed by

$$\sin E'_L = \frac{R_L \dot{R}'_L}{e'(a'GM_S)^{1/2}}$$
$$\cos E'_L = \frac{1}{e'}\left(1 - \frac{R_L}{a'}\right) \quad (2\text{–}89)$$

The mean anomaly at launch M'_L is obtained from

$$M'_L = E'_L - e' \sin E'_L \quad (2\text{–}90)$$

The mean orbital rate n' is given by

$$n' = \frac{(GM_S)^{1/2}}{a'^{3/2}} \quad (2\text{–}91)$$

The mean anomaly at the target M'_p is stated as

$$M'_p = n' T_F + M'_L \quad (2\text{–}92)$$

The eccentric anomaly at the target E'_p is obtained from the expansion

$$E'_p = E_p + \left(\frac{1}{1 - e' \cos E_p}\right)\Delta M - \frac{1}{2}\left[\frac{e' \sin E_p}{(1 - e' \cos E_p)^3}\right]\Delta M^2 + \frac{1}{6}\left[\frac{(3\,e' \sin E_p)^2 - (1 - e' \cos E_p)(e' \cos E_p)}{(1 - e' \cos E_p)^5}\right]\Delta M^3 \quad (2\text{–}93)$$

if

$$\cos E_p \geqq 0$$

However,

$$E'_p = E_p + \frac{e \cos E_p - 1 + \sqrt{(e \cos E_p - 1)^2 + (2e \sin E_p)\,\Delta M}}{e \sin E_p} \quad (2\text{–}94)$$

if

$$\cos E_p < 0$$

where

$$\Delta M = M'_p - (E_p - e' \sin E_p)$$

The true anomalies at launch and at the target, v'_L and v'_p are found from

$$\cos v'_L = \frac{p' - R_L}{e' R_L} \quad (2\text{–}95)$$

$$0 < v'_L < \pi \quad \text{if } \dot{R}'_L \text{ is positive}$$
$$\pi < v'_L < 2\pi \quad \text{if } \dot{R}'_L \text{ is negative}$$

$$\cos v'_p = \frac{\cos E'_p - e'}{1 - e' \cos E_p}$$
$$\sin v'_p = \frac{(1 - e'^2)^{1/2} \sin E'_p}{1 - e' \cos E'_p} \quad (2\text{–}96)$$

The heliocentric central angle Ψ' is given by

$$\Psi' = v'_p - v'_L \quad (2\text{–}97)$$

The angular momentum $\mathbf{h}'$ is expressed as

$$\mathbf{h}' = \mathbf{R}_L \times \mathbf{V}'_L \quad (2\text{–}98)$$

The heliocentric position vector at the target is given by

$$\mathbf{R}'_p = R'_p \left(\frac{\mathbf{R}_L}{R_L} \cos \Psi' + \frac{\mathbf{h}' \times \mathbf{R}_L}{h' R_L} \sin \Psi'\right) \quad (2\text{–}99)$$

where

$$R'_p = a'(1 - e' \cos E'_p) \quad (2\text{–}100)$$

A vector in the direction of perihelion with magnitude e' is computed from

$$\boldsymbol{\varepsilon}' = \frac{\mathbf{V}'_L \times \mathbf{h}'}{GM_S} - \frac{\mathbf{R}_L}{R_L} \quad (2\text{–}101)$$

The heliocentric velocity at the target is defined by

$$\mathbf{V}'_p = \frac{\mathbf{h}'}{p'} \times \left(\frac{\mathbf{R}'_p}{R_p} + \boldsymbol{\varepsilon}'\right) \quad (2\text{–}102)$$

The hyperbolic-excess velocity at the target is expressed by

$$\mathbf{V}'_{hp} = \mathbf{V}'_p - \mathbf{V}_2 \quad (2\text{–}103)$$

The difference between the heliocentric position vectors on the perturbed and reference trajectories is given by

$$\Delta\mathbf{R}'_p = \mathbf{R}'_p - \mathbf{R}_p \quad (2\text{–}104)$$

The impact parameter $\mathbf{B}$ is computed from

$$\mathbf{B} = -\frac{(\Delta\mathbf{R}'_p \cdot \mathbf{V}'_{hp})\,\mathbf{V}'_{hp}}{V'^2_{hp}} + \Delta\mathbf{R}'_p$$

The flight-time error is stated as

$$\Delta T_F = \frac{\Delta\mathbf{R}'_p \cdot \mathbf{V}'_{hp}}{V'^2_{hp}} \quad (2\text{–}105)$$

The partial derivatives are formed by dividing $\Delta\Theta_S$, $\Delta\Phi_S$, and ΔC_3 into the miss components $\mathbf{B} \cdot \mathbf{T}$, $\mathbf{B} \cdot \mathbf{R}$, and flight-time error ΔT_F. In addition to the component partials, the quantity $\partial B/\partial Q_i$ is defined by

$$\frac{\partial B}{\partial Q_i} = \left[\left(\frac{\partial \mathbf{B} \cdot \mathbf{T}}{\partial Q_i}\right)^2 + \left(\frac{\partial \mathbf{B} \cdot \mathbf{R}}{\partial Q_i}\right)^2\right]^{1/2} \quad (2\text{–}106)$$

The three partials, $\partial B/\partial \Theta_S$, $\partial B/\partial \Phi_S$, $\partial B/\partial C_3$, are important measures of the error sensitivity of a trajectory.

The effect of uncertainty in the knowledge of the astronomical-unit–to–kilometer conversion factor on target miss and flight time may be determined by the following formulae:

$$\frac{\partial \mathbf{B}\cdot\mathbf{T}}{\partial au} = \frac{-2C_3}{au}\frac{\partial \mathbf{B}\cdot\mathbf{T}}{\partial C_3}$$
$$\frac{\partial \mathbf{B}\cdot\mathbf{R}}{\partial au} = \frac{-2C_3}{au}\frac{\partial \mathbf{B}\cdot\mathbf{R}}{\partial C_3} \qquad (2\text{–}107)$$

whence

$$\frac{\partial B}{\partial au} = \frac{2C_3}{au}\frac{\partial B}{\partial C_3} \qquad (2\text{–}108)$$

and

$$\frac{\partial T_F}{\partial au} = \frac{-2C_3}{au}\frac{\partial T_F}{\partial C_3} \qquad (2\text{–}109)$$

where au is the astronomical-unit–to–kilometer conversion factor

The effect of solar-radiation pressure acting on the probe may also be evaluated as follows: In Eq. 2–84, let $\Delta \mathbf{V}_{hL} = 0$, but in Eqs. 2–85, 2–87, 2–89, 2–91, and 2–101, vary GM_S by adding an increment ΔGM_S. This procedure gives rise to a varied trajectory from which the impact parameter $\mathbf{B}$ and flight-time error ΔT_F may be obtained. The partials $\partial B/\partial GM_S$ and $\partial T_F/\partial GM_S$ may then be calculated. Since the acceleration caused by solar-radiation pressure acts in a direction opposite to the gravitational attraction of the Sun, radiation pressure has the effect of decreasing the Sun's gravitational attraction or decreasing GM_S. A decrease, $\Delta GM_S = -2.4 \times 10^6$ km^3/sec^2, corresponds to the solar-radiation pressure acting on a 300-kg spacecraft having a perfectly reflecting area of 3.6 m^2. Thus the miss, always being a positive number, is obtained by $\Delta B_{sp} = 2.4 \times 10^6\ \partial B/\partial GM_S$, and the corresponding flight-time error is $\Delta T_{F_{sp}} = -2.4 \times 10^6\ \partial T_F/\partial GM_S$, which is sign-sensitive.

III. DISCUSSION AND EXPLANATION OF RESULTS

A. Introduction

1. Trajectory Computations

Trajectories from Earth to Venus for the period 1962–1970 and from Earth to Mars for the period 1962–1977 were computed on the 7090 digital computer by numerically evaluating the analytical model explained in Sections I and II. Specific trajectory parameters of interest were then automatically plotted and carefully checked and analyzed. Subsequently, 313 graphs were made for 18 different trajectory parameters for each of 12 launch intervals. These graphs comprised:

(1) Curves of C_3 (*vis viva* geocentric energy) vs launch date for minimum-energy trajectories.

(2) Curves of 18 key trajectory parameters vs launch date for various *vis viva* geocentric energies.

2. Trajectory Analysis

Careful analysis of the results shows that as many as four ballistic flight paths to the target planet exist per launch date for a given *vis viva* geocentric energy, assuming trips of less than one revolution around the Sun; a more extensive analysis might reveal more than four flight paths. In reality, feasible launchings can occur only for small time intervals (1–3 months), when the relative positions of the Earth and target planet are such that the velocity requirements for ballistic transfers can be reasonably achieved by modern boost vehicles. These intervals occur once during each synodic period of the planet. A synodic period is the time interval required for the Earth and target planet to attain successive identical angular relationships in heliocentric longitude.

Thus, favorable launch opportunities occur approximately every 19.2 months for Venus and every 25.6 months for Mars. No trajectory computations were made past 1970 for Venus, or past 1977 for Mars, because of the cyclic behavior in trajectory characteristics. Approximately the same space-fixed geometry of Earth and Venus reoccurs every 8 years, or after 5 Cytherean synodic periods (1.5987 years). A similar cyclic behavior occurs for Mars about every 15 years or after 7 Martian synodic periods (2.1353 years). Thus, the Venus trajectory parameters for 1970 are virtually the same as those for 1962, whereas the parameters for 1977 Mars trajectories are essentially the same as those for 1962. The agreement here, however, is not as good as in the Venus case.

B. Classification of Trajectories

1. Type I and Type II

In observing the variation of any trajectory parameter vs launch date for fixed geocentric energies, it is noted that two separate groups of closed contours, rather than one, are described (see Fig. 3–1). These two sets of energy contours are designated as Type I and Type II trajectories, where Type I trajectories are defined as having heliocentric-transfer angles less than 180 deg, and Type II are those having heliocentric-transfer angles greater than 180 deg. A Type I trajectory traverses less than half-way around the Sun from launch to planet encounter, whereas a Type II trajectory would traverse more than half-way, but less than one full revolution, around the Sun. For a given launch day and energy, then, Type II trajectories require greater flight times than do Type I. The existence of these two sets of energy contours can be attributed to the fact that the orbits of Earth and the destination planet are not coplanar.

If the Earth and planet had coplanar orbits, only a single group of energy contours would exist. Within this single group of energy contours would be the well-known Hohmann's transfer orbit, if the orbits of Earth and the destination planet were circular as well as coplanar. The Hohmann minimum-energy trajectory *would remain constant* for each synodic period, retaining the same flight time and the same *vis viva* geocentric energy. However, even though the orbital planes of Venus and Mars are inclined to the ecliptic by only 3.39 and 1.85 deg, respectively, the three-dimensional aspect of their relationship with Earth strongly affects the free-flight trajectory and causes the single group of trajectory contours to split into two distinct parts, thus necessitating the designation of Type I and Type II trajectories.

In Fig. 3–1, note the small group of closed contours within the Type I group at the time interval around December 10. This small group has been designated as Type I-A and, again, can be attributed only to the noncoplanar relationship between the orbits of Venus and Earth. Trajectory parameters for Mars Type II transfers were not plotted for this Report; it was believed when this task began that Type II trajectories to Mars would not be used in ballistic transfers because of the long flight times and large Earth-to-probe distances at encounter. For low-energy transfers, the Mars Type II trajectories have flight times and Earth–probe distances

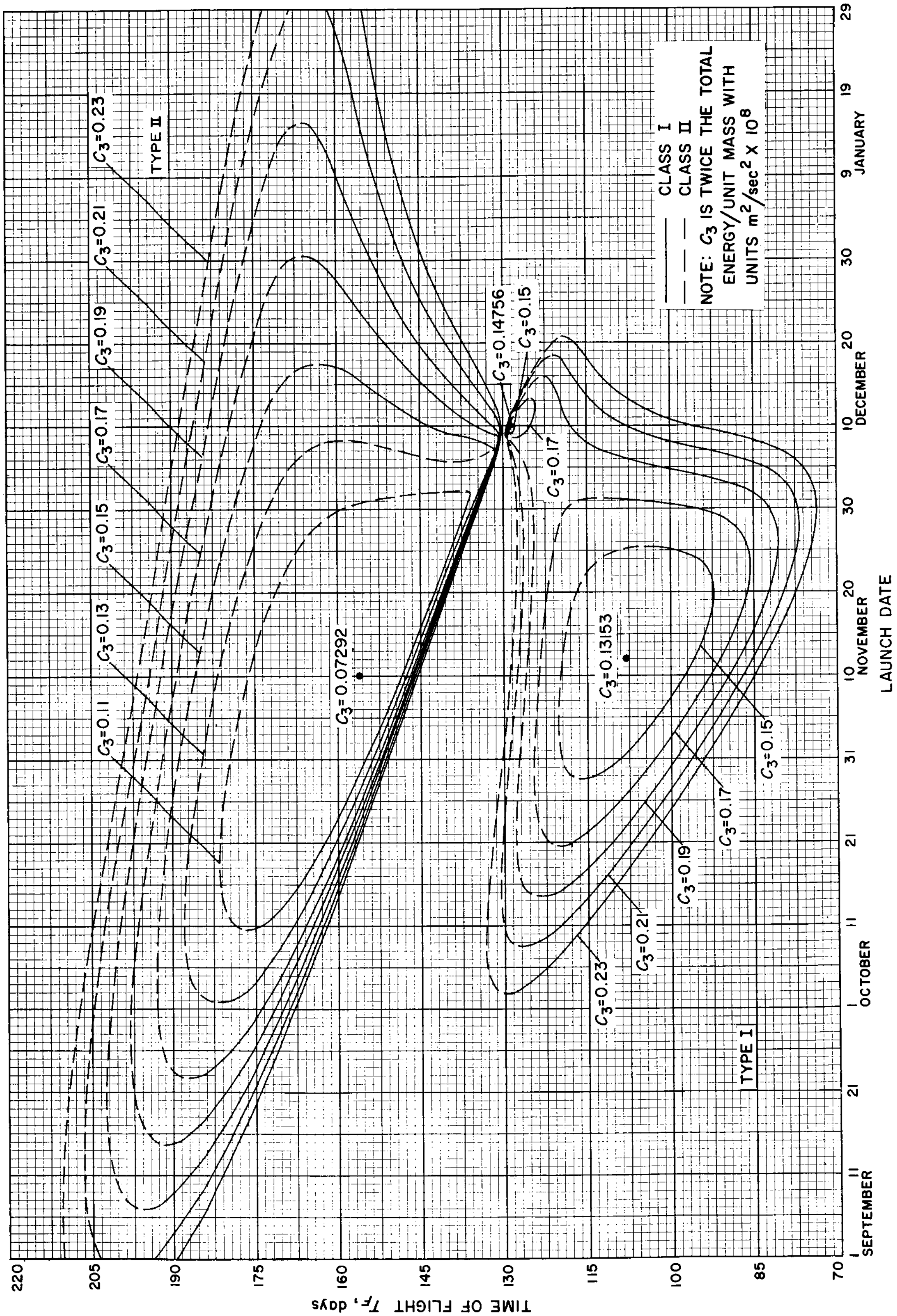

Fig. 3–1. Venus 1965: Time of flight vs launch date

at encounter far in excess of the corresponding Type I parameters.

2. Class I and Class II

For each of the two types of trajectories or energy contours, trajectories can be further divided into two classes, Class I and Class II. Inspecting a single trajectory contour, one notes that the curve is double-valued. Thus, for a given launch date, two possible trajectories exist for a given geocentric energy within each Type. These two trajectories are designated as Class I and Class II. The Class I trajectory has the lesser heliocentric central angle and, thus, the shorter flight time than that for the Class II trajectory. For a given launch date and geocentric energy, the Type I–Class I trajectory has the shortest flight time and the Type II–Class II trajectory has the longest flight time.

3. Minimum-Energy Trajectories

a. Minimum-energy loci. From the previous discussion, it is seen that a trajectory can be classified as Class I–Type I, Class II–Type I, Class I–Type II, or Class II–Type II. A further distinction must be made, however. Within each Type exist minimum-energy trajectories for each and every launch date. This is the trajectory for each Type requiring the minimum geocentric energy to encounter the planet for a given launch date. The minimum-energy locus can be found for each mission by connecting the points of intersection of vertical tangents with the energy contours of a given parameter, such as flight time. Should one do this for Fig. 3–1, he would obtain curves identical with those of Fig. 3–2, which is thus a graph of minimum *vis viva* geocentric energy vs launch date to Venus in 1965 for both Type I and Type II trajectories. Note that, for the Type I loci, two minimum points exist on the curve. One occurs on November 12 and has an energy of 0.13153×10^8 m^2/sec^2. The other, occurring on December 10, has an energy of 0.14756×10^8 m^2/sec^2. The single minimum point on the Type II loci occurs on November 10 and has an energy of 0.07292×10^8 m^2/sec^2. For clarity, these trajectories corresponding to the minimum points for each mission are called *absolute* minimum-energy trajectories. All three minimum points are reflected in Fig. 3–1. Perhaps the next question one would ask is why there are two minimum points for Type I trajectories. As previously mentioned, the only explanation that can be given is that the phenomenon is attributed to the noncoplanar relationship between the orbits of Earth and Venus. It is noted that Venus is very nearly in the ecliptic plane at arrival time for the December 10 trajectory. Similar behavior of trajectories is noted in the minimum-energy curves for Mars 1962, 1969, and 1977 for the Type I loci and Venus 1968 and 1969 for the Type II loci.

b. Absolute minimum-energy trajectories. The existence of absolute minimum-energy trajectories provides useful information concerning the lower bounds on energy requirements and gives a first approximation of launch dates, flight times, and communication distances at encounter, which are tabulated in Table 3–1. Inspection of the Table reveals several interesting characteristics. First, one notes the cyclic recurrence of trajectory characteristics for both planets, as mentioned earlier. The minimum-energy trajectories for Venus in 1962 are very similar to those for Venus in 1970, whereas Mars 1962 trajectories are similar to those for Mars 1977. Note that, for some launch intervals, the Type I minimum energy is less than that for Type II, but for others the reverse is true. The absolute minimum-energy trajectory to Venus (Fig. 3–3) is a Type II trajectory having an energy of 0.059×10^8 m^2/sec^2 and a launch date of May 30, 1967; the same trajectory to Mars is of Type I and has an energy of 0.079×10^8 m^2/sec^2 and a launch date of May 24, 1971. Note that the minimum energy for Type I transfers to Mars steadily decreases from 1964 to 1971, then abruptly increases in 1973, as shown in Fig. 3–4. The reverse is true for Venus, with the energy steadily increasing to 1965, then dropping abruptly in 1967. Also, the energy required to reach Venus in 1964–1965 for Type I transfers is greater than that required for Mars in the period 1964–1971. This result may seem surprising, but can be explained by observation of two major quantities: the celestial latitude of the target planet at arrival and the Sun–target-planet distance at arrival. Although Venus' orbit is fairly circular (eccentricity = 0.0068) compared with that of Mars (eccentricity = 0.0934), it is more inclined to the ecliptic (3.39 deg) than that of Mars (1.85 deg). In 1965, for example, the probe encounters Venus when it is quite far out of the ecliptic, causing the energy requirement to rise. In 1967, however, the probe encounters Venus when it is very nearly in the ecliptic, resulting in a near-Hohmann transfer and low energy requirements. Thus, for Venus, energy requirements are closely correlated with the celestial latitude of the planet at encounter, the small variation of Sun–planet distances having little effect. For Mars, the effect of Sun–planet distance is more pronounced. In Table 3–1, note that, as Sun–planet distance decreases, the energy stays almost constant in the interval 1964–1969, as the celestial latitude increases. This increase in latitude tends to offset any reduction in energy requirements which would be caused from the decreasing Sun–planet distance at encounter. In 1971, however, both celestial

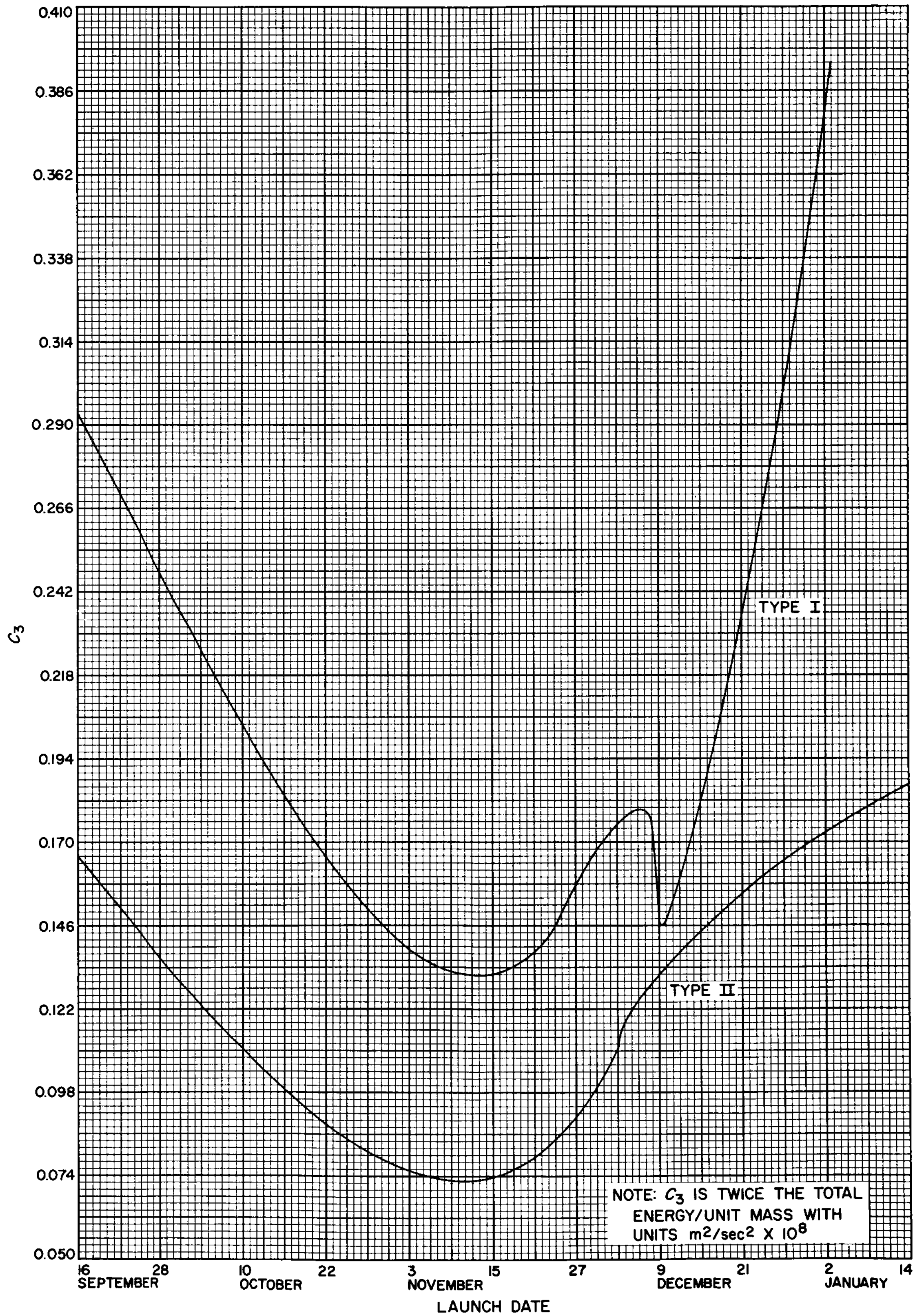

Fig. 3–2. Venus 1965: Minimum injection energy vs launch date

Table 3–1. Characteristics of minimum-energy transfer

Planet	Trajectory type	Launch date	Flight time, days	Geocentric injection energy[a], $m^2/sec^2 \times 10^8$	Heliocentric central angle[b], deg	Sun–planet distance at arrival, 10^6 km	Earth–planet distance at arrival, 10^6 km	Celestial latitude of planet at arrival, deg
Venus	I	8–23–62	114	0.087	132.4	107.5	58	1.46
	II	9–19–62	166	0.104	234.0	108.2	145	1.53
	I	3–30–64	112	0.123	126.8	108.9	61	−2.93
	II	4–9–64	170	0.081	225.4	107.8	137	−0.698
	I	11–12–65	108	0.132	129.5	107.6	60	3.31
	IA	12–10–65	128	0.148	178.2	108.6	114	0.030
	II	11–10–65	156	0.073	205.3	108.5	112	0.218
	I	6–11–67	142	0.065	175.6	107.7	92	−0.082
	II	5–30–67	156	0.059	190.4	107.7	94	0.110
	I	1–13–69	126	0.077	150.5	108.6	70	−0.393
	II	2–12–69	174	0.125	243.7	108.3	161	−2.59
	I	8–19–70	116	0.085	134.5	107.5	58	1.36
	II	9–16–70	166	0.106	233.6	108.2	145	1.71
Mars	I	10–30–62	232	0.151	158.2	243.5	246	1.06
	IA	11–13–62	290	0.161	178.8	232.1	312	0.010
	II	10–19–62	321	0.099	206.4	231.1	315	−0.070
	I	11–19–64	244	0.090	174.1	231.2	222	−0.047
	II	11–12–64	304	0.088	209.9	220.8	268	−0.911
	I	1–5–67	202	0.091	152.2	221.9	160	−0.833
	II	1–21–67	332	0.085	224.4	206.8	277	−1.672
	I	3–2–69	178	0.088	139.3	209.7	177	−1.75
	IA	5–11–69	284	0.128	178.5	219.9	288	−0.022
	II	4–1–69	294	0.080	200.6	214.8	257	−0.562
	I	5–24–71	210	0.079	156	216.6	164	−0.352
	II	5–10–71	244	0.096	181.1	220.4	189	0.012
	I	7–30–73	192	0.146	141.4	234.2	179	1.16
	II	8–28–73	407	0.160	223.7	242.6	391	0.956
	I	9–15–75	206	0.187	144.7	247.6	221	1.85
	II	9–19–75	379	0.133	220.2	237.0	376	0.440
	I	10–19–77	224	0.170	152.9	247.1	244	1.44
	IA	11–13–77	308	0.226	179.5	232.0	340	−0.001
	II	10–9–77	338	0.108	211.4	232.9	337	0.080

[a] Actually, twice the total energy per unit mass, or *vis viva* integral.
[b] The heliocentric central angle subtended at the Sun between the Sun–Earth line at launch time and the Sun–planet line at arrival time.

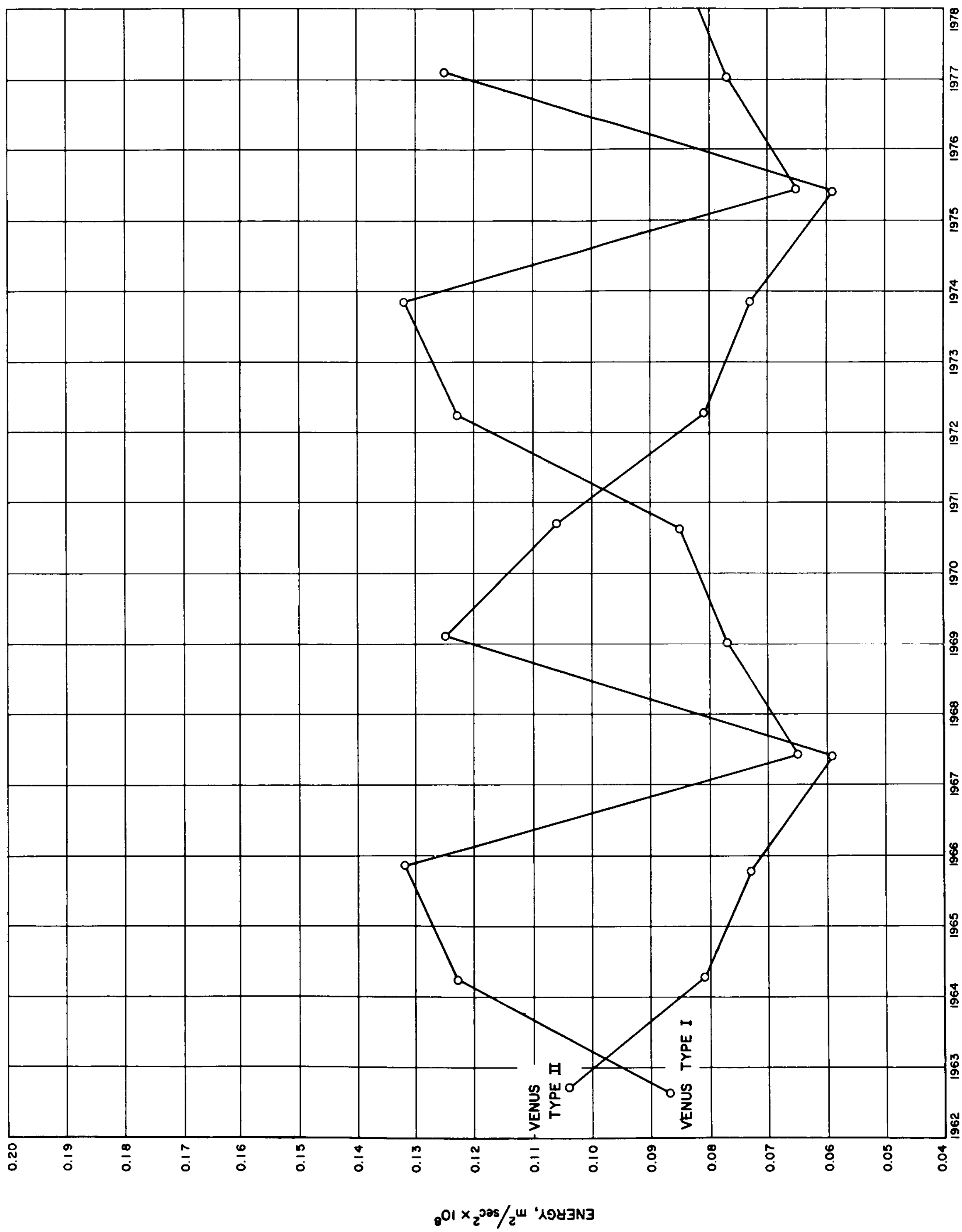

Fig. 3–3. Absolute minimum energy for Venus 1962–1977

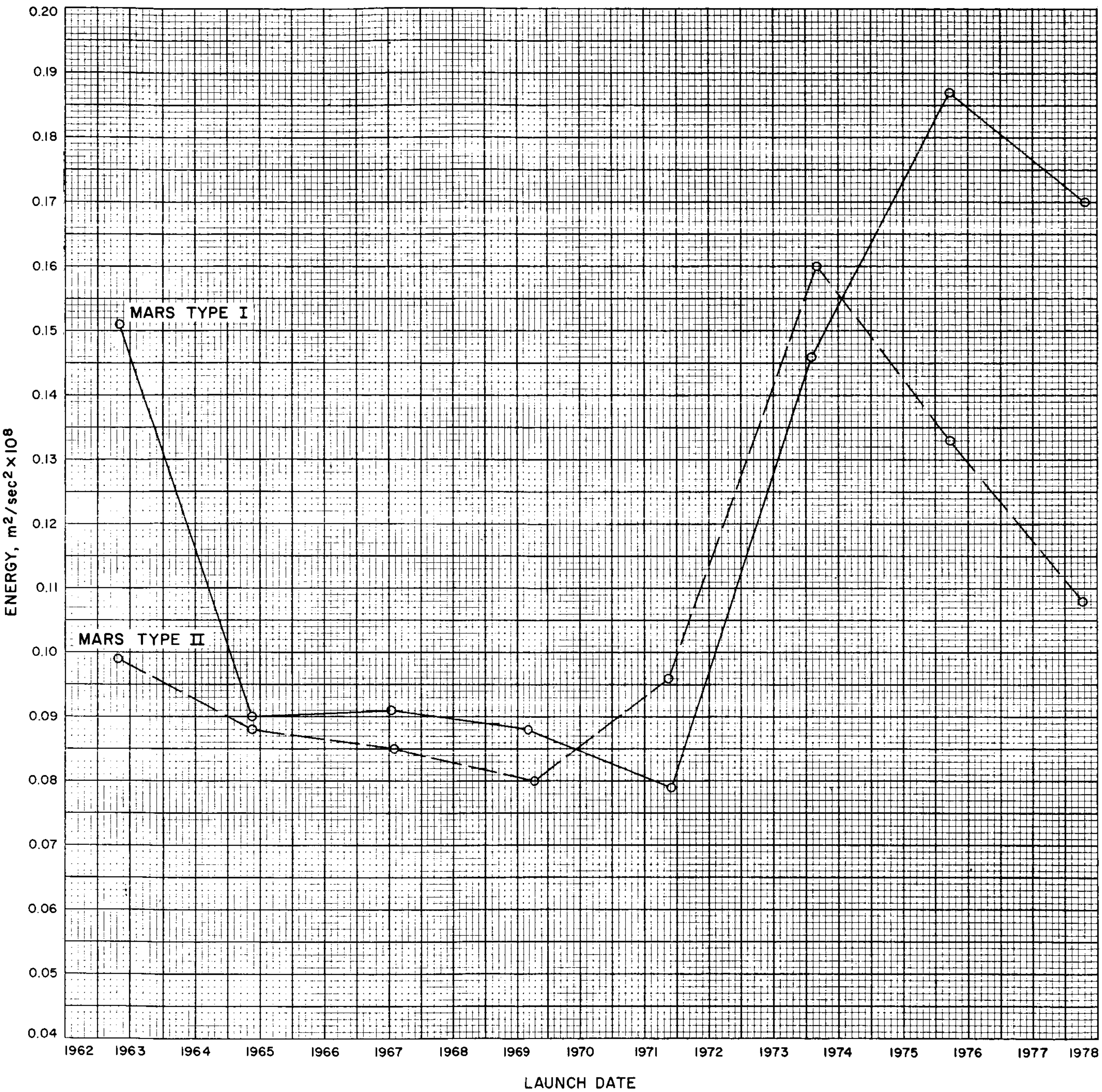

Fig. 3–4. Absolute minimum energy for Mars 1962–1977

latitude and Sun–planet distance are nearly minimum at encounter, resulting in low energy requirements. From 1973 on, both quantities increase, with a subsequent steep rise in energy.

C. *Launch Period*

The curve of minimum geocentric energy vs launch date can be most helpful in determining the maximum allowable launch period for a given geocentric energy. By treating the energy as the independent variable, one finds two extreme launch dates corresponding to a chosen energy (above the minimum energy, of course). The difference between the two launch dates is the permissible launch period for the chosen energy. If a launch period is arbitrarily selected, one can find the required injection energy from the graphs. These energy values are given in Tables 3–2 to 3–4 for launch periods of 15, 30, 45, and 60 days for Types I and II trajectories to Venus and Mars. In addition, trajectory parameters such as flight time, communication distance at encounter, asymptotic speed relative to the target planet, and geocentric asymptotic declinations are tabulated for each launch interval. For these parameters, the maximum values are given for Class I and Class II trajectories separately. Careful interpretation of these maxima and minima is necessary. They correspond to the largest and smallest values of these parameters under the conditions that the vehicle would be launched within the prescribed launch interval and would have an injection energy lying between the minimum value and the one corresponding to the launch interval. For example, according to Table 3–2 (Venus Type I trajectories), if a probe is launched in the 15-day interval, August 13–28, 1962, and has an injection energy between 0.087×10^8 m²/sec² (the minimum possible) and 0.09×10^8 m²/sec² (the energy necessary for a 15-day launch interval) it can have, for Class I transfers, maximum and minimum flight times of 122 and 108 days, maximum and minimum communication distances of 59 and 54 million km, maximum and minimum hyperbolic approach speeds to Venus of 5.92 and 5.40 km/sec, and maximum and minimum geocentric asymptotic declinations of −0.6 and −7.8 deg. Similar boundary values of these parameters for Class II transfers are also given.

The geocentric asymptotic declination is included in Tables 3–2 to 3–4 because it is an important parameter in determining the injection location (Ref. 4) over the Earth's surface. Acceptable values for this parameter are estimated to lie between −34 and +34 deg. Values outside this range result in severe restrictions for Cape Canaveral launchings.

D. General Characteristics of Trajectories

After review of the previous paragraphs, there are, no doubt, many questions concerning the characteristics of planetary trajectories that remain unanswered in the reader's mind. A majority of the questions can be answered only by probing deeply into the graphs in Sections IV to XVIII of this Report. In the following discussion, an attempt is made to reveal specific trajectory characteristics of paramount importance, in the hope of answering pertinent questions that might be confronting the reader. These characteristics or properties may be divided into three categories: geocentric, heliocentric, and planetocentric.

1. Geocentric Parameters

To describe the probe's outgoing asymptotic direction as it leaves the influence of the Earth, four parameters are plotted as functions of launch date for various energies: (1) declination and (2) right ascension of the outgoing asymptote; (3) celestial latitude of the outgoing asymptote; and (4) the angle between the outgoing asymptote and the Sun–Earth vector.

a. Declination and celestial latitude of outgoing asymptote. As mentioned earlier, perhaps the most important parameter in determining the preinjection trajectory is the declination of the outgoing asymptote. This parameter is equivalent to the declination of the probe measured at the Earth's center (positive if above the Earth's equator) from a few hours to several days past launch. Injection locations over the surface of the Earth and permissible firing windows for a given range of launch azimuths are highly dependent on the asymptotic declinations. From mission to mission, the range in asymptotic declinations varies for a given energy. Notice in Figs. 3–5 to 3–8, for instance, that the ranges in the asymptotic declination for an energy of 0.15×10^8 m²/sec² are −24 to +27 deg, −20 to +8 deg, and −28 to +23 deg for Venus 1962, 1964, 1965 Type I trajectories, whereas, for Type II trajectories, the ranges are −18 to −64 deg, −5 to +69 deg, and −58 to +20 deg. In observing all asymptotic-declination curves, one finds that the parameter takes on values as high as ±80 deg for the energies considered. Both the declination and the right ascension of the outgoing asymptote can be expressed as functions of the celestial latitude γ_L and longitude λ_S of the outgoing asymptote. Now, for a given launch date and flight time to planet encounter, the three parameters C_3, γ_L, and λ_S can be made *essentially* functions of the path angle of the probe's heliocentric velocity at launch Γ_L, the magnitude of the probe's heliocentric velocity at launch V_L, and, finally, the inclination i of the heliocentric-transfer orbital plane to the ecliptic. The ellipticity of the Earth's heliocentric orbit should also be included, but is a secondary effect (see Fig. 3–9).

The hyperbolic-excess velocity vector $\mathbf{V}_{hL}$ is expressed by

$$\mathbf{V}_{hL} = \mathbf{R}^1 V_L \sin\Gamma_L + (\mathbf{K}' \times \mathbf{R}^1)(V_L \cos\Gamma_L \cos i - V_E) + \mathbf{K}' V_L \cos\Gamma_L \sin i \qquad (3\text{–}1)$$

and, since the geocentric injection energy is given by

$$C_3 = V_{hL}^2 \qquad (3\text{–}2)$$

then

$$C_3 = V_L^2 + V_E^2 - 2V_L V_E \cos\Gamma_L \cos i \qquad (3\text{–}3)$$

Table 3–2. Venus Type I transfer characteristics

Launch dates	Launch period, days	Geocentric injection energy, $m^2/sec^2 \times 10^8$	Class I trajectories: Flight time, days		Communication distance, 10^6 km		Planetocentric asymptotic speed, km/sec		Declination of geocentric asymptote, deg		Class II trajectories: Flight time, days		Communication distance, 10^6 km		Planetocentric asymptotic speed, km/sec		Declination of geocentric asymptote, deg	
			Min	Max	Min	Max	Min	Max	Min	Max	Min	Max	Min	Max	Min	Max	Min	Max
Aug 13–Aug 28 1962	15	0.09	108	122	54	59	5.40	5.92	−7.8	−0.6	110	123	57	62	5.20	5.58	−2.7	5.9
Aug 4–Sept 3 1962	30	0.0985	101	127	50	60	5.23	6.49	−13.5	0.08	105	130	56	66	4.98	5.73	−4.2	12.6
July 26–Sept 9 1962	45	0.112	94	135	47	61	5.13	7.18	−18.0	1.6	100	138	53	69	4.78	5.84	−5.8	18.3
July 15–Sept 13 1962	60	0.1295	88	143	45	62	5.04	7.91	−21.4	2.3	96	145	51	73	4.61	6.03	−7.5	23.0
Mar 22–Apr 6 1964	15	0.128	104	115	55	61	5.78	6.82	−6.0	0.7	105	119	58	66	5.39	6.32	−11.1	−4.0
Mar 14–Apr 13 1964	30	0.142	96	122	51	63	5.55	7.74	−6.0	5.8	101	125	55	71	4.82	6.65	−17.1	−2.5
Mar 5–Apr 19 1964	45	0.1645	88	128	48	65	5.32	8.71	−6.0	9.8	97	132	53	78	4.34	6.98	−22.2	−0.8
Feb 24–Apr 24 1964	60	0.19475	81	135	46	67	5.13	9.72	−6.0	13.0	93	138	50	84	3.98	7.25	−26.5	1.0
Nov 5–Nov 20 1965	15	0.1370	99	112	54	64	4.30	5.75	9.2	16.5	104	115	57	69	3.73	5.10	11.6	19.0
Oct 27–Nov 26 1965	30	0.1537	91	117	48	75	3.50	6.94	4.9	17.2	104	121	53	81	3.02	5.70	8.0	24.1
Oct 19–Dec 3 1965	45	0.1750	84	129	45	94	2.99	7.92	2.0	17.2	104	126	51	96	2.99	6.16	5.5	27.8
Oct 16–Dec 15 1965	60	0.183	82	124	44	114	2.91	8.23	−23.5	17.2	104	127	49	116	2.99	6.34	−41.1	28.9
June 8–June 23 1967	15	0.0842	128	144	81	91	2.81	3.95	−18.5	15.0	133	146	93	96	3.70	4.90	−16.0	35.9
May 30–June 29 1967	30	0.1065	110	144	60	93	3.31	5.15	−23.7	19.0	127	145	68	98	2.88	5.61	−27.3	44.4
May 21–July 5 1967	45	0.1344	96	144	51	96	3.45	6.96	−27.4	22.0	122	146	61	100	3.13	6.27	−33.7	48.0
May 12–July 11 1967	60	0.1700	86	144	47	99	3.62	8.48	−29.0	27.0	119	146	56	103	3.54	6.82	−38.2	52.0
Jan 4 1969–Jan 19 1969	15	0.0805	119	132	66	71	4.53	4.73	−2.2	8.8	120	134	70	74	4.49	4.62	−8.4	2.2
Dec 27 1968–Jan 26 1969	30	0.0894	111	140	61	72	4.45	5.22	−4.0	15.4	115	141	68	78	4.44	4.85	−16.3	4.8
Dec 17 1968–Jan 31 1969	45	0.1035	103	148	56	73	4.26	5.92	−4.4	20.3	110	149	67	82	4.39	5.21	−23.1	8.0
Dec 9 1968–Feb 7 1969	60	0.1315	93	156	51	74	3.63	7.12	−6.8	26.2	105	157	66	86	4.30	5.80	−30.6	10.5
Aug 9 1970–Aug 24 1970	15	0.088	109	122	54	58	5.31	5.80	−8.2	−1.0	112	124	56	62	5.17	5.55	−1.8	5.5
Aug 1–Aug 31 1970	30	0.0965	102	129	51	60	5.15	6.40	−13.6	0	105	131	55	66	4.98	5.57	−3.2	12.4
July 23–Sept 6 1970	45	0.1105	95	137	48	61	5.00	7.13	−18.3	0.7	100	139	53	70	4.79	5.65	−5	18.6
July 12–Sept 10 1970	60	0.1272	89	144	45	62	4.88	7.81	−21.5	1.0	97	146	51	73	4.63	5.81	−7.8	23.1

Table 3–3. Venus Type II transfer characteristics

Launch dates	Launch period, days	Geocentric injection energy, $m^2/sec^2 \times 10^8$	Class I trajectories: Flight time, days		Class I: Communication distance, 10^6 km		Class I: Planetocentric asymptotic speed, km/sec		Class I: Declination of geocentric asymptote, deg		Class II trajectories: Flight time, days		Class II: Communication distance, 10^6 km		Class II: Planetocentric asymptotic speed, km/sec		Class II: Declination of geocentric asymptote, deg	
			Min	Max	Min	Max	Min	Max	Min	Max	Min	Max	Min	Max	Min	Max	Min	Max
Sept 10–Sept 25 1962	15	0.106	162	168	138	149	6.02	6.52	−45.8	−35.6	162	167	138	151	6.05	6.58	−44.7	−34.0
Sept 2–Oct 2 1962	30	0.1103	159	172	132	153	5.78	6.75	−50.6	−31.0	159	173	133	156	5.83	6.84	−48.0	−28.9
Aug 24–Oct 8 1962	45	0.118	155	173	125	159	5.48	7.0	−55.3	−26.0	155	177	127	163	5.57	7.16	−51.0	−23.3
Aug 15–Oct 14 1962	60	0.1275	152	176	118	164	5.17	7.23	−59.0	−21.6	152	179	120	169	5.33	7.45	−52.5	−18.6
Mar 31–Apr 15 1964	15	0.0835	165	174	130	141	5.20	5.55	28.0	41.3	167	176	131	142	5.25	5.62	26.6	38.0
Mar 23–Apr 22 1964	30	0.090	160	177	124	146	5.06	5.70	22.0	48.7	165	181	127	149	5.12	5.96	17.0	40.8
Mar 15–Apr 29 1964	45	0.1007	155	181	119	152	4.92	5.98	15.8	55.4	163	187	121	157	4.95	6.38	10.1	43.2
Mar 7–May 6 1964	60	0.114	151	185	113	158	4.78	6.30	10.0	60.7	162	191	117	164	4.80	6.84	4.4	45.0
Nov 3–Nov 18 1965	15	0.0761	150	161	108	114	4.18	4.43	−29.4	−18.6	150	163	110	118	4.10	4.27	−22.3	−10.0
Oct 25–Nov 24 1965	30	0.0850	144	167	103	116	4.18	4.76	−39.2	−15.5	145	170	107	126	4.10	4.47	−24.5	−0.8
Oct 16–Nov 30 1965	45	0.0993	138	173	99	117	4.18	5.19	−46.5	−22.8	140	177	103	136	4.31	4.88	−26.8	6.8
Oct 6–Dec 5 1965	60	0.1197	133	178	93	118	4.0	5.68	−52.5	−21.3	135	185	98	149	4.50	5.53	−28.7	13.6
May 23–June 7 1967	15	0.0614	147	160	92	93	3.56	4.02	6.0	19.3	147	161	93	96	3.22	3.66	−3.0	7.3
May 9–June 8 1967	30	0.078	147	171	87	96	3.56	4.88	6.0	34.6	147	176	92	107	2.92	3.83	−18.2	9.5
Apr 28–June 12 1967	45	0.0978	147	181	83	115	2.98	5.49	−24.7	41.8	147	187	88	122	3.70	4.38	−25.5	12.5
Apr 21–June 20 1967	60	0.1125	147	187	81	130	2.98	5.88	−28.2	45.7	147	193	86	134	3.70	5.14	−28.9	14.5
Feb 6–Feb 21 1969	15	0.126	170	174	154	168	6.00	6.88	29.4	43.1	172	176	156	168	6.11	6.93	37.0	42.4
Jan 28–Feb 27 1969	30	0.1292	167	176	145	172	5.47	7.27	32.0	45.7	171	179	147	175	5.57	7.33	33.6	44.8
Jan 19–Mar 5 1969	45	0.1332	165	178	136	177	4.91	7.52	34.3	47.5	170	181	139	179	5.02	7.67	30.8	46.1
Jan 9–Mar 10 1969	60	0.138	163	178	124	181	4.25	7.80	37.5	48.8	169	184	127	183	4.35	7.95	28.4	46.8
Sept 8–Sept 23 1970	15	0.1075	162	168	138	149	6.04	6.58	−46.4	−36.8	169	171	122	152	6.09	6.66	−44.4	−34.2
Aug 31–Sept 30 1970	30	0.1115	159	172	132	154	5.80	6.80	−50.6	−33.0	165	175	127	157	5.80	6.91	−48.2	−29.6
Aug 22–Oct 6 1970	45	0.1190	156	175	125	161	5.48	7.08	−55.2	−27.5	162	179	133	164	5.55	7.23	−51.2	−24.1
Aug 13–Oct 12 1970	60	0.1276	153	178	119	166	5.17	7.30	−58.4	−22.2	160	183	139	169	5.30	7.50	−52.2	−19.8

Table 3–4. Mars Type I transfer characteristics

Launch dates	Launch period, days	Geocentric injection energy, $m^2/sec^2 \times 10^8$	Class I trajectories: Flight time, days		Communication distance, 10^6 km		Planetocentric asymptotic speed, km/sec		Declination of geocentric asymptote, deg		Class II trajectories: Flight time, days		Communication distance, 10^6 km		Planetocentric asymptotic speed, km/sec		Declination of geocentric asymptote, deg	
			Min	Max	Min	Max	Min	Max	Min	Max	Min	Max	Min	Max	Min	Max	Min	Max
Oct 23–Nov 7 1962	15	0.1612	206	241	214	264	3.35	5.24	30.0	42.2	225	260	231	281	2.88	4.44	32.6	48.3
Oct 18–Nov 17 1962	30	0.1821	188	288	193	313	3.16	6.30	6.0	42.2	221	292	218	315	2.53	5.00	−4.5	56.8
Oct 11–Nov 25 1962	45	0.232	163	290	167	316	2.80	7.94	1.0	42.2	216	294	202	320	2.80	5.64	−14.5	68.0
Oct 4–Dec 3 1962	60	0.3004	144	290	148	316	2.50	9.52	1.0	42.2	211	298	188	325	3.13	6.30	−19.8	76.7
Nov 12–Nov 27 1964	15	0.094	233	246	214	225	3.96	4.45	8.0	16.2	240	248	220	229	3.90	4.15	−1.8	8.5
Nov 10–Dec 10 1964	30	0.1257	196	246	182	227	3.96	6.24	8.0	30.0	229	253	207	244	3.59	4.15	−20.9	37.8
Nov 5–Dec 20 1964	45	0.1759	167	246	157	227	3.96	8.16	8.0	30.4	224	259	186	257	3.41	4.30	−32.1	50.1
Oct 31–Dec 30 1964	60	0.24350	146	246	139	227	3.55	9.96	8.0	31.8	223	265	172	270	3.50	4.30	−38.1	54.2
Dec 28 1966– Jan 12 1967	15	0.0962	189	204	149	162	5.25	6.25	−26.5	−14.3	198	212	155	171	4.87	5.70	−29.3	−15.7
Dec 21 1966– Jan 20 1967	30	0.1120	173	206	138	166	5.04	7.23	−28.7	−9.3	193	220	150	182	4.38	6.06	−37.7	−11.3
Dec 13 1966– Jan 27 1967	45	0.1397	158	207	127	172	4.89	8.41	−29.3	−5.6	189	227	144	194	4.01	6.45	−44.6	−8.4
Dec 6 1966–Feb 4 1967	60	0.178	143	207	118	182	4.75	9.64	−29.3	−3.1	183	233	138	206	3.81	6.87	−51.3	−7.5
Feb 24–Mar 11 1969	15	0.092	165	178	108	119	4.92	5.88	−51.9	−43.6	176	189	115	129	4.34	5.22	−56.1	−46.7
Feb 16–Mar 18 1969	30	0.1049	151	181	98	128	4.40	6.72	−55.1	−38.1	176	201	109	139	3.79	5.70	−63.3	−43.3
Feb 9–Mar 26 1969	45	0.1235	140	193	92	151	3.66	7.86	−55.1	−34.3	176	212	105	163	3.62	5.72	−68.9	−43.3
Feb 3–Apr 4 1969	60	0.1433	131	201	87	165	3.64	8.64	−55.1	−31.8	176	224	102	178	3.87	6.27	−72.8	−43.3
May 16–May 31 1971	15	0.0815	186	212	130	175	2.83	2.99	−27.2	−15.6	202	230	142	191	2.82	3.04	−25.0	−6.7
May 8–June 7 1971	30	0.0896	164	216	106	190	2.86	3.64	−30.0	−8.0	196	240	126	208	2.84	3.24	−29.5	5.8
May 1–June 15 1971	45	0.1033	147	222	90	208	2.91	4.52	−33.6	−4.5	192	242	113	223	2.88	3.51	−33.6	16.2
Apr 24–June 23 1971	60	0.1222	132	228	79	225	2.95	5.47	−35.3	−0.3	188	246	100	240	2.95	3.75	−38.5	24.4
July 21–Aug 5 1973	15	0.1507	176	195	154	186	2.90	3.53	23.8	31.5	191	209	172	206	2.71	3.17	26.0	35.6
July 13–Aug 12 1973	30	0.166	159	196	132	202	2.78	4.26	19.9	32.0	194	223	160	233	2.49	3.35	24.0	42.6
July 5–Aug 19 1973	45	0.1903	143	197	114	218	2.70	5.10	16.9	32.1	201	235	148	259	2.45	3.54	23.0	49.1
June 26–Aug 25 1973	60	0.2228	130	197	100	240	2.65	5.98	14.7	31.0	210	246	138	283	2.48	3.70	22.5	54.9
Sept 7–Sept 22 1975	15	0.1964	186	209	191	230	3.60	4.68	41.7	51.5	206	226	203	254	3.10	3.98	43.2	54.9
Aug 31–Sept 30 1975	30	0.2237	165	210	164	243	3.42	5.78	37.2	52.2	203	245	190	285	2.62	4.30	38.7	62.6
Aug 23–Oct 7 1975	45	0.2683	147	210	143	257	3.20	6.99	33.7	52.4	200	264	177	315	2.39	4.72	36.6	69.7
Aug 15–Oct 14 1976	60	0.3263	132	211	126	268	2.90	8.18	31.8	52.4	199	283	167	342	2.54	5.22	36.3	75.6
Oct 11–Oct 26 1977	15	0.1806	198	225	209	255	3.62	5.33	37.0	48.0	220	247	228	275	3.10	4.57	40.0	54.0
Oct 4–Nov 3 1977	30	0.2122	176	238	182	273	3.18	6.66	32.0	48.8	216	273	210	308	2.49	5.10	35.0	63.0
Sept 30–Nov 4 1977	45	0.2376	164	306	170	339	2.46	7.44	17.0	47.8	213	309	206	340	2.51	5.35	3.5	68.0
Sept 23–Nov 22 1977	60	0.301	145	306	149	339	2.56	8.94	10.0	48.8	210	309	192	344	2.92	5.85	−10.0	76.0

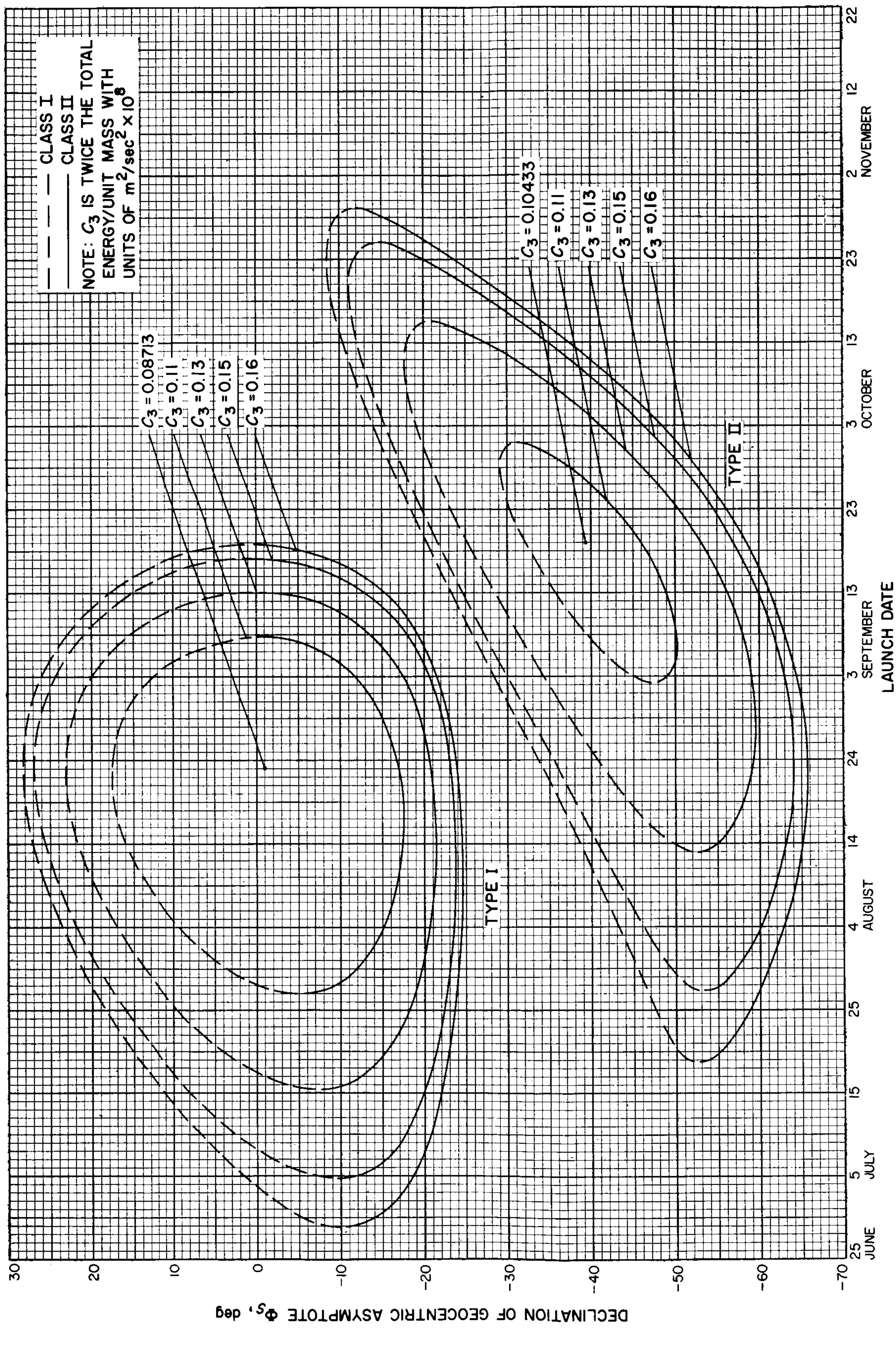

Fig. 3–5. Venus 1962: Declination of geocentric asymptote vs launch date

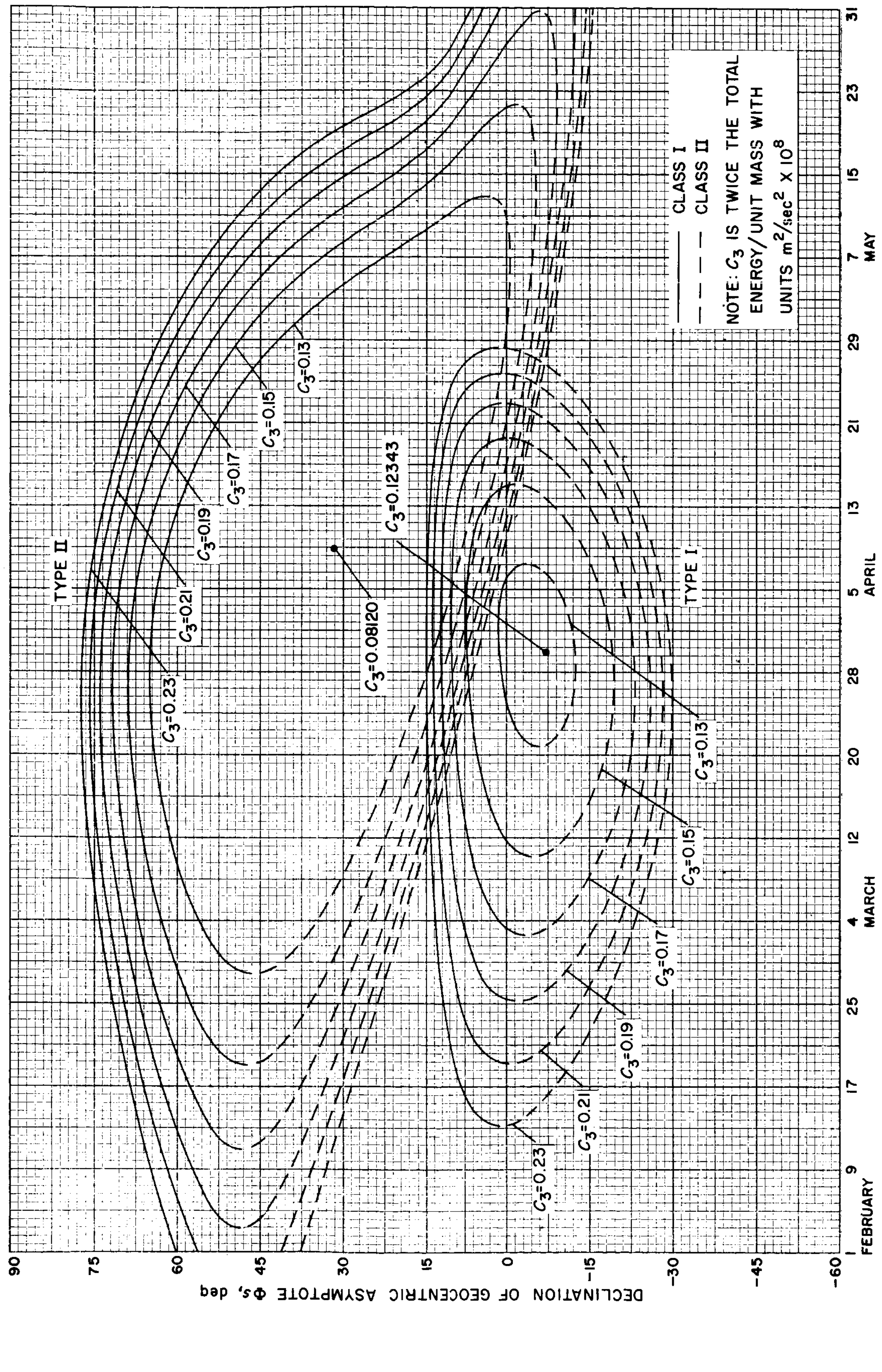

Fig. 3–6. Venus 1964: Declination of geocentric asymptote vs launch date

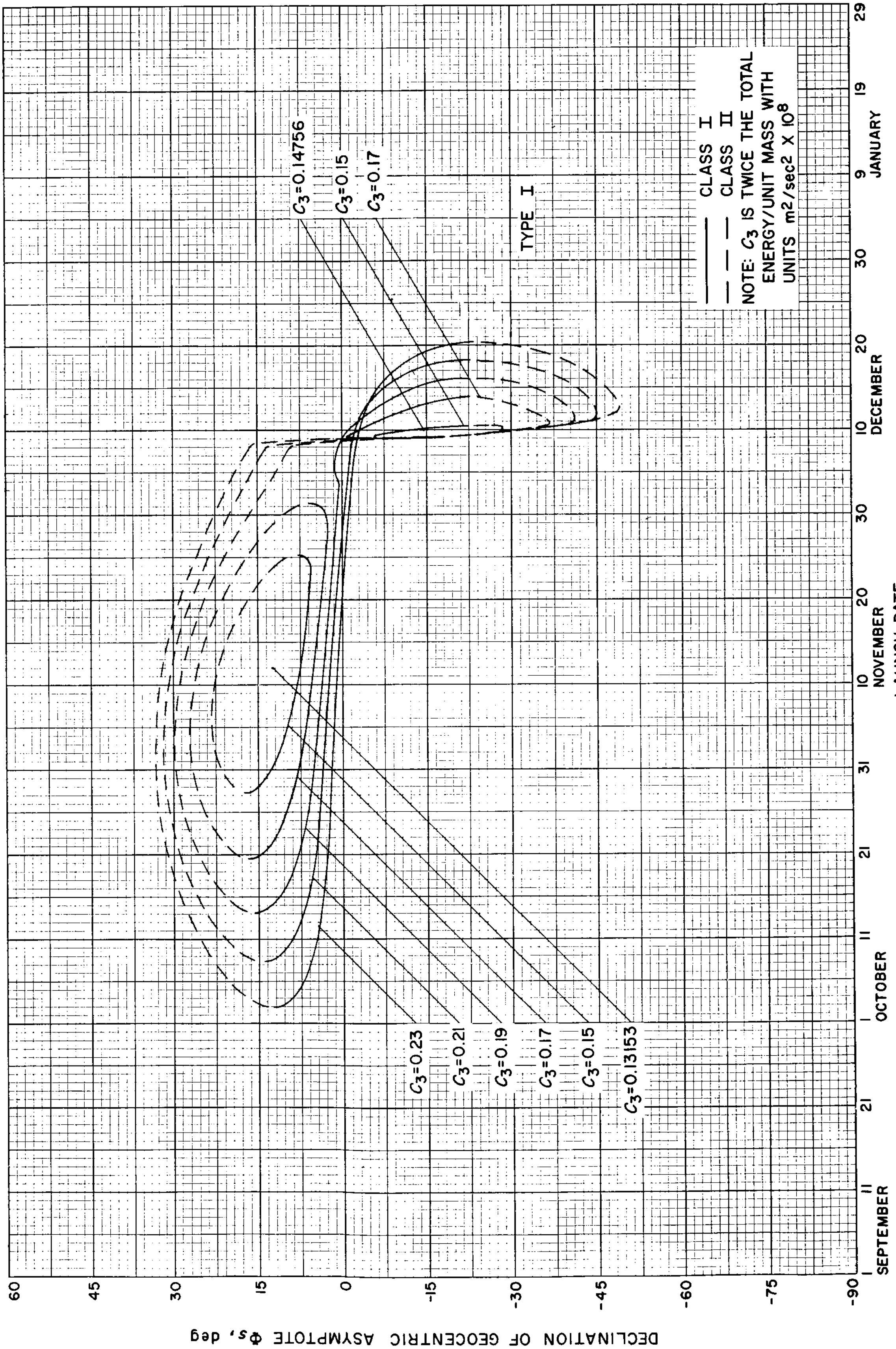

Fig. 3–7. Venus 1965: Declination of geocentric asymptote vs launch date, Type I

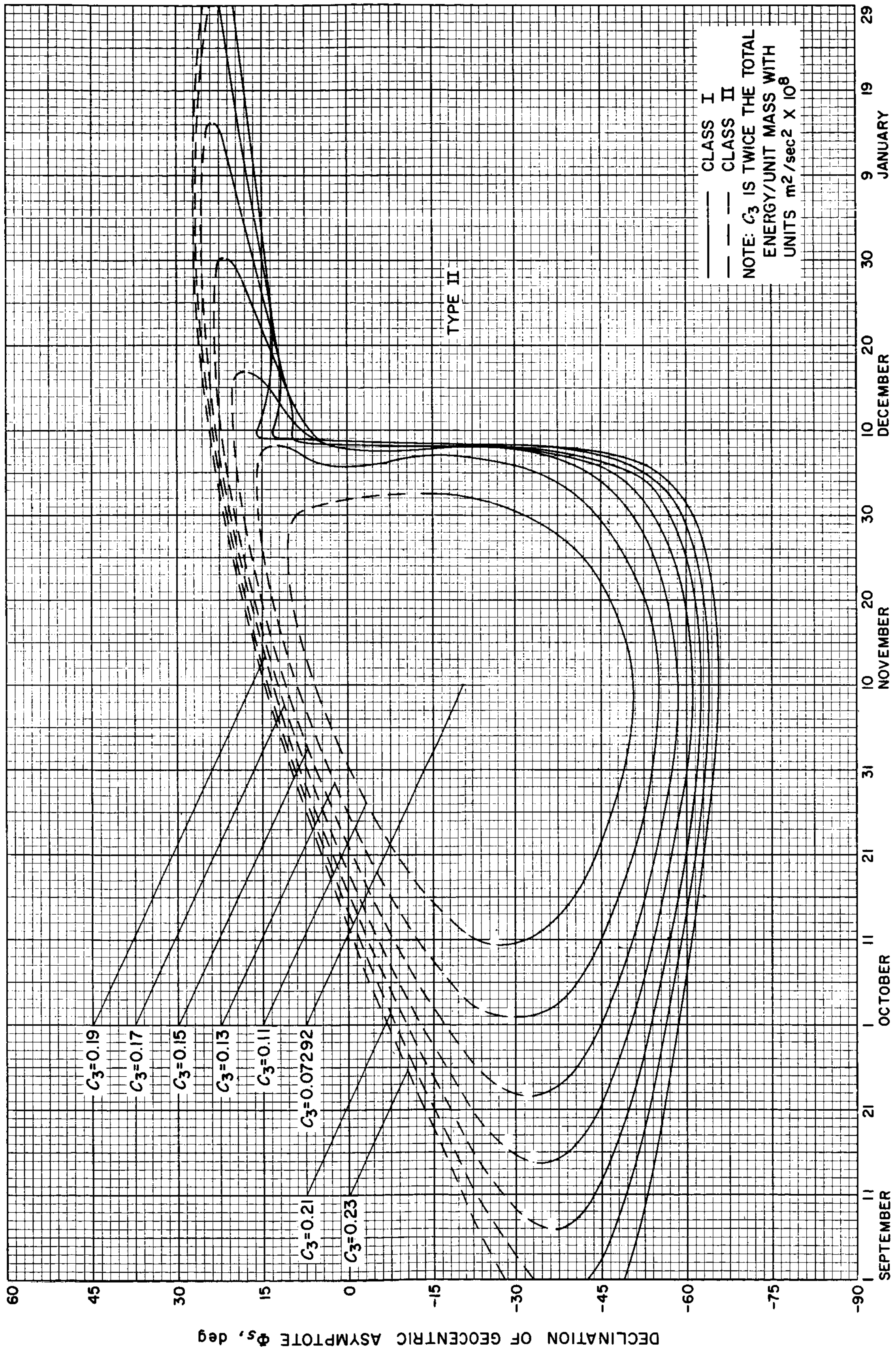

Fig. 3–8. Venus 1965: Declination of geocentric asymptote vs launch date, Type II

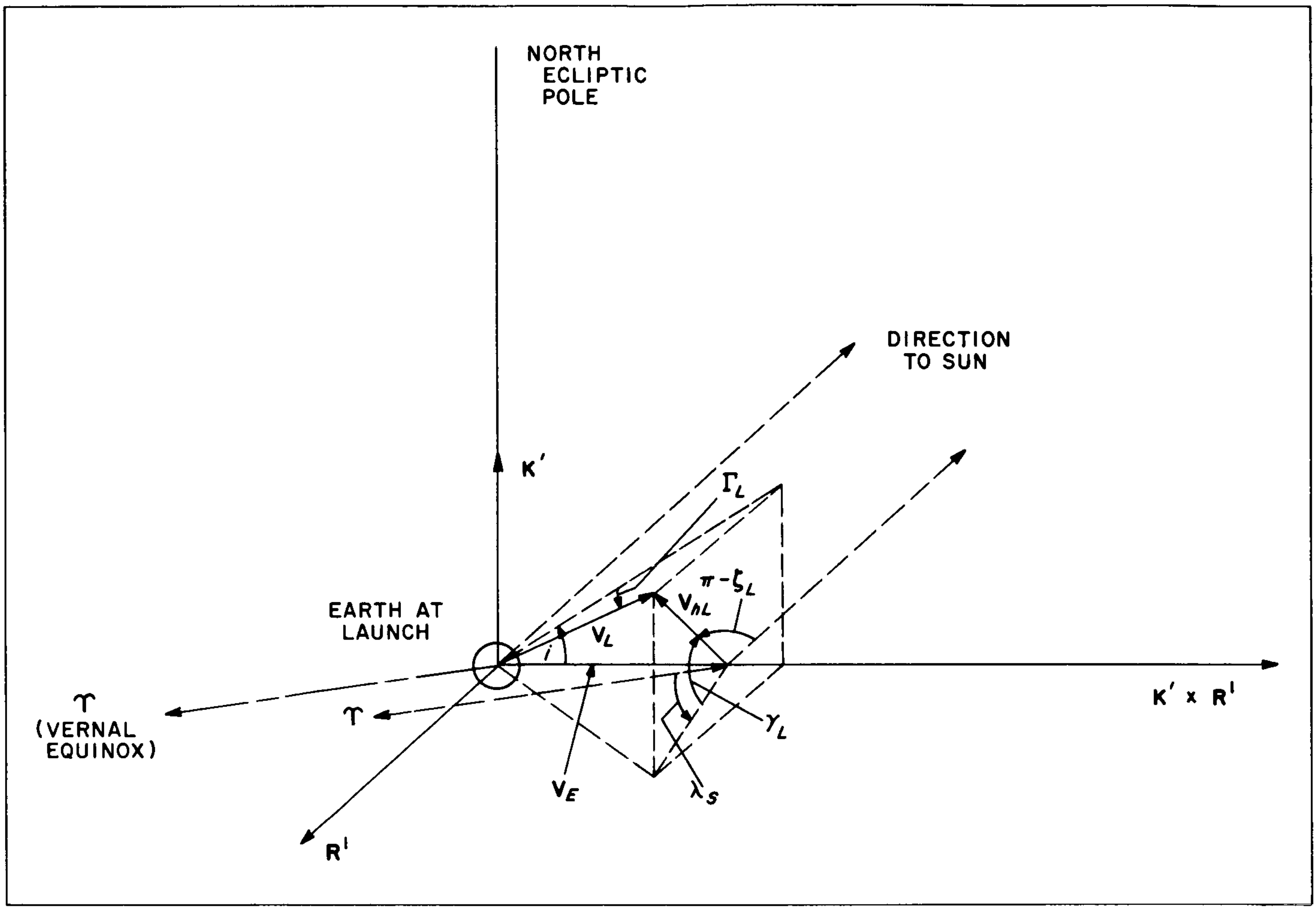

Fig. 3–9. Geometry of heliocentric injection

The celestial latitude γ_L of $\mathbf{V}_{hL}$ is obtained by

$$\sin\gamma_L = \frac{\mathbf{K}'\cdot\mathbf{V}_{hL}}{V_{hL}} = \frac{V_L\cos\Gamma_L\sin i}{V_{hL}} \qquad -\frac{\pi}{2}\le\gamma_L\le\frac{\pi}{2} \tag{3–4}$$

The celestial longitude λ_s of $\mathbf{V}_{hL}$ is given by

$$\left.\begin{aligned}
\cos\lambda_S &= \frac{\mathbf{I}'\cdot[\mathbf{R}^1 V_L\sin\Gamma_L + (\mathbf{K}'\times\mathbf{R}^1)(V_L\cos\Gamma_L\cos i - V_E)]}{V_{hL}\cos\gamma_L}\\
\cos\lambda_S &= \frac{V_L\cos\lambda_E\sin\Gamma_L - \sin\lambda_E(V_L\cos\Gamma_L\cos i - V_E)}{V_{hL}\cos\gamma_L}\\
\sin\lambda_S &= \frac{V_L\sin\lambda_E\sin\Gamma_L + \cos\lambda_E(V_L\cos\Gamma_L\cos i - V_E)}{V_{hL}\cos\gamma_L}
\end{aligned}\right\} \quad 0\le\lambda_S\le 2\pi \tag{3–5}$$

where λ_E is the celestial longitude of the Earth at launch time, $\mathbf{I}'$ is a unit vector in the direction of the vernal equinox, $\mathbf{K}'$ is a unit vector along the ecliptic north pole, $\mathbf{R}^1$ is a unit vector from Sun to Earth at launch, and V_E is the speed of the Earth. It is apparent, from Fig. 3–9 and these Equations, that even though the inclination i of the heliocentric orbital plane to the ecliptic may be only a few degrees, the celestial latitude of the outgoing asymptote γ_L may take on values quite large. Taking a simple example, where $\Gamma_L = 0$ deg, $i = 3$ deg, $V_E = 30$ km/sec, and $V_L = 27$ km/sec, one finds C_3 to be 11.22 km²/sec² and γ_L to be 24.9 deg. Although, for this particular case, the elliptical orbit of the probe with respect to the Sun is inclined only 3 deg to the ecliptic, the outgoing asymptote $\mathbf{V}_{hL}$, along which the probe must leave the Earth in order to encounter the planet, is inclined to the ecliptic by 24.1 deg, a considerable difference. From Eq. 3–4, it is noted that the quantity $V_L \cos \Gamma_L / V_{hL}$ acts as a magnification factor (equal to about 8 in the cited example); i.e., for small angles, $\gamma_L \approx (V_L/V_{hL})\, i$.

Since the Earth's equatorial plane is inclined to the ecliptic by 23.5 deg, the declination of the outgoing geocentric asymptote may differ from the celestial latitude by as much as ± 23.5 deg, depending on the required celestial longitude of the outgoing asymptote. Figures 3–10 and 3–11 show curves of the celestial latitude of the outgoing asymptote[9] for Venus 1962 and 1964 trajectories. Note the similarity of these graphs to the curves presented in Figs. 3–5 and 3–6.

The maximum value of γ_L is arc sin V_L/V_E for Venus trajectories, assuming that $\Gamma_L = 0$. Upon maximizing V_L/V_E, maximum γ_L will be attained (see Fig. 3–12). On the other hand, γ_L may take on values as high as ± 90 deg for a Mars encounter. Observing the curves of celestial latitude of the outgoing geocentric asymptote for Venus and Mars transfers in Sections V to XVIII, one finds that, for the injection energies considered (up to 23 km²/sec²), γ_L takes on values up to ± 55 deg and ± 70 deg for Cytherian and Martian trajectories, respectively.

b. Variation of celestial latitude of geocentric asymptote with celestial latitude of planet at encounter. Upon observing the curves of celestial latitude of the outgoing asymptote vs launch date for various injection energies, such as those in Figs. 3–10 and 3–11, one may at first become confused at the manner in which the parameter varies. These few remarks may help, however. The celestial latitude of the outgoing asymptote γ_L is equal to zero only if the planet at arrival is passing through the ecliptic plane.

For Type I trajectories, the celestial latitude of the outgoing asymptote (measured from Earth) is negative when the celestial latitude of the planet at arrival (measured from the Sun) is negative, and positive when the celestial latitude at arrival is positive (see Fig. 3–13). For Type II trajectories, however, the celestial latitude of the outgoing asymptote is positive when the celestial latitude of the planet at arrival is negative, and negative when the celestial latitude of the planet at arrival is positive. These statements may be verified by comparing Fig. 3–11 with Fig. 3–13. The geometrical configurations are illustrated in Fig. 3–14.

This property is easily seen, since the hyperbolic-excess velocity must be directed *above* the ecliptic so that the resultant heliocentric velocity of the probe at launch will also be directed *above* the ecliptic. This allows the probe to encounter Venus *above* the ecliptic for heliocentric-transfer angles less than 180 deg (Type I trajectories) and *below* the ecliptic for heliocentric-transfer angles greater than 180 deg but less than 360 deg (Type II trajectories), as illustrated.

c. Angle between outgoing geocentric asymptote and Sun–Earth vector. The angle between the outgoing asymptote and the Sun–Earth vector ζ_L, (Fig. 3–9) is equivalent to the Earth–probe–Sun angle a few days after launch. One may note from the curves that, for both Type I and Type II trajectories to Venus, this parameter increases in general as launch date is delayed. For Mars trajectories, however, the parameter decreases with launch-date delay. For Type I trajectories, the range of values does not change appreciably for the range of injection energies plotted on a given launch date. In observing this parameter on two Venus launch dates, March 12 and April 13, 1964, note in Figs. 3–15 and 3–16 that on March 12 the parameter ranges from 64 to 80 deg for Type I trajectories and from 43 to 80 deg for Type II trajectories, whereas on April 13 the variation of the parameter ζ_L over the range of energies considered is only about 15 and 55 deg for Type I and Type II, respectively. In observing the Mars 1964 plots for ζ_L, one finds that the maximum range of this parameter for the energies plotted on a given launch date is only about 35 deg. This implies that, for any feasible Type I trajectory to Venus for a given launch date, the Earth–probe–Sun angle will remain essentially the same at a few days after launch; the same statement applies to Martian trajectories. Another interesting characteristic of this parameter is indicated in Figs. 3–17 and 3–18. These graphs show the Earth–probe–Sun angle vs time from launch for two trajectories to Venus and two to Mars in 1964. The Venus trajectories are computed for launching on March 15 with a 122-day flight time, and for an April 10

[9]Note that, in these Figures, the title "angle between outgoing geocentric asymptote and launch planet's orbital plane" is used, rather than "celestial latitude of outgoing asymptote." These two titles are synonymous.

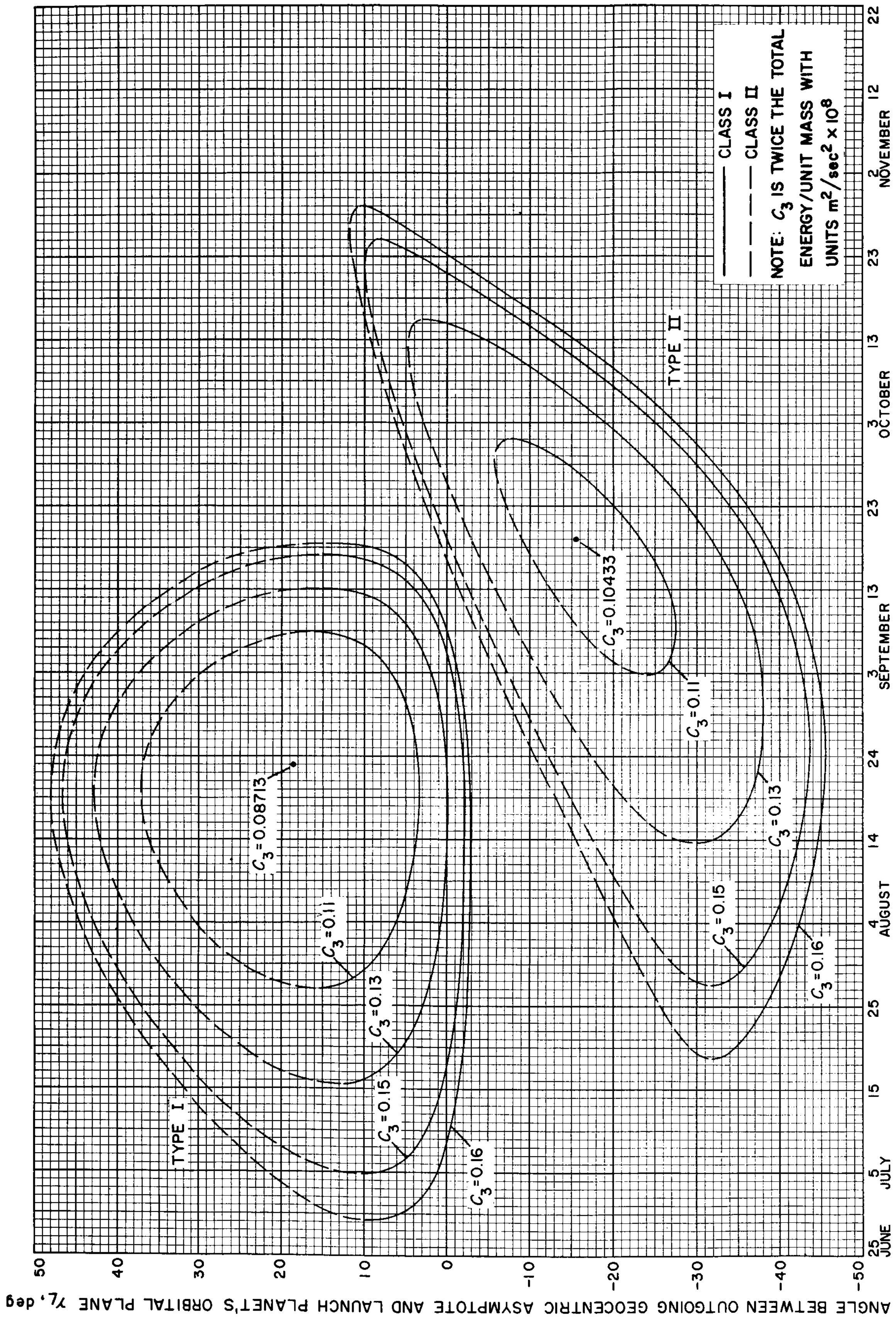

Fig. 3-10. Venus 1962: Angle between outgoing geocentric asymptote and launch planet's orbital plane vs launch date

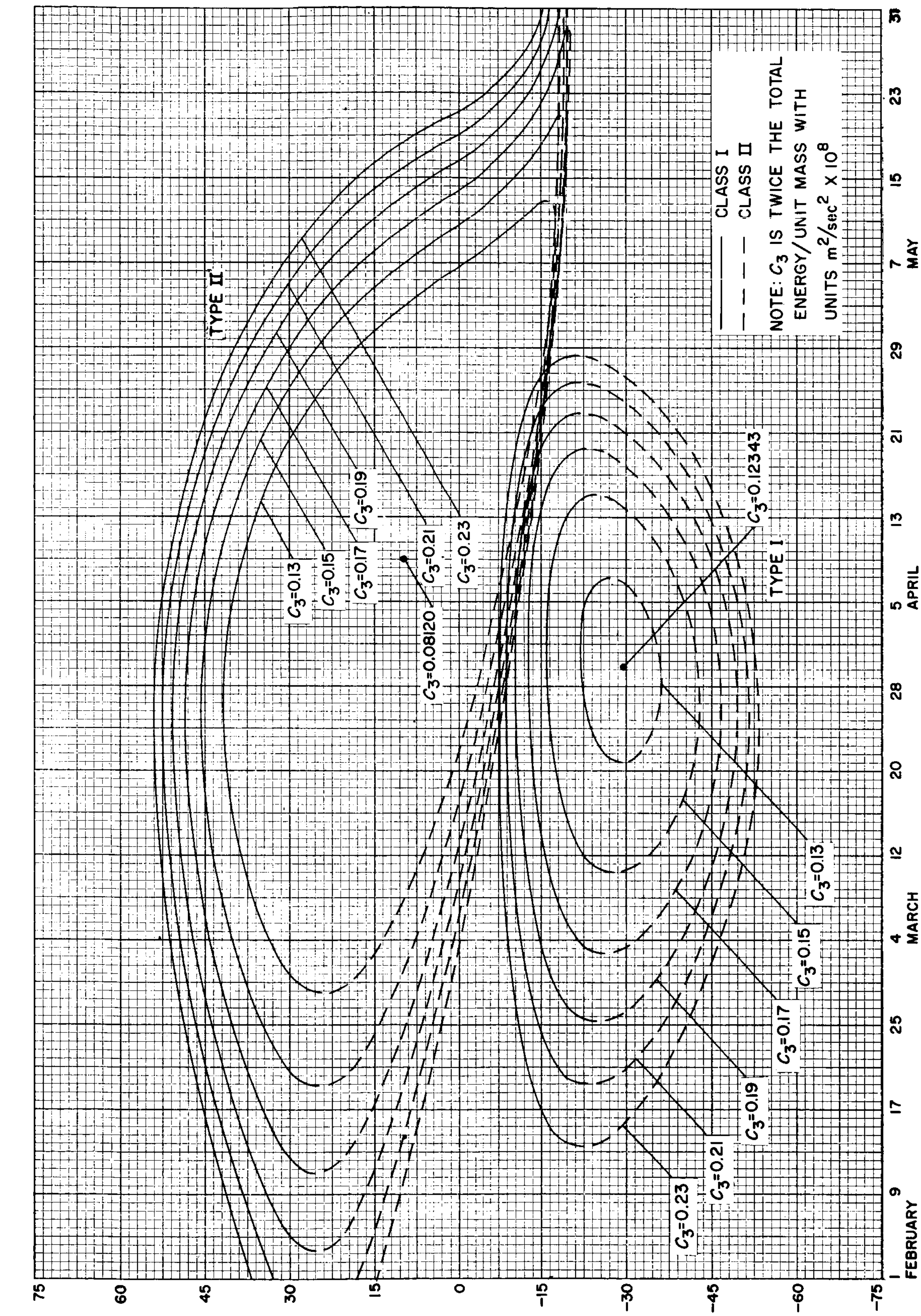

Fig. 3-11. Venus 1964: Angle between outgoing geocentric asymptote and launch planet's orbital plane vs launch date

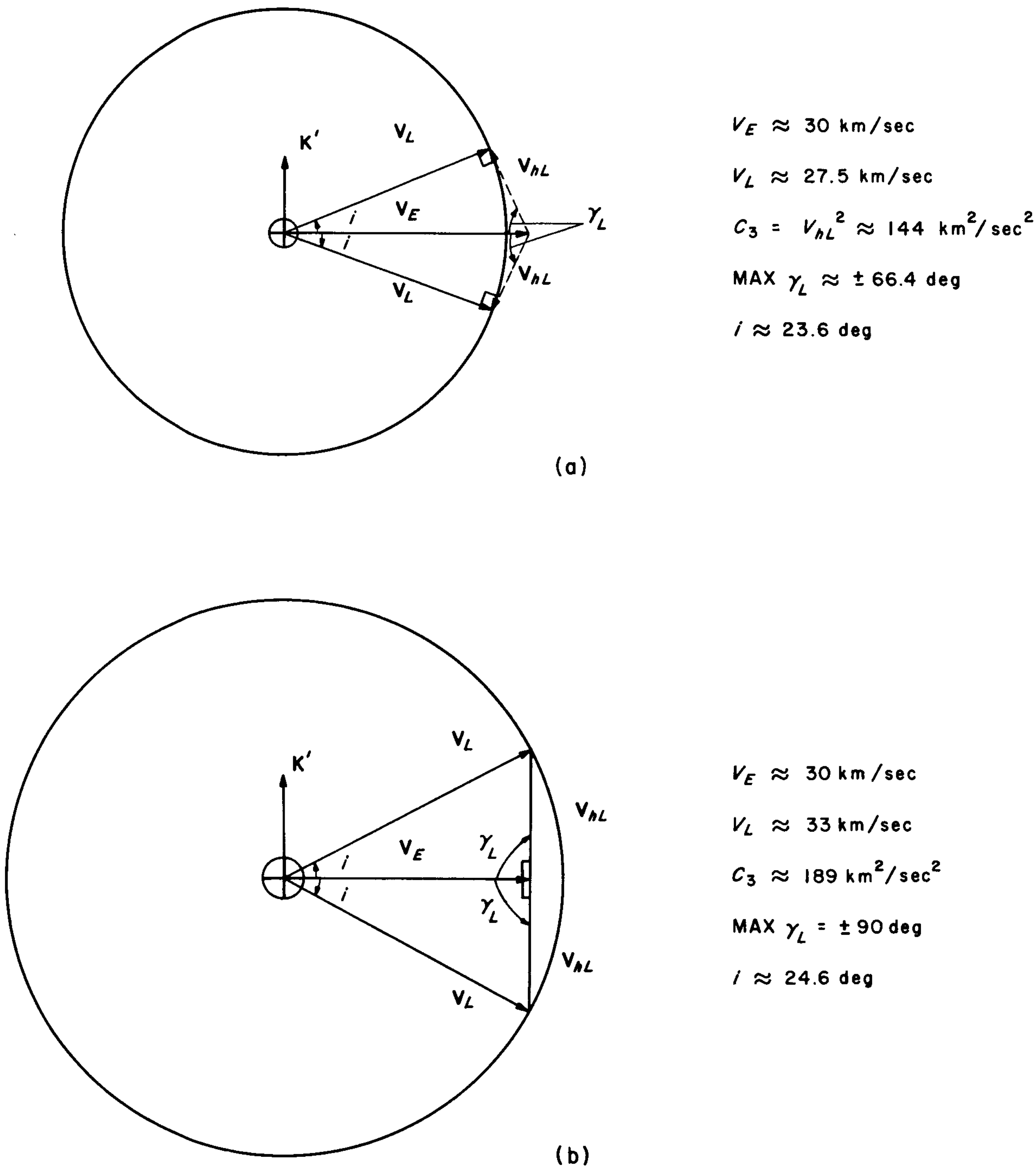

NOTE: PLANE OF PAPER IS PERPENDICULAR TO SUN-EARTH LINE
K' IS UNIT VECTOR ALONG ECLIPTIC NORTH POLE

Fig. 3–12. Geometry for maximum celestial latitude of outgoing asymptote: (a) Rendezvous with Venus; (b) Rendezvous with Mars

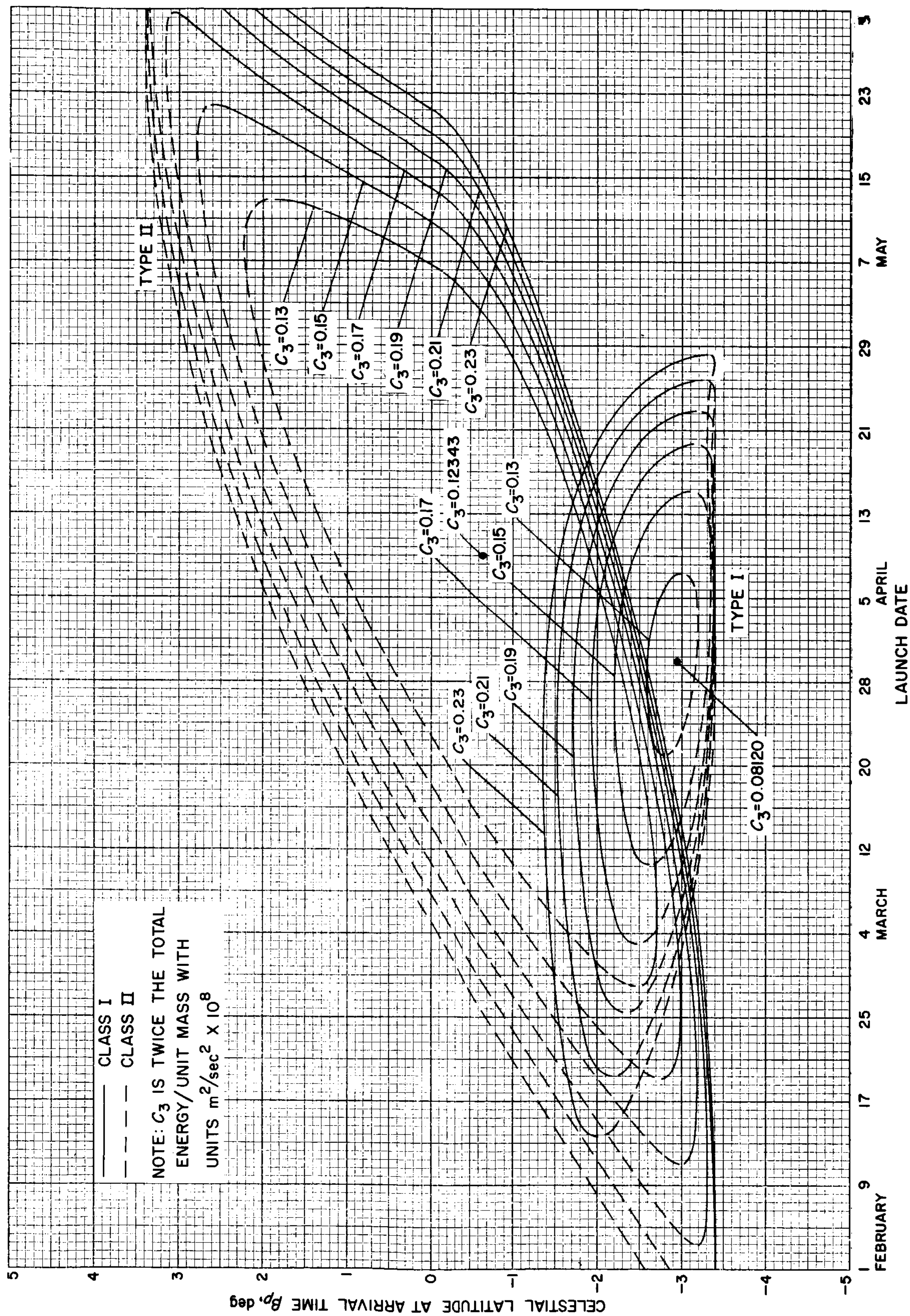

Fig. 3–13. Venus 1964: Celestial latitude at arrival time vs launch date

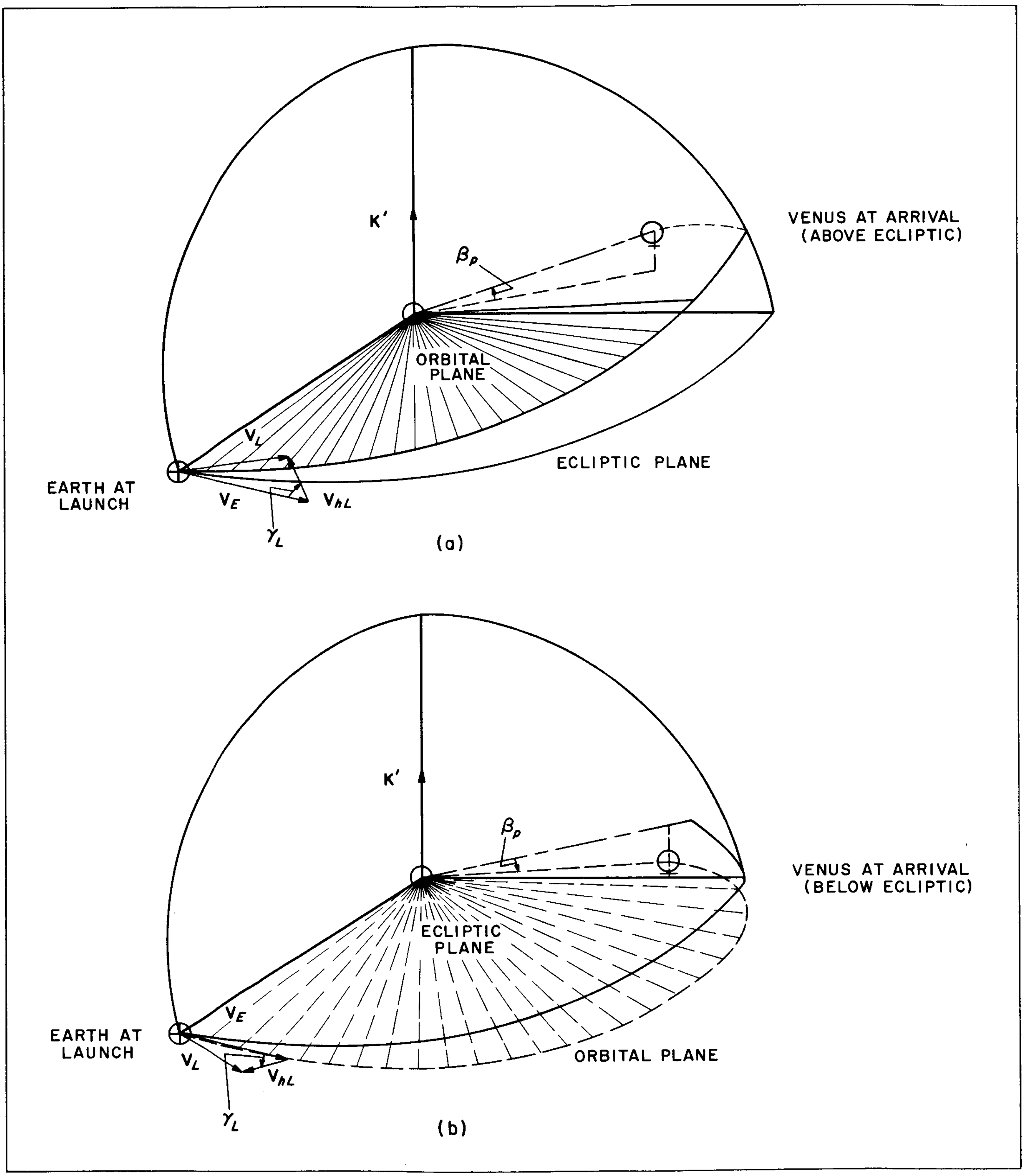

Fig. 3–14. Demonstration of variation of celestial latitude of outgoing asymptote with celestial latitude of Venus at arrival for Type I trajectories: (a) $\beta_p > 0$, $\gamma_L > 0$; (b) $\beta_p < 0$, $\gamma_L < 0$

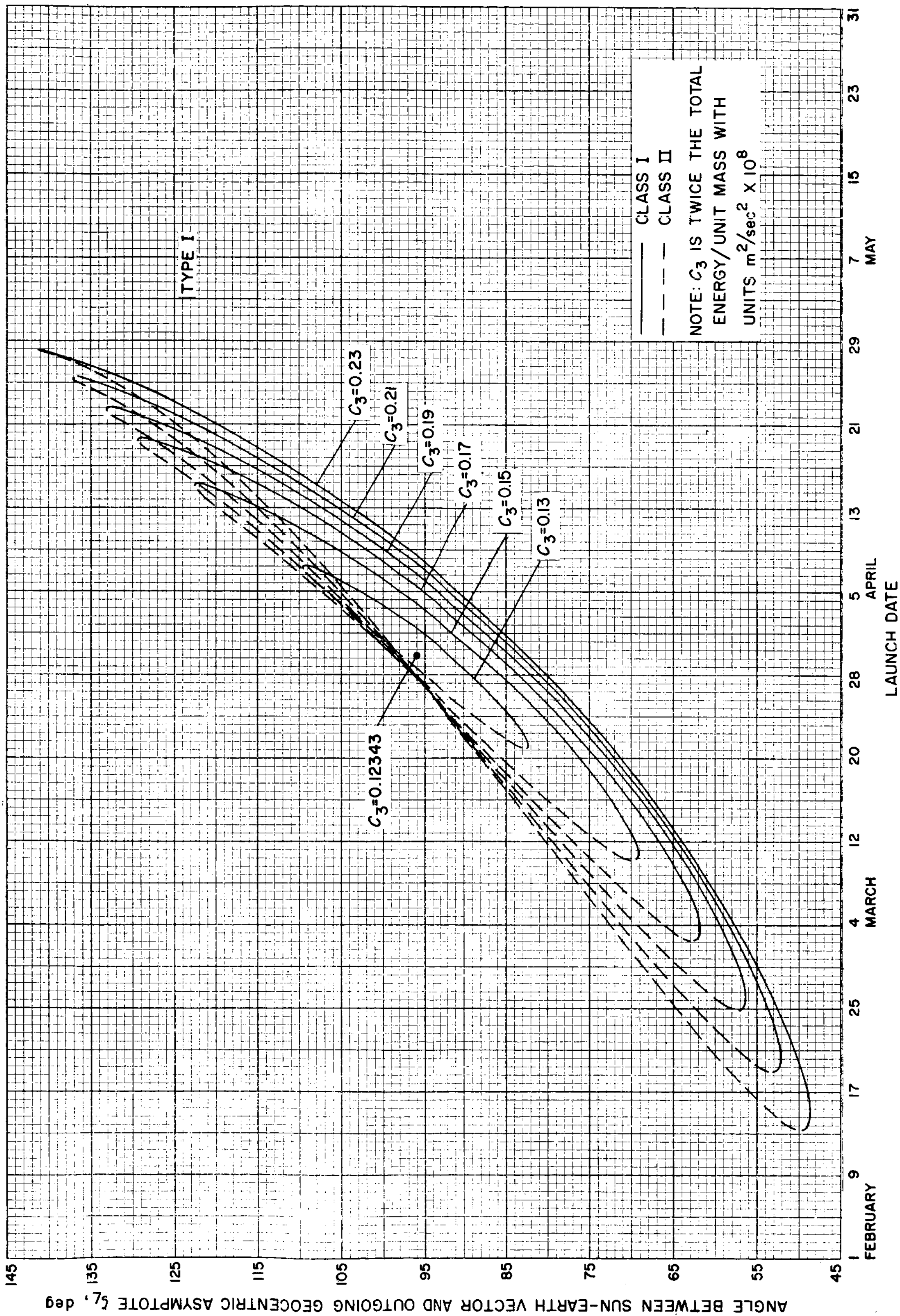

Fig. 3–15. Venus 1964: Angle between Sun–Earth vector and outgoing geocentric asymptote vs launch date, Type I

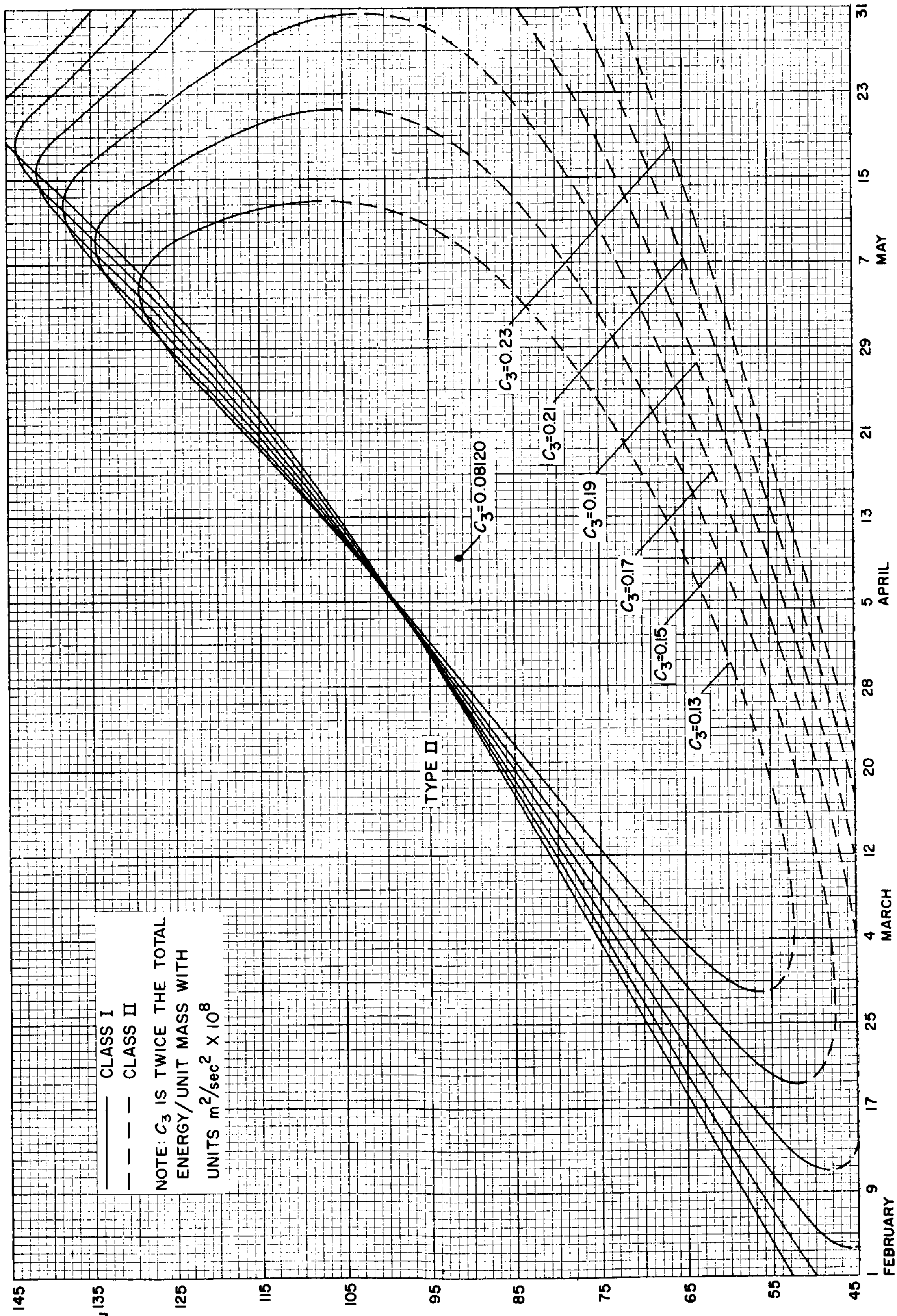

Fig. 3–16. Venus 1964: Angle between Sun–Earth vector and outgoing geocentric asymptote vs launch date, Type II

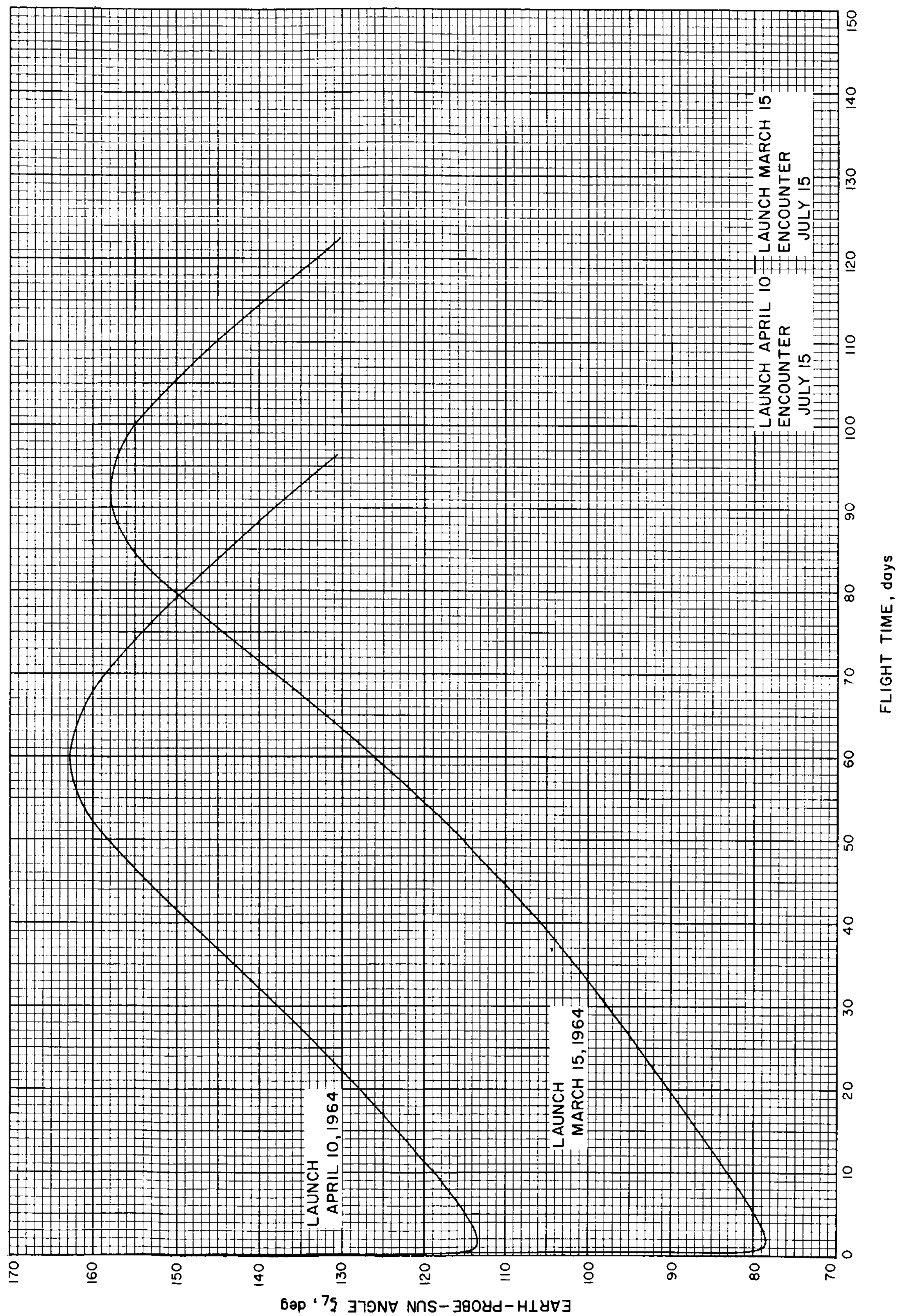

Fig. 3-17. Venus 1964: Earth-probe-Sun angle vs flight time for two launch dates

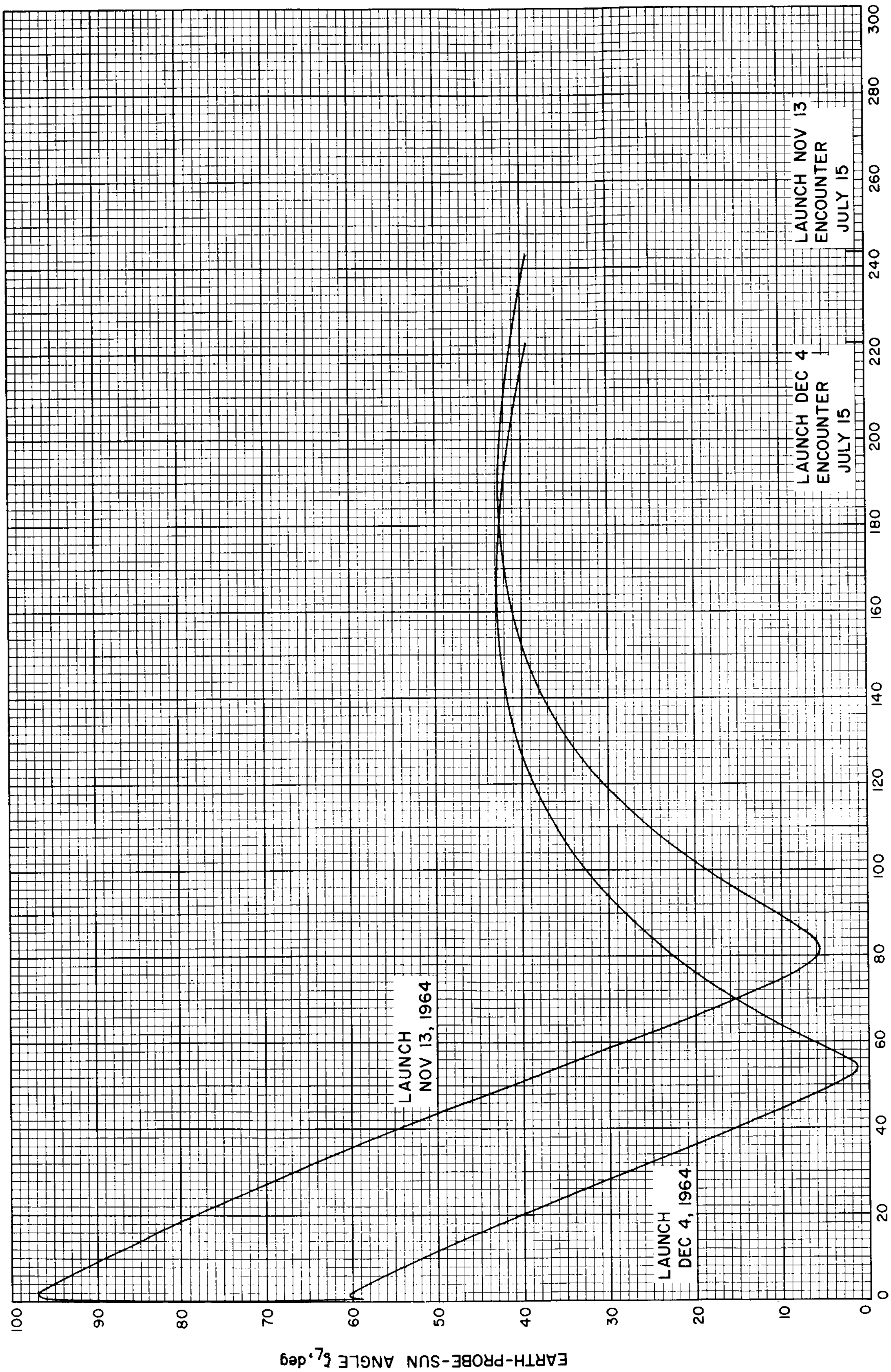

Fig. 3–18. Mars 1964: Earth–probe–Sun angle vs flight time for two launch dates

launch with a 96-day flight time. The Mars trajectories correspond to November 13 and December 4 launchings, with 242- and 221-day flight times, respectively. Inspection of the ζ_L curves in Figs. 3–15 and 3–16, corresponding to the Venus trajectories, shows the angles to be 76 and 111 deg. Corresponding values for the Mars trajectories are 100 and 63 deg. In Figs. 3–17 and 3–18, notice that these four values correspond roughly to the Earth–probe–Sun angle at a few days after launch, and roughly to the part of the curve where the slope is zero. If ζ_L is less than 90 deg for Venus trajectories, it is essentially the minimum Earth–probe–Sun angle during flight to the planet, occurring a few days after launch. If ζ_L is greater than 90 deg, the value still corresponds to the Earth–probe–Sun angle at a few days after launch, but is not necessarily the minimum value during flight. For Mars trajectories, if the parameter ζ_L is roughly greater than 45 deg, it is essentially the maximum Earth–probe–Sun angle during flight to the planet, occurring a few days after launch. If ζ_L is less than 45 deg, the parameter still corresponds to the Earth–probe–Sun angle at a few days after launch, but is not necessarily the maximum Earth–probe–Sun angle during flight.

2. Heliocentric Parameters

To visualize the heliocentric path of the probe from Earth to the target planet, nine key parameters were plotted as functions of launch date and injection energy: flight time, Earth–probe communication distance at encounter, heliocentric central angle, true anomaly of launch and true anomaly of encounter in the heliocentric-transfer orbit, perihelion and aphelion distances[10], inclination of the heliocentric orbital plane to the ecliptic, and celestial latitude of the planet at encounter (with respect to the Sun).

a. True anomaly at launch. As previously mentioned, ζ_L does not vary appreciably over the range of injection energies plotted for a given launch date for Type I trajectories. This implies that the true anomaly at launch in the heliocentric-transfer orbit does not change appreciably for a given launch date. In the curves of true anomaly at launch vs launch date for Venus and Mars 1964 Type I trajectories (Figs. 3–19 and 3–20), it is observed that the variation in true anomoly for a given launch date is less than 10 deg for Venus and less than 20 deg for Mars. In general, for Venus trajectories, if ζ_L is less than 90 deg, the true anomaly at launch in the transfer orbit is less than 180 deg, and heliocentric injections will take place before aphelion of the transfer orbit. However, if ζ_L is greater than 90 deg, the true anomaly at launch will be greater than 180 deg, and heliocentric injection will take place after aphelion of the transfer orbit. For those Venus trajectories having heliocentric injection before aphelion, the maximum Sun–probe distance (aphelion distance) during flight can be found from the curves of aphelion distance vs launch date. For the Venus trajectories having heliocentric injection after aphelion, the maximum Sun–probe distance during flight occurs essentially at launch. From the Venus and Mars 1964 true-anomaly curves, one notes that the true anomaly at launch increases with launch-date delay from the second quadrant to the third, and from the fourth quadrant to the first, respectively. *Thus, toward the beginning of the firing period, heliocentric injection takes place before aphelion for Venus trajectories and, toward the end of the firing period, it occurs after aphelion.* In general, this statement holds for all feasible Type I and Type II trajectories to Venus for each synodic period. A similar conclusion can be drawn for Mars trajectories. *Toward the beginning of the firing period, heliocentric injection takes place before perihelion for Mars trajectories, and after perihelion toward the end of the firing period.* For the Mars trajectories having heliocentric injection before perihelion, the minimum Sun–probe distance (perihelion distance) during flight can be found from the curves of perihelion vs launch date (see Fig. 3–27).

b. True anomaly at arrival. Another parameter of interest is the true anomaly at arrival in the heliocentric-transfer orbit. In observing the graphs, one finds that, for most Type I trajectories to Venus, the true anomaly at arrival is in the fourth quadrant. Thus, planet encounter takes place before perihelion of the transfer orbit, whereas, for most Type II trajectories, encounter occurs after perihelion of the transfer orbit. However, for Venus 1965, one finds that the true anomaly at encounter falls in the fourth and first quadrants for Type I trajectories (see Fig. 3–21). Thus, in this case, encounter occurs before and after perihelion of the transfer orbit for Type I trajectories. Upon observing the Type I trajectories to Mars (Fig. 3–22), one finds that the true anomaly at arrival in the transfer orbit lies in the second and third quadrants. Thus, encounter of Mars occurs *before and after aphelion* for Type I trajectories.

c. Inclination of heliocentric-transfer orbit. The inclination i of the heliocentric-transfer orbit to the ecliptic

[10]These quantities are plotted, even though the probe may not transit perihelion or aphelion. Inspection of the launch and encounter true anomalies will reveal whether they are transversed.

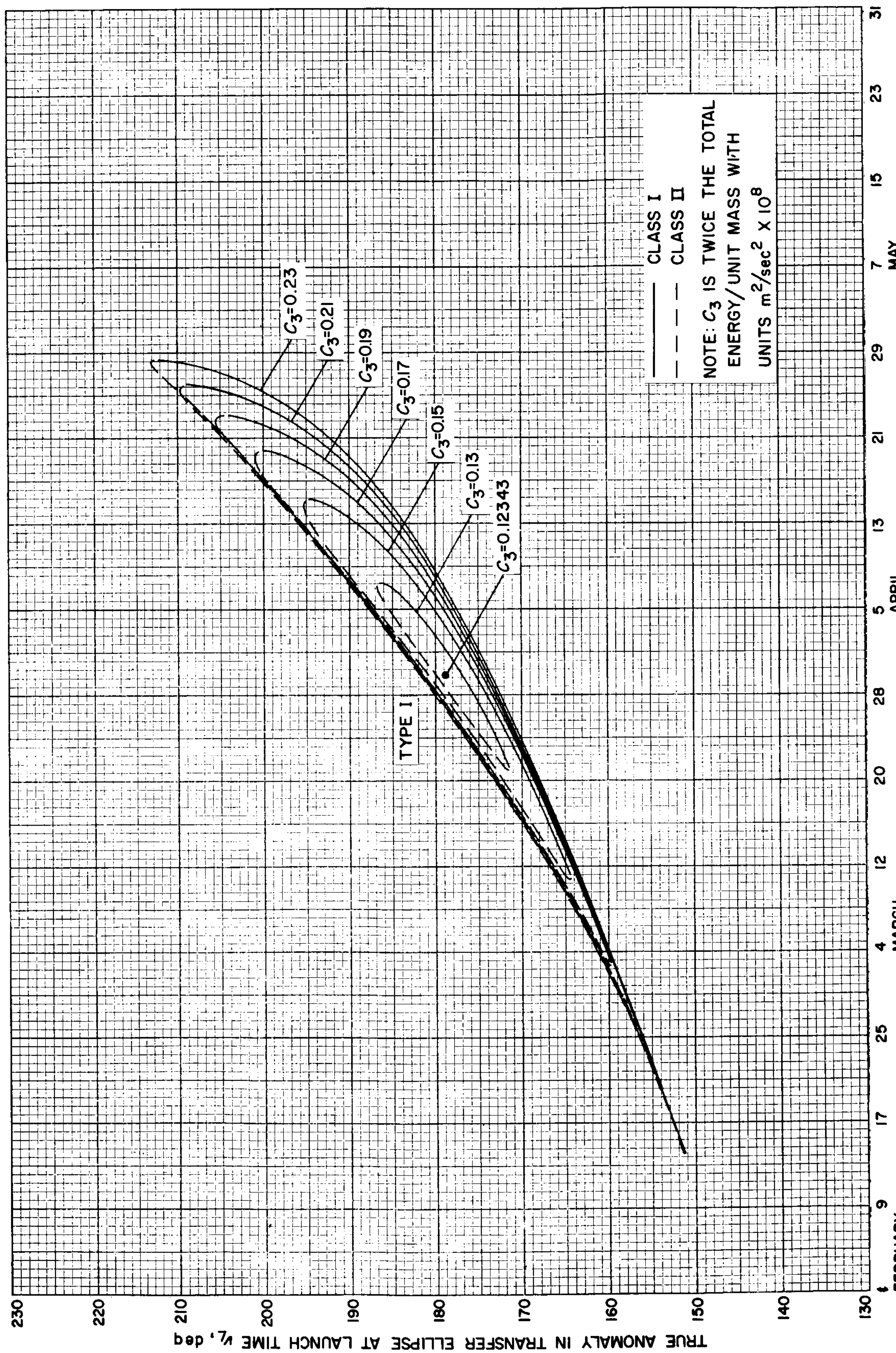

Fig. 3–19. Venus 1964: True anomaly in transfer ellipse at launch time vs launch date, Type I

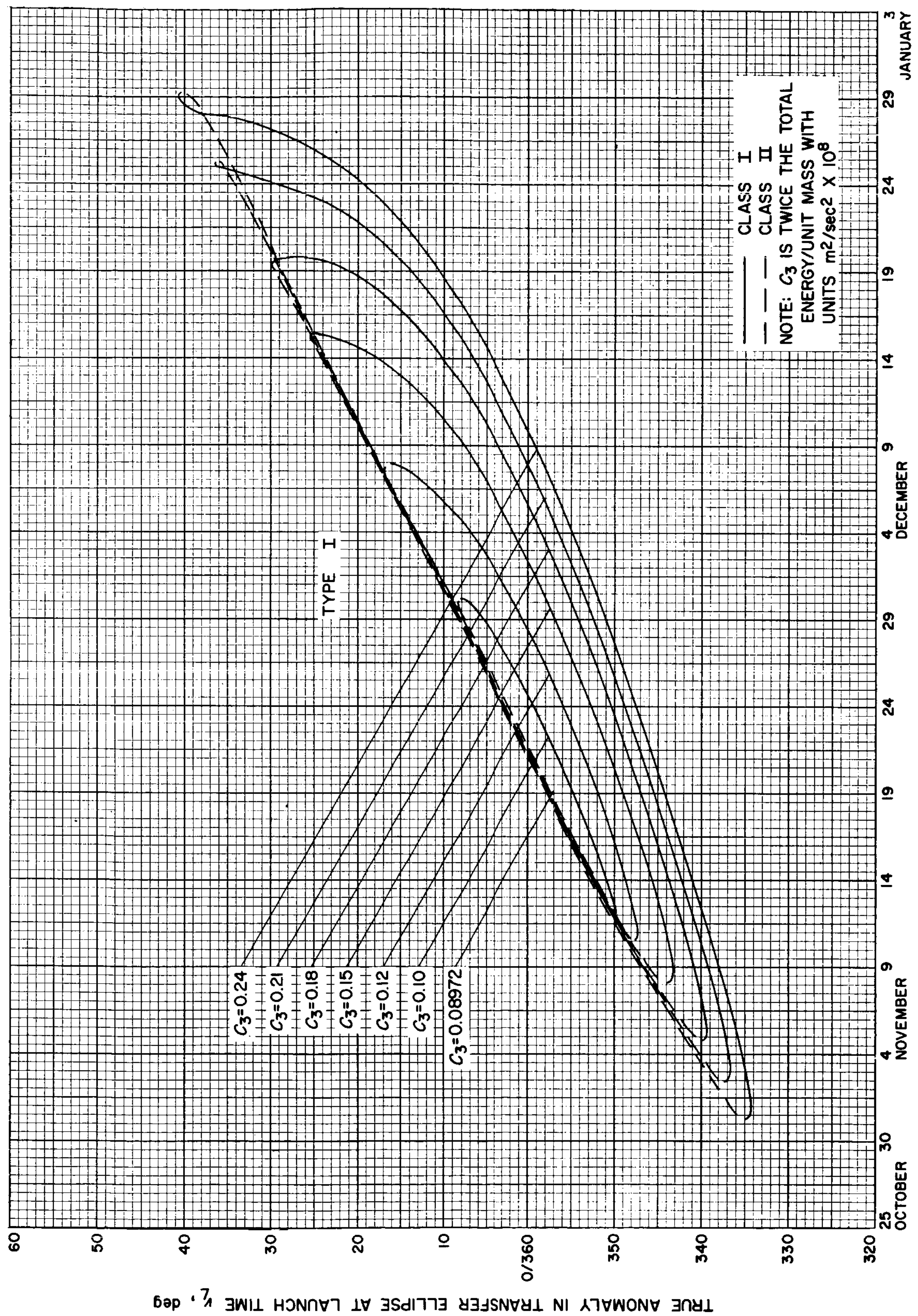

Fig. 3–20. Mars 1964: True anomaly in transfer ellipse at launch time vs launch date, Type I

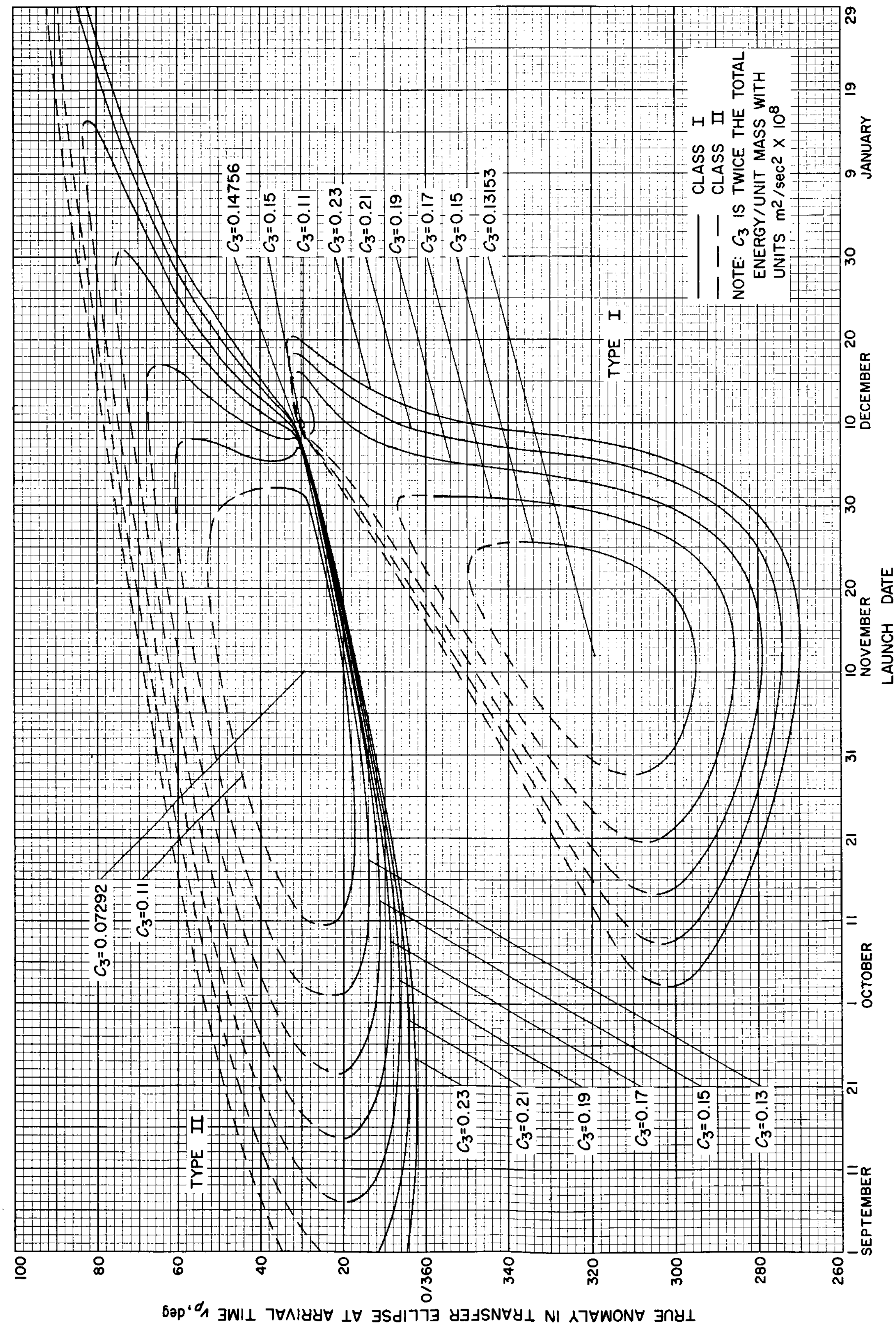

Fig. 3–21. Venus 1965: True anomaly in transfer ellipse at arrival time vs launch date

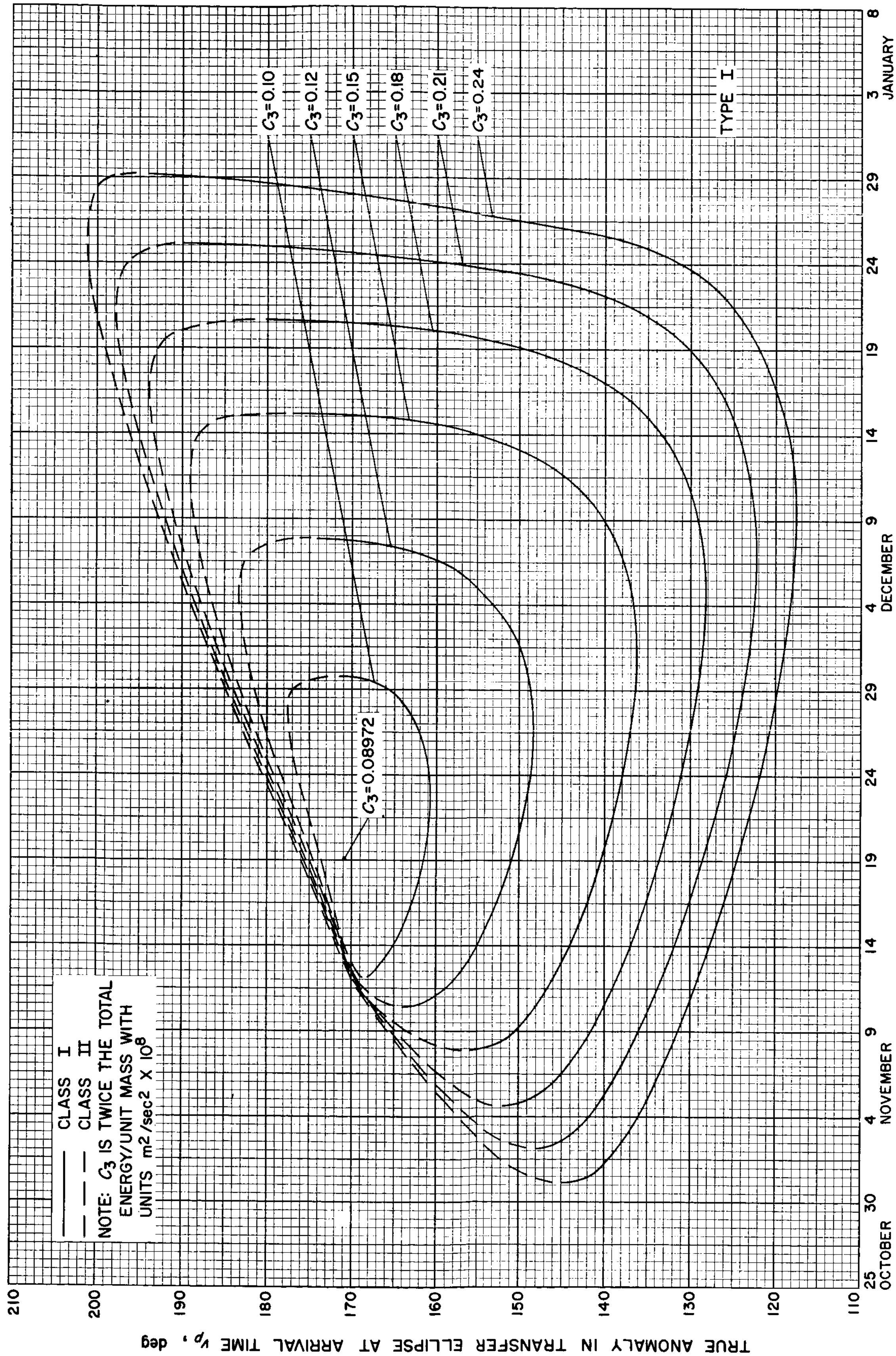

Fig. 3-22. Mars 1964: True anomaly in transfer ellipse at arrival time vs launch date, Type I

plane is essentially a function of two parameters, (1) the heliocentric central angle Ψ, and (2) the celestial latitude β_p of the planet at arrival, since

$$\sin i = \left| \frac{\sin \beta_p}{\sin \Psi} \right| \tag{3-6}$$

If the heliocentric central angle is fixed, and the absolute magnitude of the celestial latitude at arrival is increased, the inclination also increases. If the celestial latitude of the planet at arrival is zero, the inclination is equal to zero, no matter what the heliocentric central angle may be (with the exception of a central angle of 180 deg). However, as shown in Fig. 3-23, if the celestial latitude β_p of the planet at encounter is fixed at an absolute value greater than zero, and the central angle is varied, the inclination will reach its minimum value (equal to β_p) at central angles of 90 and 270 deg, or its maximum value of 90 deg at the central angles equal to β_p, $180 - \beta_p$, $180 + \beta_p$, and $360 - \beta_p$. It is because of the fact that the inclination increases near the central angles of $180 \pm \beta_p$ that Type I–Class II and Type II–Class I trajectories come into existence. The increasing heliocentric inclination eventually results in a sharp increase in energy C_3 as the central angle approaches 180 deg $\pm\beta_p$, thereby bringing the two groups of energy contours into existence. It may now become apparent that the inclination of the heliocentric orbital plane may take on values greater than the celestial latitude of the planet at arrival because of the varying helio-

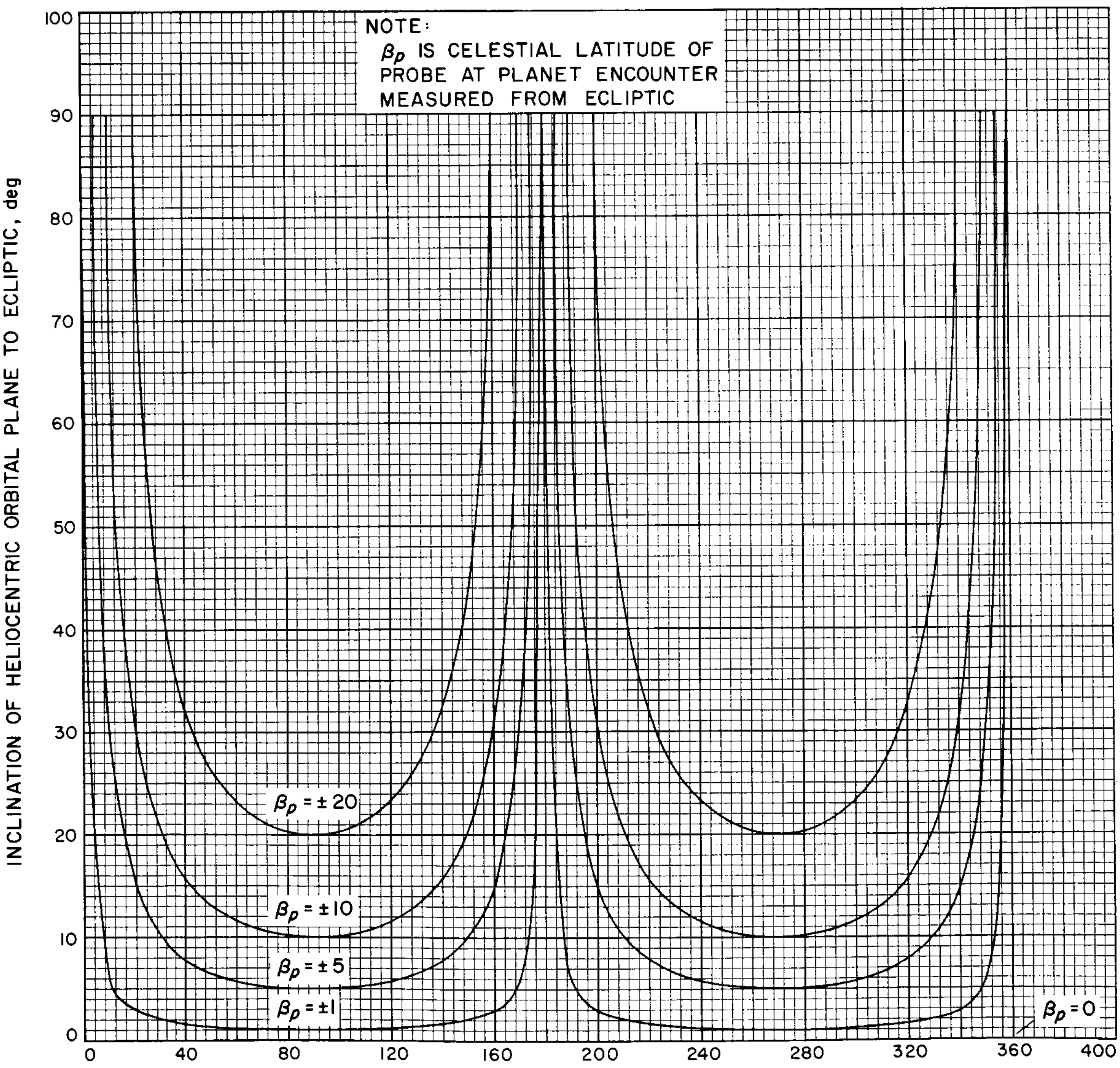

Fig. 3-23. Inclination of heliocentric orbital plane to ecliptic vs heliocentric central angle

centric central angle. In fact, upon observing curves of the inclination vs launch date, one finds the value as high as 8 deg for the range of energies considered here. By definition, the inclination parameter is positive whether the planet at encounter is above or below the ecliptic plane.

3. Planetocentric Parameters

The magnitude and direction of the hyperbolic-excess velocity with respect to the planet are most important in designing and analyzing trajectories near the planet. The planetocentric parameters presented graphically in this Report are: the hyperbolic-excess speed V_{hp}; the right ascension Θ_{sp} and declination Φ_{sp} of the incoming asymptote of the approach hyperbola; the angle between the incoming asymptote and the planet–Sun vector ζ_p, and the angle between the incoming asymptote and the planet's orbital plane γ_p. All these parameters are shown as functions of launch date for various energies.

a. Asymptotic approach speeds. In examining the curves of asymptotic approach velocity V_{hp} (hyperbolic-excess velocity) with respect to the arrival planet, it is quickly found that the range in speed is about the same for a given mission for both Type I and Type II trajectories. For instance, note in the curve of Venus 1964 asymptotic approach speed (Fig. 3–24) that, for a maximum energy of 23 km^2/sec^2, the range in V_{hp} is roughly 3.75 to 10.7 km/sec for both Type I and Type II transfers. Note that the absolute minimum-energy trajectories of both types have different asymptotic speeds: 6.1 km/sec for Type I and 5.4 km/sec for Type II. Also, the Type I trajectory which has the minimum hyperbolic-excess speed at the planet is a Class II–Type I trajectory. For the range of energies considered in the Venus 1964 graph, the trajectory for minimum asymptotic approach speed would have a launch date of April 27 and a flight time of 108 days. If larger energies had been plotted, this minimum-asymptotic-approach-speed trajectory would probably still remain a Class II trajectory; however, the launch date and flight time would be different. In general, one finds that, for both Venus and Mars trajectories, the minimum-asymptotic-approach-speed trajectory is of Type I, Class II, or of Type II, Class I, and varies from mission to mission.

b. Angle between approach asymptote and planet's orbital plane. A second parameter of interest is γ_p, the angle between the approach asymptote and the planet's orbital plane. This parameter varies between −70 and +70 deg for the curves given herein. At first, this variation may appear to be unrealistically high, but one must remember that the approach velocity is taken with respect to the arrival planet and not with respect to the Sun. For an observer on the Sun, the probe at planet encounter appears to be traveling in a direction inclined by only a few degrees to the planet's orbital plane (for low-energy trajectories). When the planet's heliocentric velocity is subtracted from the probe's heliocentric velocity at encounter, the resultant vector (which is, of course, the hyberbolic-excess velocity with respect to the planet) may be greatly inclined to the orbital plane of the arrival planet. The angle between the approach asymptote and the planet's orbital plane is zero only if the probe's heliocentric orbital plane and the arrival planet's orbital plane are exactly coplanar. For Type I trajectories to Venus in 1962, this parameter takes on negative values (approaching from above the planet's orbital plane) from −16 to −62 deg, whereas for 1964 the angle will have the positive range of 8 to 57 deg (approaching from below the planet's orbital plane) as seen from Figs. 3–25 and 3–26. The range of values for the parameter varies from mission to mission. In conclusion, one may add that the parameters V_{hp}, γ_p, and ζ_p (discussed in the following paragraphs) are all essentially functions of the magnitudes of the heliocentric velocities of the probe and planet at encounter, the path angles of the two velocities, and the inclination of the probe's heliocentric velocity to the arrival planet's orbital plane.

c. Angle between approach asymptote and planet–Sun vector. A third parameter to be analyzed is ζ_p, the angle between the approach asymptote and the planet–Sun vector at arrival. This parameter is equivalent to the Sun–probe–planet angle at a few days before encounter. For the Venus trajectories studied, the heliocentric speed of the probe at encounter is greater than that of Venus; thus, the probe essentially "catches up" with Venus in its orbit around the Sun, approaching Venus along its trailing edge (see Figs. 3–27 and 3–28). For the Mars trajectories, the exact opposite is true. The heliocentric speed of Mars at encounter is greater than that of the probe; thus, Mars "catches up" with the probe in its heliocentric orbit. An observer on Mars sees the probe in its heliocentric orbit, approaching from the leading edge of Mars (see Figs. 3–27 and 3–29). For most 1964 Type I trajectories to Venus, ζ_p is an acute angle, whereas, for most of Type II, the angle is obtuse (see Fig. 3–30). However, for the Venus 1965 curve, notice that the angle is obtuse, as well as acute, for Type I trajectories (Fig. 3–31). For most Type I trajectories to Mars, the parameter is an

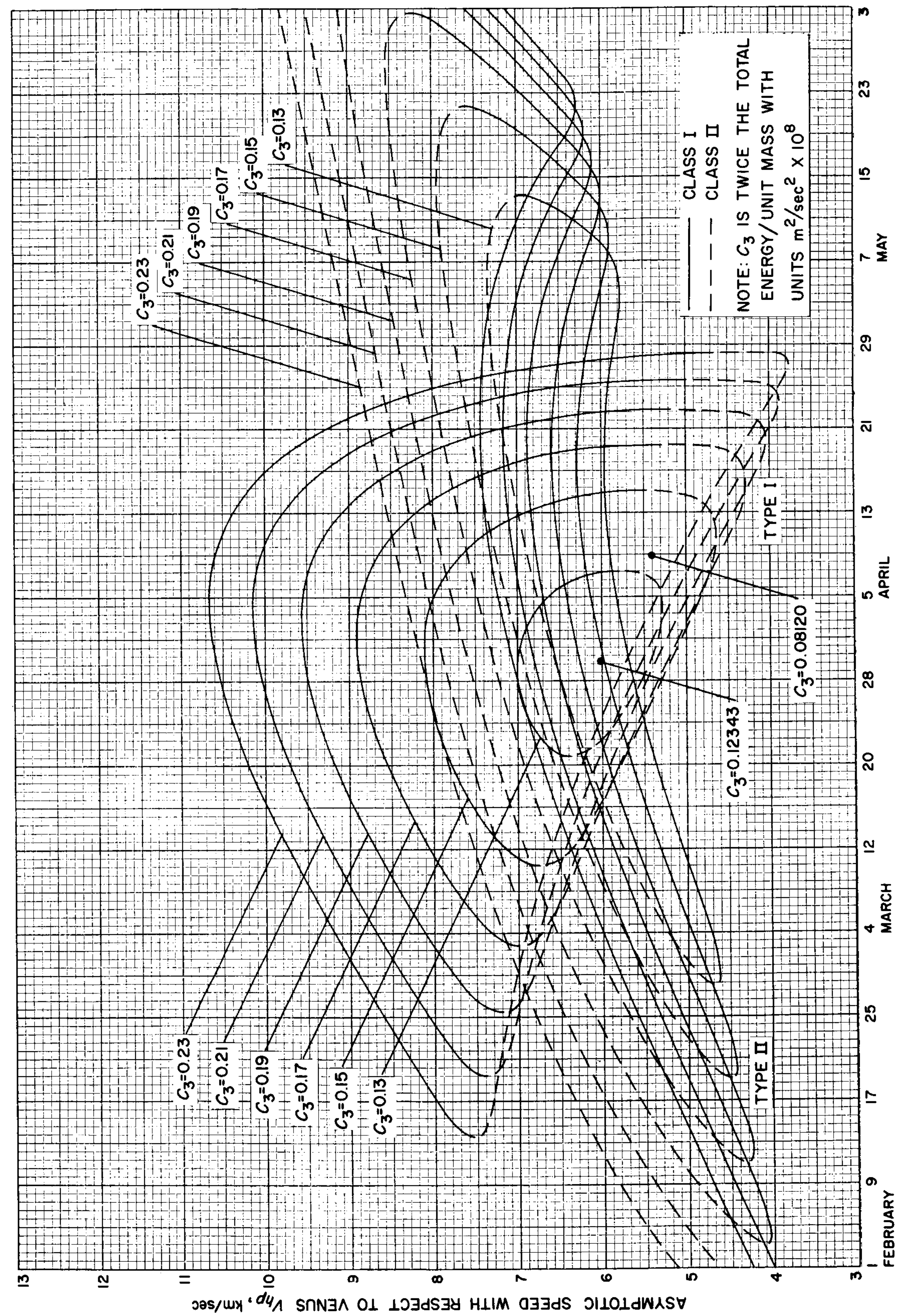

Fig. 3-24. Venus 1964: Asymptotic speed with respect to Venus vs launch date

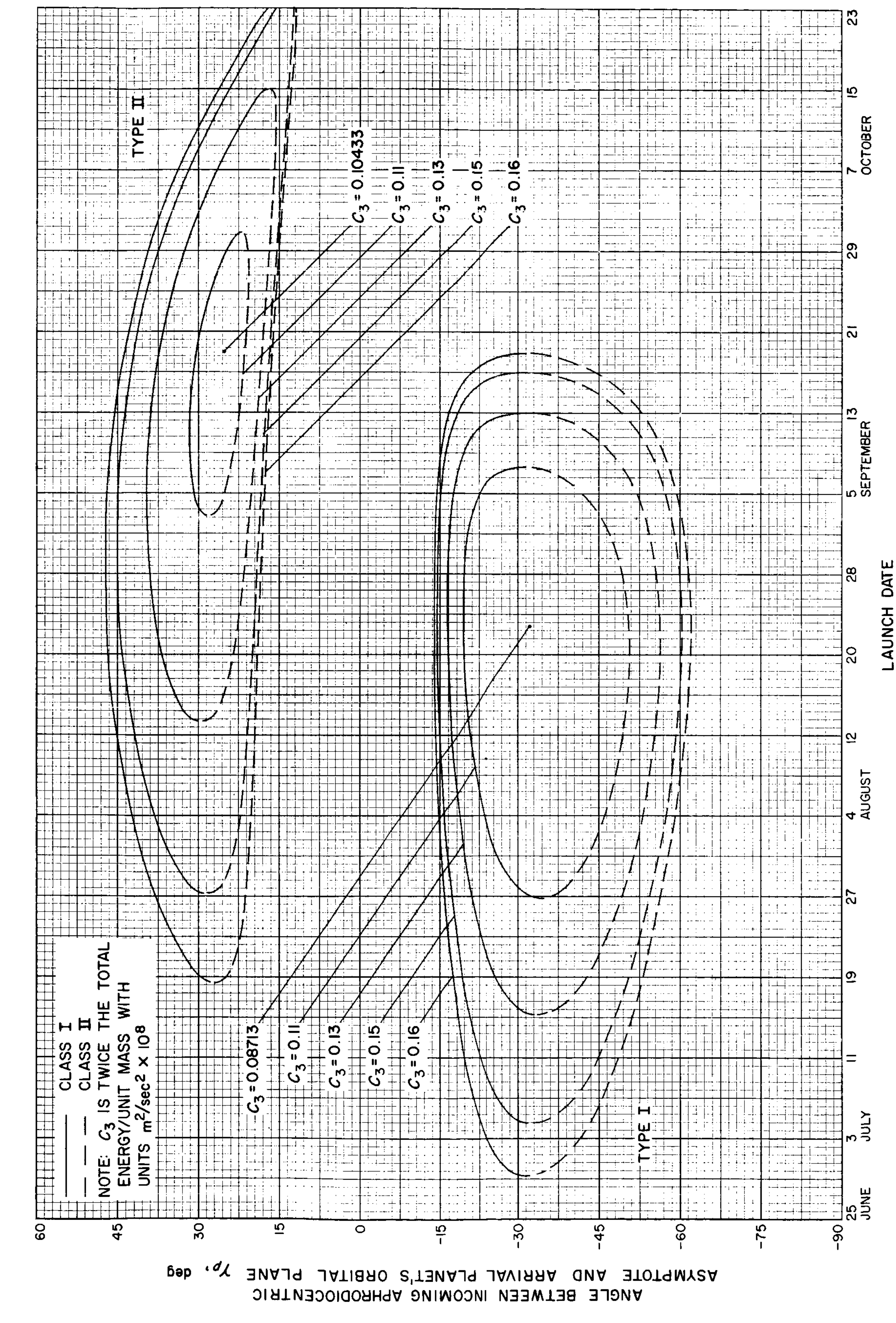

Fig. 3-25. Venus 1962: Angle between incoming aphrodiocentric asymptote and arrival planet's orbital plane vs launch date

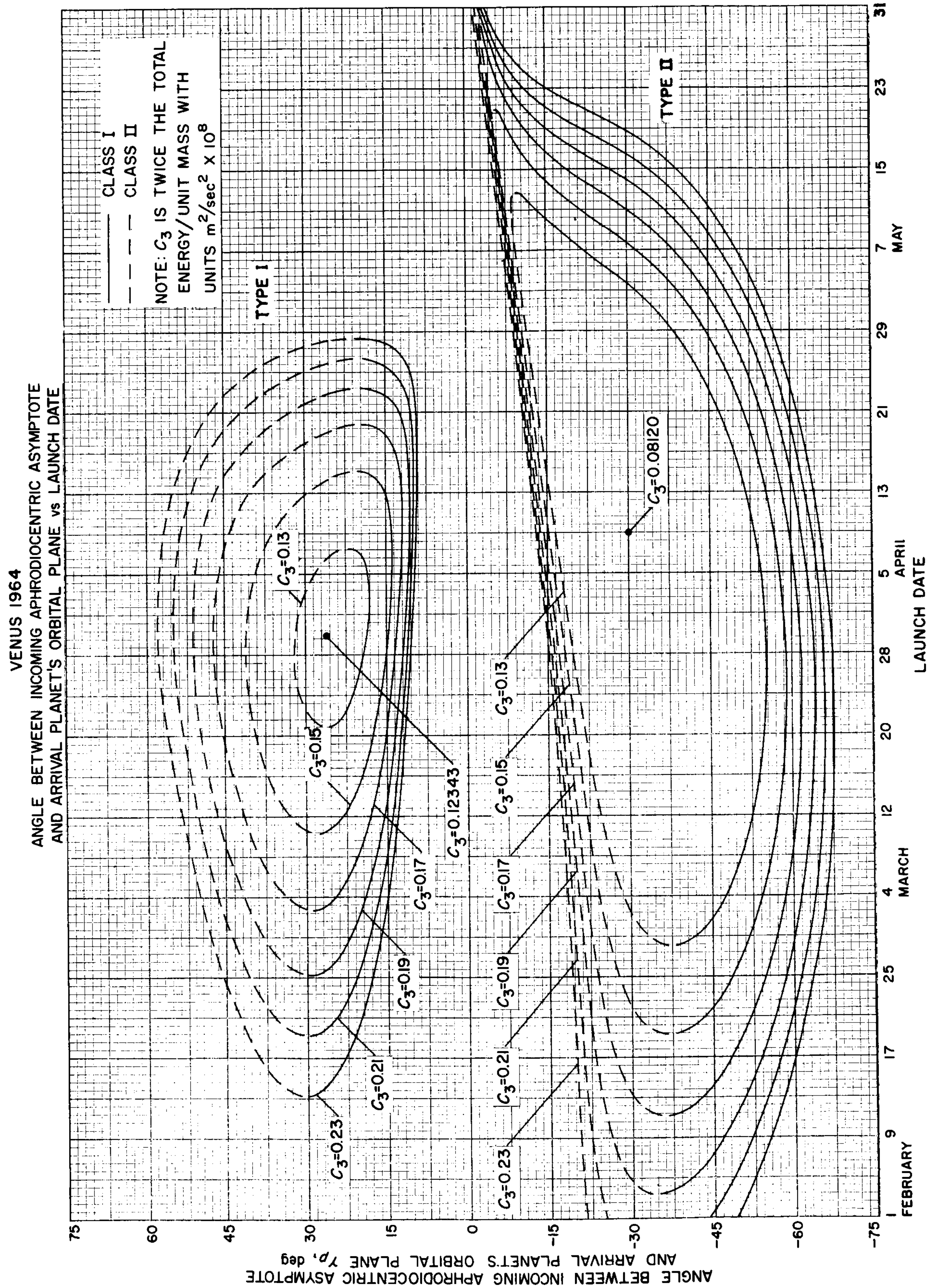

Fig. 3-26. Venus 1964: Angle between incoming aphrodiocentric asymptote and arrival planet's orbital plane vs launch date

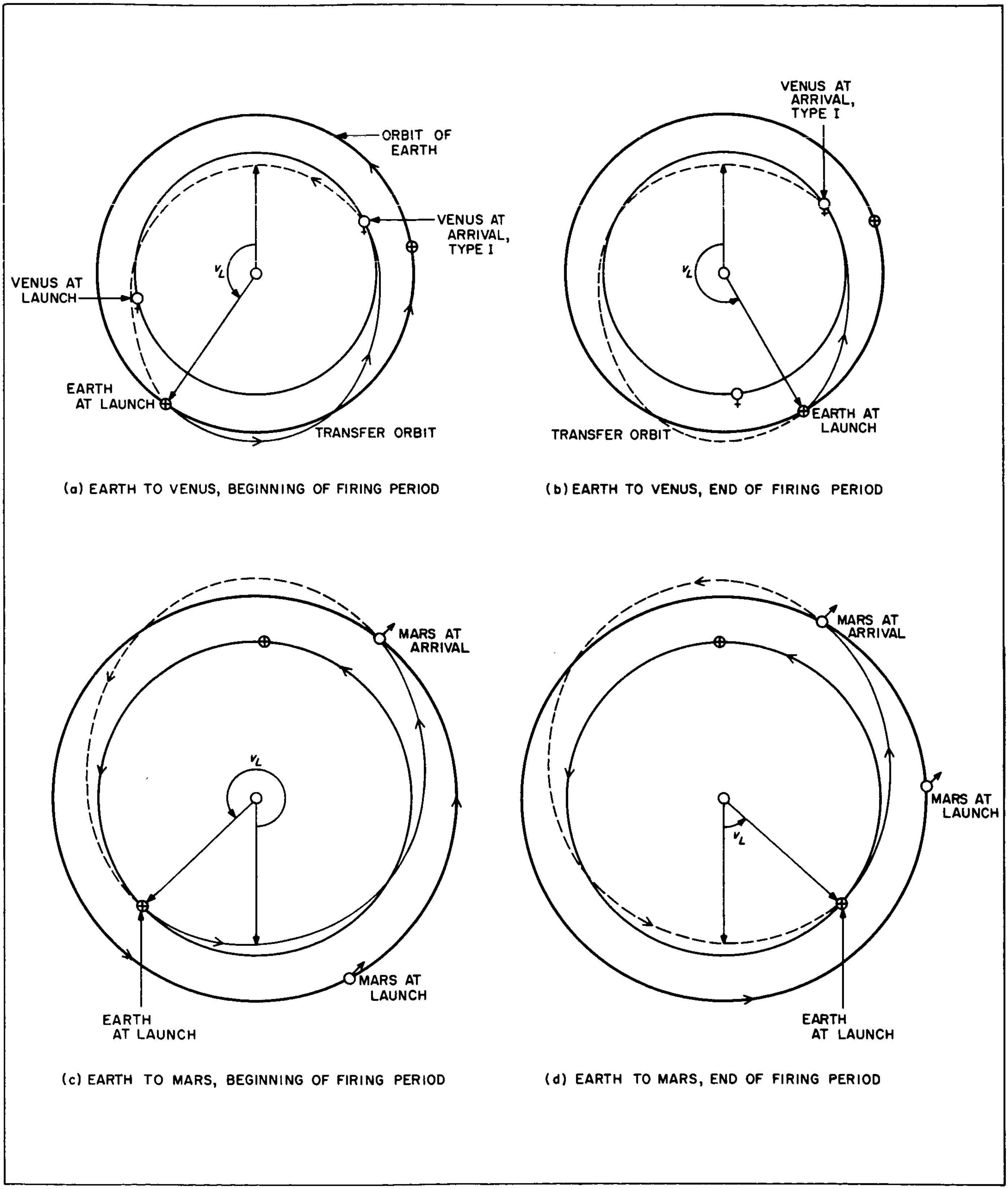

Fig. 3–27. Projection of typical heliocentric-transfer orbits onto ecliptic plane, viewed from above ecliptic plane

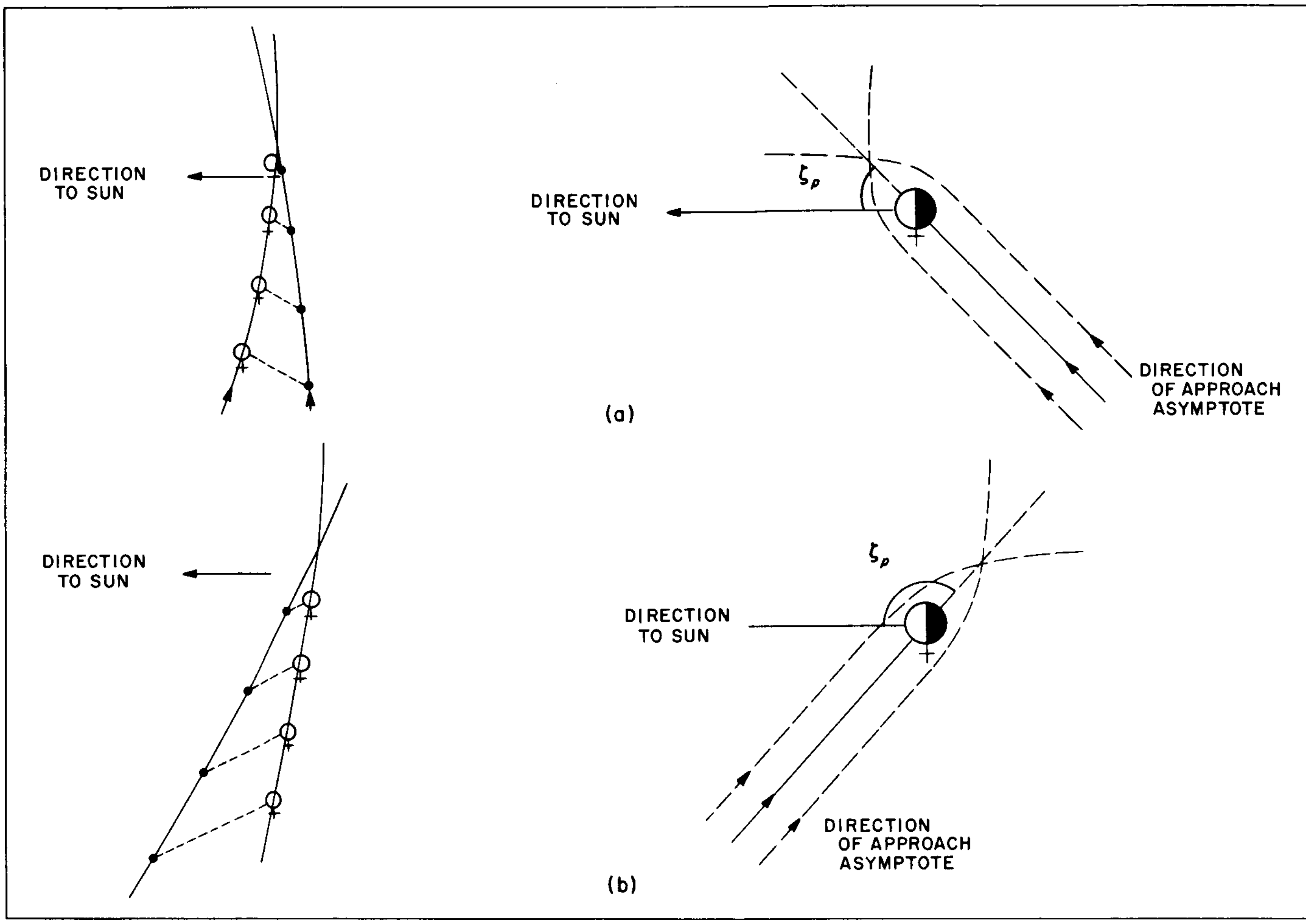

Fig. 3–28. Near-Venus geometry for typical trajectories, viewed from above ecliptic plane: (a) Type I trajectory, encountering Venus before perihelion; (b) Type II trajectory, encountering Venus after perihelion

obtuse angle; however, for some, the angle is acute. Figure 3–32 shows ζ_p for 1964 Mars trajectories. Typical crescent orientations of the illuminated planet, as viewed along the incoming asymptote, are presented in Fig. 3–33.

d. Declination and right ascension of approach asymptote. Two other parameters are plotted which also give the direction of the incoming asymptote: the declination and the right ascension of the incoming asymptote with respect to the arrival planet. The coordinate system is a vernal-equinox equatorial (Earth's) system centered at the planet.

E. Procedures for Utilization of Graphs in Design of Planetary Trajectories

For a trajectory design, a source of information must be available which can be quickly scanned to determine the range of feasible trajectories for a mission. The graphs presented in Sections IV to XVIII of this Report constitute such a source. The order and procedure for actual use of these graphs by the trajectory engineer in the design and analysis of trajectories are now reviewed.

(1) Both Type I and Type II transfers should be scanned. Those trajectories should be selected for which the declination of the outgoing geocentric asymptote lies roughly between −34 and +34 deg. These are the feasible trajectories for launchings from AMR. The algebraic value of the declination reveals vital information concerning the preinjection trajectory (see Ref. 4).

(2) For the trajectories of paragraph (1), the energy requirements (C_3) for various firing periods should be observed. If it is found that booster payload capability and the desired payload weight

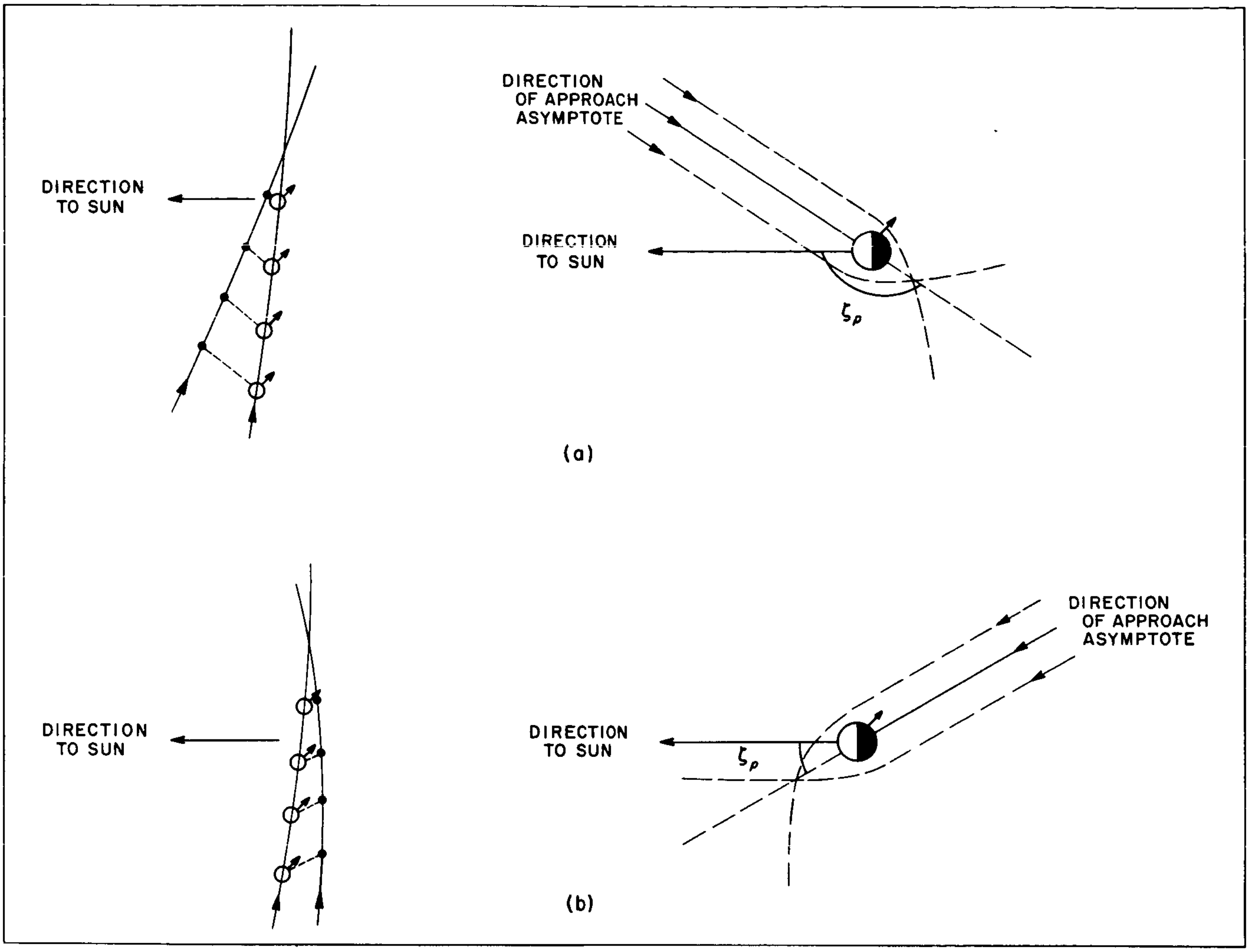

Fig. 3–29. Near-Mars geometry for typical trajectories, viewed from above ecliptic plane; (a) Type I trajectory, encountering Mars before aphelion; (b) Type I trajectory, encountering Mars after aphelion

match the required injection energy for a given firing period (for example, 30 days) and also satisfy paragraph (1) for Type I and Type II trajectories, a decision must then be made to utilize either Type I or Type II trajectories or, perhaps, both.

(3) In making the decision to utilize either the Type I or the Type II trajectory, or both, the curves of flight time and Earth–probe communication distance vs launch date are most helpful. In general, Type II trajectories have longer flight times and Earth–probe distances at encounter than do Type I. The actual differences in magnitude depend on the mission and range of injection energy. In general, the longer the flight time, the greater is the sensitivity of the trajectory to injection errors.

(4) Next, the parameter ζ_L, the angle between the outgoing asymptote and the Sun–Earth vector at heliocentric injection, should be studied. It will be recalled that this is equivalent to the Earth–probe–Sun angle at a few days after launch. Since there are usually many limitations on a spacecraft which is stabilized and controlled in attitude by optical references (such as the Earth and Sun), the Earth–probe–Sun angle may be restricted near the Earth and, perhaps, throughout the flight. The parameter ζ_L is most helpful in trajectory design for determining the constraint near the Earth.

(5) If the value of ζ_L is less than 90 deg for Venus trajectories, the probe is usually being injected into the heliocentric-transfer orbit before aphelion and will travel outside the Earth's orbit before

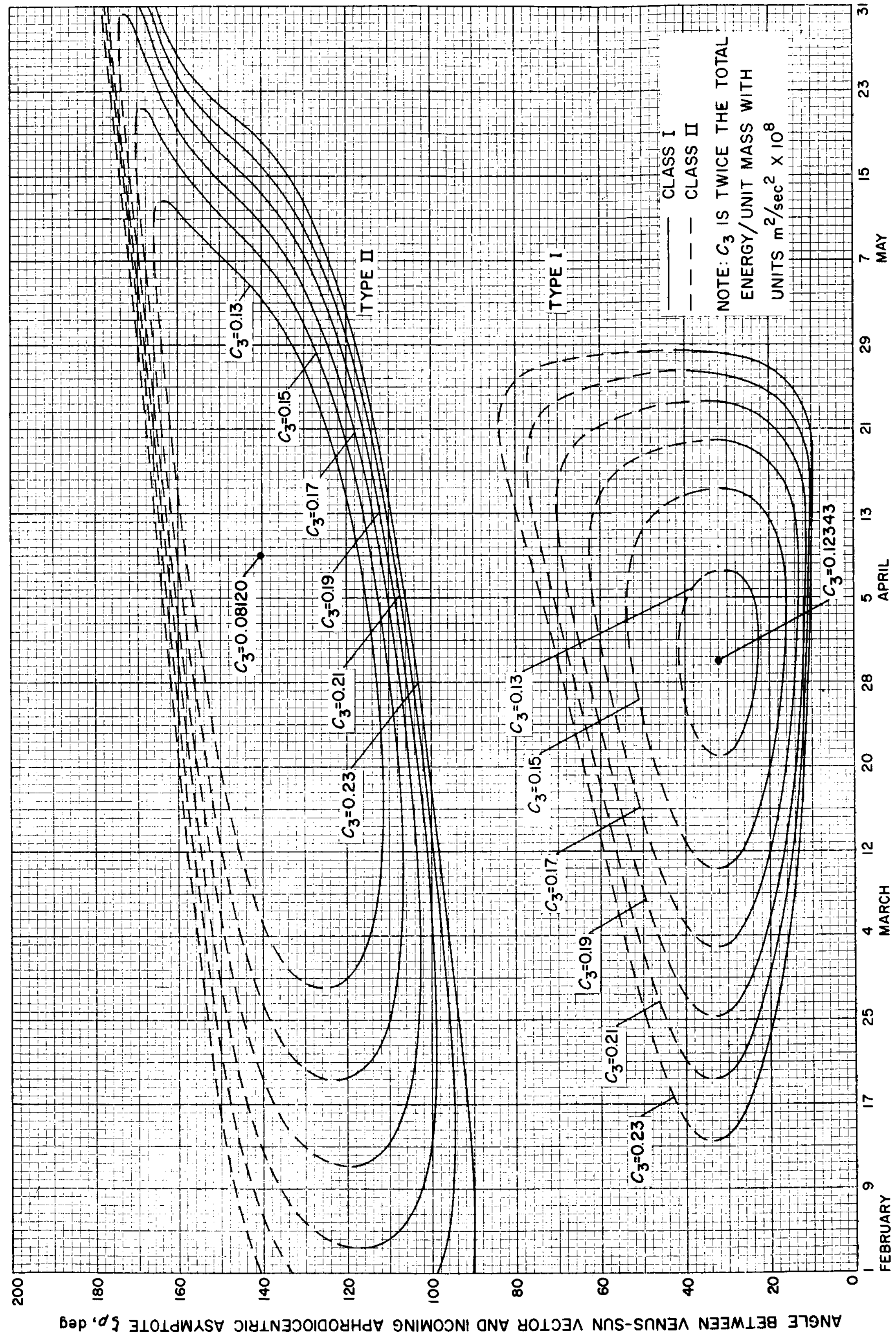

Fig. 3–30. Venus 1964: Angle between Venus–Sun vector and incoming aphrodiocentric asymptote vs launch date

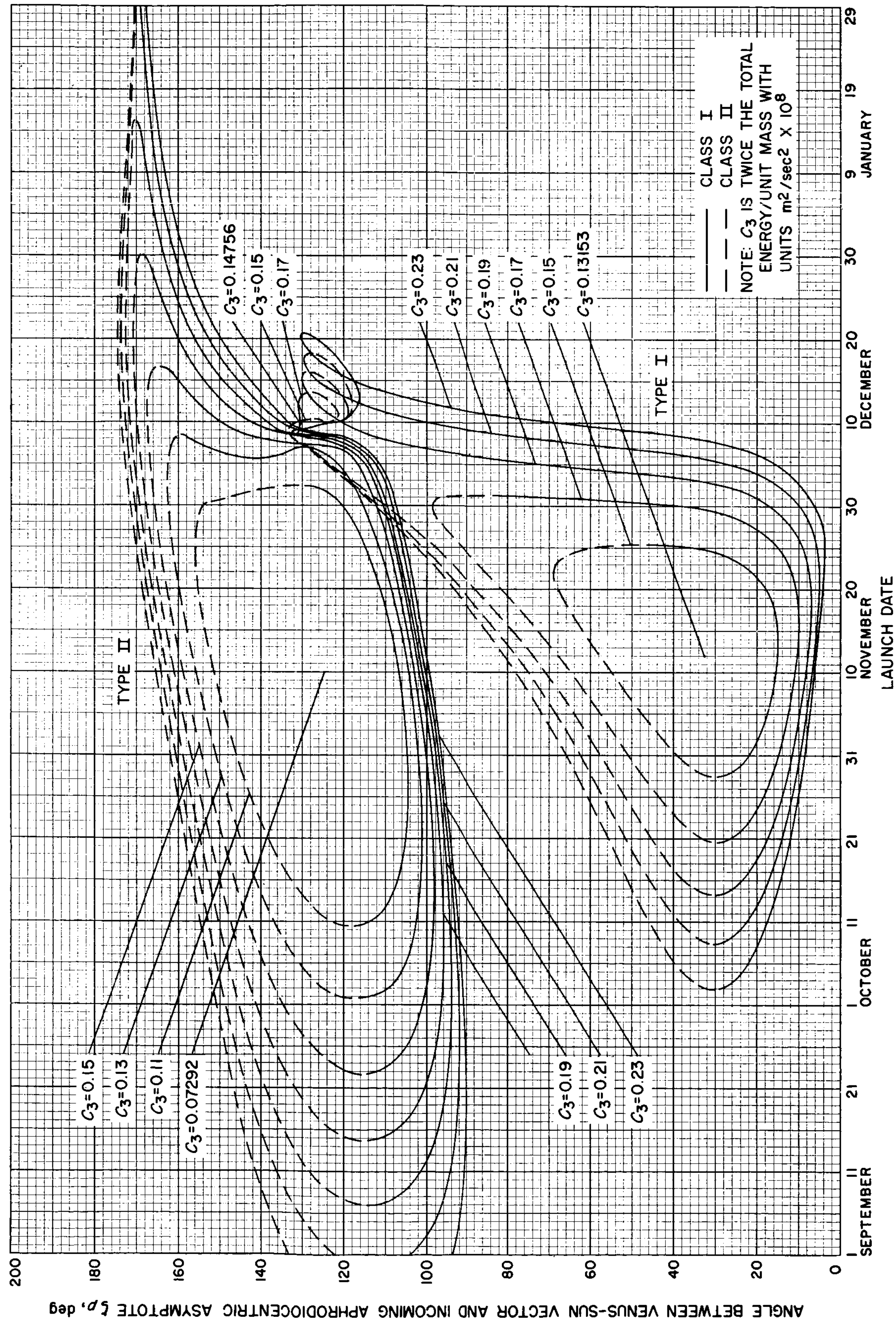

Fig. 3–31. Venus 1965: Angle between Venus–Sun vector and incoming aphrodiocentric asymptote vs launch date

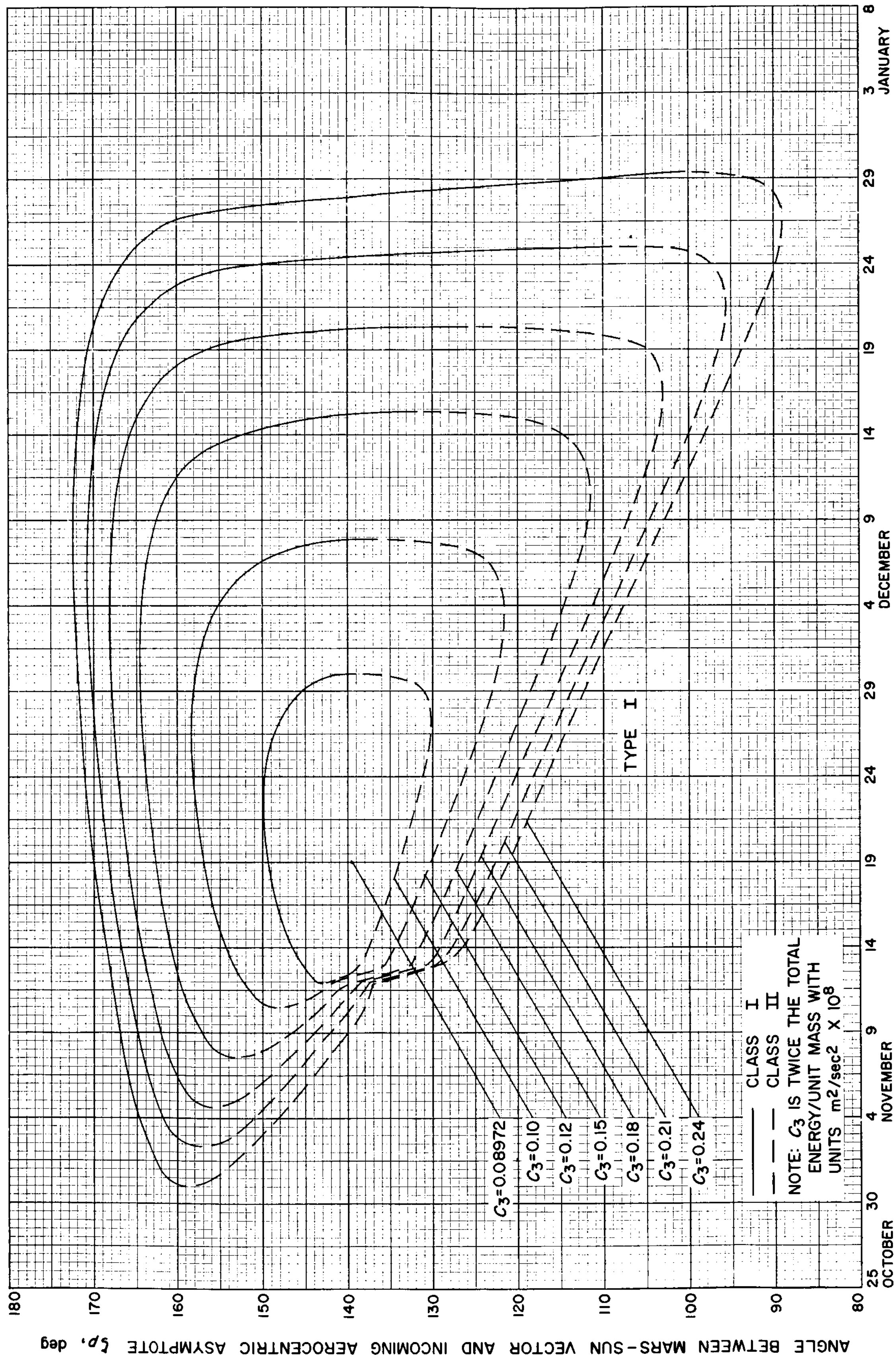

Fig. 3-32. Mars 1964: Angle between Mars–Sun vector and incoming aerocentric asymptote vs launch date, Type I

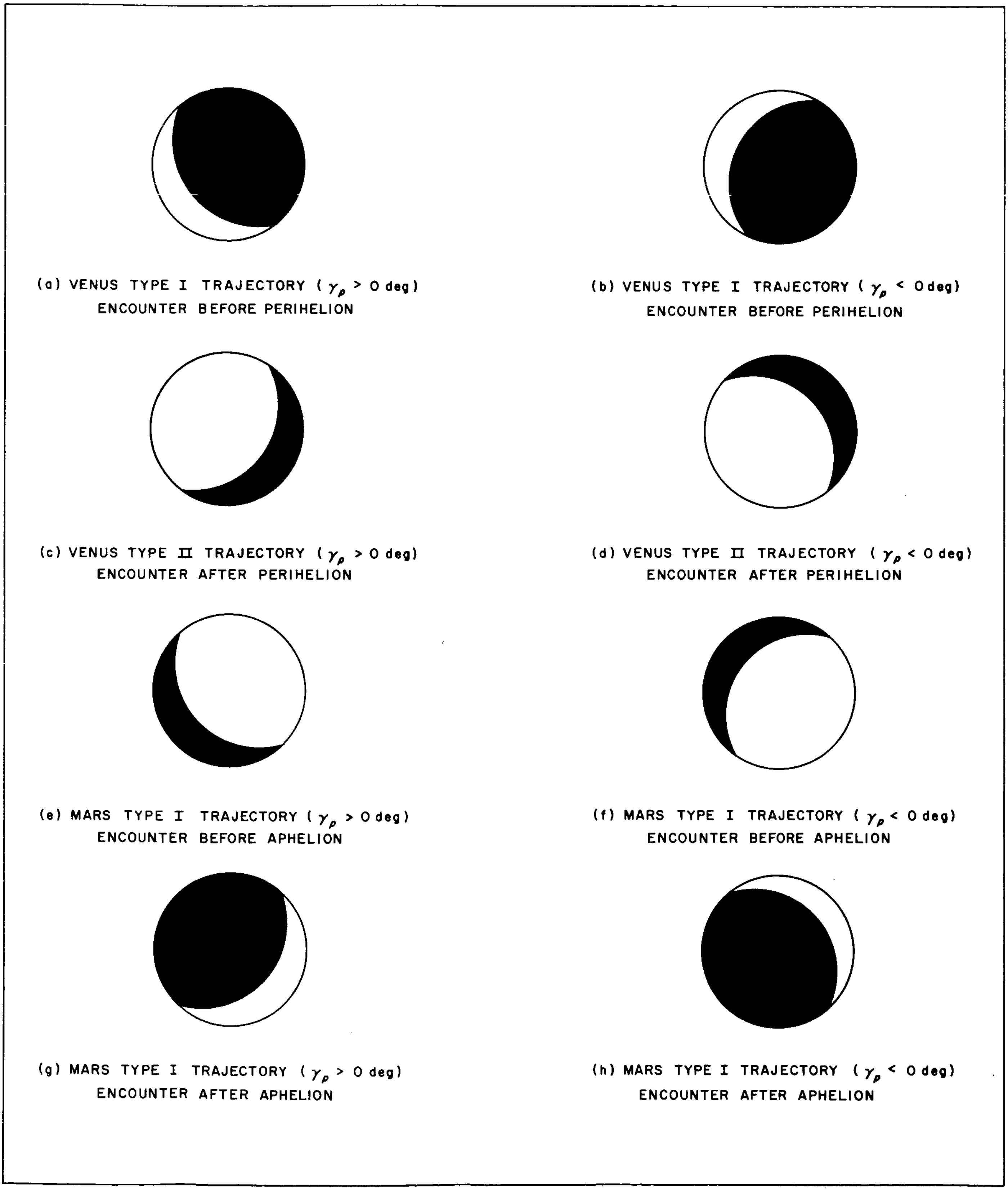

Fig. 3–33. Crescent orientations for typical trajectories to Venus and Mars as observed from approaching spacecraft

"falling" in toward Venus. To be precise, one can observe the curves of true anomaly at launch. Because of temperature-control problems, there may be a restriction on the maximum Sun–probe distance during flight. To determine this maximum distance during flight, one simply finds the aphelion distance of the probe from the graphs. If ζ_L is greater than 90 deg, then the maximum distance during flight to Venus is essentially the Sun–probe distance at launch.

(6) If the value of ζ_L is greater than 90 deg for Mars trajectories, the probe is usually being injected into the heliocentric-transfer orbit before perihelion and will "fall" inside the Earth's orbit before traversing out to Mars. Temperature-control considerations may restrict the minimum Sun–probe distance during flight. To determine the minimum distance, simply find the perihelion of the probe's transfer orbit for the desired trajectory or range of trajectories. If ζ_L is less than 90 deg, the minimum Sun–probe distance during flight to Mars is the distance at launch.

(7) For a spacecraft stabilized and controlled in attitude by Sun and Earth optical references, a constraint may exist which will restrict the Earth–probe–Sun angle to a value greater than 0 deg by a few degrees or less than 180 deg by a few degrees. This immediately implies that a trajectory must be chosen that has an inclination of the heliocentric orbital plane to the ecliptic which is *greater than 0 deg*. To satisfy the above constraint, the inclination may have to be 0.25, 0.50, or even 1.0 deg, depending on the restriction and on the trajectory itself. The values of the orbital inclinations for specific trajectories can be found from the graphs in Sections V to XVIII.

(8) For essentially all feasible Type II trajectories to Venus and a few of Type I, Venus encounter for some missions will take place *after* perihelion of the transfer orbit. This means that the probe will pass closest to the Sun several days or, perhaps, several weeks before encounter, depending on the trajectory. Because of temperature-control requirements, there may be a restriction on the minimum Sun–probe distance during flight. To determine the value of this parameter, one finds the perihelion distance of the probe for the desired trajectory from the graphs. This parameter is the minimum Sun–probe distance during flight to Venus if the true anomaly of arrival is in the first or second quadrant.

(9) For Type I trajectories to Mars, encounter usually takes place before aphelion of the transfer orbit. For those trajectories having true anomalies at arrival in the third or fourth quadrant, however, encounter will take place after aphelion. This means that the maximum Sun–probe distance during flight occurs before encounter. Temperature-control considerations may restrict the maximum Sun–probe distance during flight. To determine this maximum for the necessary trajectories, find the value of the aphelion distance from the graphs in Sections XII to XVIII.

(10) For planetary missions such as landers or orbiters, it will probably become necessary to utilize trajectories for which the hyperbolic-excess speed at the planet is nearly minimum. In fact, in order to maximize the scientific-payload weight, a "trade-off" must be made in minimizing the geocentric energy or planetocentric energy. Such trajectories will allow the heaviest payloads to be landed on the planet or injected in a desired elliptical orbit around the planet with the use of retro-maneuvers. The trajectory designer can find the values of the hyperbolic-excess speeds at the planet for various trajectories from the graphs in Sections V to XVIII, and can determine the feasibility of the trajectories from the procedures in paragraphs (1) to (9).

(11) For a spacecraft which is stabilized and controlled in attitude by optical references, there may be certain restrictions on the Sun–probe–planet angle as the probe approaches the planet. Such restrictions may be necessary because of approach-guidance considerations. The parameter ζ_p, the angle between the approach asymptote and the target-planet–Sun vector, is equivalent to the Sun–probe–planet angle a few days before encounter. The parameter can be most helpful in analyzing permissible trajectories near the planet.

(12) Regarding the design of trajectories near the planet, it is needless to say that, by altering the parameters in the preinjection trajectory near Earth by small increments, the probe can be made to pass on any side of the planet. However, the inclinations of the planetocentric hyperbolic orbit (or elliptical orbit, assuming that the required retro-maneuver is made in the orbital plane of the hyperbola) to the planet's orbital plane depends

on the aiming point at the planet, as well as on the parameter γ_p, the angle between the approach asymptote and the planet's orbital plane. The minimum inclination which can be attained is equal to γ_p. If γ_p is zero, the inclination of the orbit to the planet's orbital plane will range from 0 to 180 deg, depending on the aiming point. Inclinations of 0 to 90 deg imply direct motion (in the direction of the planet's orbital rotation), whereas inclinations from 90 to 180 deg imply retrograde motion (opposite to the planet's orbital rotation). If $\gamma_p = \pm 45$ deg, the inclination may range from 45 to 135 deg for all aiming points. If $\gamma_p = \pm 90$ deg, the inclination will equal 90 deg for any aiming point which is chosen at the planet. For $\gamma_p > 0$ deg, the probe will approach the planet from a path below the planet's orbital plane; for $\gamma_p < 0$ deg, the approach will be from above. In many cases, it may be desirable to design the near-planet trajectory with a prescribed inclination in mind such that the probe will pass the target body in the planet's orbital or, perhaps, equatorial plane. It is thus apparent that the parameter γ_p may or may not permit the selected pass. To find the value of γ_p for a given trajectory, observe the curve of γ_p vs launch date for the desired mission.

(13) To comprehend fully the significance of each parameter and its variation with launch date and arrival date, it may be advantageous to construct the loci of constant arrival dates on each pertinent graph in Sections V to XVIII. This may be done in three steps, as shown in Fig. 3–34:

(a) Construct the loci of desired arrival dates on the curves of flight time vs launch date.

(b) Mark the launch dates and geocentric energies for which intersection of the arrival loci and the various energy contours occur.

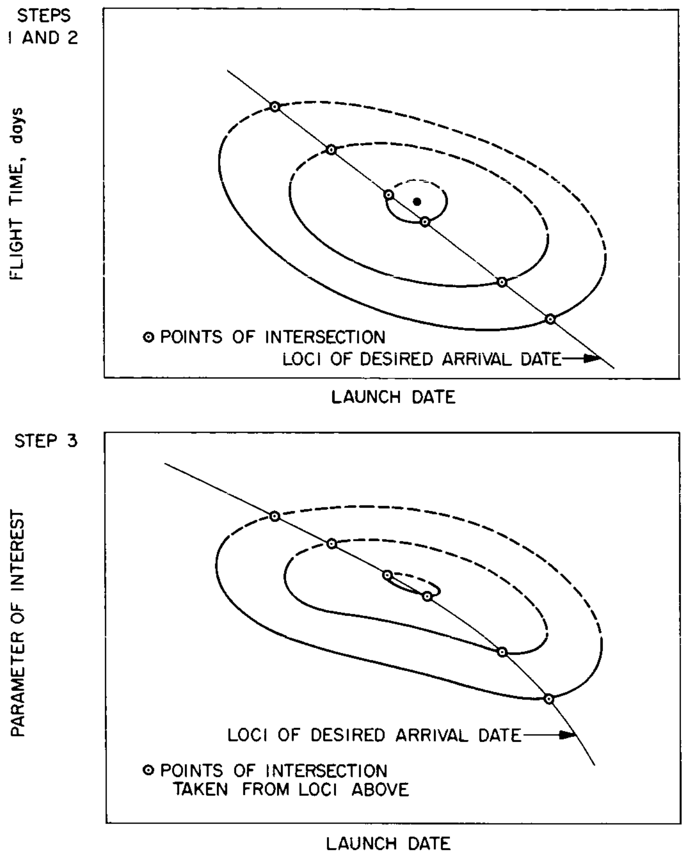

Fig. 3–34. Steps for construction of arrival-date loci

(c) Take the intersection points of (b) and construct the arrival-date loci on the graph of interest.

Experience has shown that trajectory parameters tend to exhibit an invariance if the arrival date is held fixed while the launch date is varied. This fact has proved very useful in trajectory design.

IV. MINIMUM-ENERGY GRAPHS FOR VENUS AND MARS TRANSFERS

Figure

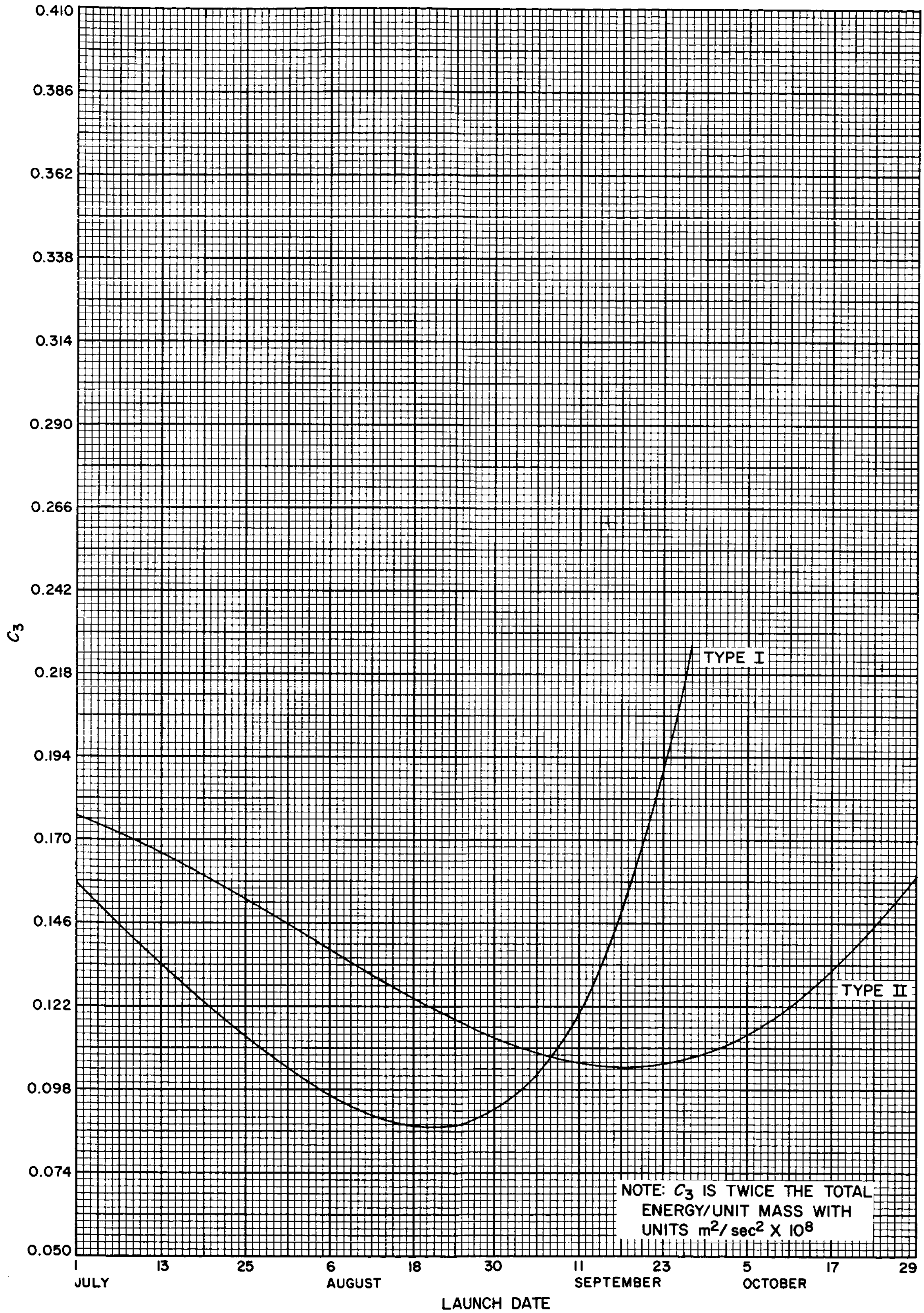

Fig. 4–1. Venus 1962: Minimum injection energy vs launch date

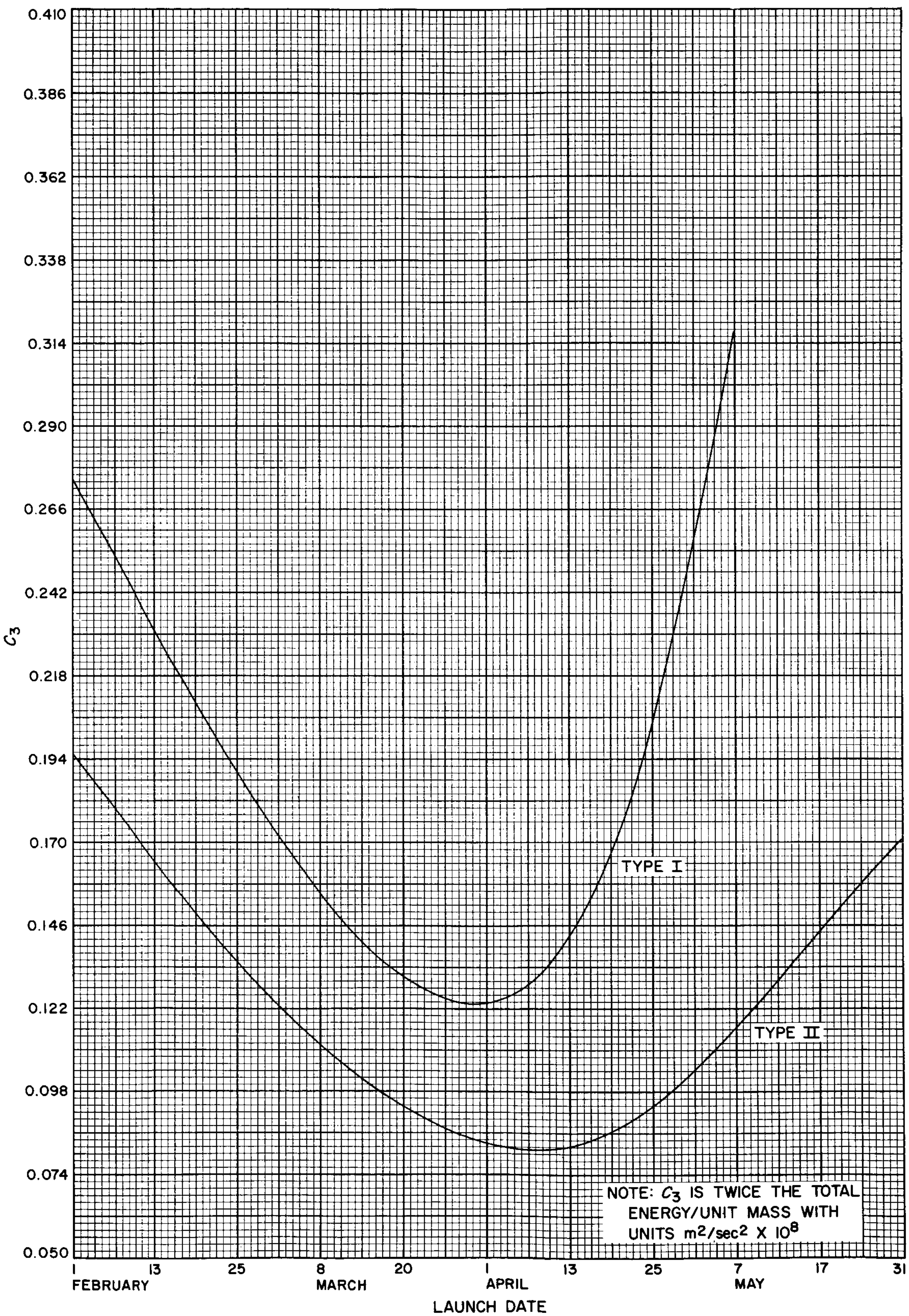

Fig. 4–2. Venus 1964: Minimum injection energy vs launch date

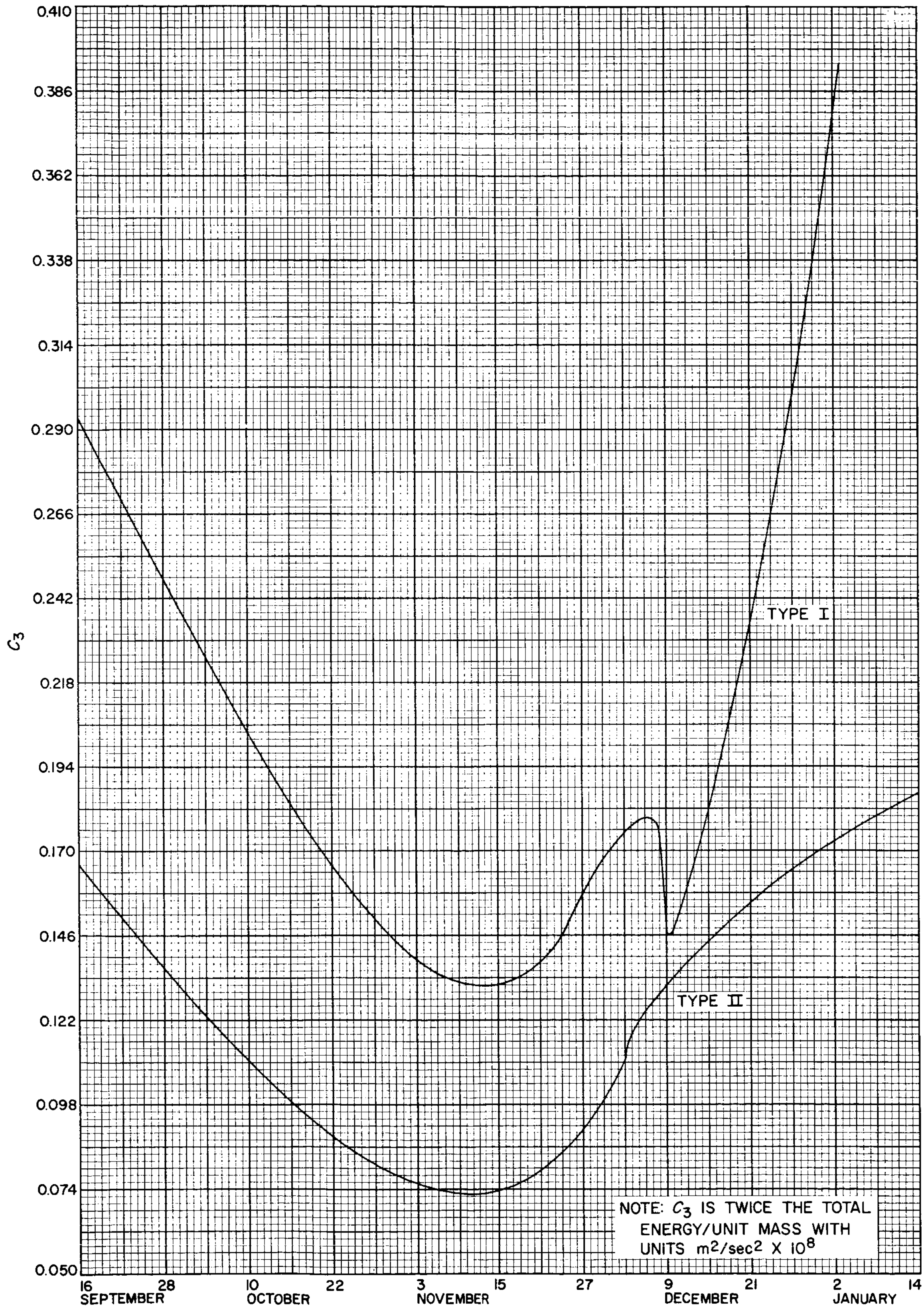

Fig. 4–3. Venus 1965: Minimum injection energy vs launch date

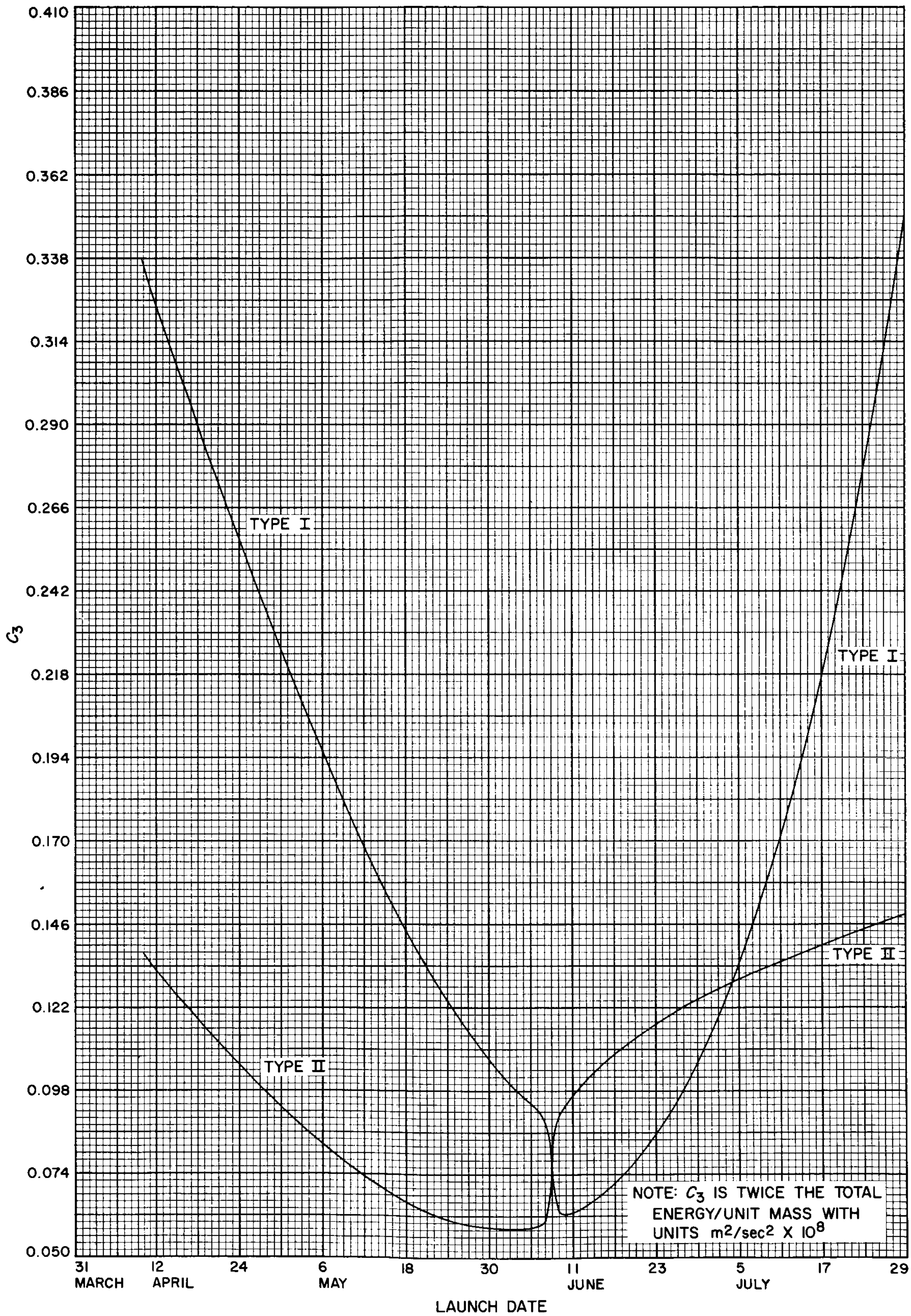

Fig. 4–4. Venus 1967: Minimum injection energy vs launch date

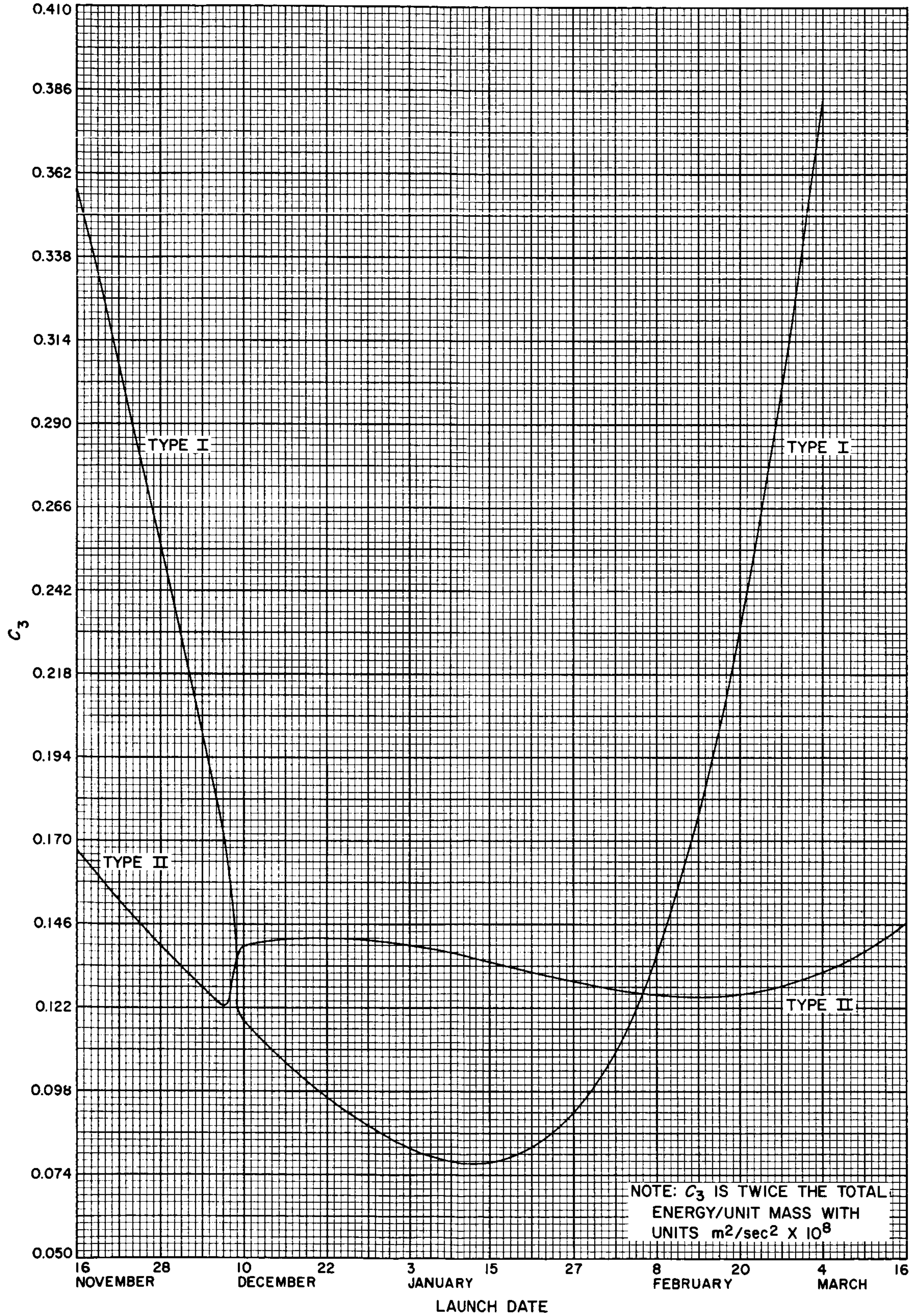

Fig. 4–5. Venus 1968–1969: Minimum injection energy vs launch date

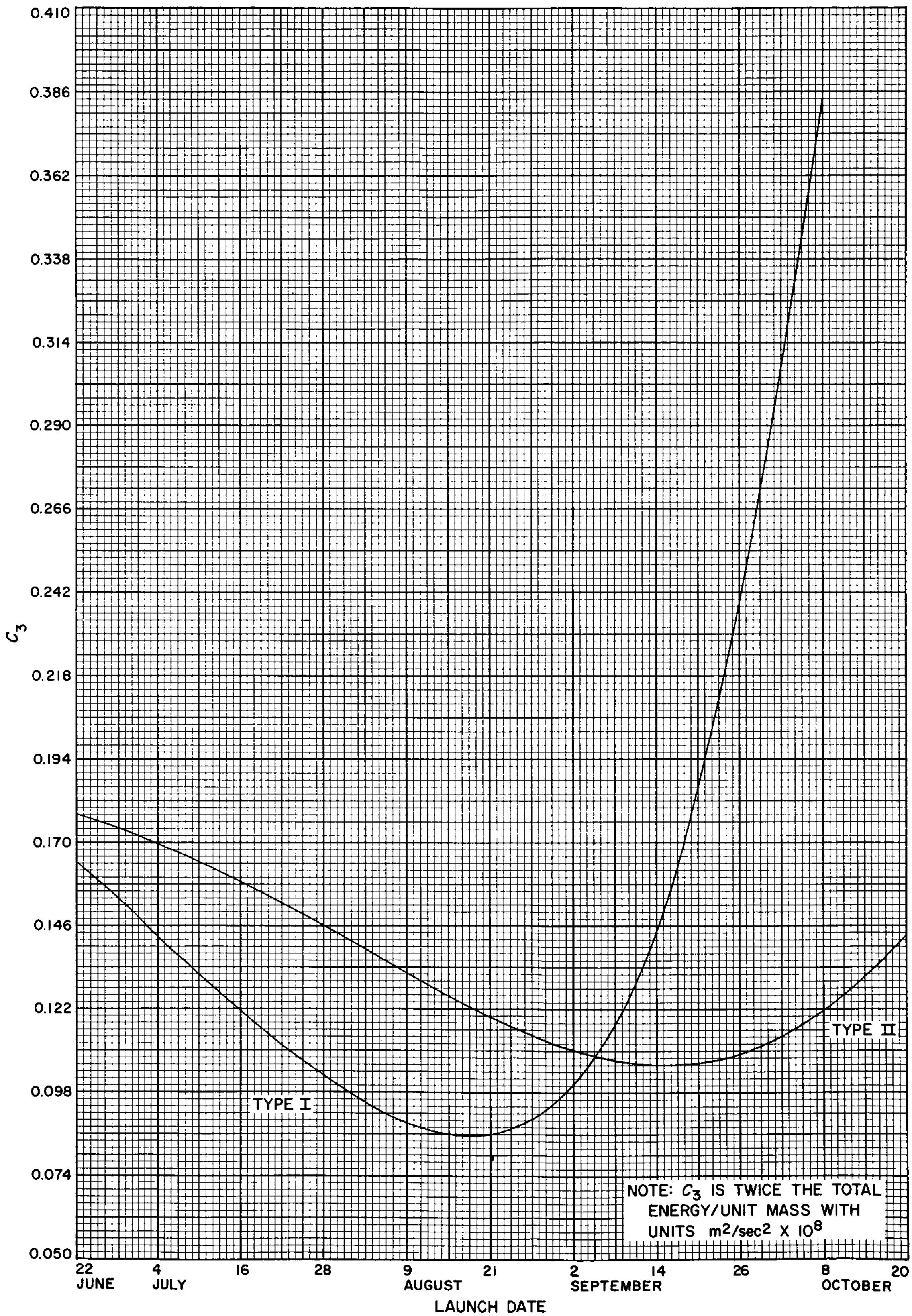

Fig. 4–6. Venus 1970: Minimum injection energy vs launch date

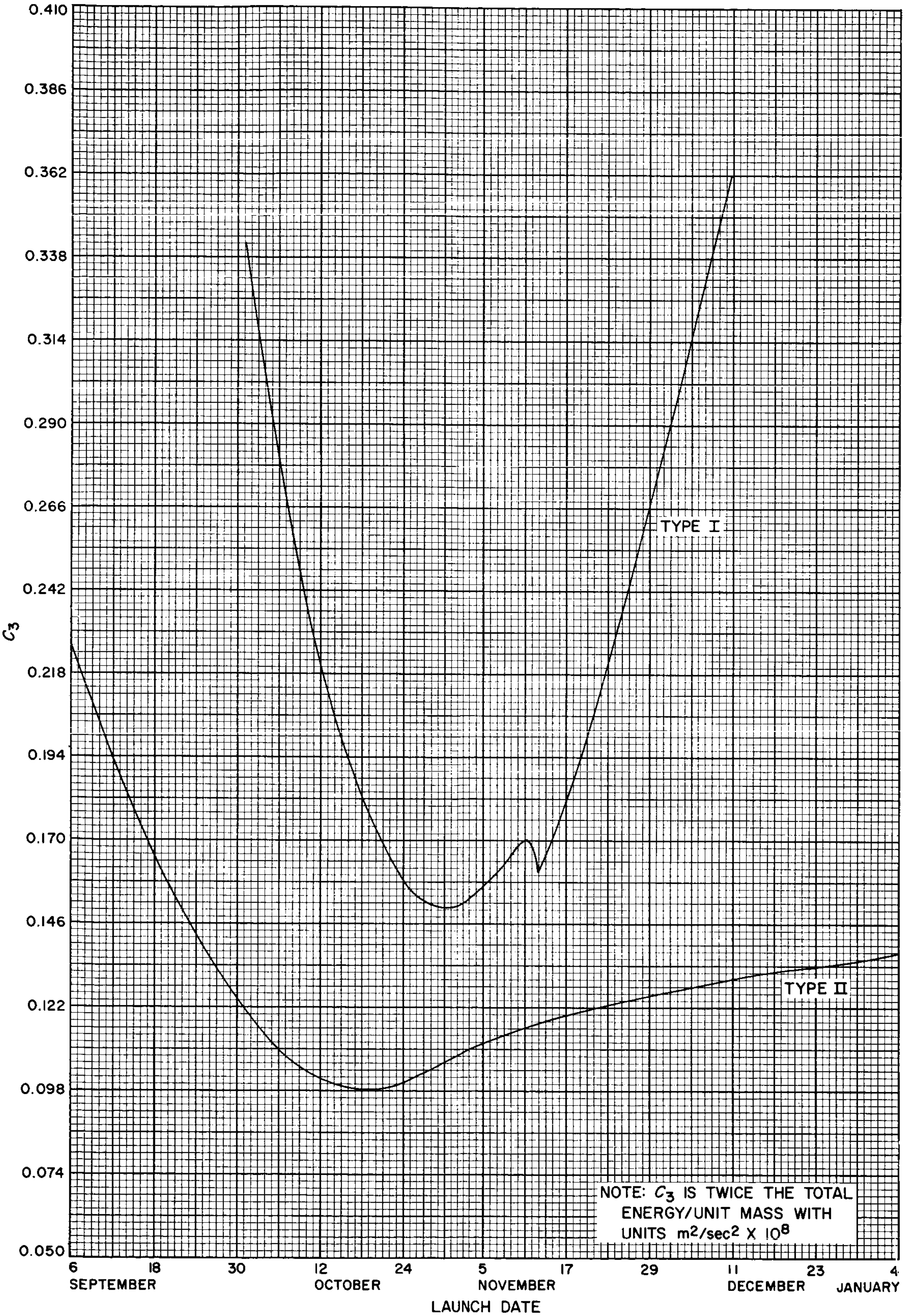

Fig. 4–7. Mars 1962: Minimum injection energy vs launch date

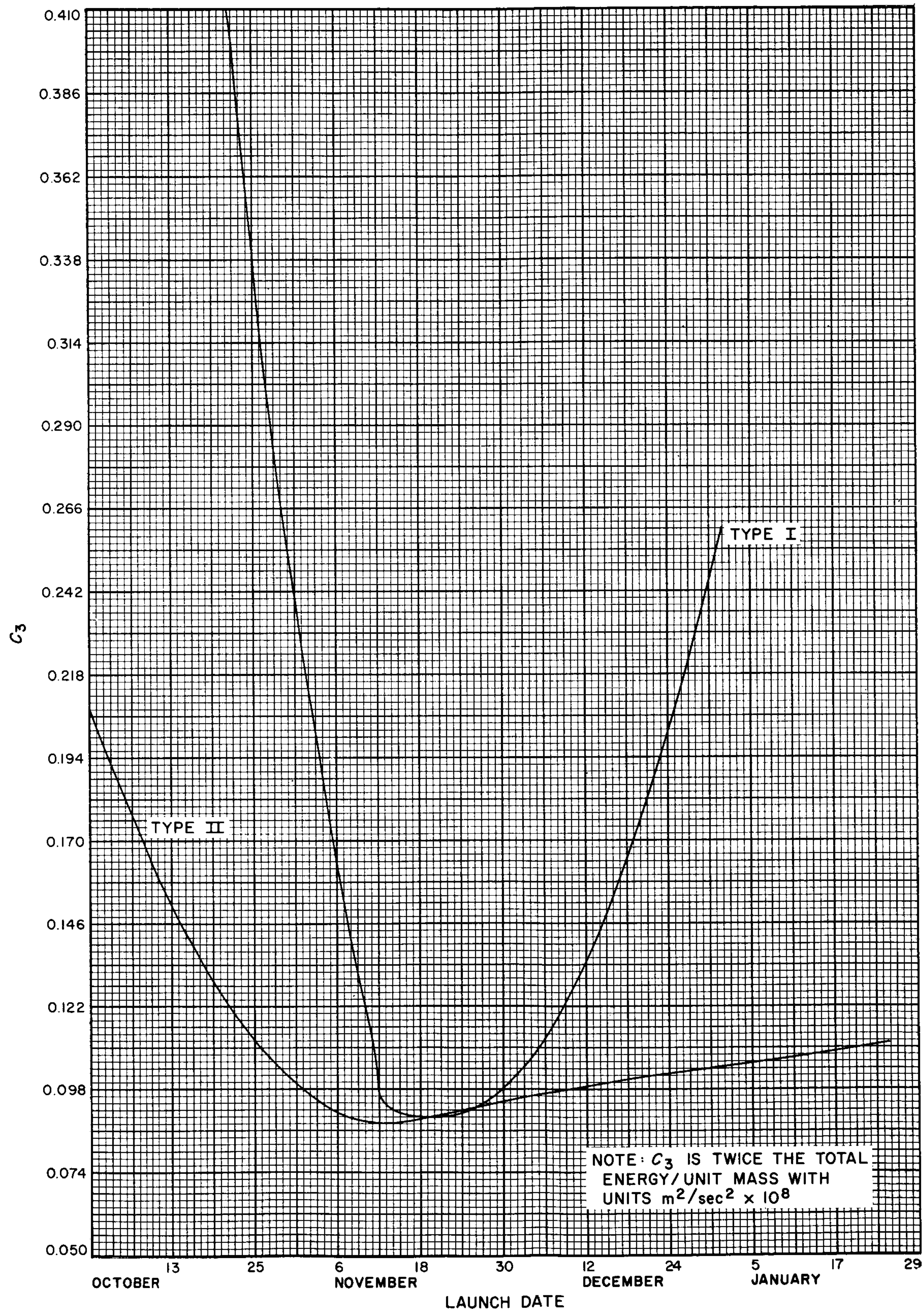

Fig. 4–8. Mars 1964: Minimum injection energy vs launch date

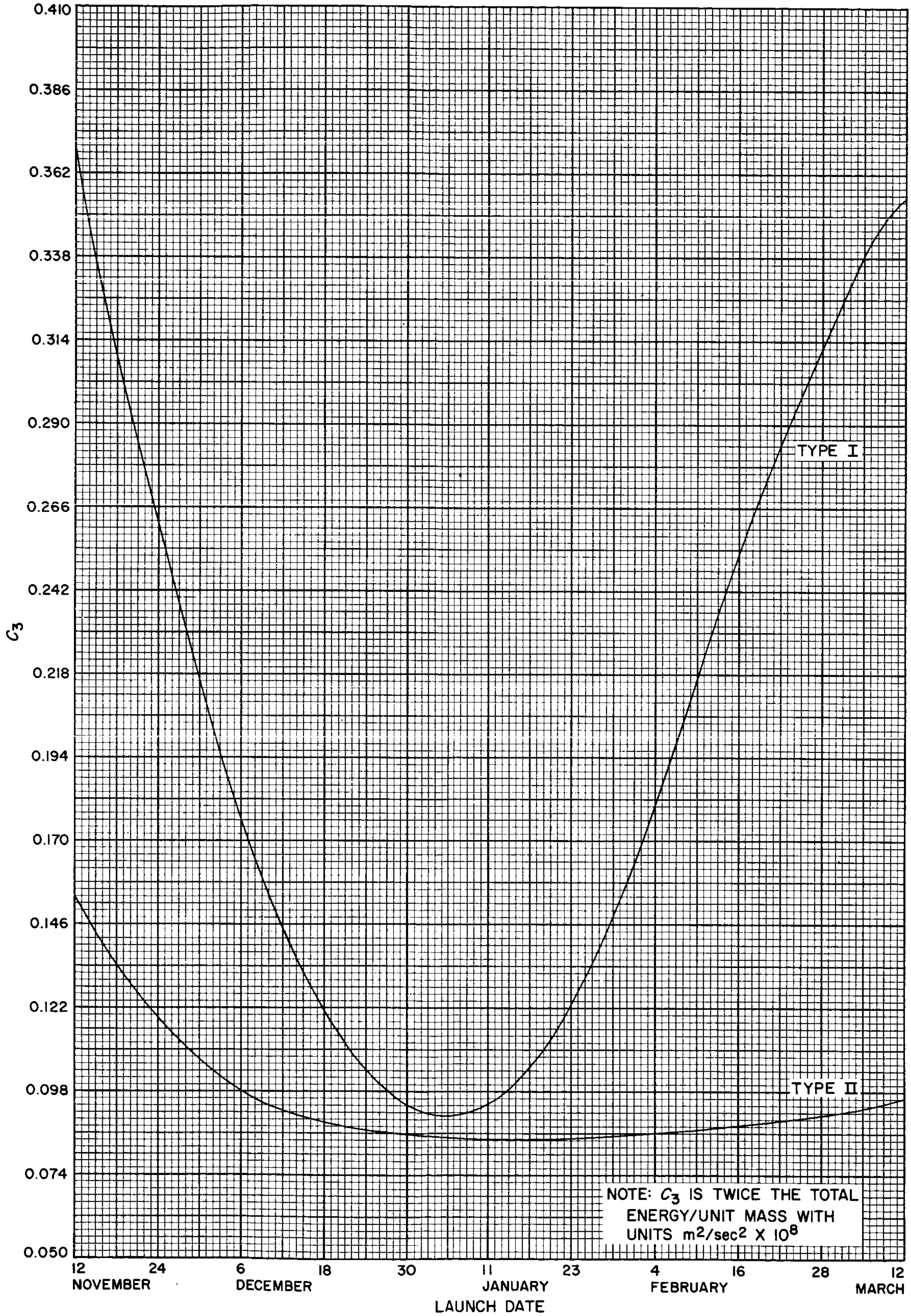

Fig. 4–9. Mars 1966: Minimum injection energy vs launch date

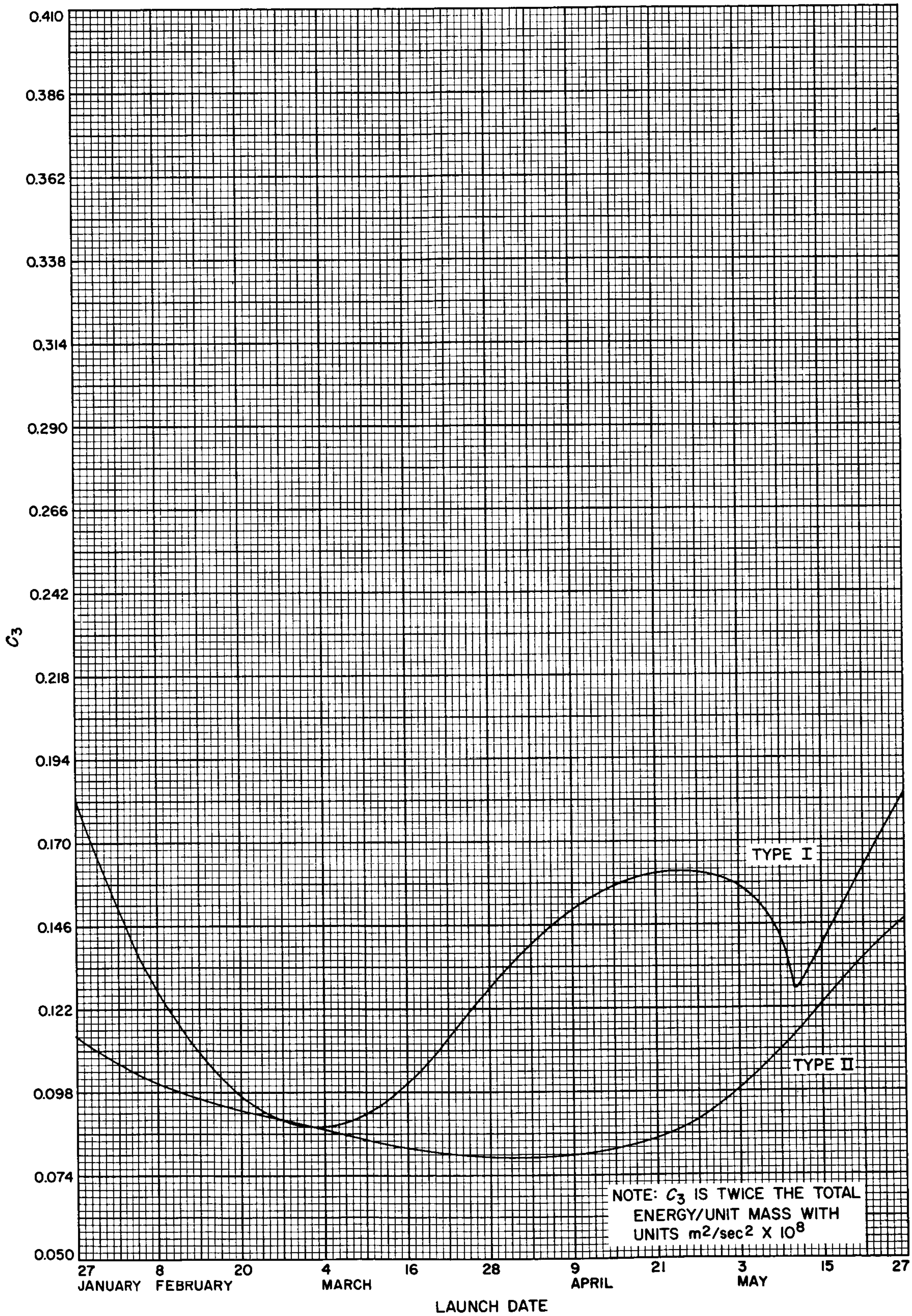

Fig. 4–10. Mars 1969: Minimum injection energy vs launch date

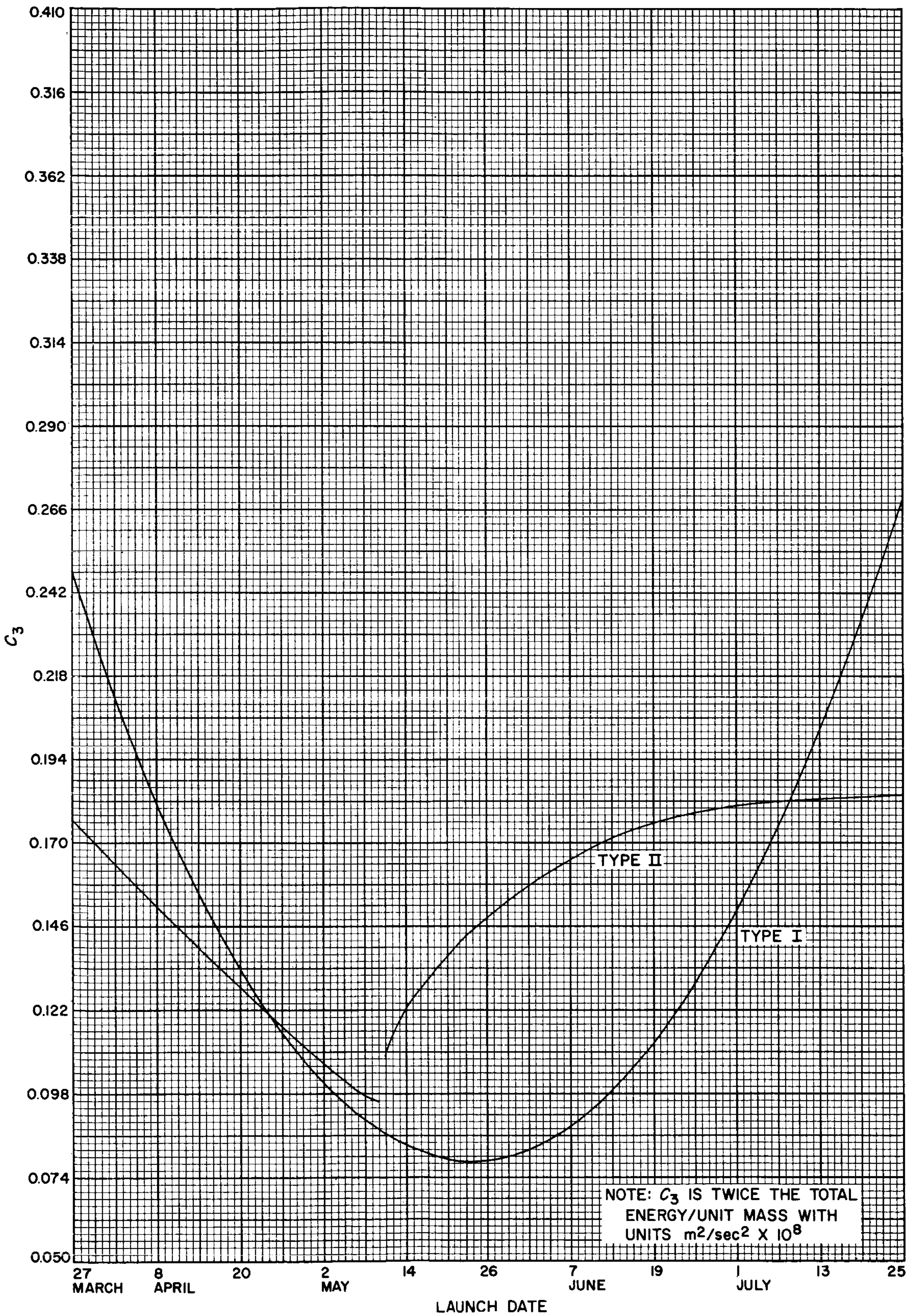

Fig. 4–11. Mars 1971: Minimum injection energy vs launch date

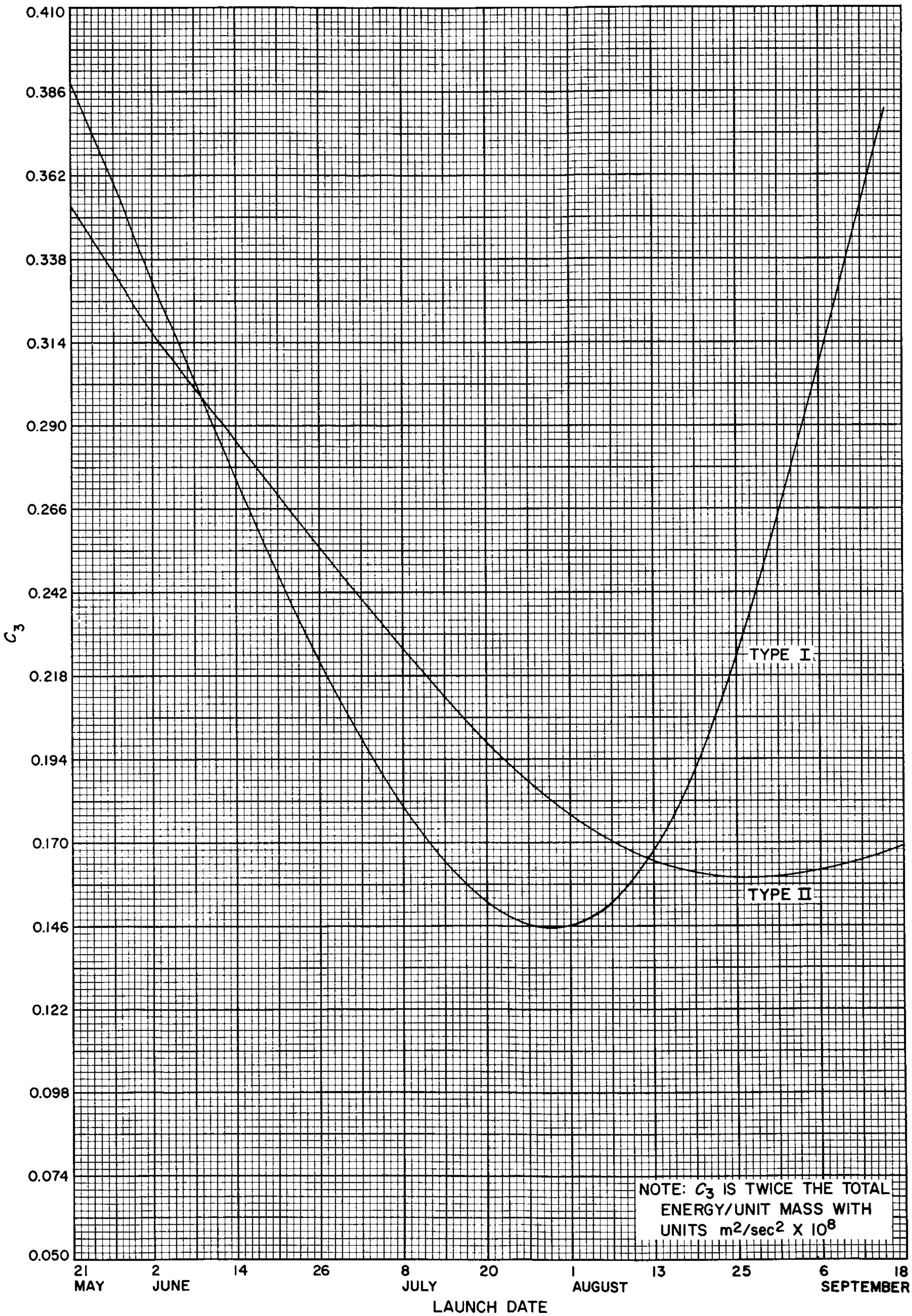

Fig. 4–12. Mars 1973: Minimum injection energy vs launch date

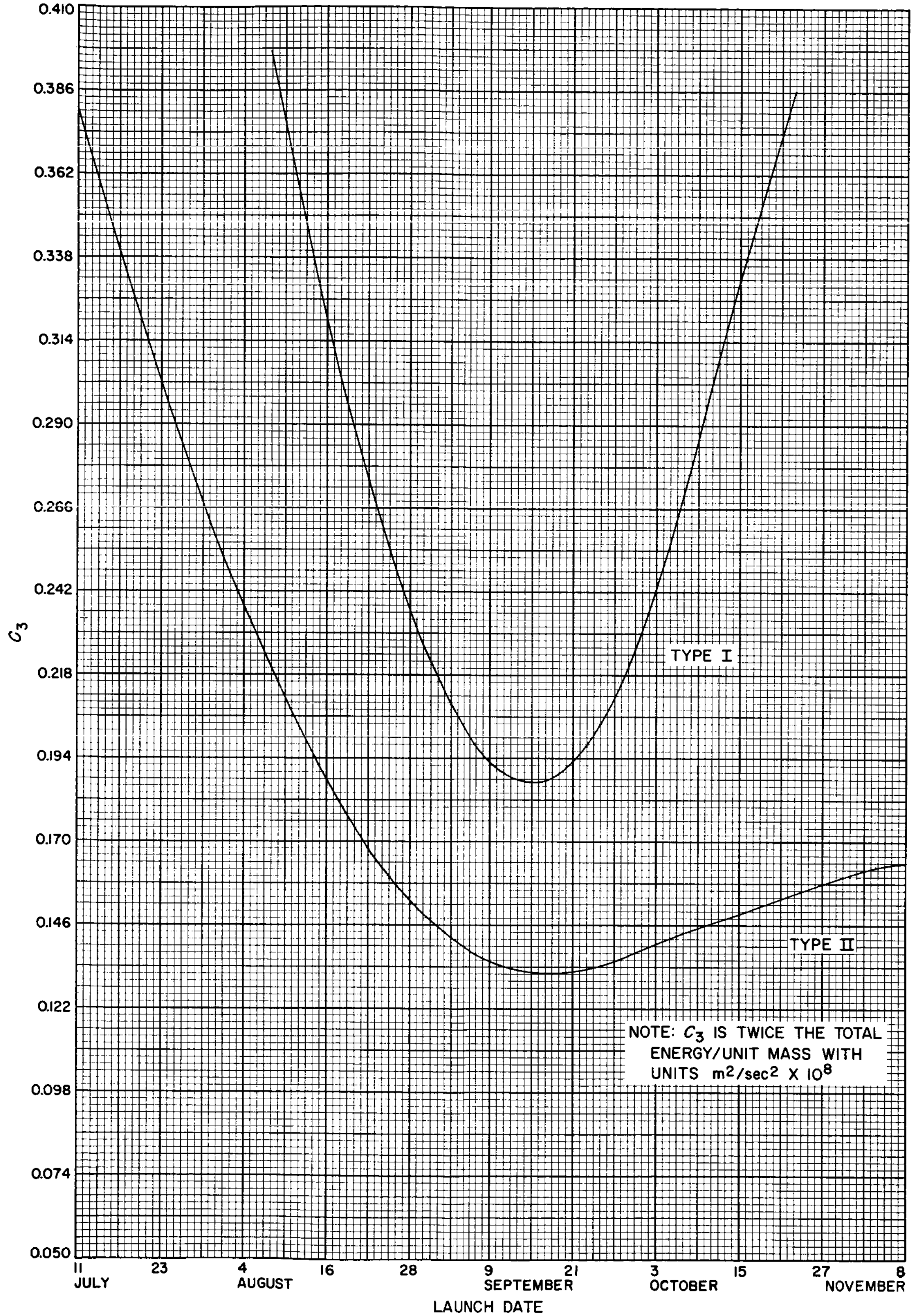

Fig. 4–13. Mars 1975: Minimum injection energy vs launch date

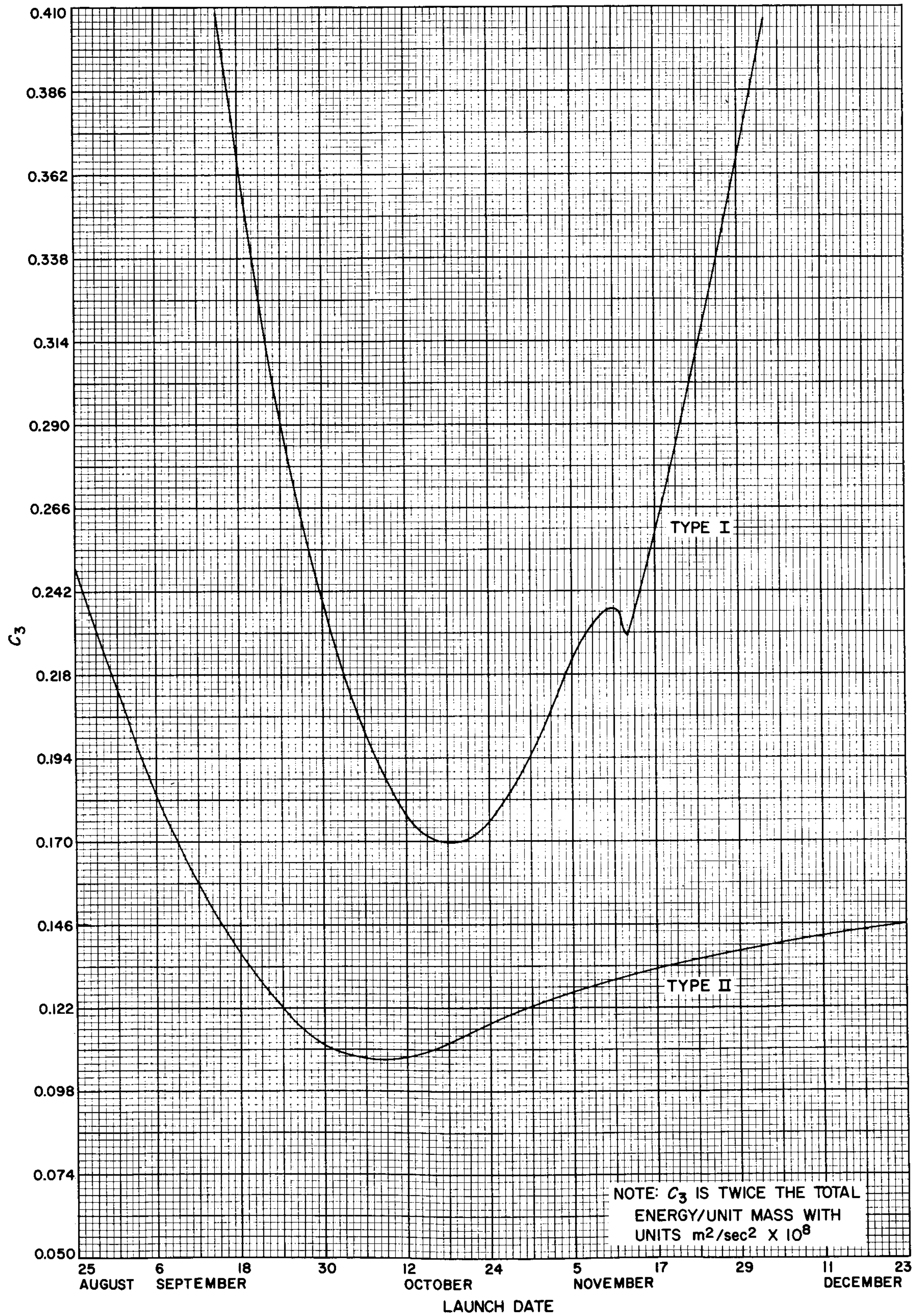

Fig. 4–14. Mars 1977: Minimum injection energy vs launch date

V. VENUS 1962: TRAJECTORY-PARAMETER GRAPHS

Figure

V. VENUS 1962: TRAJECTORY-PARAMETER GRAPHS (Cont'd)

Figure

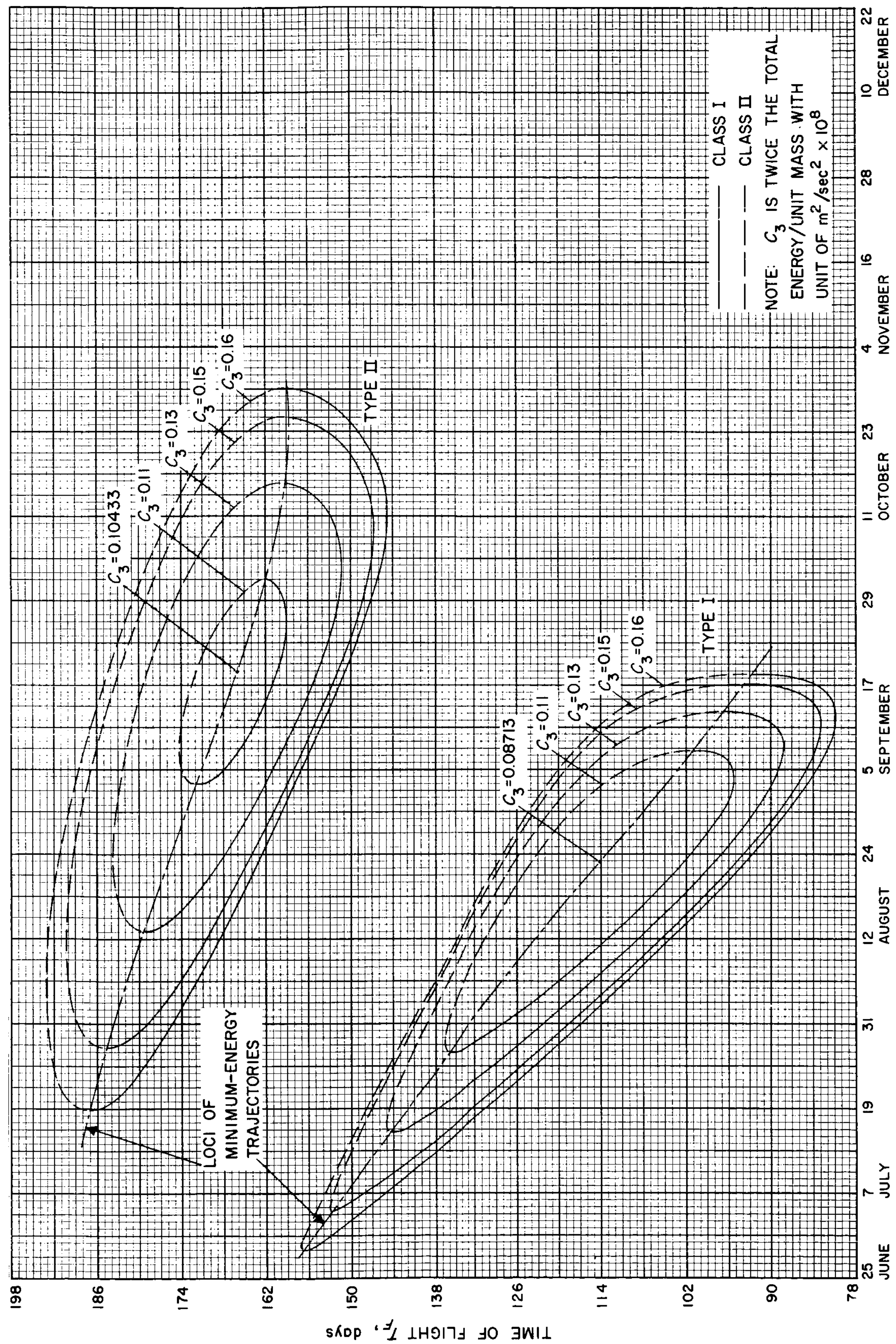

Fig. 5-1. Venus 1962: Time of flight vs launch date

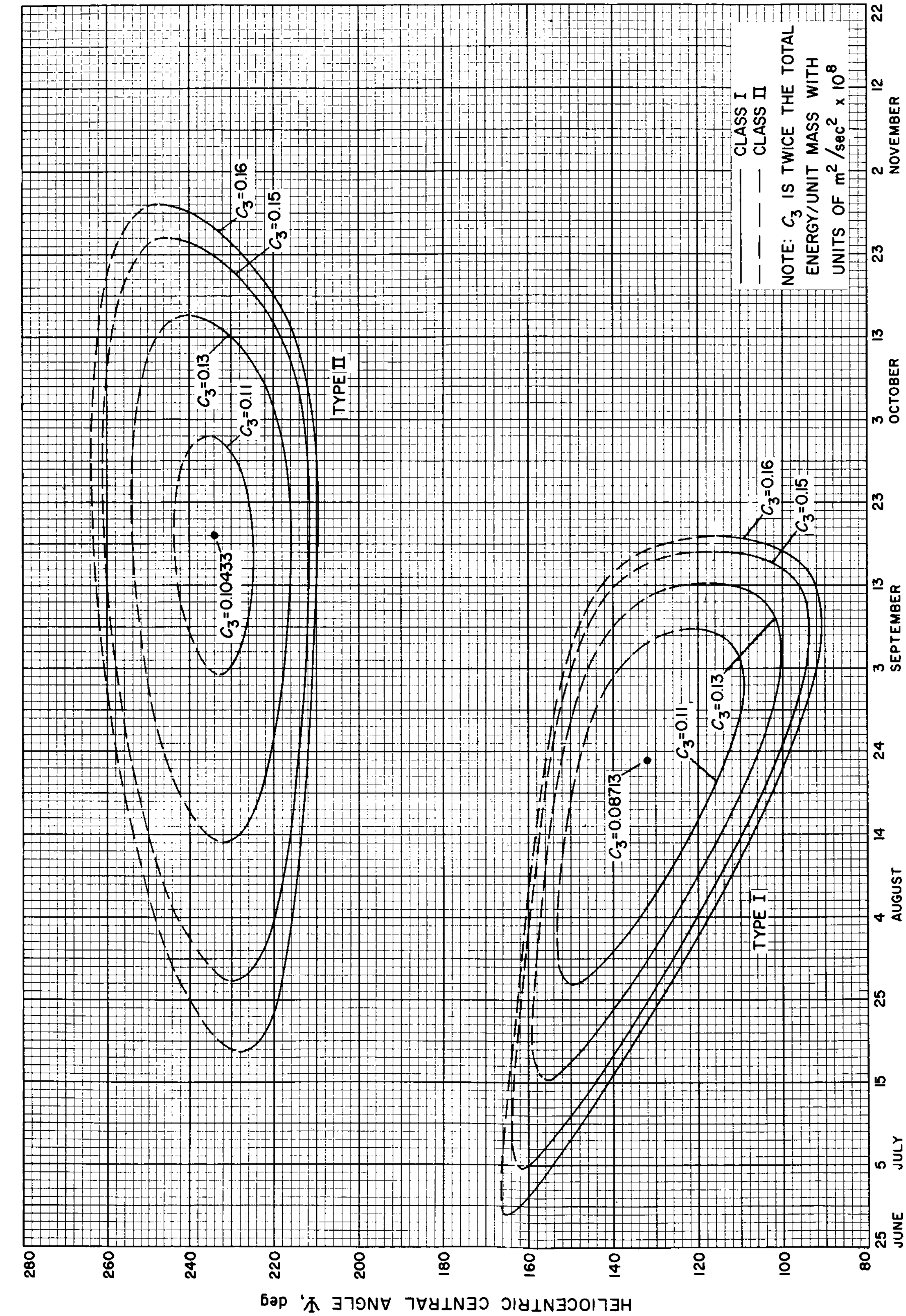

Fig. 5–2. Venus 1962: Heliocentric central angle vs launch date

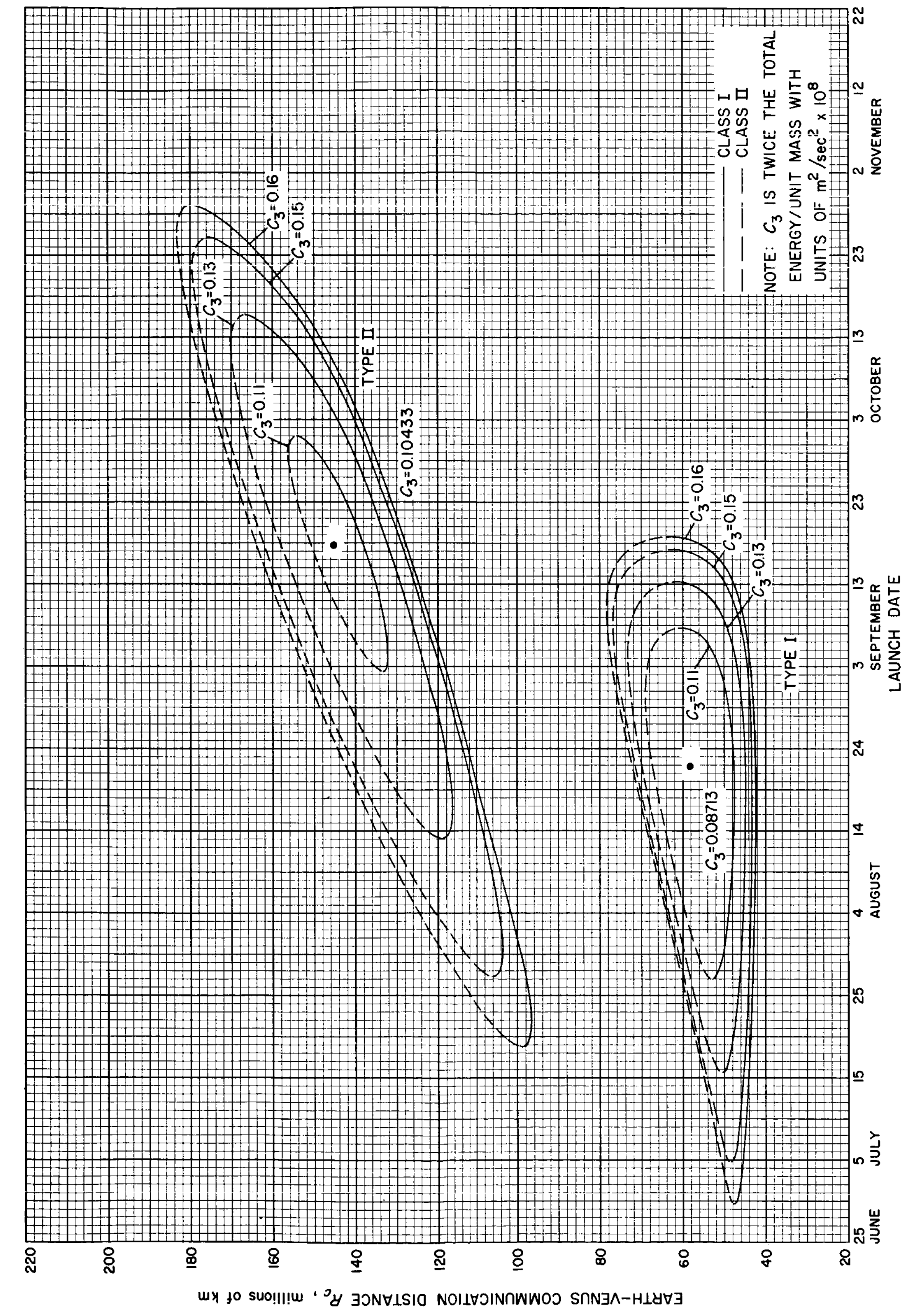

Fig. 5-3. Venus 1962: Earth–Venus communication distance vs launch date

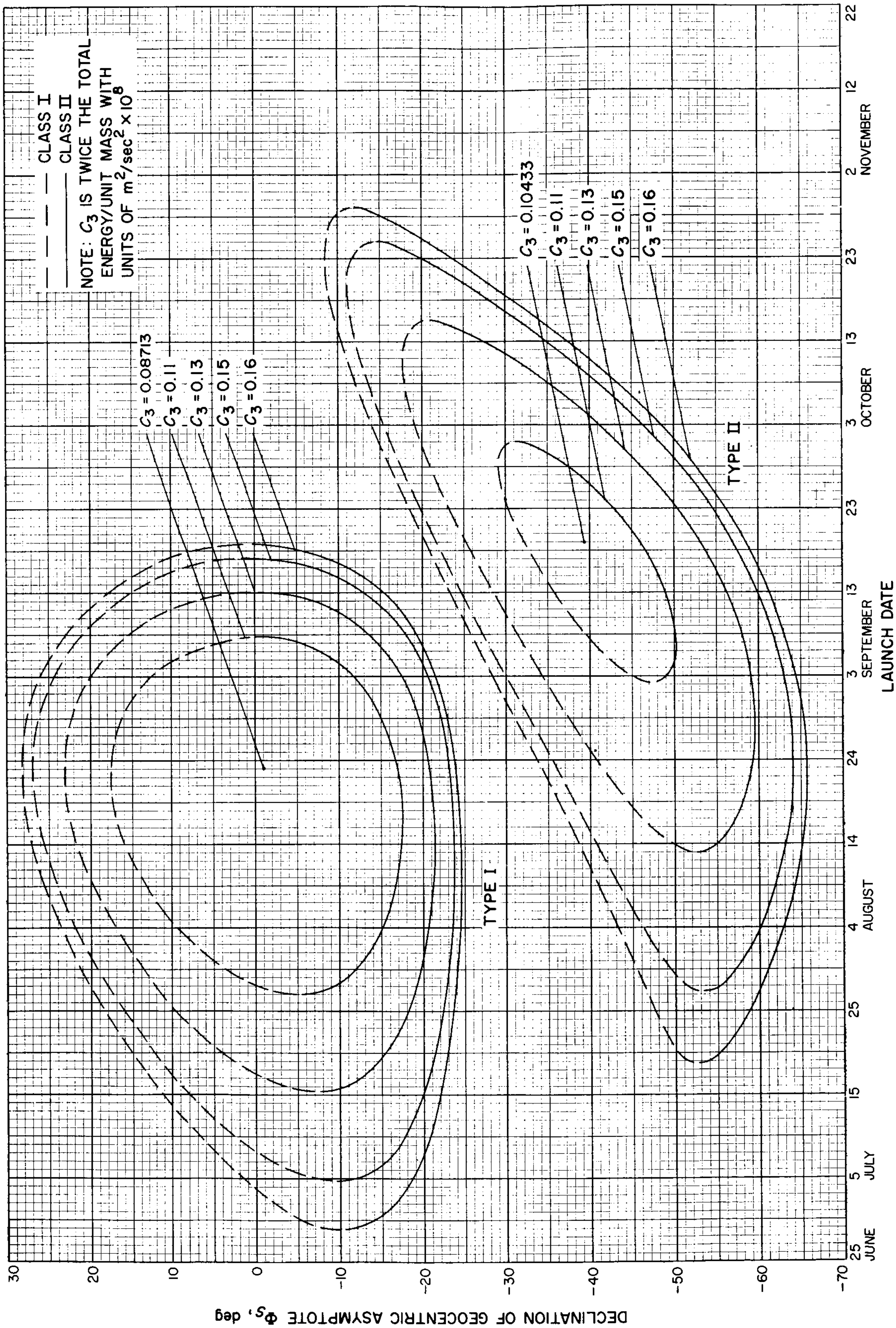

Fig. 5–4. Venus 1962: Declination of geocentric asymptote vs launch date

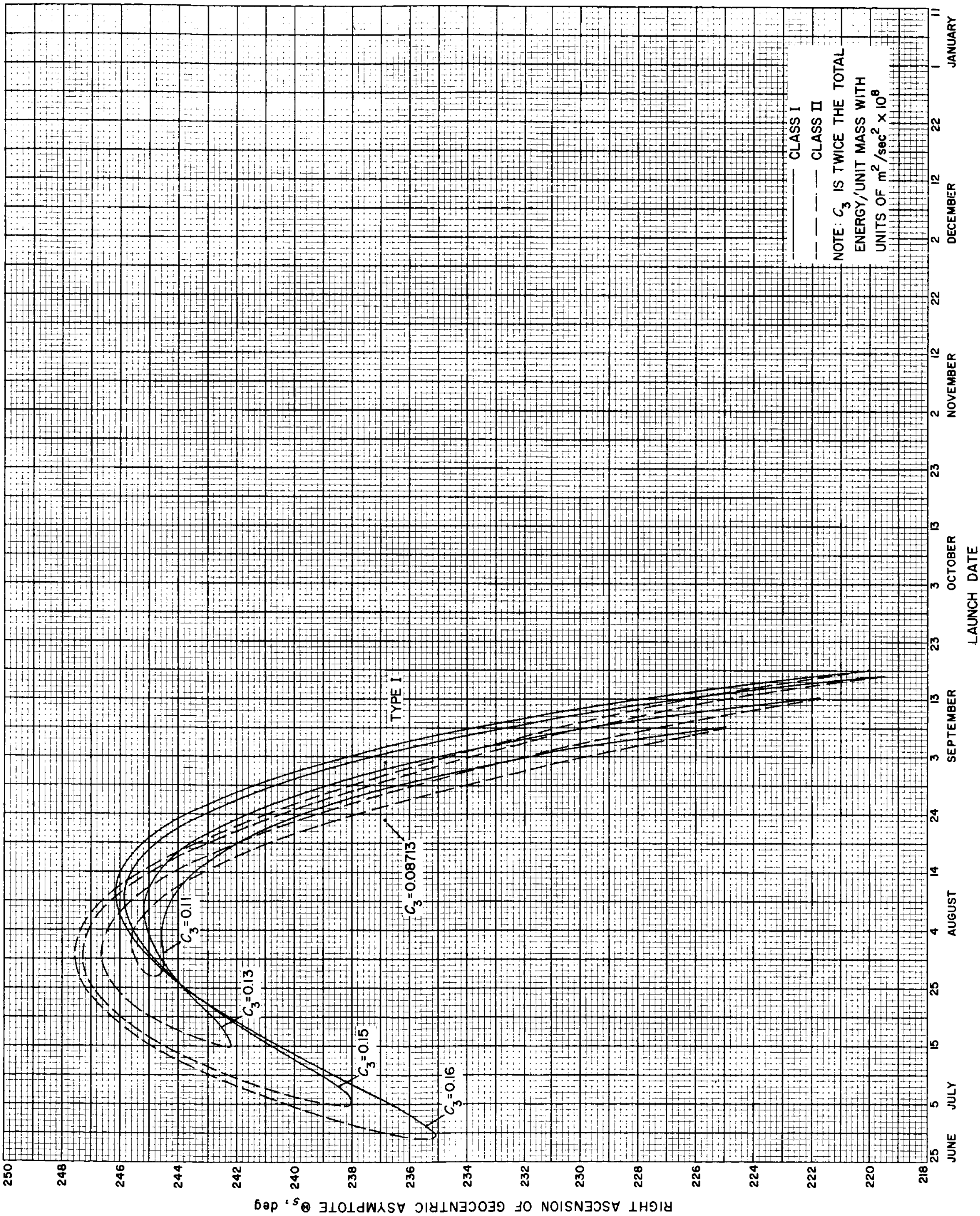

Fig. 5–5. Venus 1962: Right ascension of geocentric asymptote vs launch date, Type I

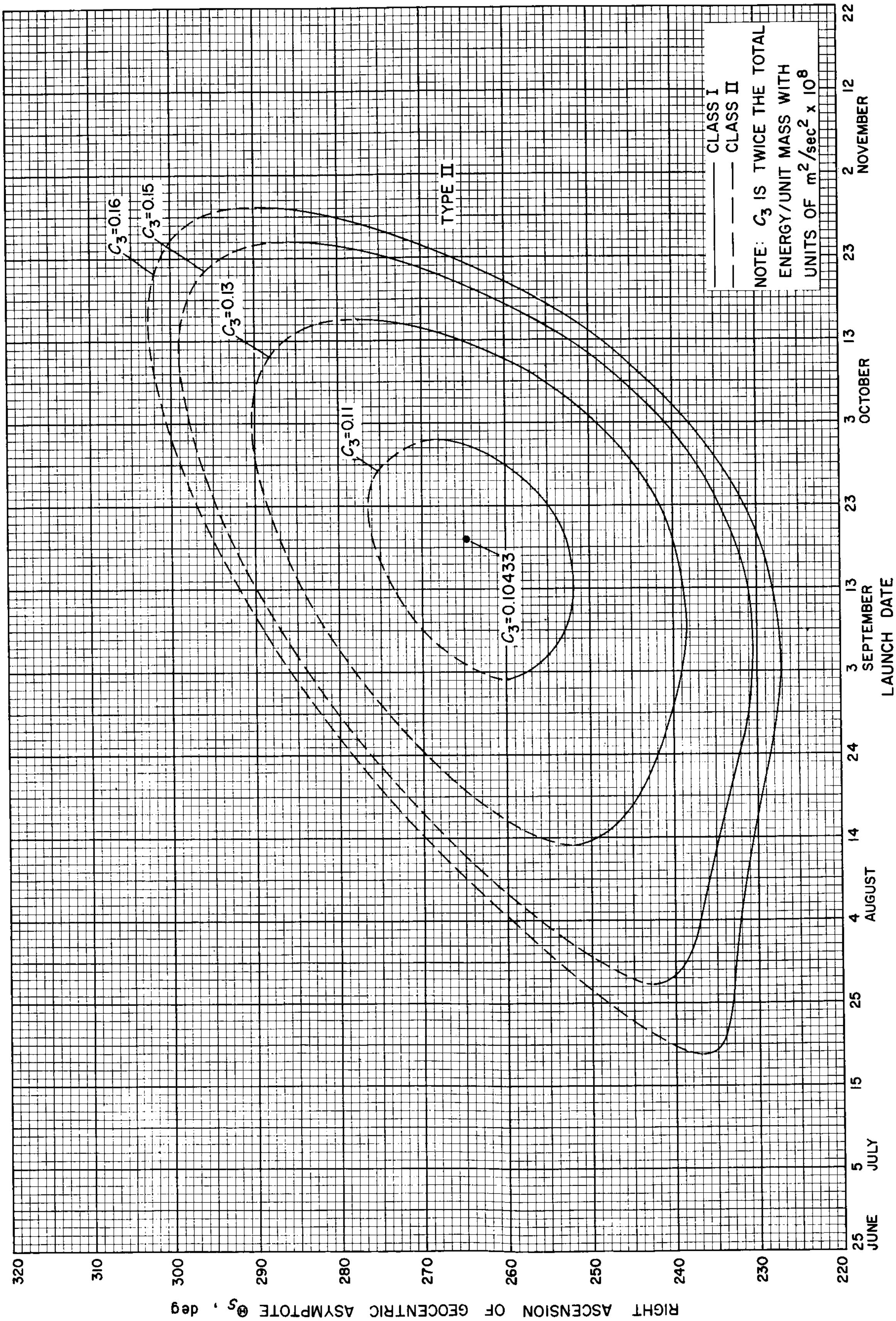

Fig. 5-6. Venus 1962: Right ascension of geocentric asymptote vs launch date, Type II

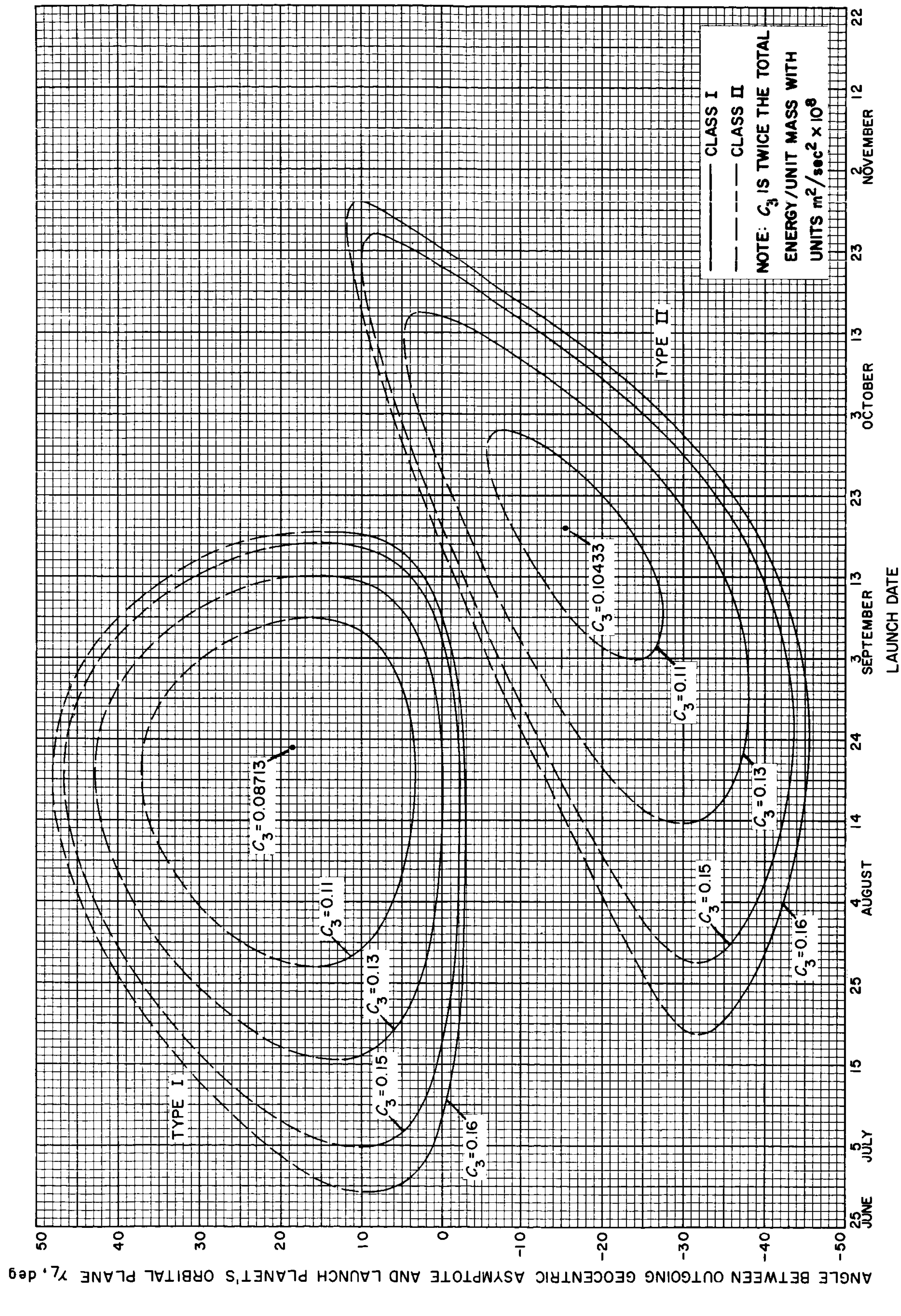

Fig. 5-7. Venus 1962: Angle between outgoing geocentric asymptote and launch planet's orbital plane vs launch date

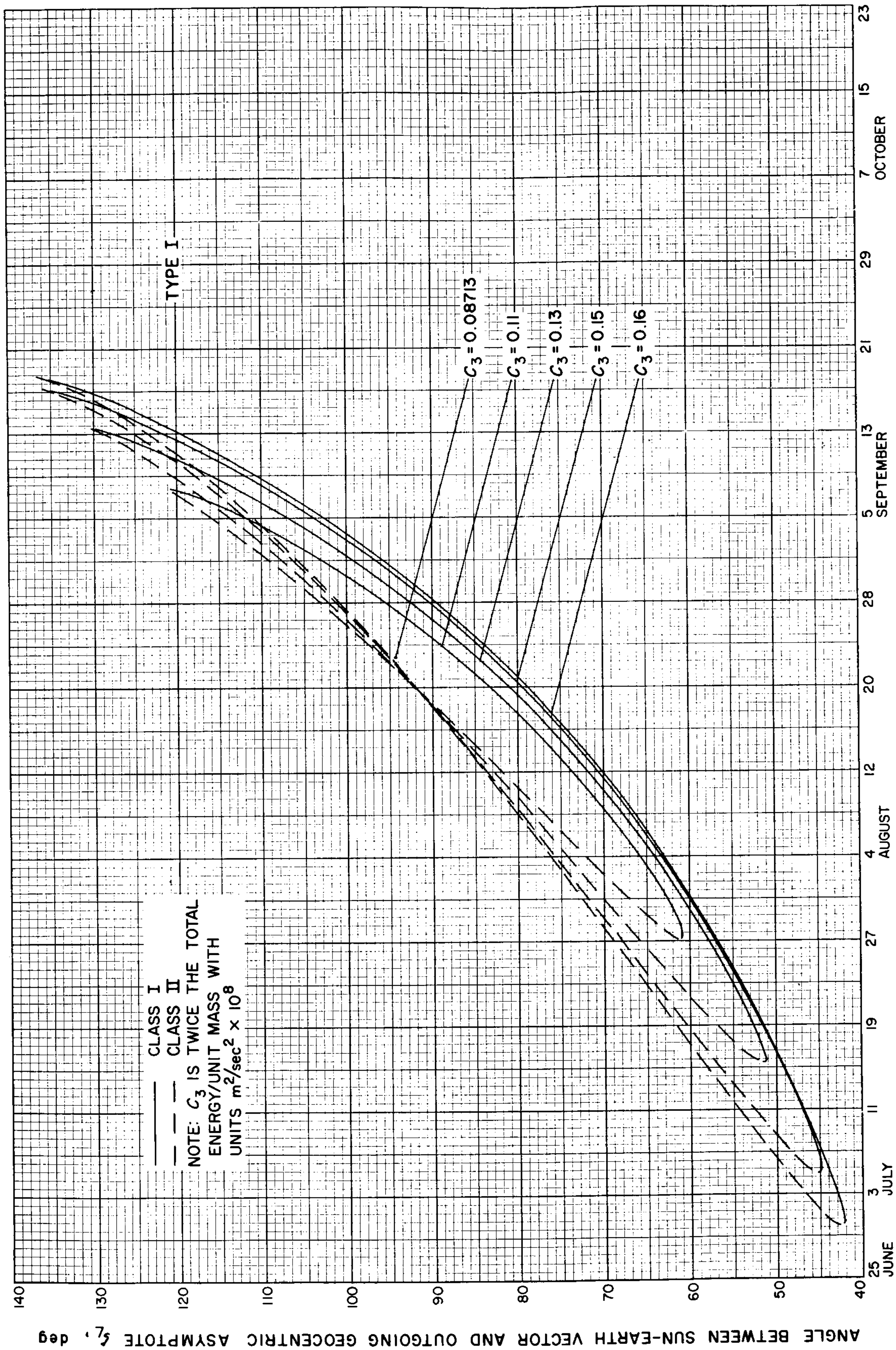

Fig. 5–8. Venus 1962: Angle between Sun–Earth vector and outgoing geocentric asymptote vs launch date, Type I

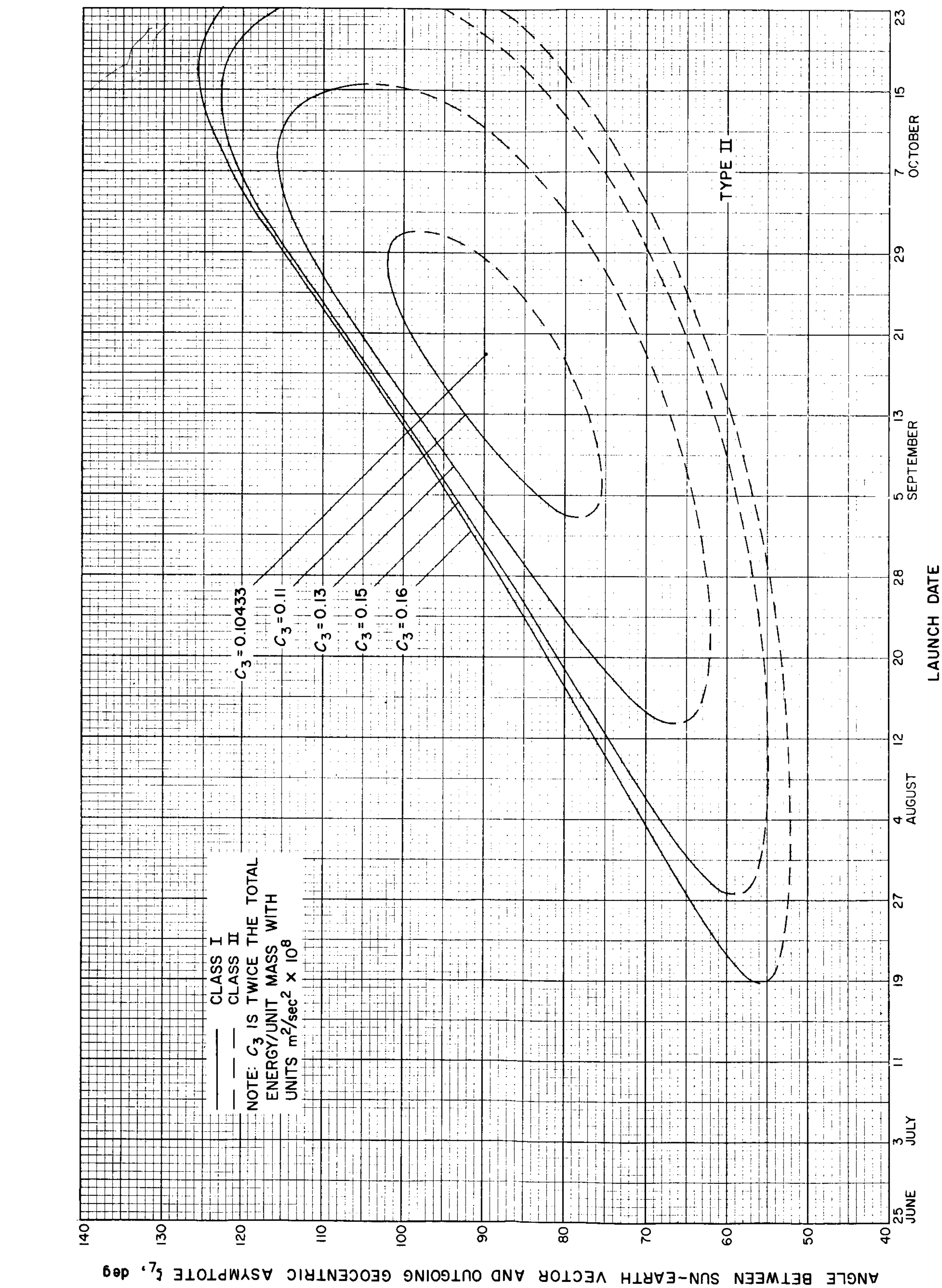

Fig. 5-9. Venus 1962: Angle between Sun–Earth vector and outgoing geocentric asymptote vs launch date, Type II

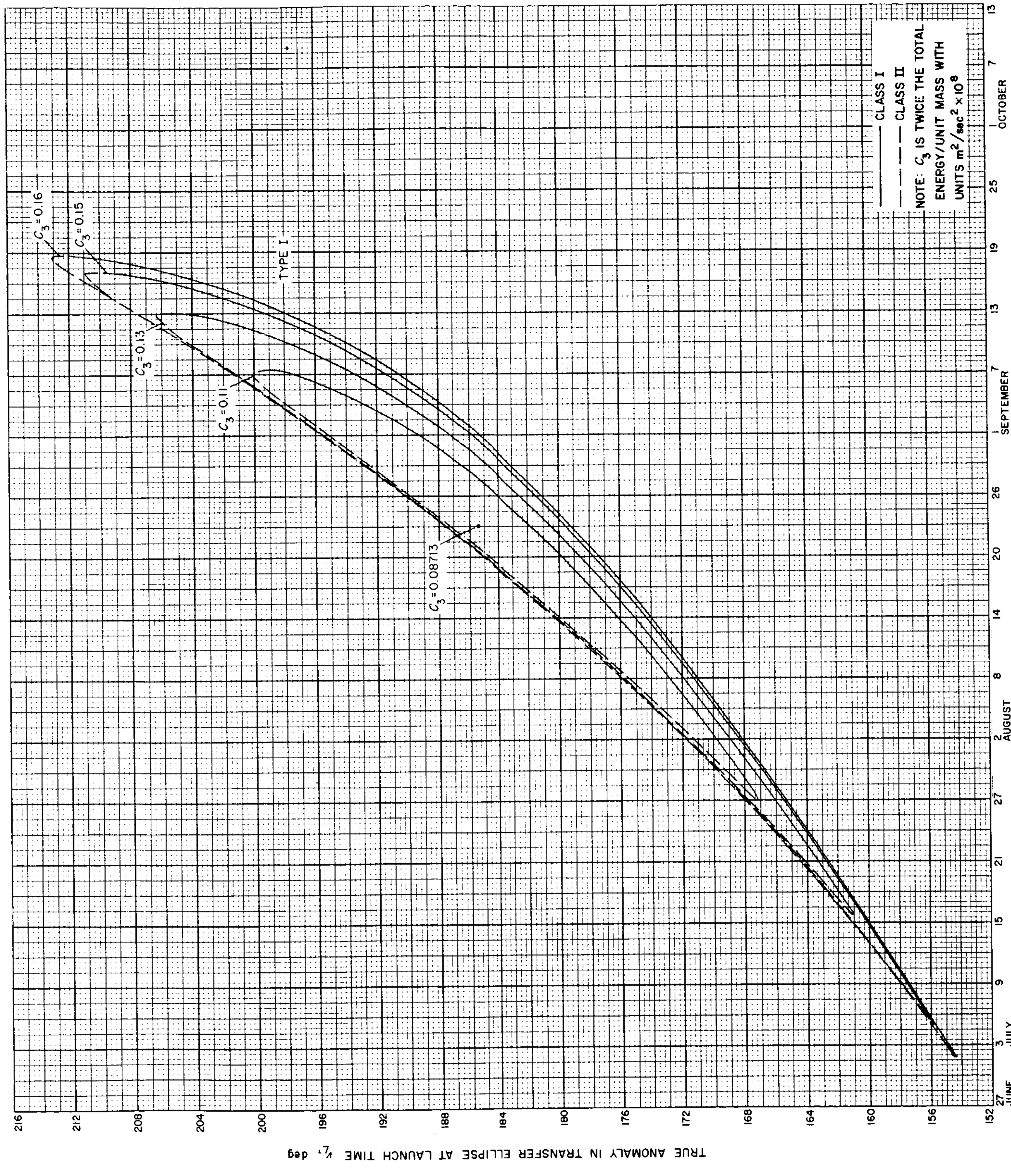

Fig. 5-10. Venus 1962: True anomaly in transfer ellipse at launch time vs launch date, Type I

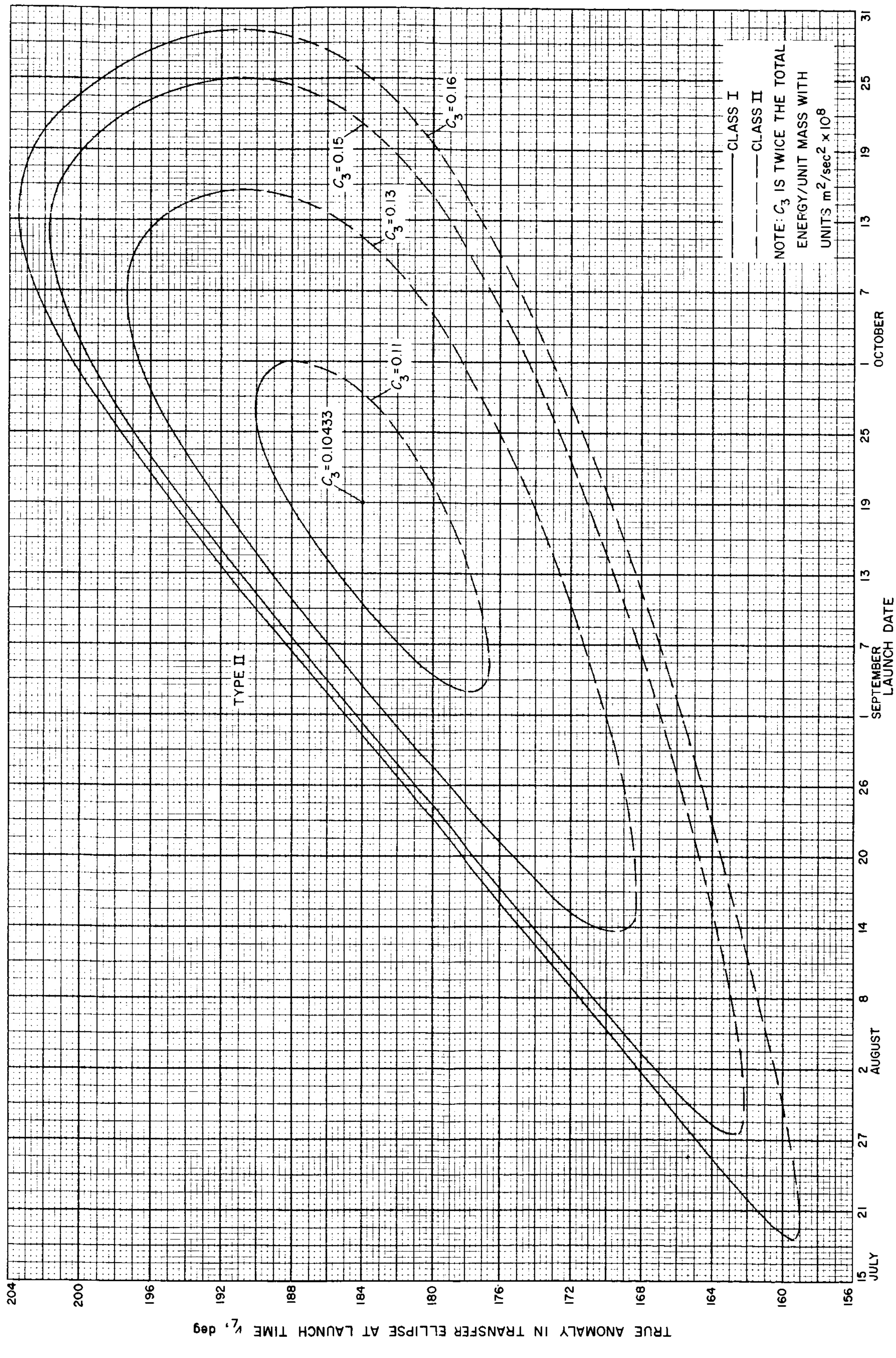

Fig. 5-11. Venus 1962: True anomaly in transfer ellipse at launch time vs launch date, Type II

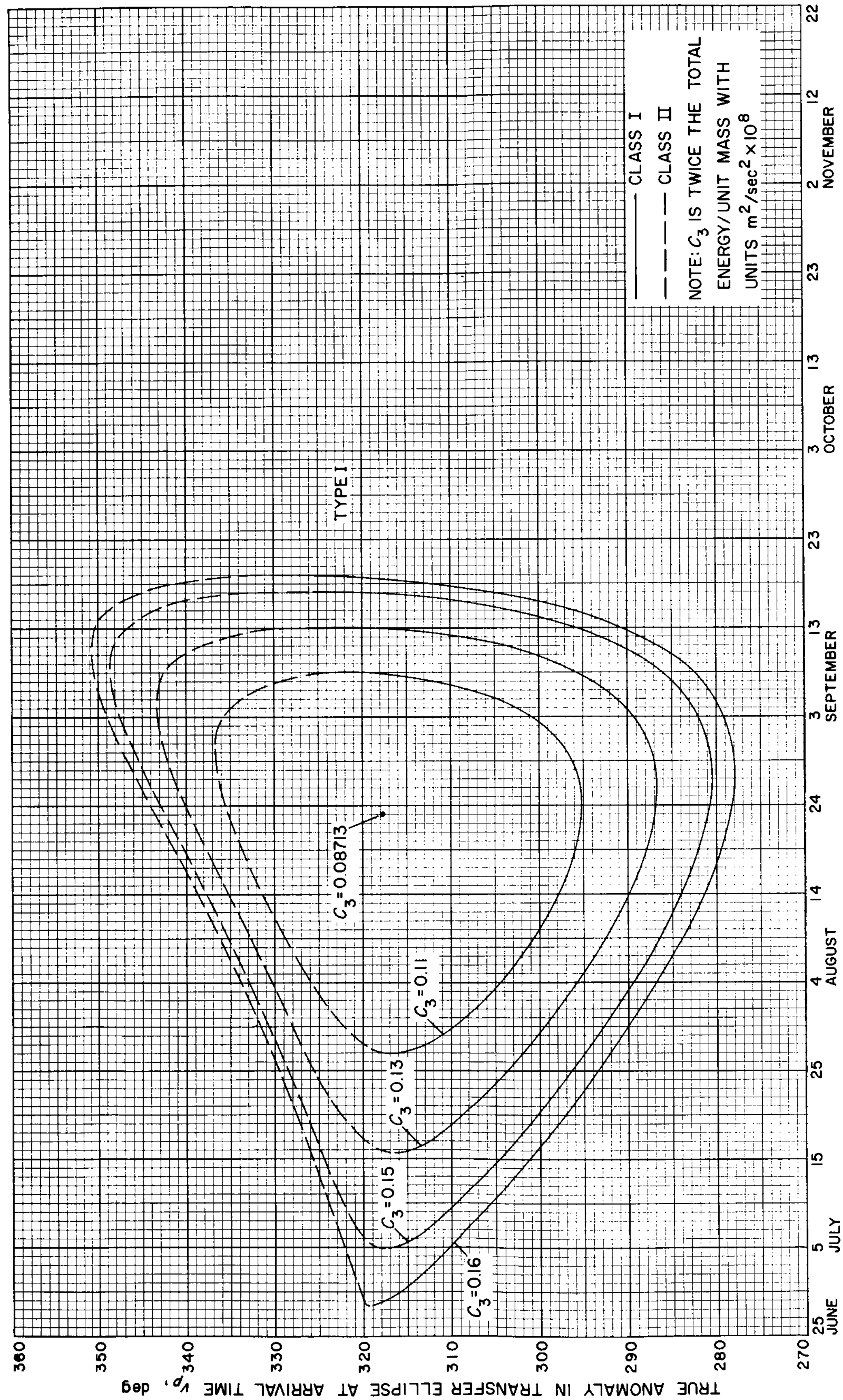

Fig. 5–12. Venus 1962: True anomaly in transfer ellipse at arrival time vs launch date, Type I

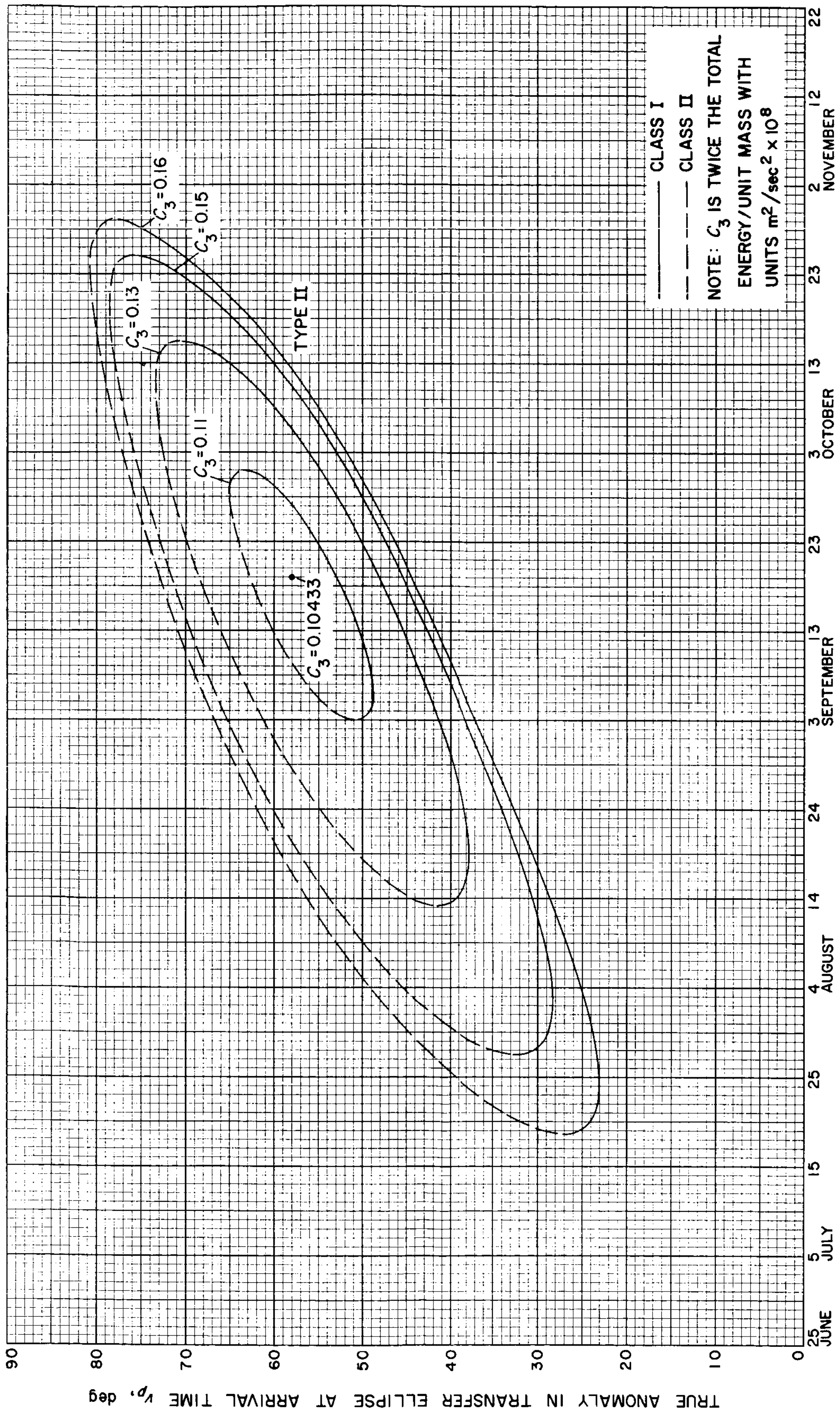

Fig. 5-13. Venus 1962: True anomaly in transfer ellipse at arrival time vs launch date, Type II

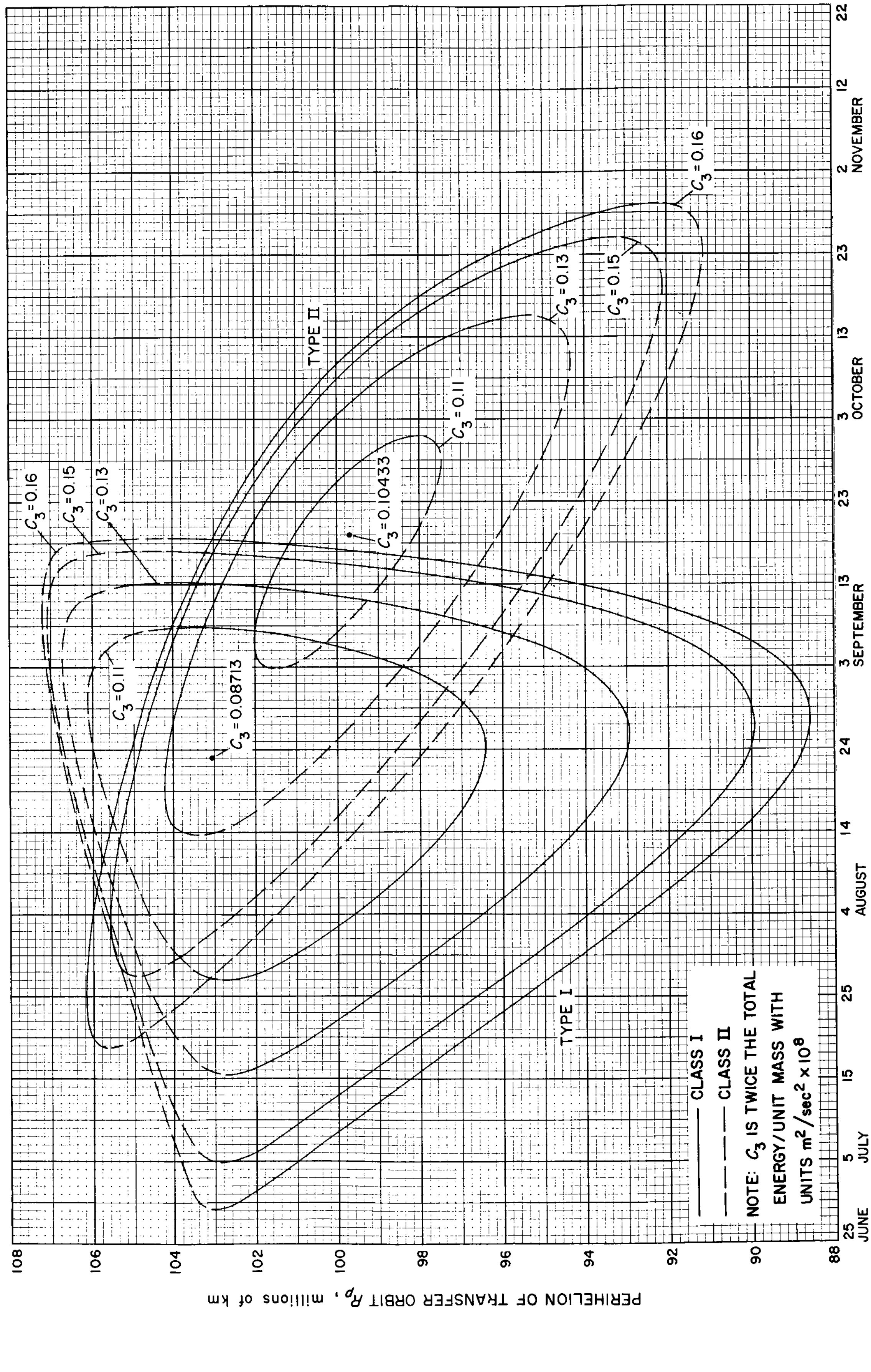

Fig. 5-14. Venus 1962: Perihelion of transfer orbit vs launch date

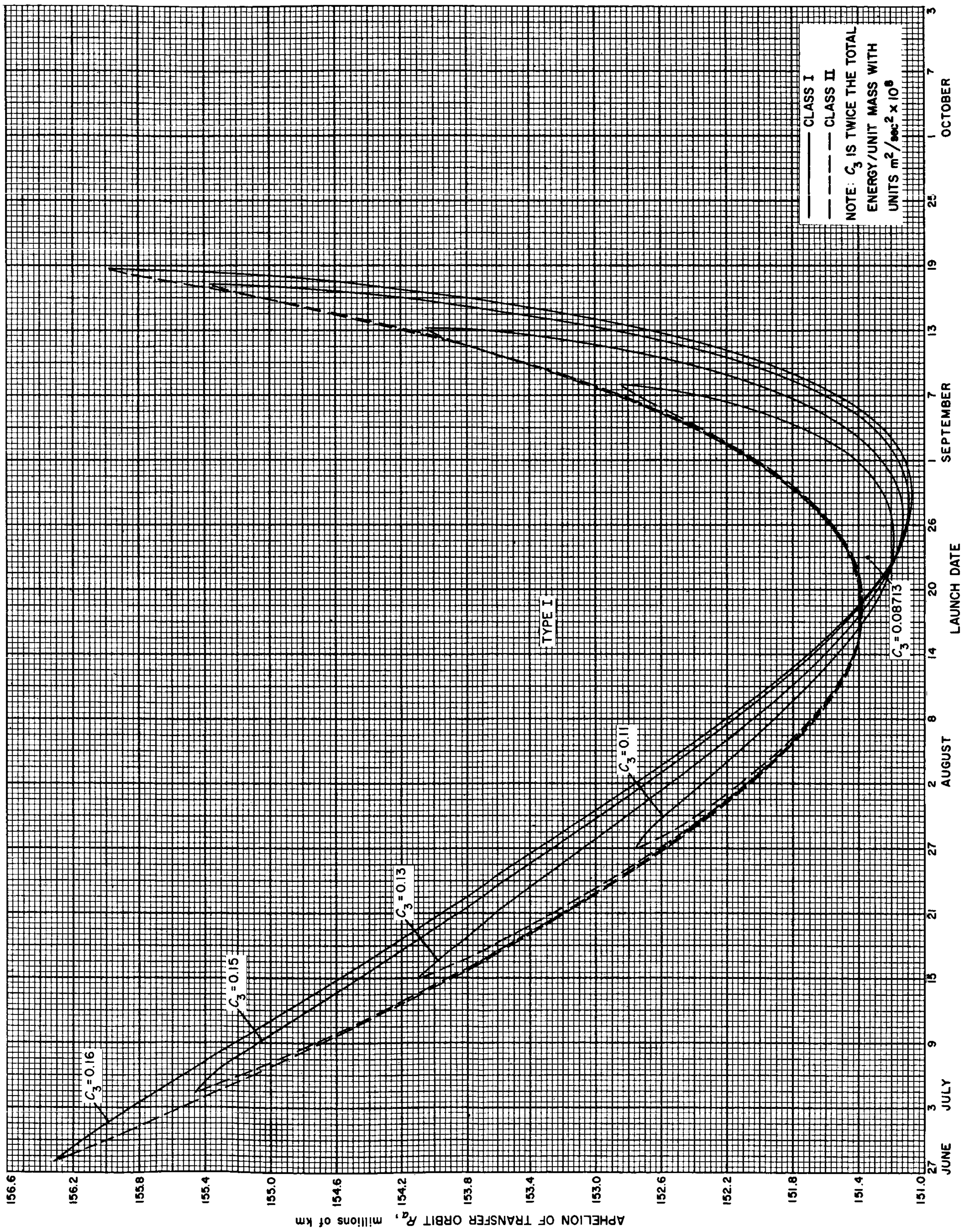

Fig. 5–15. Venus 1962: Aphelion of transfer orbit vs launch date, Type I

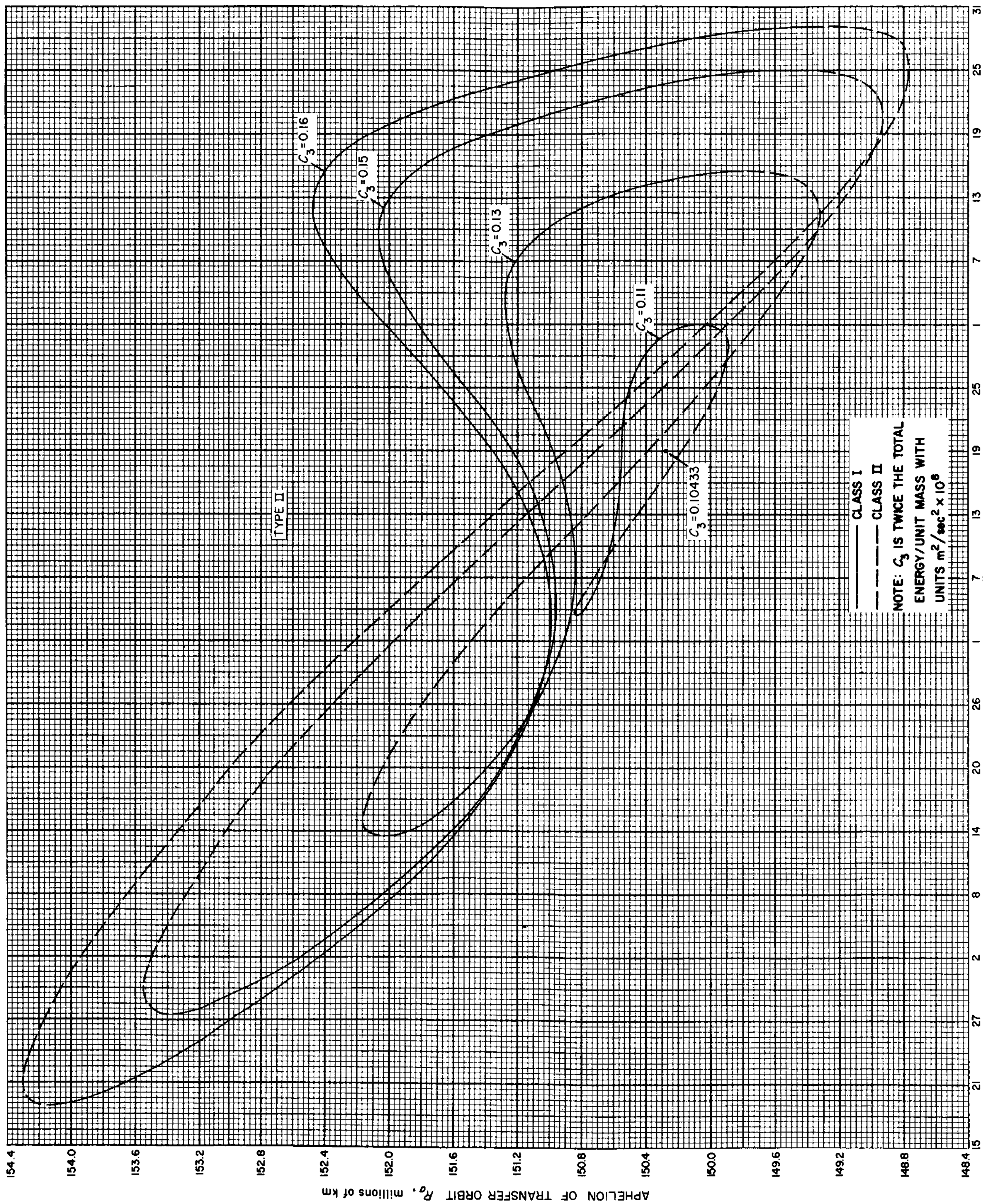

Fig. 5–16. Venus 1962: Aphelion of transfer orbit vs launch date, Type II

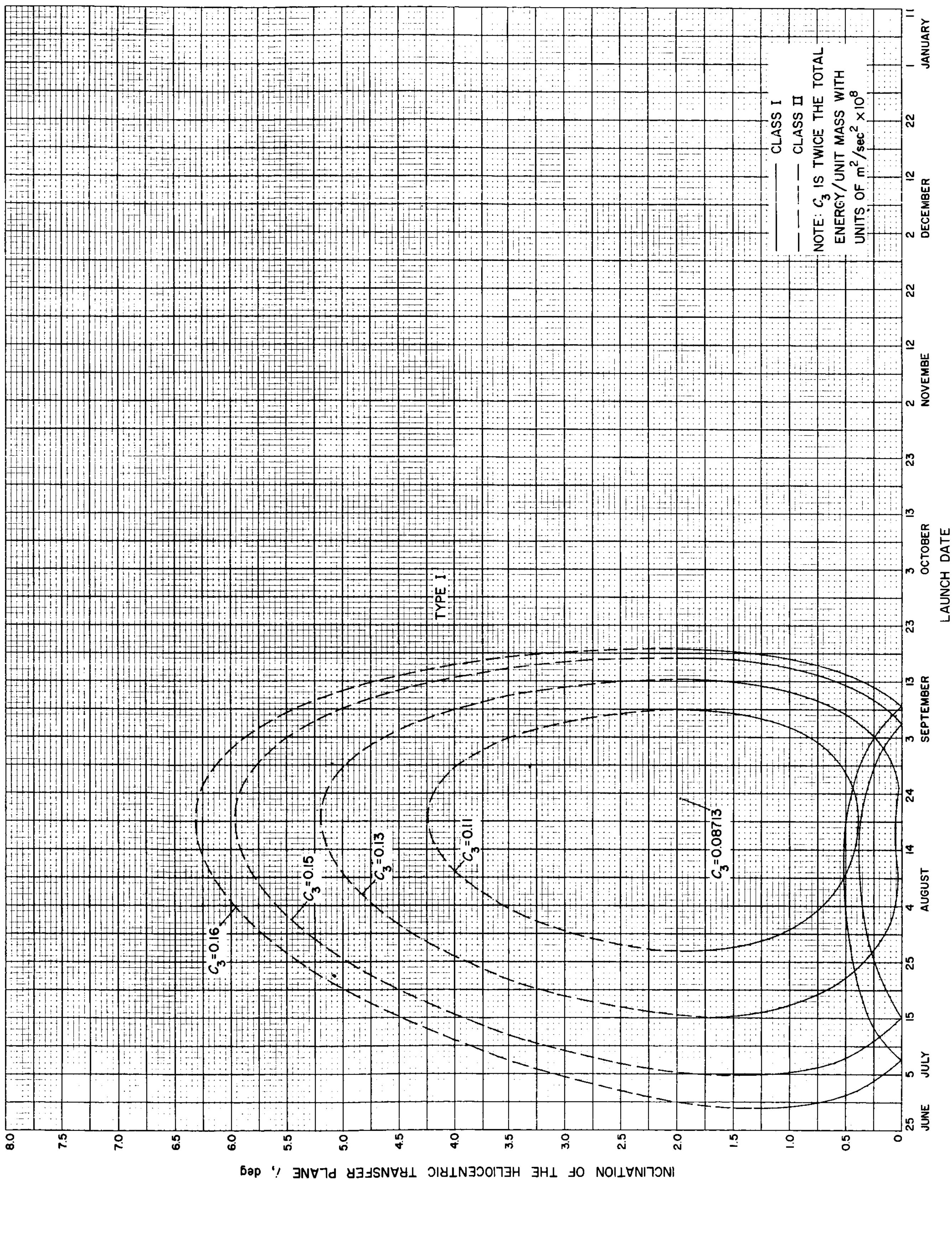

Fig. 5–17. Venus 1962: Inclination of heliocentric-transfer plane vs launch date, Type I

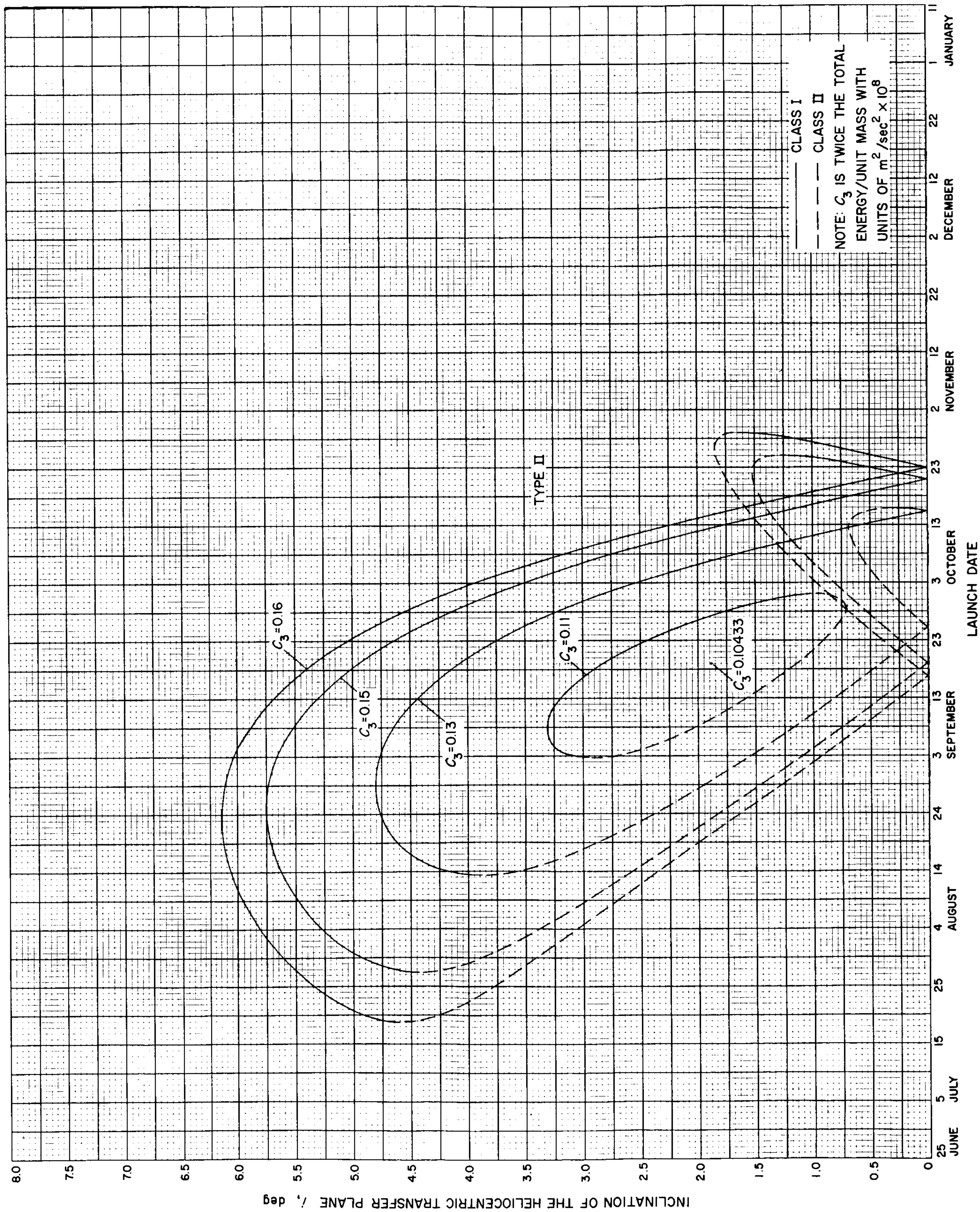

Fig. 5–18. Venus 1962: Inclination of heliocentric-transfer plane vs launch date, Type II

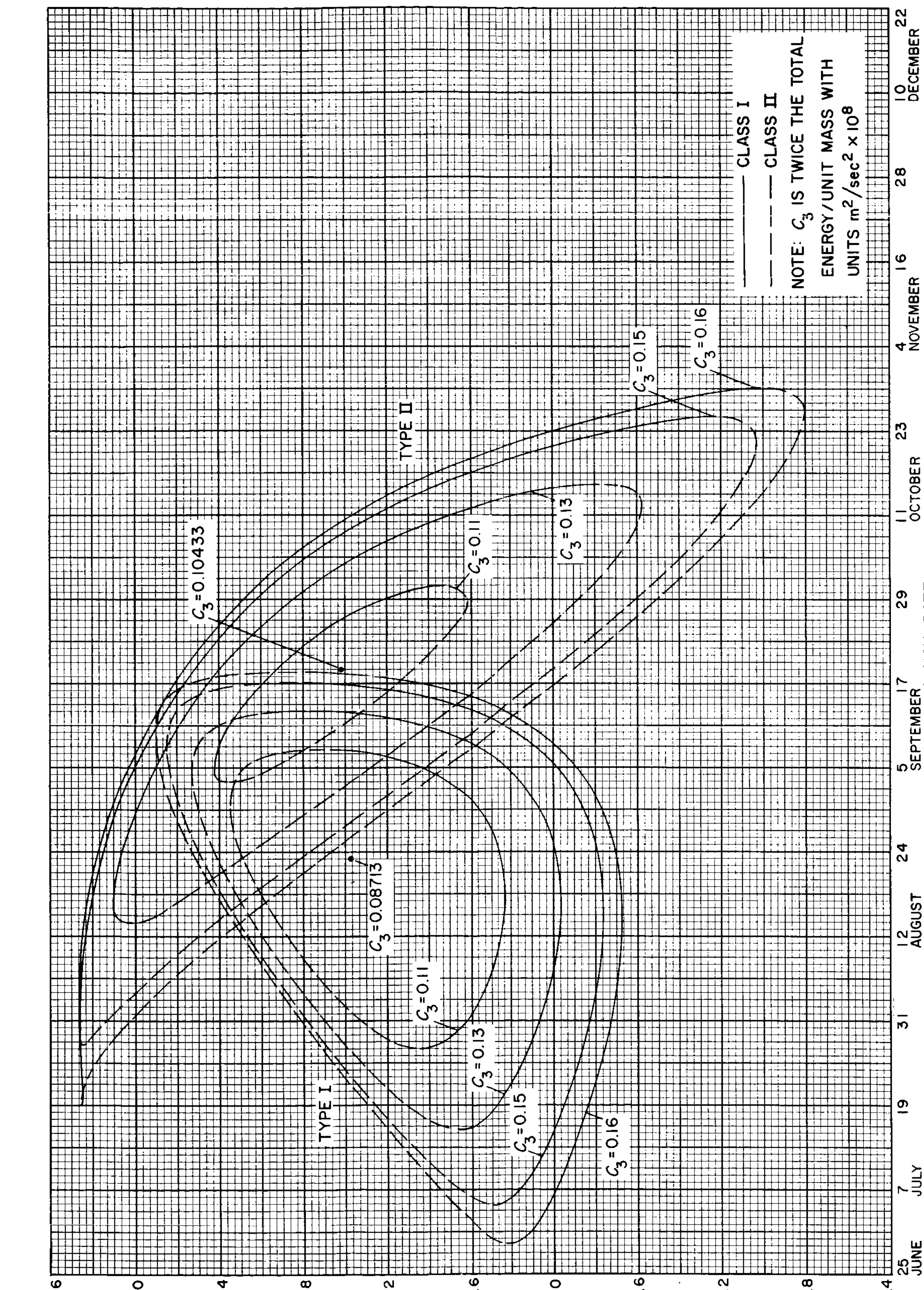

Fig. 5–19. Venus 1962: Celestial latitude at arrival time vs launch date

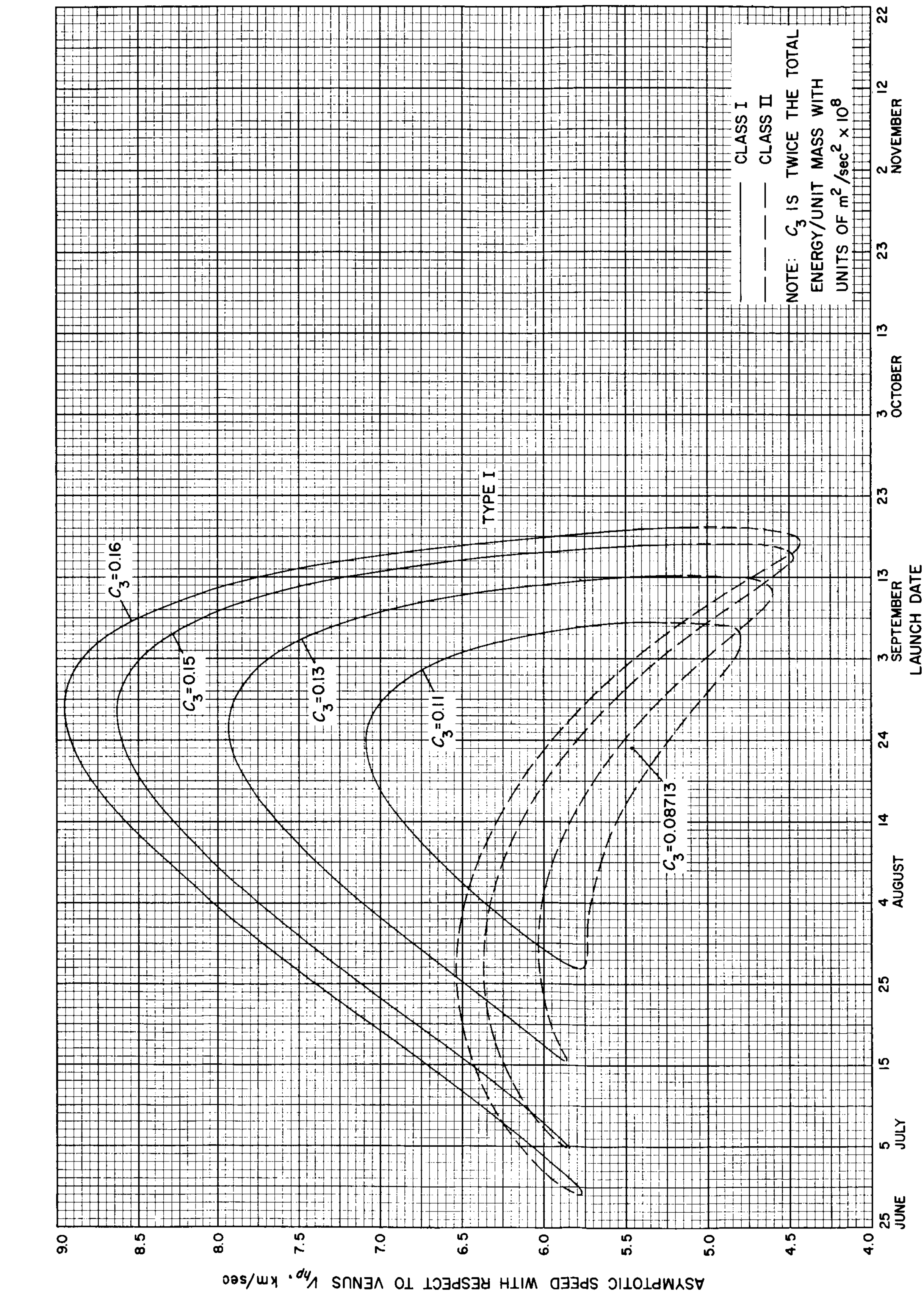

Fig. 5-20. Venus 1962: Asymptotic speed with respect to Venus vs launch date, Type I

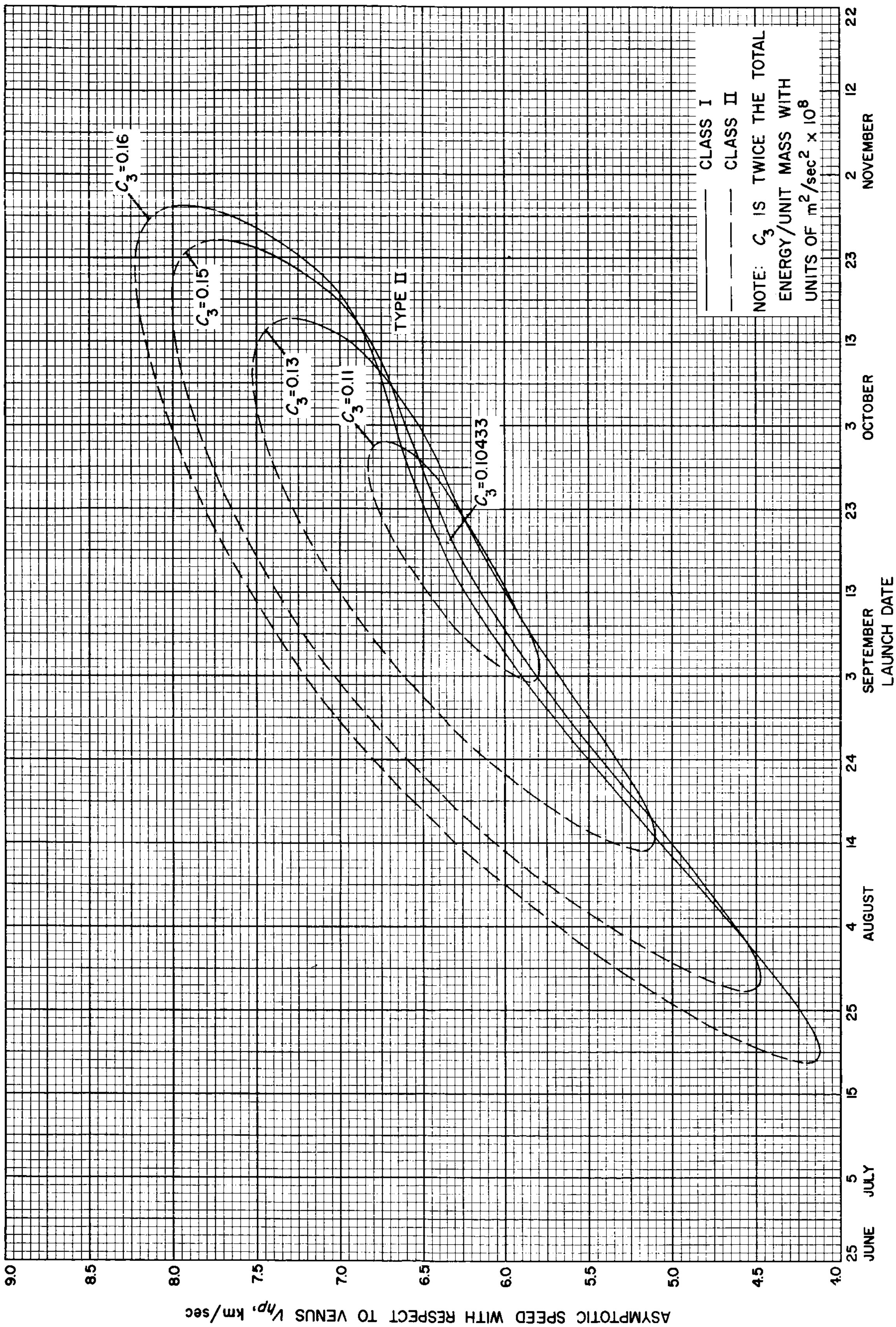

Fig. 5-21. Venus 1962: Asymptotic speed with respect to Venus vs launch date, Type II

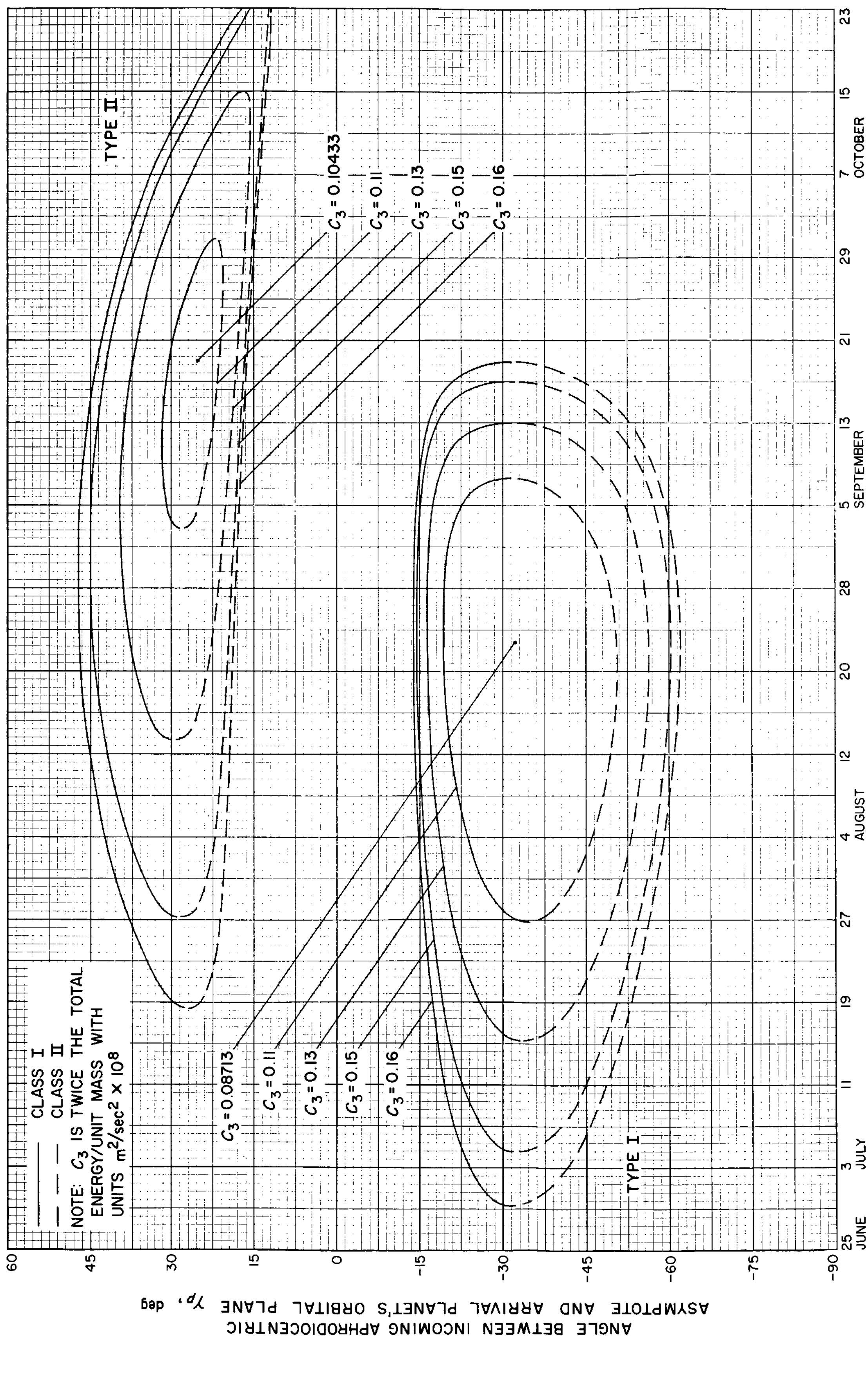

Fig. 5–22. Venus 1962: Angle between incoming aphrodiocentric asymptote and arrival planet's orbital plane vs launch date

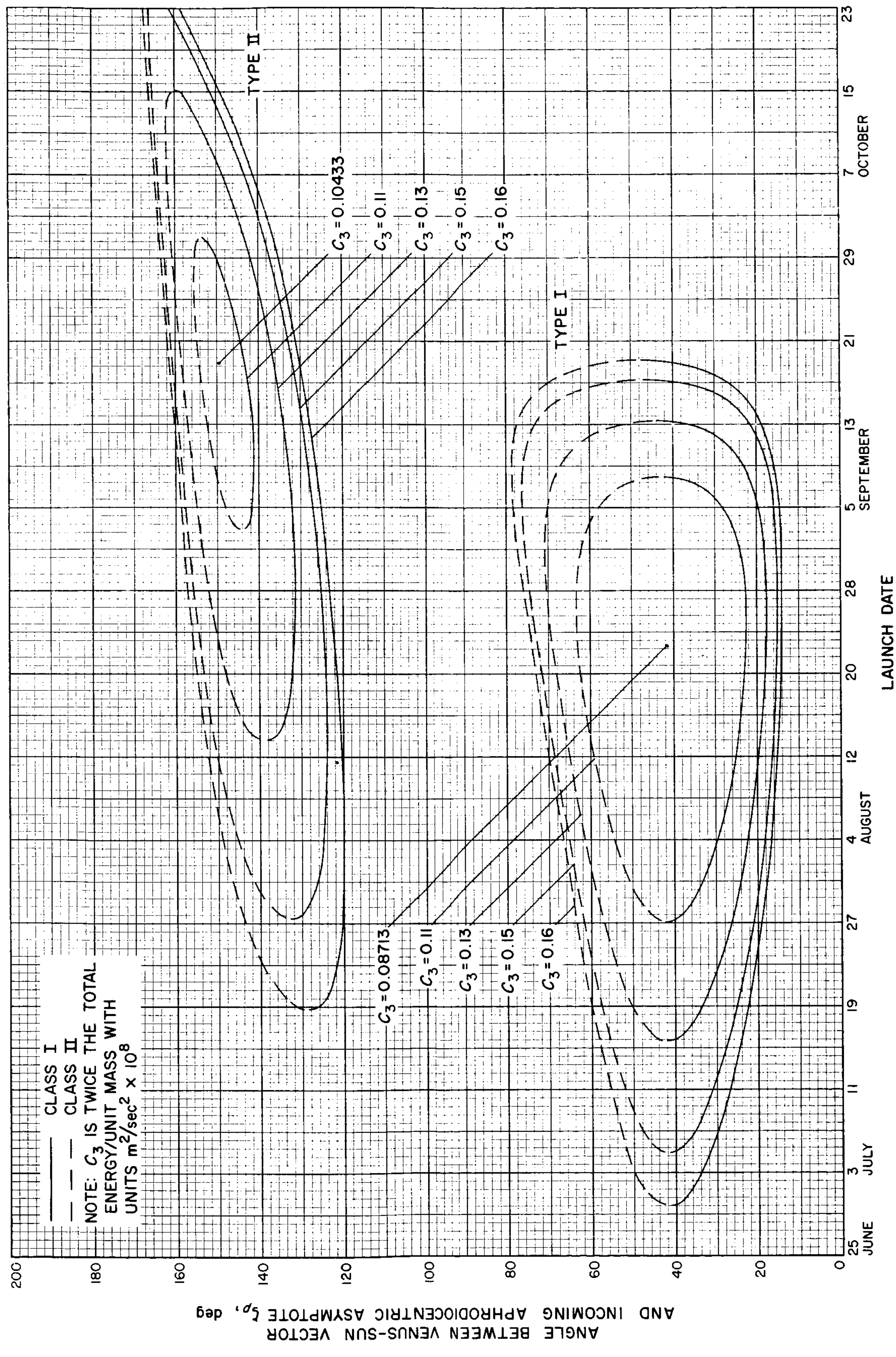

Fig. 5–23. Venus 1962: Angle between Venus–Sun vector and incoming aphrodiocentric asymptote vs launch date

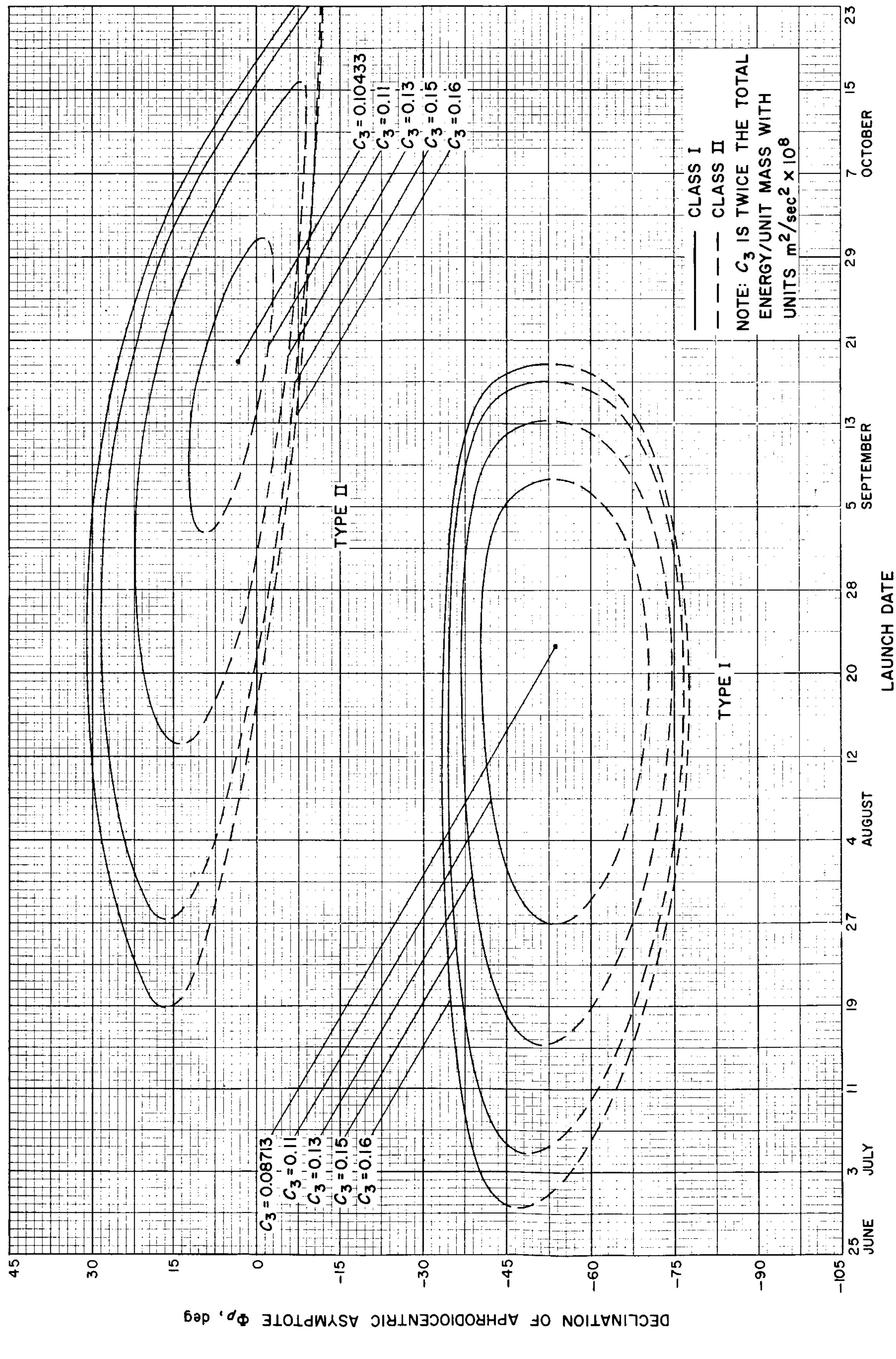

Fig. 5-24. Venus 1962: Declination of aphrodiocentric asymptote vs launch date

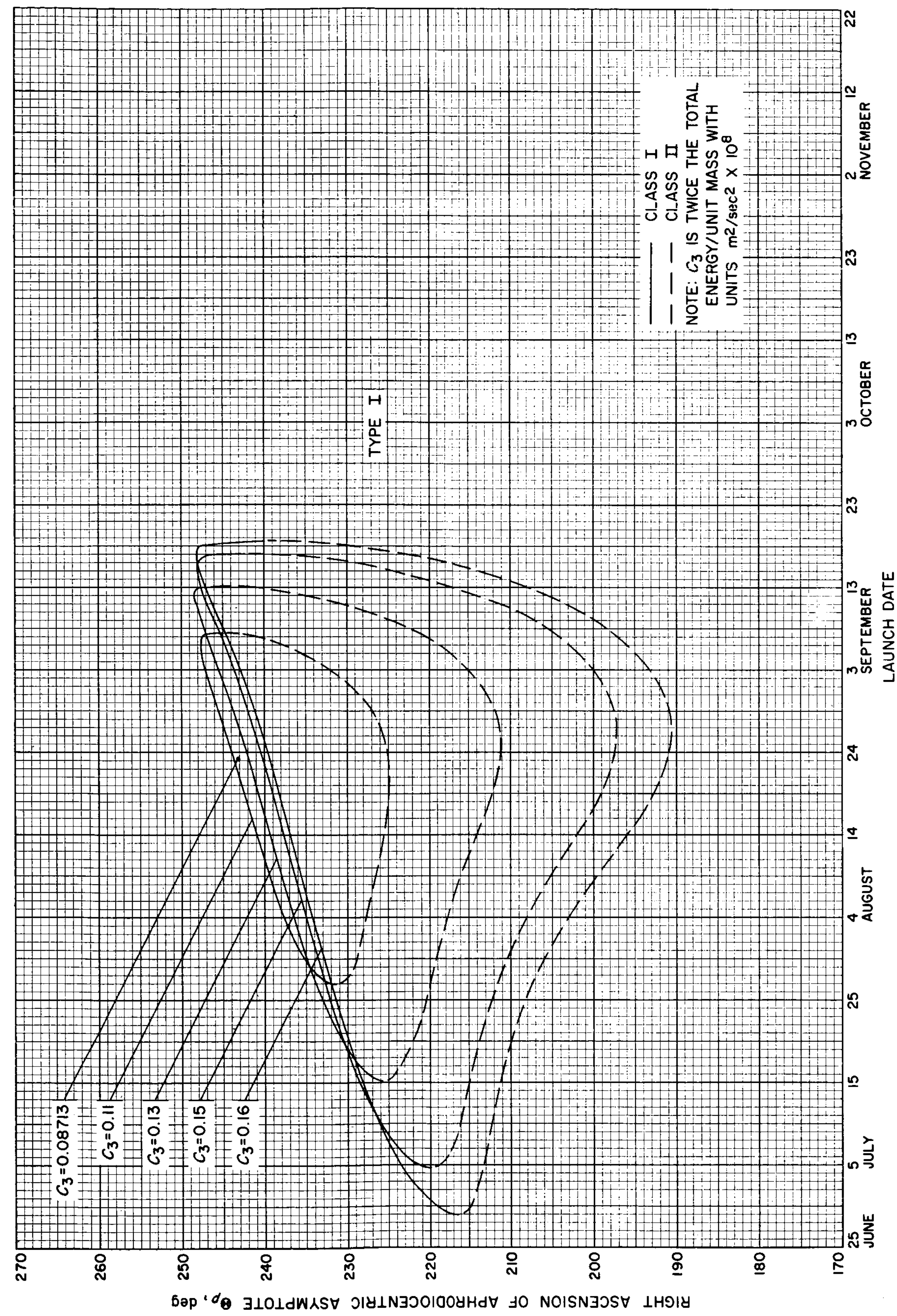

Fig. 5-25. Venus 1962: Right ascension of aphrodiocentric asymptote vs launch date, Type I

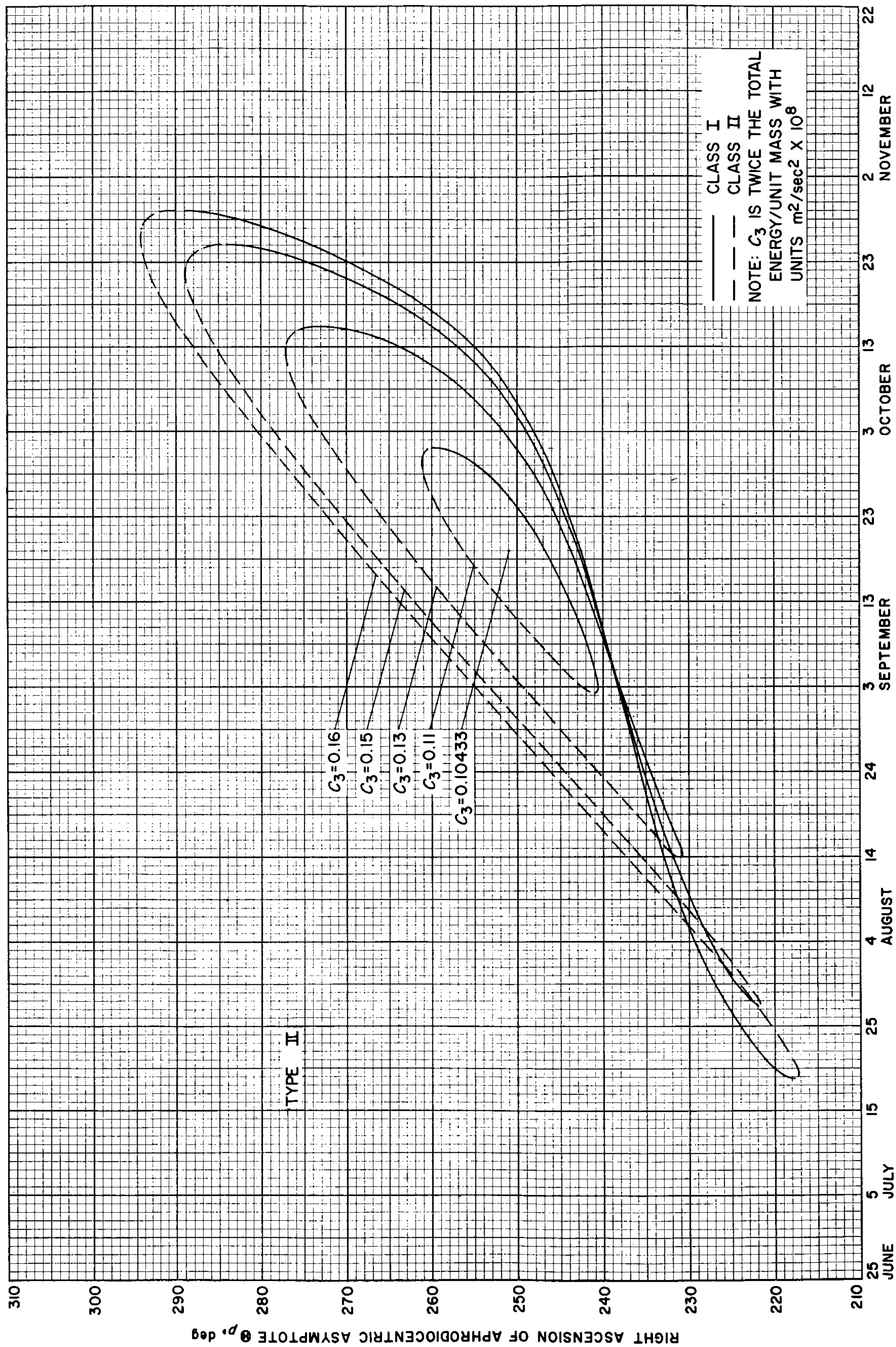

Fig. 5-26. Venus 1962: Right ascension of aphrodiocentric asymptote vs launch date, Type II

VI. VENUS 1964: TRAJECTORY-PARAMETER GRAPHS

Figure

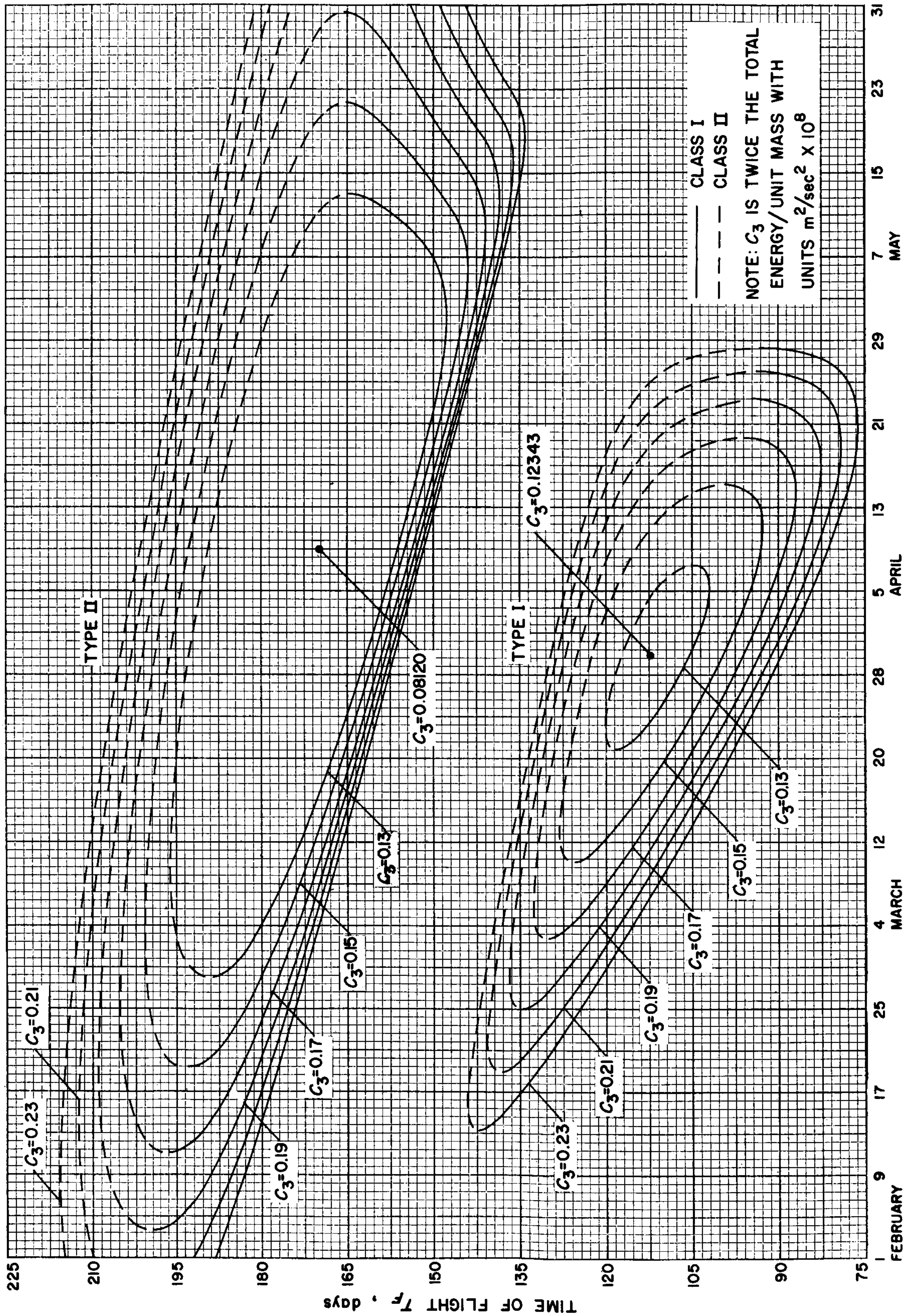

Fig. 6–1. Venus 1964: Time of flight vs launch date

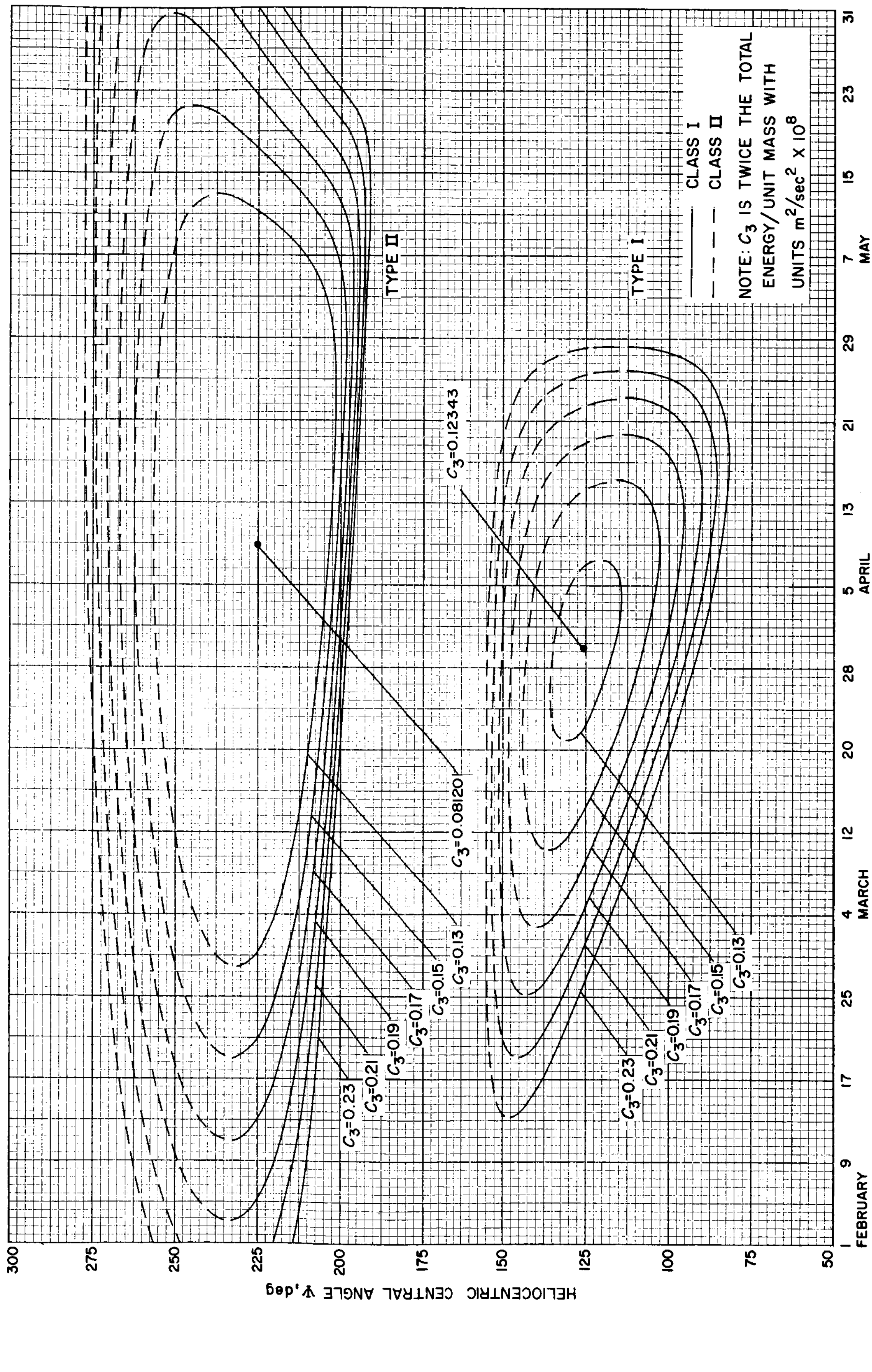

Fig. 6–2. Venus 1964: Heliocentric central angle vs launch date

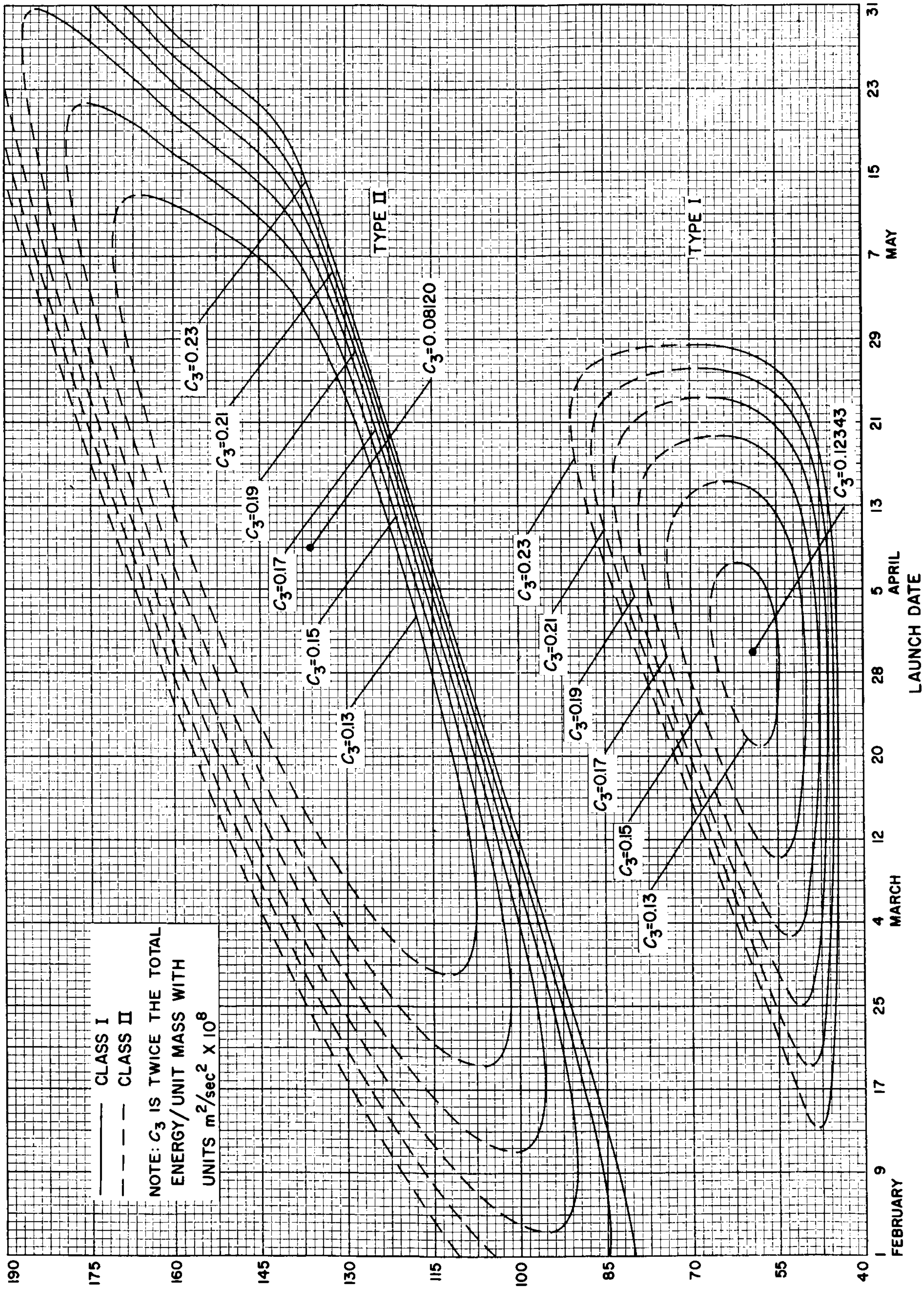

Fig. 6–3. Venus 1964: Earth–Venus communication distance vs launch date

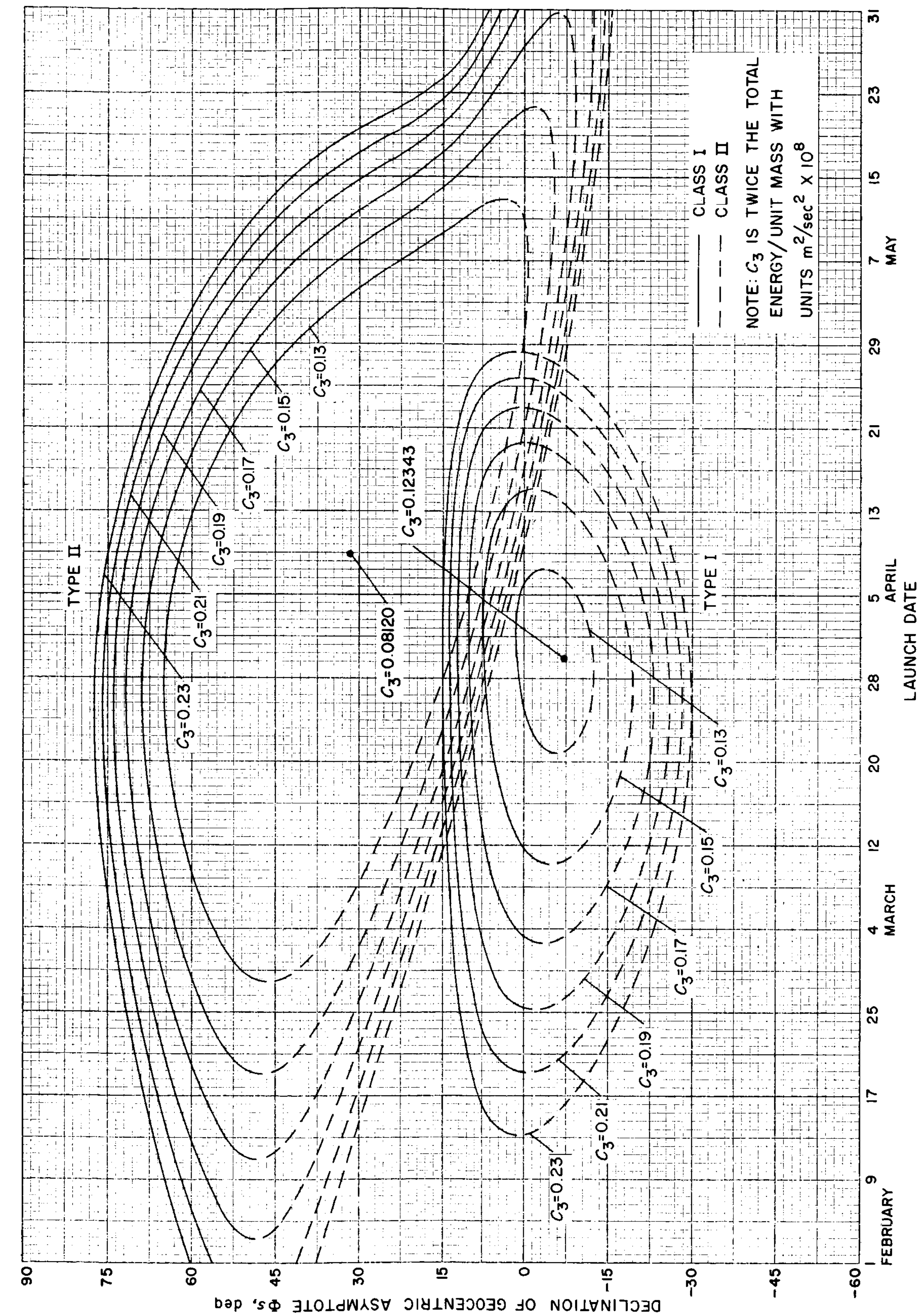

Fig. 6–4. Venus 1964: Declination of geocentric asymptote vs launch date

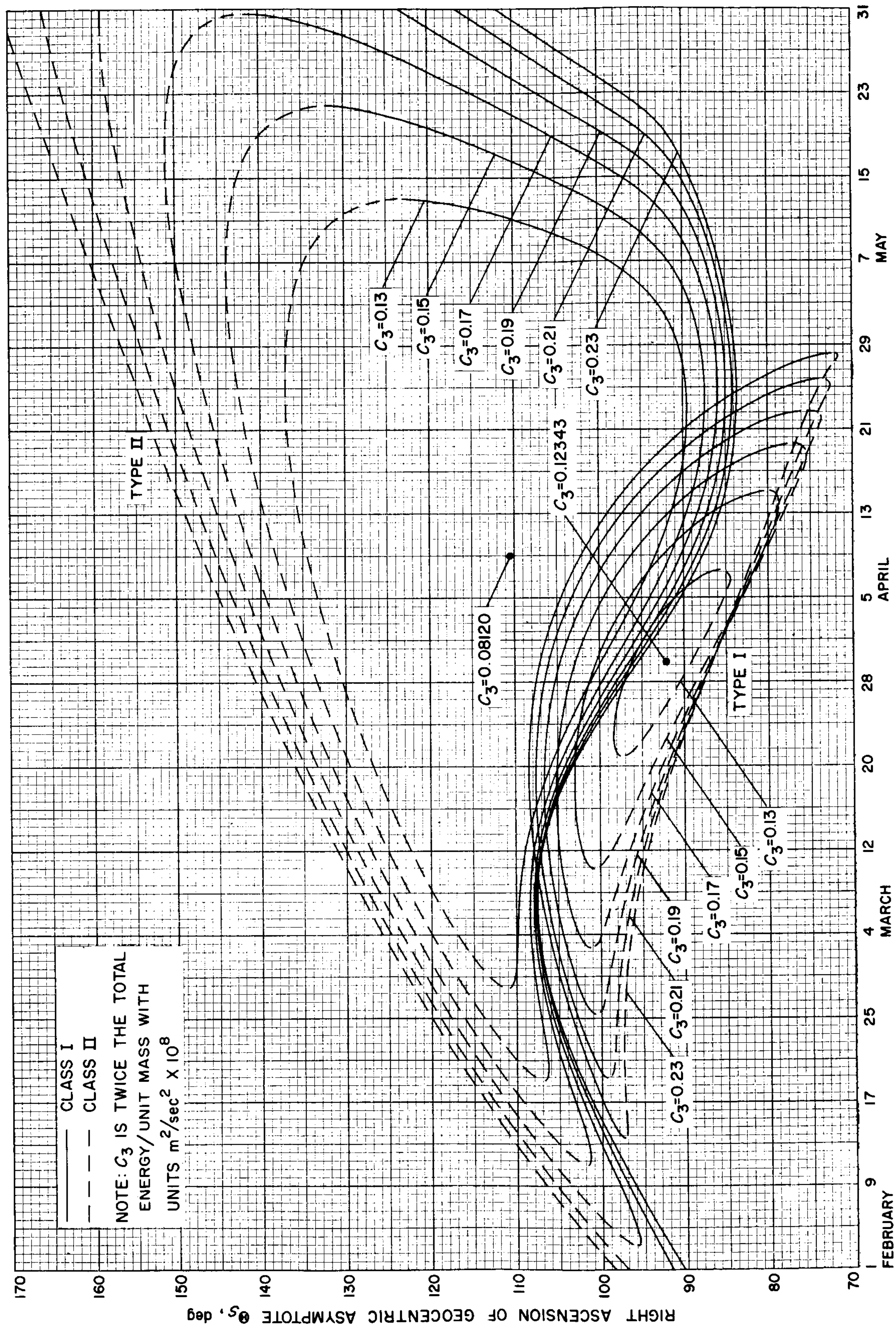

Fig. 6–5. Venus 1964: Right ascension of geometric asymptote vs launch date

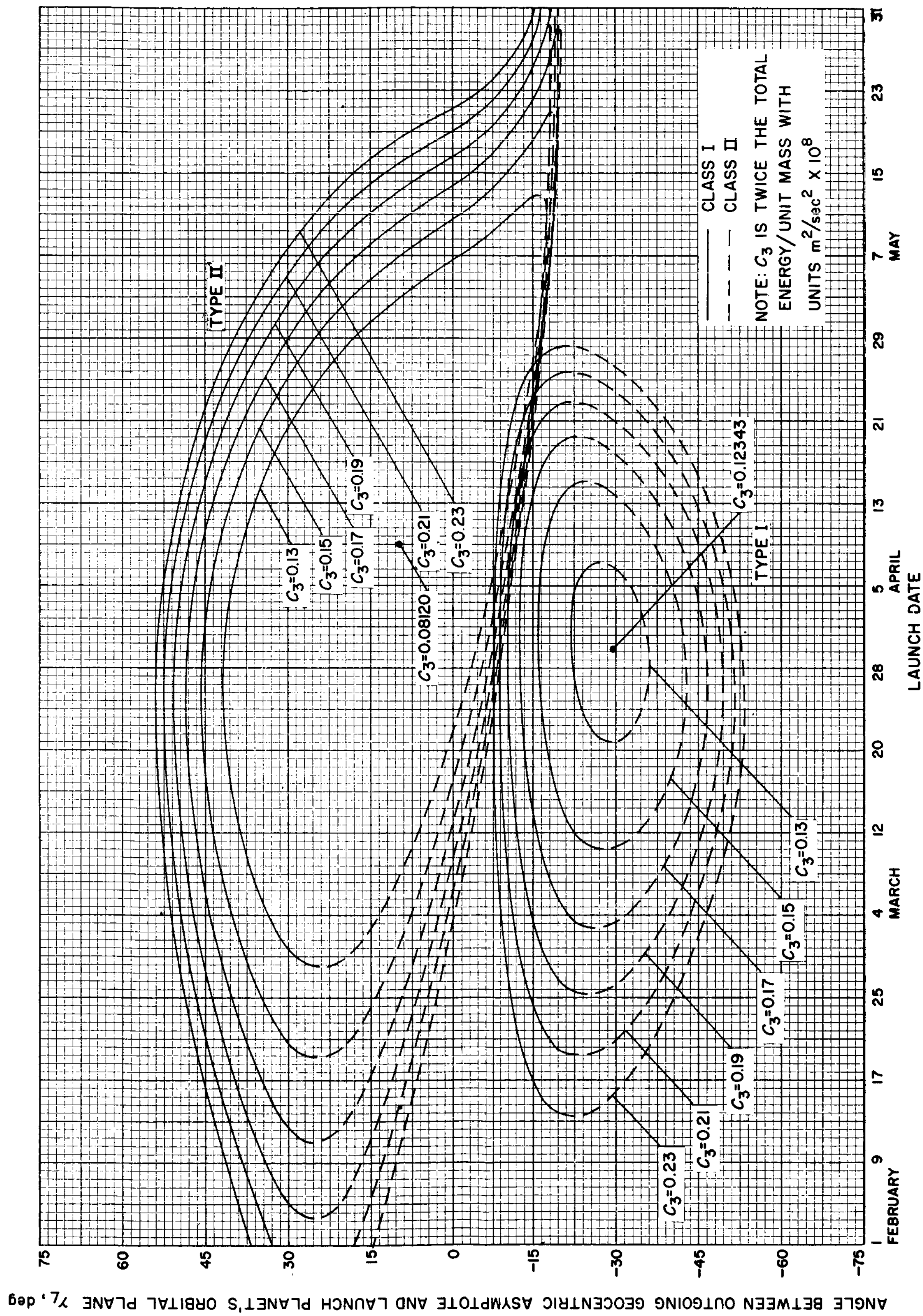

Fig. 6-6. Venus 1964: Angle between outgoing geocentric asymptote and launch planet's orbital plane vs launch date

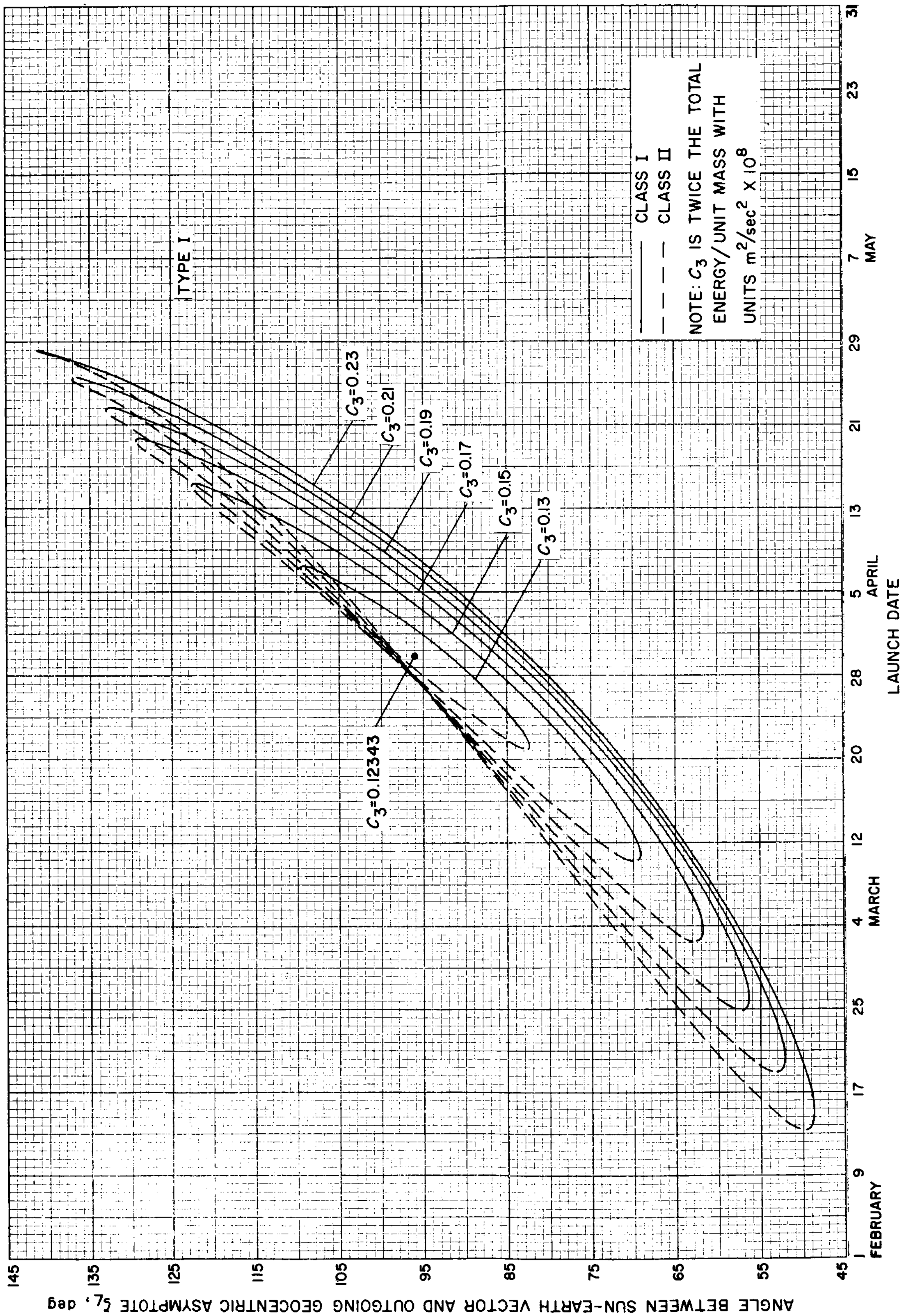

Fig. 6-7. Venus 1964: Angle between Sun–Earth vector and outgoing geocentric asymptote launch date, Type I

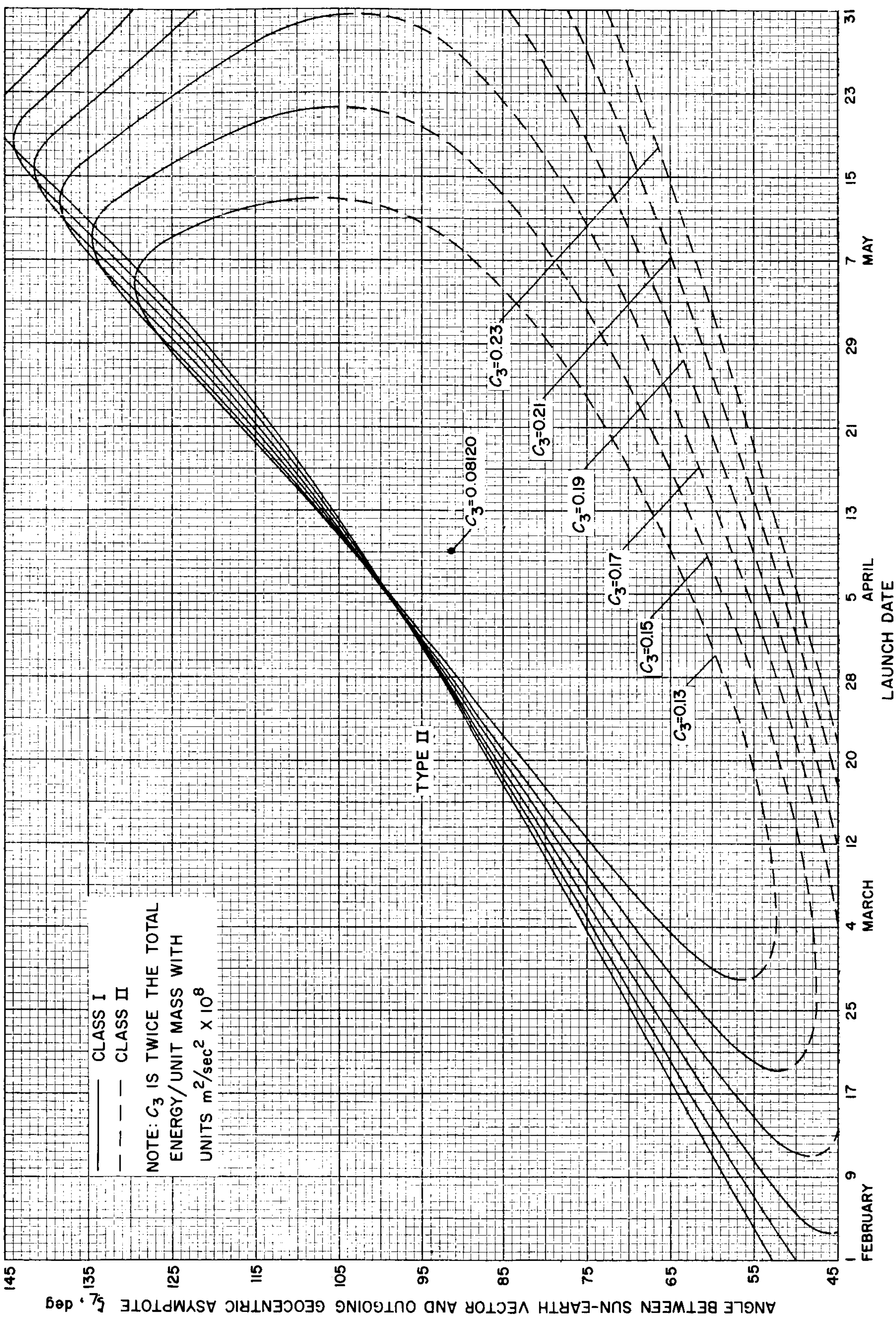

Fig. 6–8. Venus 1964: Angle between Sun–Earth vector and outgoing geocentric asymptote vs launch date, Type II

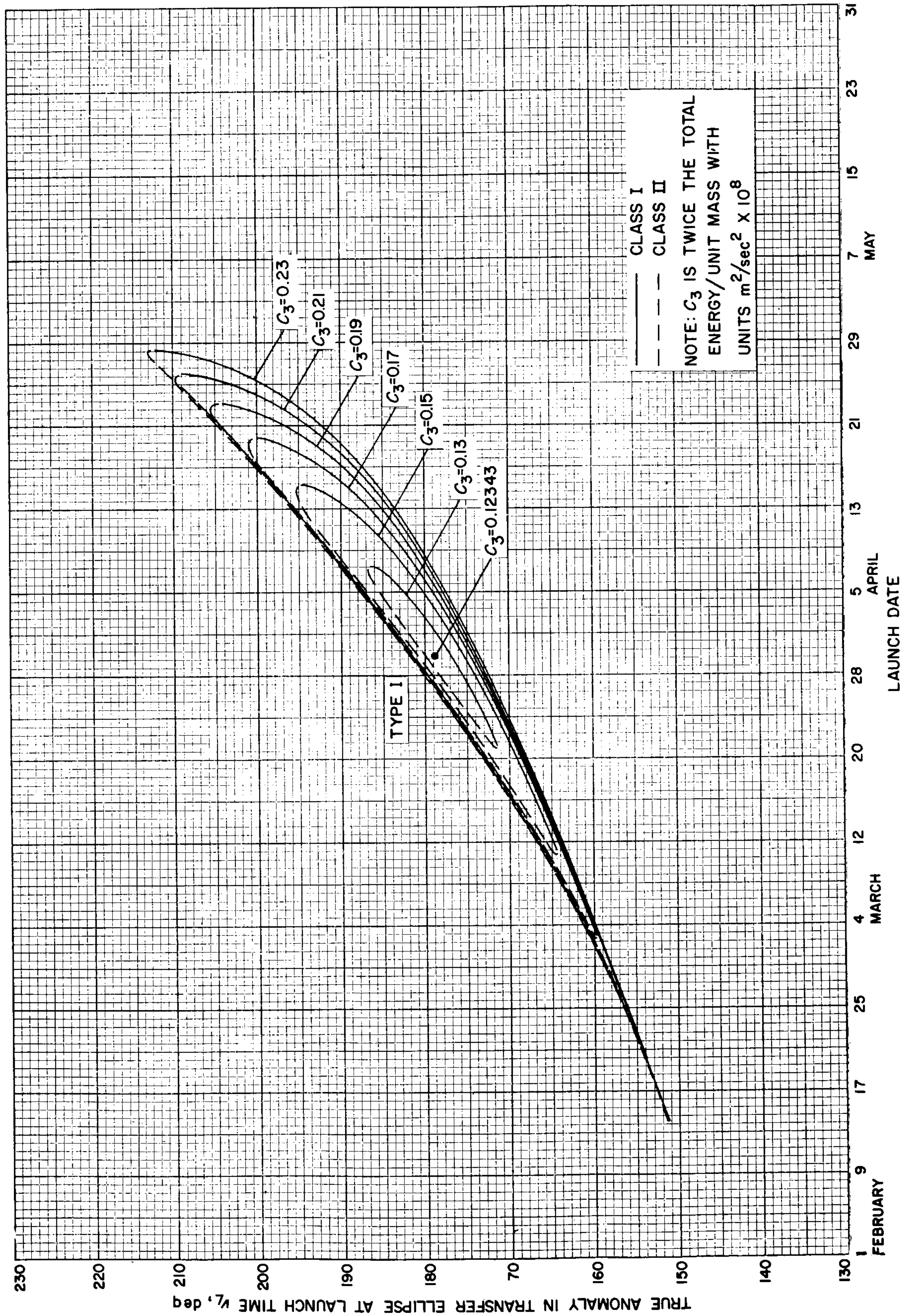

Fig. 6-9. Venus 1964: True anomaly in transfer ellipse at launch time vs launch date, Type I

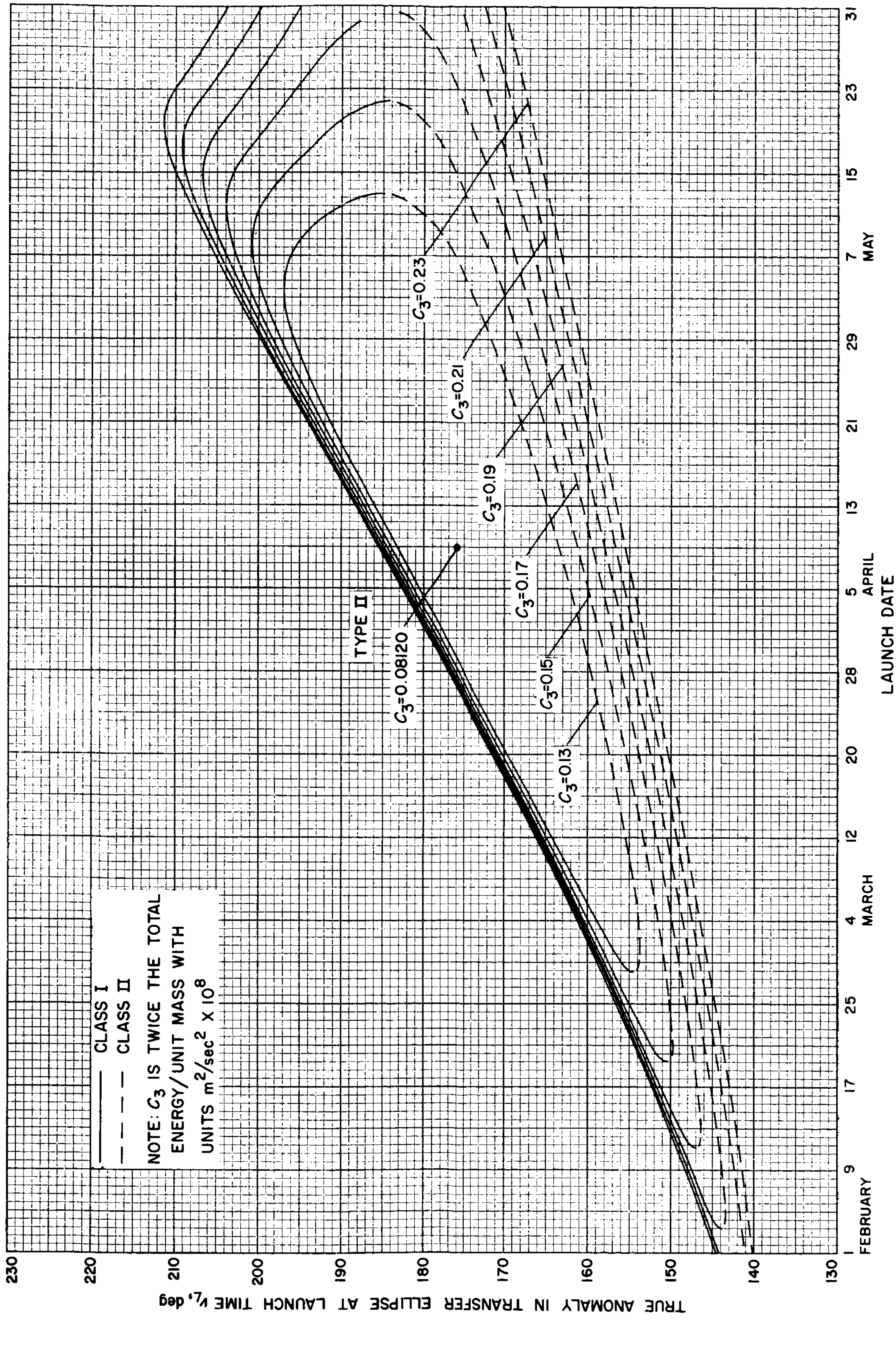

Fig. 6–10. Venus 1964: True anomaly in transfer ellipse at launch time vs launch date, Type II

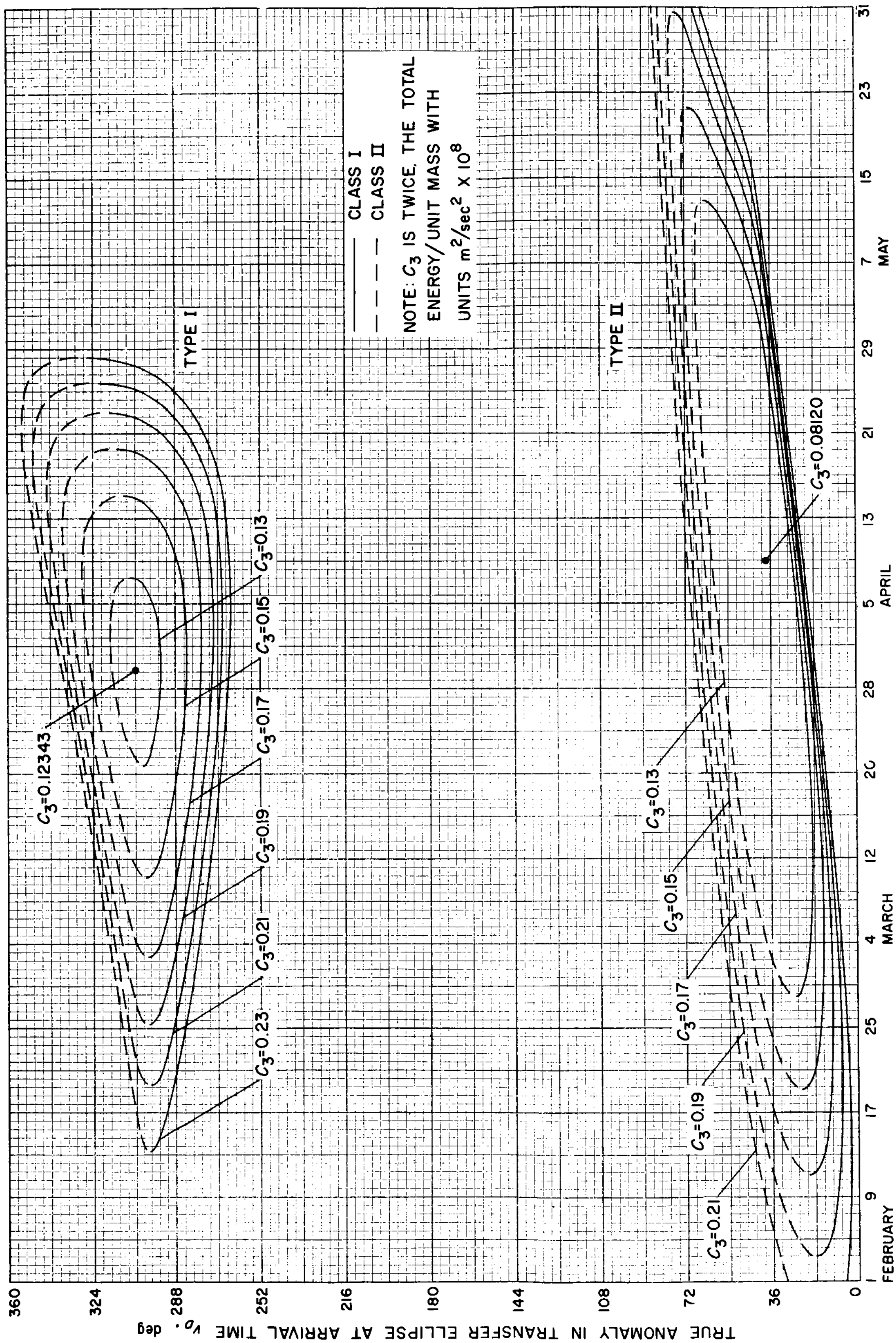

Fig. 6-11. Venus 1964: True anomaly in transfer ellipse at arrival time vs launch date

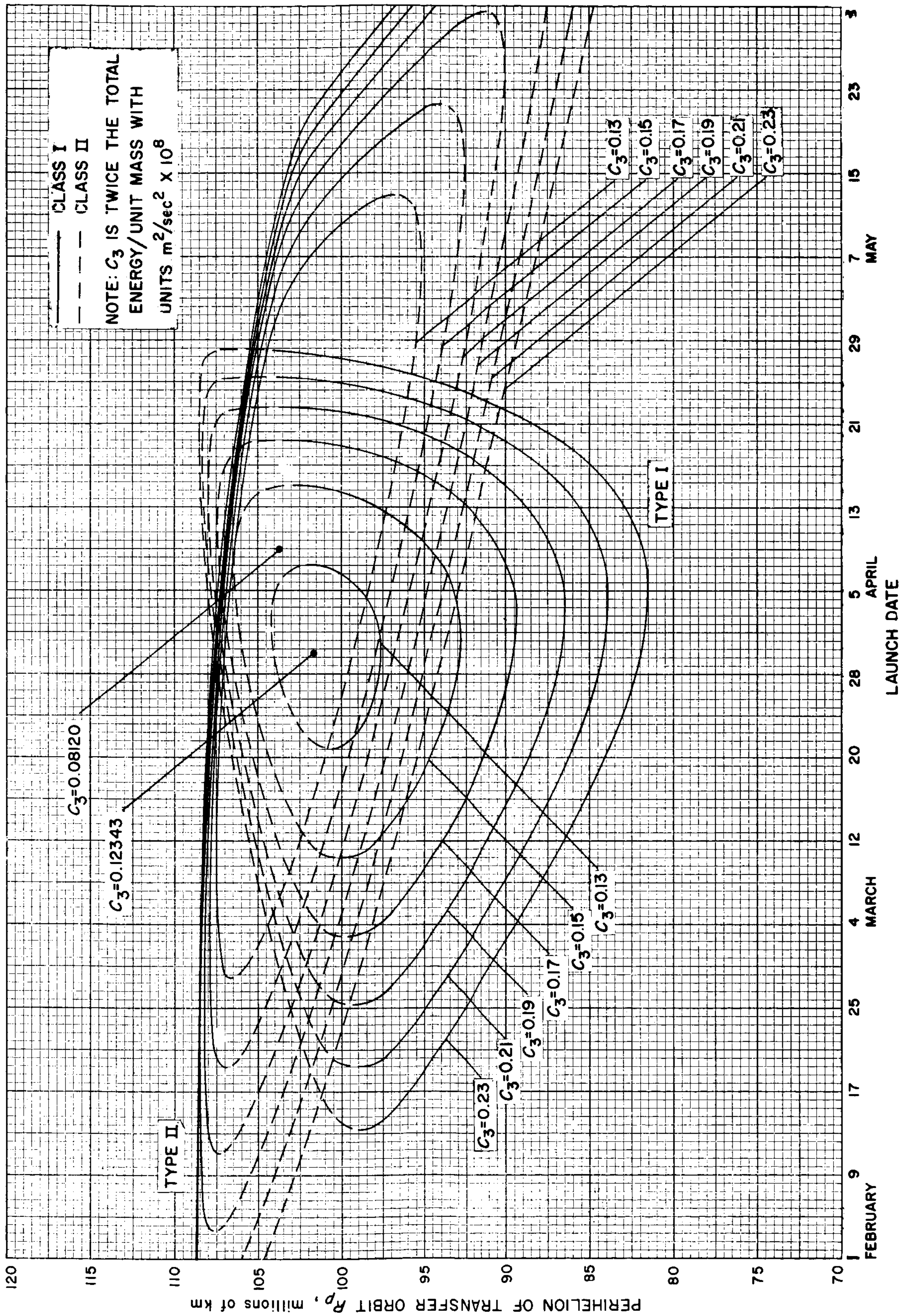

Fig. 6–12. Venus 1964: Perihelion of transfer orbit vs launch date

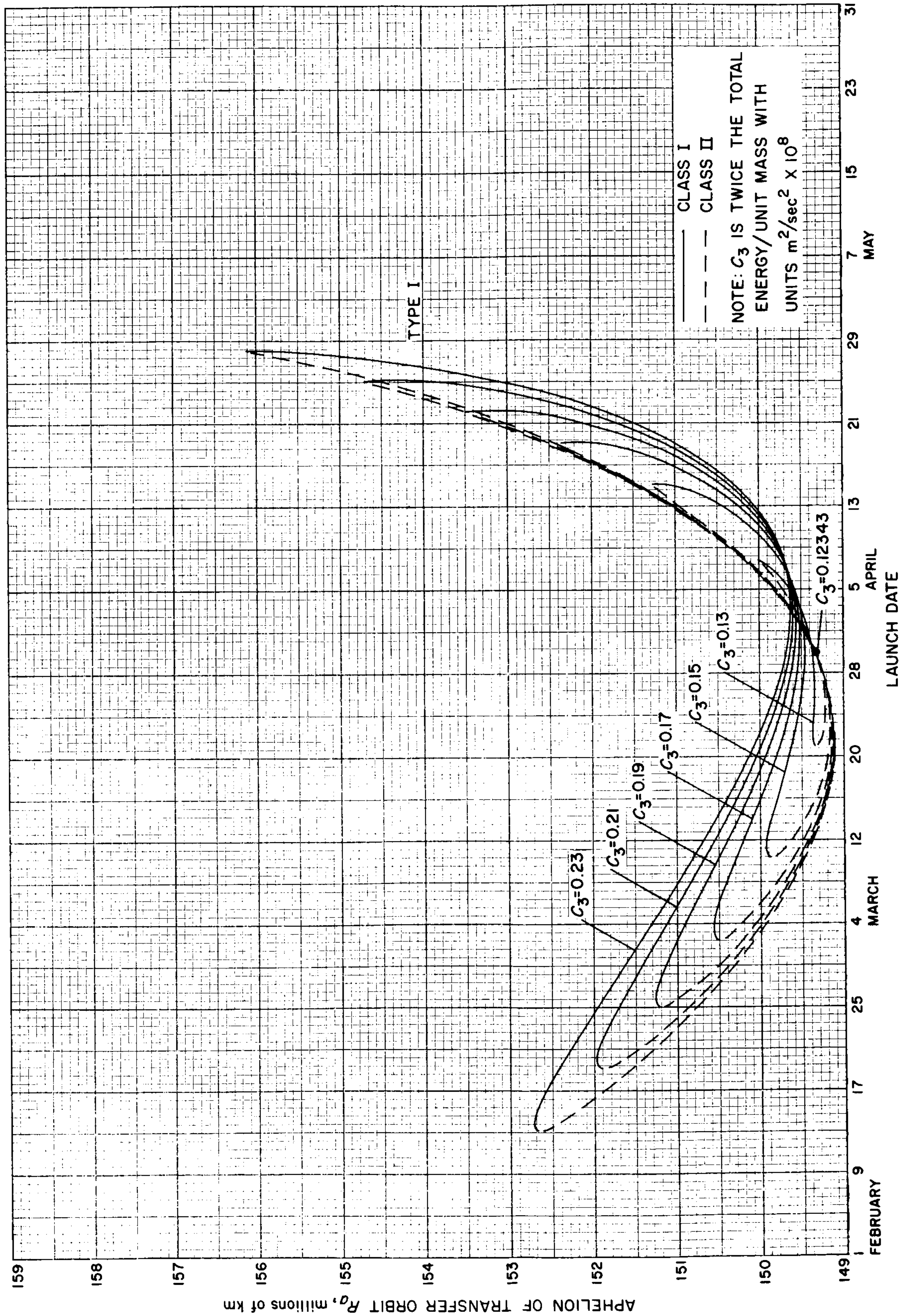

Fig. 6-13. Venus 1964: Aphelion of transfer orbit vs launch date, Type I

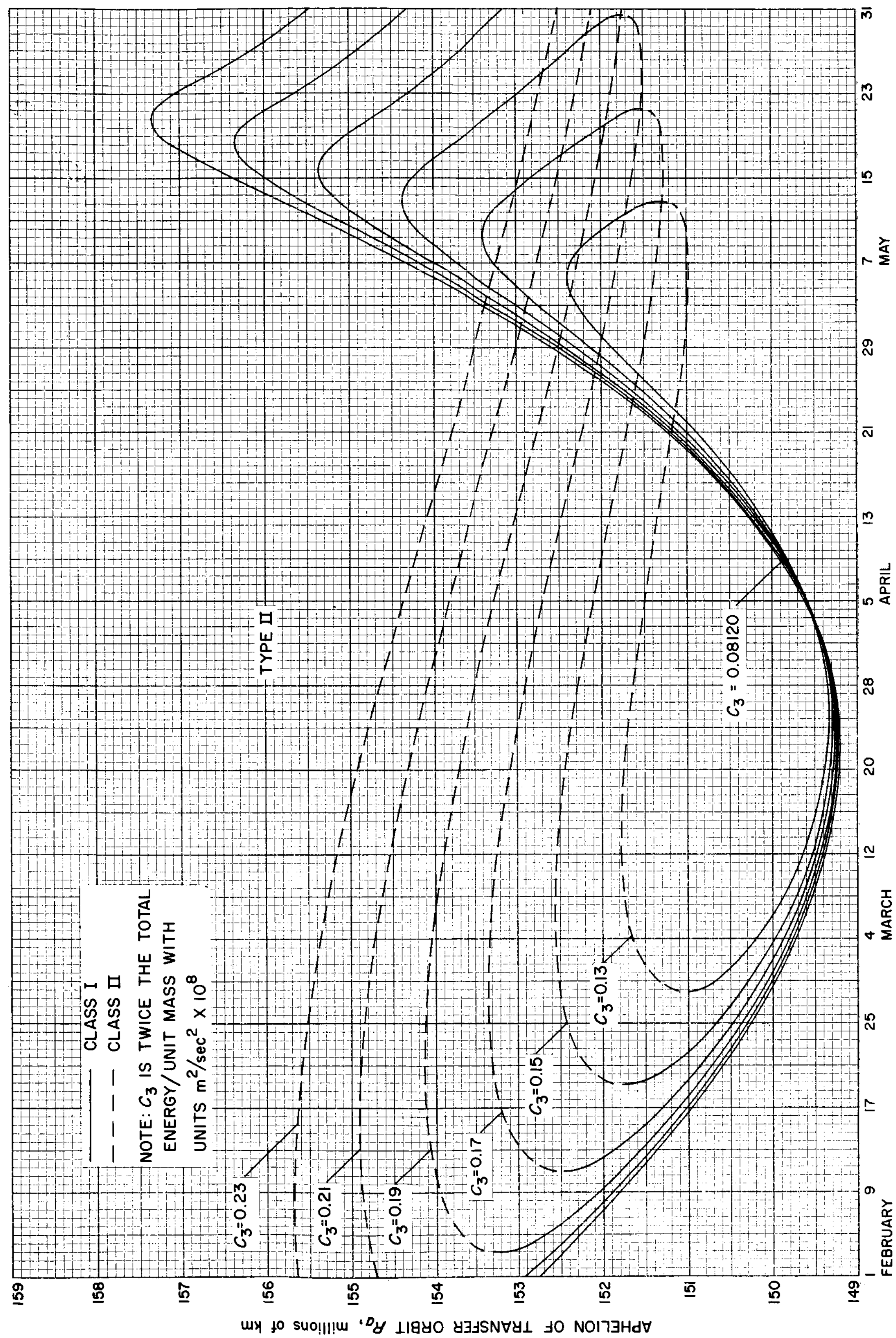

Fig. 6–14. Venus 1964: Aphelion of transfer orbit vs launch date, Type II

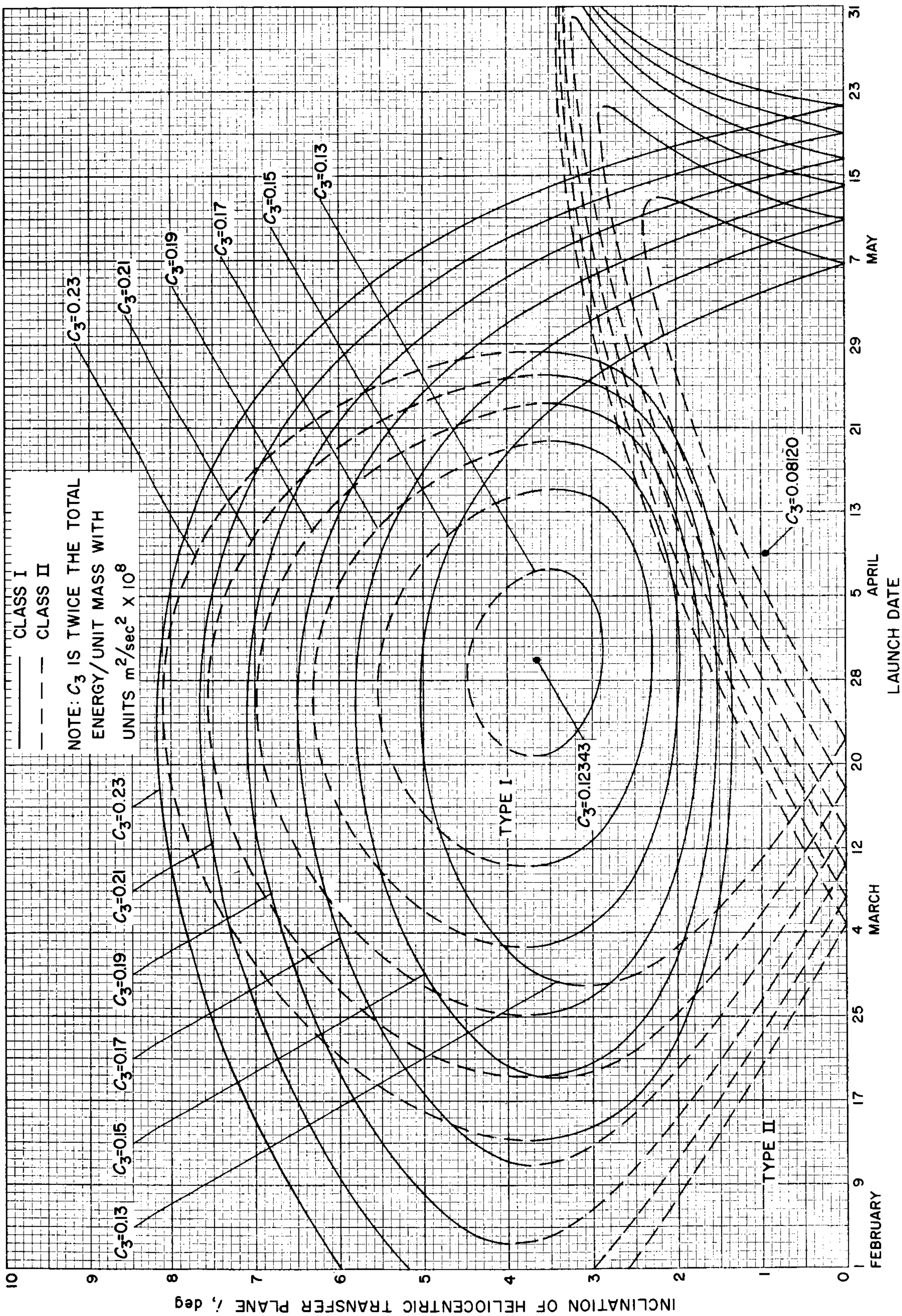

Fig. 6–15. Venus 1964: Inclination of heliocentric-transfer plane vs launch date

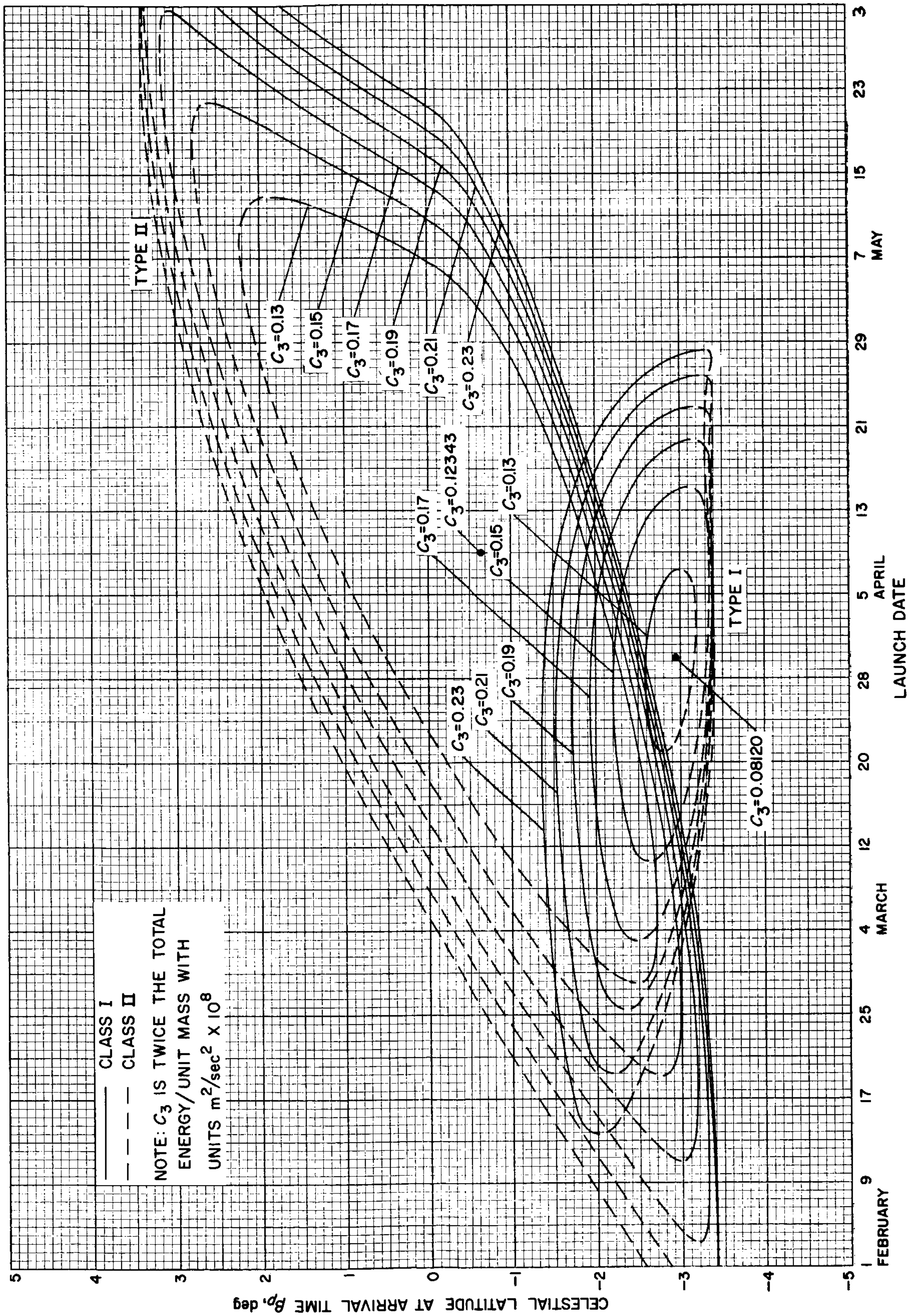

Fig. 6–16. Venus 1964: Celestial latitude at arrival time vs launch date

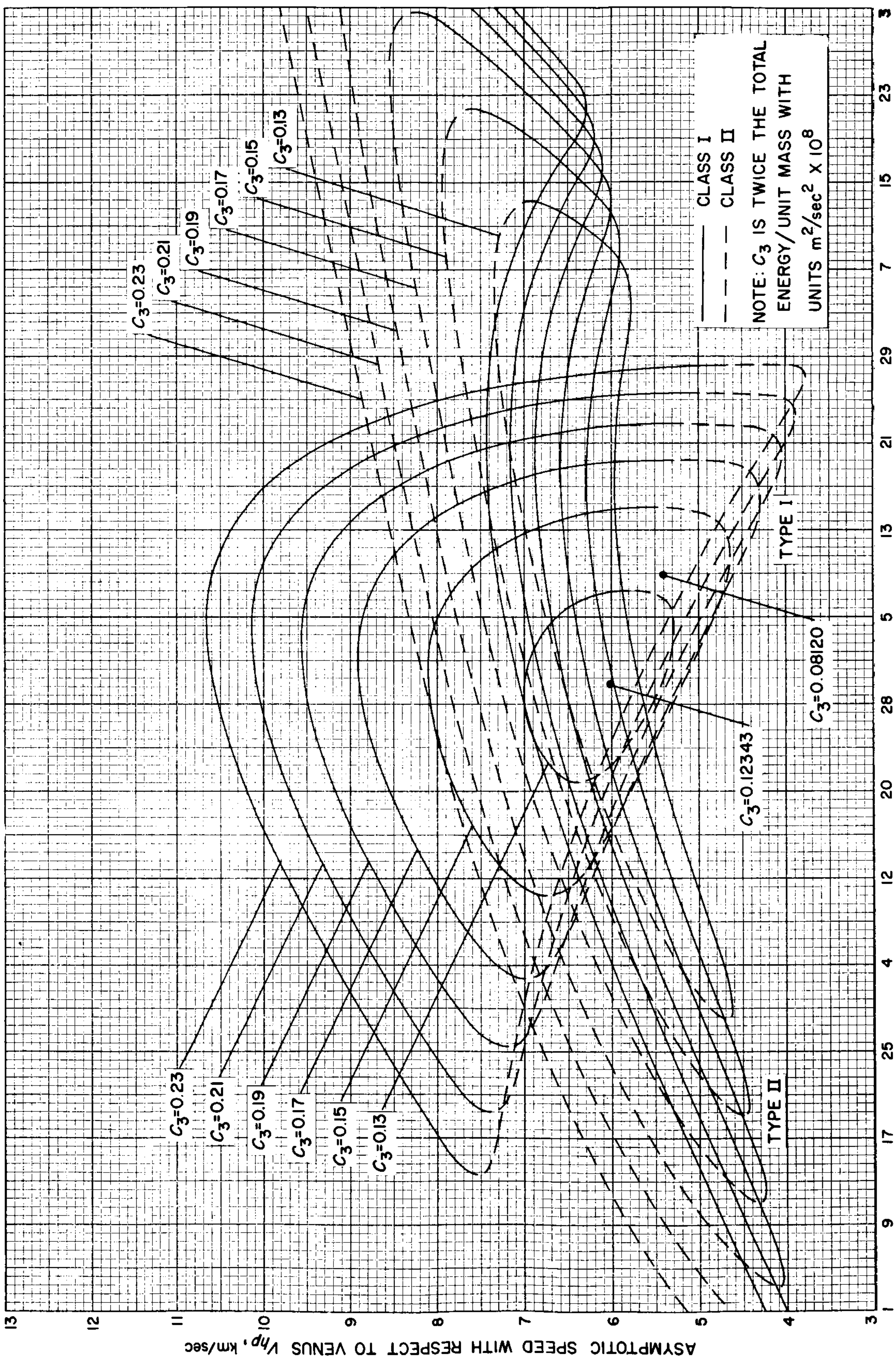

Fig. 6–17. Venus 1964: Asymptotic speed with respect to Venus vs launch date

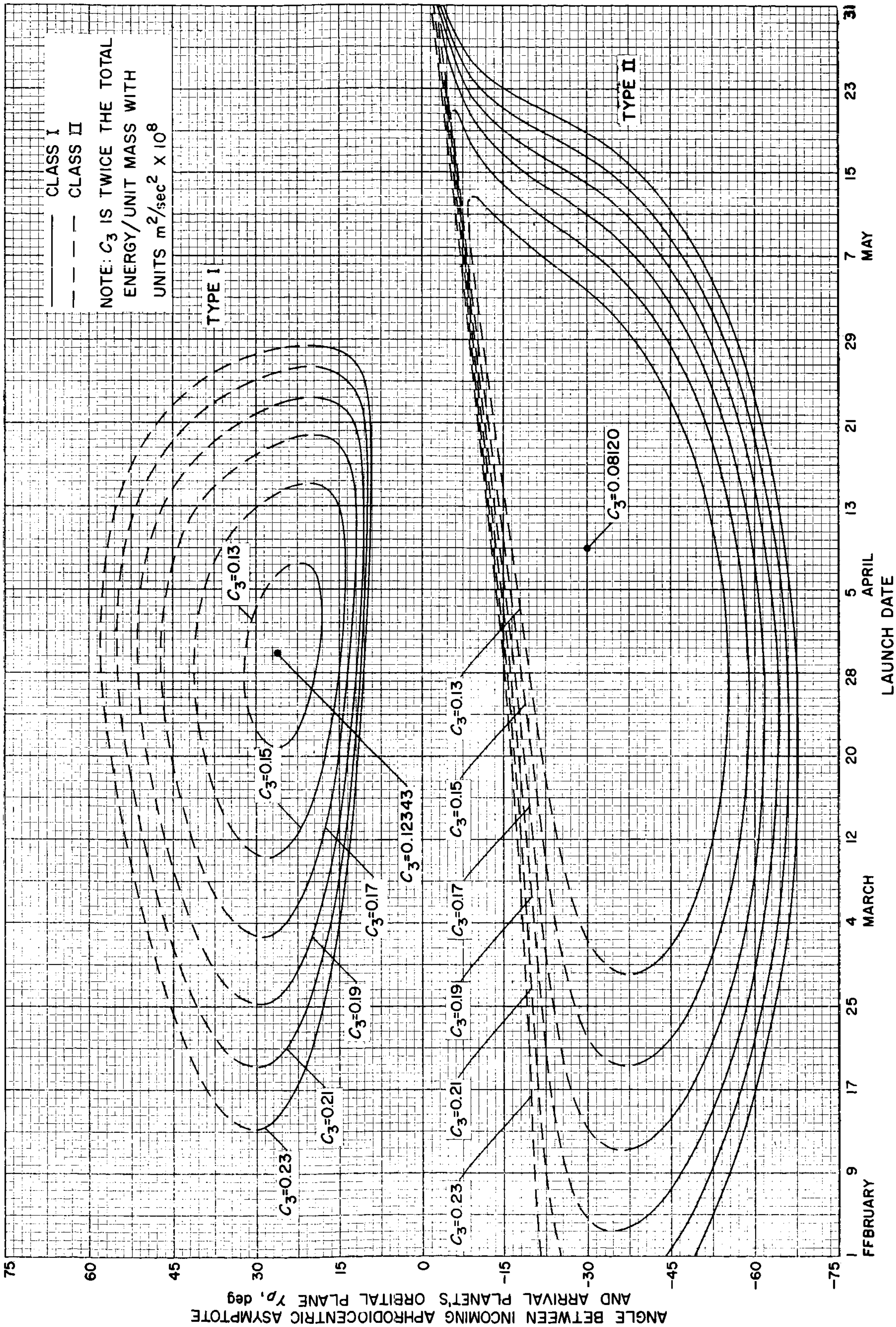

Fig. 6–18. Venus 1964: Angle between incoming aphrodiocentric asymptote and arrival planet's orbital plane vs launch date

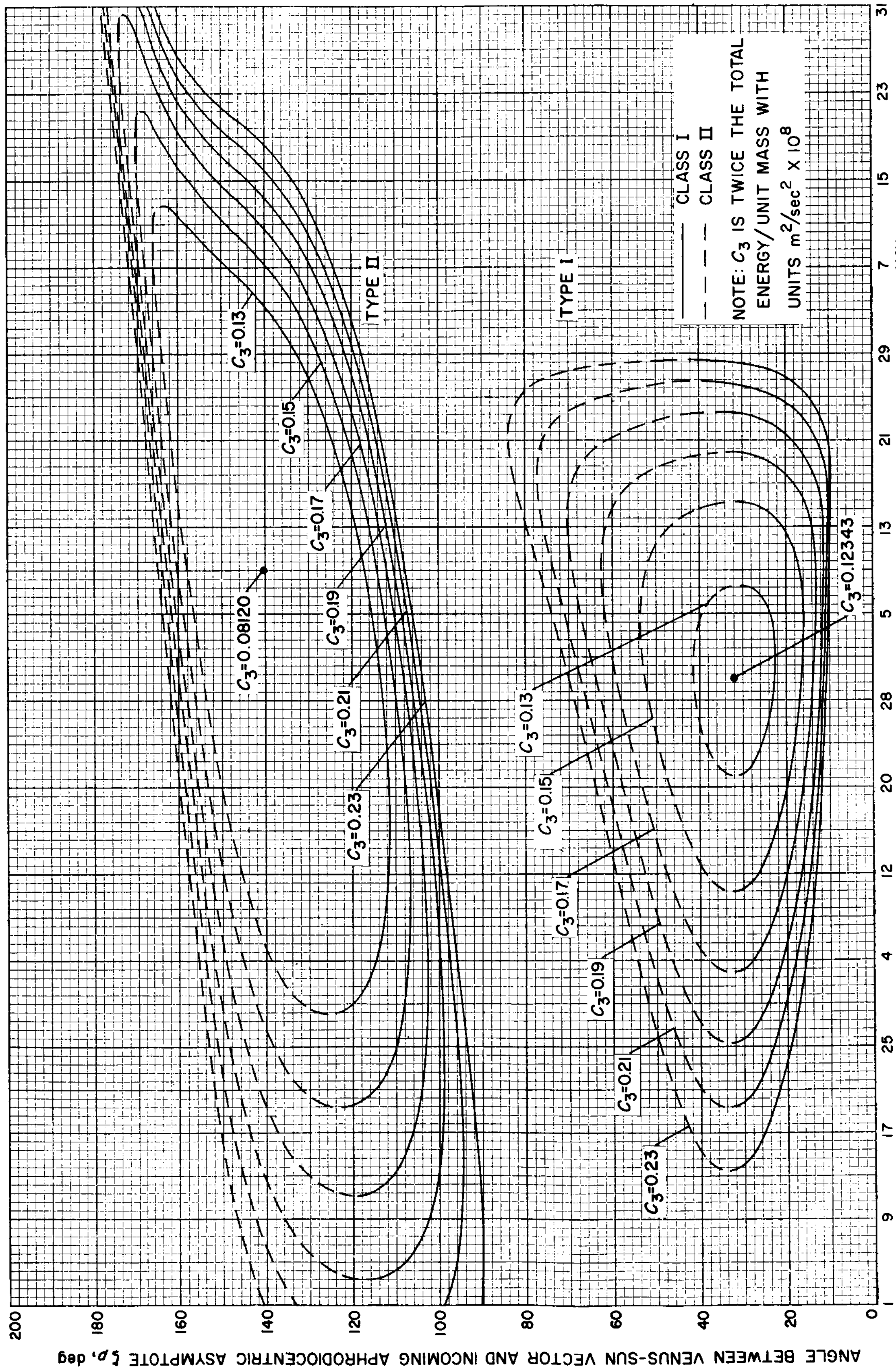

Fig. 6–19. Venus 1964: Angle between Venus–Sun vector and incoming aphrodiocentric asymptote vs launch date

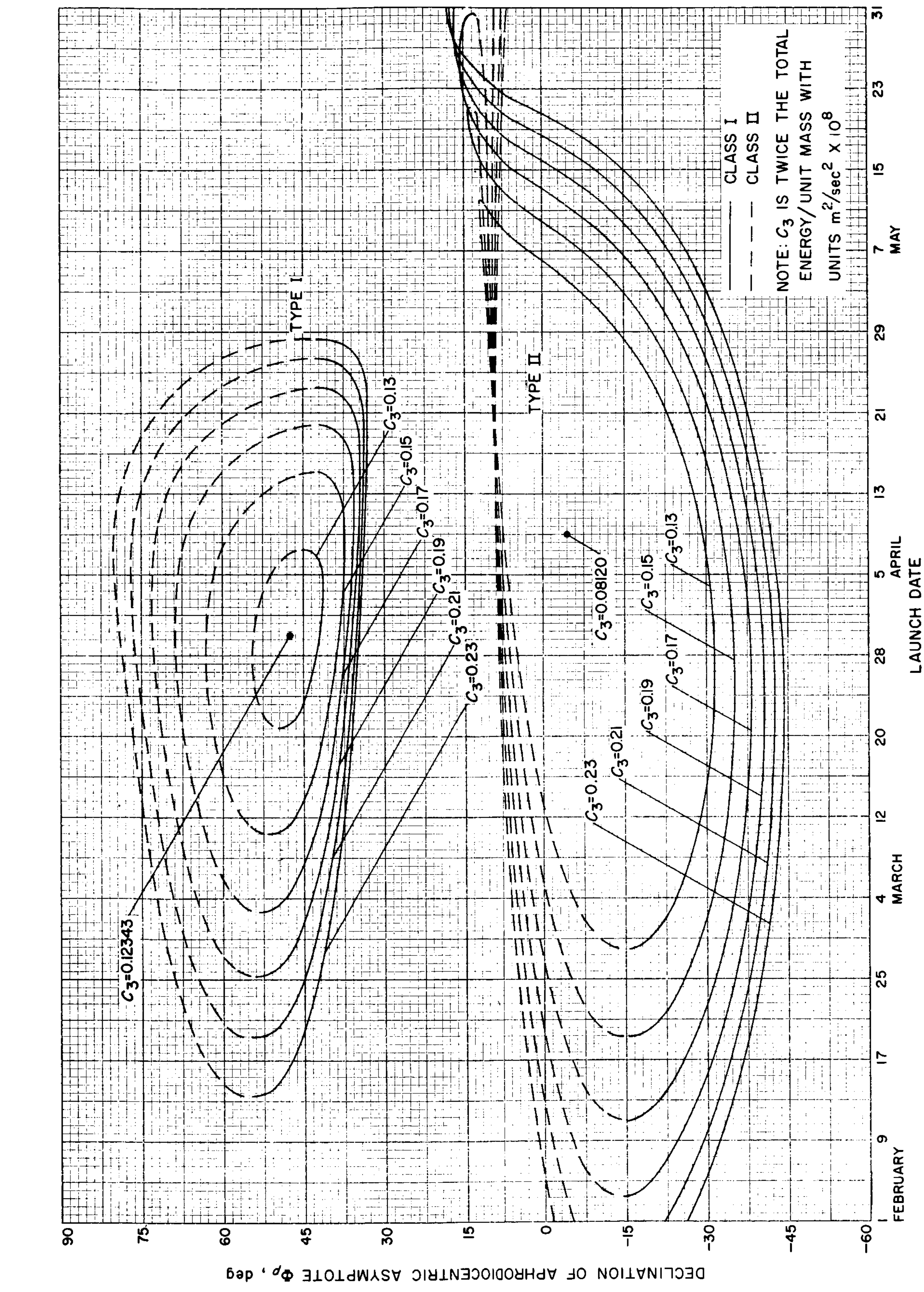

Fig. 6–20. Venus 1964: Declination of aphrodiocentric asymptote vs launch date

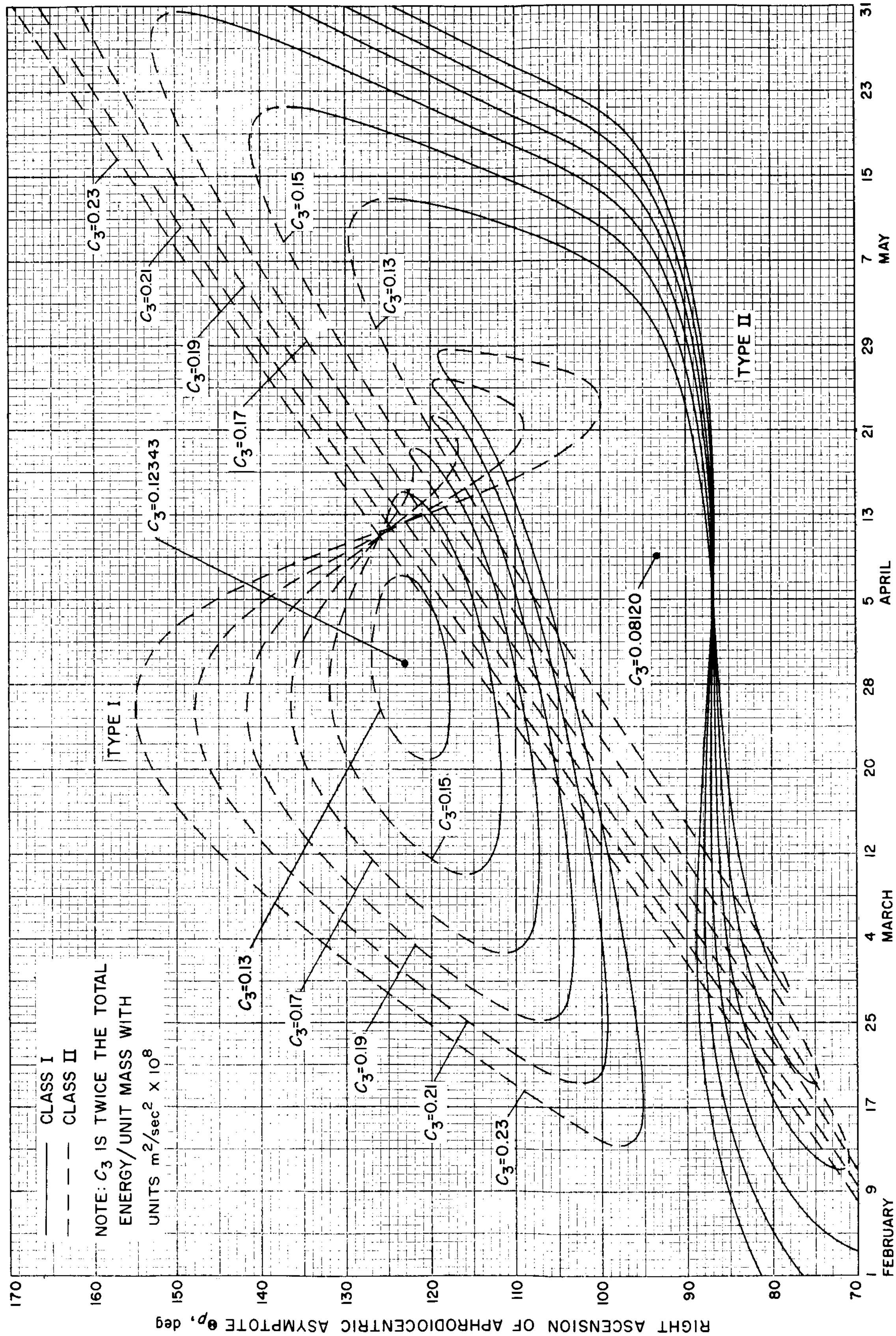

Fig. 6–21. Venus 1964: Right ascension of aphrodiocentric asymptote vs launch date

VII. VENUS 1965: TRAJECTORY-PARAMETER GRAPHS

Figure

VII. VENUS 1965: TRAJECTORY-PARAMETER GRAPHS (Cont'd)

Figure

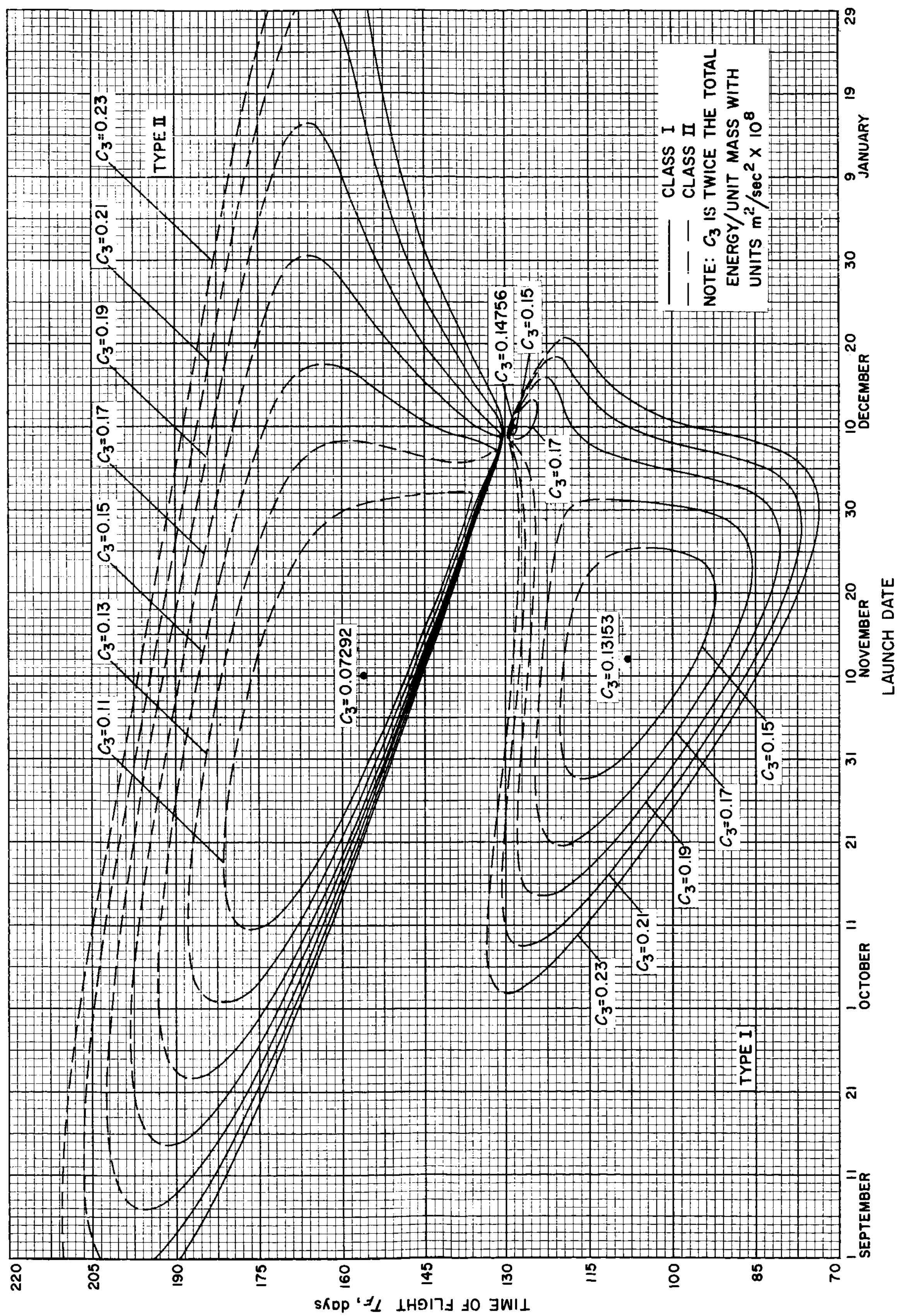

Fig. 7–1. Venus 1965: Time of flight vs launch date

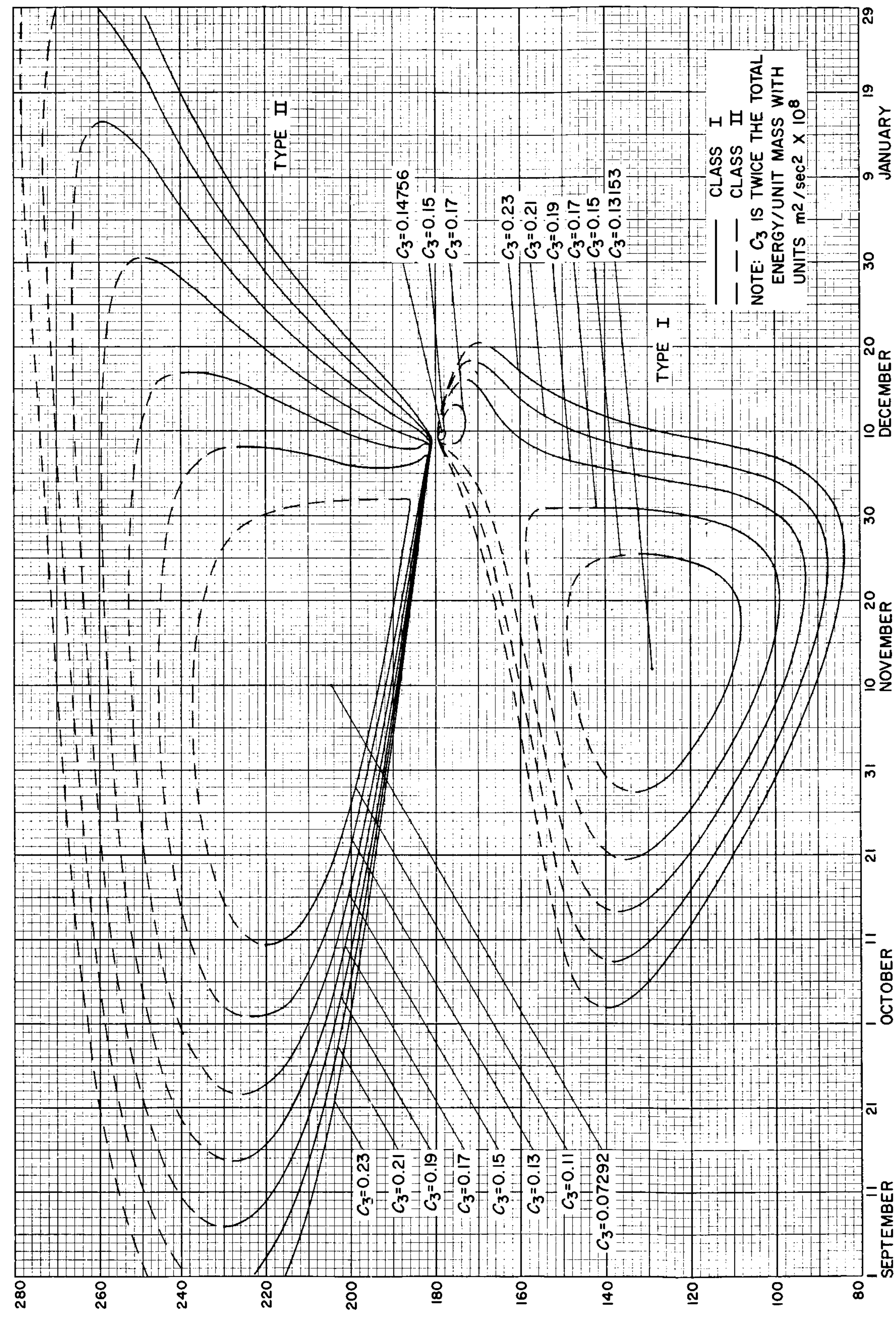

Fig. 7-2. Venus 1965: Heliocentric central angle vs launch date

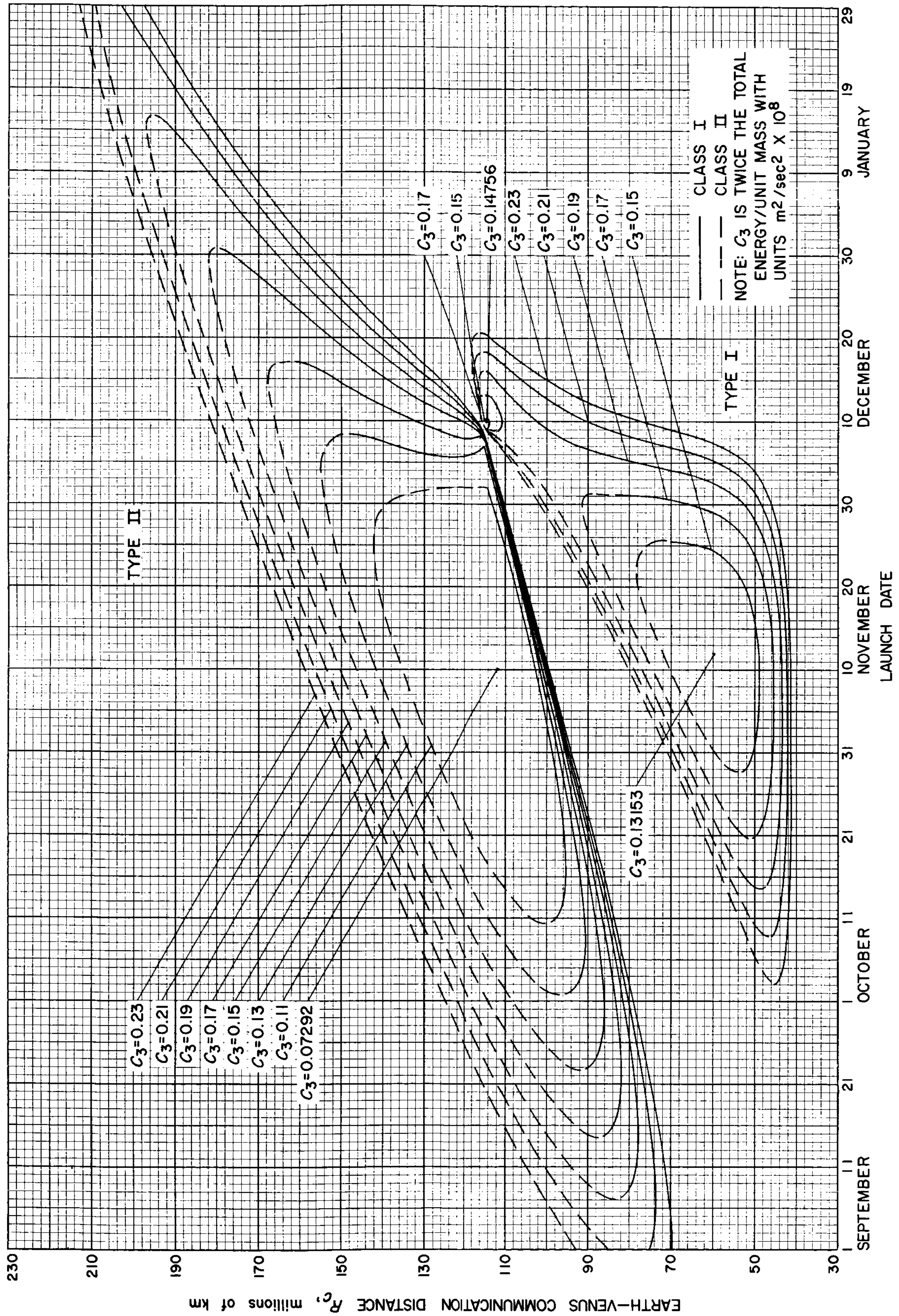

Fig. 7–3. Venus 1965: Earth–Venus communication distance vs launch date

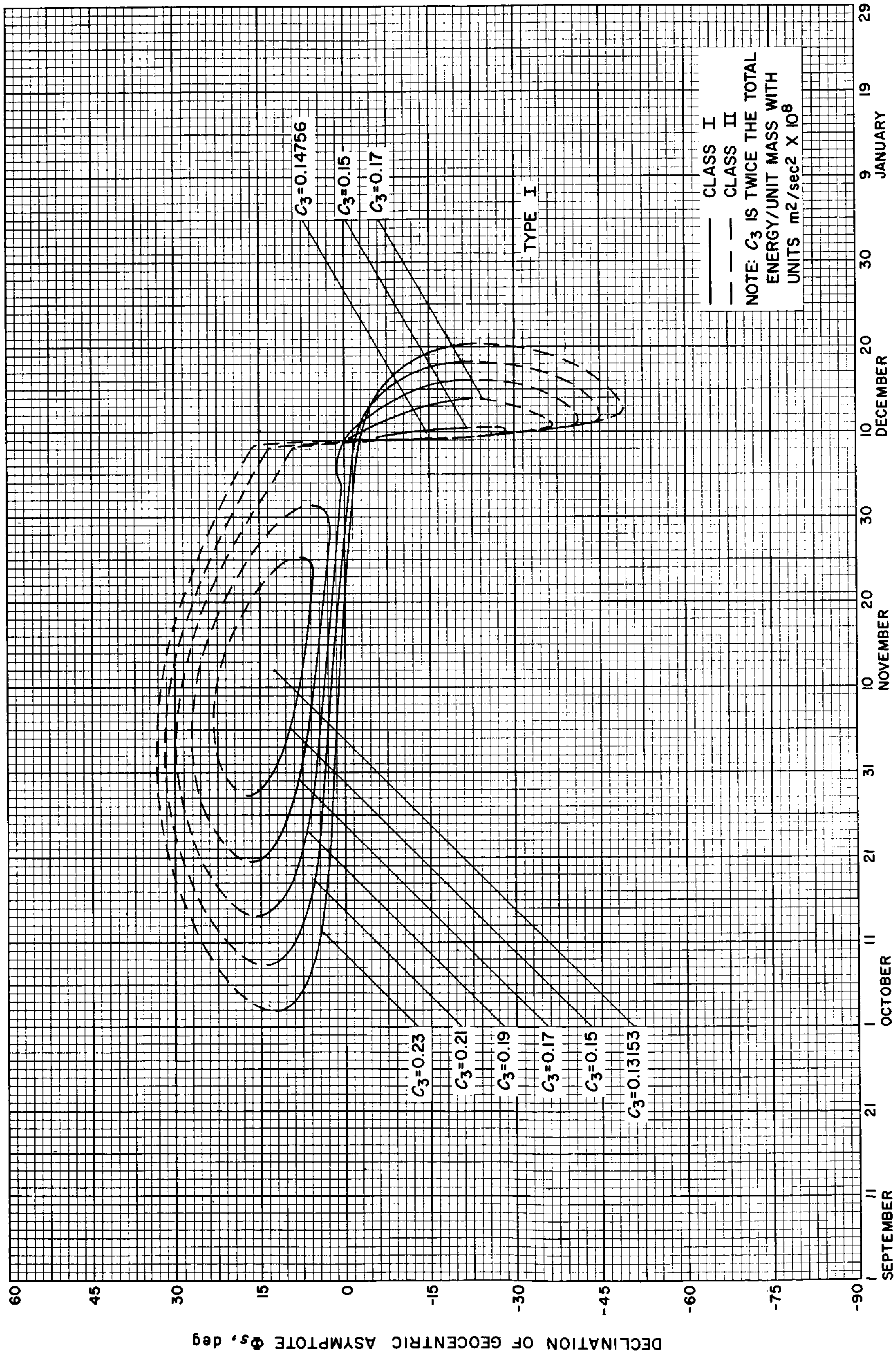

Fig. 7–4. Venus 1965: Declination of geocentric asymptote vs launch date, Type I

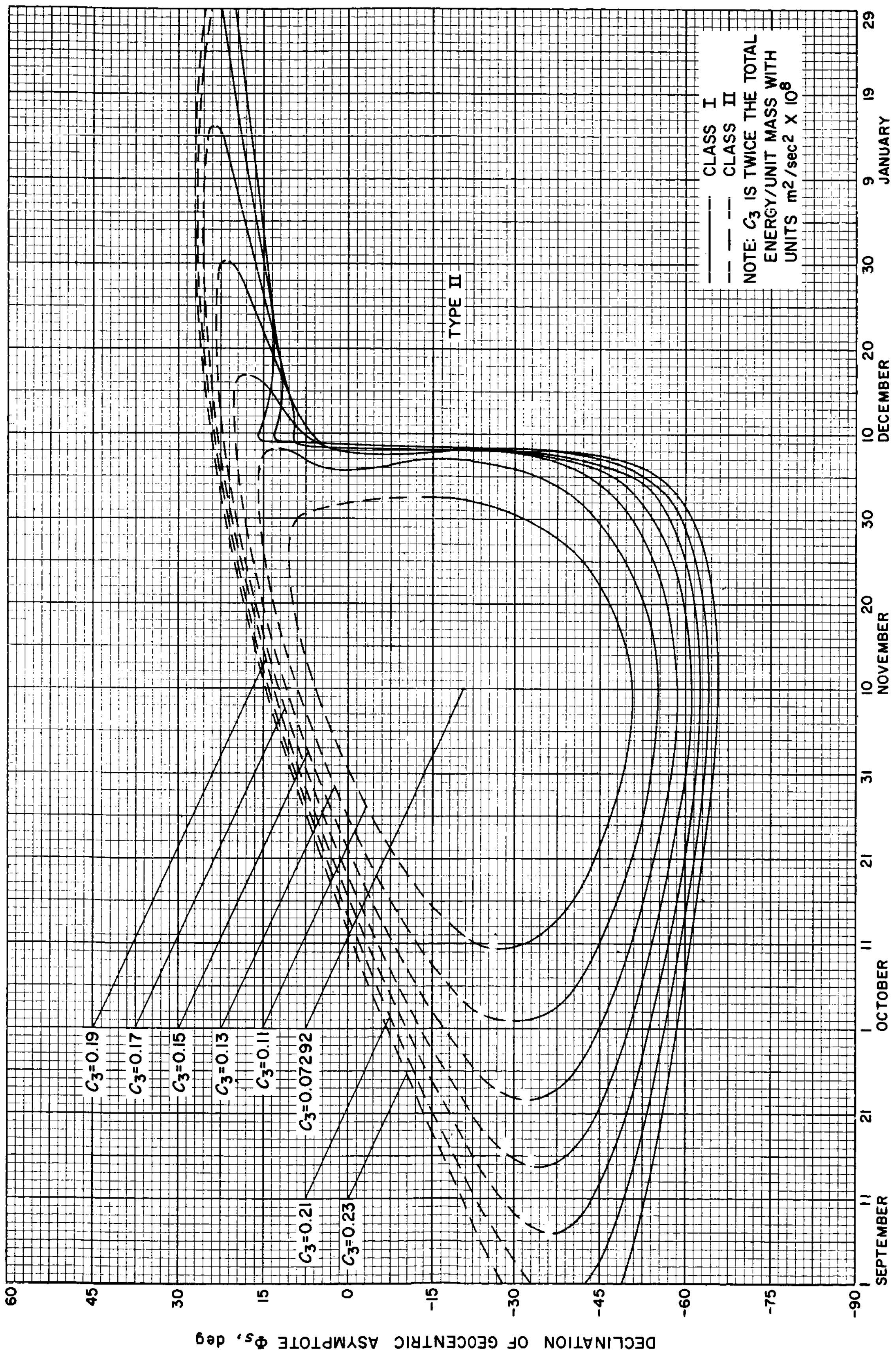

Fig. 7–5. Venus 1965: Declination of geocentric asymptote vs launch date, Type II

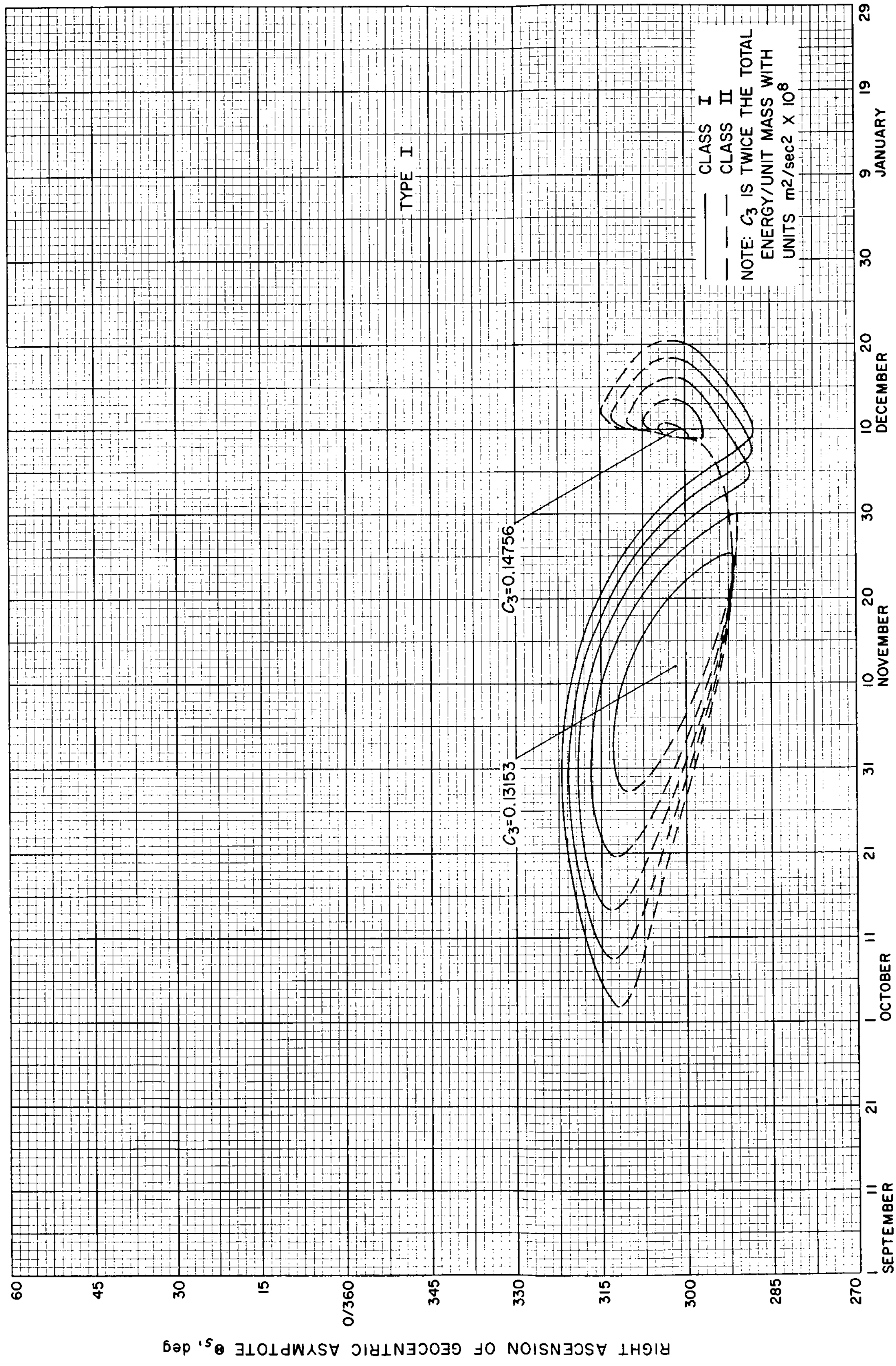

Fig. 7–6. Venus 1965: Right ascension of geocentric asymptote vs launch date, Type I

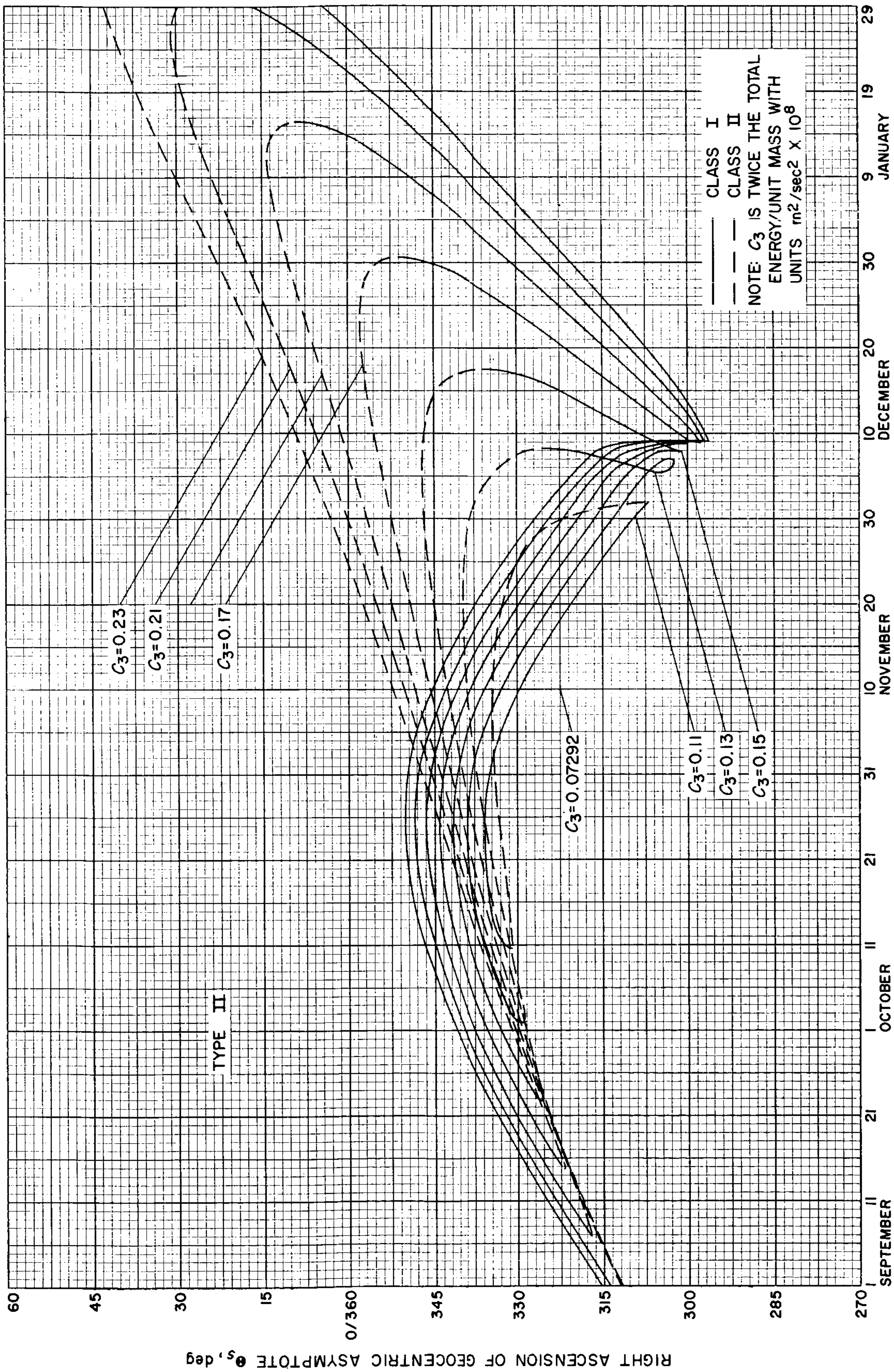

Fig. 7-7. Venus 1965: Right ascension of geocentric asymptote vs launch date, Type II

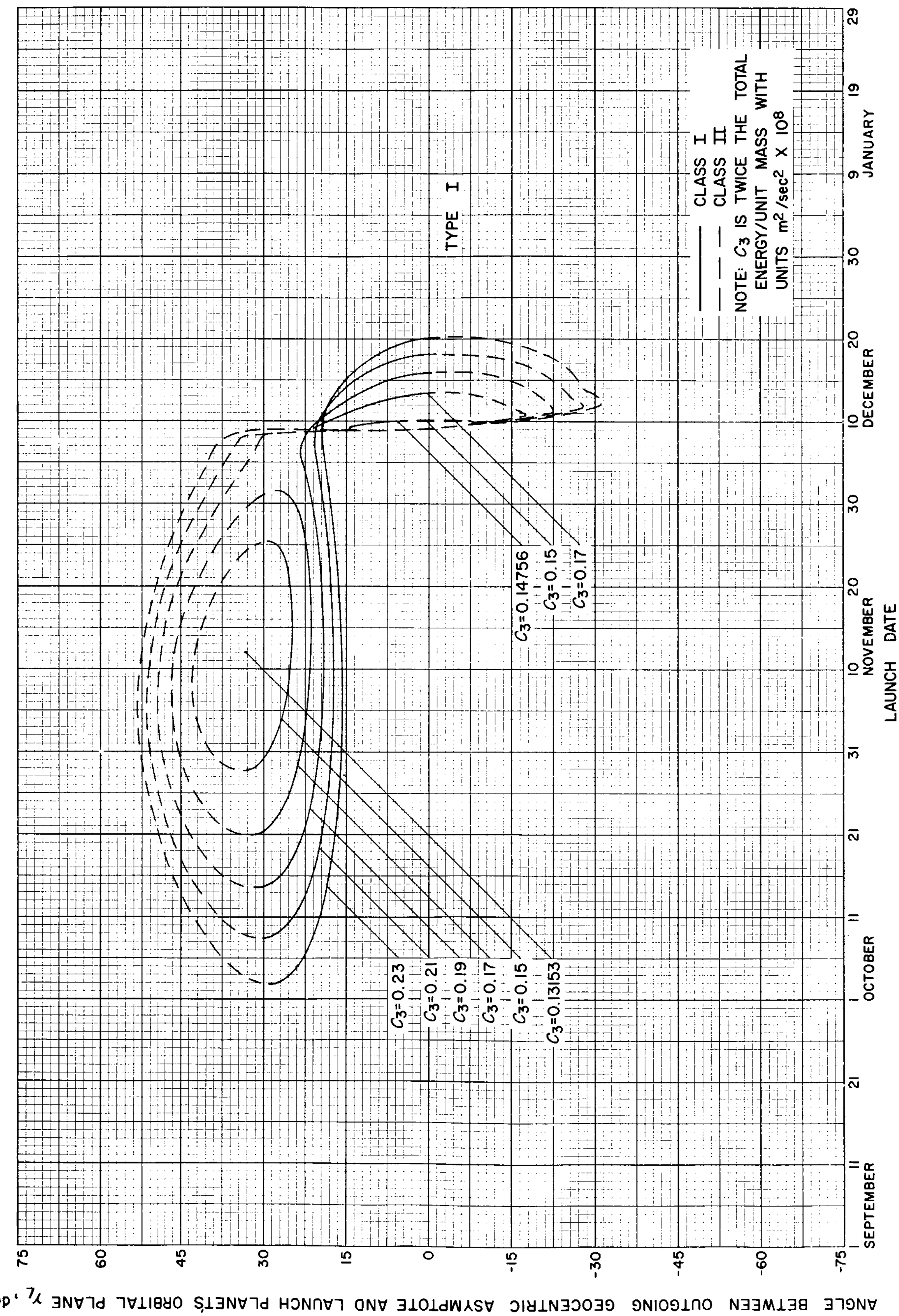

Fig. 7–8. Venus 1965: Angle between outgoing geocentric asymptote and launch planet's orbital plane vs launch date, Type I

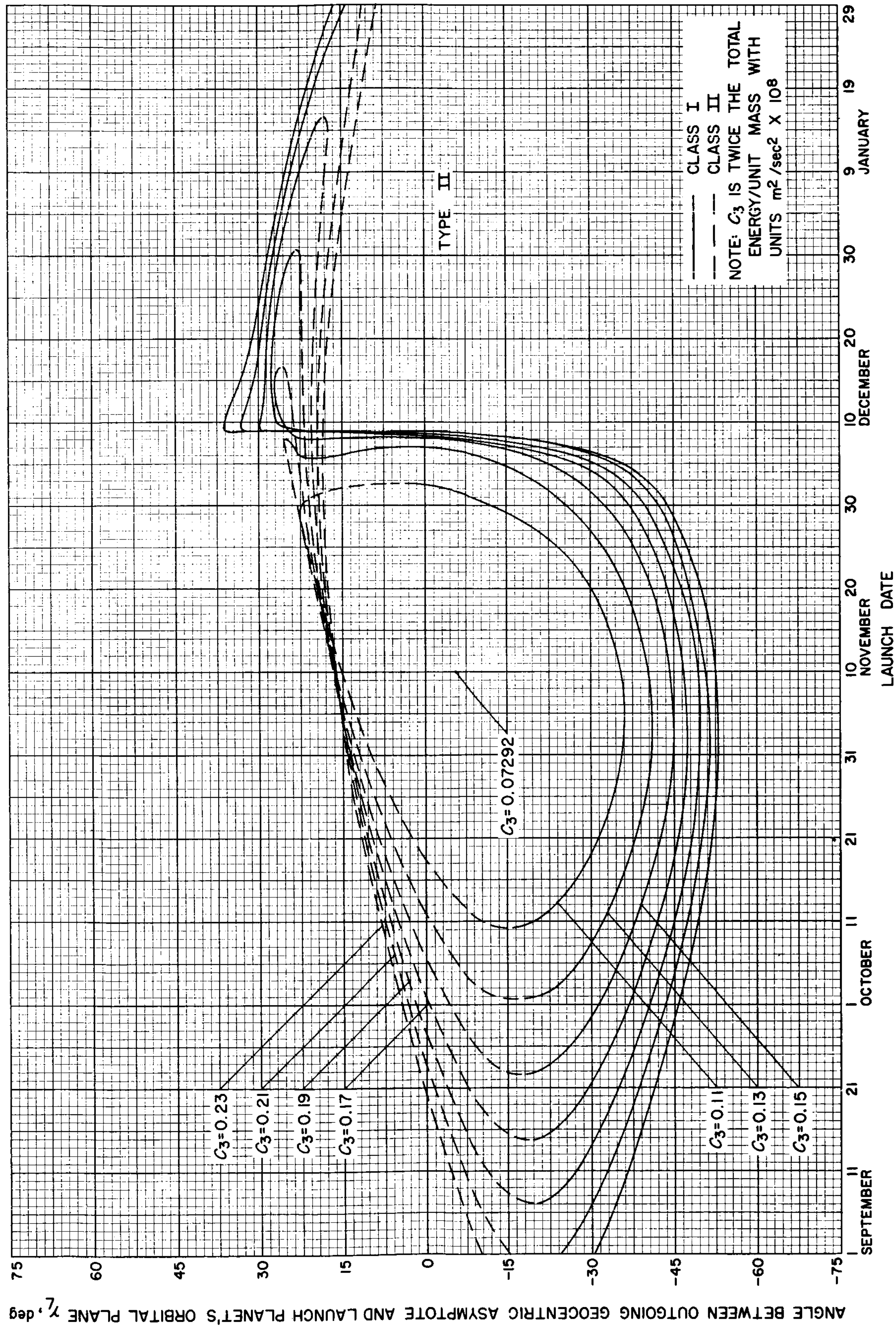

Fig. 7–9. Venus 1965: Angle between outgoing geocentric asymptote and launch planet's orbital plane vs launch date, Type II

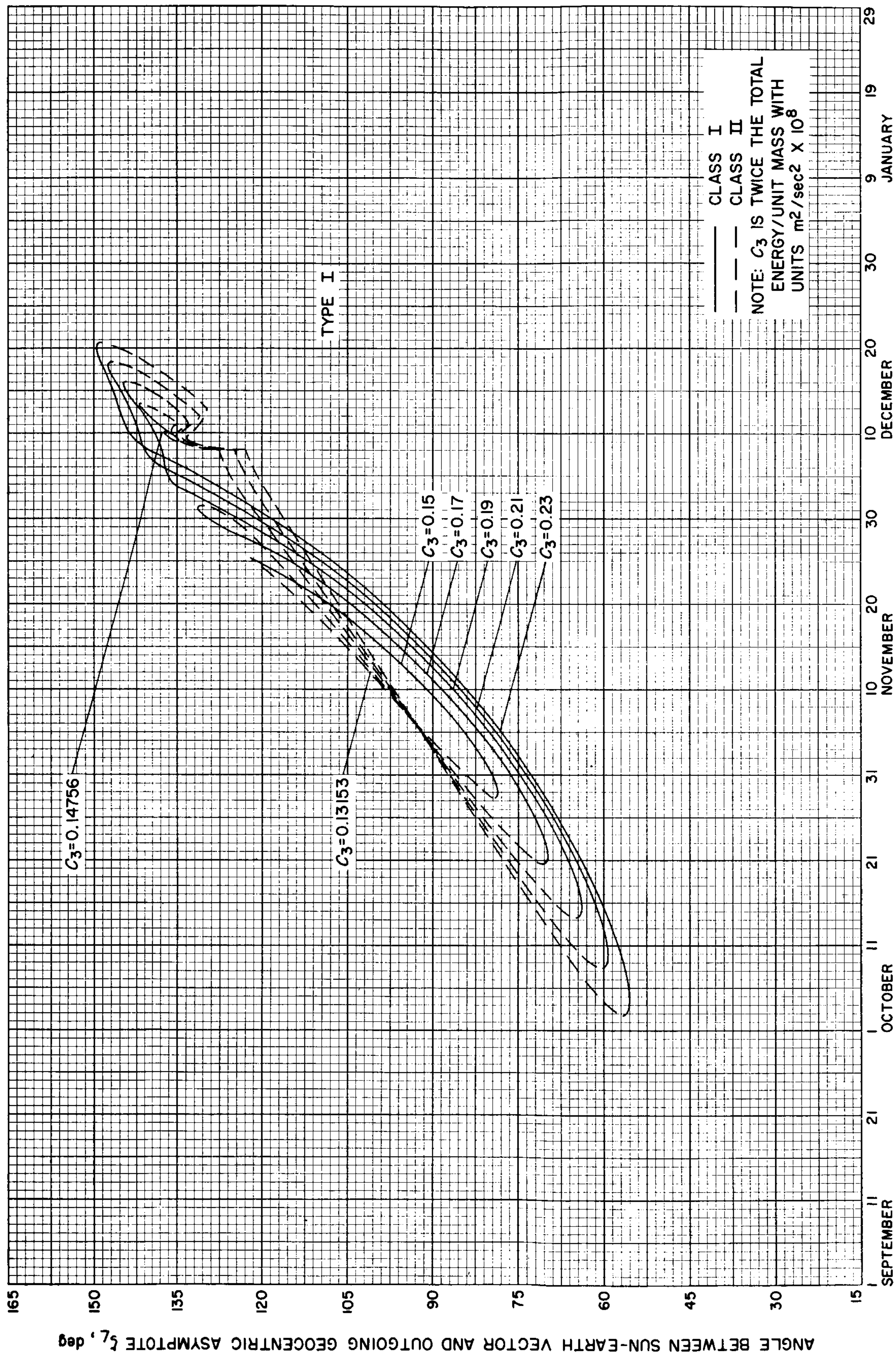

Fig. 7–10. Venus 1965: Angle between Sun–Earth vector and outgoing geocentric asymptote vs launch date, Type I

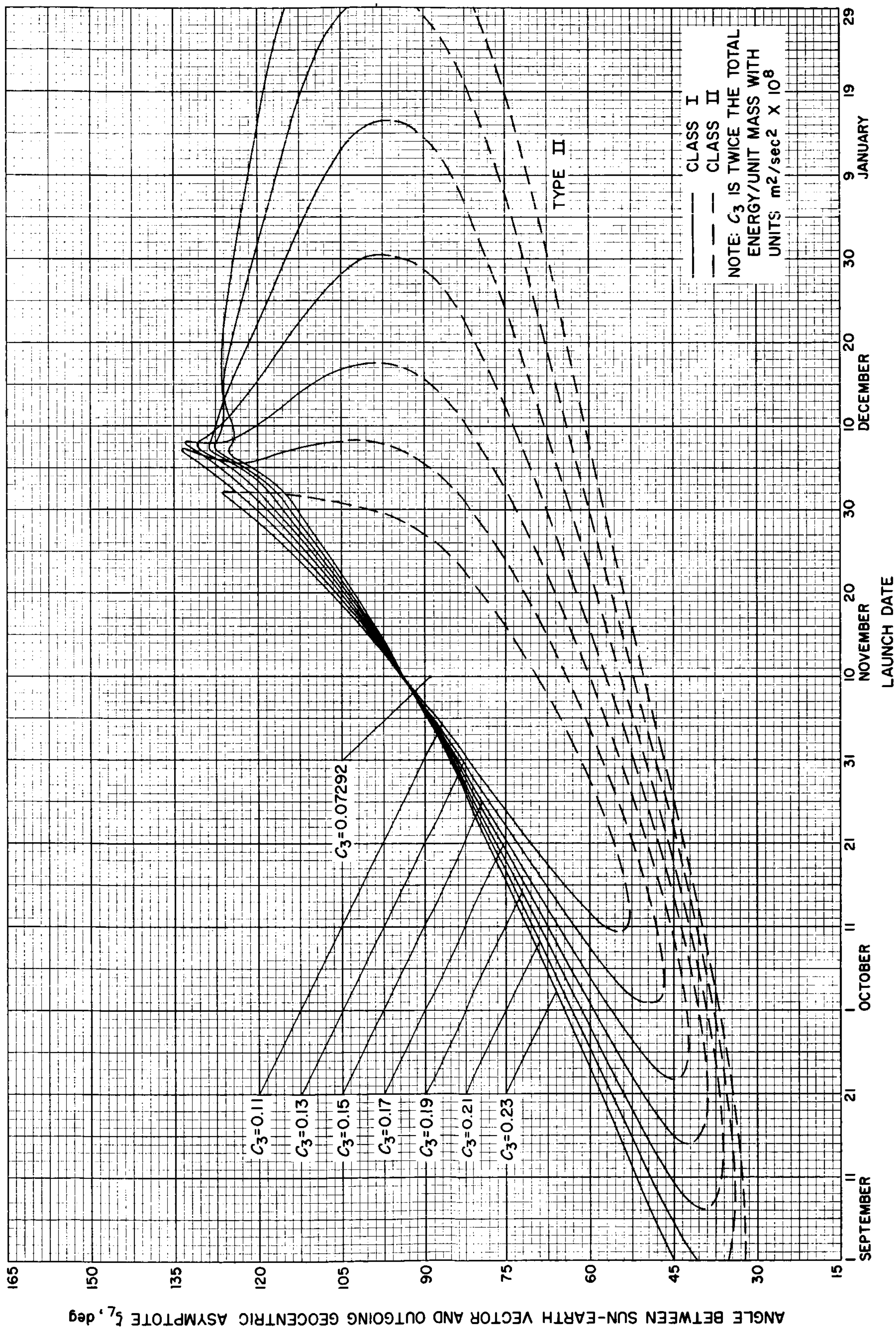

Fig. 7-11. Venus 1965: Angle between Sun–Earth vector and outgoing geocentric asymptote vs launch date, Type II

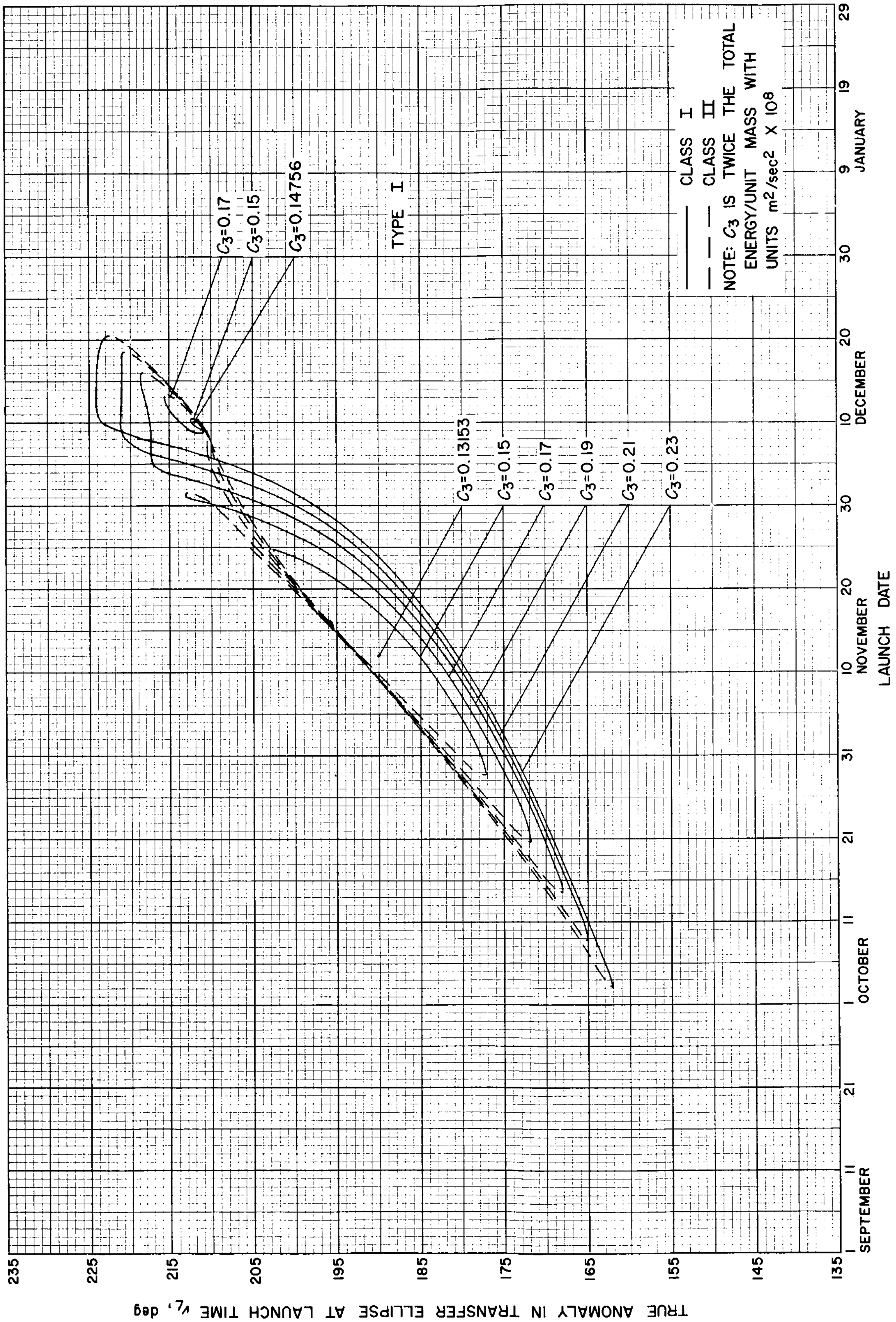

Fig. 7–12. Venus 1965: True anomaly in transfer ellipse at launch time vs launch date, Type I

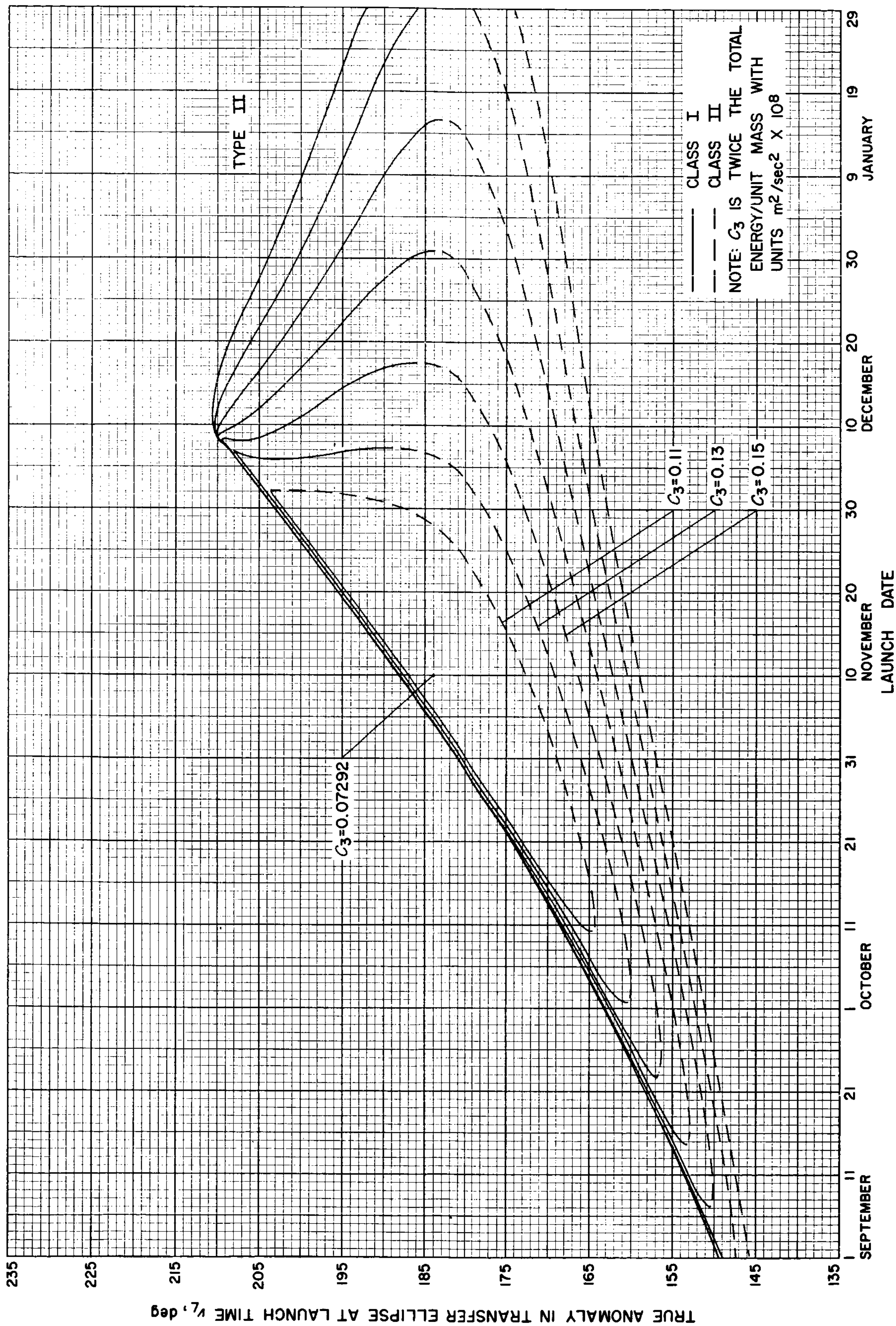

Fig. 7–13. Venus 1965: True anomaly in transfer ellipse at launch time vs launch date, Type II

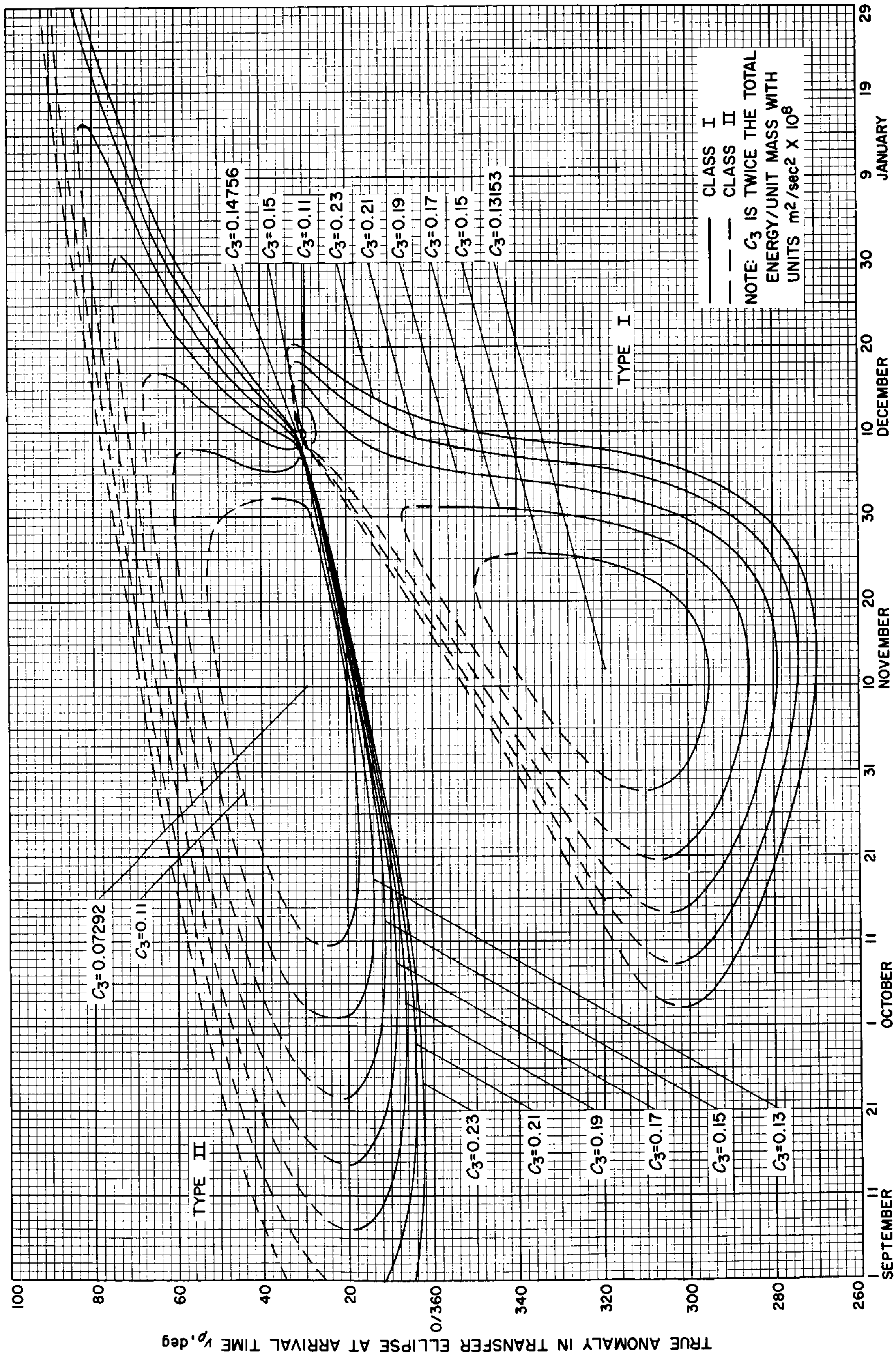

Fig. 7–14. Venus 1965: True anomaly in transfer ellipse at arrival time vs launch date

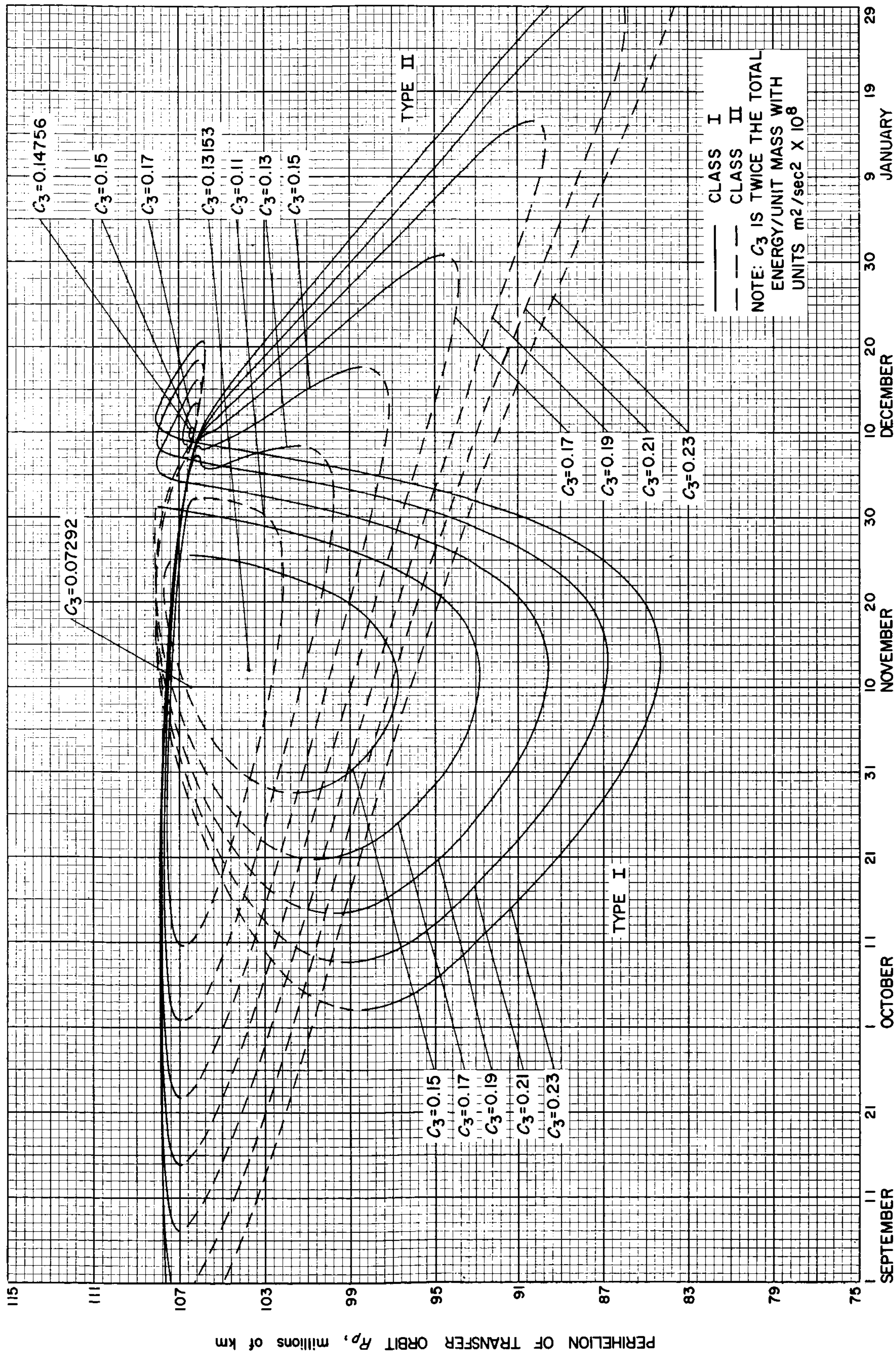

Fig. 7–15. Venus 1965: Perihelion of transfer orbit vs launch date

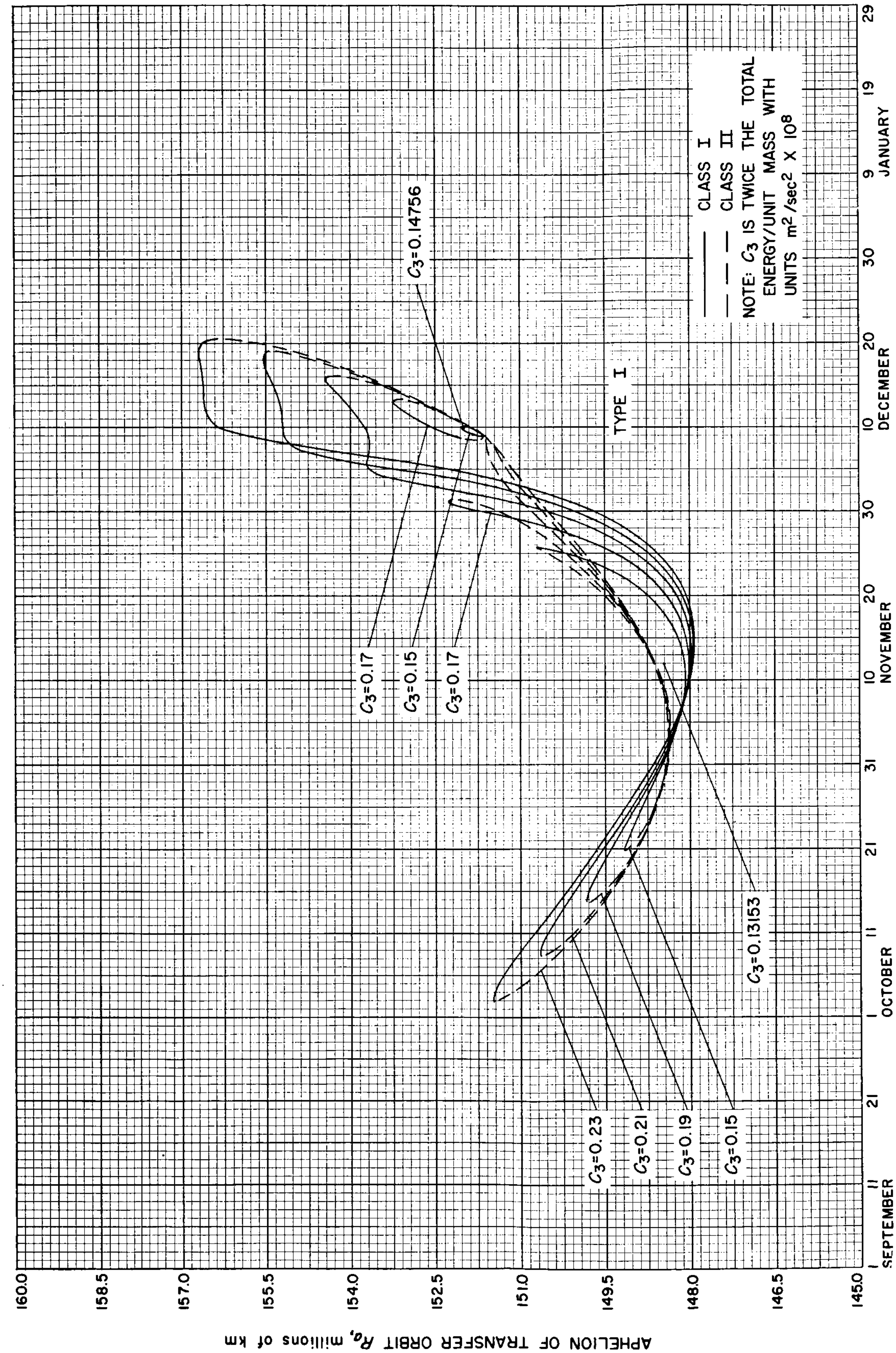

Fig. 7–16. Venus 1965: Aphelion of transfer orbit vs launch date, Type I

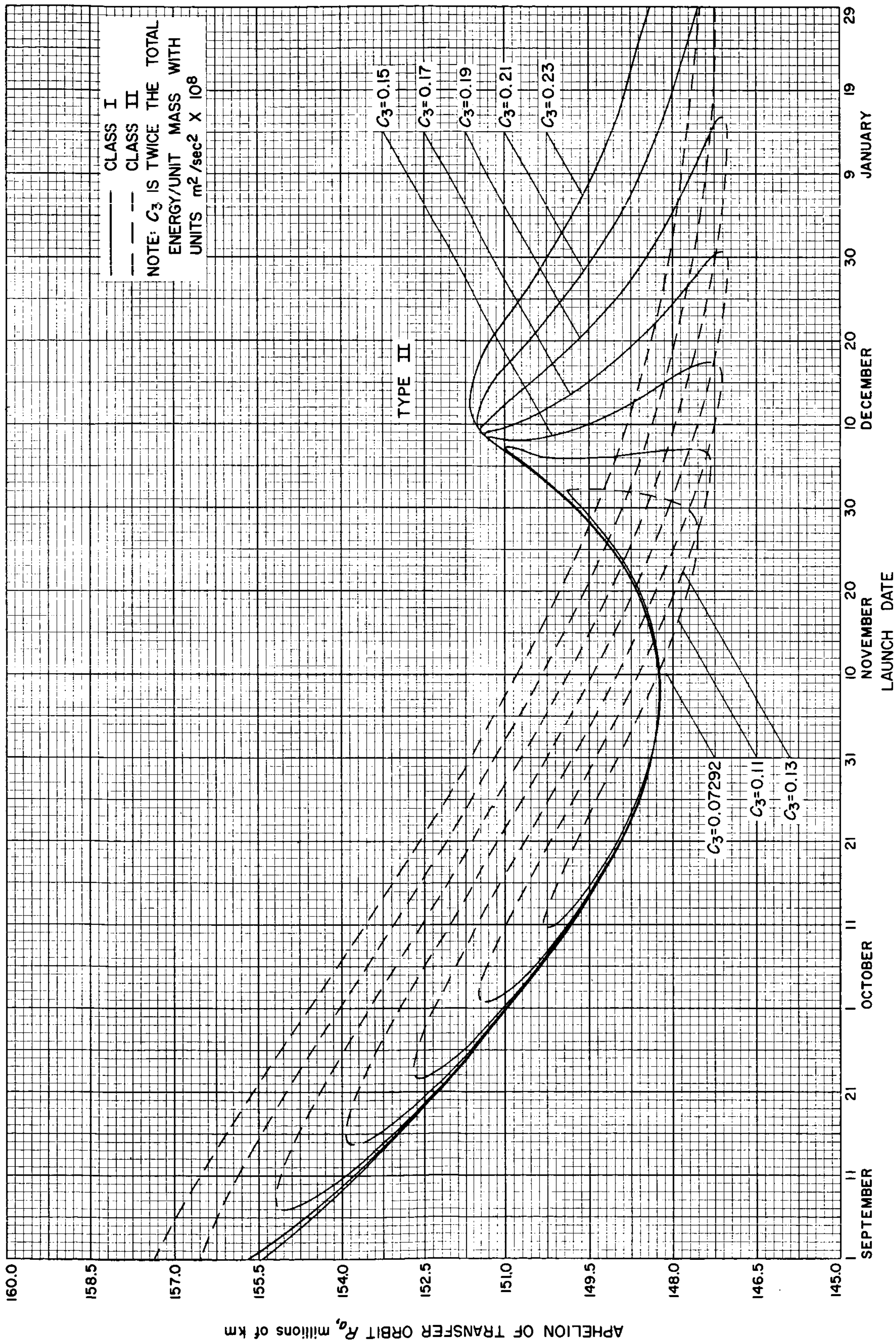

Fig. 7–17. Venus 1965: Aphelion of transfer orbit vs launch date, Type II

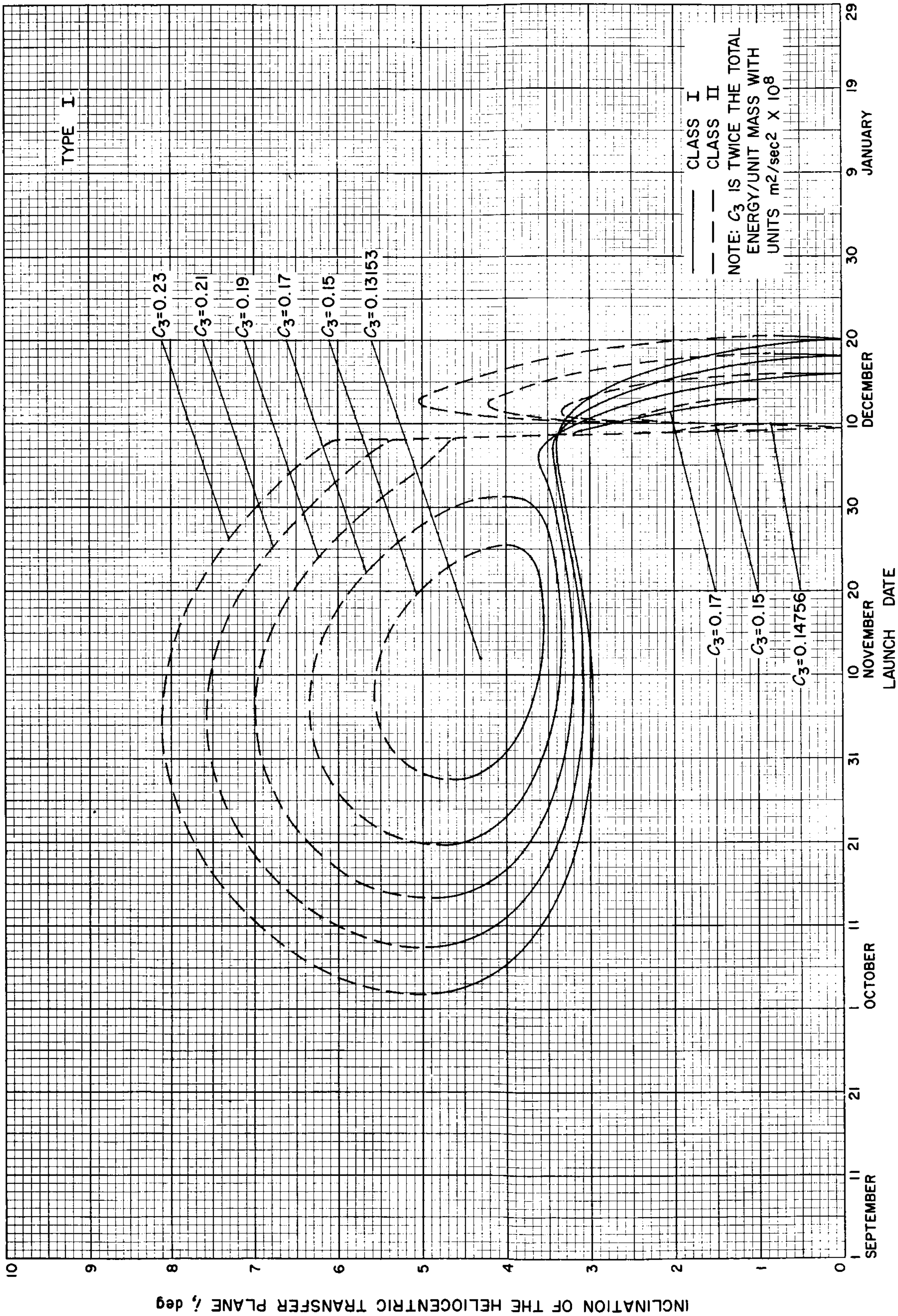

Fig. 7–18. Venus 1965: Inclination of heliocentric-transfer plane vs launch date, Type I

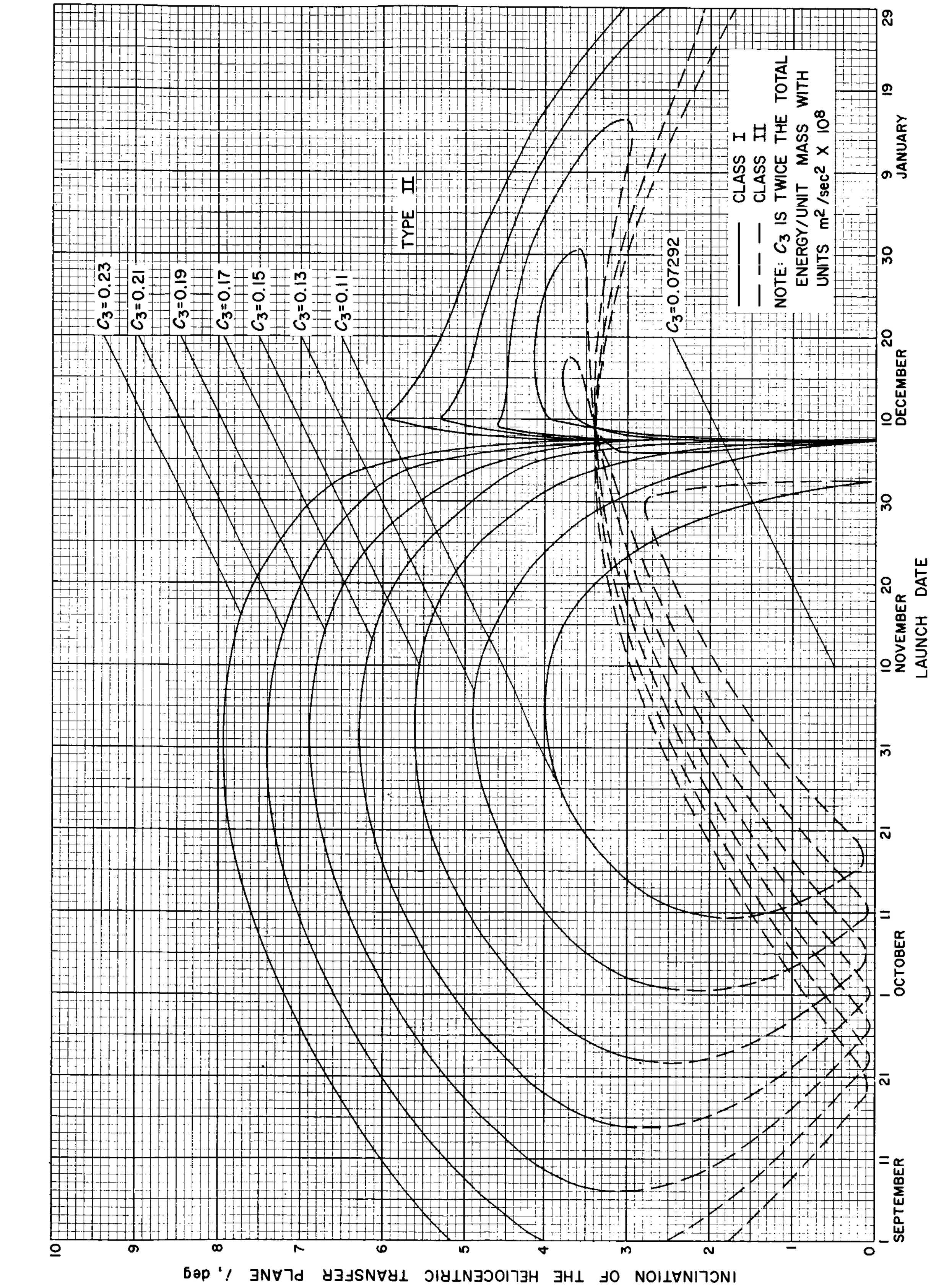

Fig. 7–19. Venus 1965: Inclination of heliocentric-transfer plane vs launch date, Type II

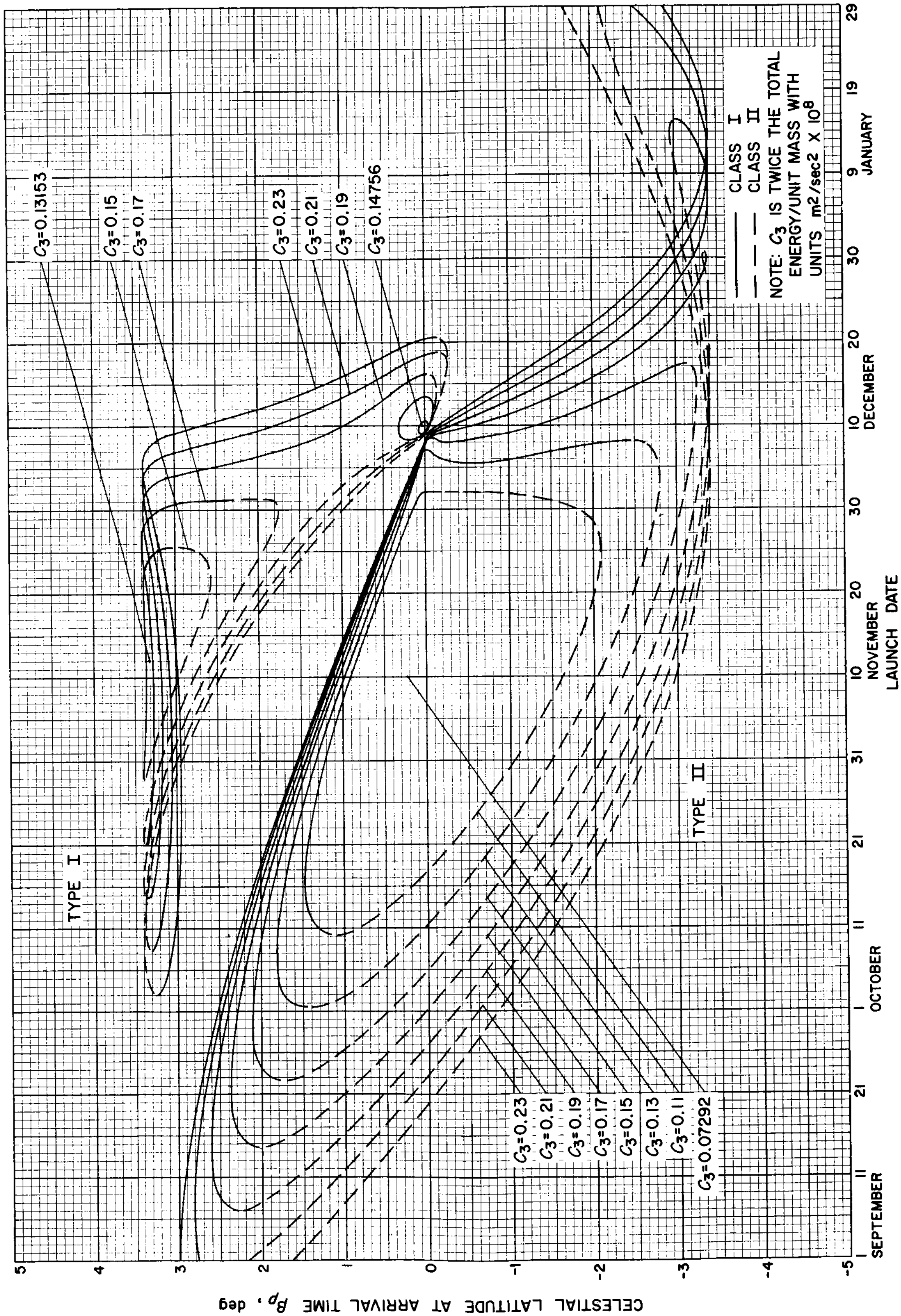

Fig. 7-20. Venus 1965: Celestial latitude at arrival time vs launch date

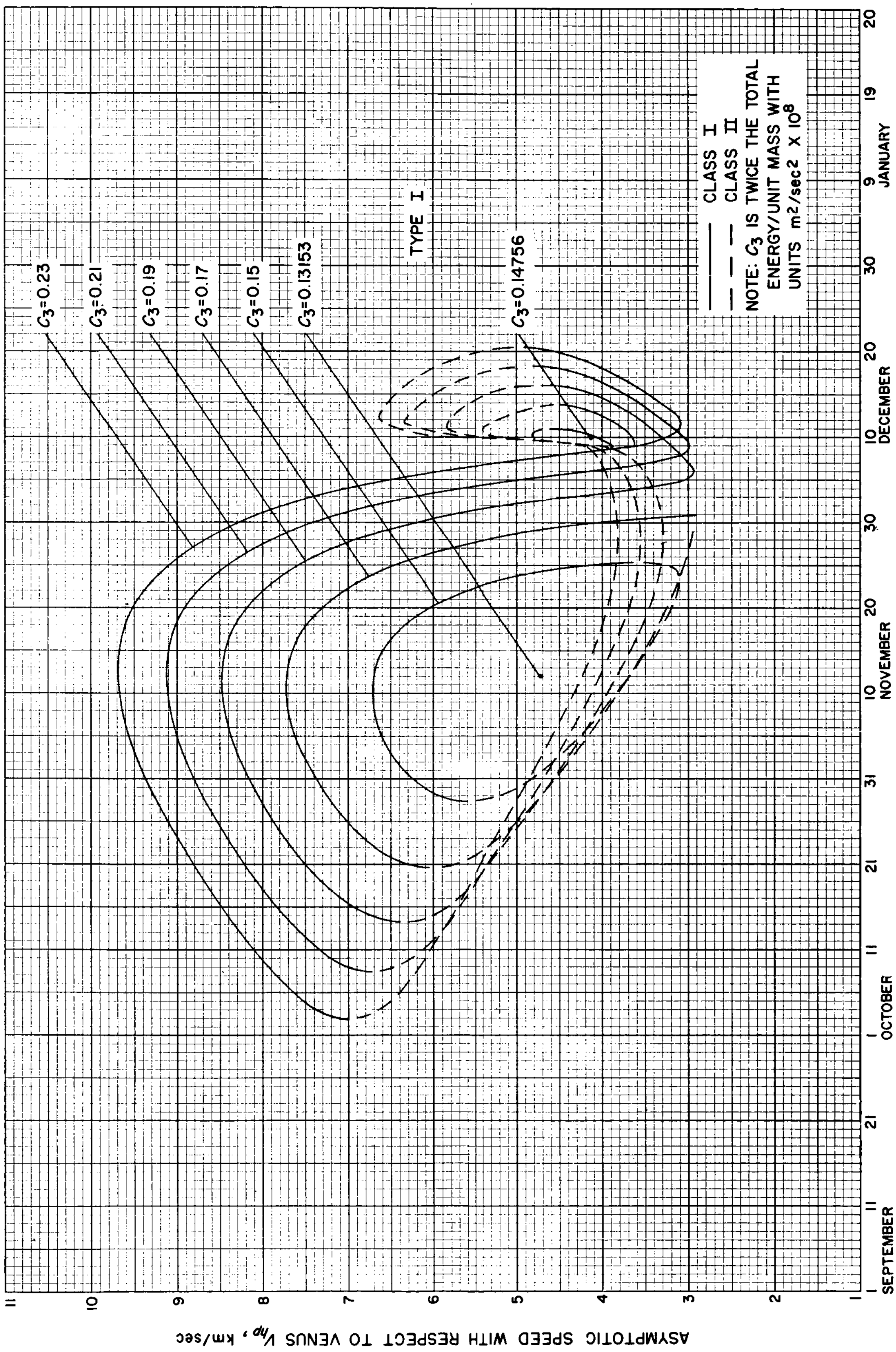

Fig. 7-21. Venus 1965: Asymptotic speed with respect to Venus vs launch date, Type I

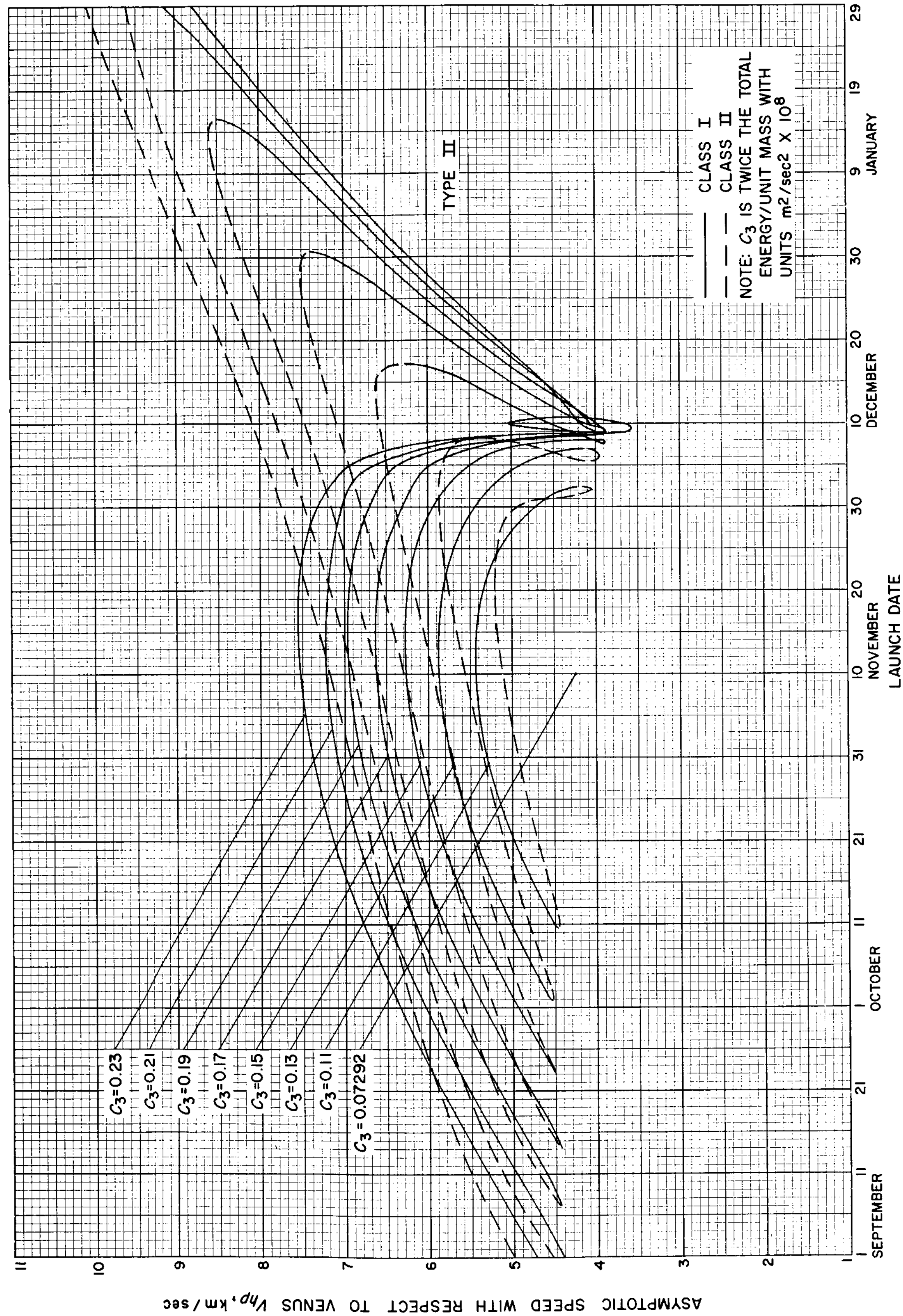

Fig. 7–22. Venus: 1965: Asymptotic speed with respect to Venus vs launch date, Type II

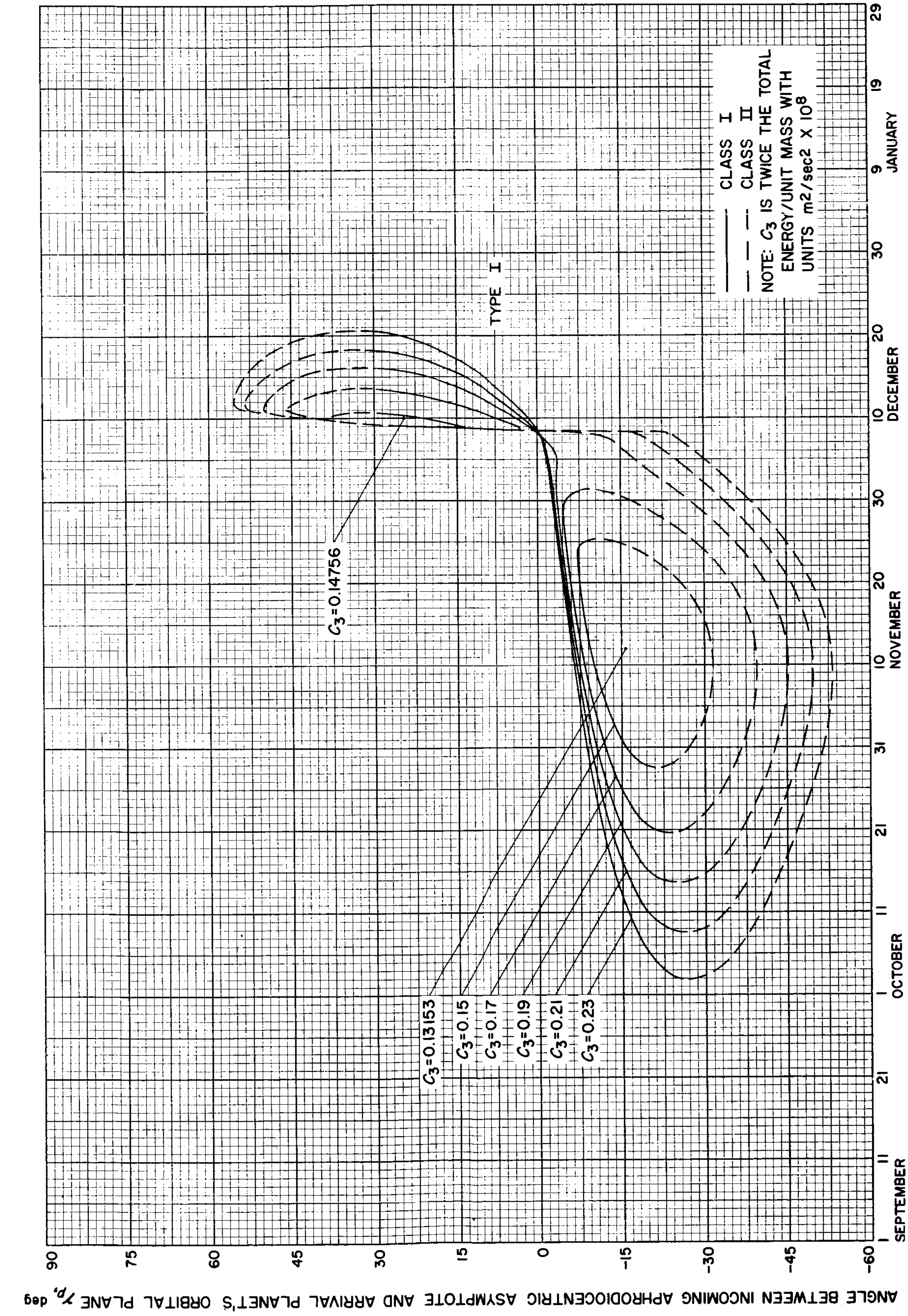

Fig. 7–23. Venus 1965: Angle between incoming aphrodiocentric asymptote and arrival planet's orbital plane vs launch date, Type I

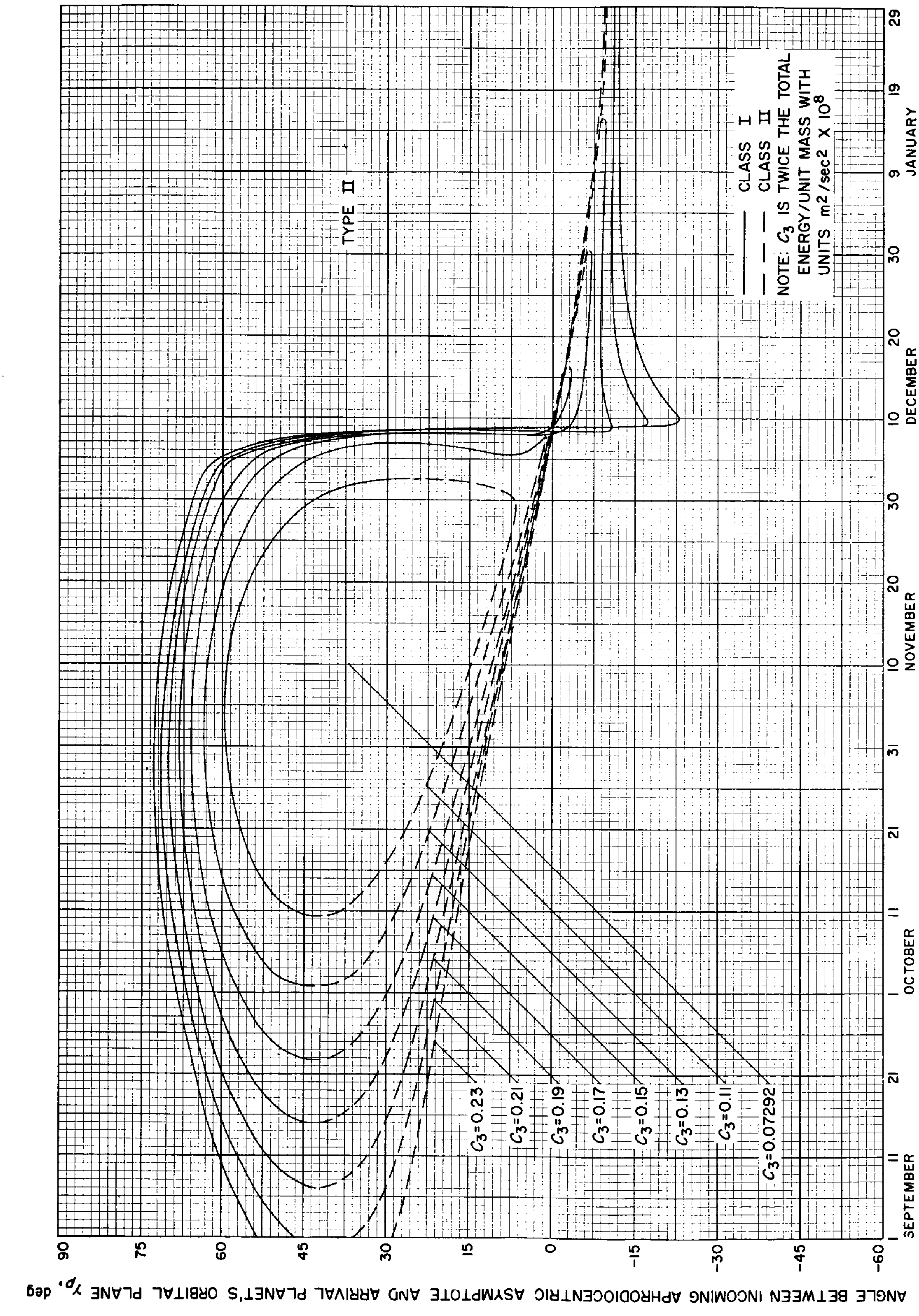

Fig. 7–24. Venus 1965: Angle between incoming aphrodiocentric asymptote and arrival planet's orbital plane vs launch date, Type II

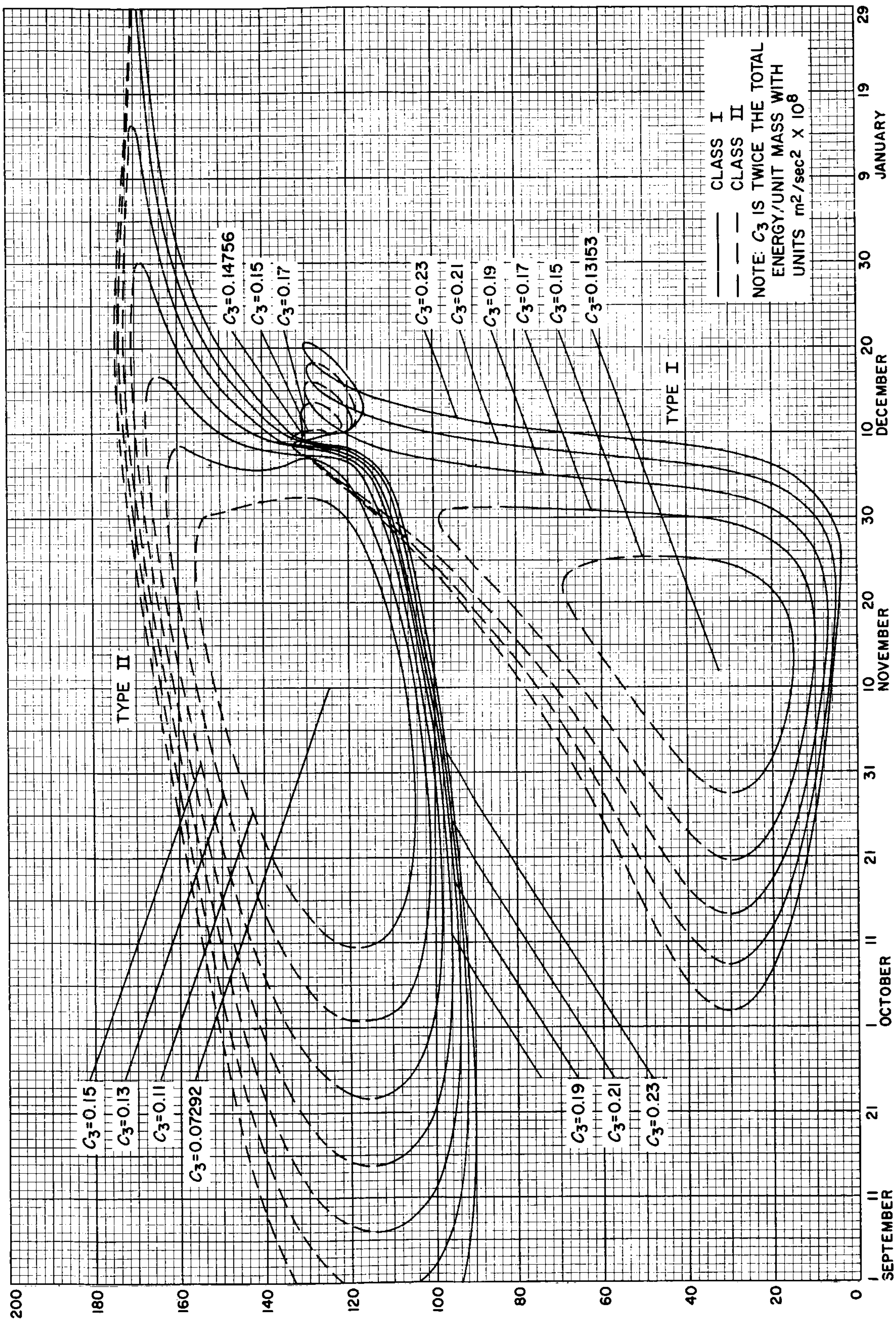

Fig. 7-25. Venus 1965: Angle between Venus–Sun vector and incoming aphrodiocentric asymptote vs launch date

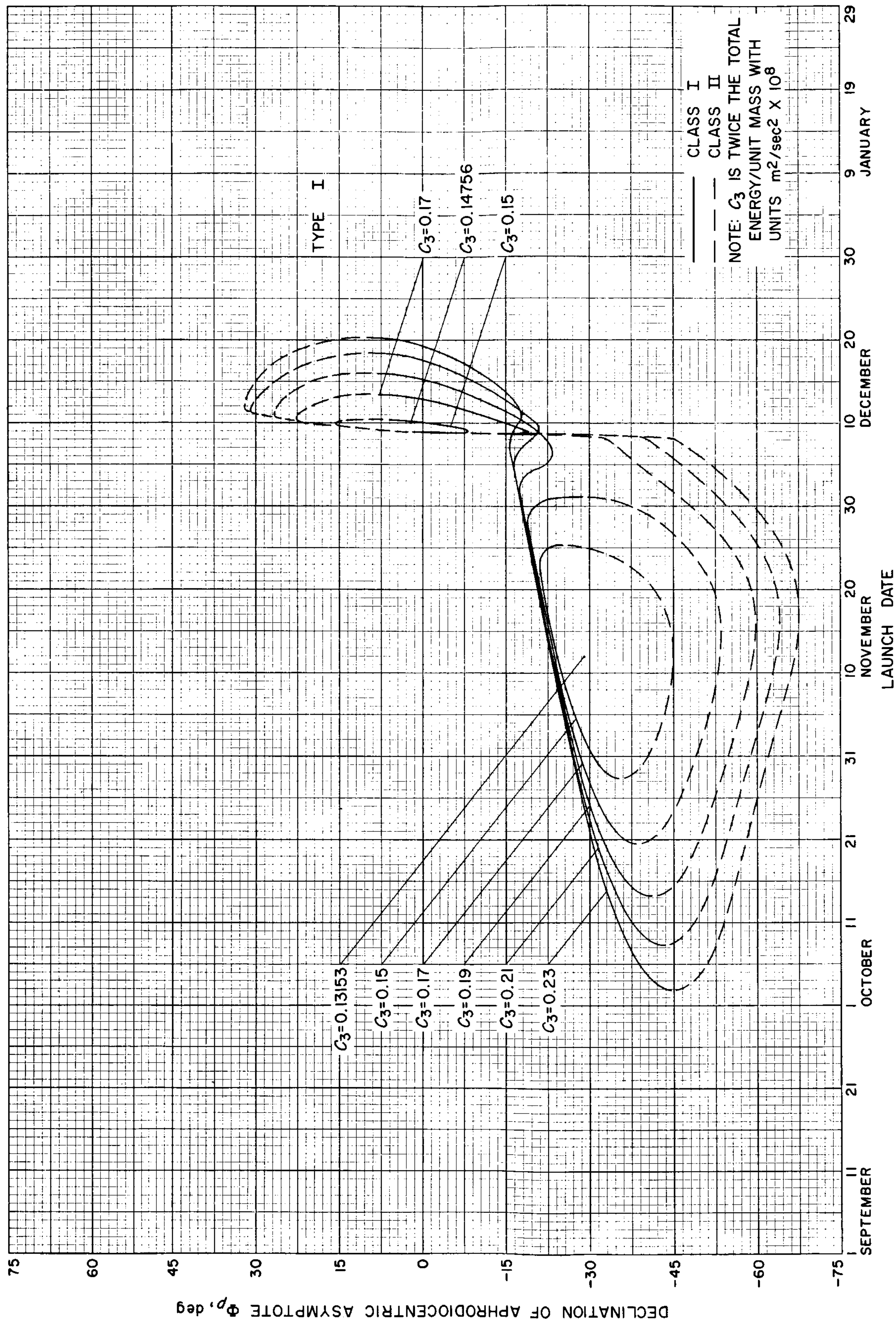

Fig. 7–26. Venus 1965: Declination of aphrodiocentric asymptote vs launch date, Type I

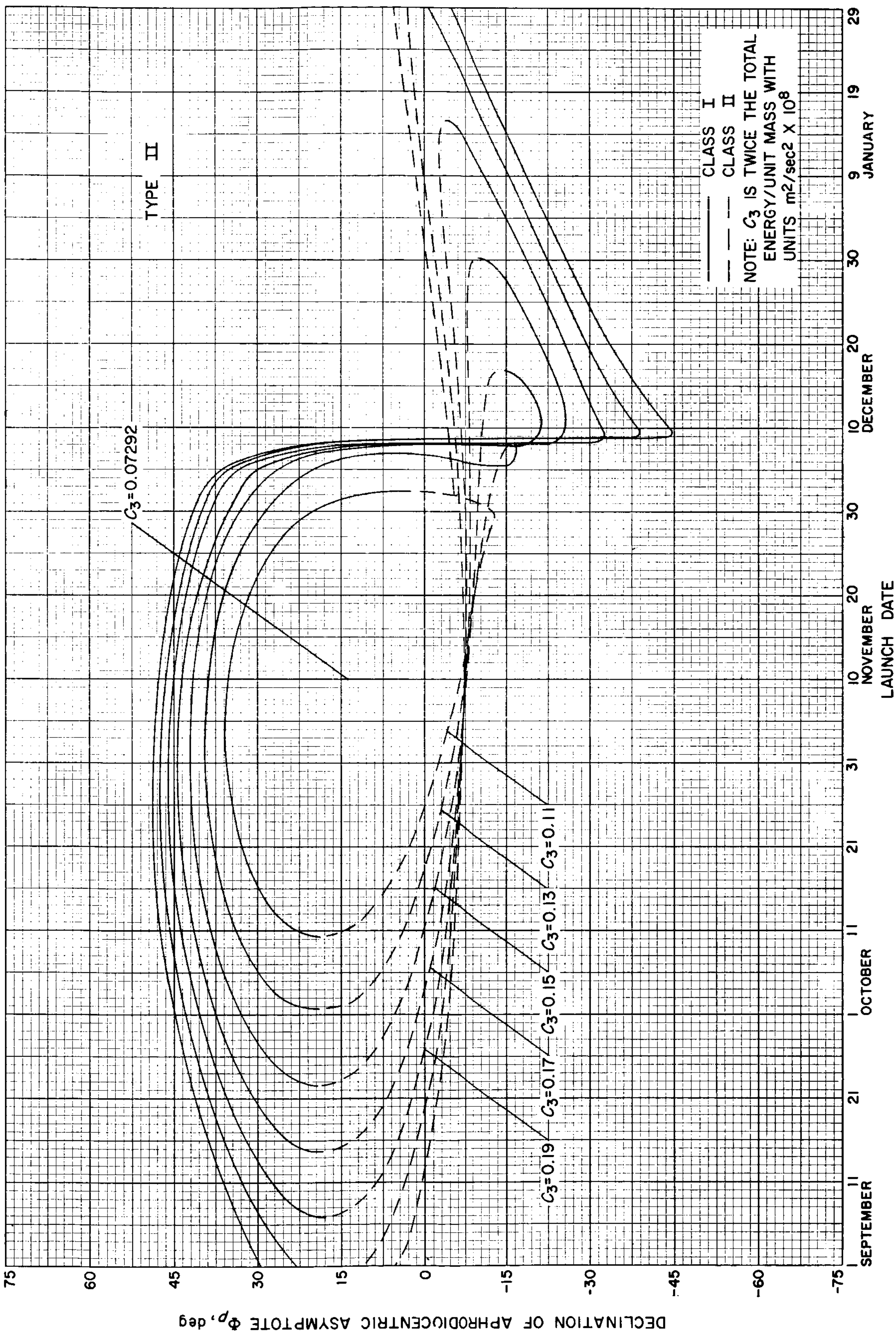

Fig. 7-27. Venus 1965: Declination of aphrodiocentric asymptote vs launch date, Type II

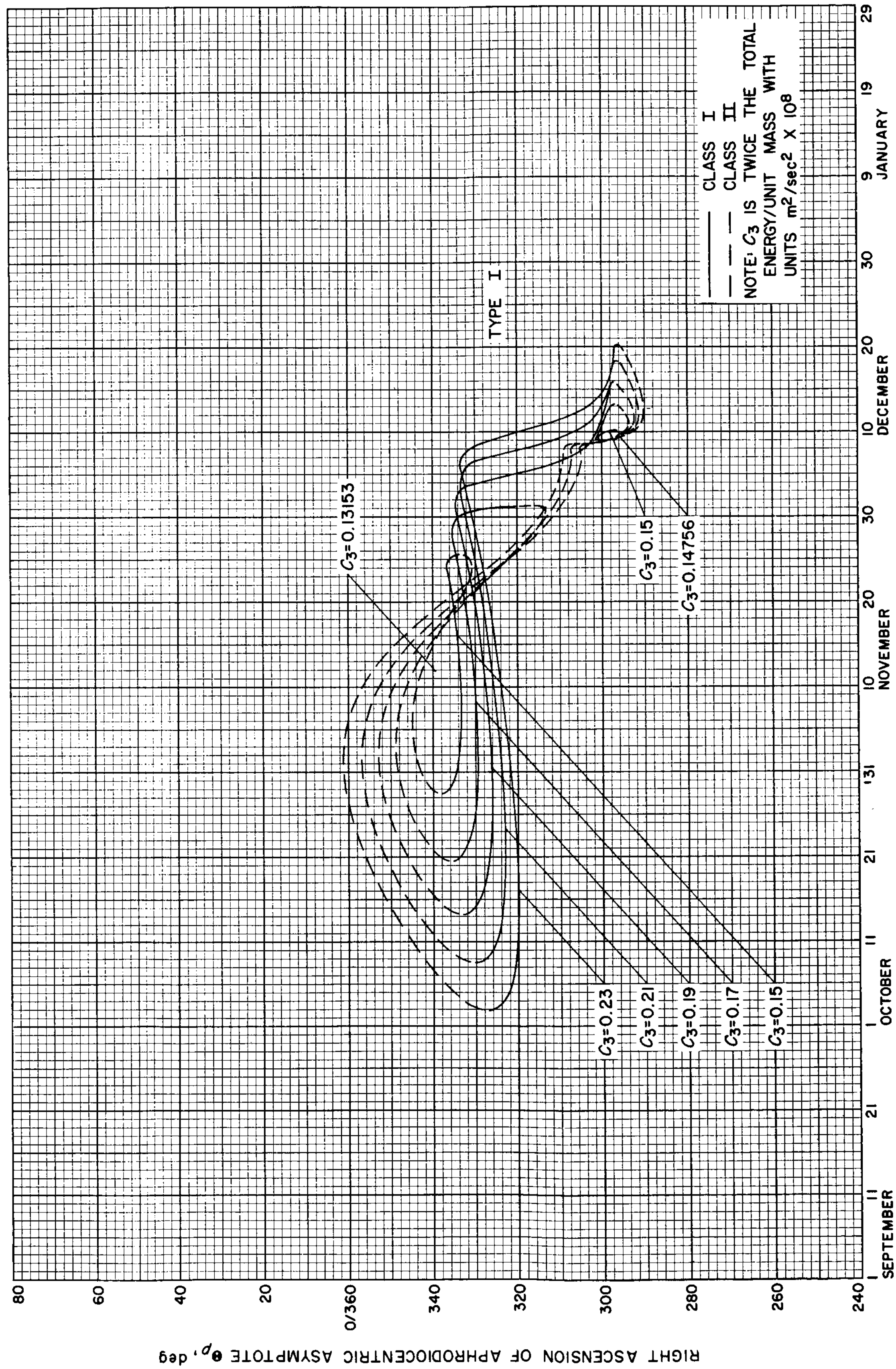

Fig. 7–28. Venus 1965: Right ascension of aphrodiocentric asymptote vs launch date, Type I

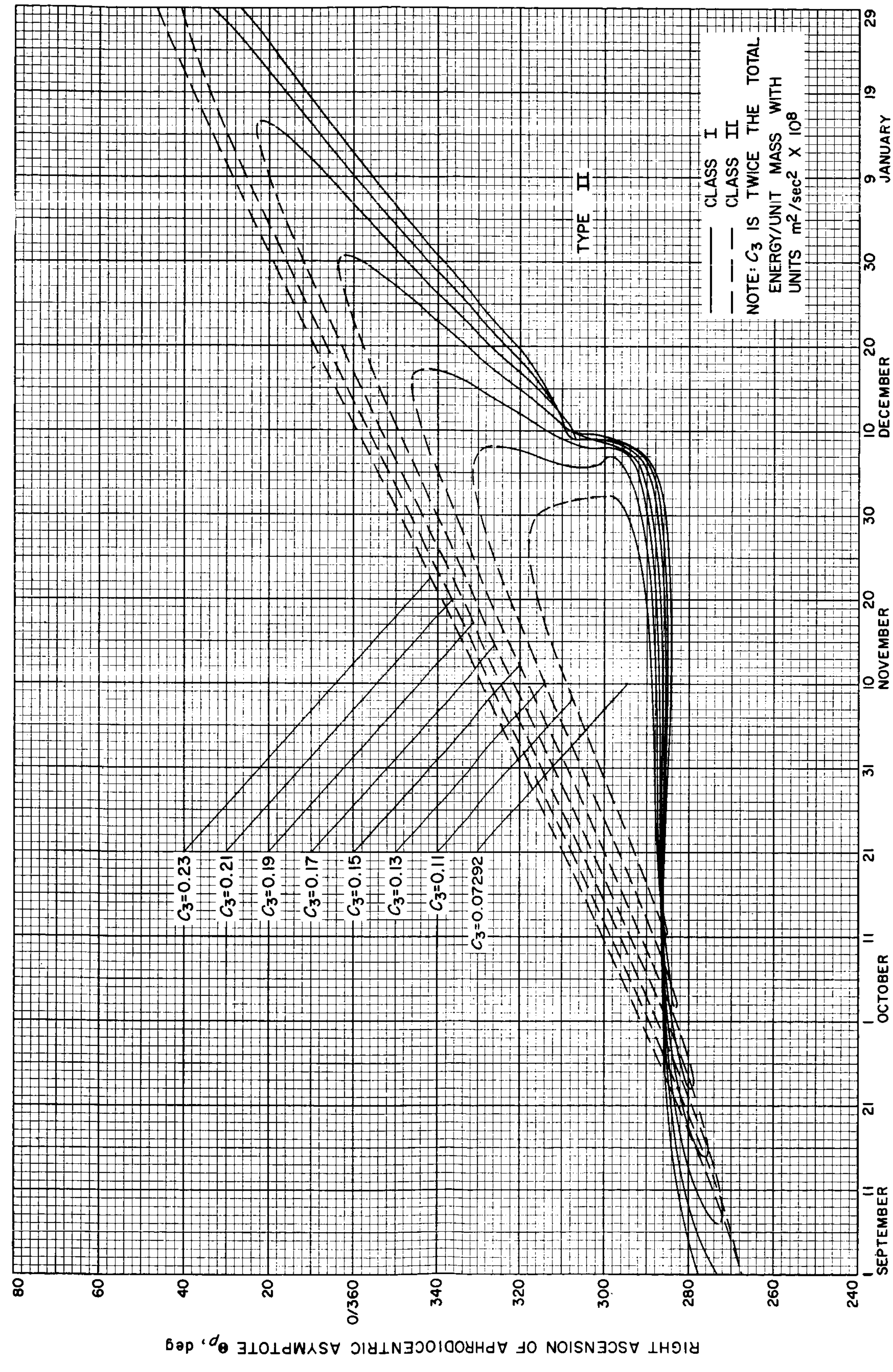

Fig. 7-29. Venus 1965: Right ascension of aphrodiocentric asymptote vs launch date, Type II

VIII. VENUS 1967: TRAJECTORY-PARAMETER GRAPHS

Figure

VIII. VENUS 1967: TRAJECTORY-PARAMETER GRAPHS (Cont'd)

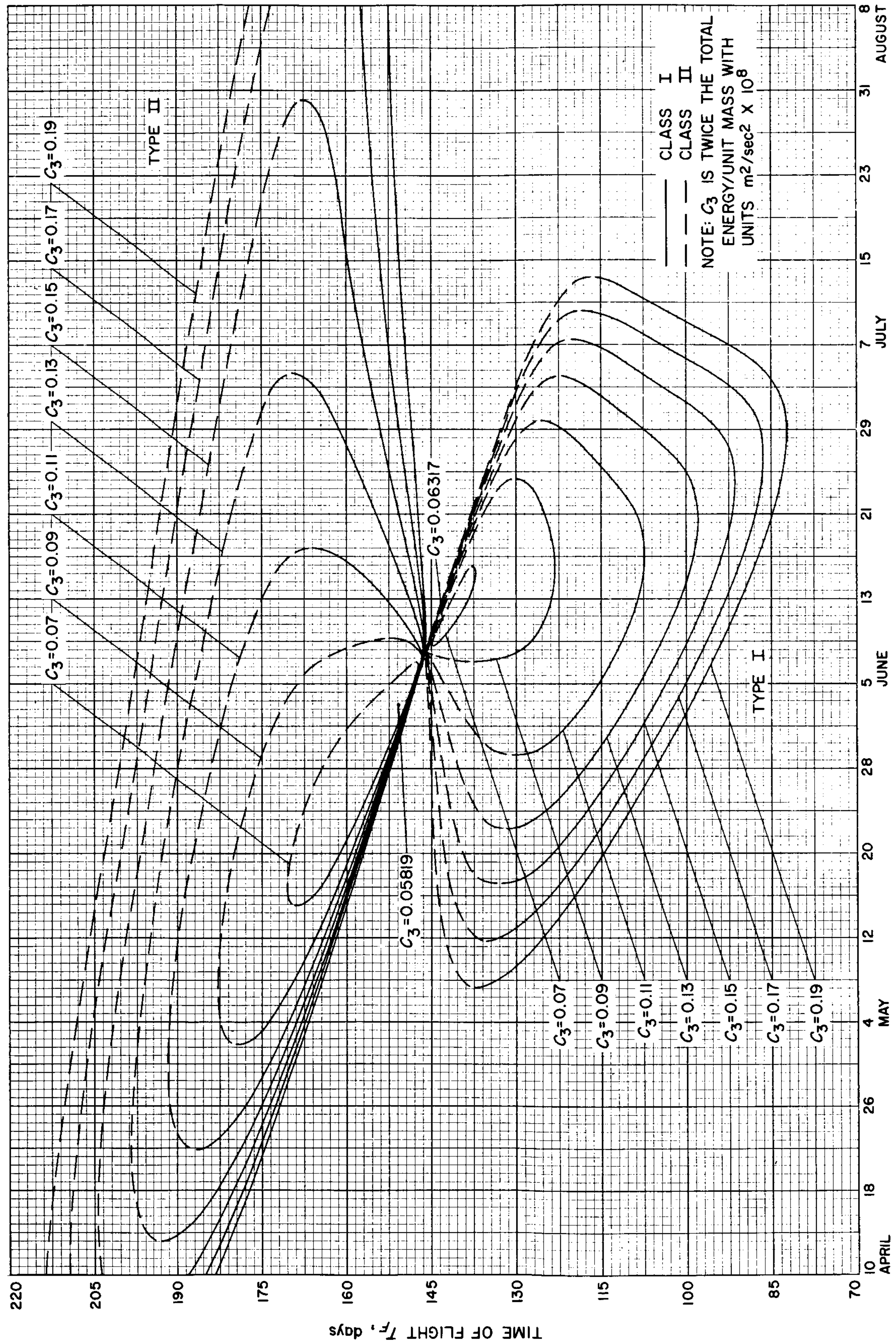

Fig. 8–1. Venus 1967: Time of flight vs launch date

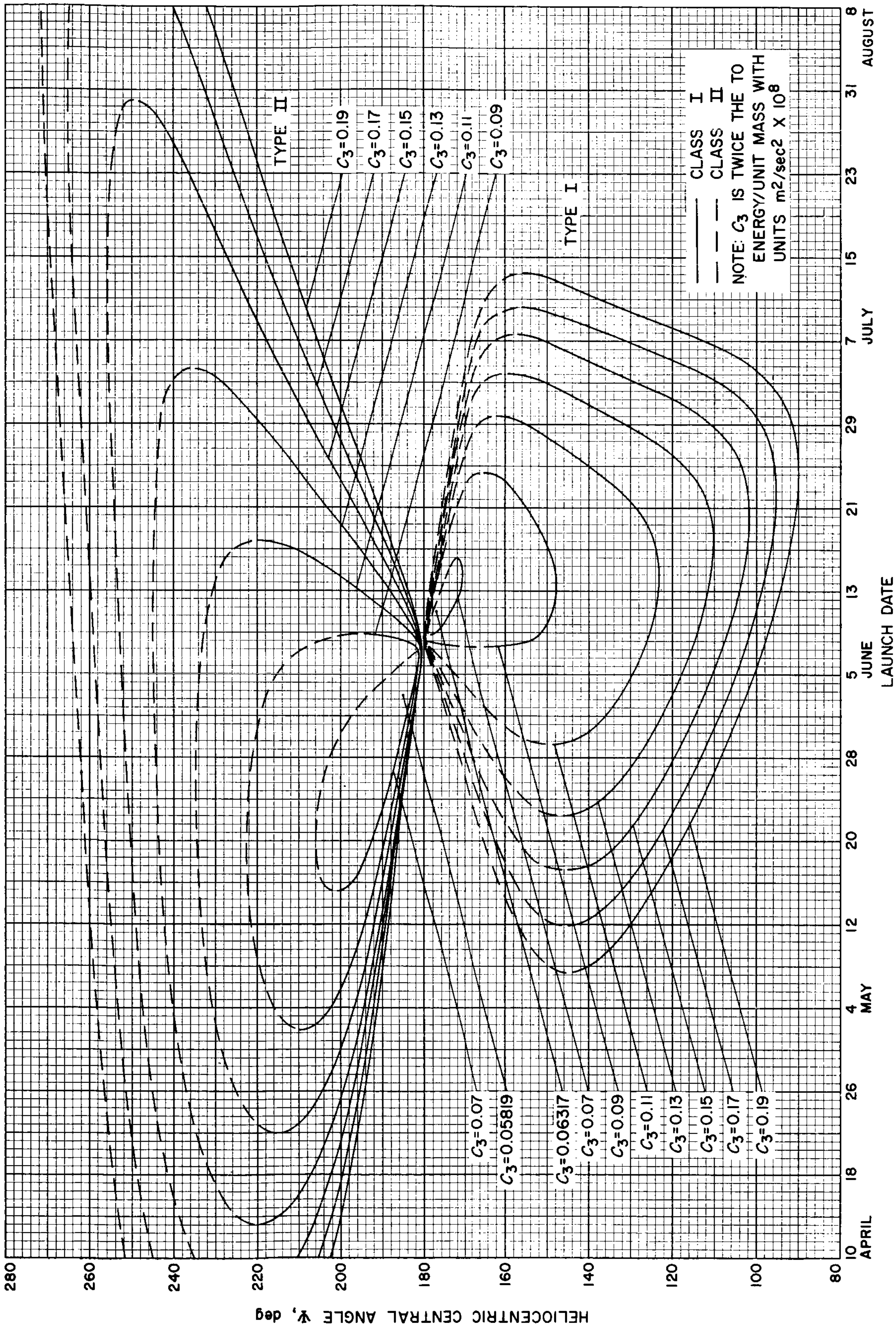

Fig. 8–2. Venus 1967: Heliocentric central angle vs launch date

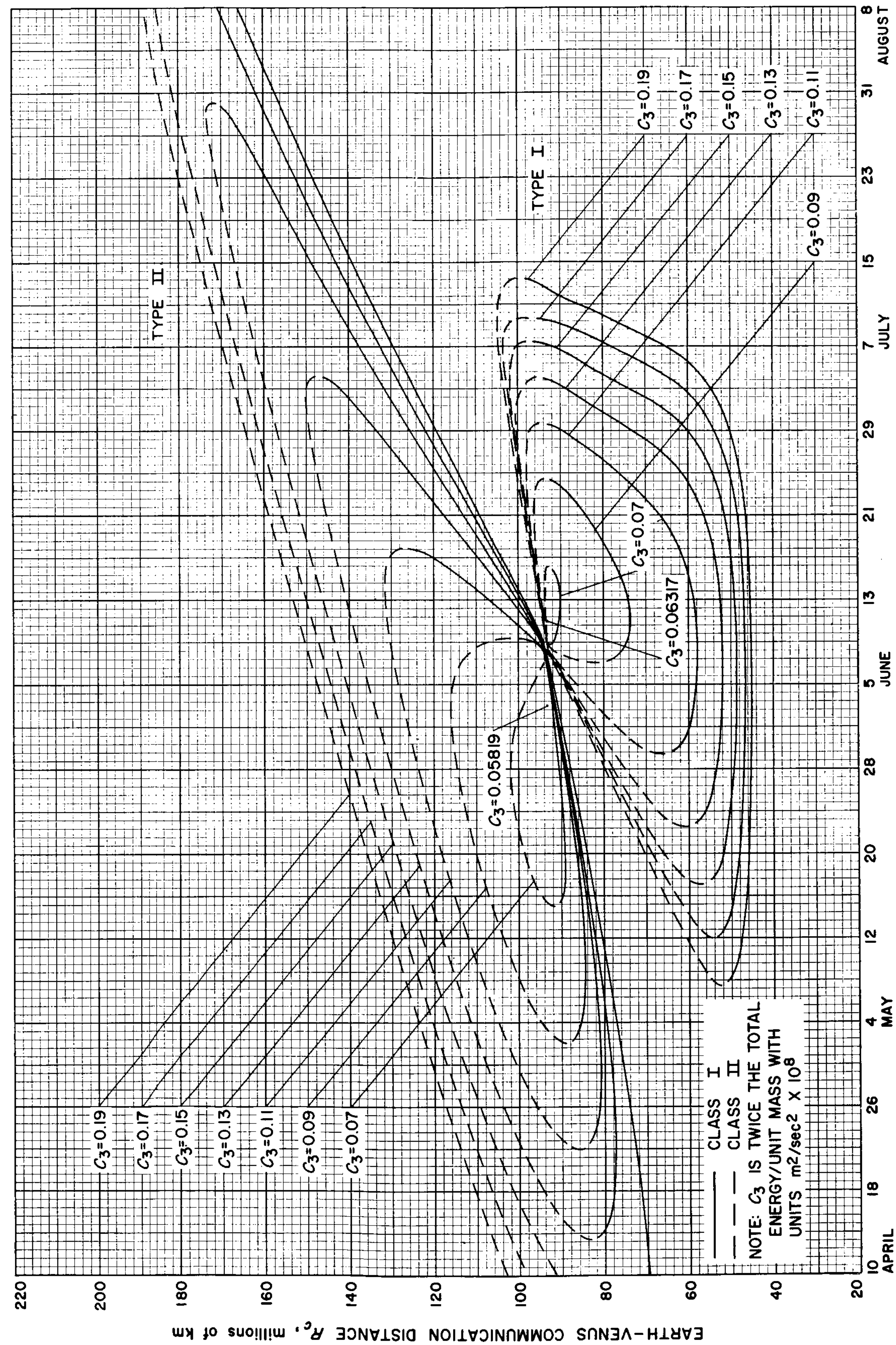

Fig. 8-3. Venus 1967: Earth–Venus communication distance vs launch date

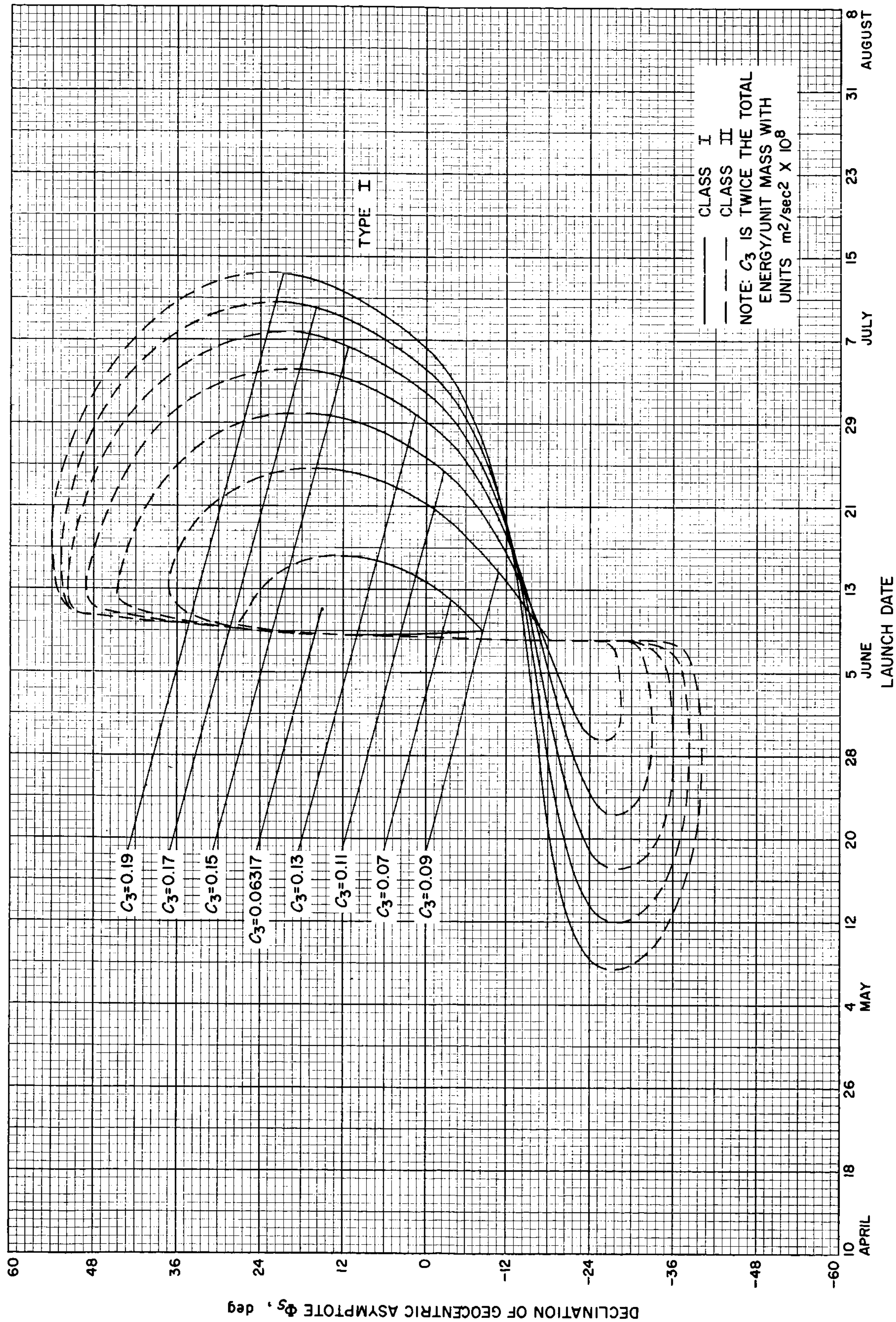

Fig. 8–4. Venus 1967: Declination of geocentric asymptote vs launch date, Type I

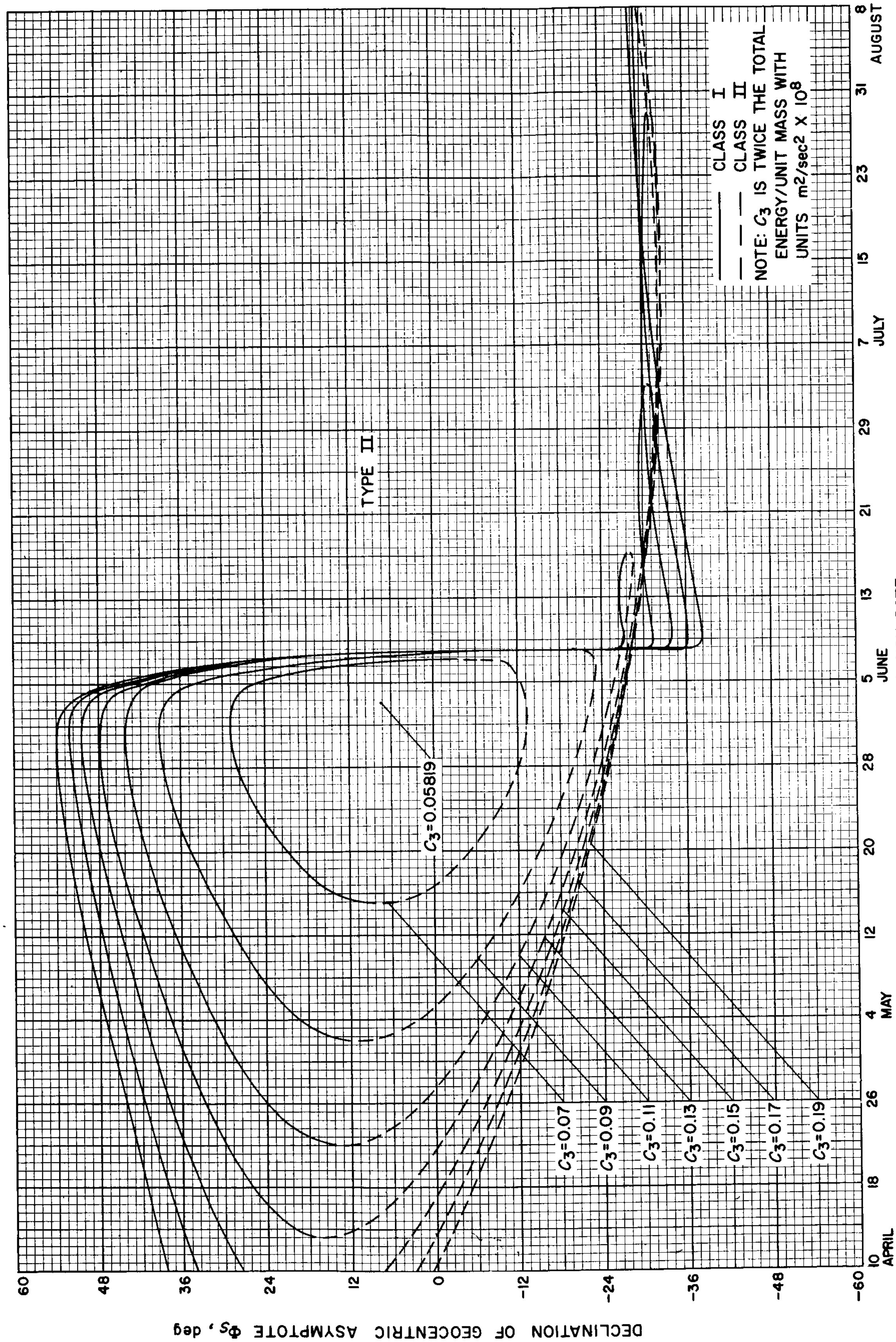

Fig. 8-5. Venus 1967: Declination of geocentric asymptote vs launch date, Type II

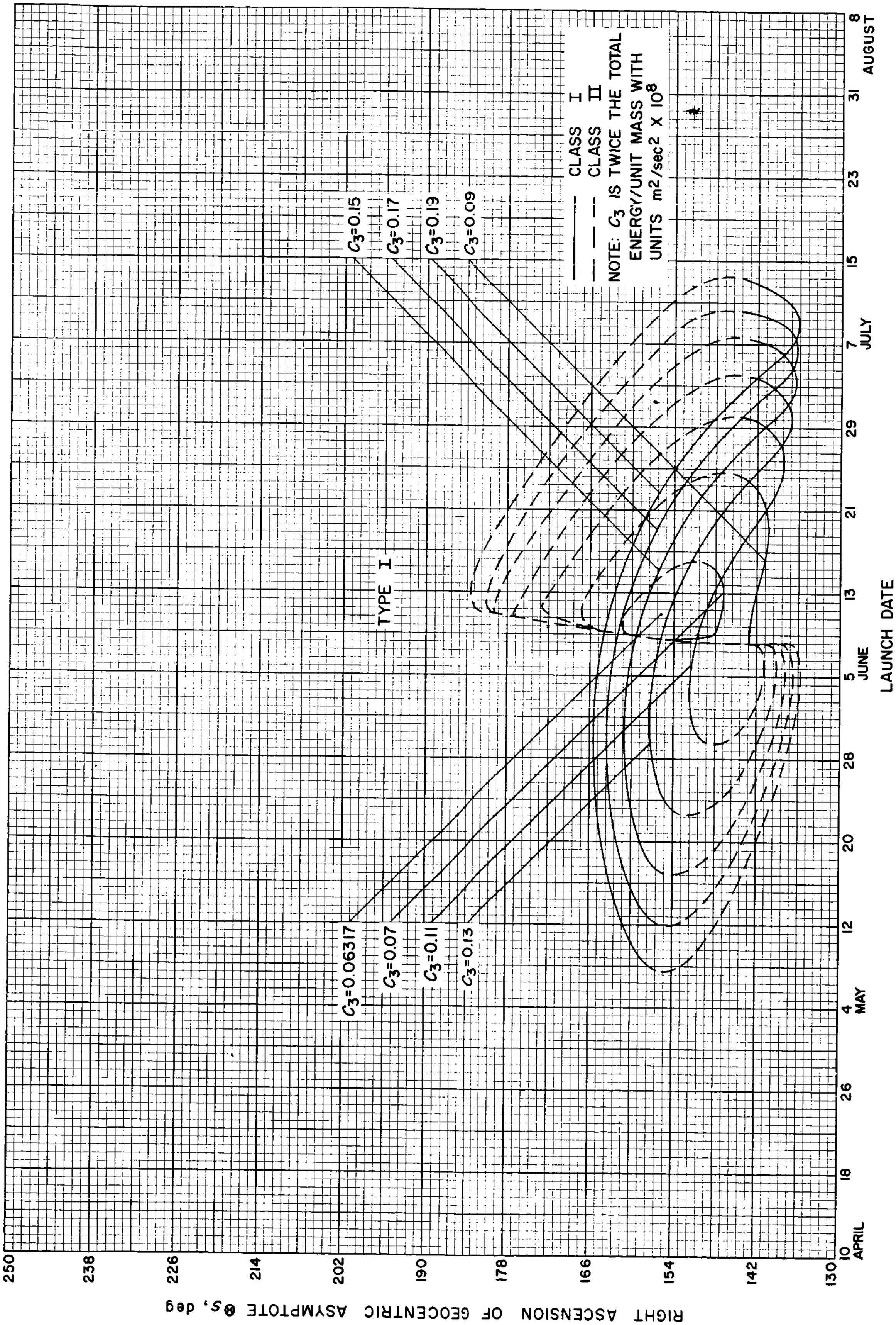

Fig. 8-6. Venus 1967: Right ascension of geocentric asymptote vs launch date, Type I

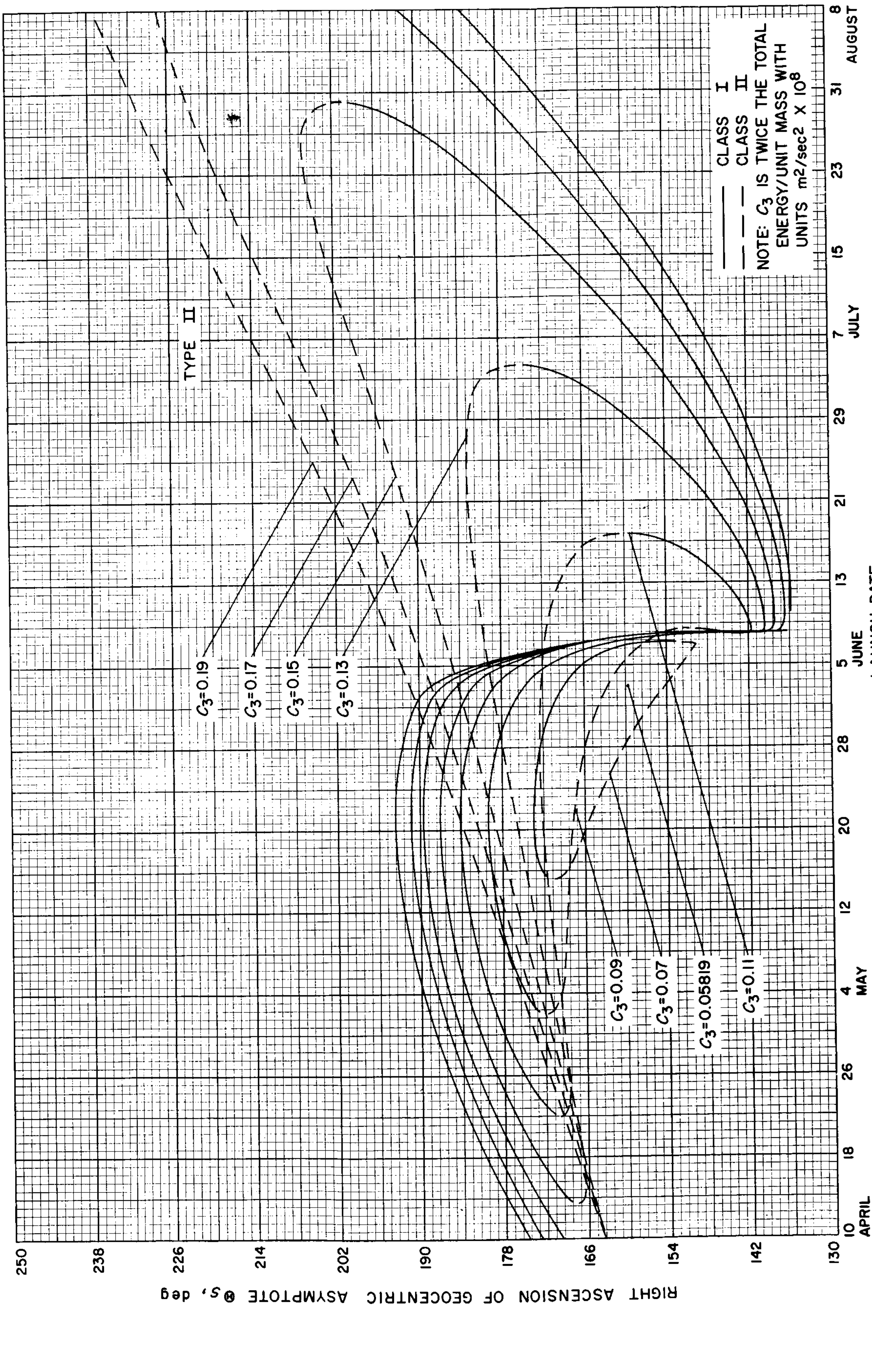

Fig. 8-7. Venus 1967: Right ascension of geocentric asymptote vs launch date, Type II

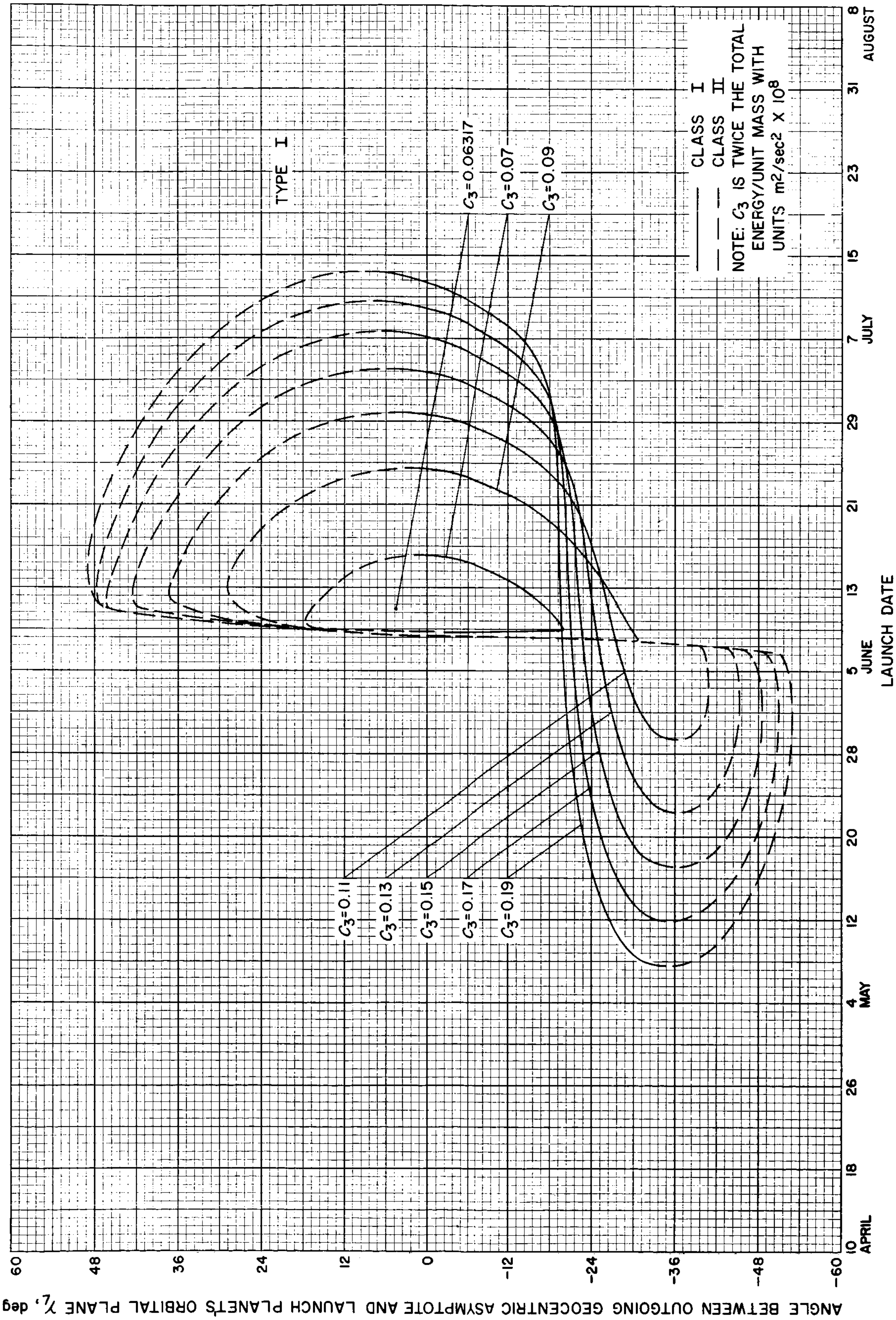

Fig. 8–8. Venus 1967: Angle between outgoing geocentric asymptote and launch planet's orbital plane vs launch date, Type I

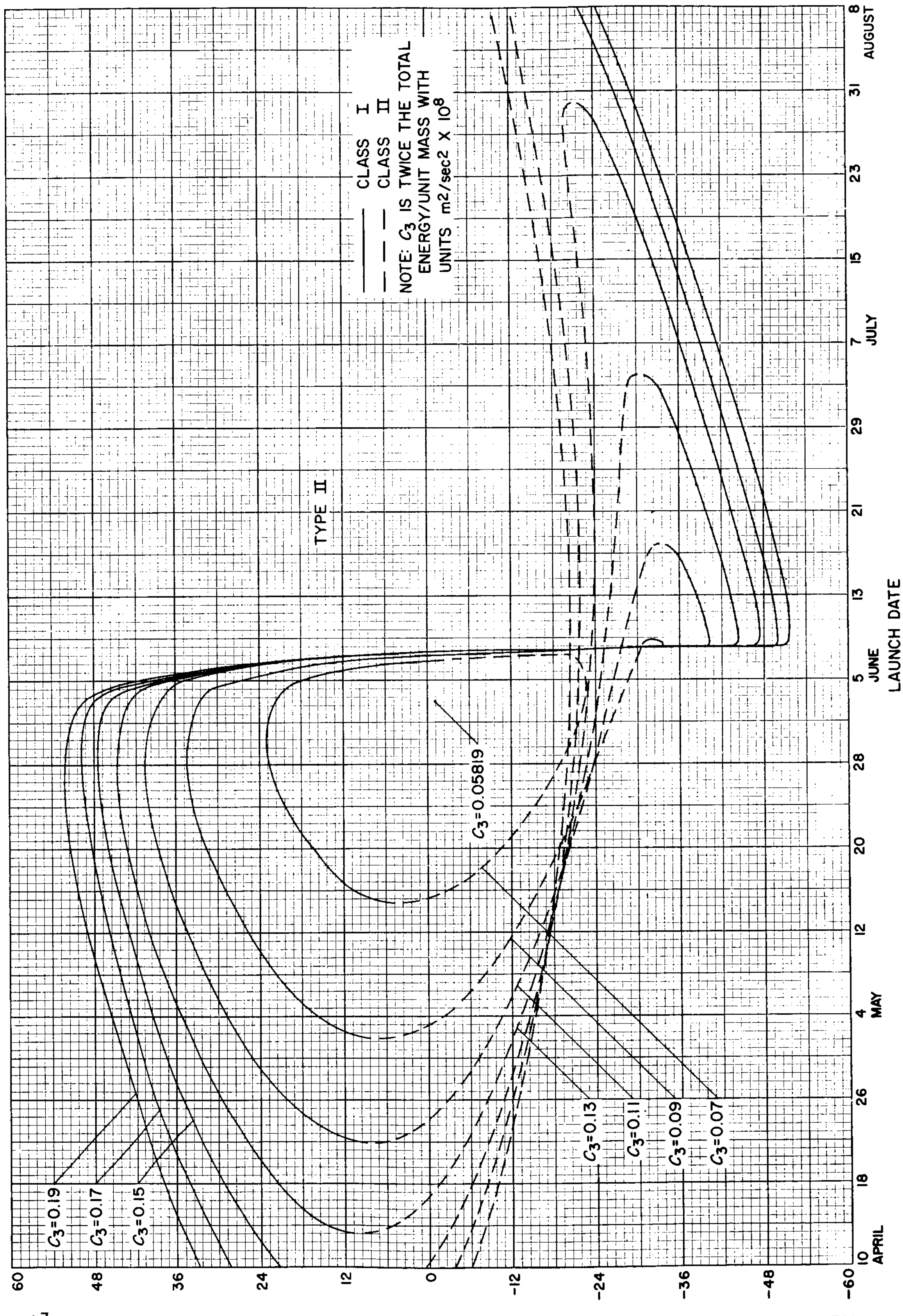

Fig. 8-9. Venus 1967: Angle between outgoing geocentric asymptote and launch planet's orbital plane vs launch date, Type II

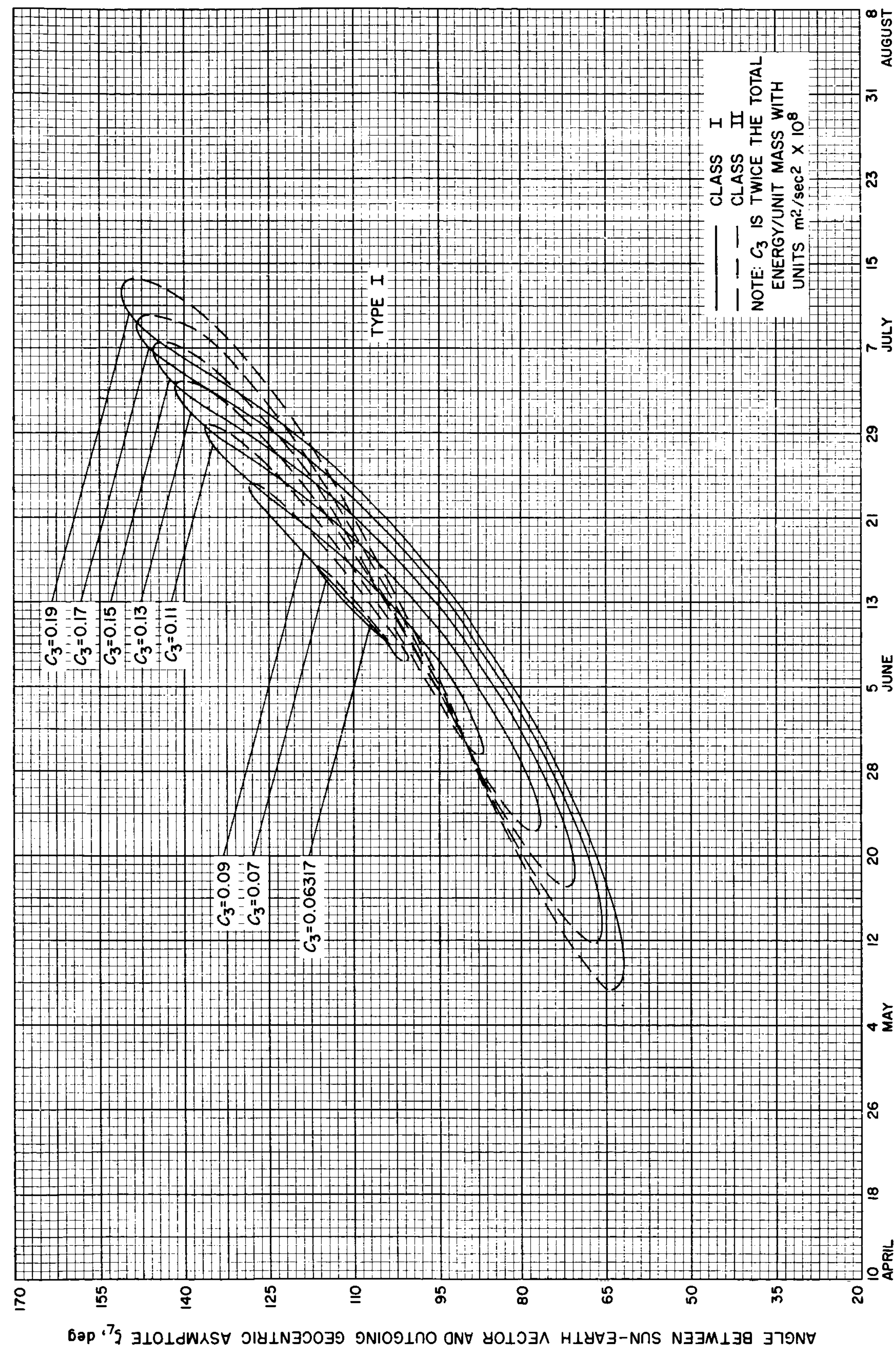

Fig. 8-10. Venus 1967: Angle between Sun–Earth vector and outgoing geocentric asymptote vs launch date, Type I

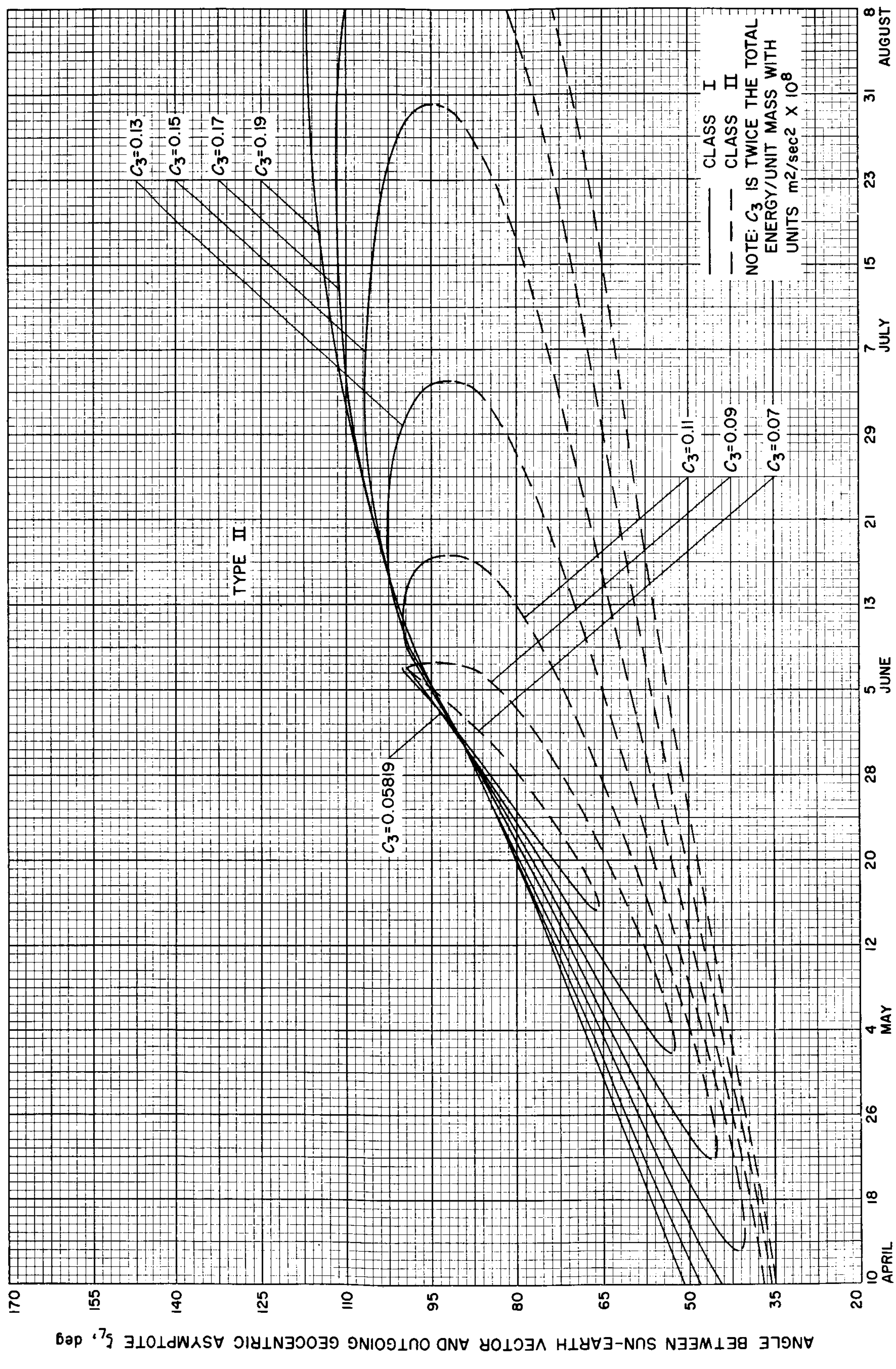

Fig. 8–11. Venus 1967: Angle between Sun–Earth vector and outgoing geocentric asymptote vs launch date, Type II

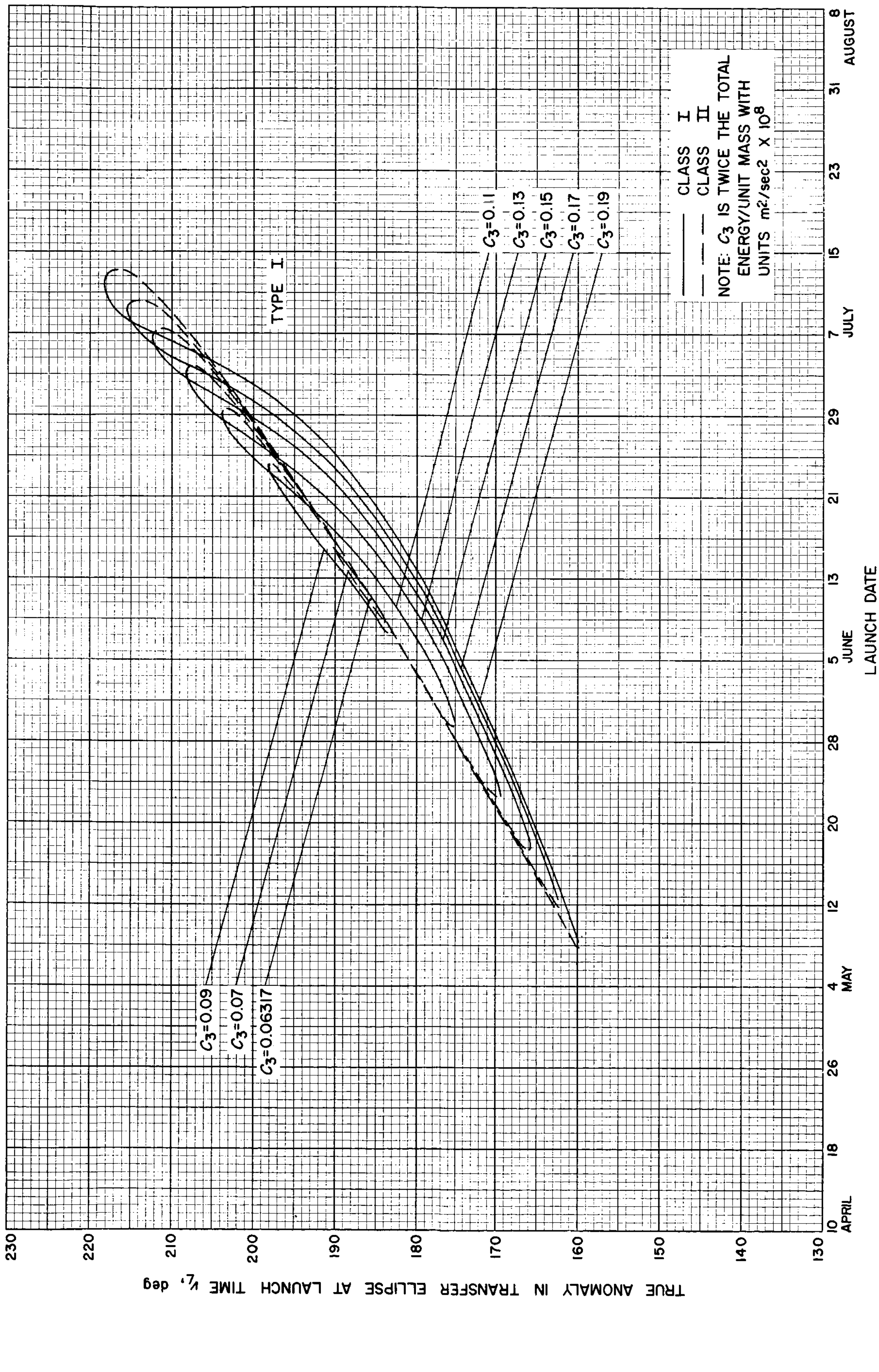

Fig. 8–12. Venus 1967: True anomaly in transfer ellipse at launch time vs launch date, Type I

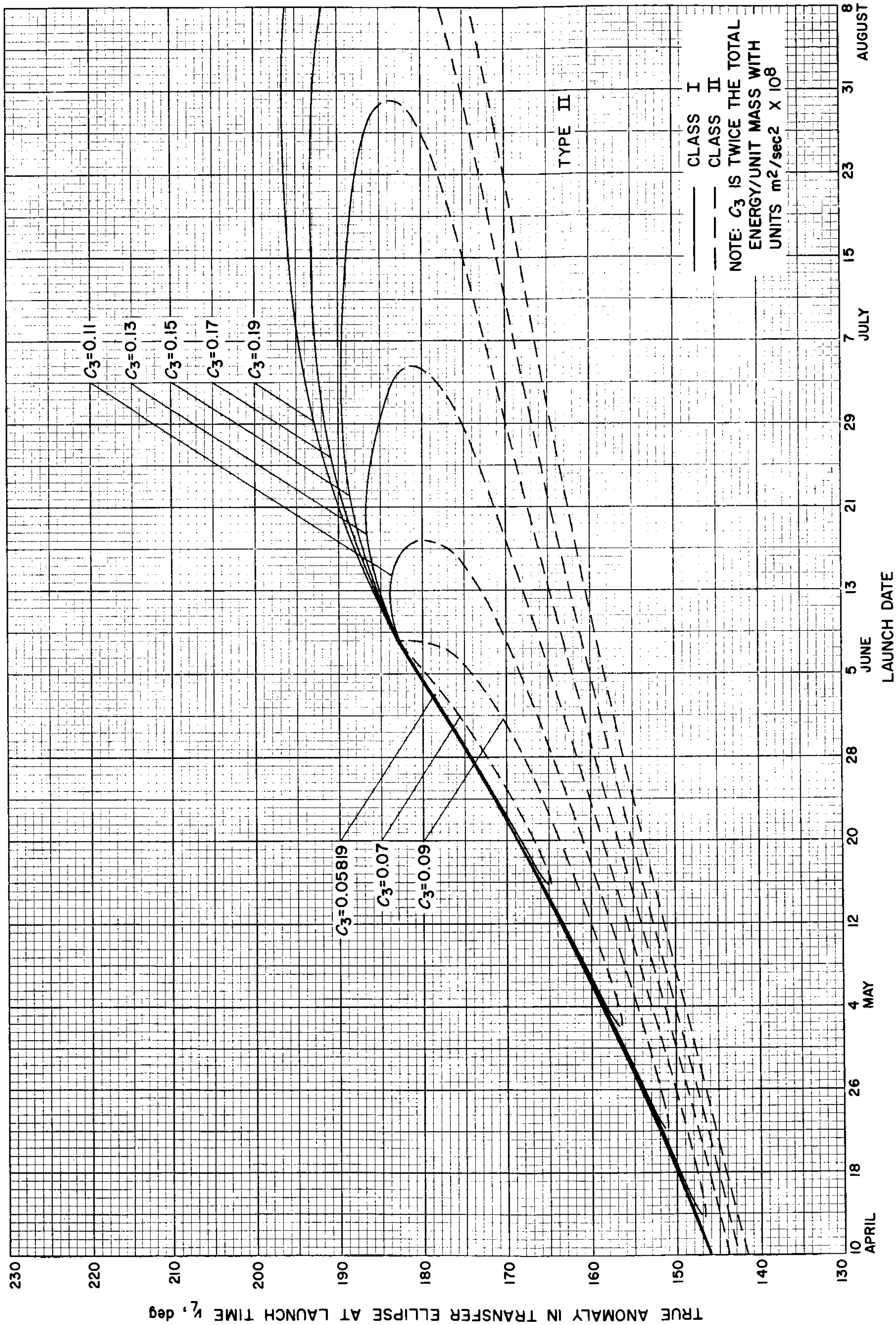

Fig. 8–13. Venus 1967: True anomaly in transfer ellipse at launch time vs launch date, Type II

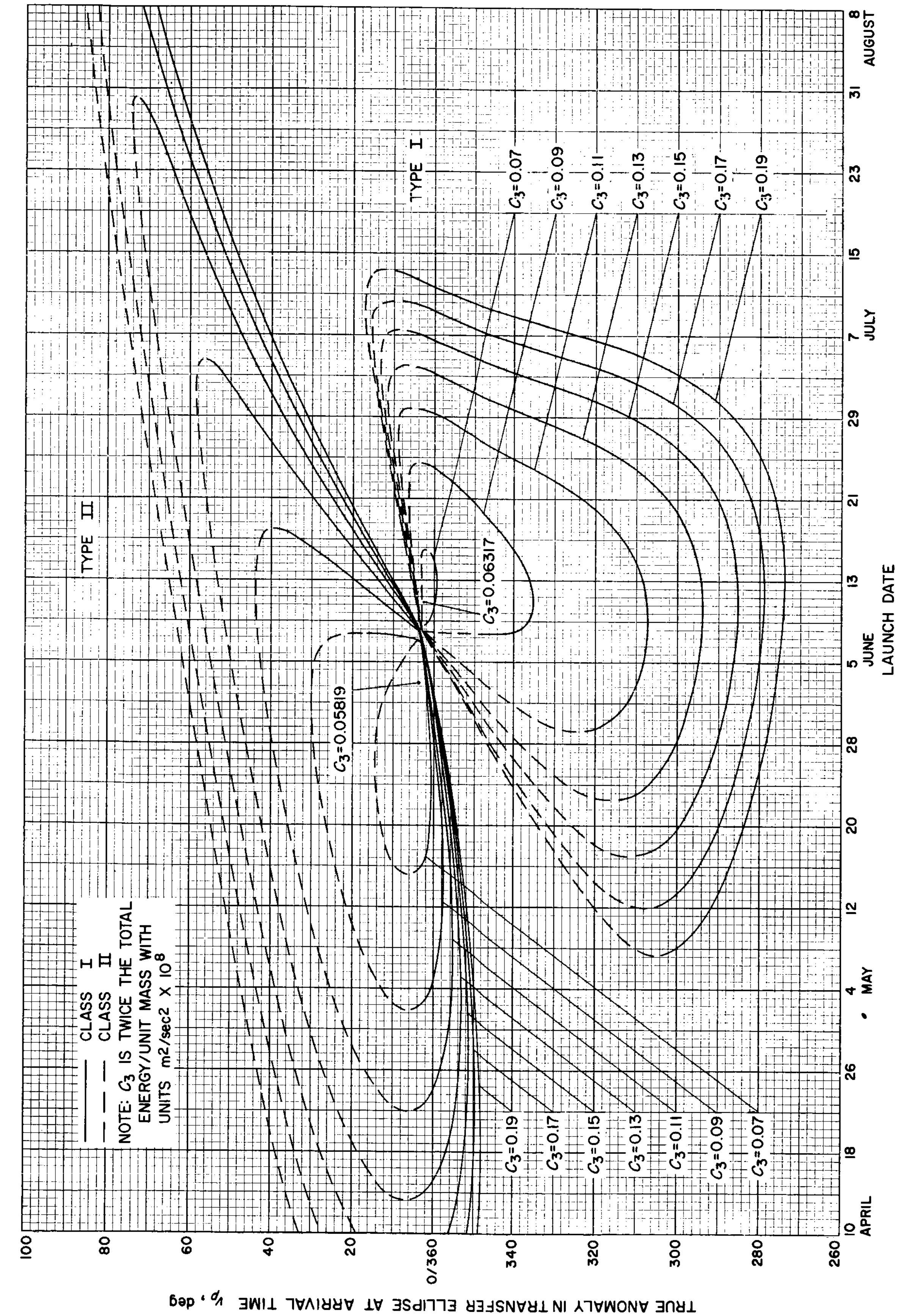

Fig. 8–14. Venus 1967: True anomaly in transfer ellipse at arrival time vs launch date

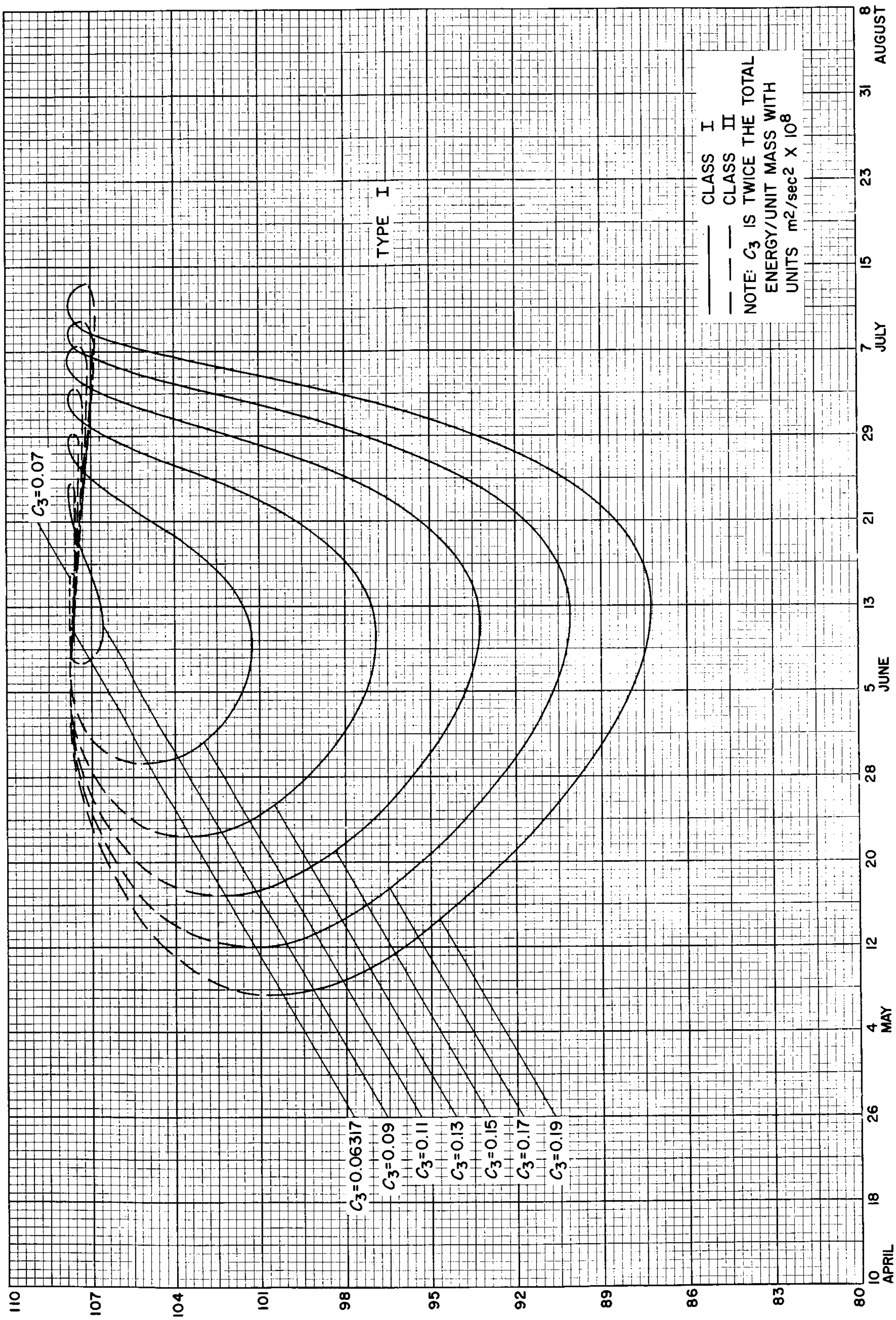

Fig. 8-15. Venus 1967: Perihelion of transfer orbit vs launch date, Type I

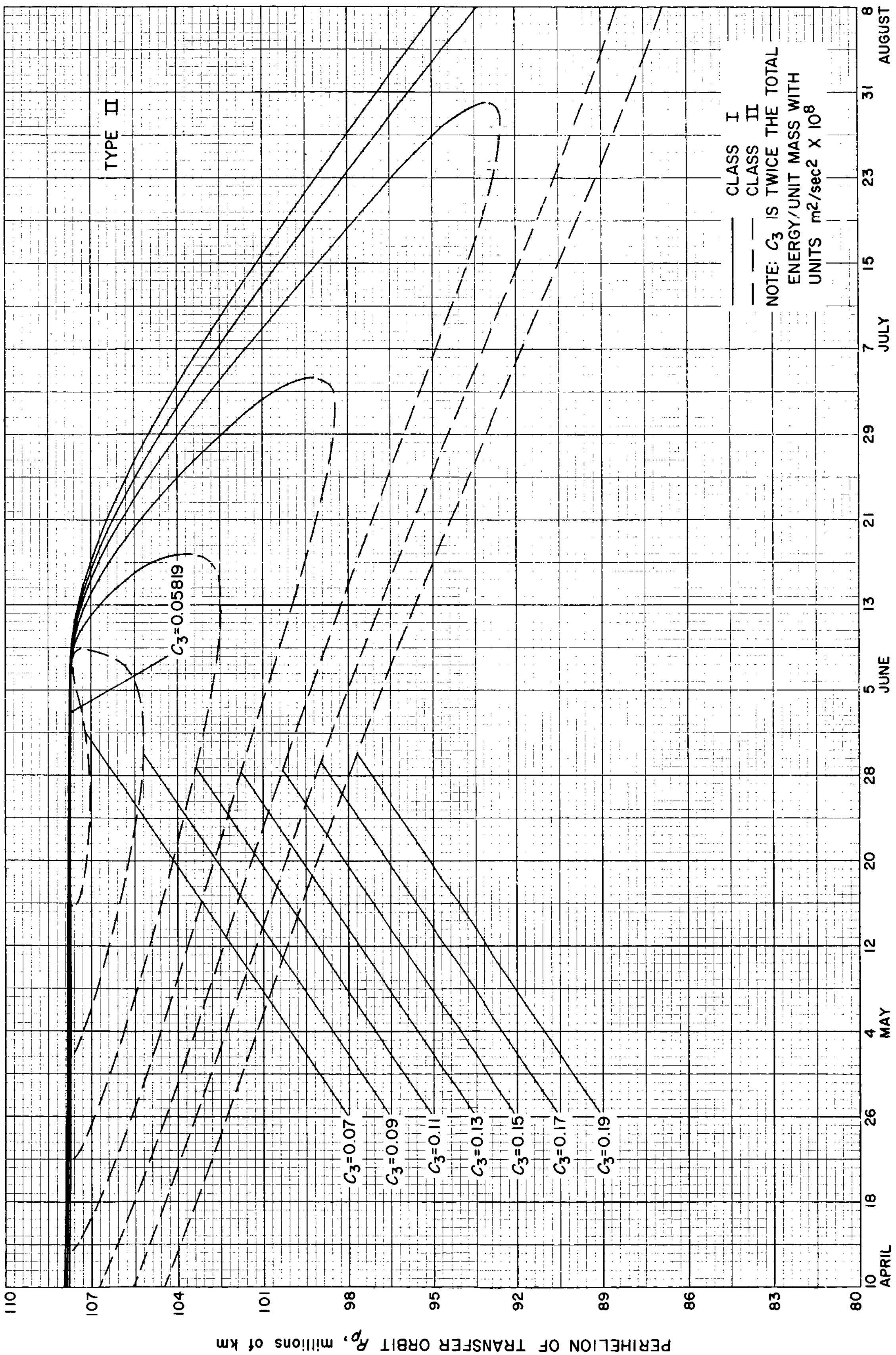

Fig. 8–16. Venus 1967: Perihelion of transfer orbit vs launch date, Type II

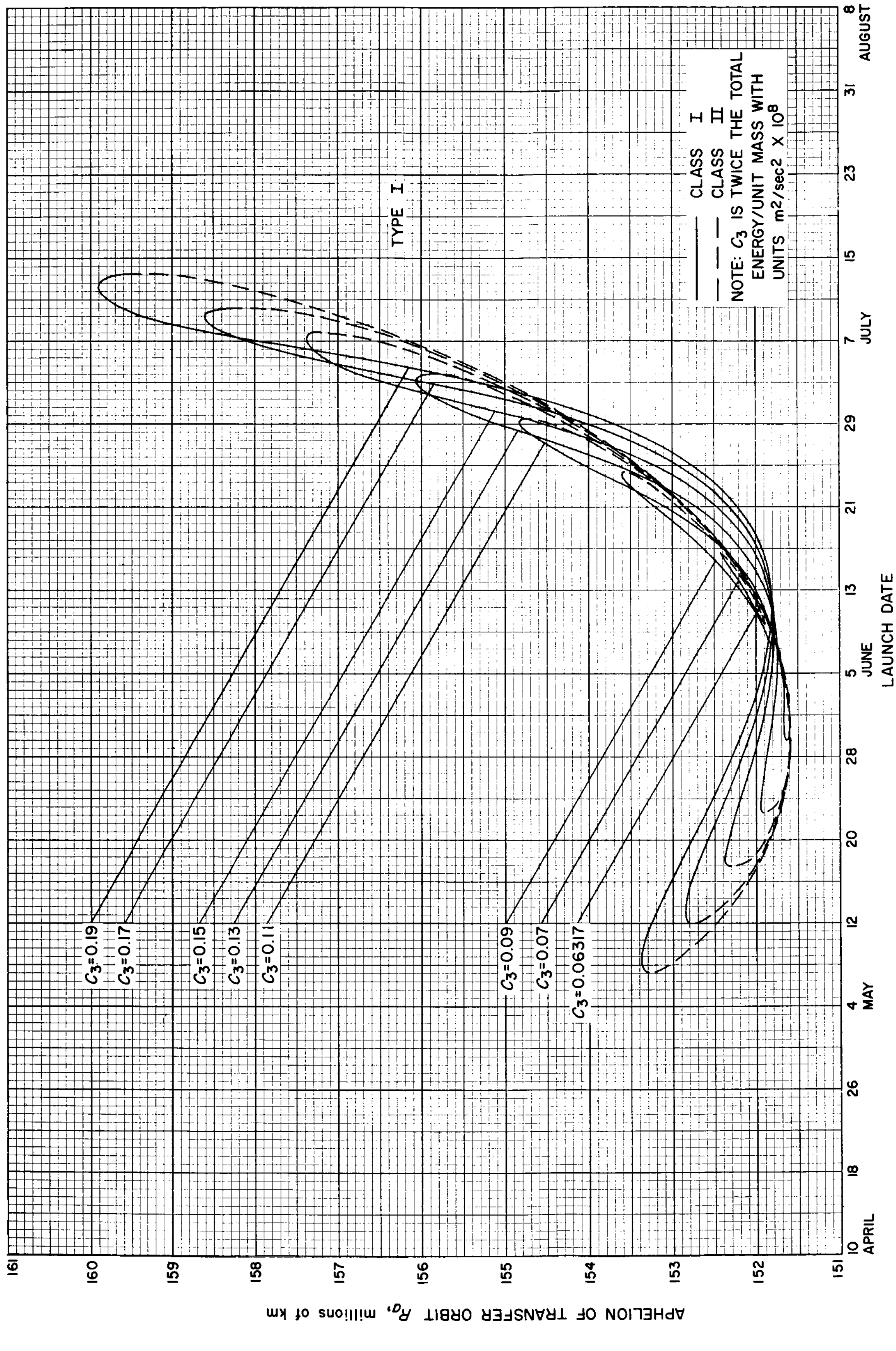

Fig. 8-17. Venus 1967: Aphelion of transfer orbit vs launch date, Type I

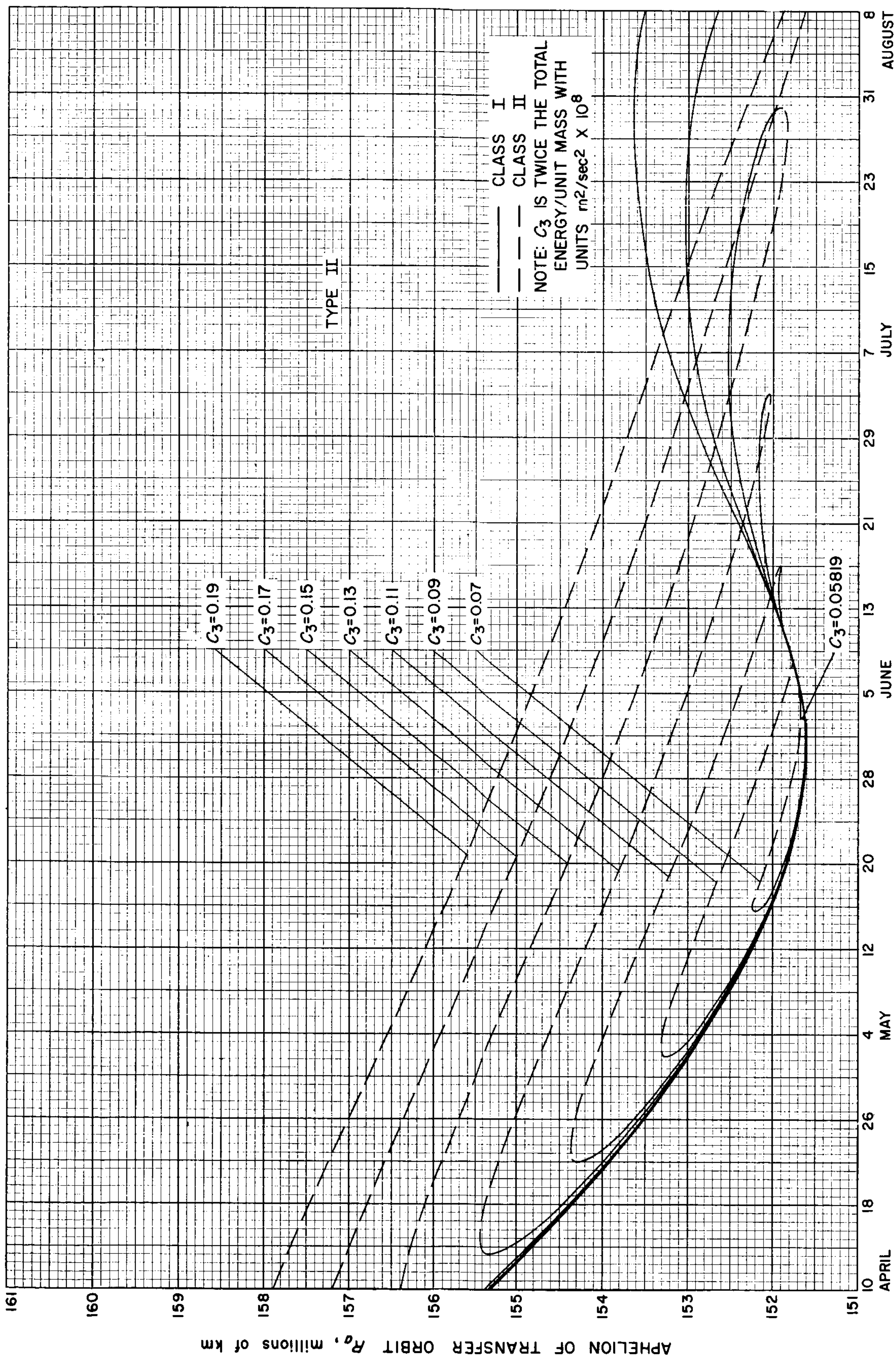

Fig. 8–18. Venus 1967: Aphelion of transfer orbit vs launch date, Type II

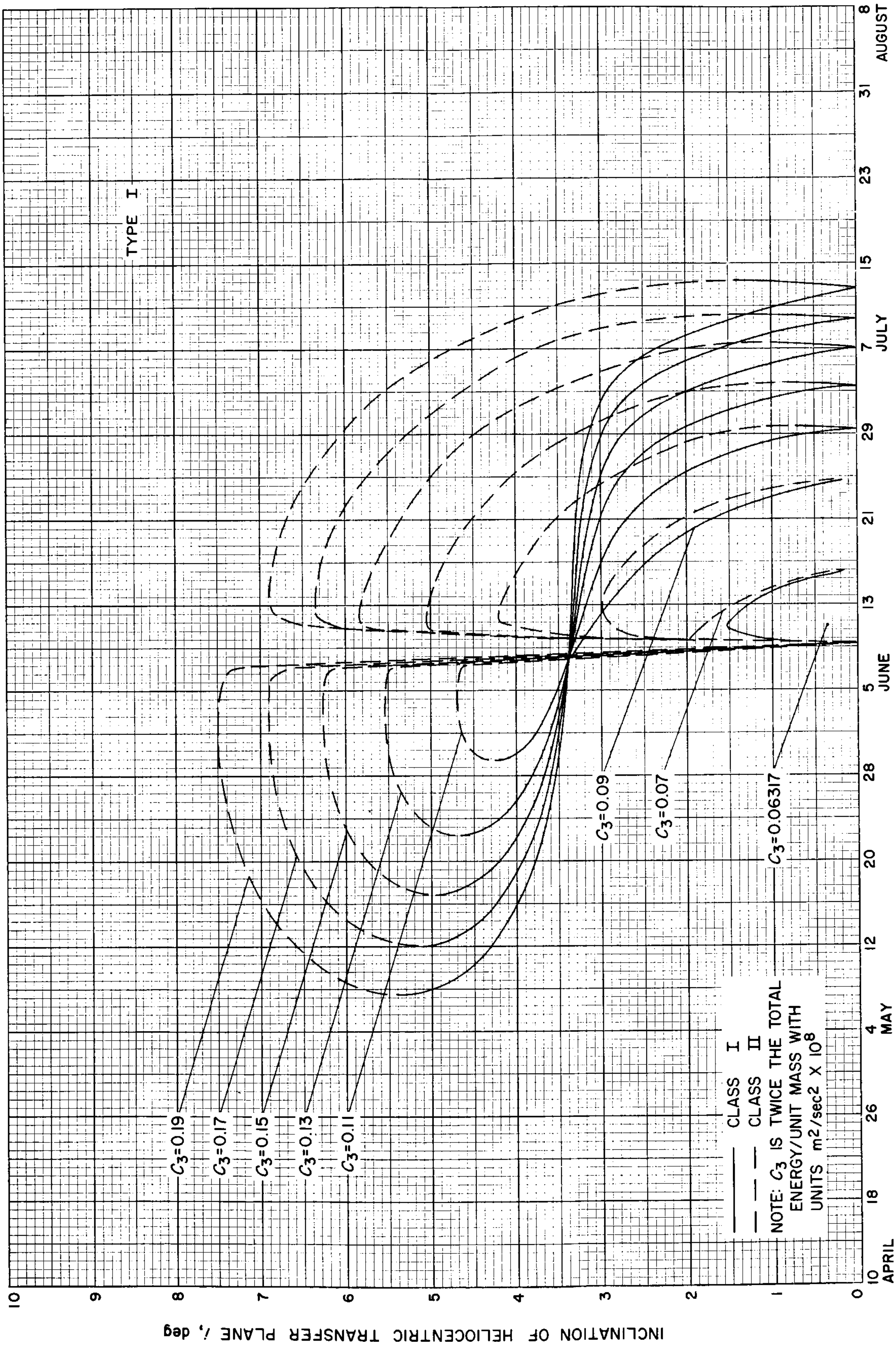

Fig. 8–19. Venus 1967: Inclination of heliocentric-transfer plane vs launch date, Type I

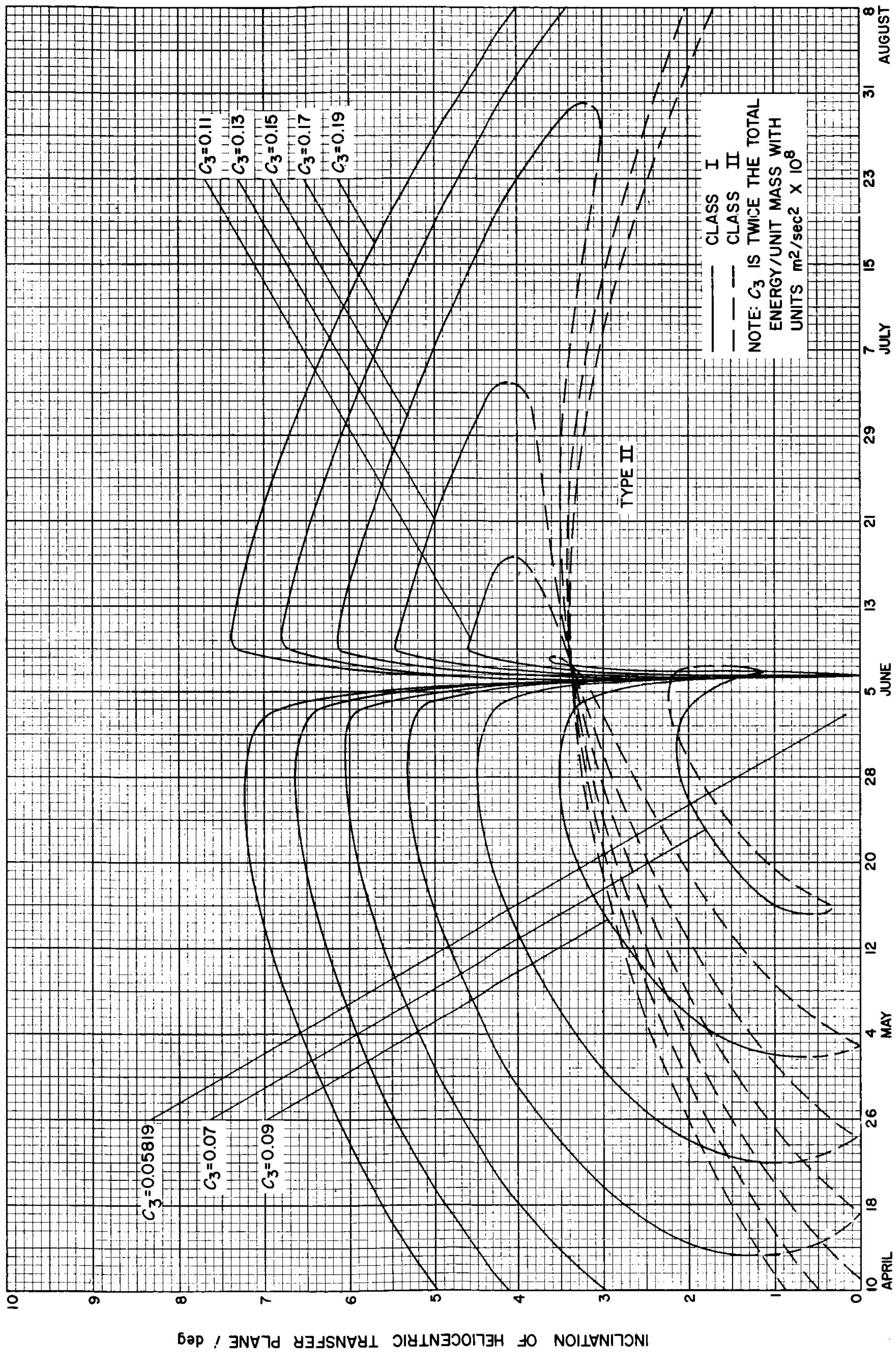

Fig. 8–20. Venus 1967: Inclination of heliocentric-transfer plane vs launch date, Type II

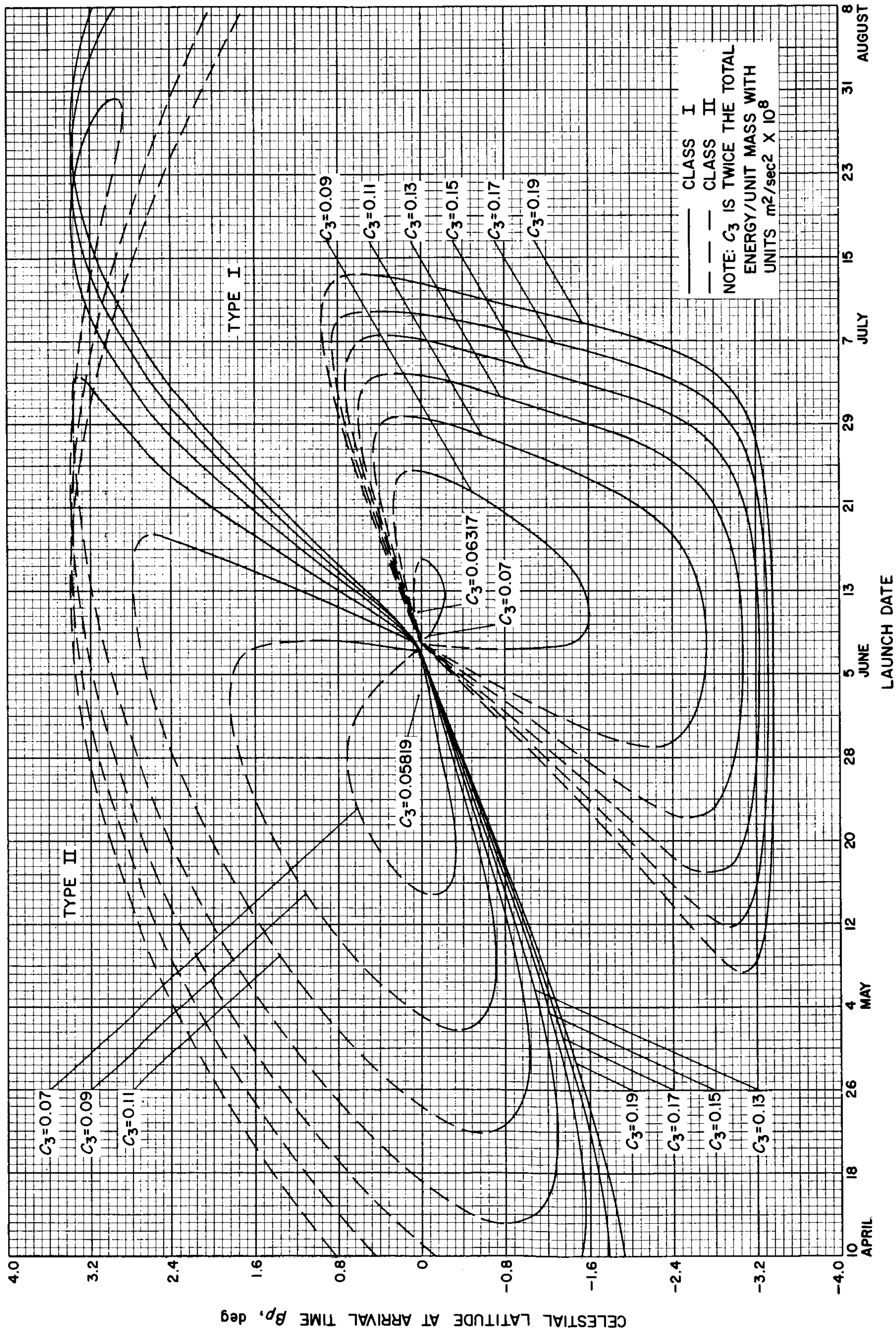

Fig. 8-21. Venus 1967: Celestial latitude at arrival time vs launch date

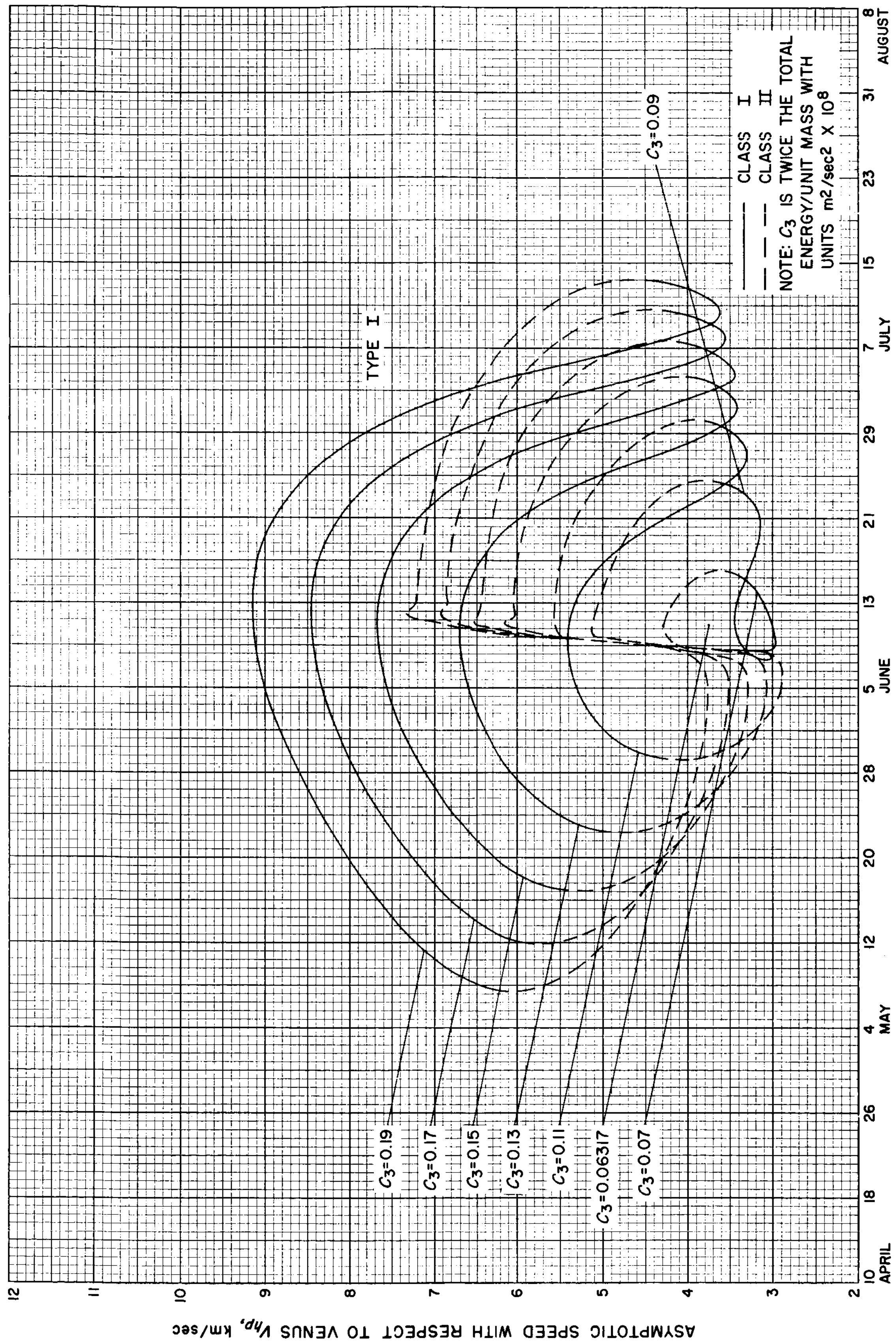

Fig. 8–22. Venus 1967: Asymptotic speed with respect to Venus vs launch date, Type I

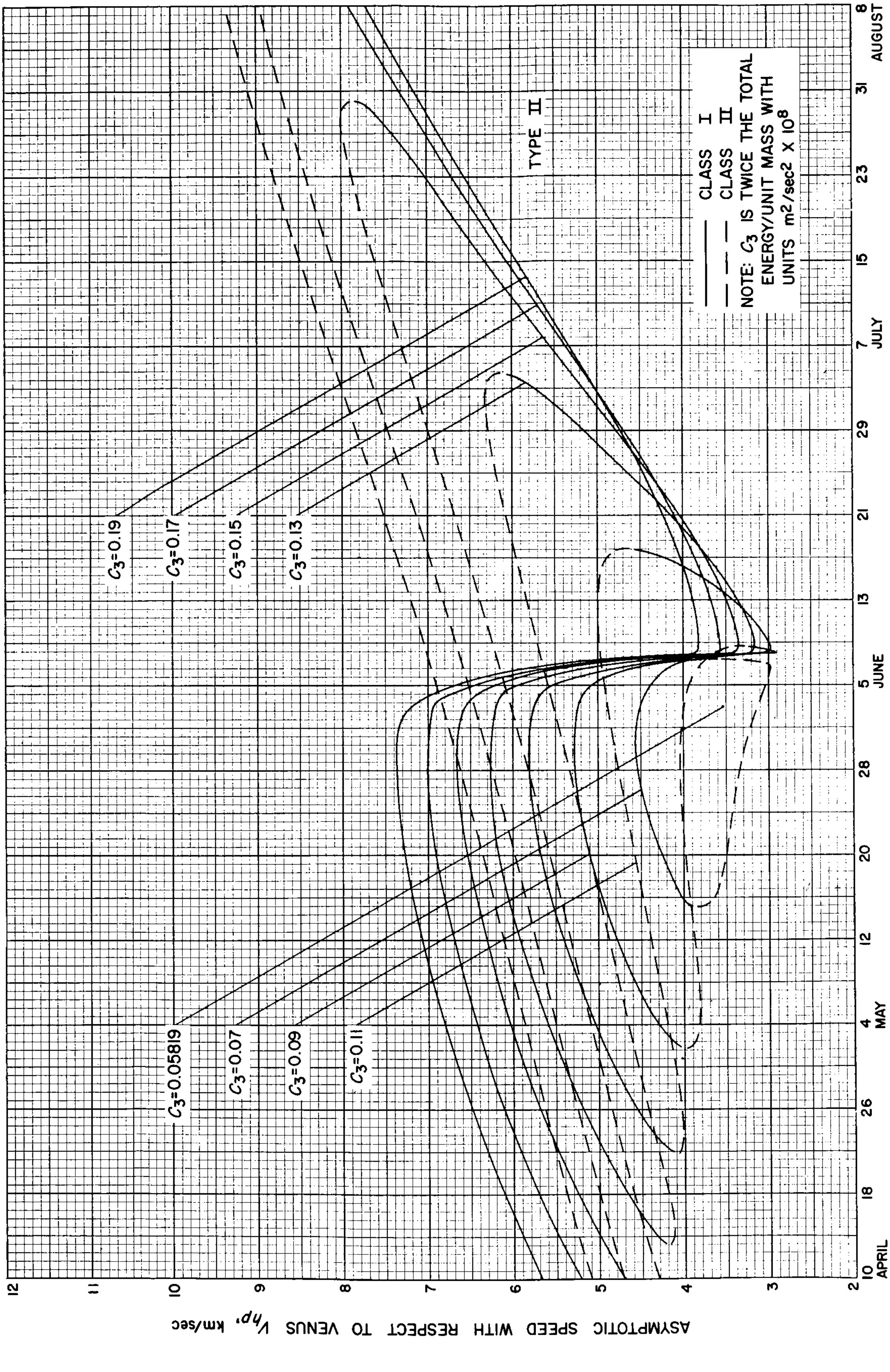

Fig. 8–23. Venus 1967: Asymptotic speed with respect to Venus vs launch date, Type II

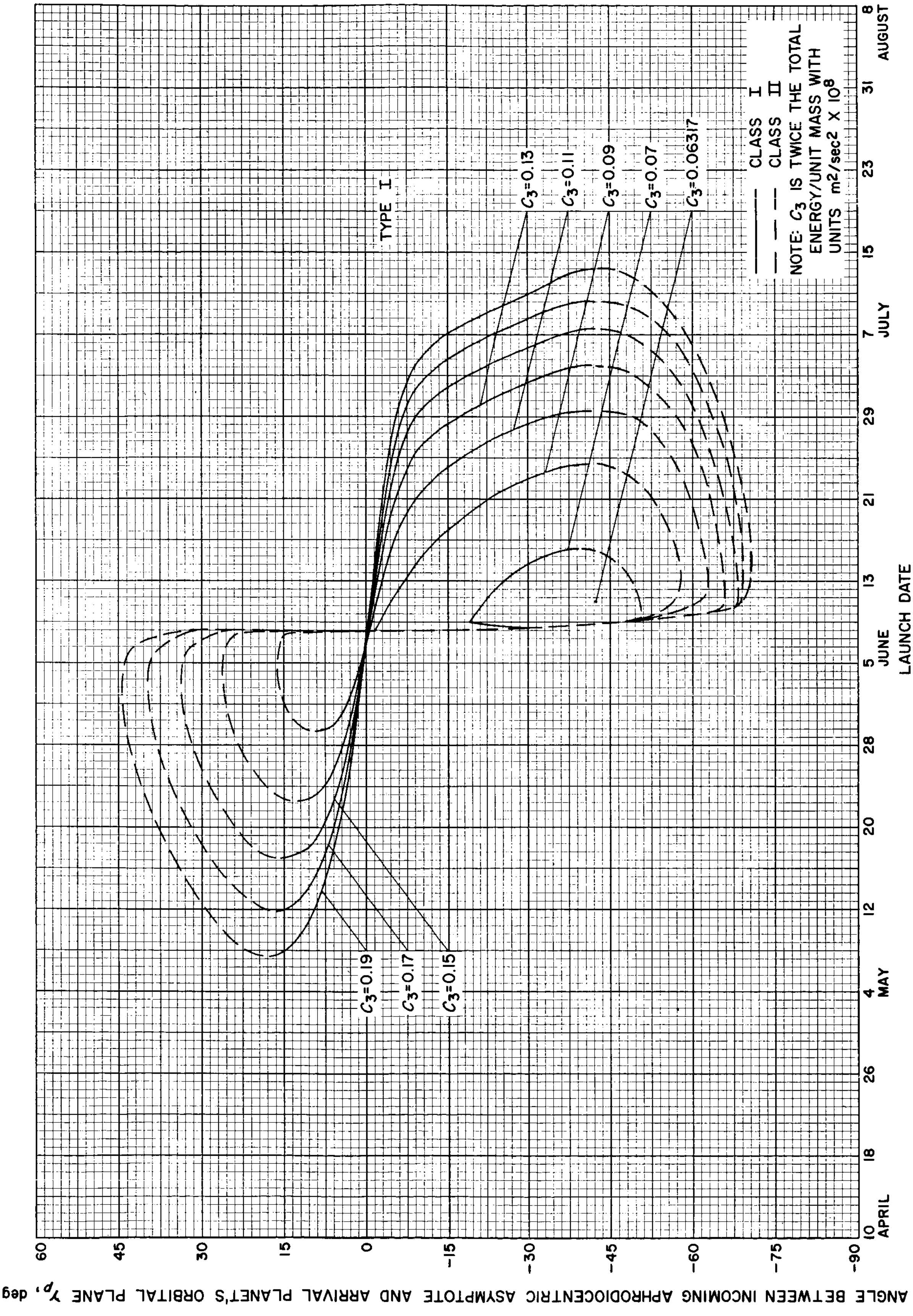

Fig. 8-24. Venus 1967: Angle between incoming aphrodiocentric asymptote and arrival planet's orbital plane vs launch date, Type I

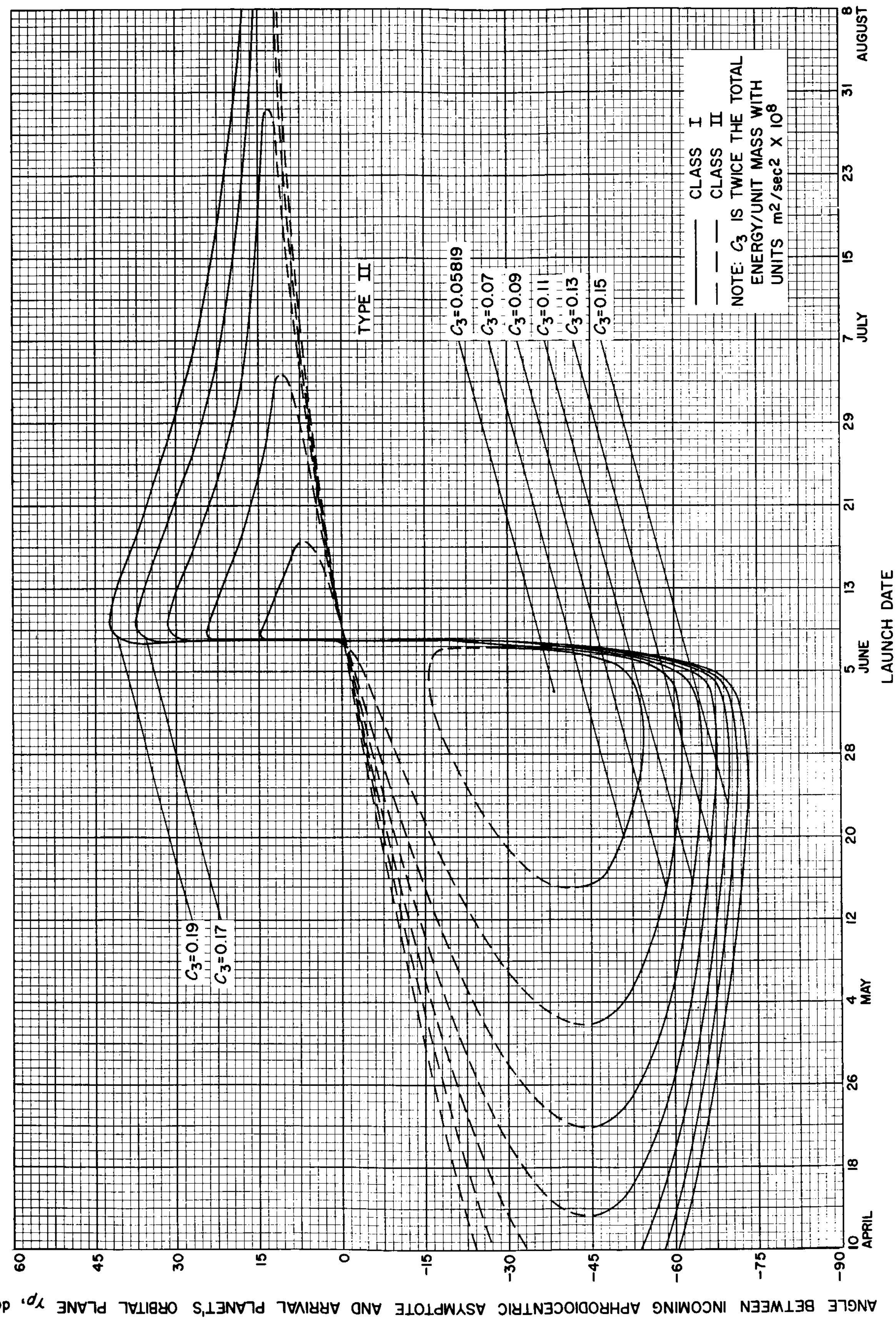

Fig. 8–25. Venus 1967: Angle between incoming aphrodiocentric asymptote and arrival planet's orbital plane vs launch date, Type II

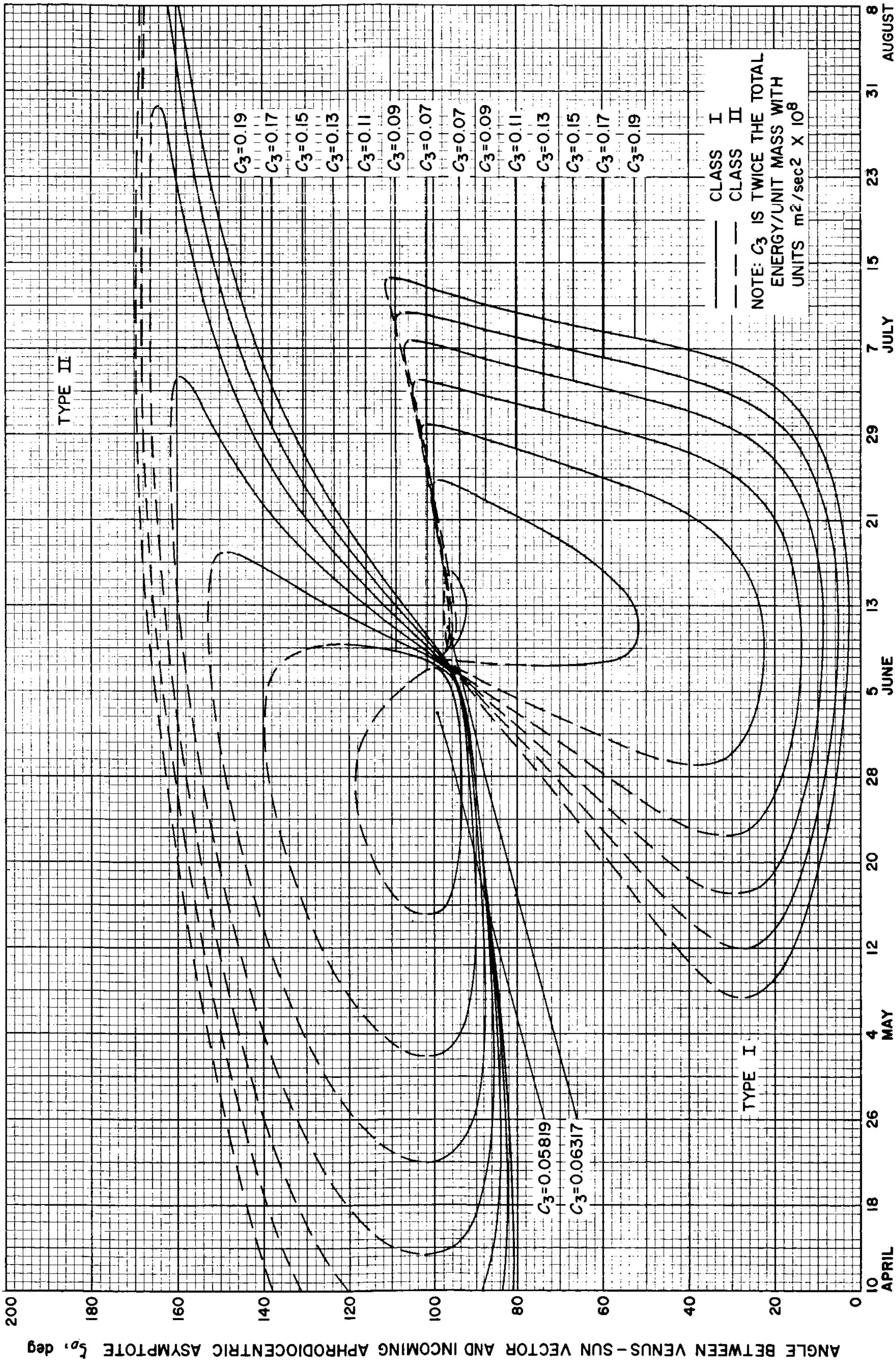

Fig. 8–26. Venus 1967: Angle between Venus–Sun vector and incoming aphrodiocentric asymptote vs launch date

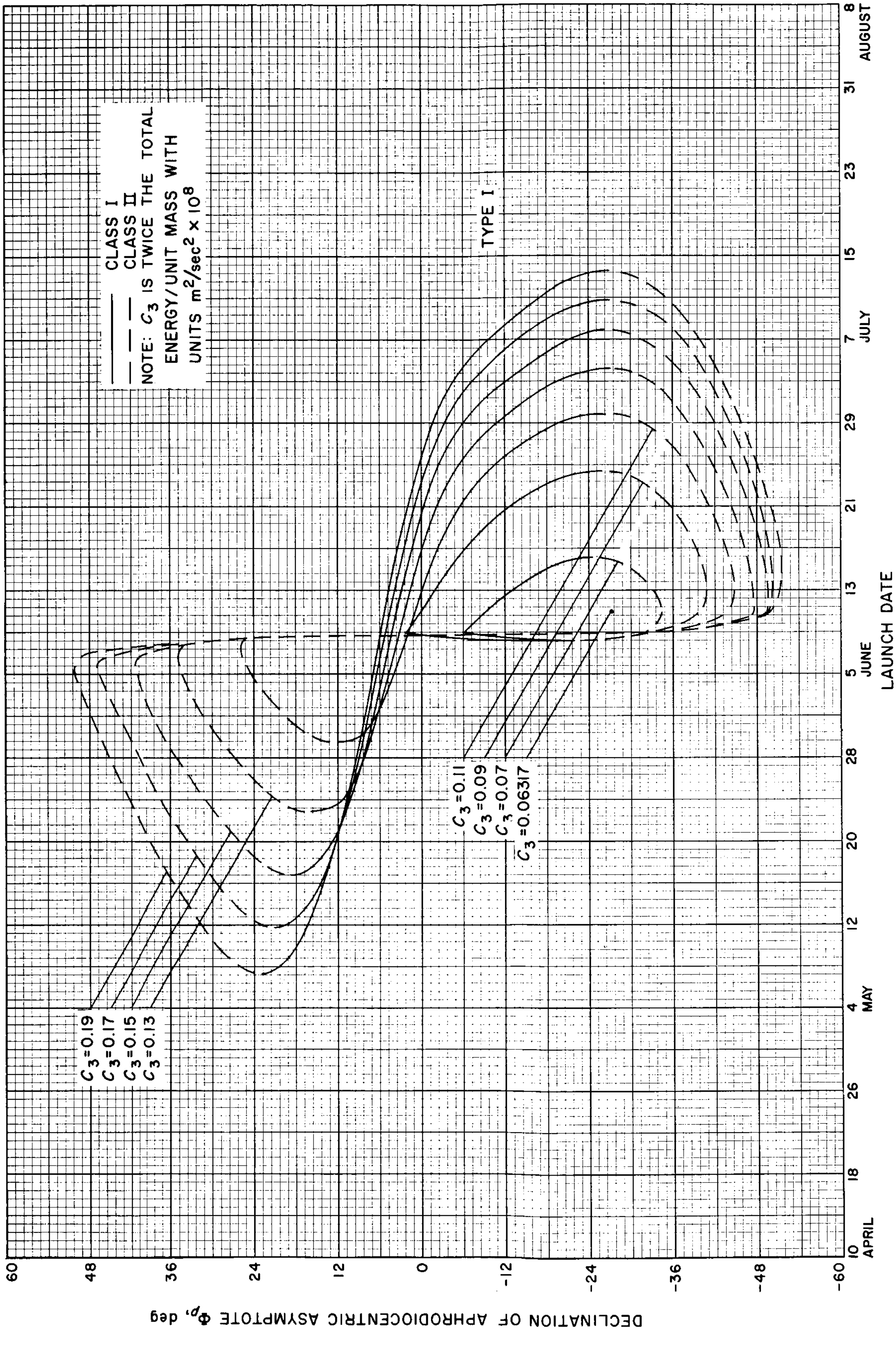

Fig. 8–27. Venus 1967: Declination of aphrodiocentric asymptote vs launch date, Type I

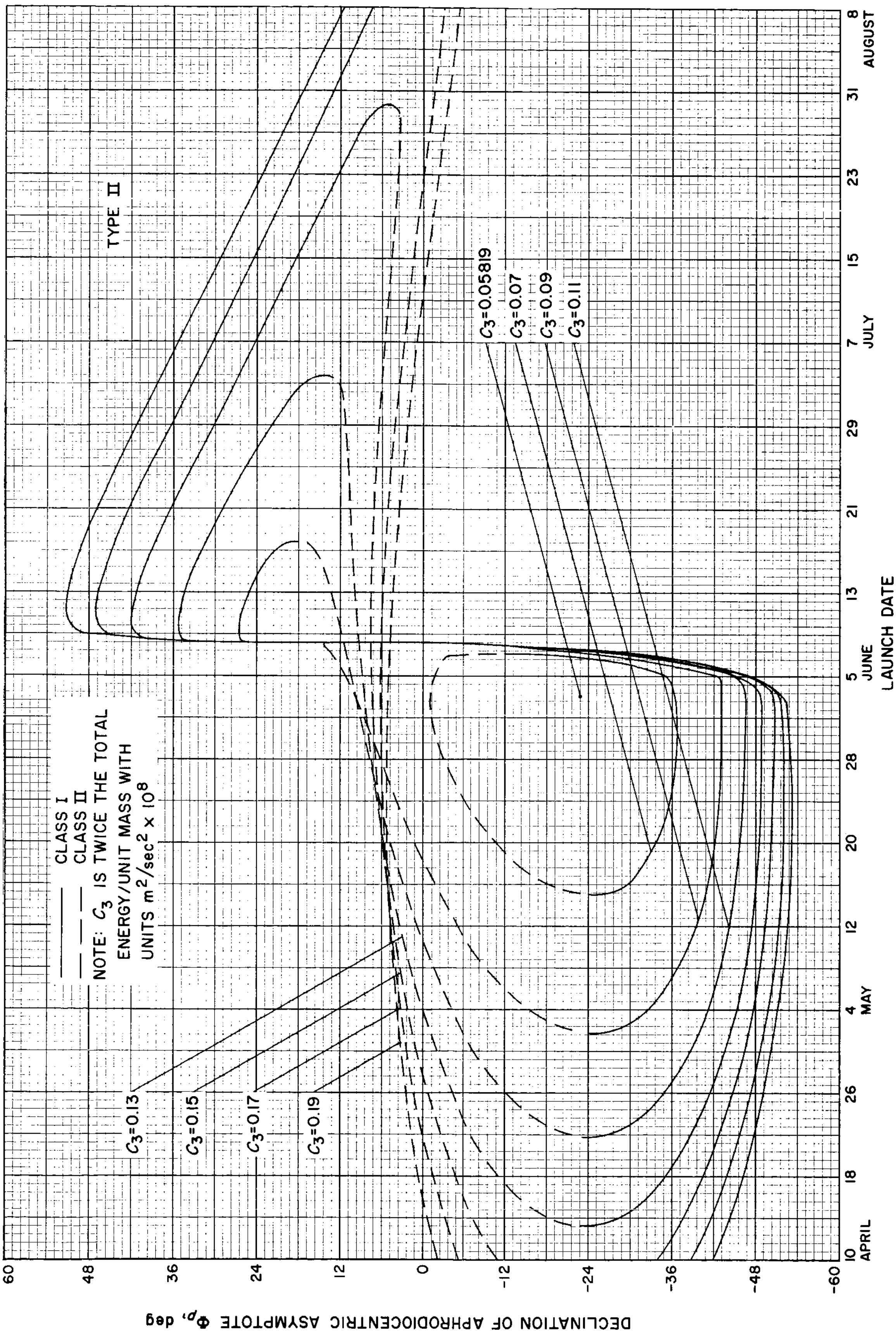

Fig. 8–28. Venus 1967: Declination of aphrodiocentric asymptote vs launch date, Type II

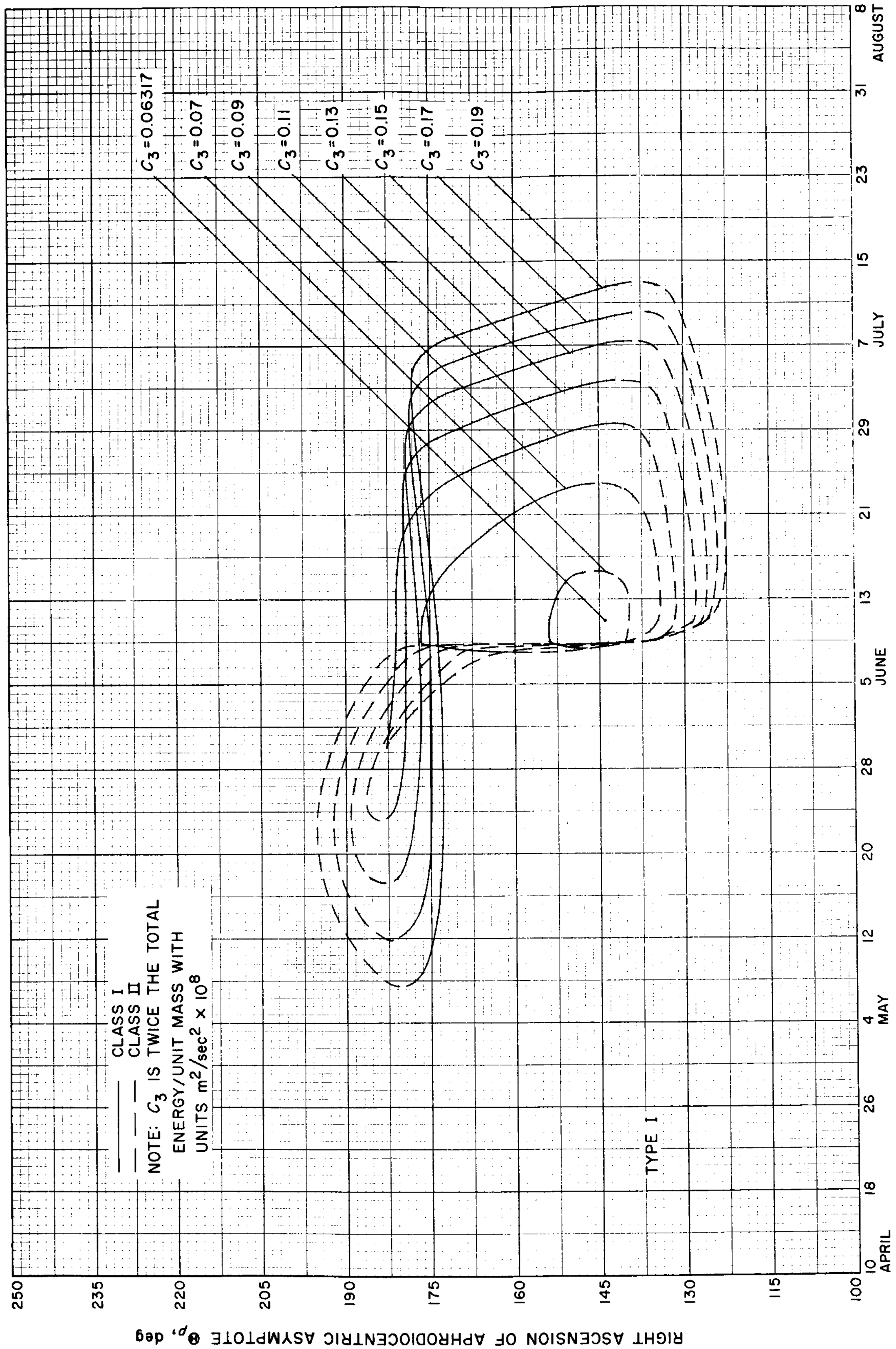

Fig. 8–29. Venus 1967: Right ascension of aphrodiocentric asymptote vs launch date, Type I

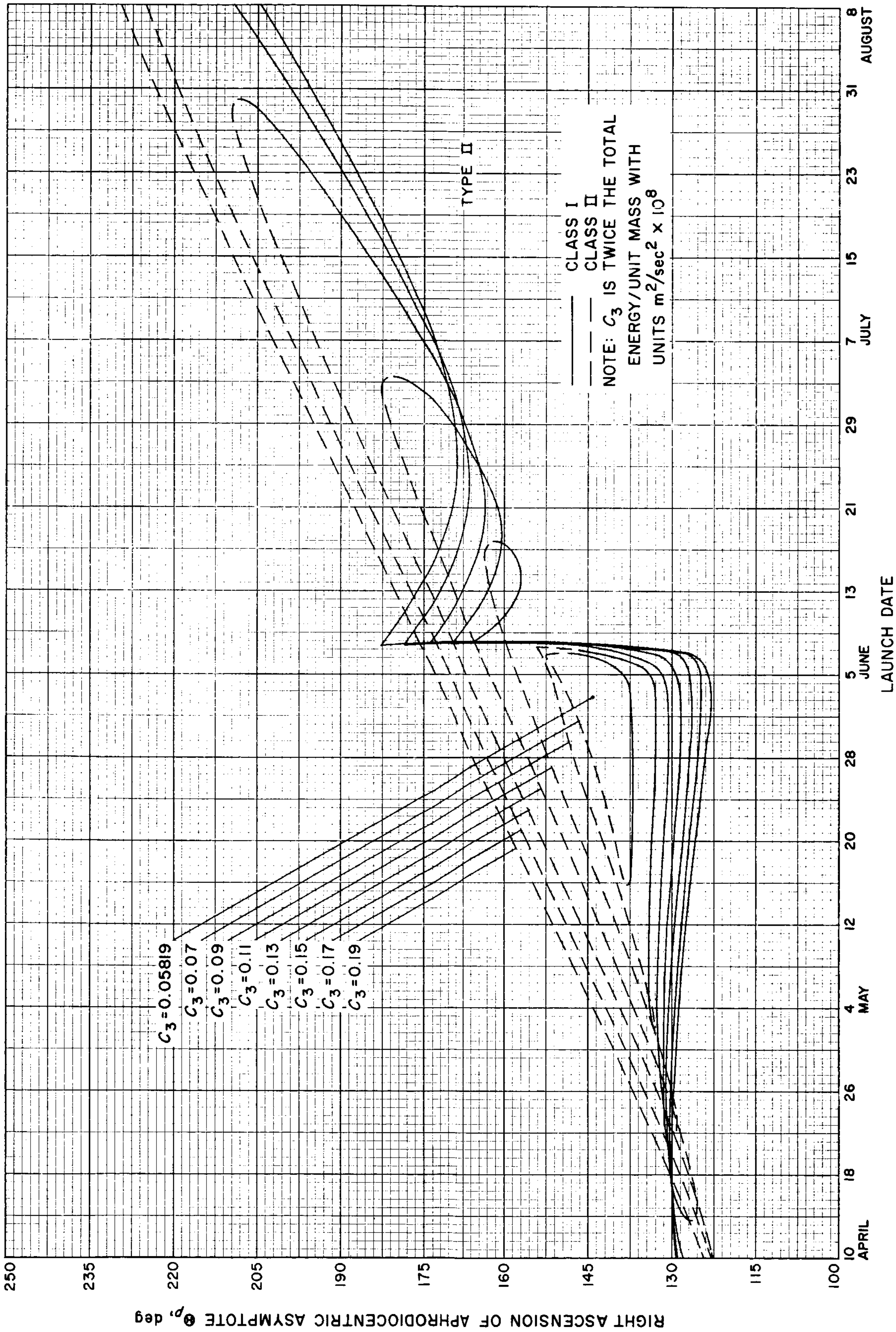

Fig. 8–30. Venus 1967: Right ascension of aphrodiocentric asymptote vs launch date, Type II

IX. VENUS 1968–1969: TRAJECTORY-PARAMETER GRAPHS

Figure

IX. VENUS 1968-1969: TRAJECTORY-PARAMETER GRAPHS (Cont'd)

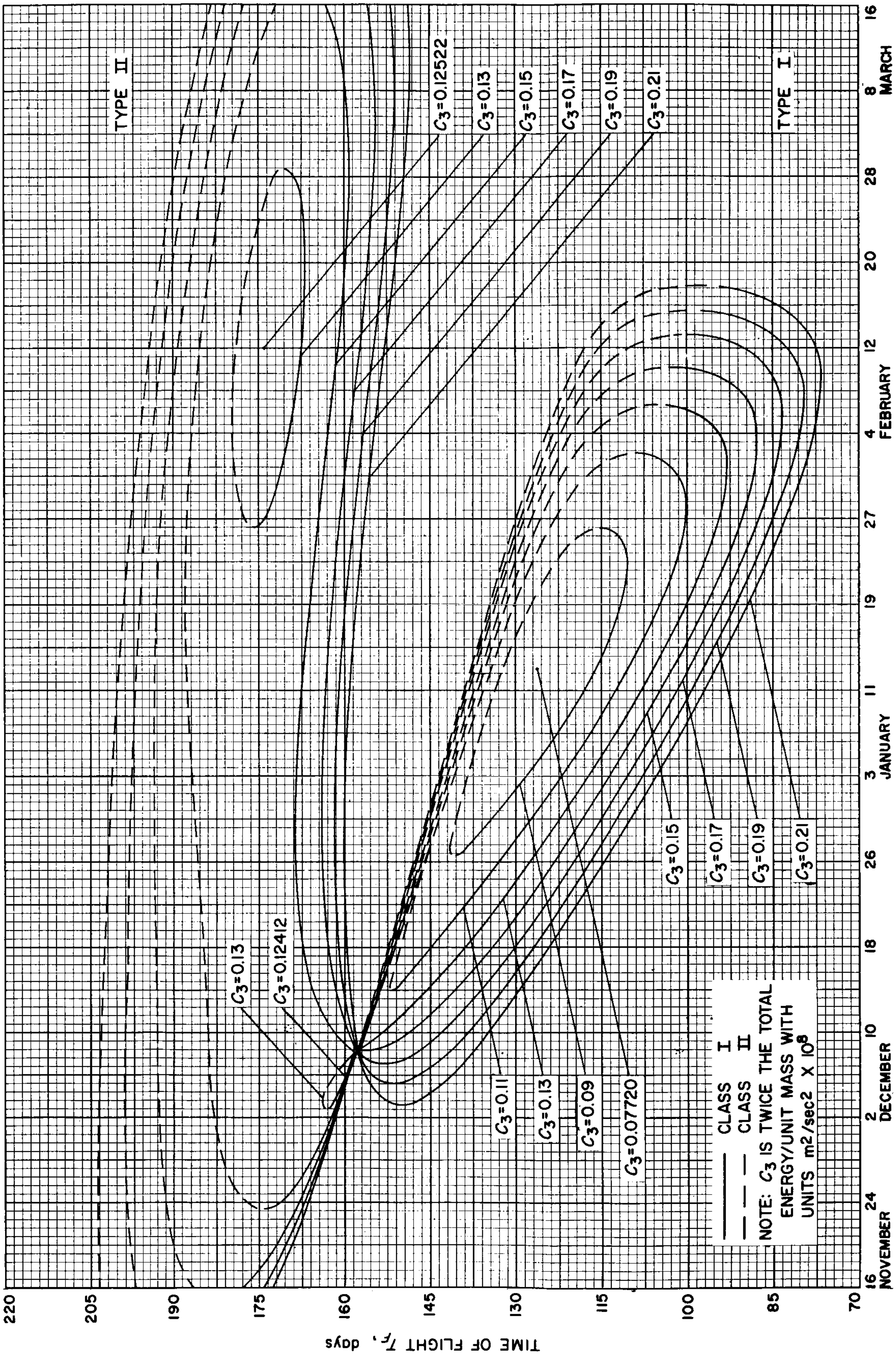

Fig. 9–1. Venus 1968–1969: Time of flight vs launch date

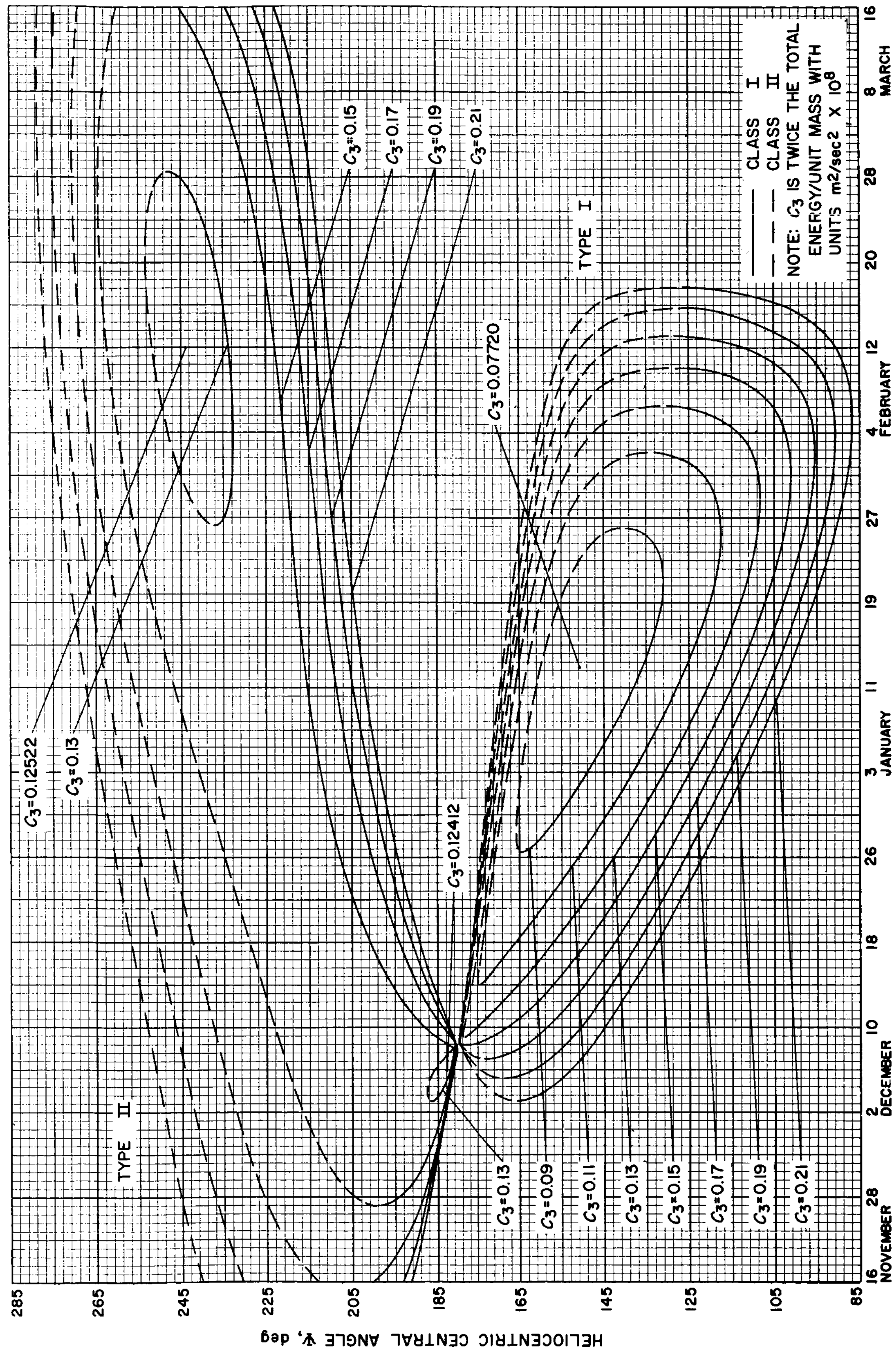

Fig. 9–2. Venus 1968–1969: Heliocentric central angle vs launch date

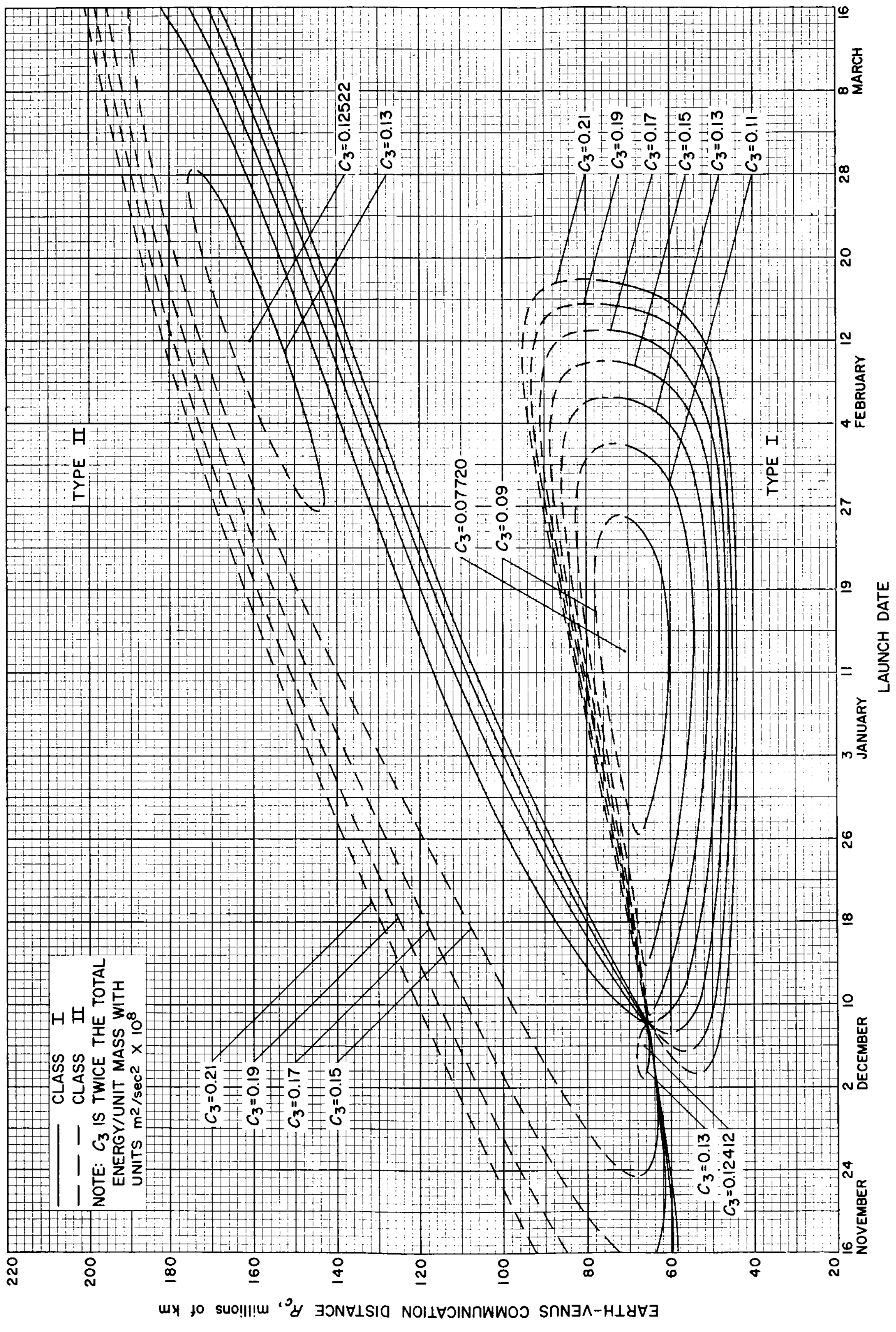

Fig. 9-3. Venus 1968–1969: Earth–Venus communication distance vs launch date

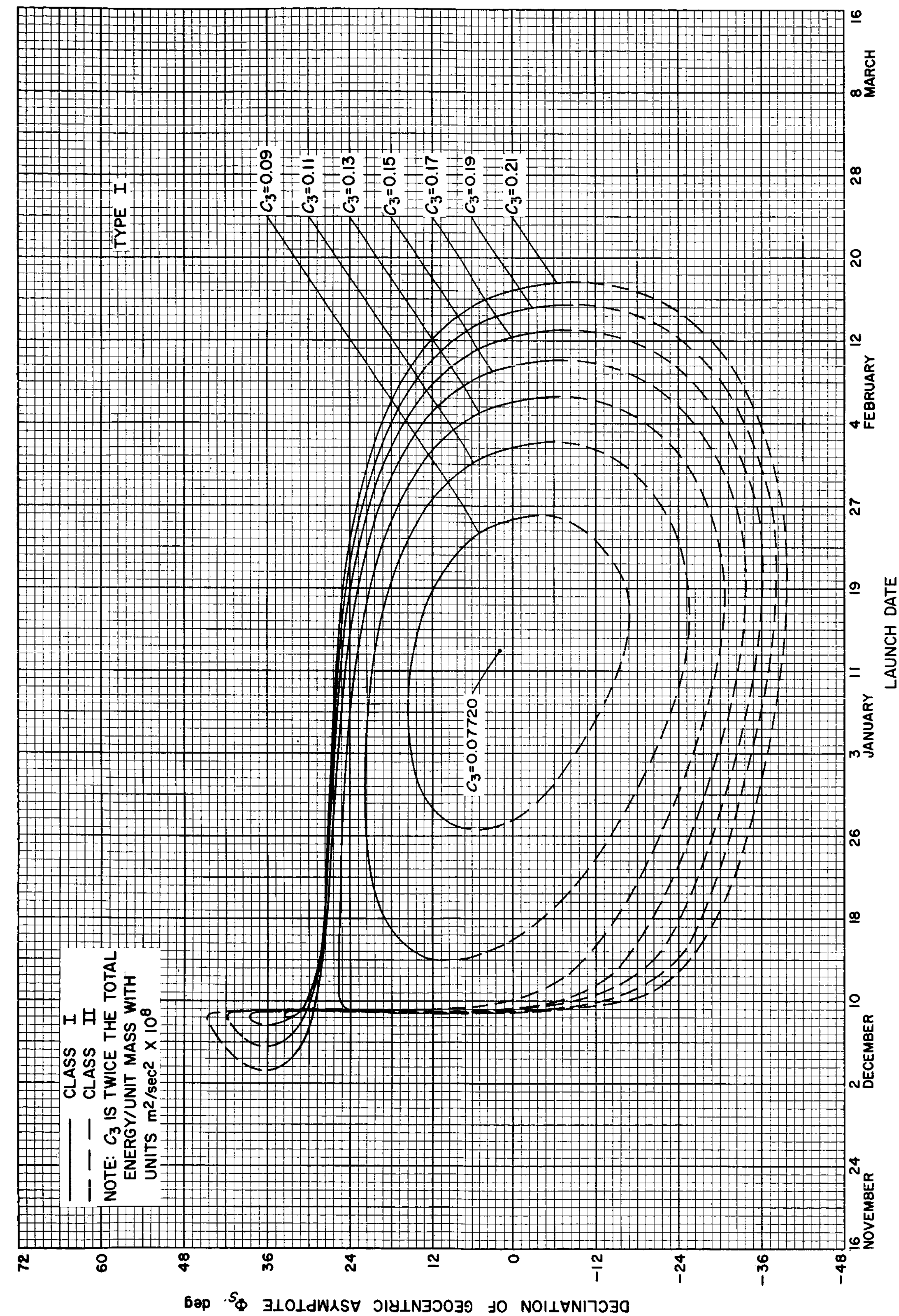

Fig. 9–4. Venus 1968–1969: Declination of geocentric asymptote vs launch date, Type I

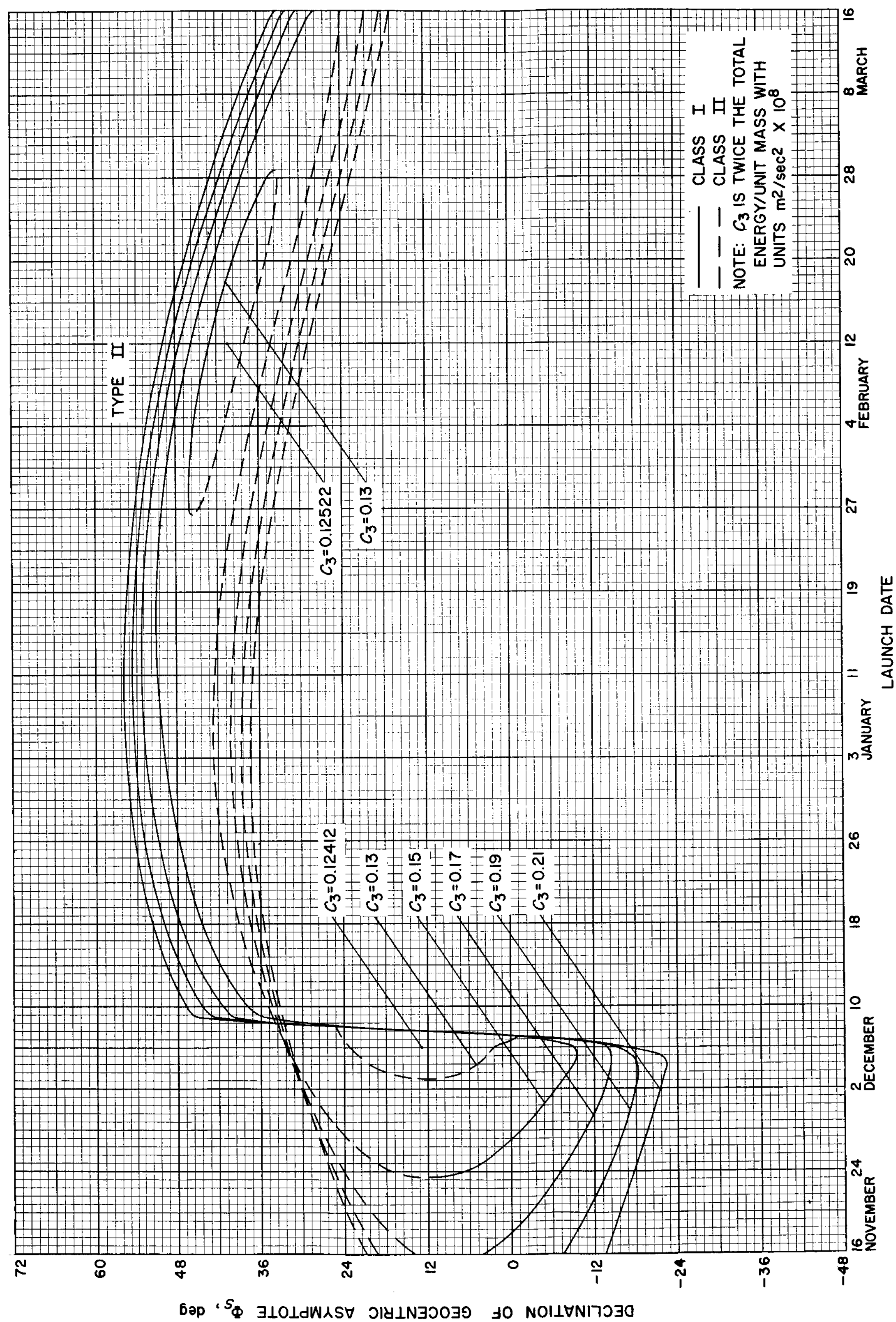

Fig. 9-5. Venus 1968–1969: Declination of geocentric asymptote vs launch date, Type II

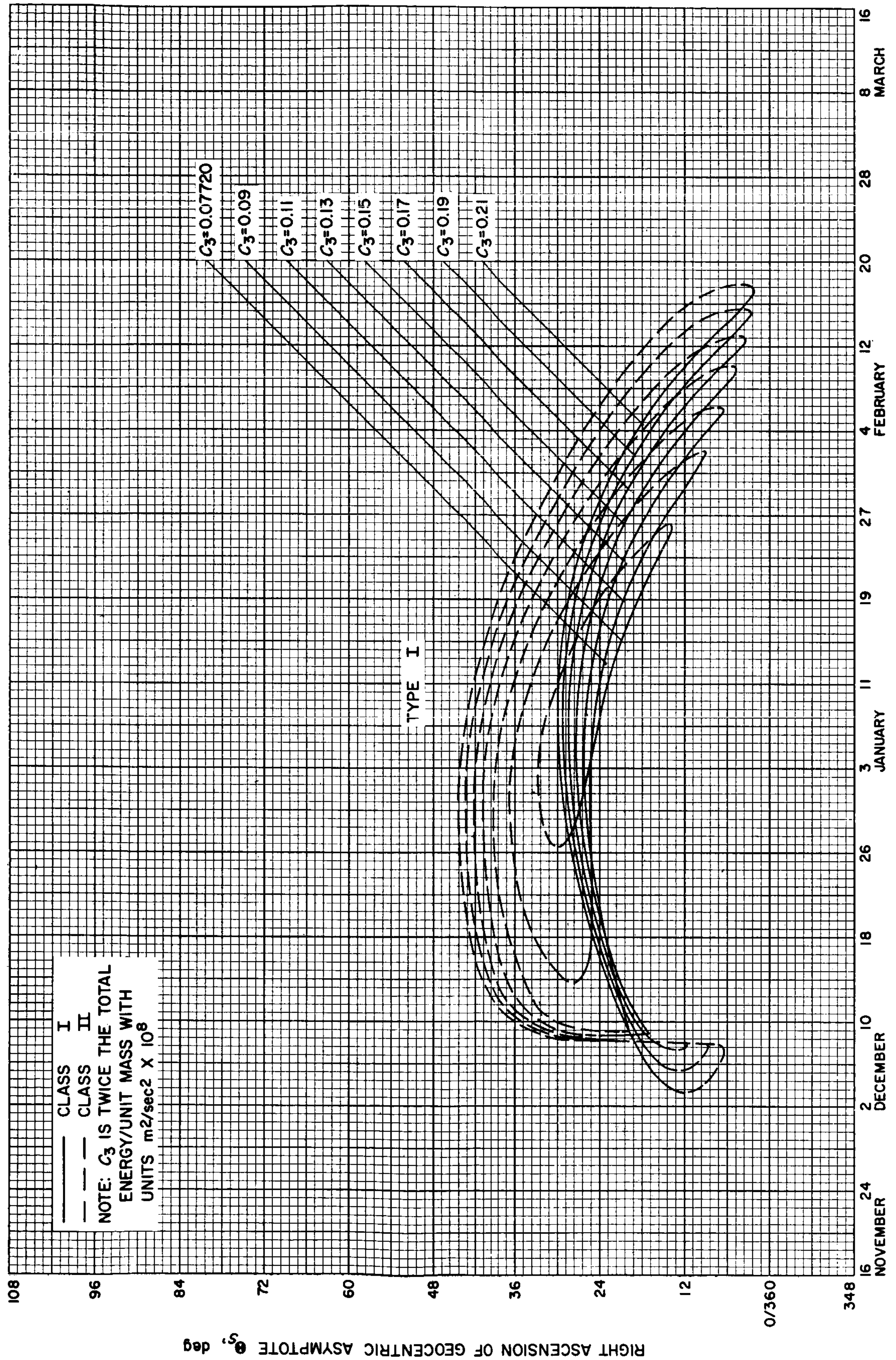

Fig. 9–6. Venus 1968–1969: Right ascension of geocentric asymptote vs launch date, Type I

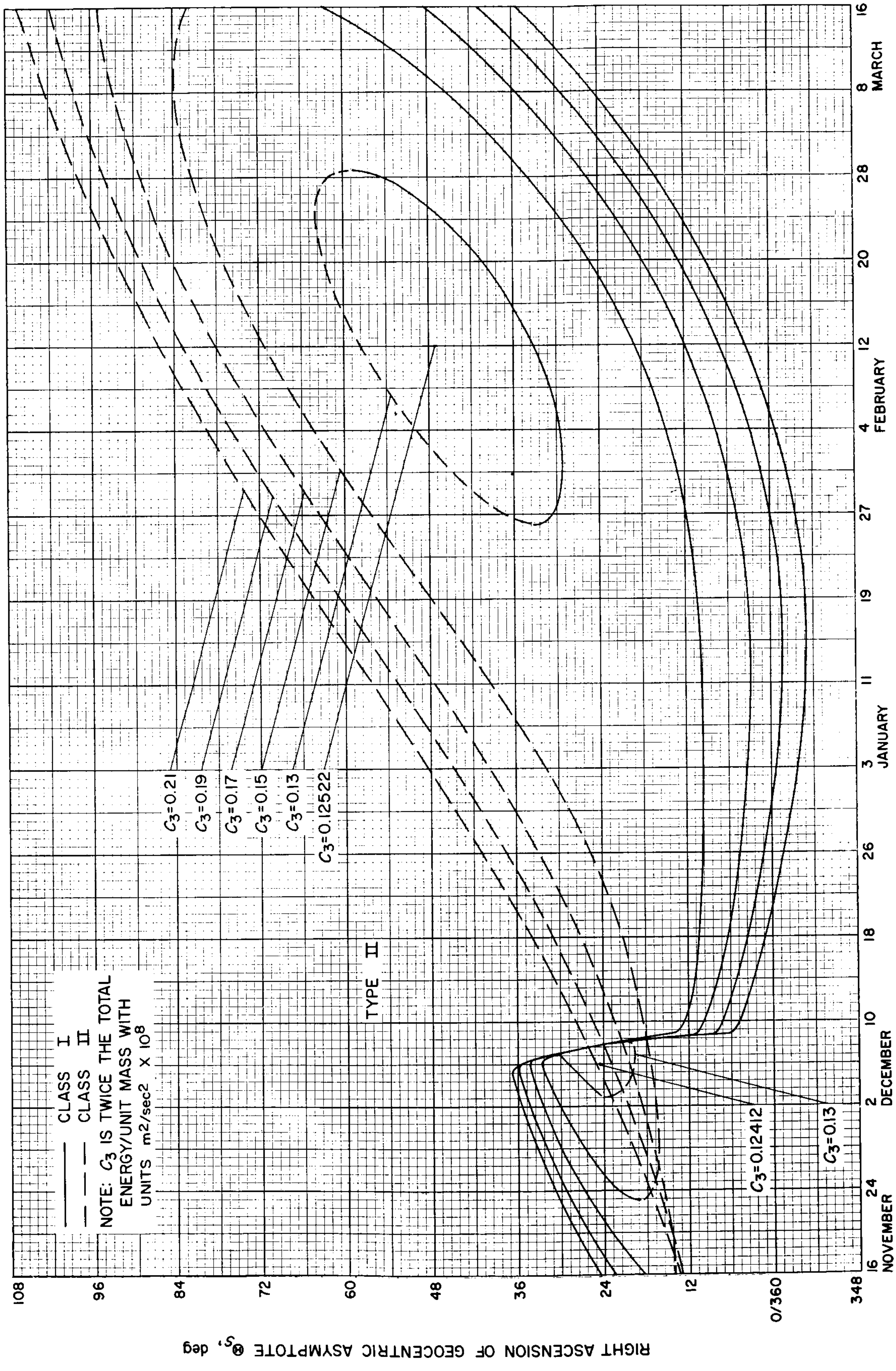

Fig. 9–7. Venus 1968–1969: Right ascension of geocentric asymptote vs launch date, Type II

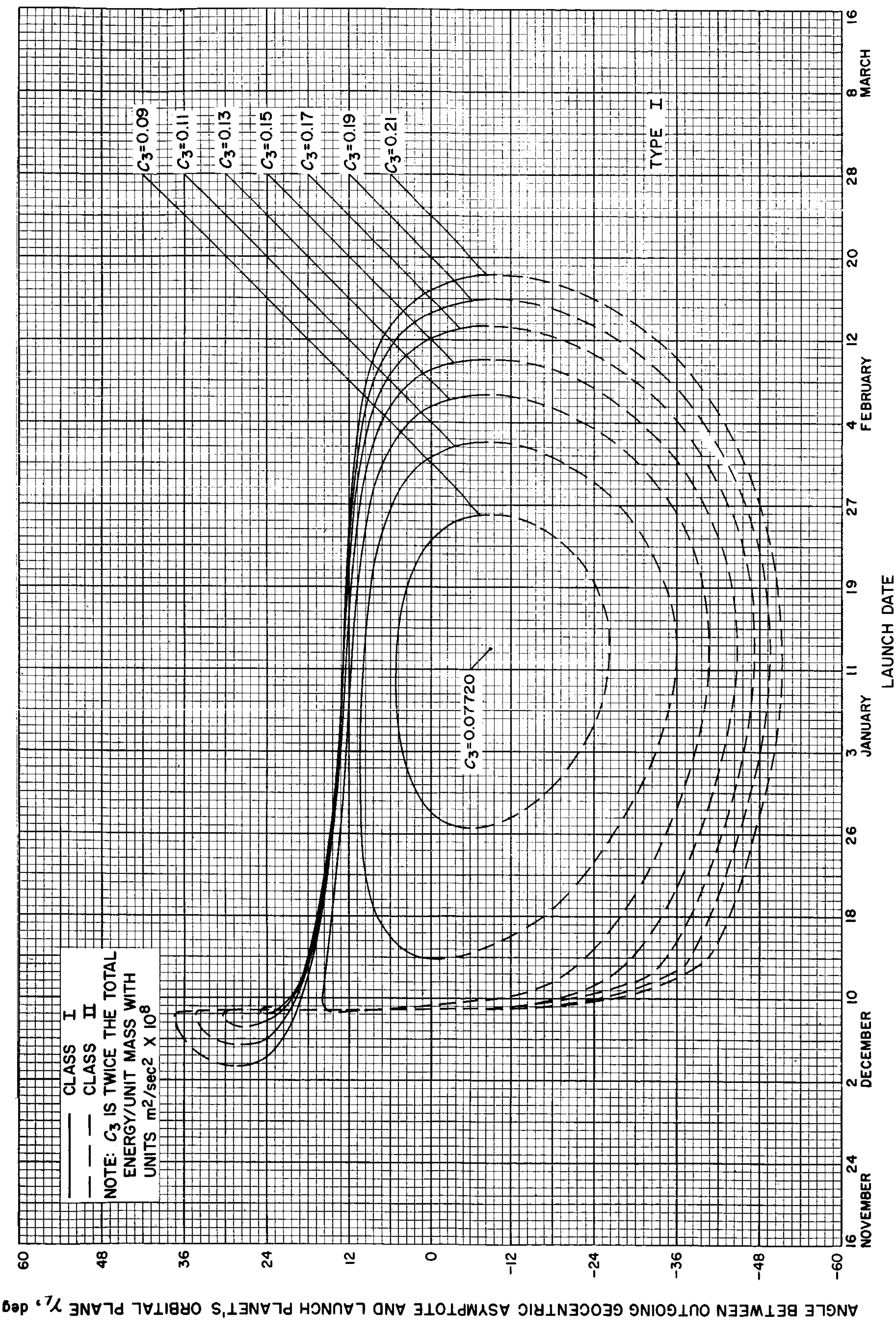

Fig. 9–8. Venus 1968–1969: Angle between outgoing geocentric asymptote and launch planet's orbital plane vs launch date, Type I

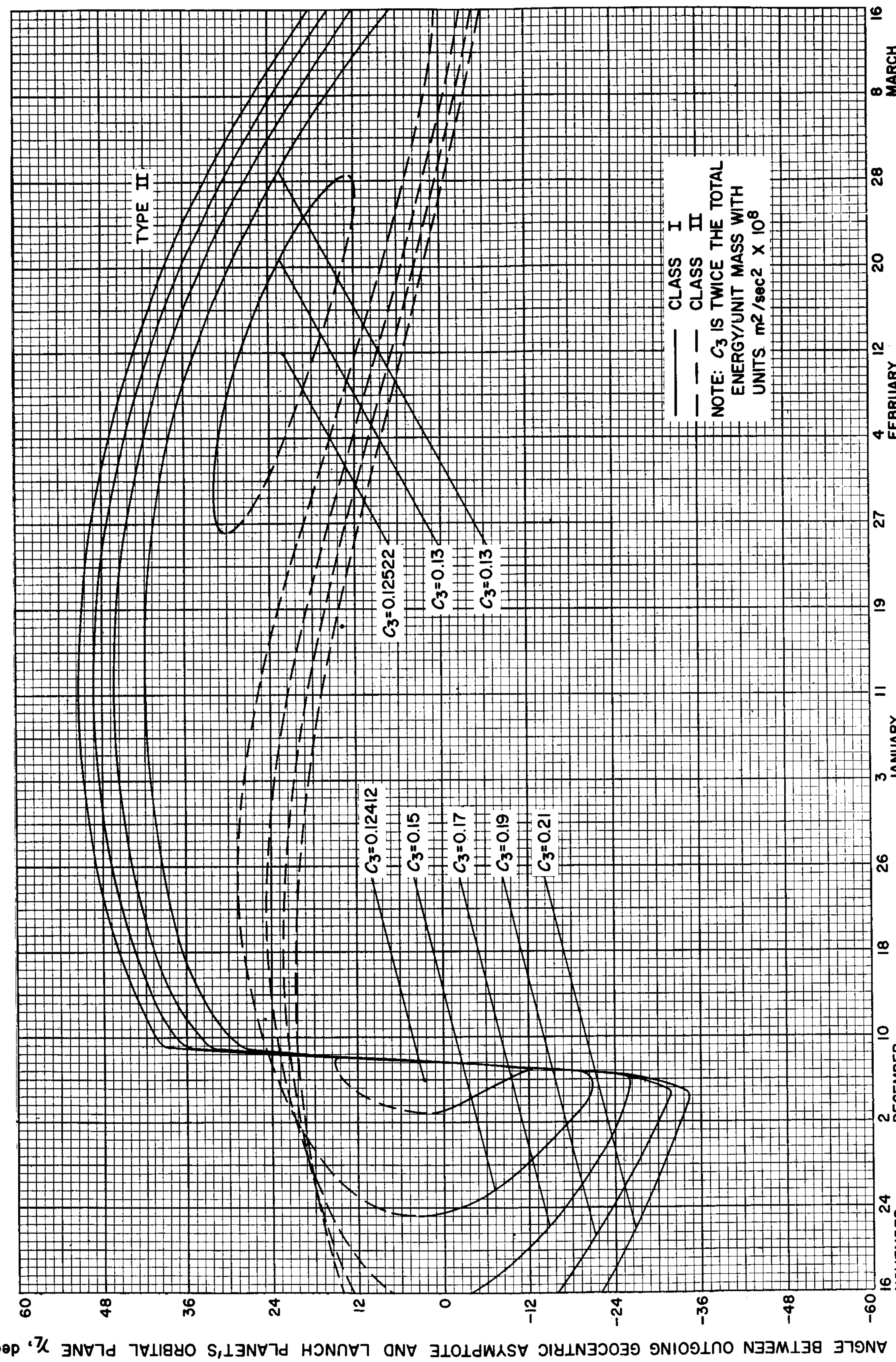

Fig. 9–9. Venus 1968–1969: Angle between outgoing geocentric asymptote and launch planet's orbital plane vs launch date, Type II

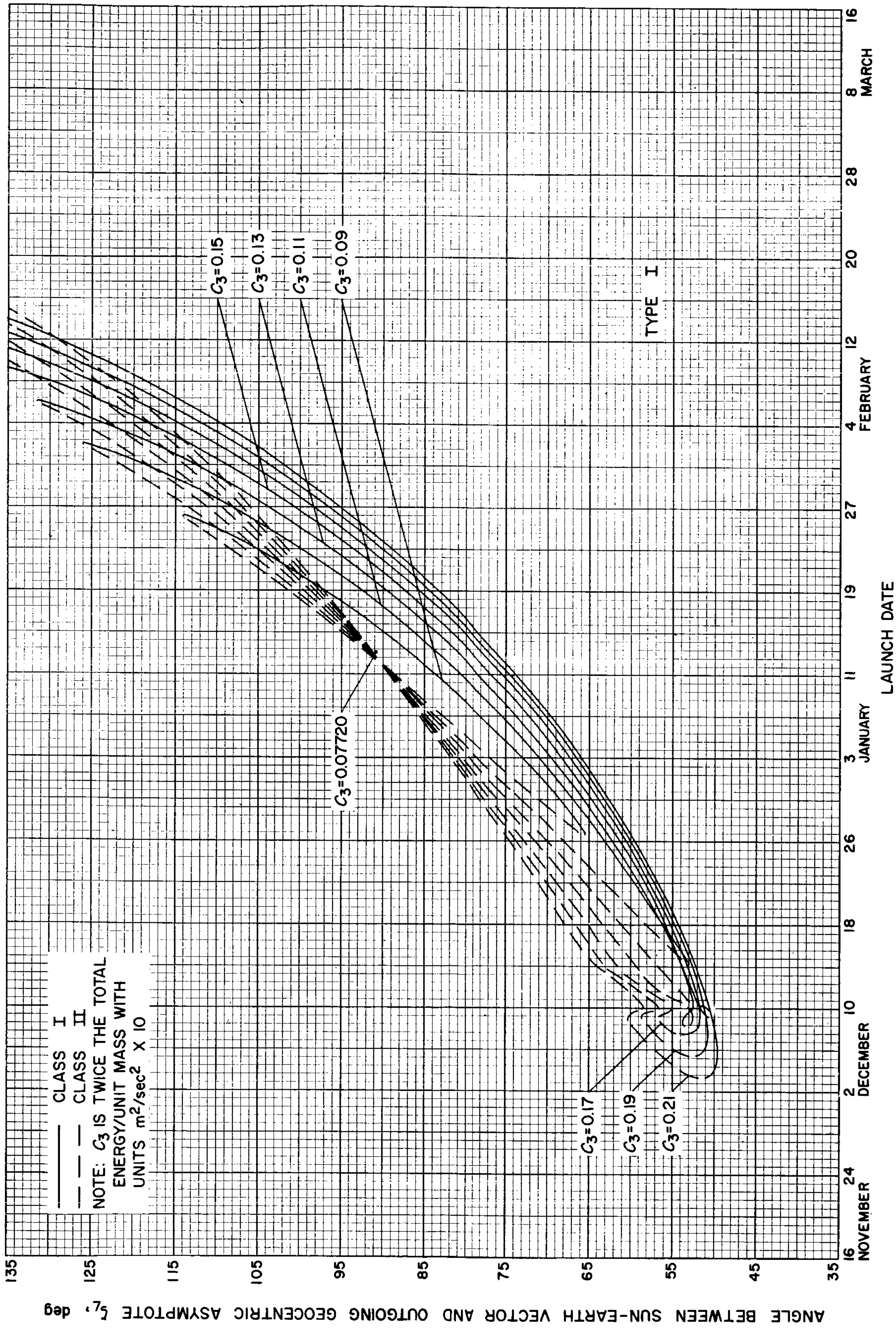

Fig. 9–10. Venus 1968–1969: Angle between Sun–Earth vector and outgoing geocentric asymptote vs launch date, Type I

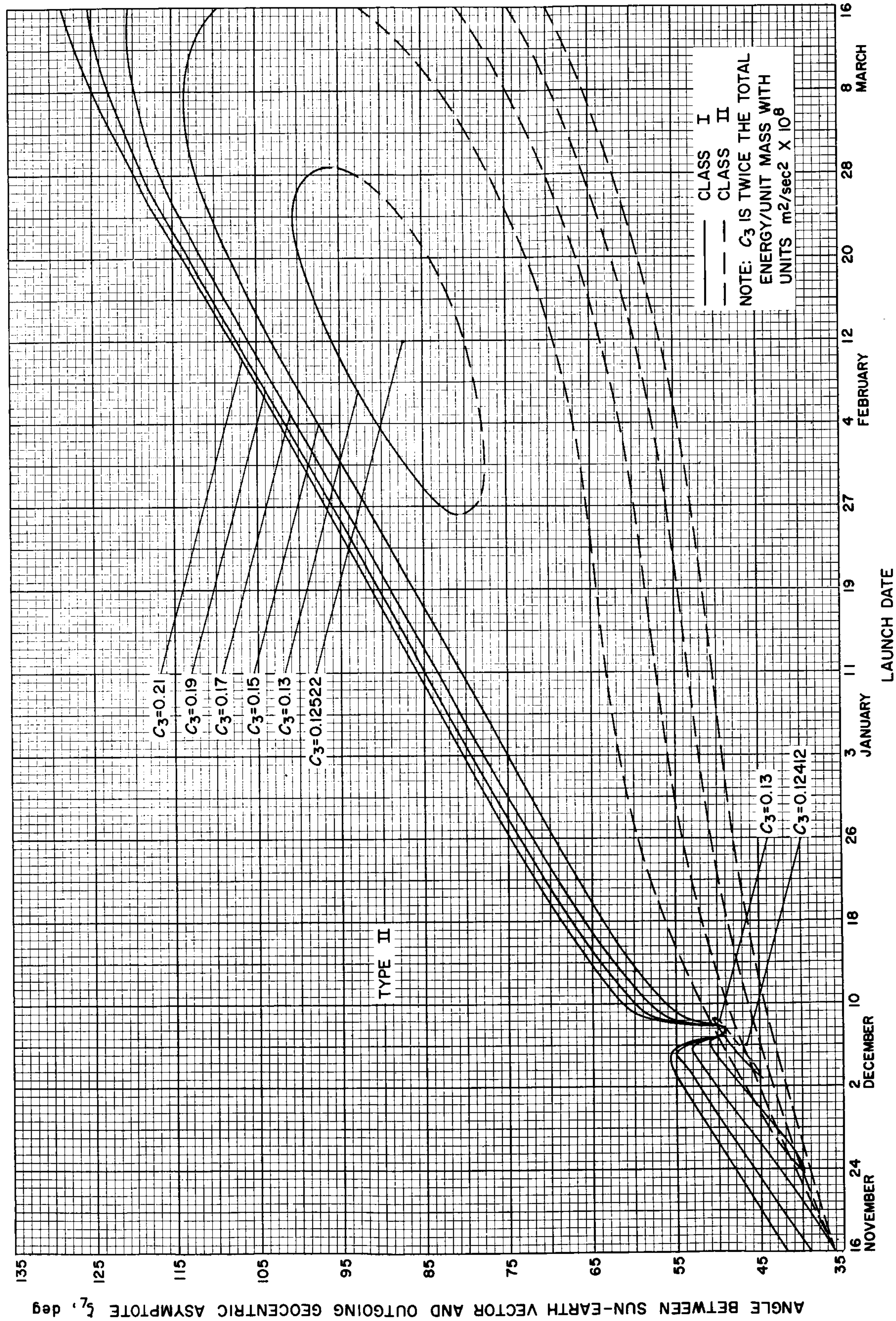

Fig. 9–11. Venus 1968–1969: Angle between Sun–Earth vector and outgoing geocentric asymptote vs launch date, Type II

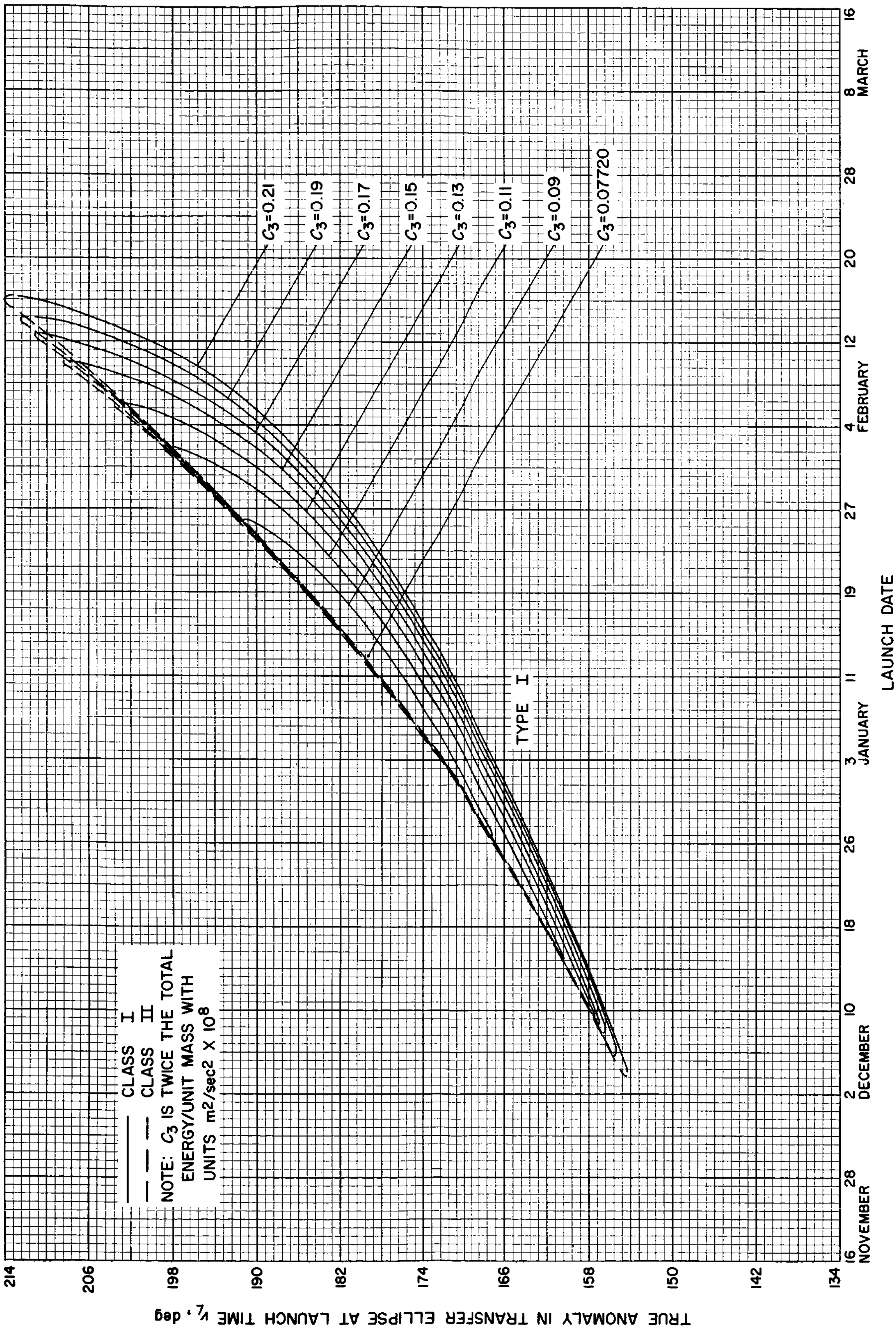

Fig. 9-12. Venus 1968-1969: True anomaly in transfer ellipse at launch time vs launch date, Type I

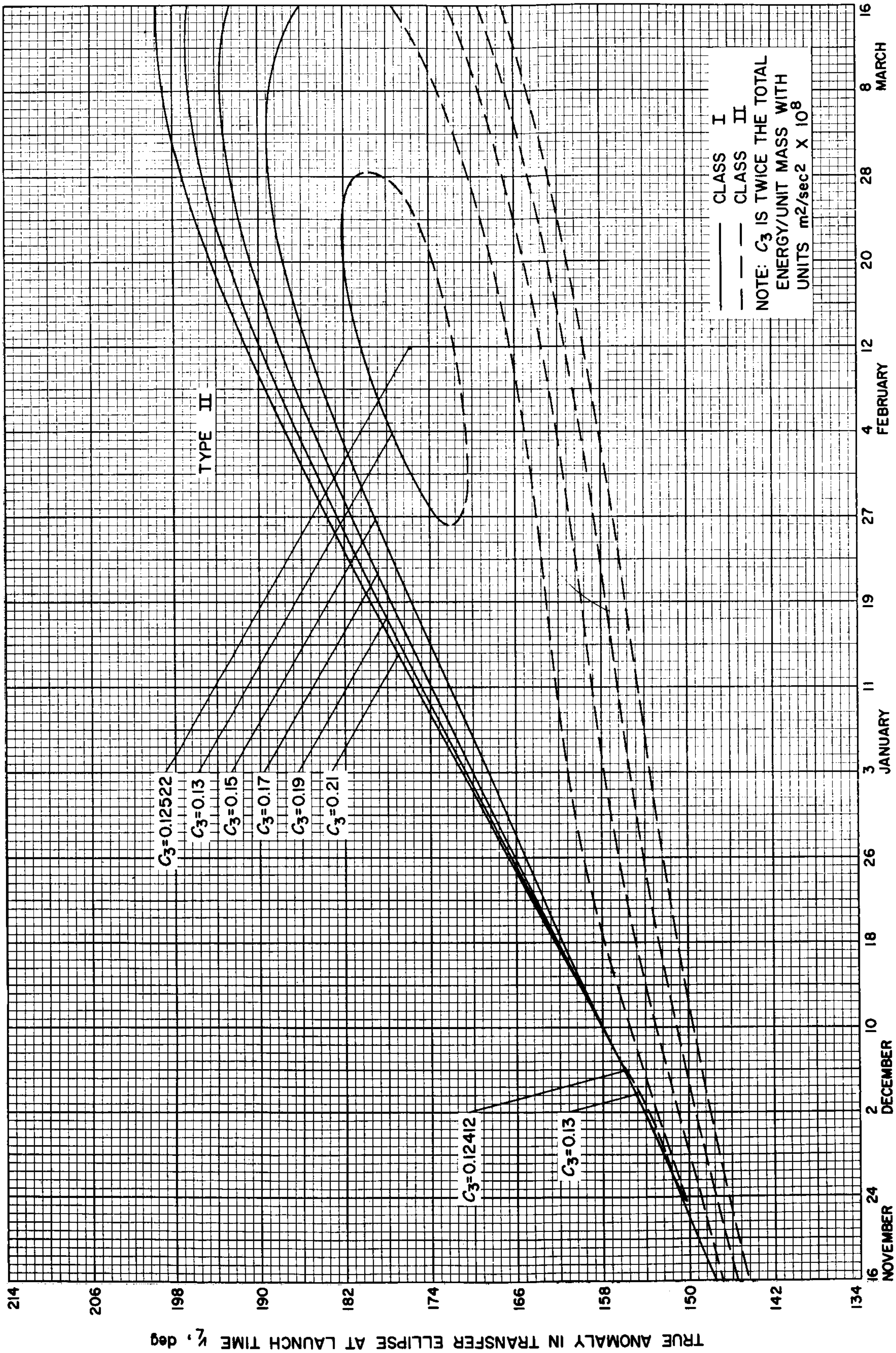

Fig. 9–13. Venus 1968–1969: True anomaly in transfer ellipse at launch time vs launch date, Type II

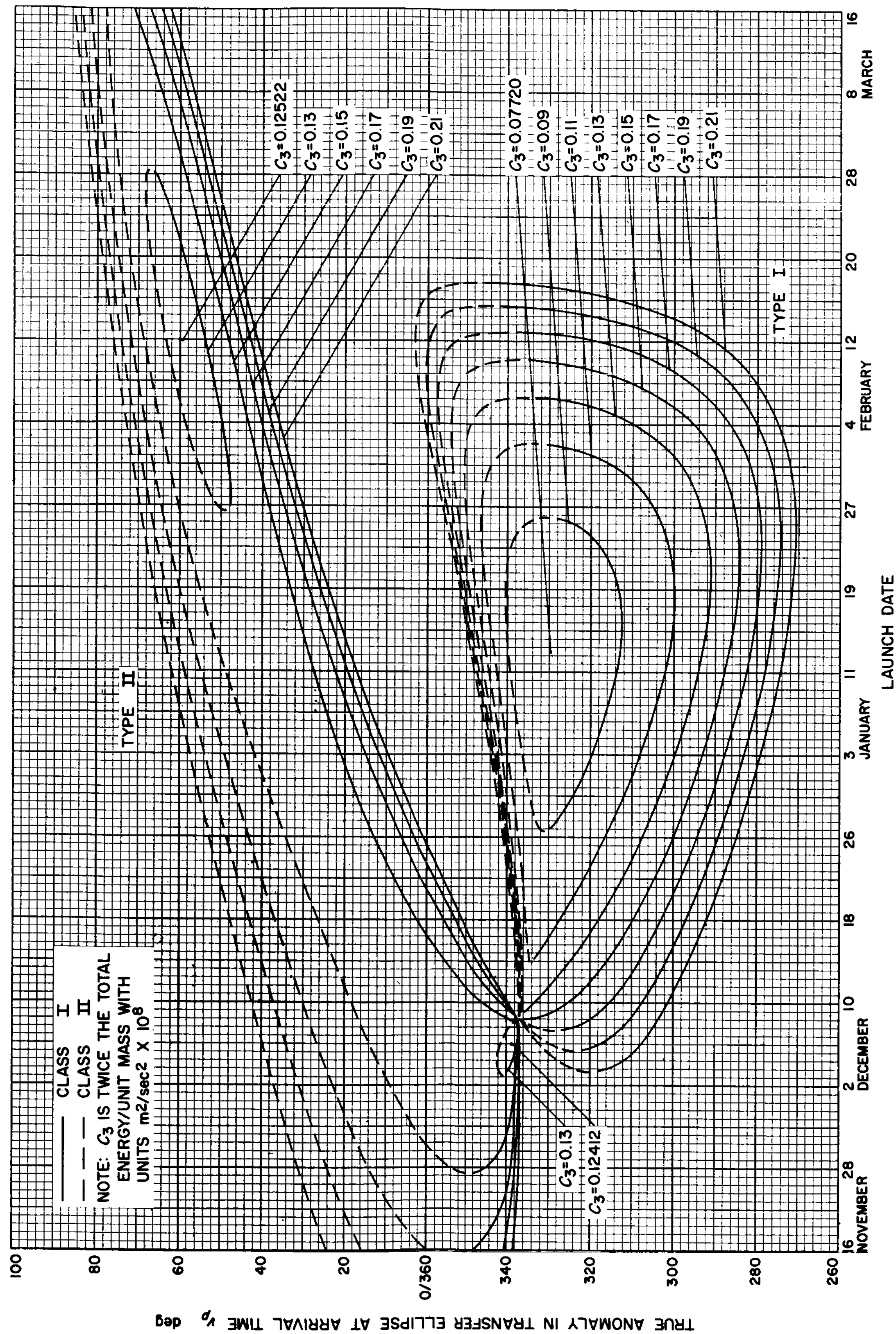

Fig. 9-14. Venus 1968–1969: True anomaly in transfer ellipse at arrival time vs launch date

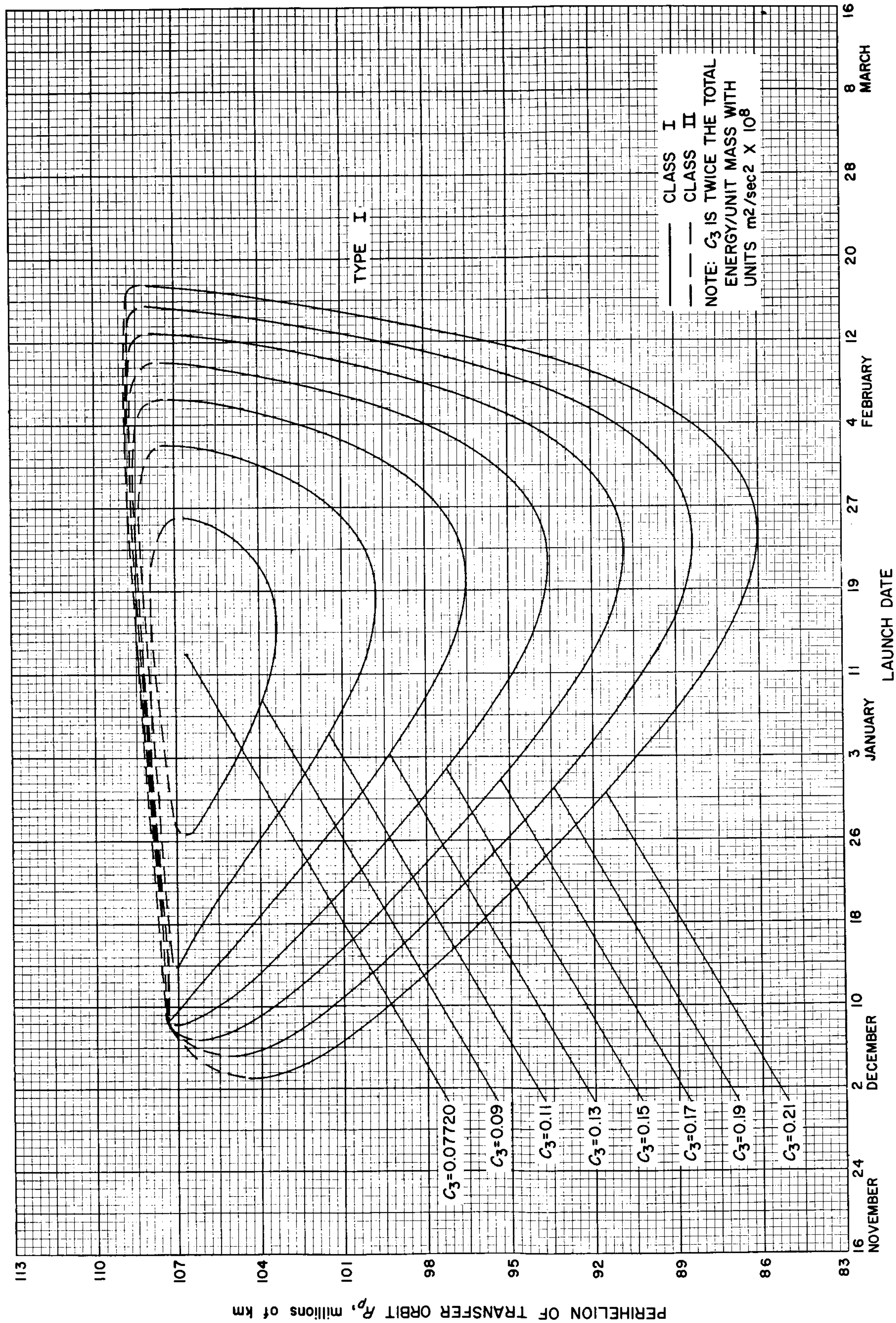

Fig. 9–15. Venus 1968–1969: Perihelion of transfer orbit vs launch date, Type I

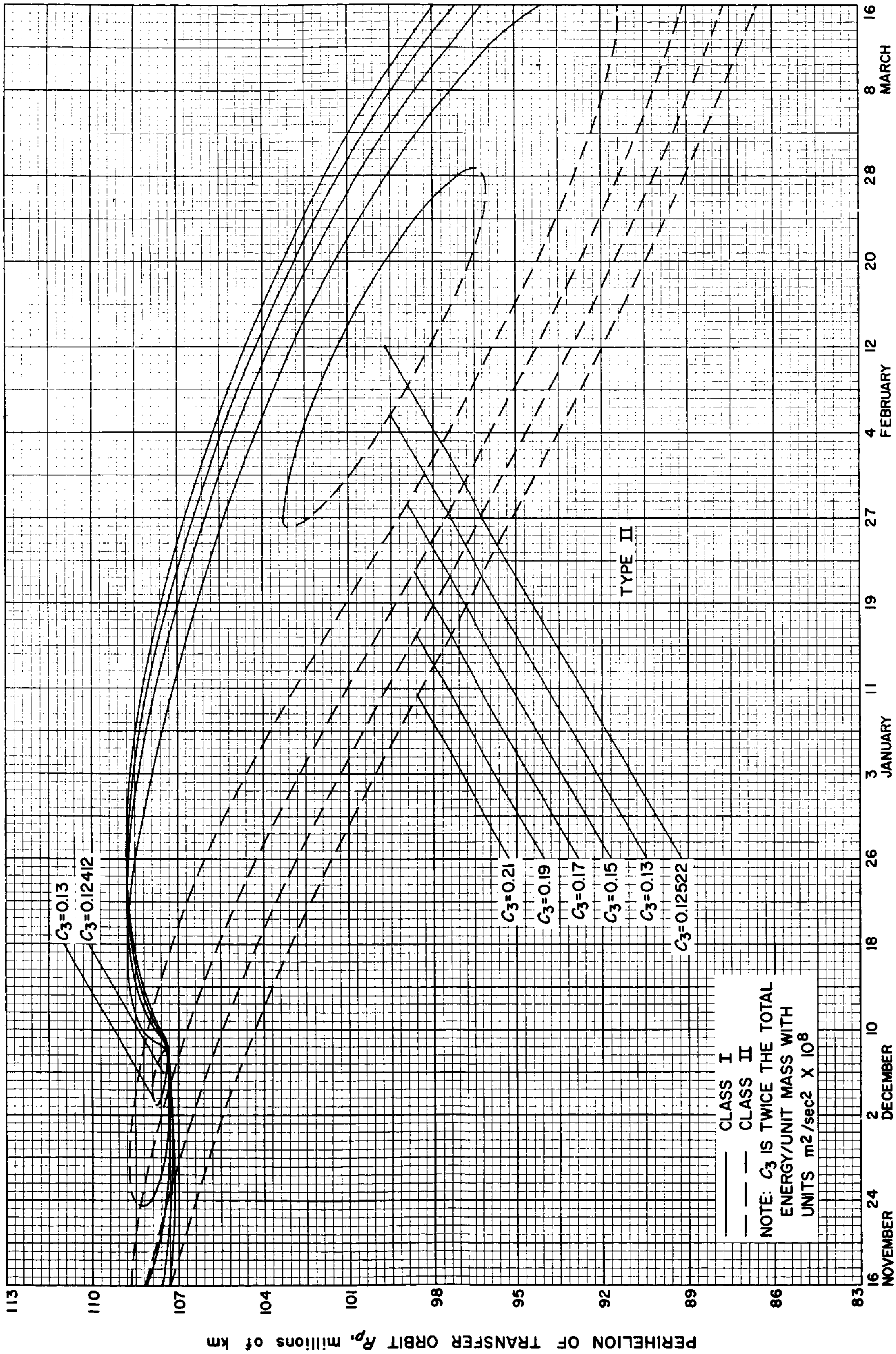

Fig. 9-16. Venus 1968–1969: Perihelion of transfer orbit vs launch date, Type II

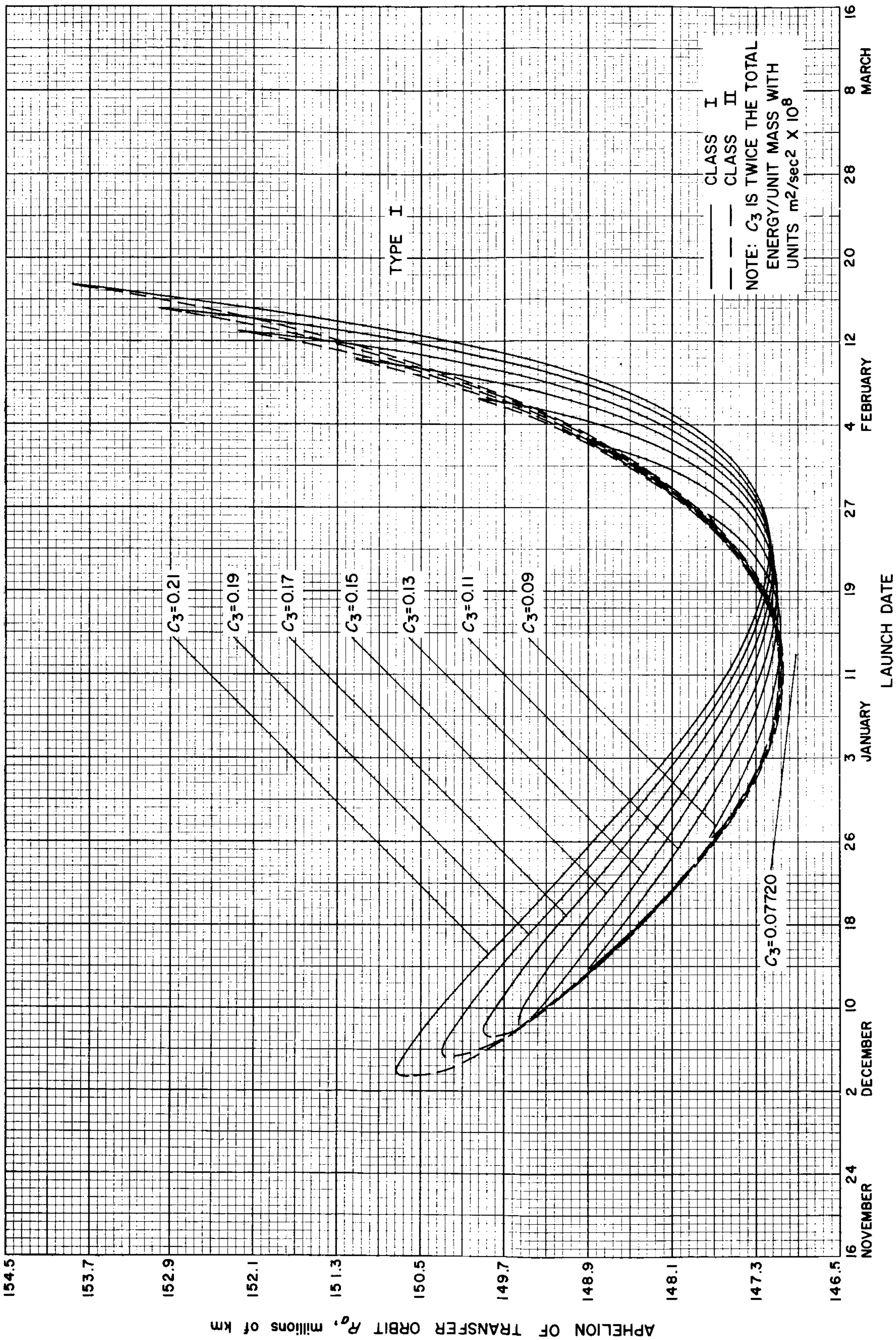

Fig. 9–17. Venus 1968–1969: Aphelion of transfer orbit vs launch date, Type I

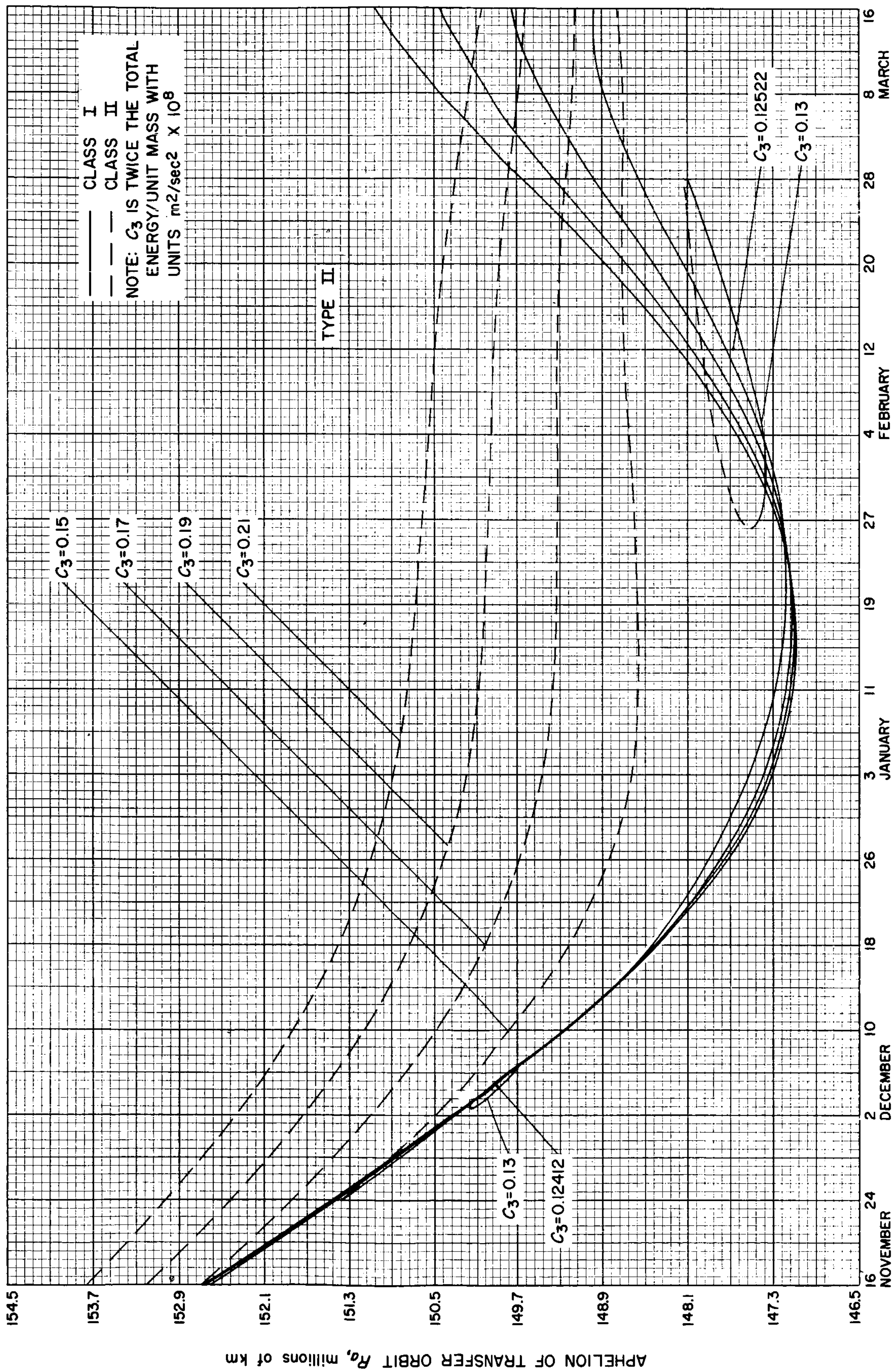

Fig. 9–18. Venus 1968–1969: Aphelion of transfer orbit vs launch date, Type II

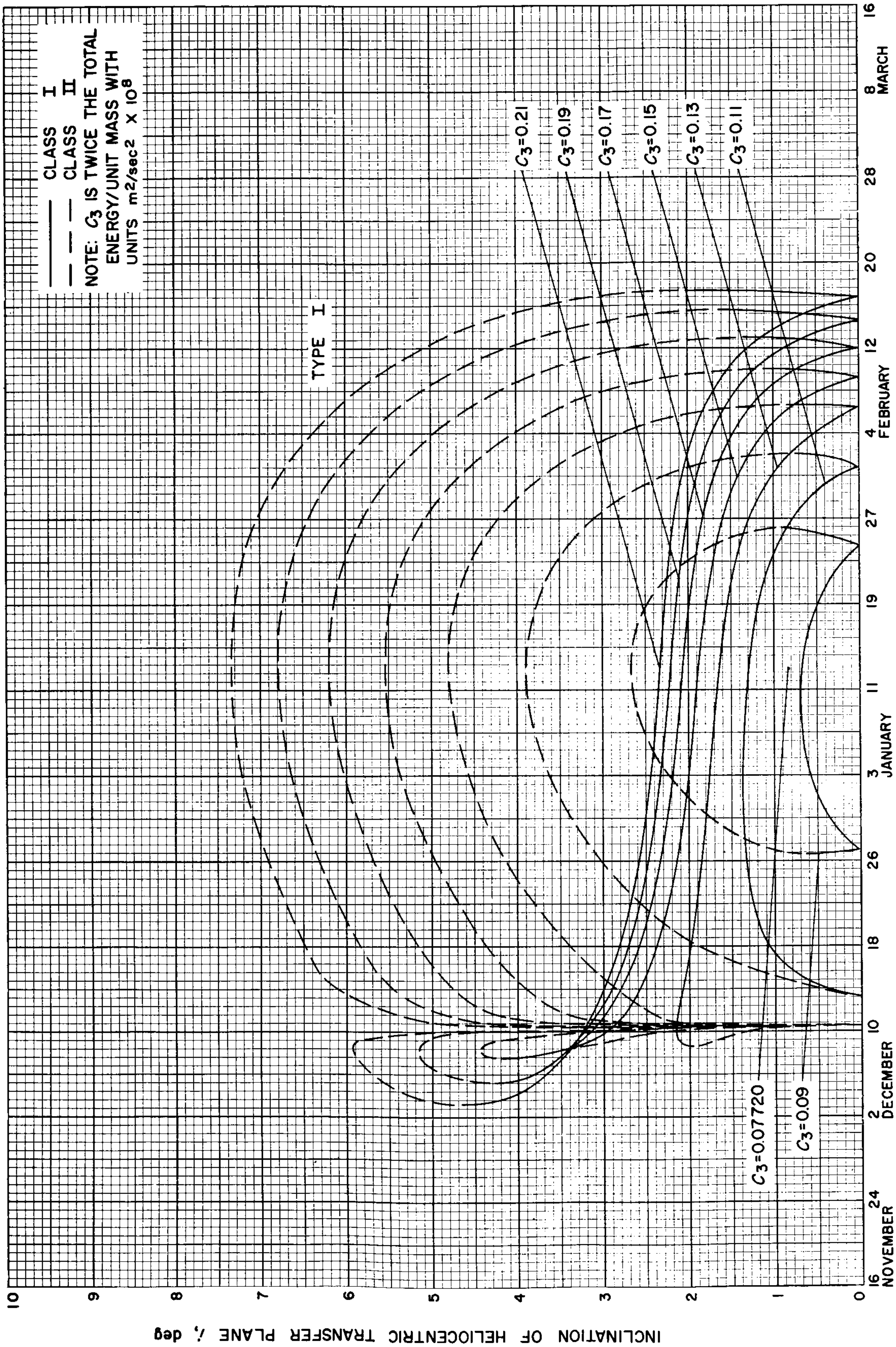

Fig. 9-19. Venus 1968–1969: Inclination of heliocentric-transfer plane vs launch date, Type I

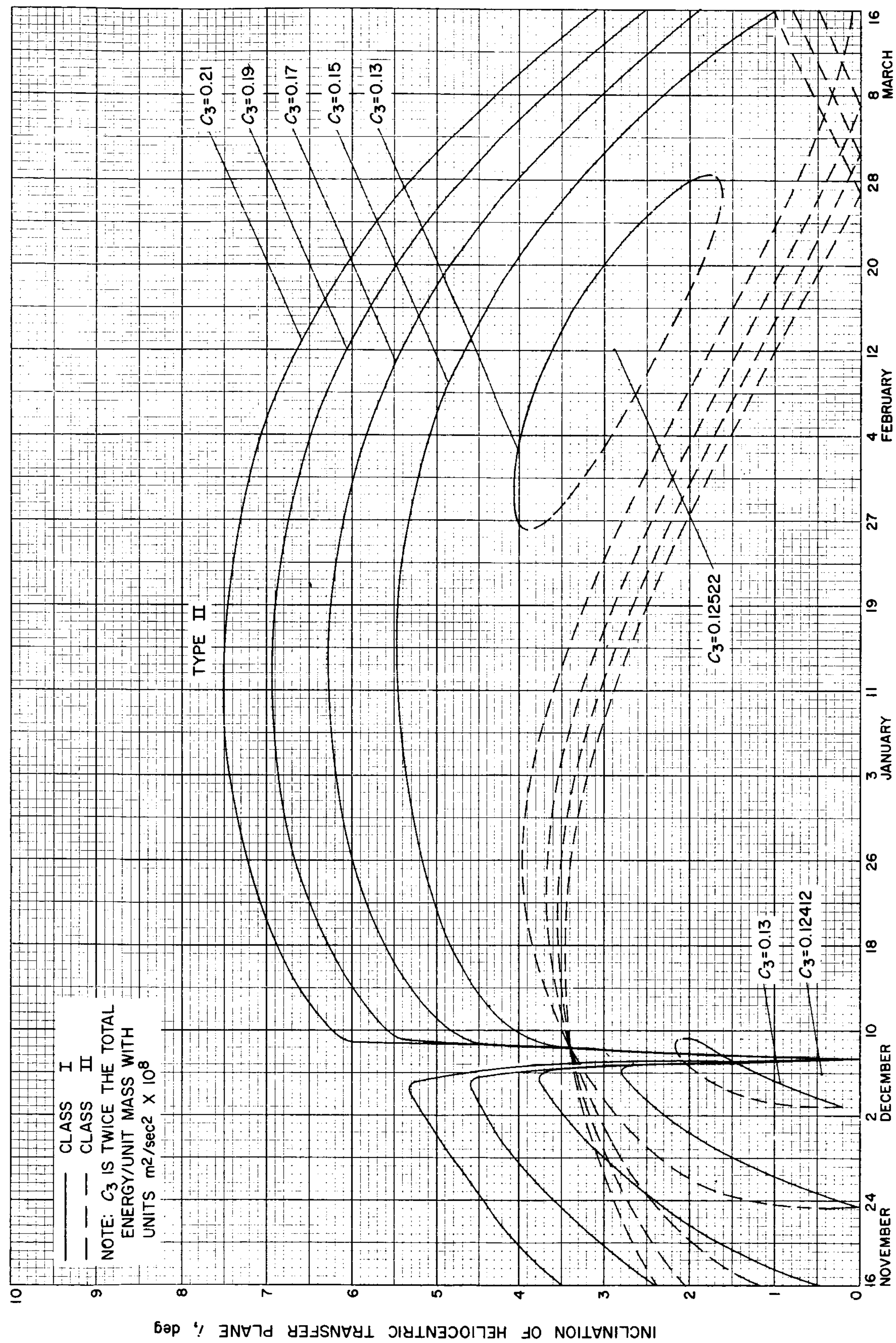

Fig. 9–20. Venus 1968–1969: Inclination of heliocentric-transfer plane vs launch date, Type II

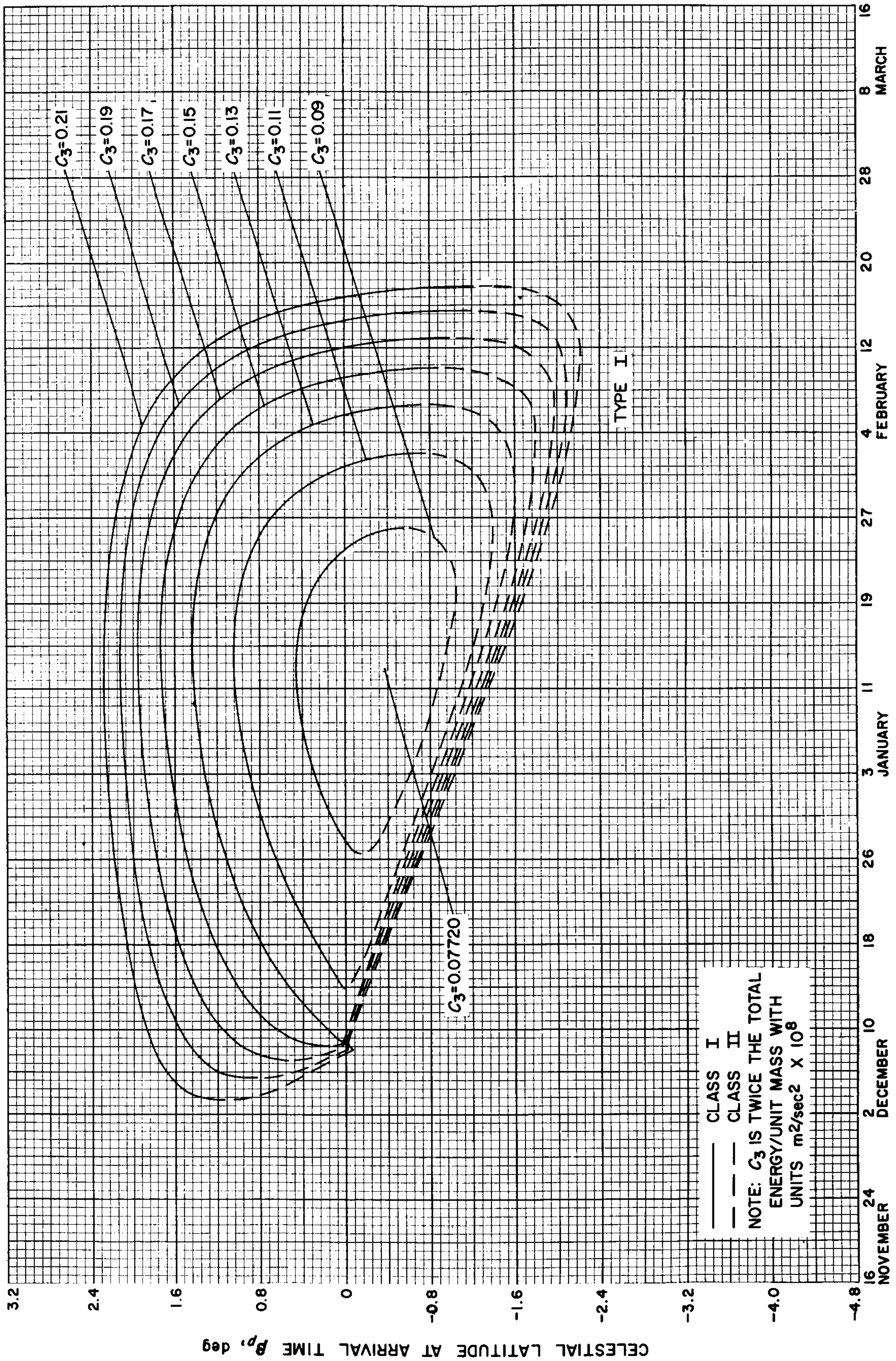

Fig. 9-21. Venus 1968–1969: Celestial latitude at arrival time vs launch date, Type I

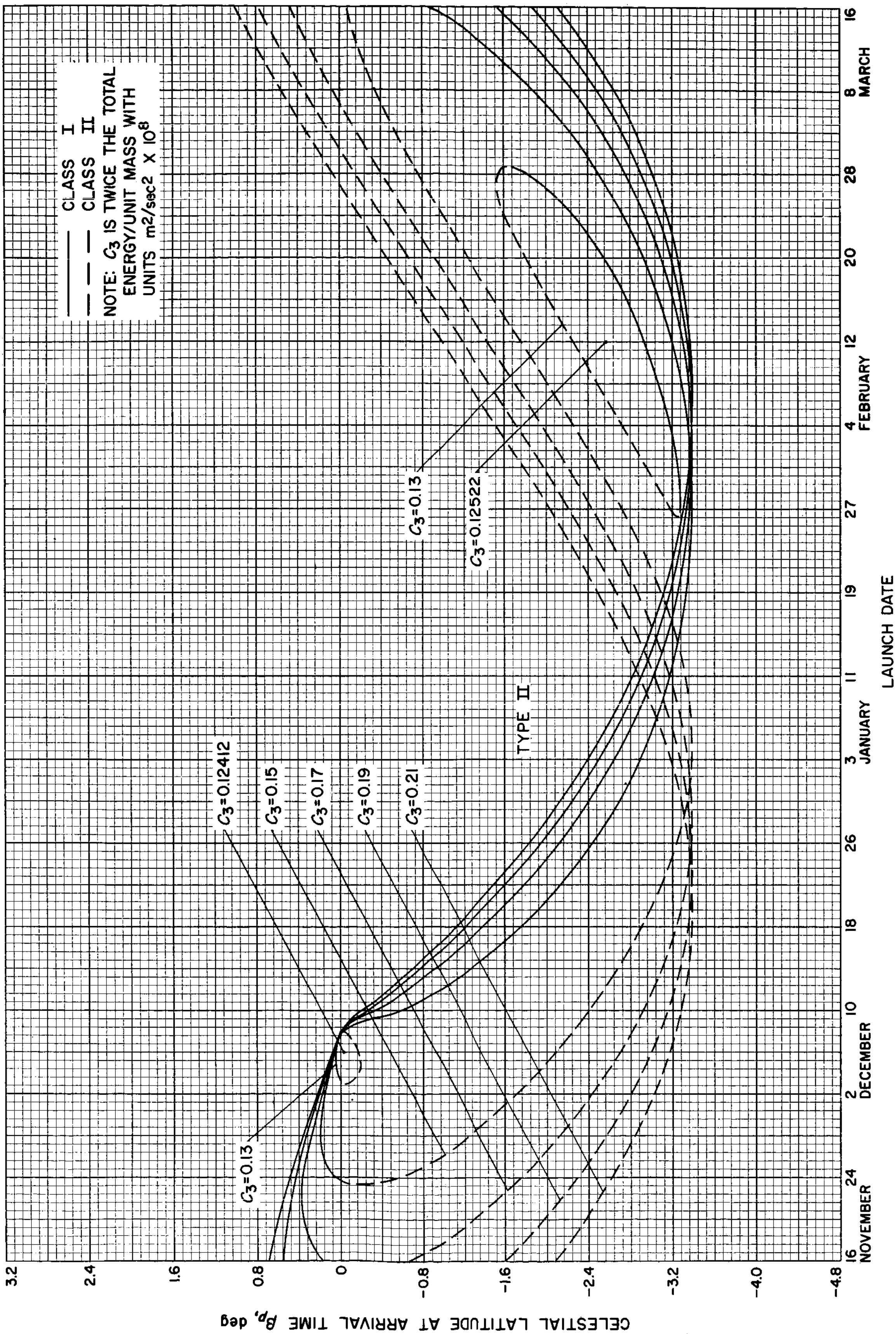

Fig. 9–22. Venus 1968–1969: Celestial latitude at arrival time vs launch date, Type II

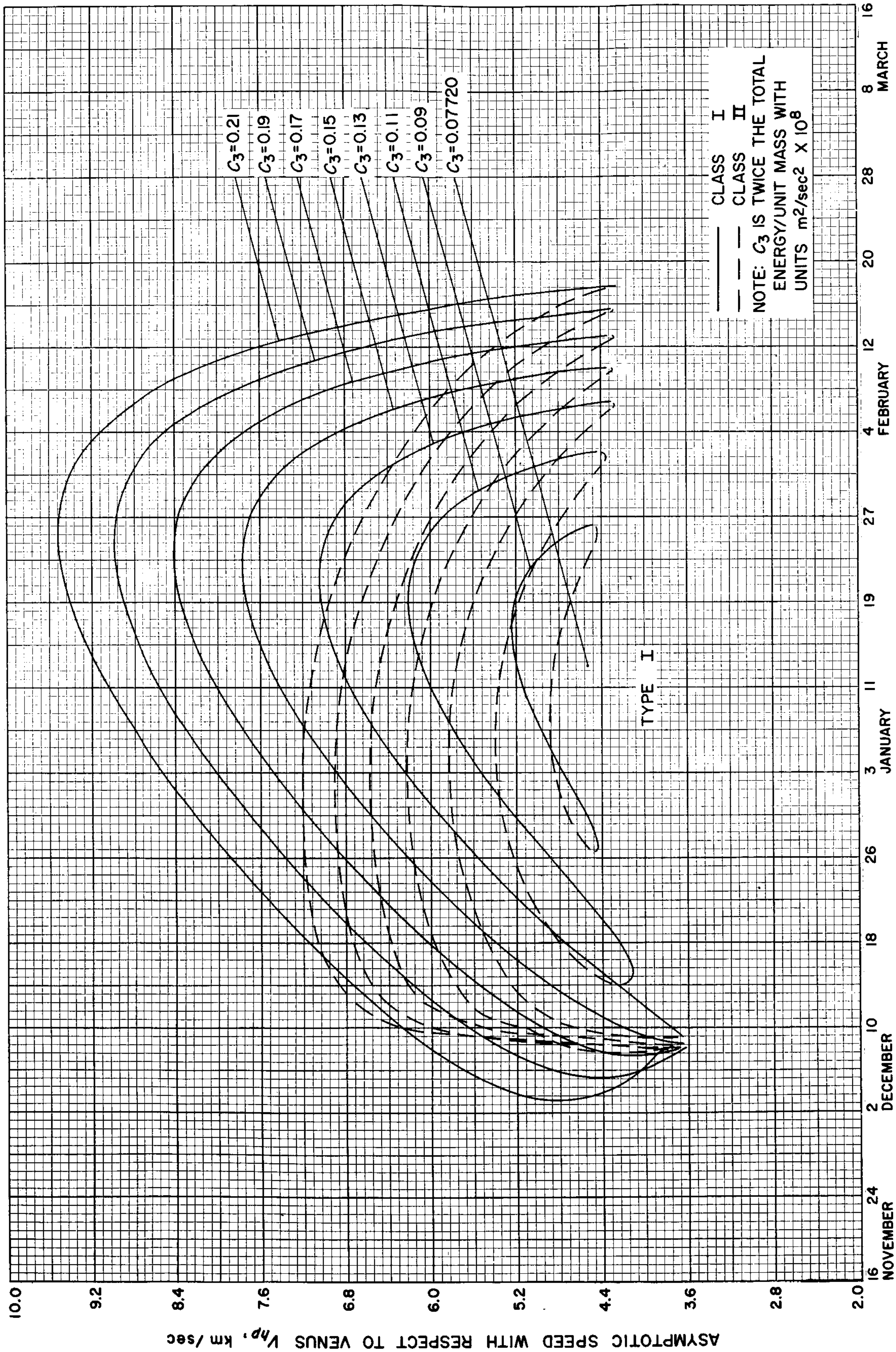

Fig. 9–23. Venus 1968–1969: Asymptotic speed with respect to Venus vs launch date, Type I

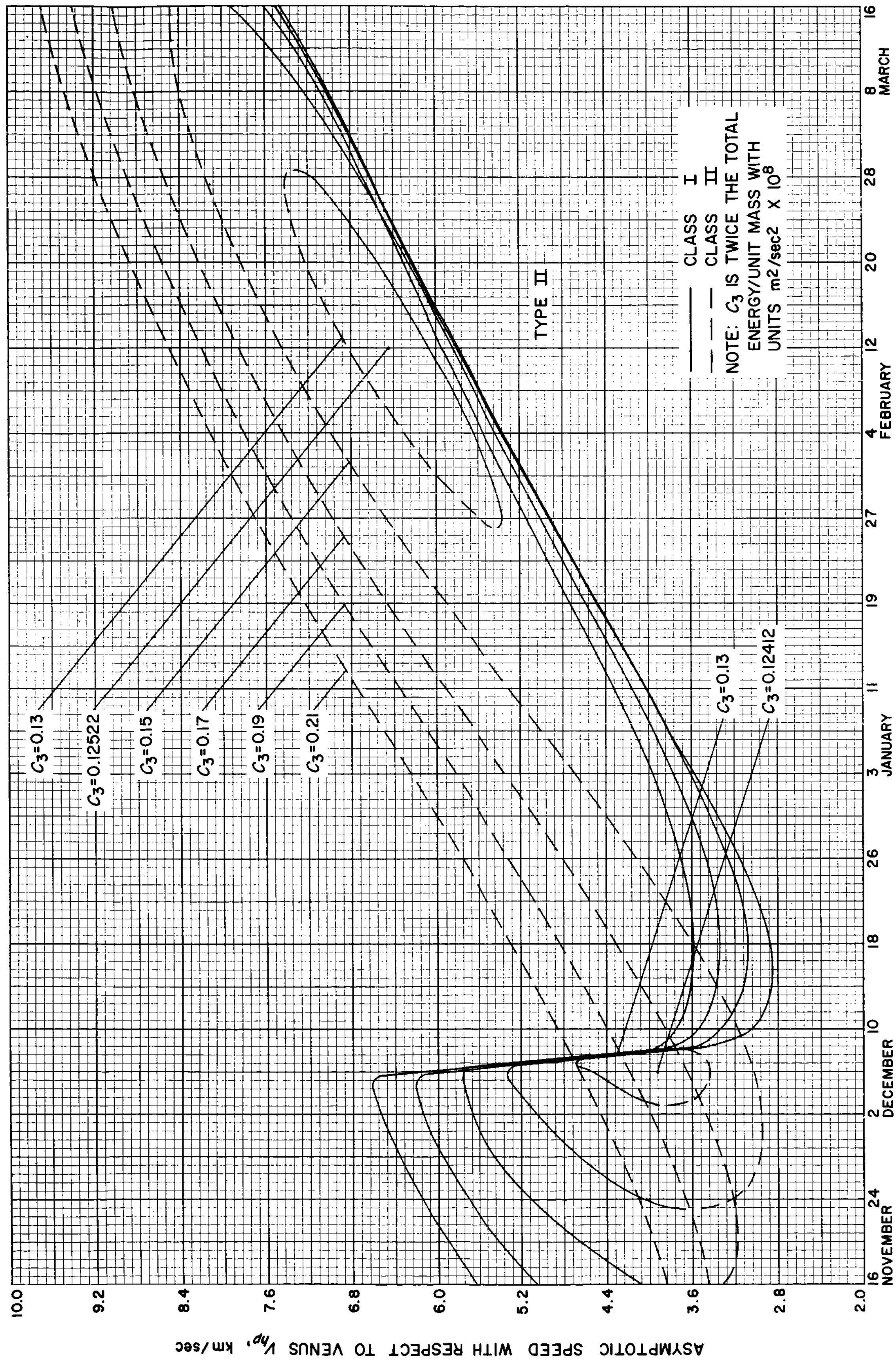

Fig. 9–24. Venus 1968–1969: Asymptotic speed with respect to Venus vs launch date, Type II

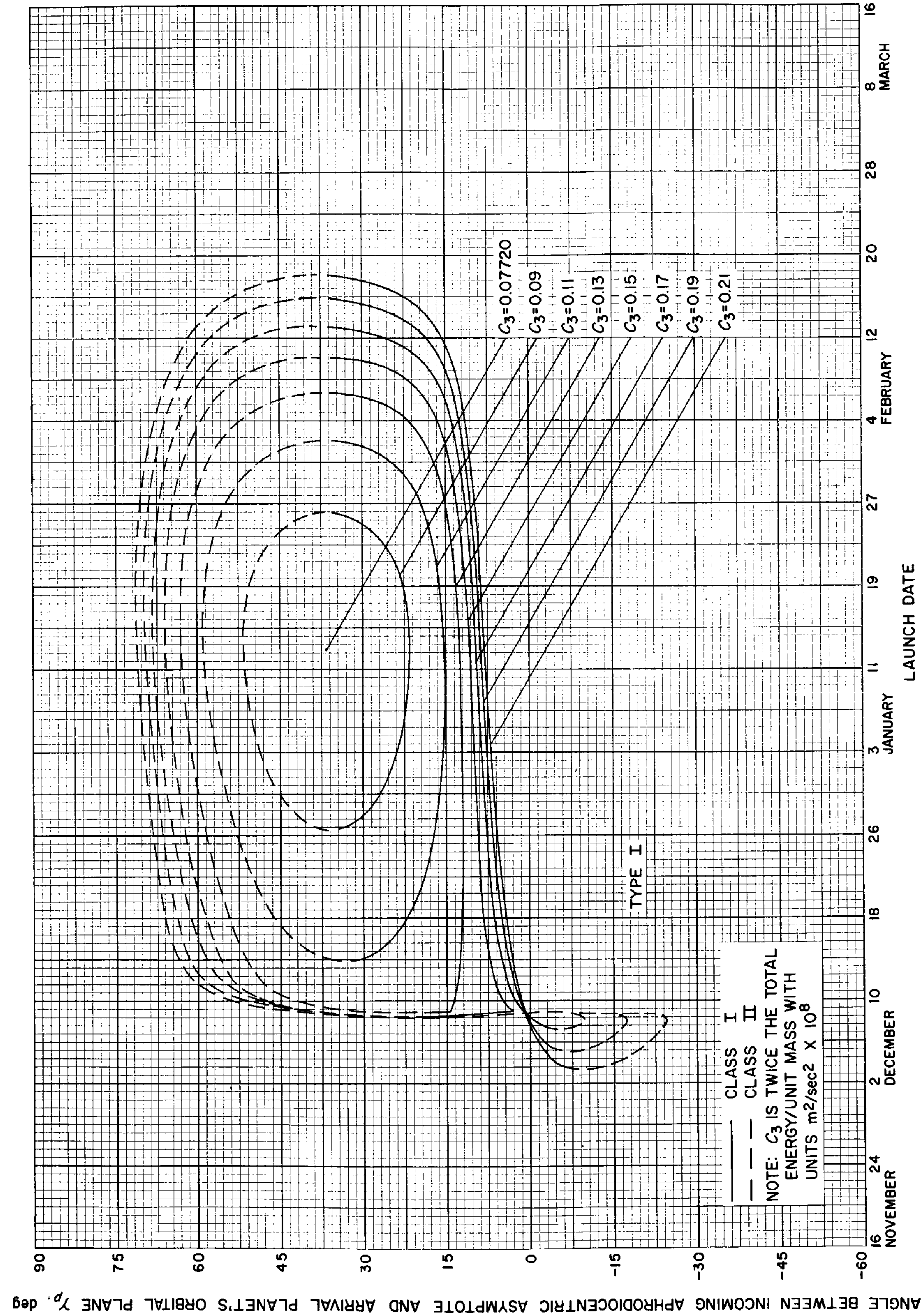

Fig. 9–25. Venus 1968–1969: Angle between incoming aphrodiocentric asymptote and arrival planet's orbital plane vs launch date, Type I

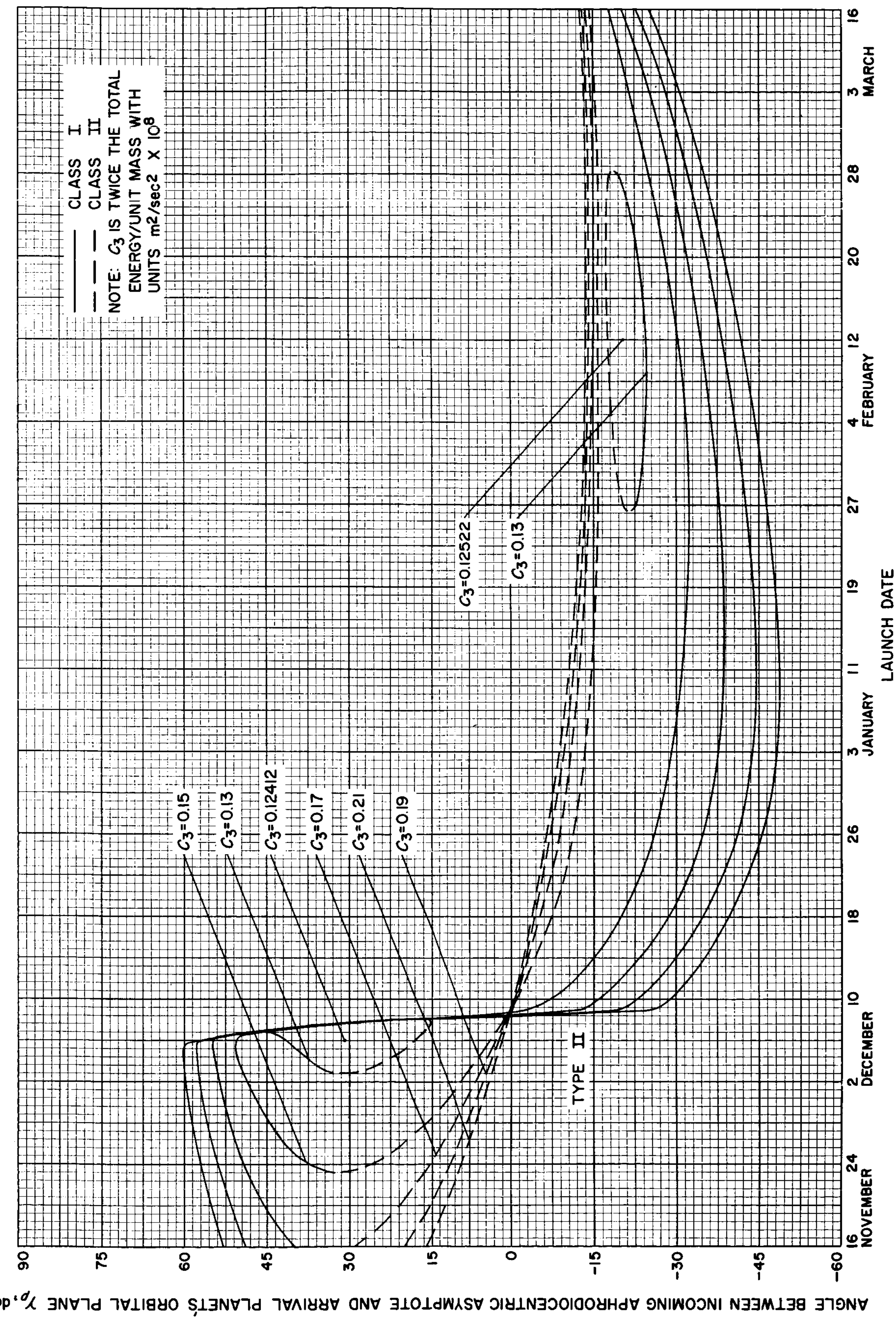

Fig. 9-26. Venus 1968–1969: Angle between incoming aphrodiocentric asymptote and arrival planet's orbital plane vs launch date, Type II

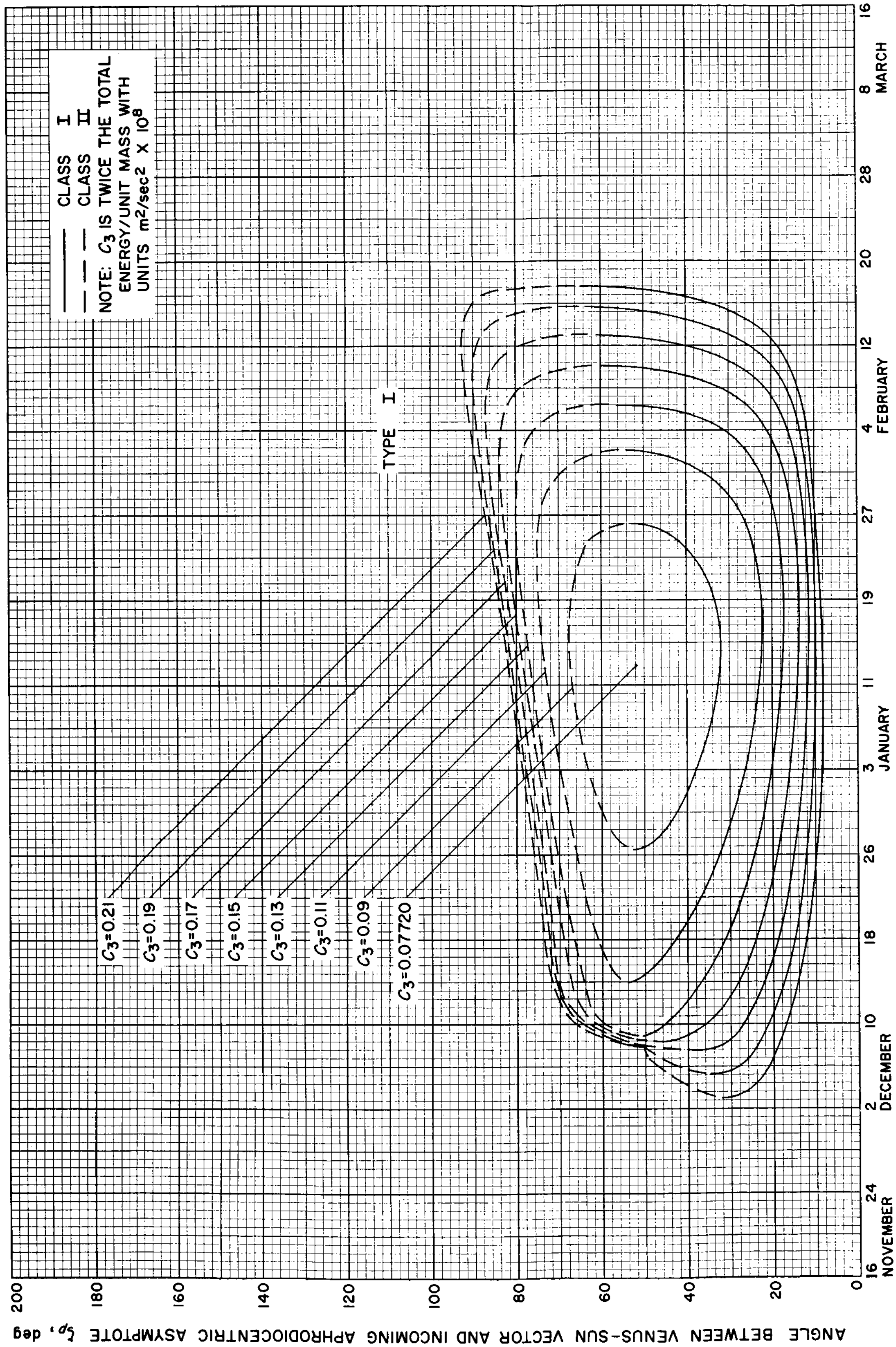

Fig. 9-27. Venus 1968–1969: Angle between Venus–Sun vector and incoming aphrodiocentric asymptote vs launch date, Type I

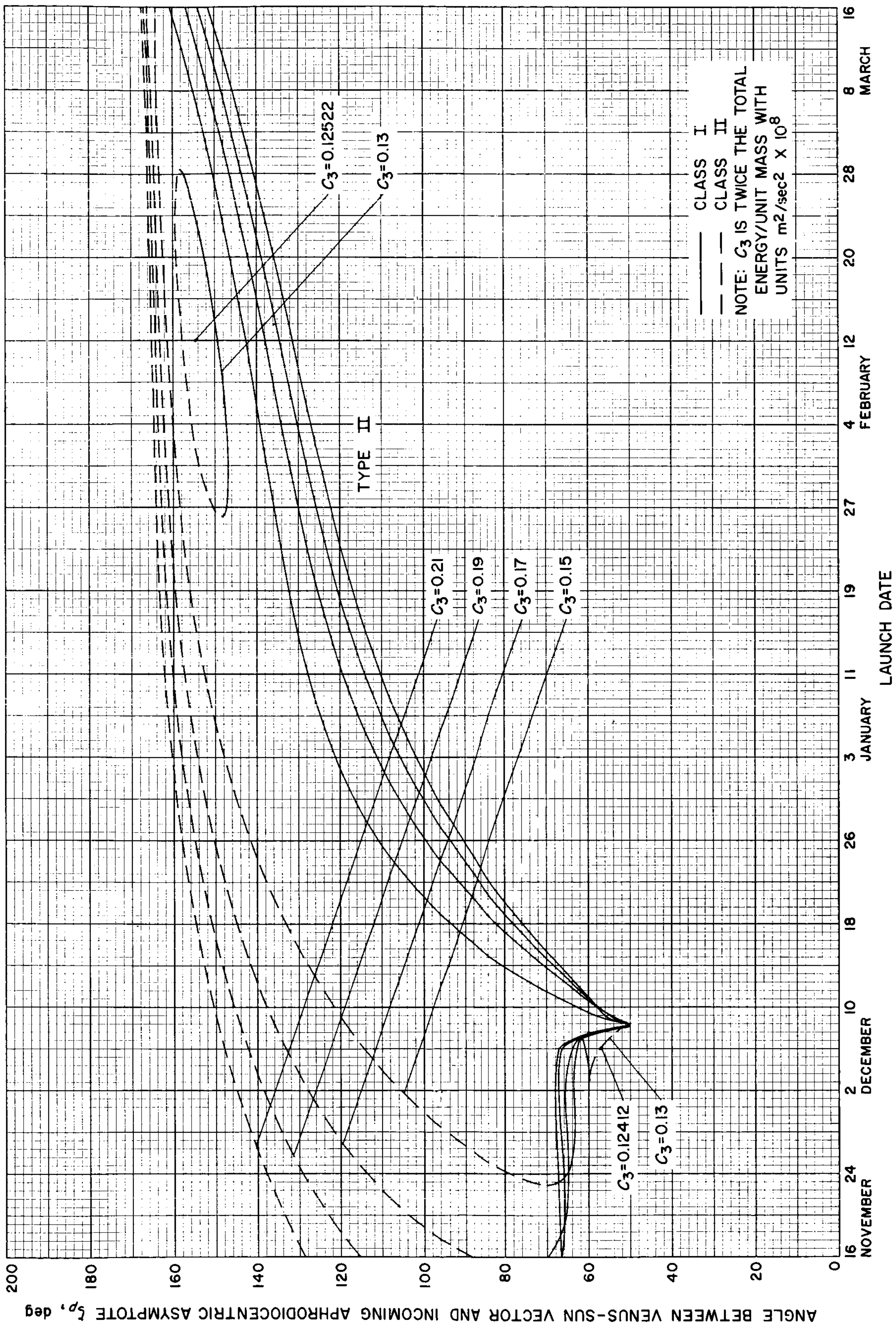

Fig. 9-28. Venus 1968–1969: Angle between Venus–Sun vector and incoming aphrodiocentric asymptote vs launch date, Type II

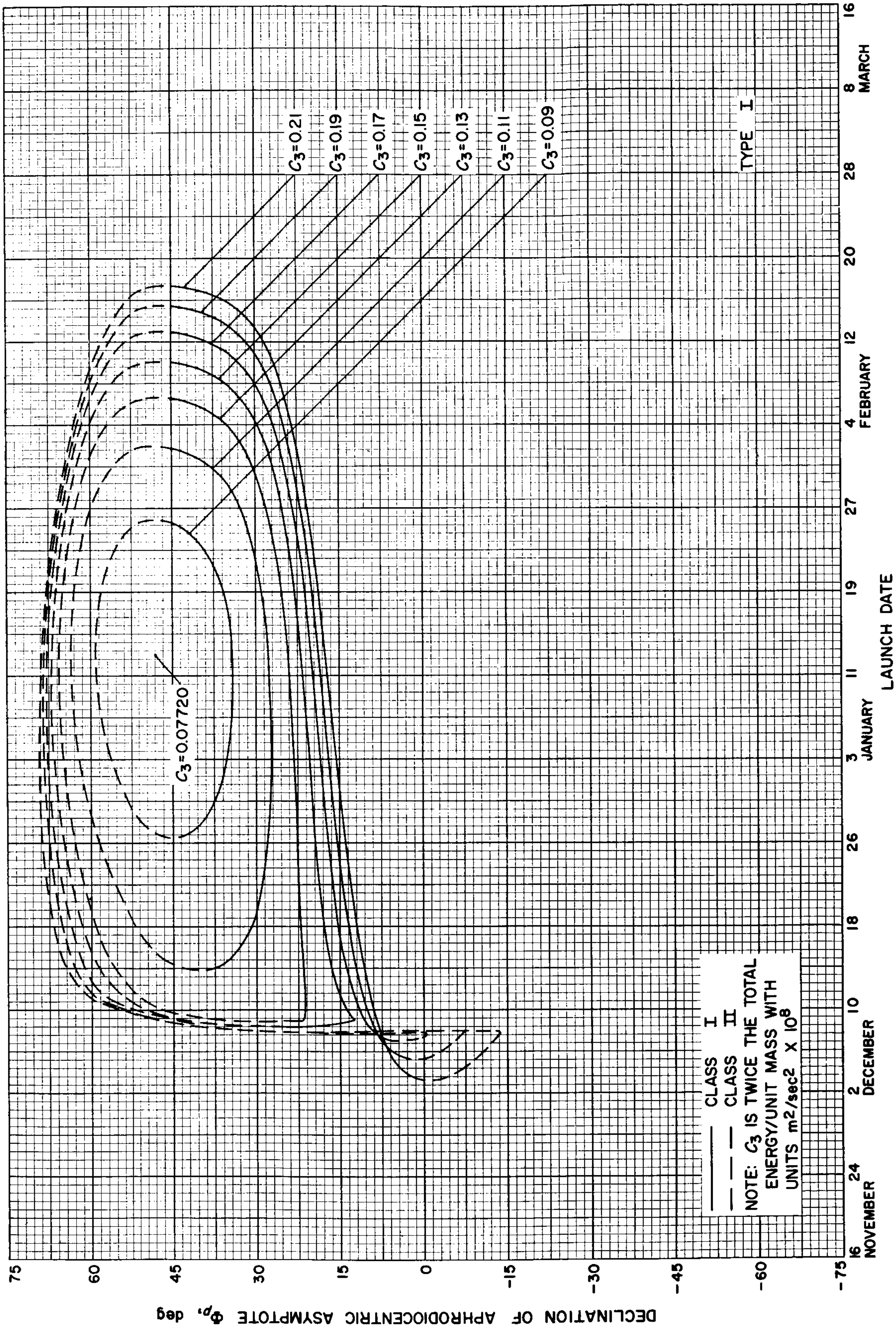

Fig. 9-29: Venus 1968–1969: Declination of aphrodiocentric asymptote vs launch date, Type I

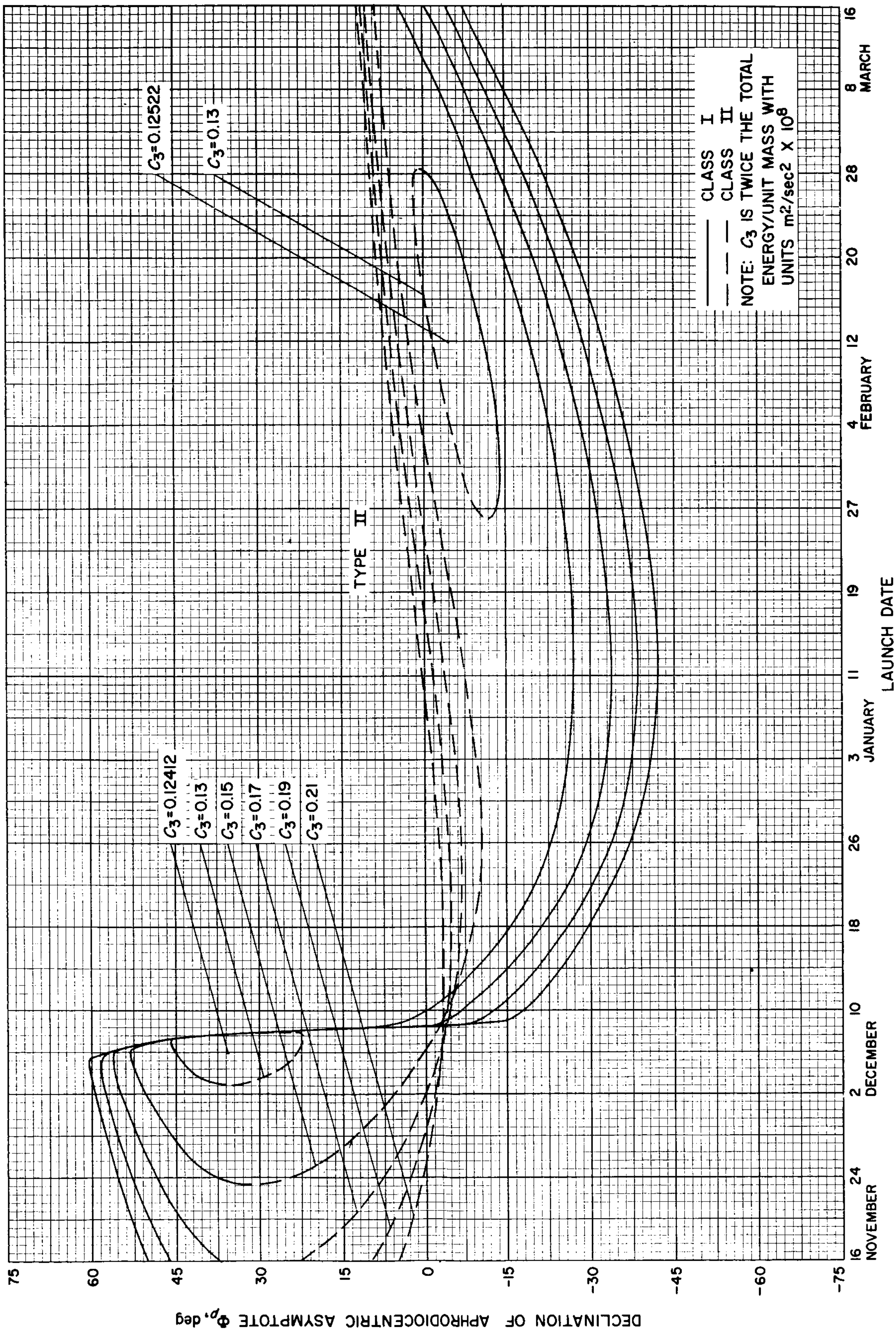

Fig. 9–30. Venus 1968–1969: Declination of aphrodiocentric asymptote vs launch date, Type II

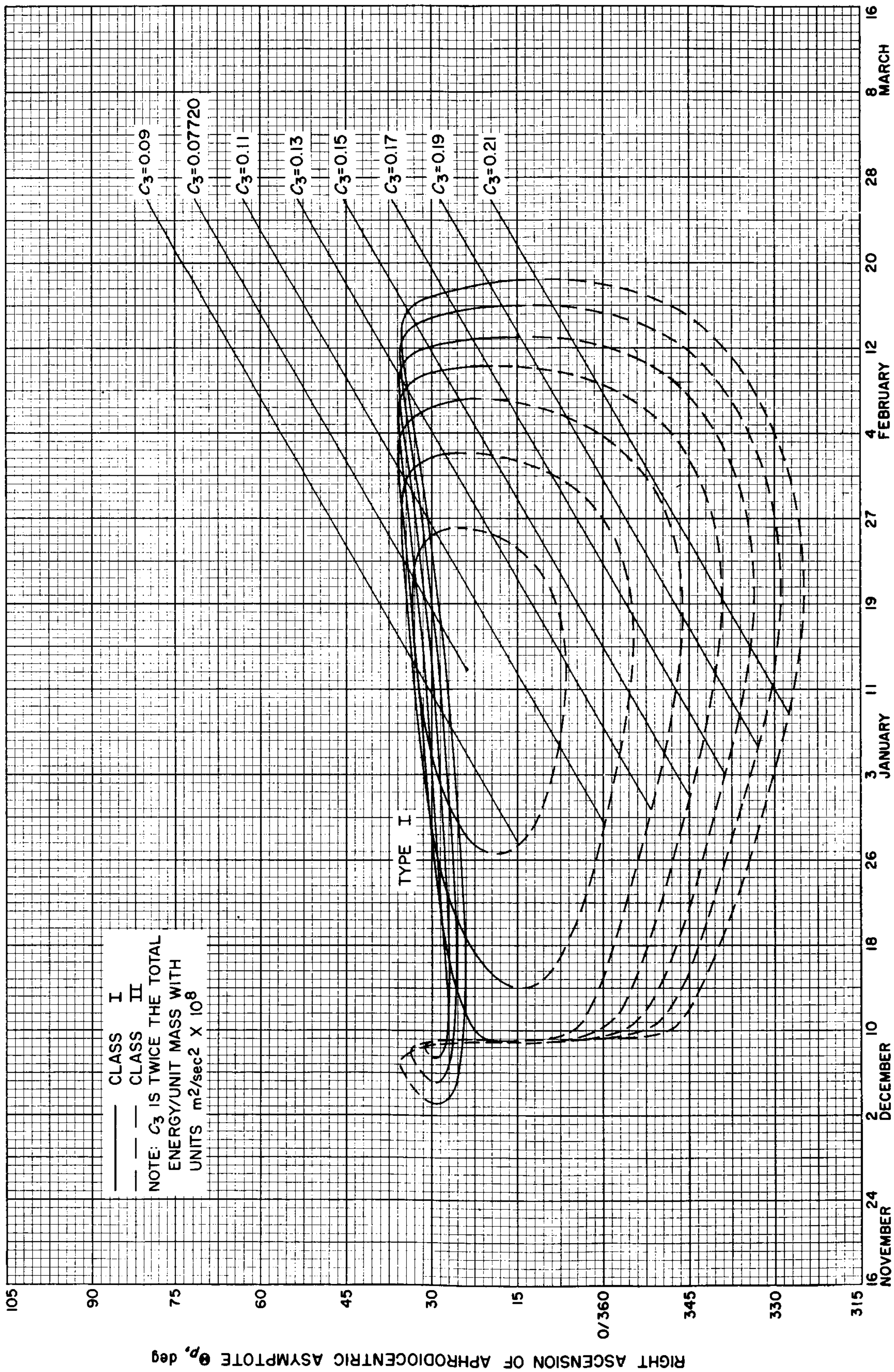

Fig. 9–31. Venus 1968–1969: Right ascension of aphrodiocentric asymptote vs launch date, Type I

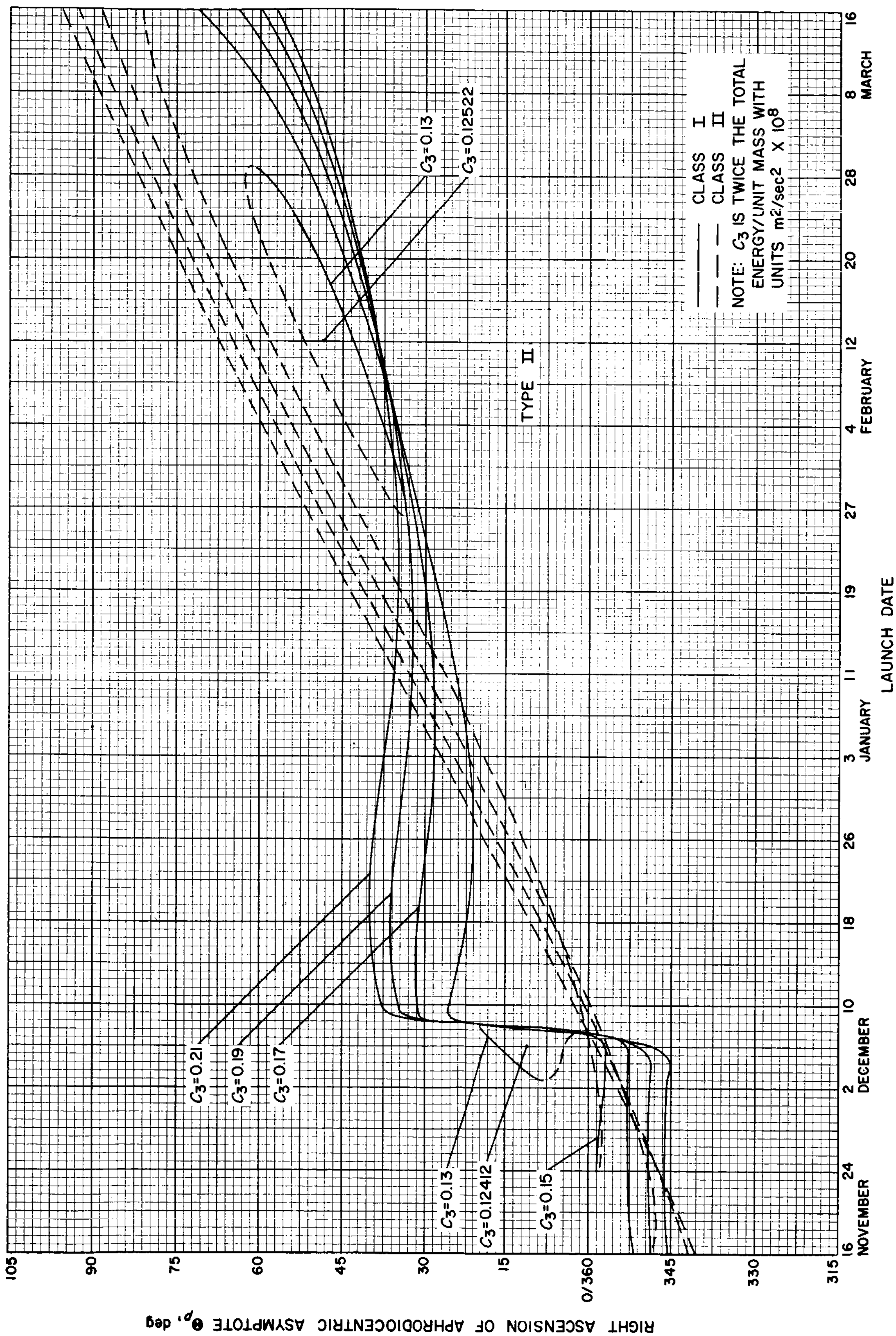

Fig. 9–32. Venus 1968–1969: Right ascension of aphrodiocentric asymptote vs launch date, Type II

X. VENUS 1970: TRAJECTORY-PARAMETER GRAPHS

Figure

X. VENUS 1970: TRAJECTORY-PARAMETER GRAPHS (Cont'd)

Figure

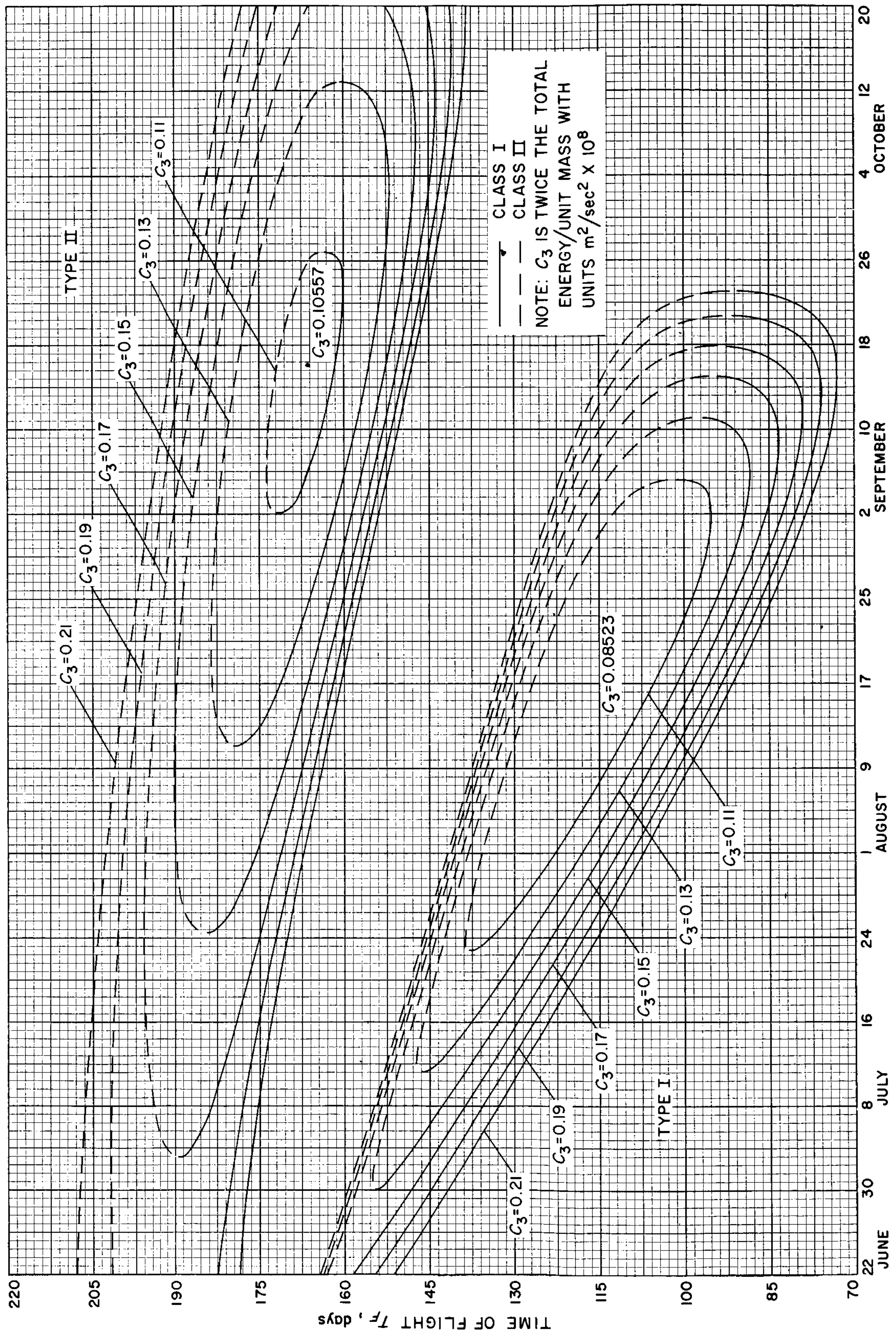

Fig. 10–1. Venus 1970: Time of flight vs launch date

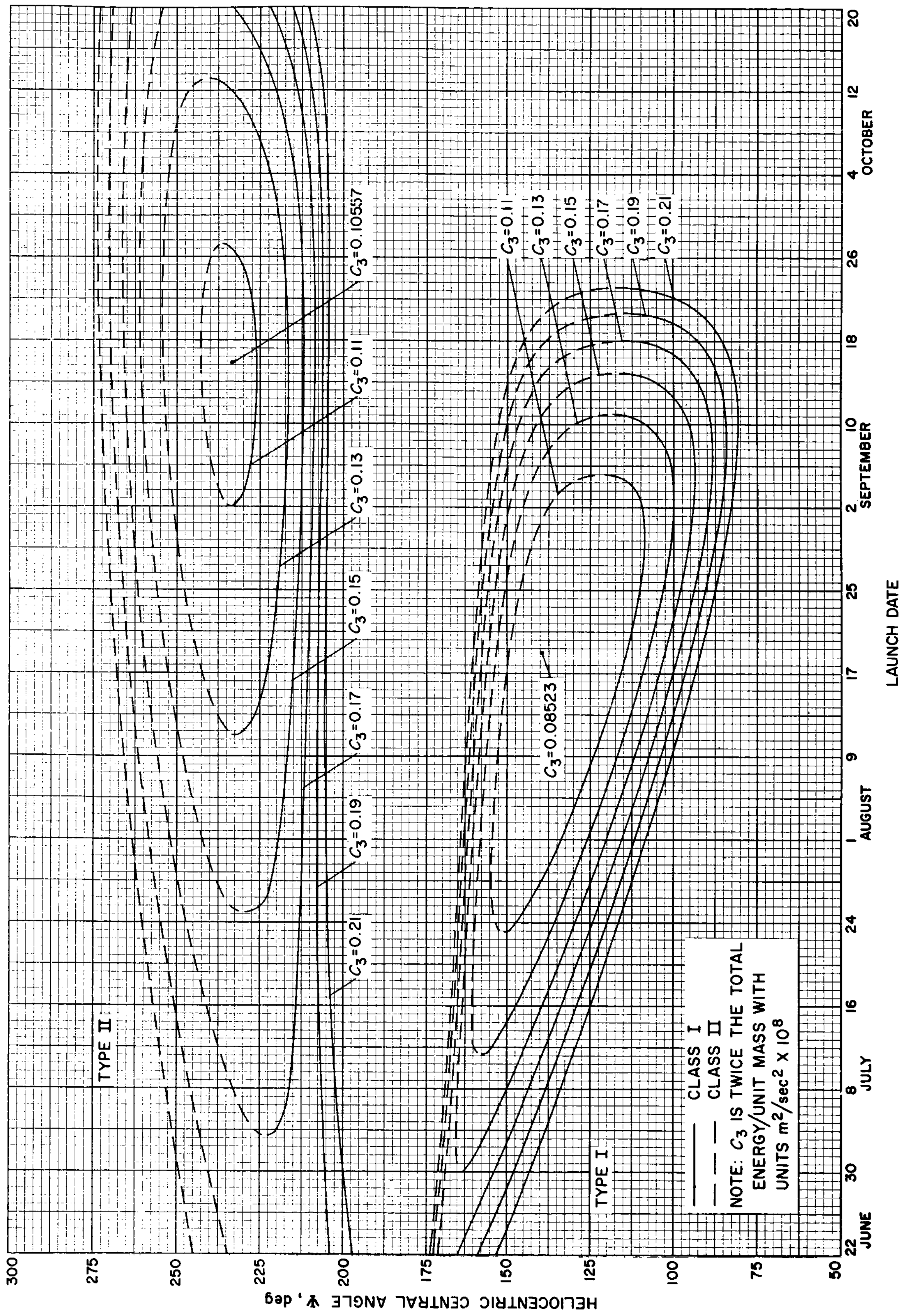

Fig. 10–2. Venus 1970: Heliocentric central angle vs launch date

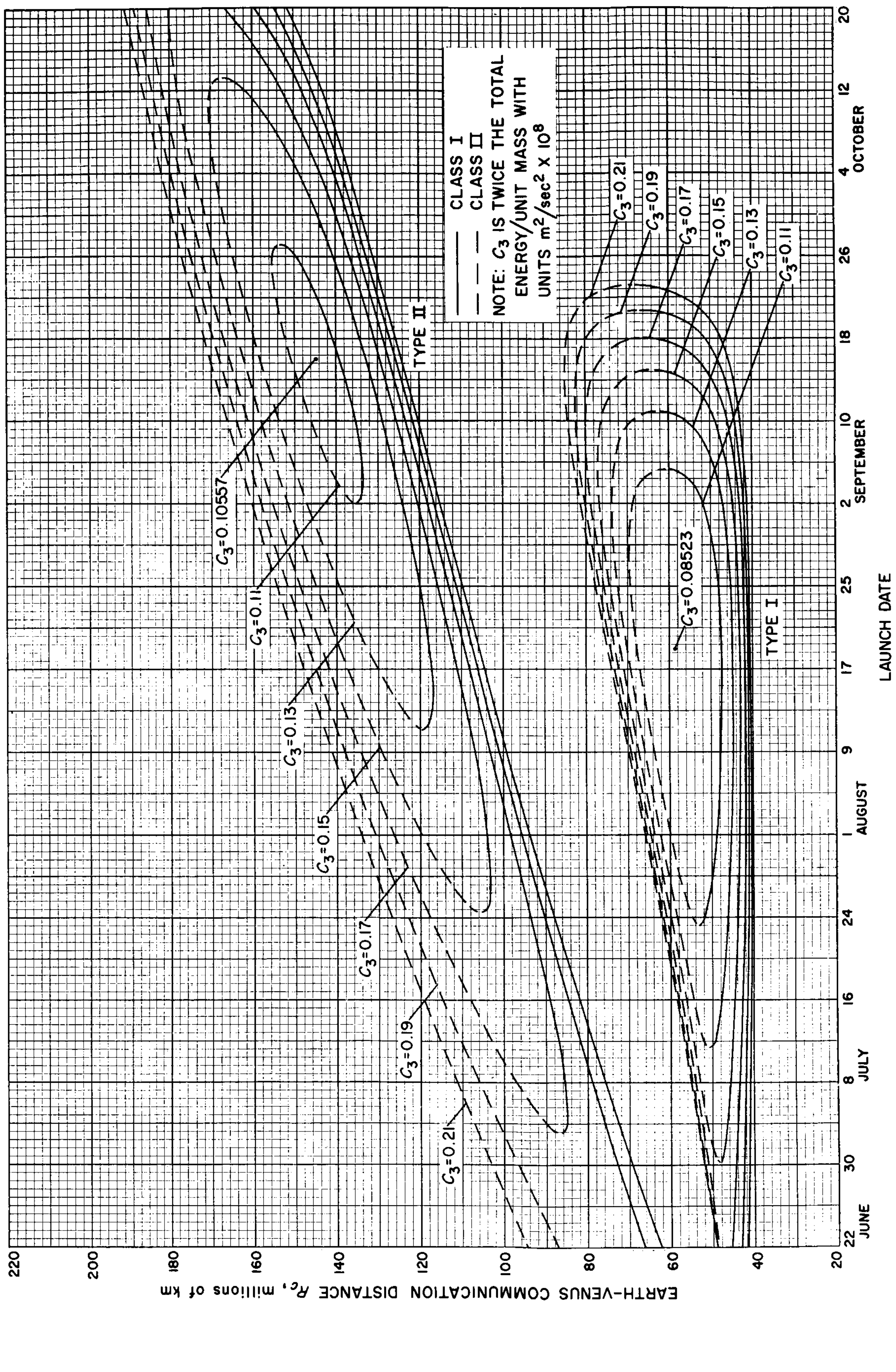

Fig. 10–3. Venus 1970: Earth–Venus communication distance vs launch date

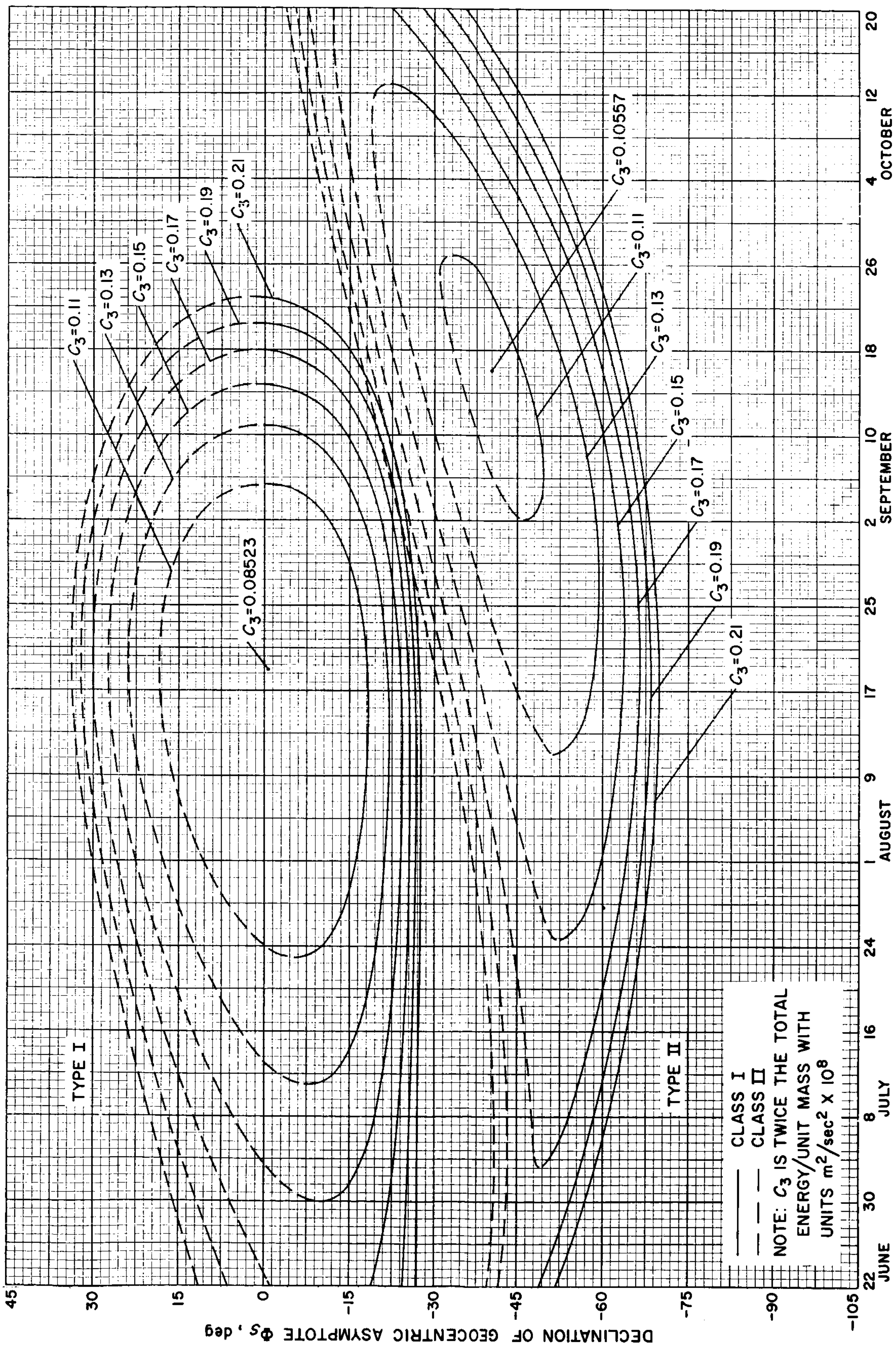

Fig. 10–4. Venus 1970: Declination of geocentric asymptote vs launch date

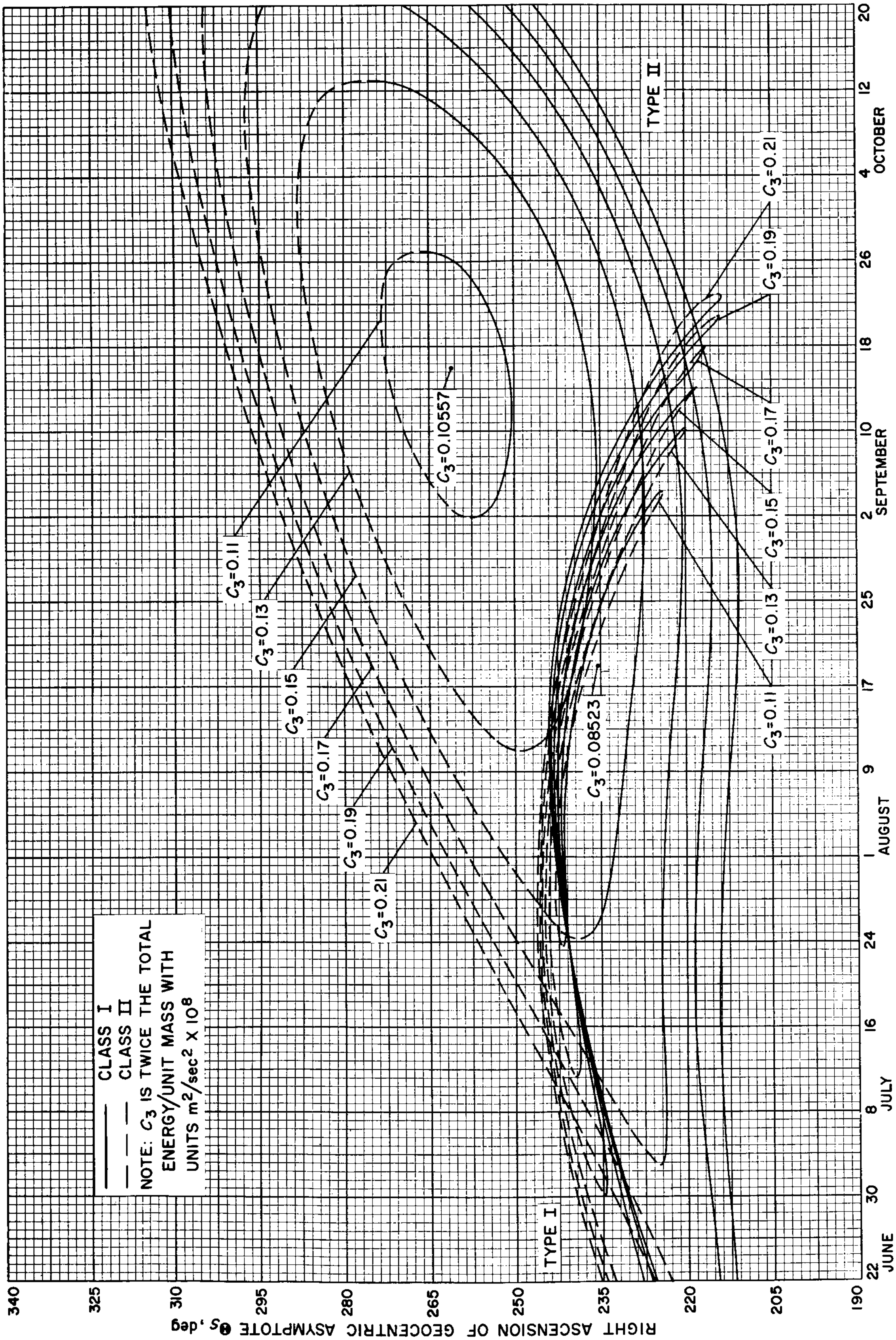

Fig. 10–5. Venus 1970: Right ascension of geocentric asymptote vs launch date

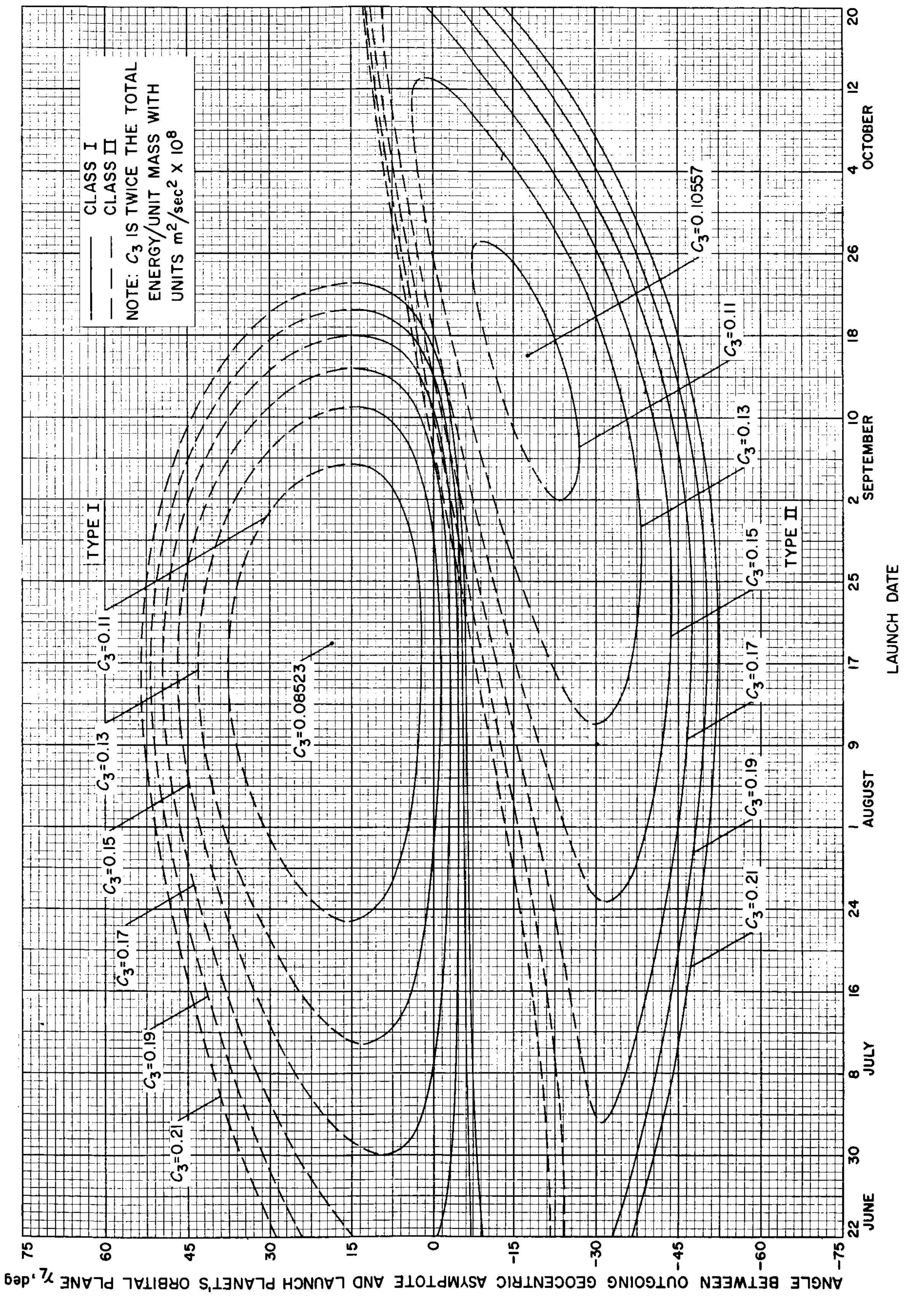

Fig. 10–6. Venus 1970: Angle between outgoing geocentric asymptote and launch planet's orbital plane vs launch date

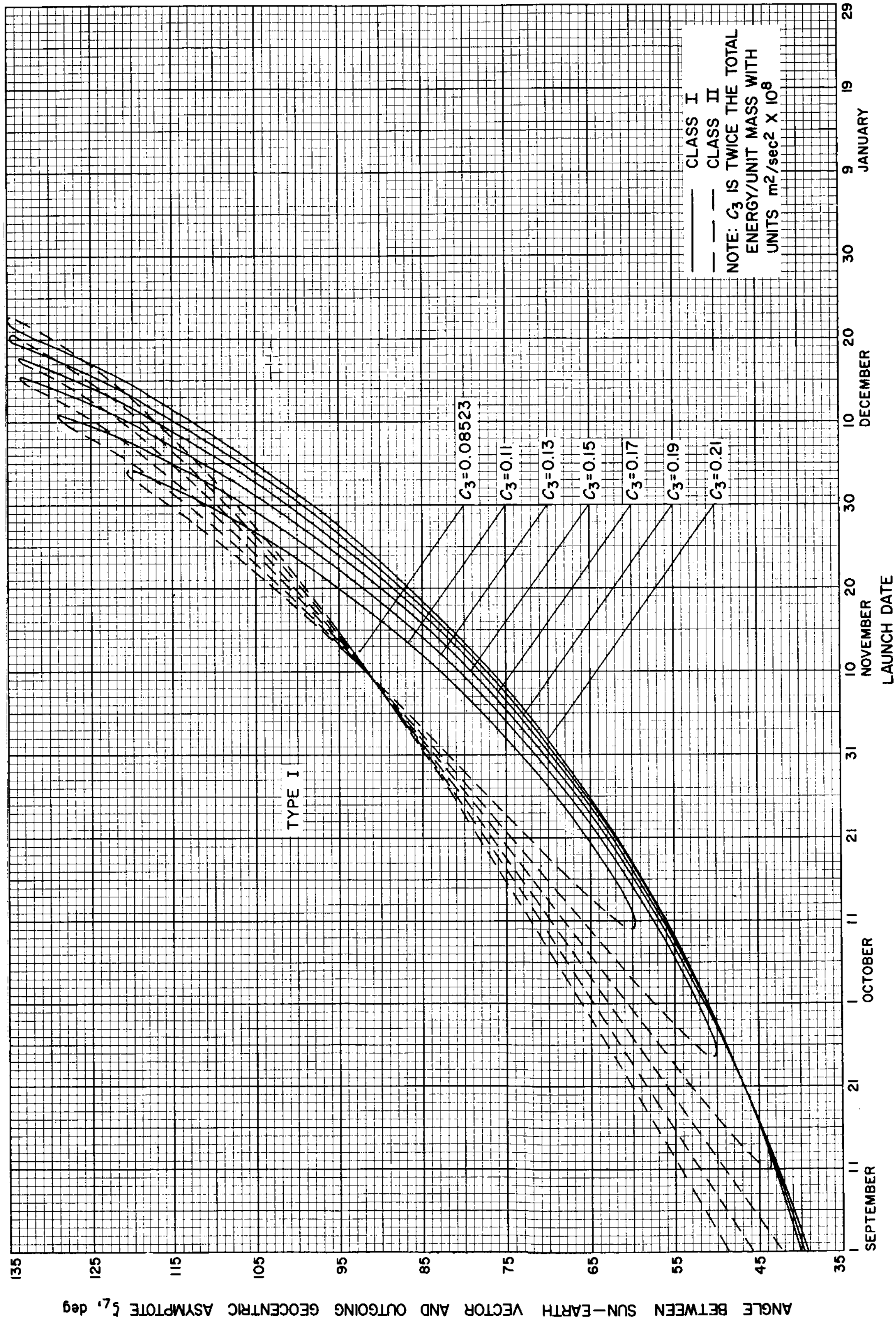

Fig. 10–7. Venus 1970: Angle between Sun–Earth vector and outgoing geocentric asymptote vs launch date, Type I

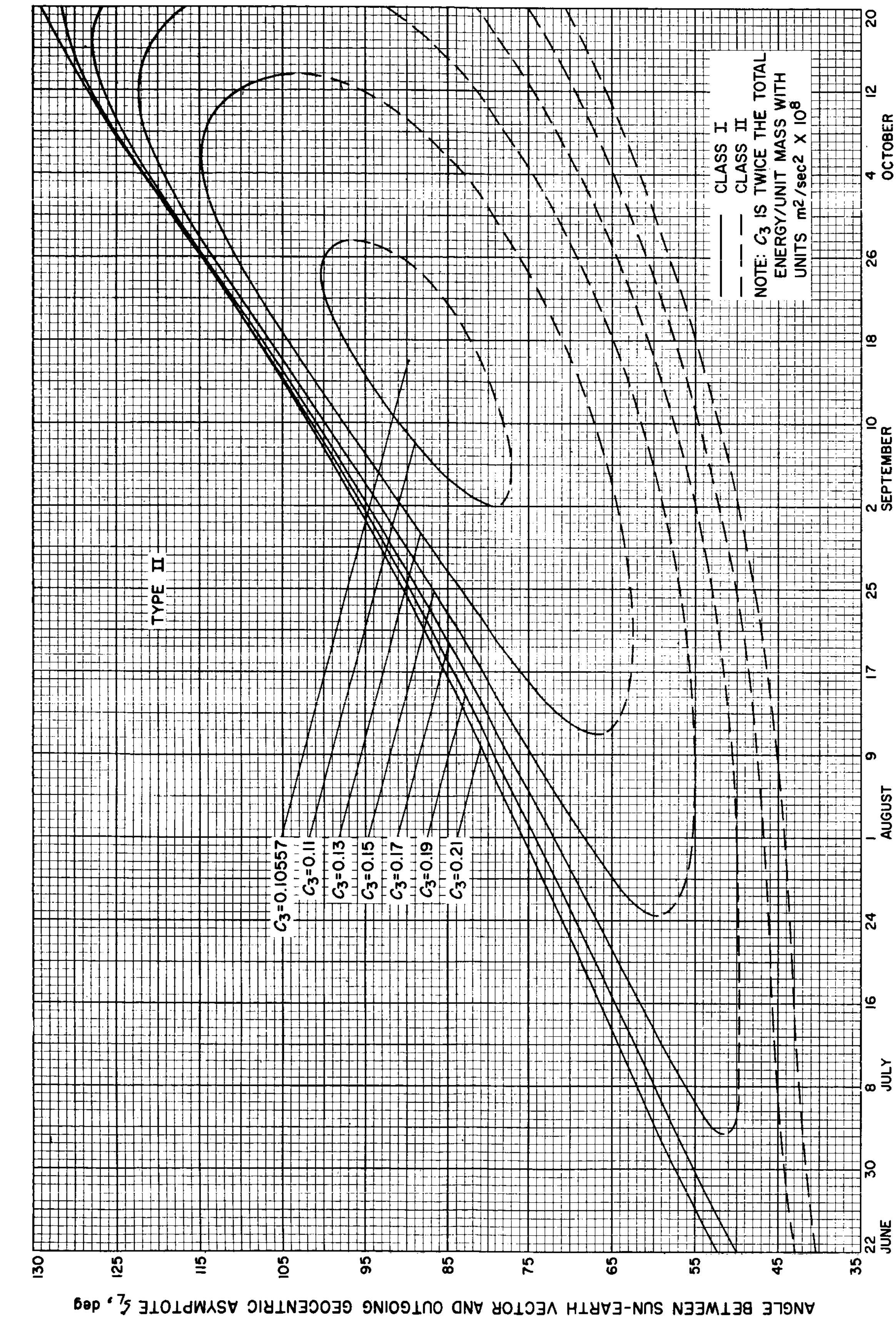

Fig. 10-8. Venus 1970: Angle between Sun–Earth vector and outgoing geocentric asymptote vs launch date, Type II

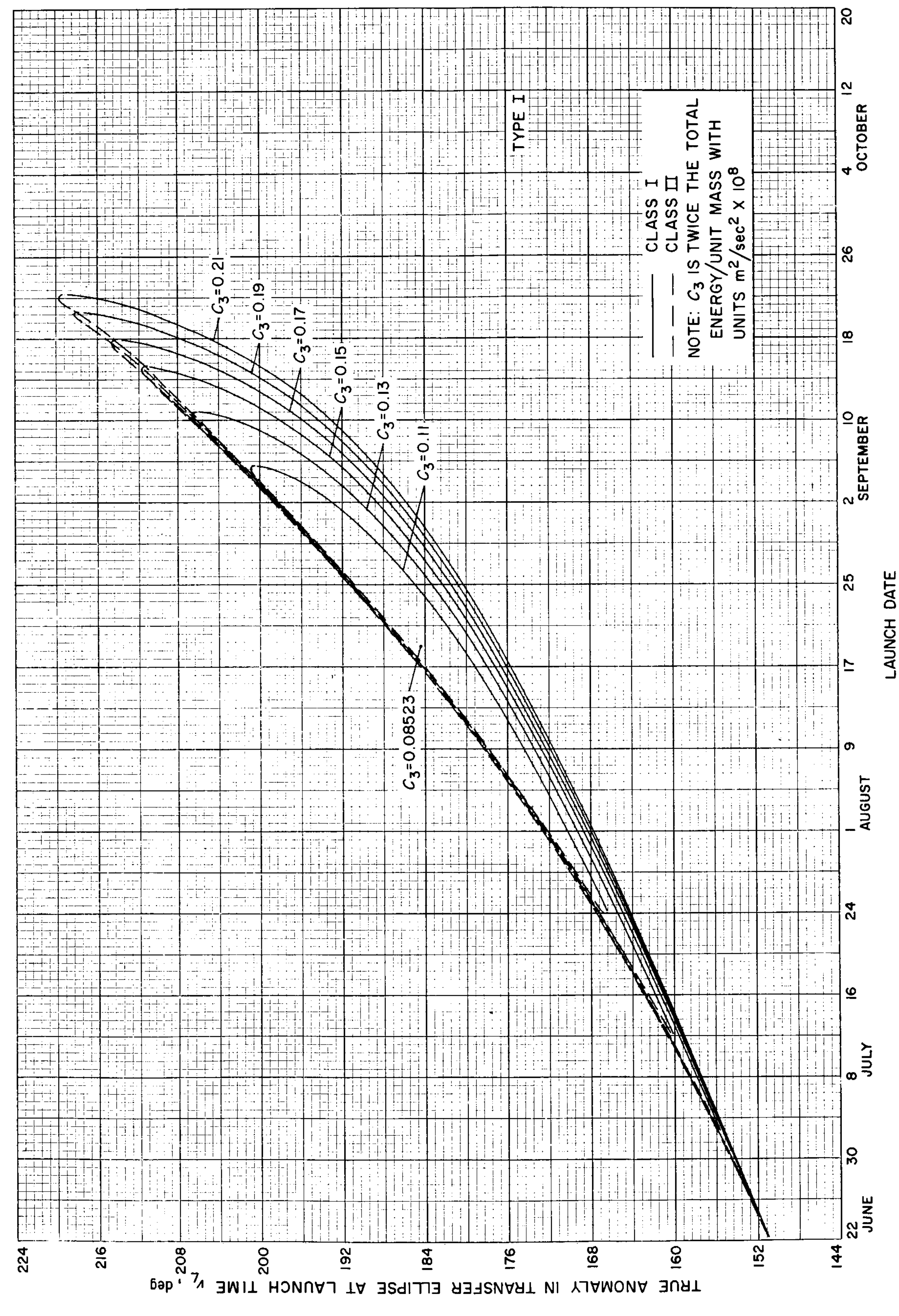

Fig. 10–9. Venus 1970: True anomaly in transfer ellipse at launch time vs launch date, Type I

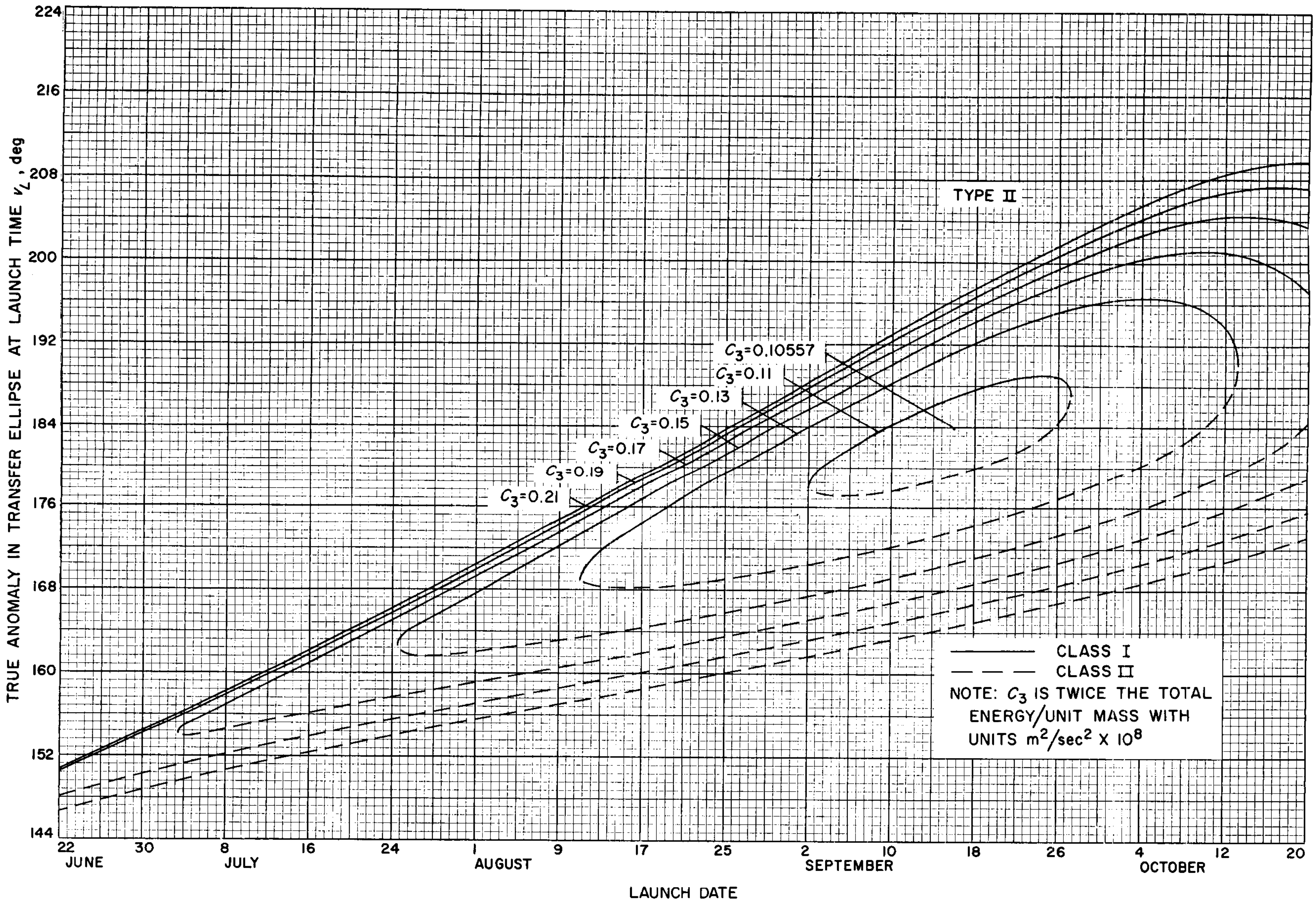

Fig. 10–10. Venus 1970: True anomaly in transfer ellipse at launch time vs launch date, Type II

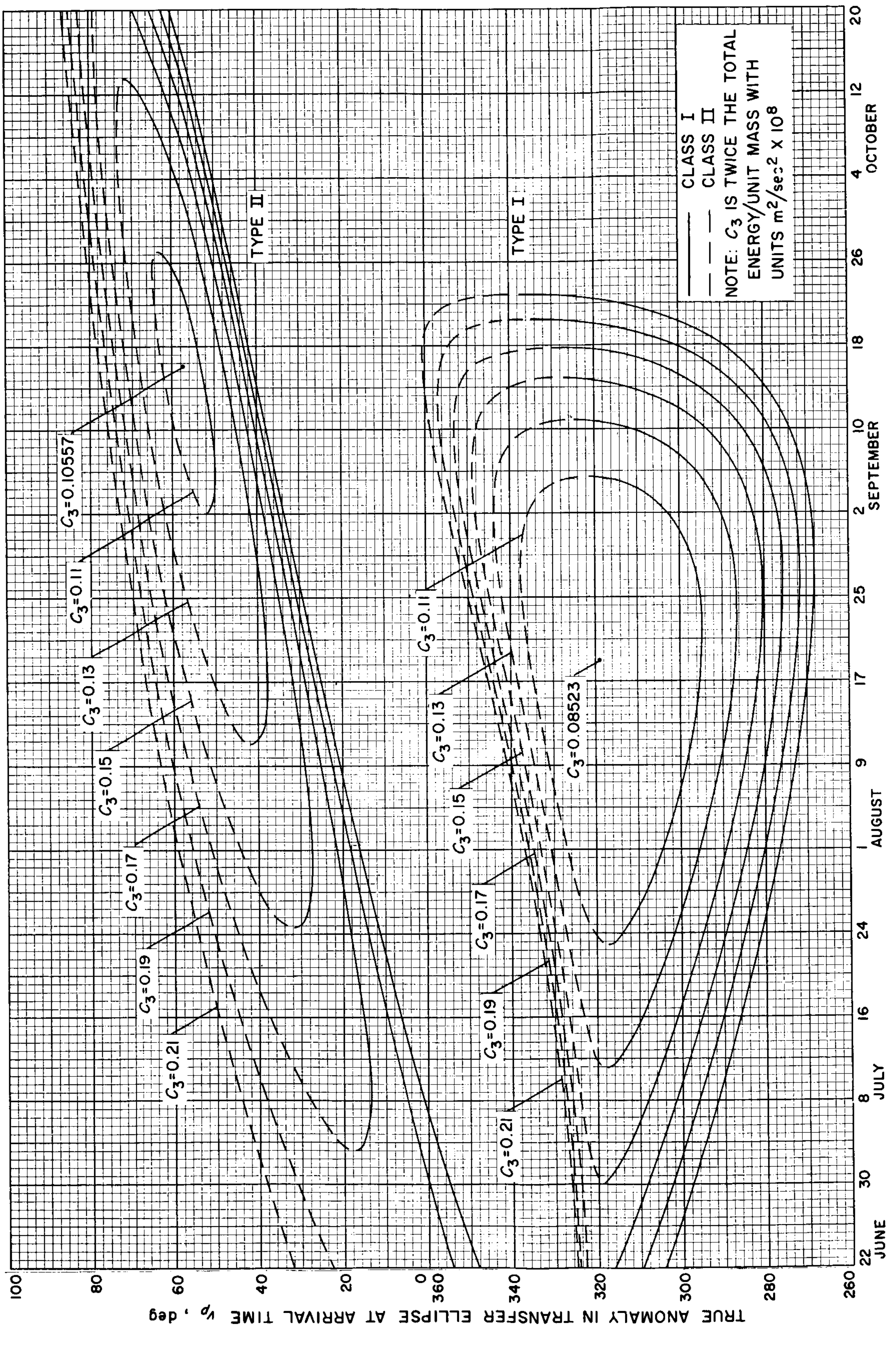

Fig. 10-11. Venus 1970: True anomaly in transfer ellipse at arrival time vs launch date

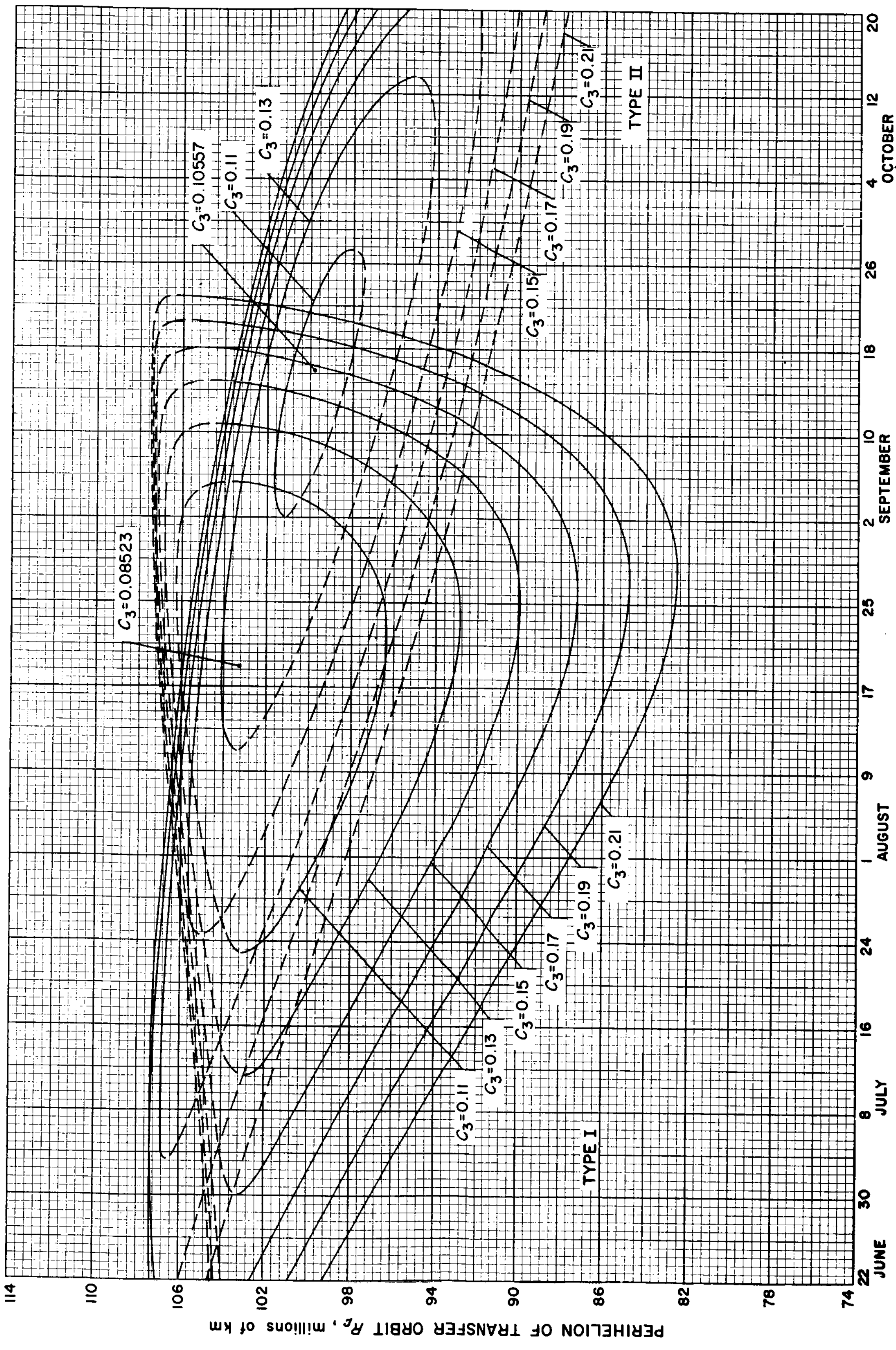

Fig. 10–12. Venus 1970: Perihelion of transfer orbit vs launch date

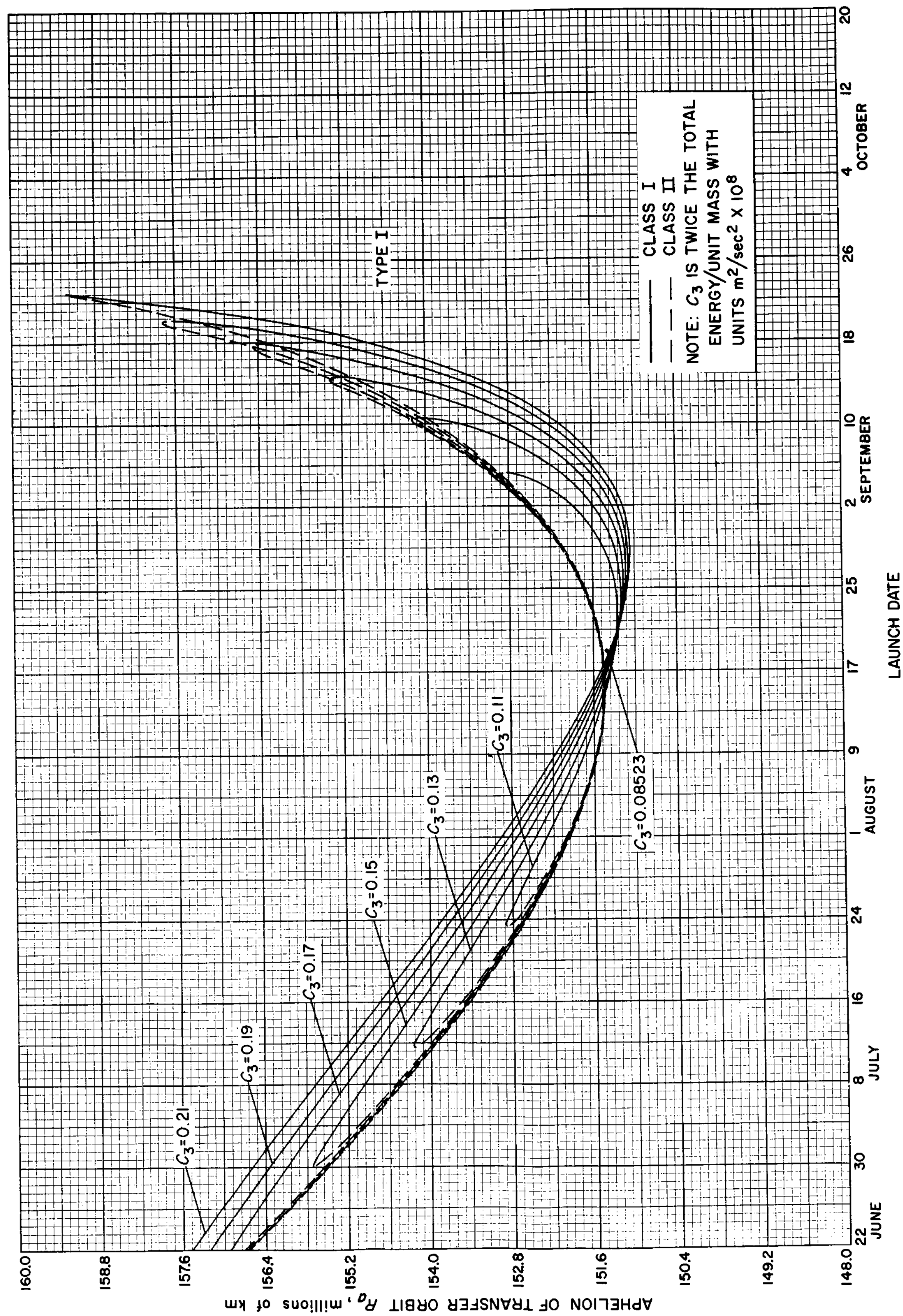

Fig. 10–13. Venus 1970: Aphelion of transfer orbit vs launch date, Type I

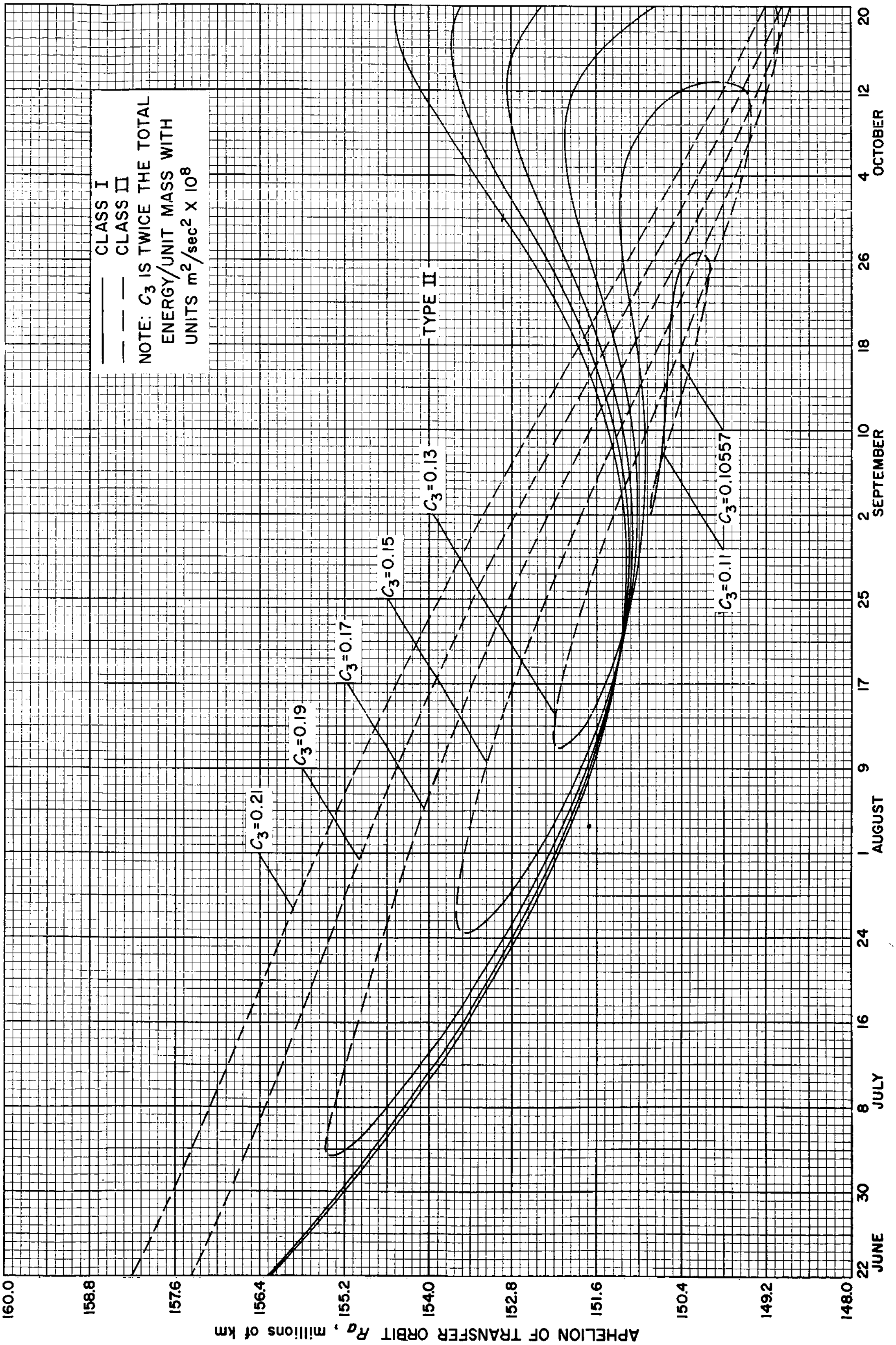

Fig. 10-14. Venus 1970: Aphelion of transfer orbit vs launch date, Type II

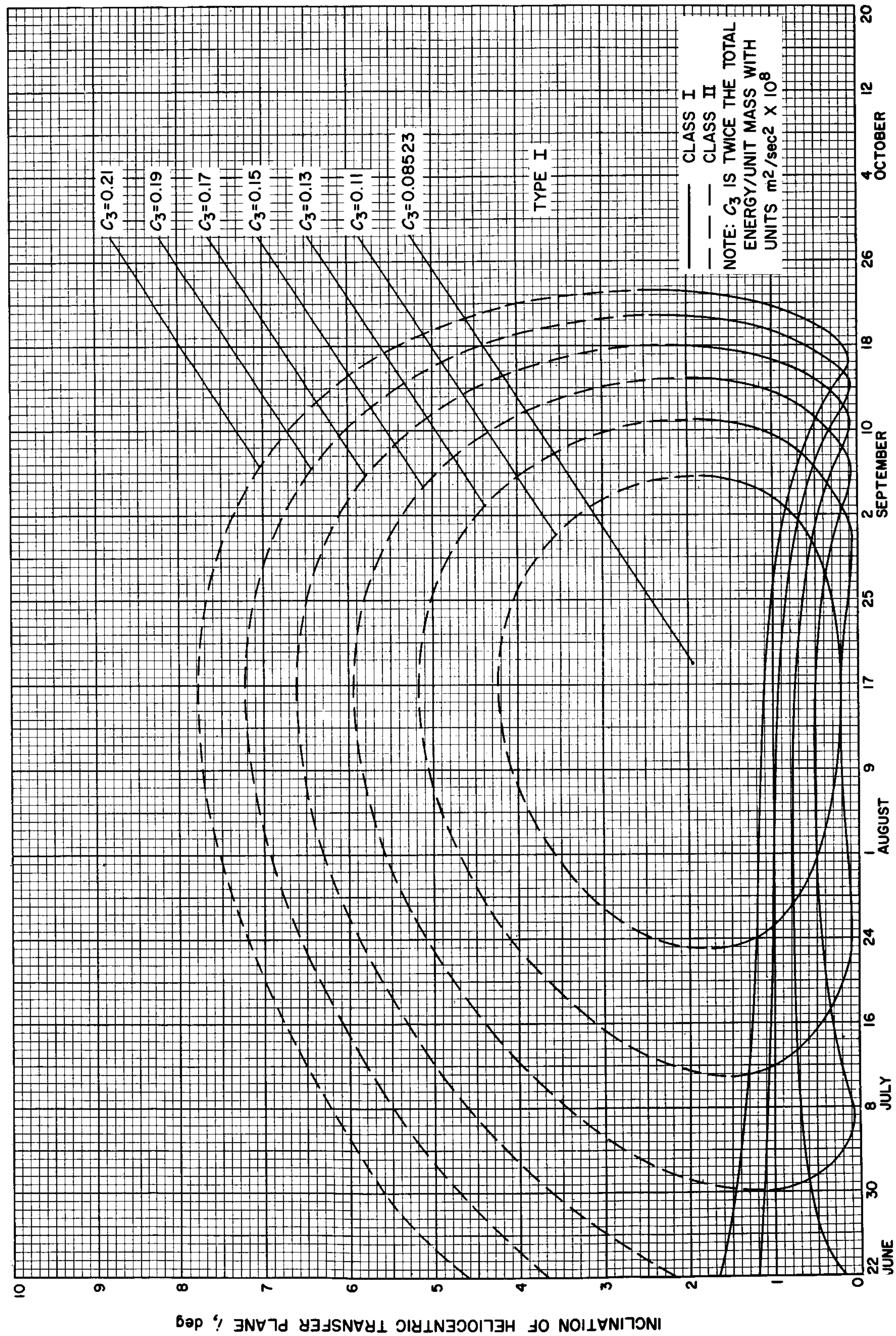

Fig. 10-15. Venus 1970: Inclination of heliocentric-transfer plane vs launch date, Type I

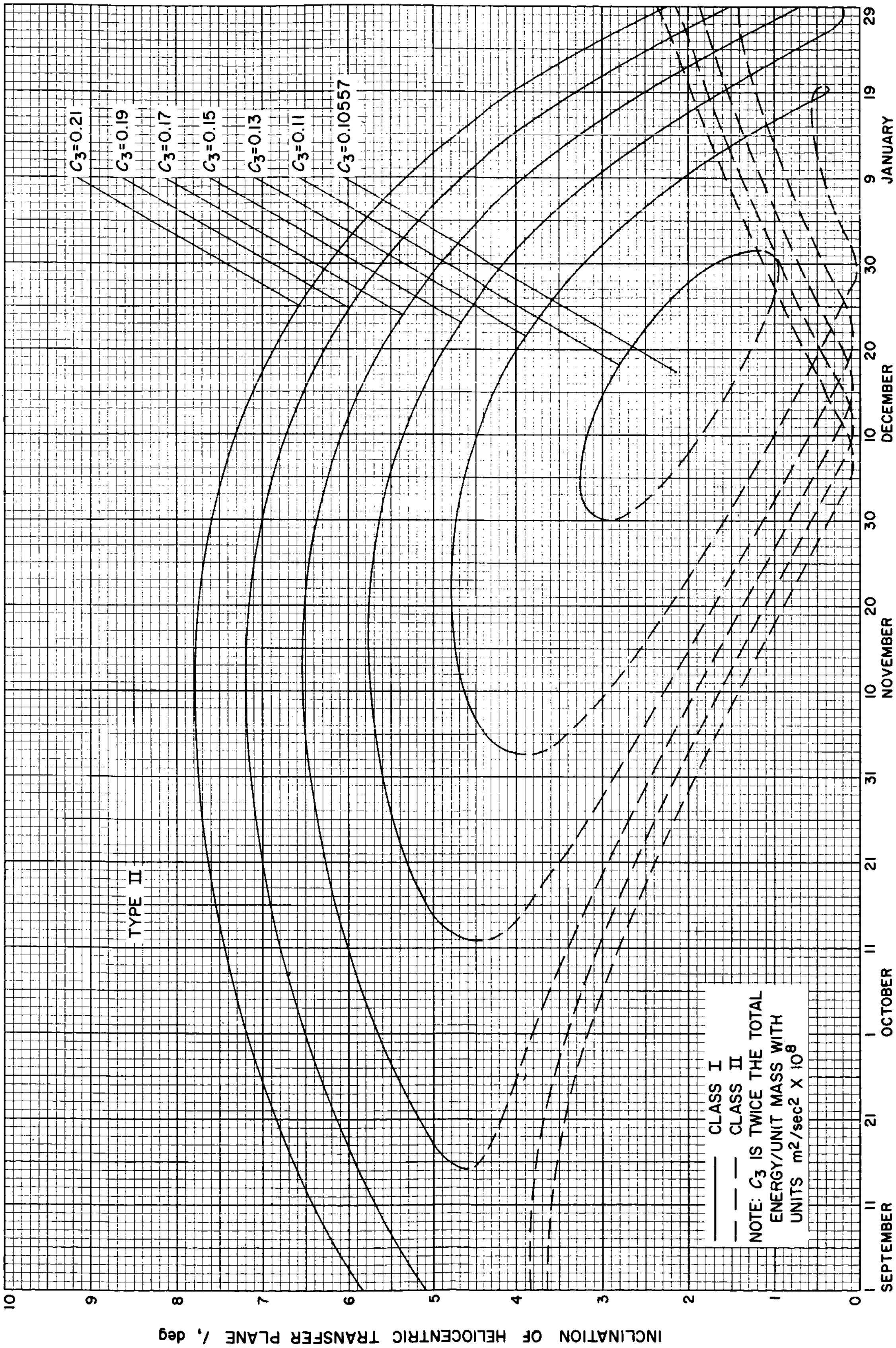

Fig. 10–16. Venus 1970: Inclination of heliocentric-transfer plane vs launch date, Type II

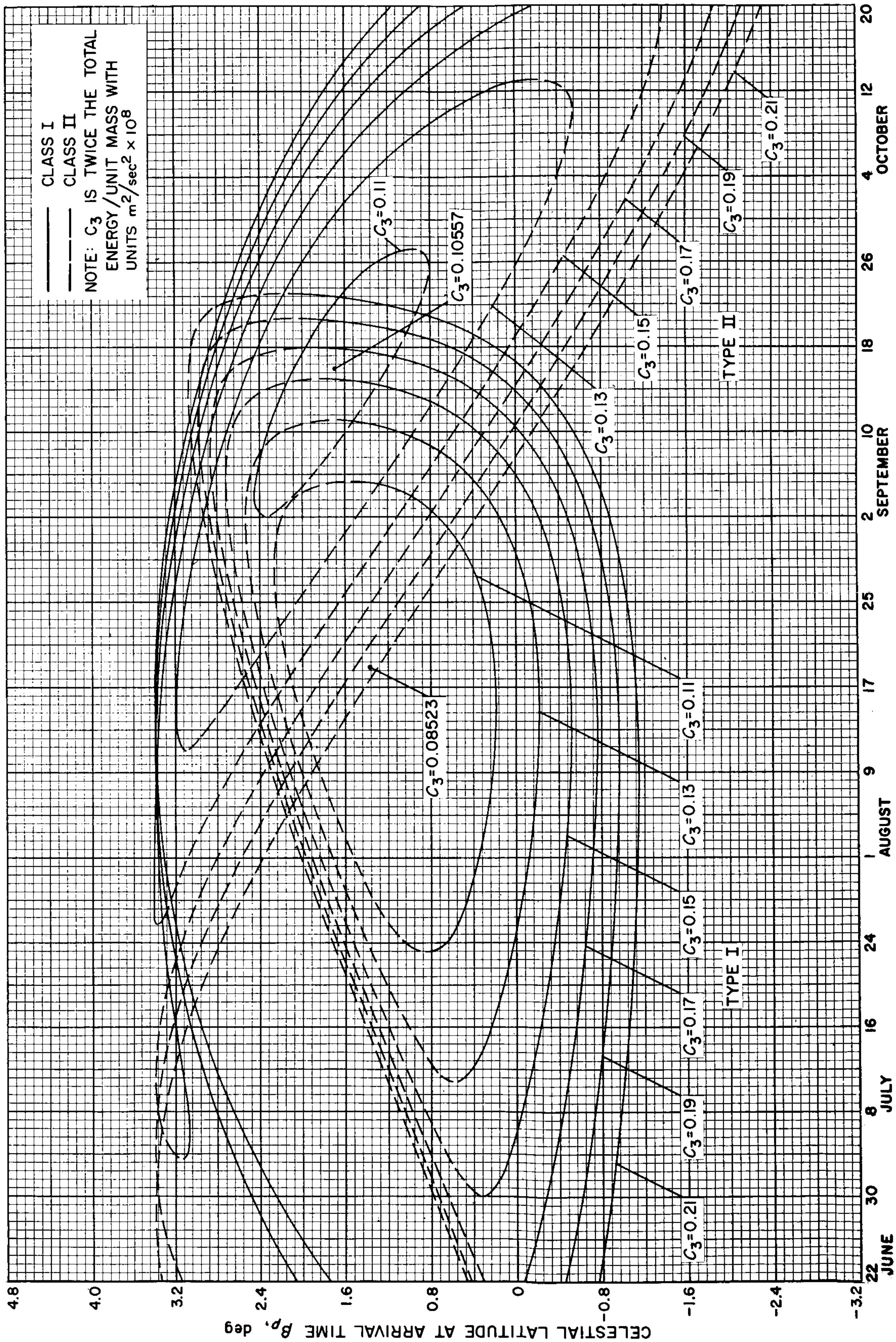

Fig. 10–17. Venus 1970: Celestial latitude at arrival time vs launch date

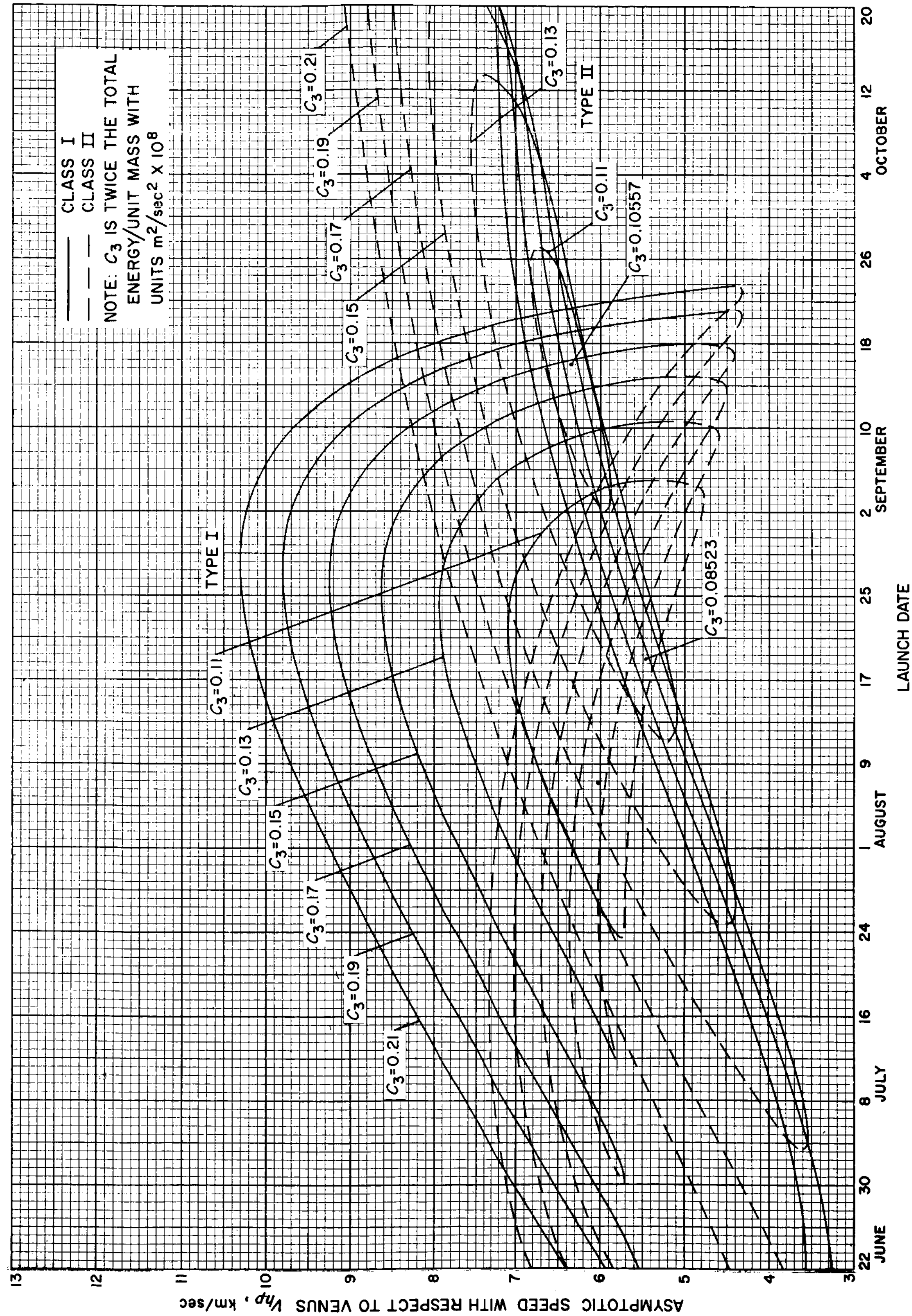

Fig. 10–18. Venus 1970: Asymptotic speed with respect to Venus vs launch date

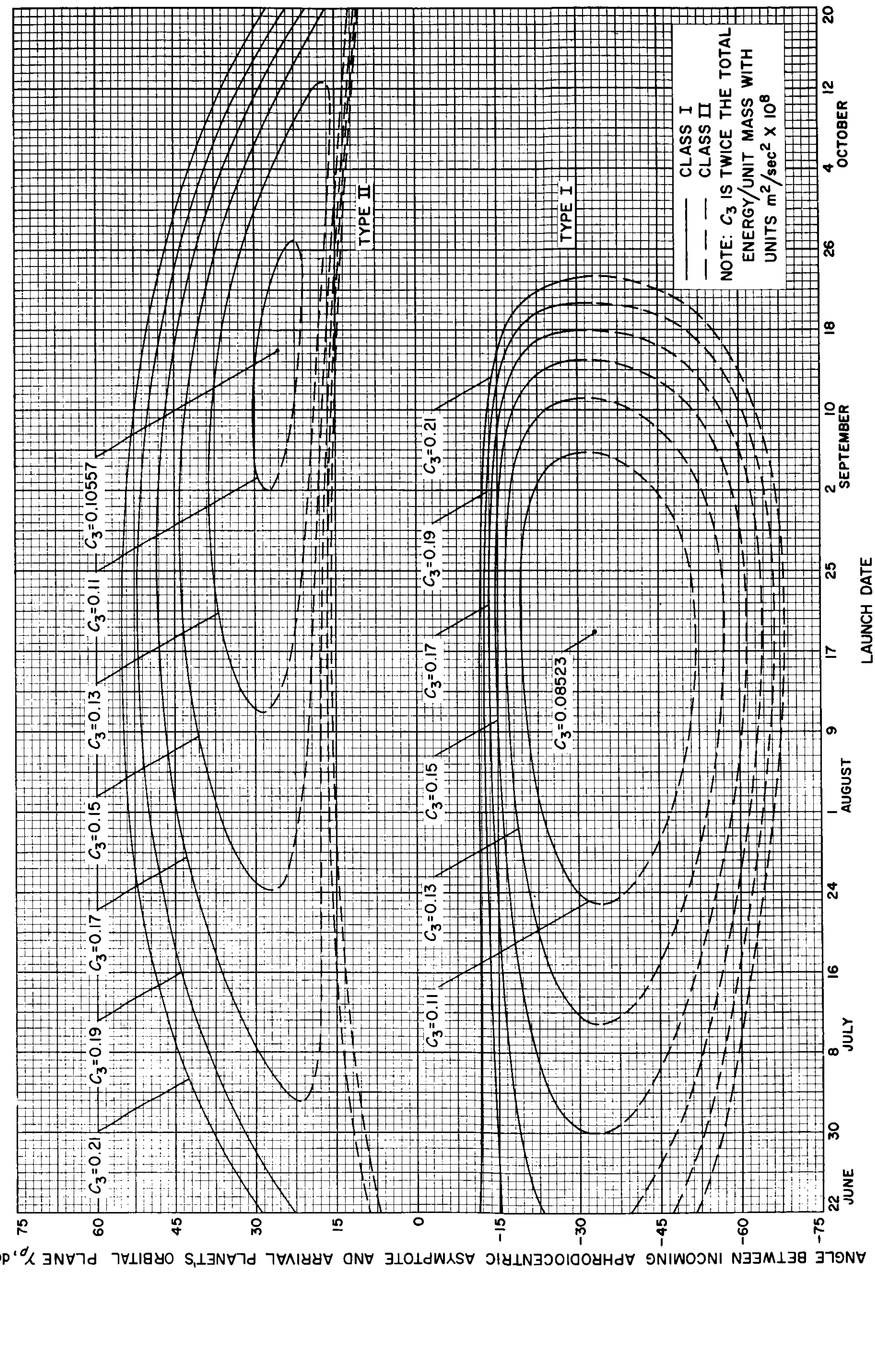

Fig. 10-19. Venus 1970: Angle between incoming aphrodiocentric asymptote and arrival planet's orbital plane vs launch date

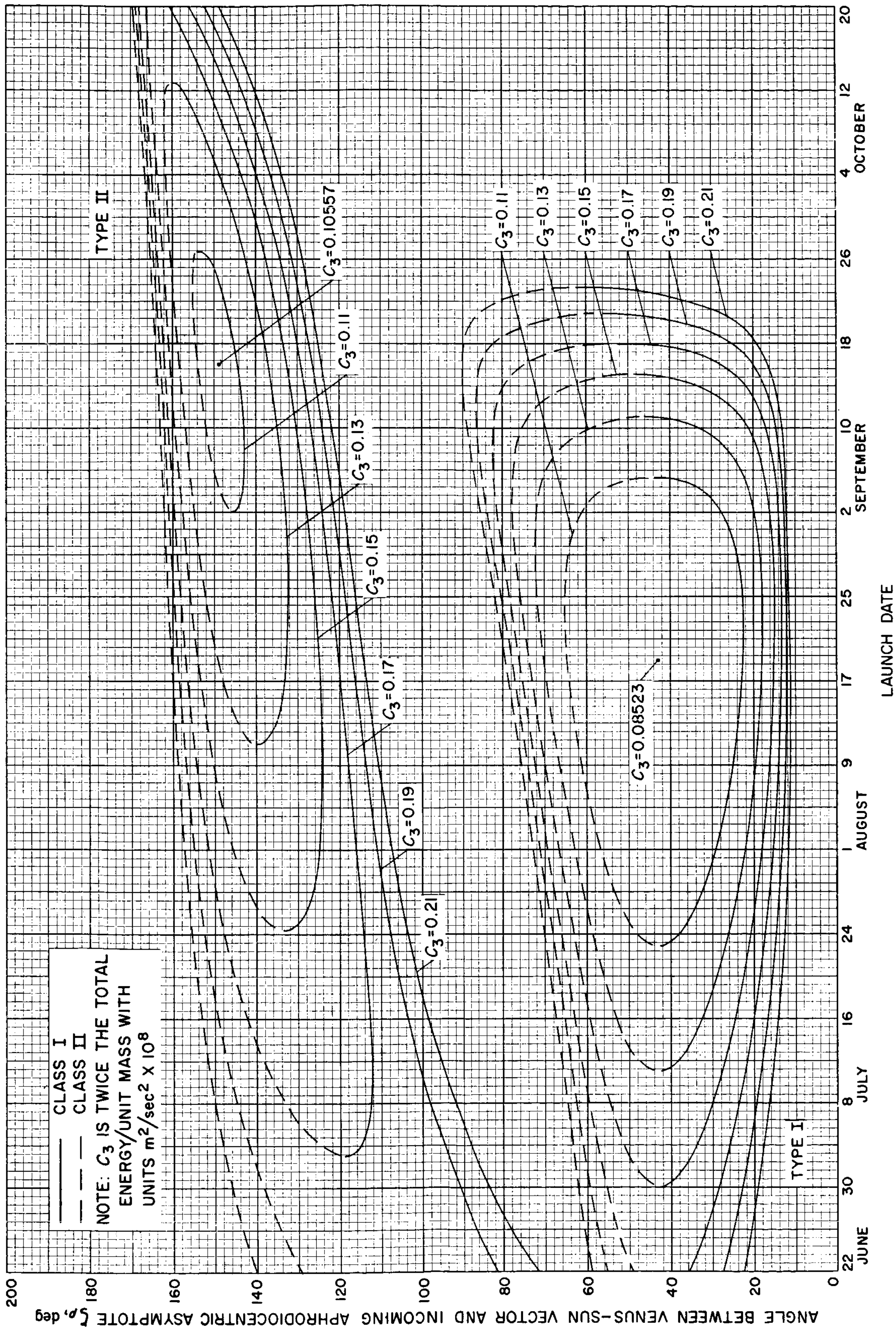

Fig. 10–20. Venus 1970: Angle between Venus–Sun vector and incoming aphrodiocentric asymptote vs launch date

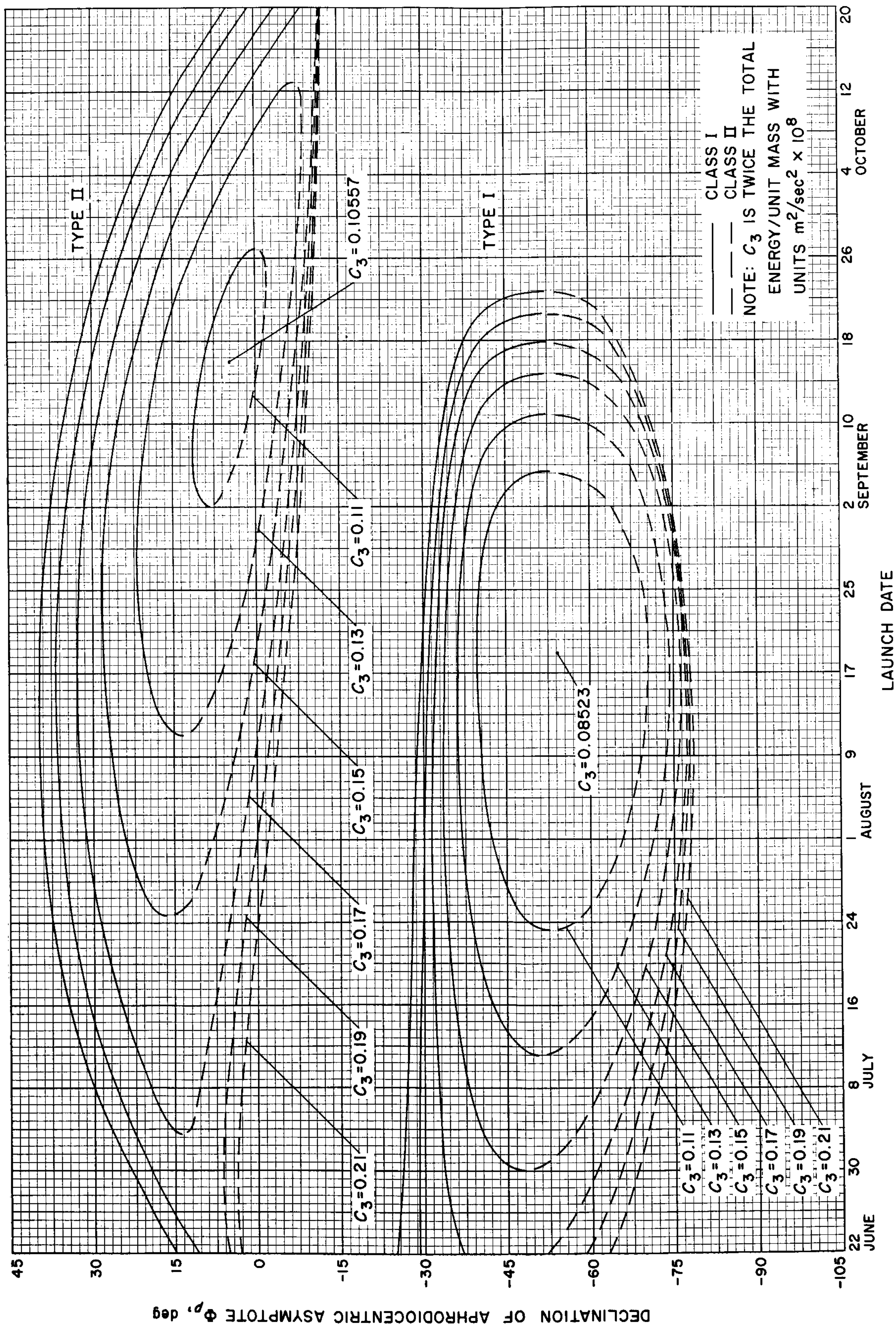

Fig. 10–21. Venus 1970: Declination of aphrodiocentric asymptote vs launch date

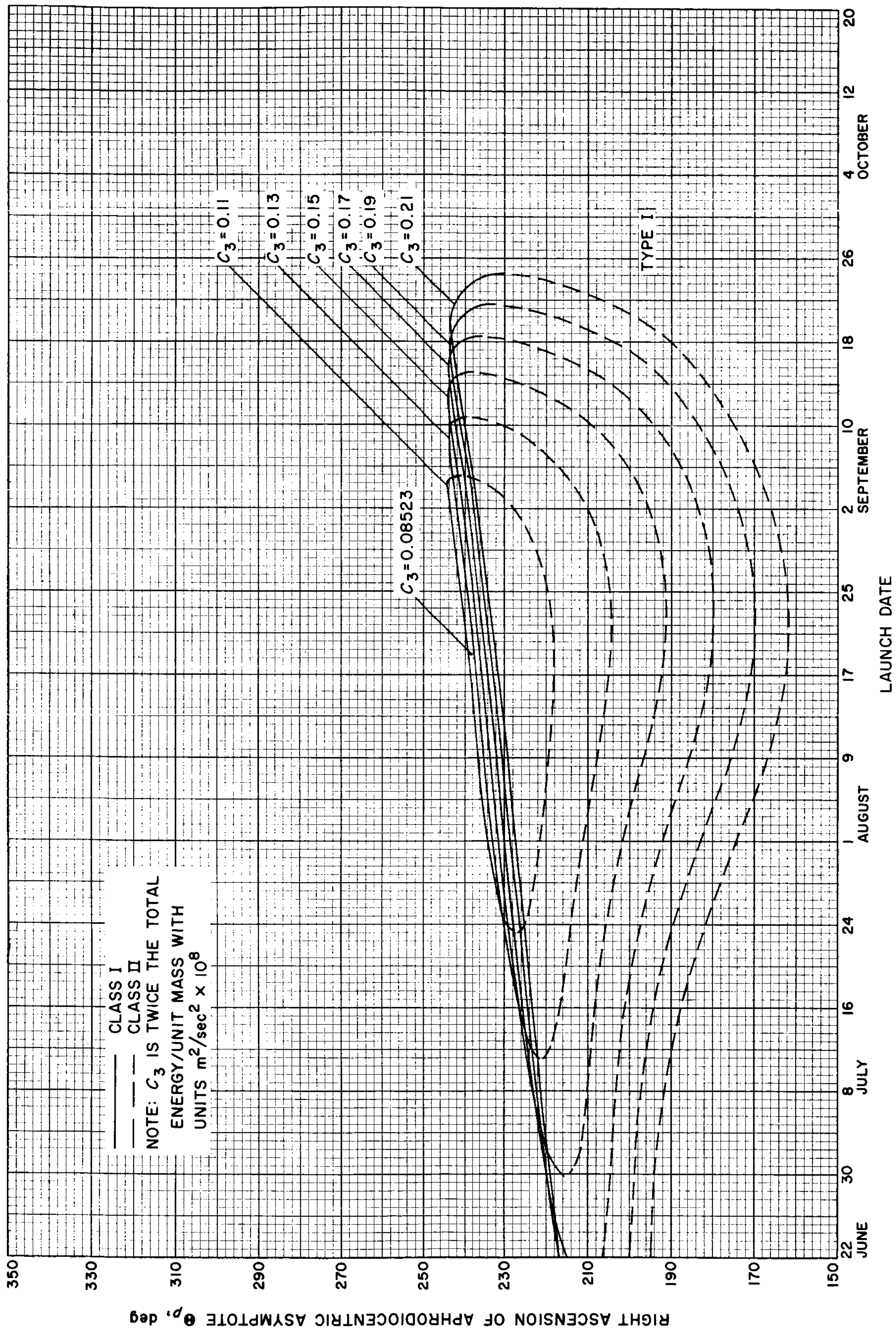

Fig. 10–22. Venus 1970: Right ascension of aphrodiocentric asymptote vs launch date, Type I

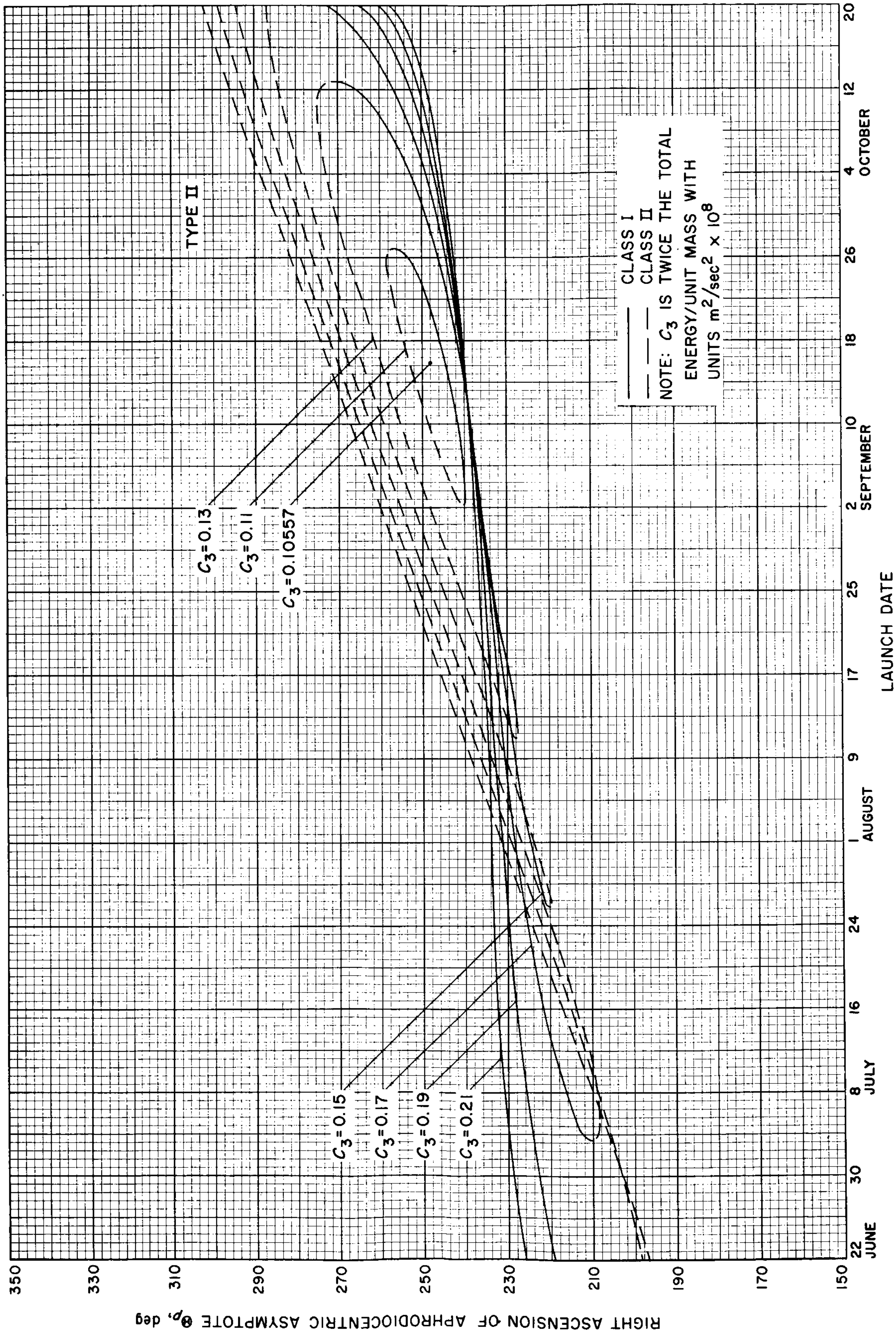

Fig. 10–23. Venus 1970: Right ascension of aphrodiocentric asymptote vs launch date, Type II

XI. MARS 1962: TRAJECTORY-PARAMETER GRAPHS

Figure

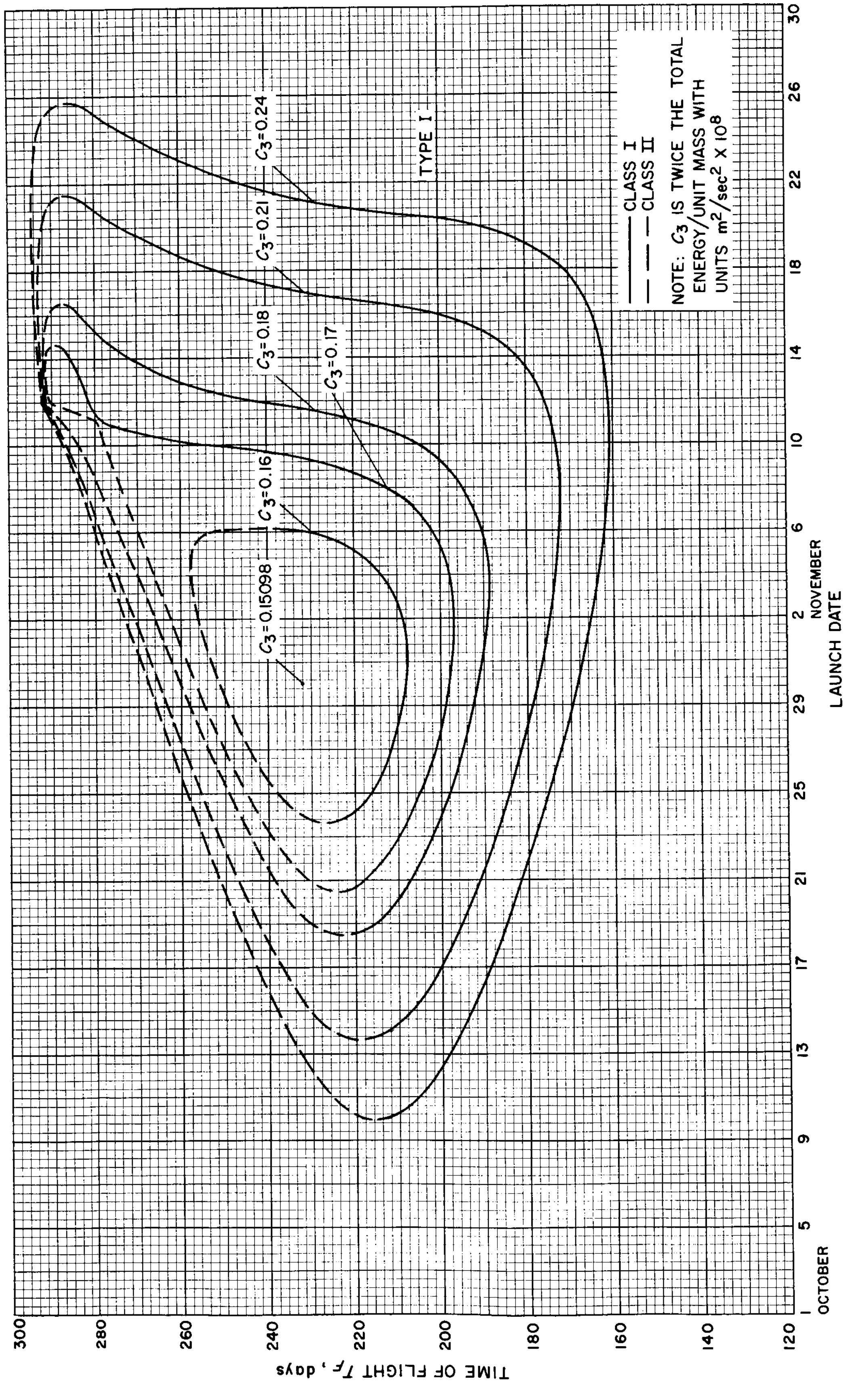

Fig. 11–1. Mars 1962: Time of flight vs launch date

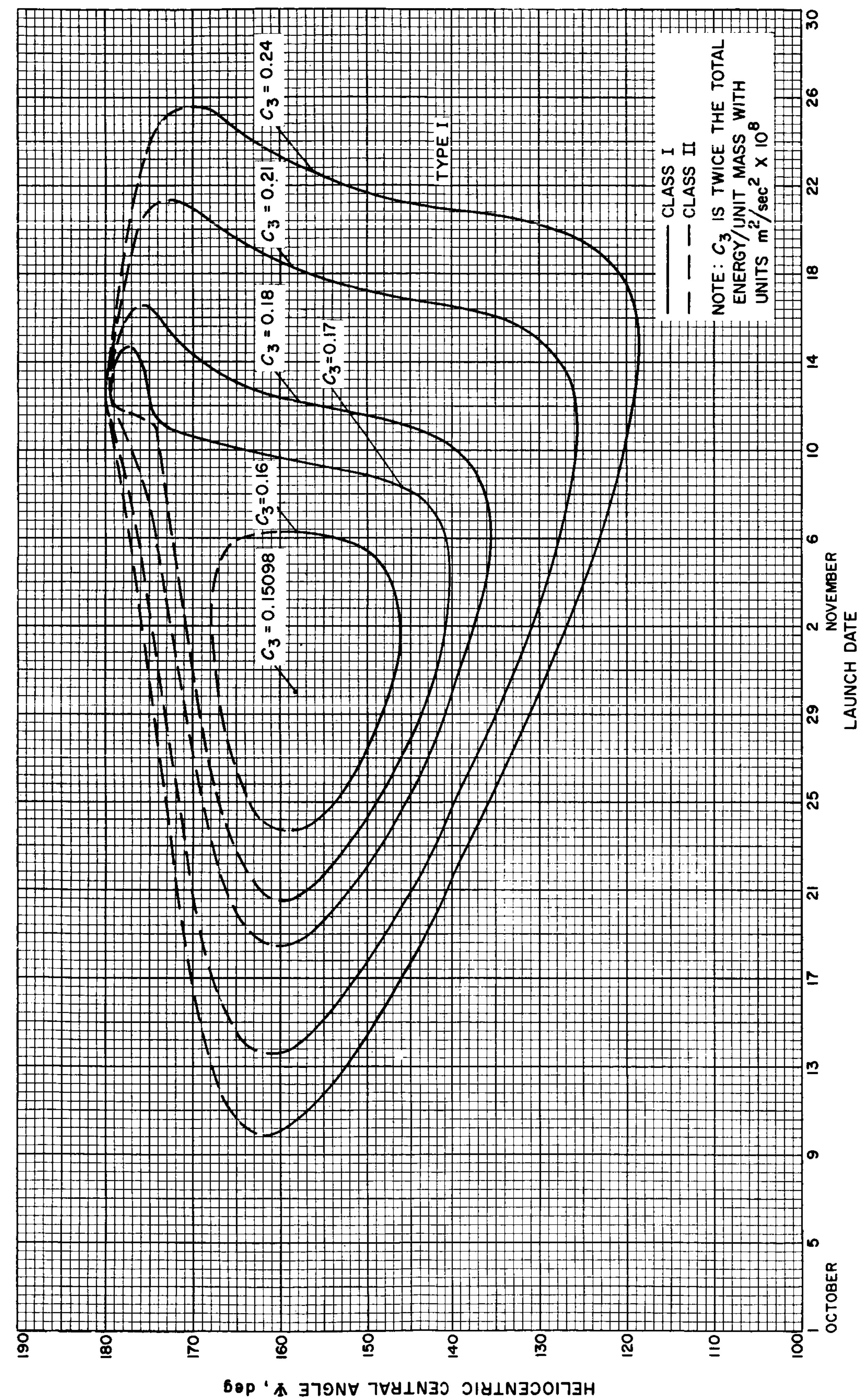

Fig. 11-2. Mars 1962: Heliocentric central angle vs launch date

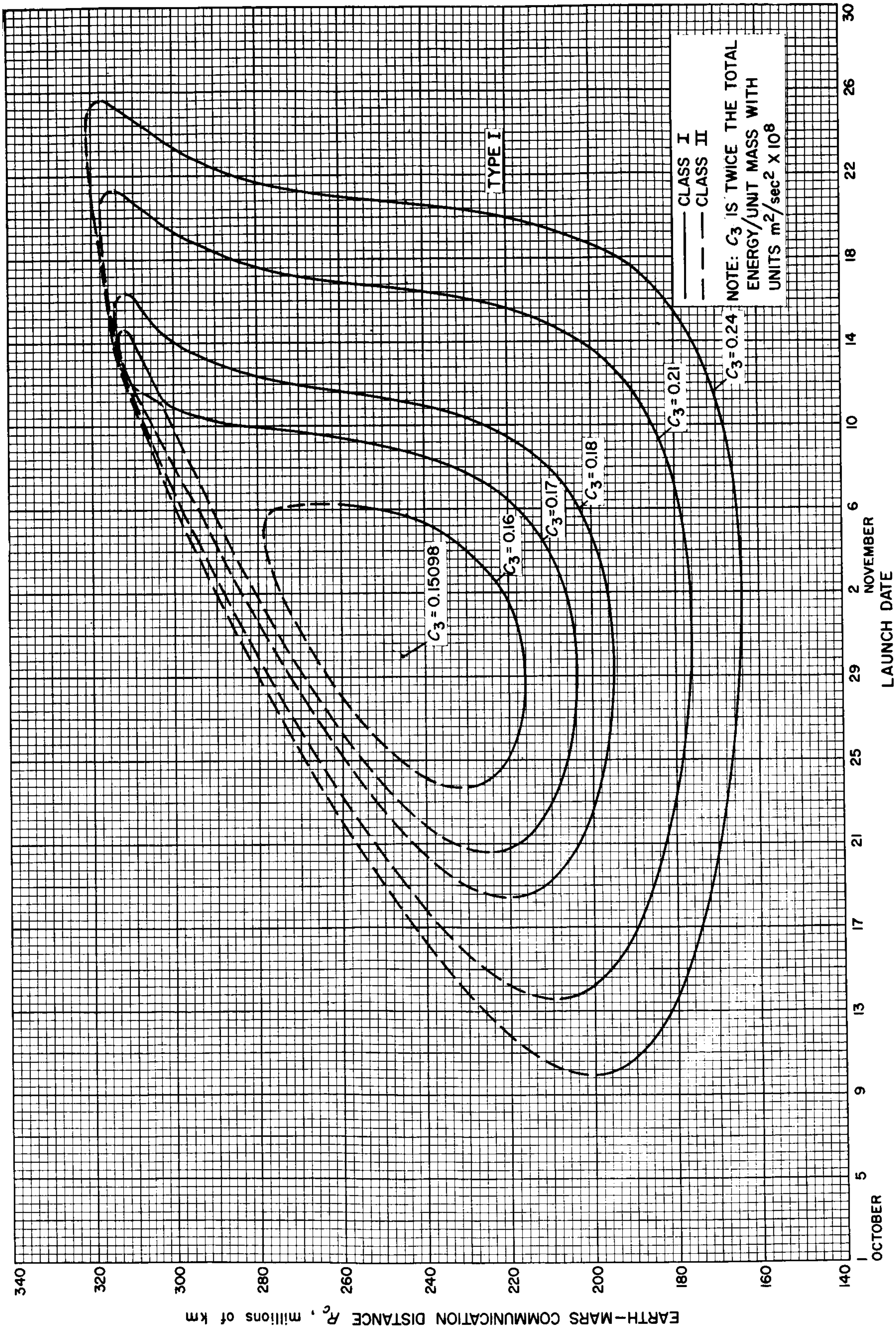

Fig. 11–3. Mars 1962: Earth–Mars communication distance vs launch date

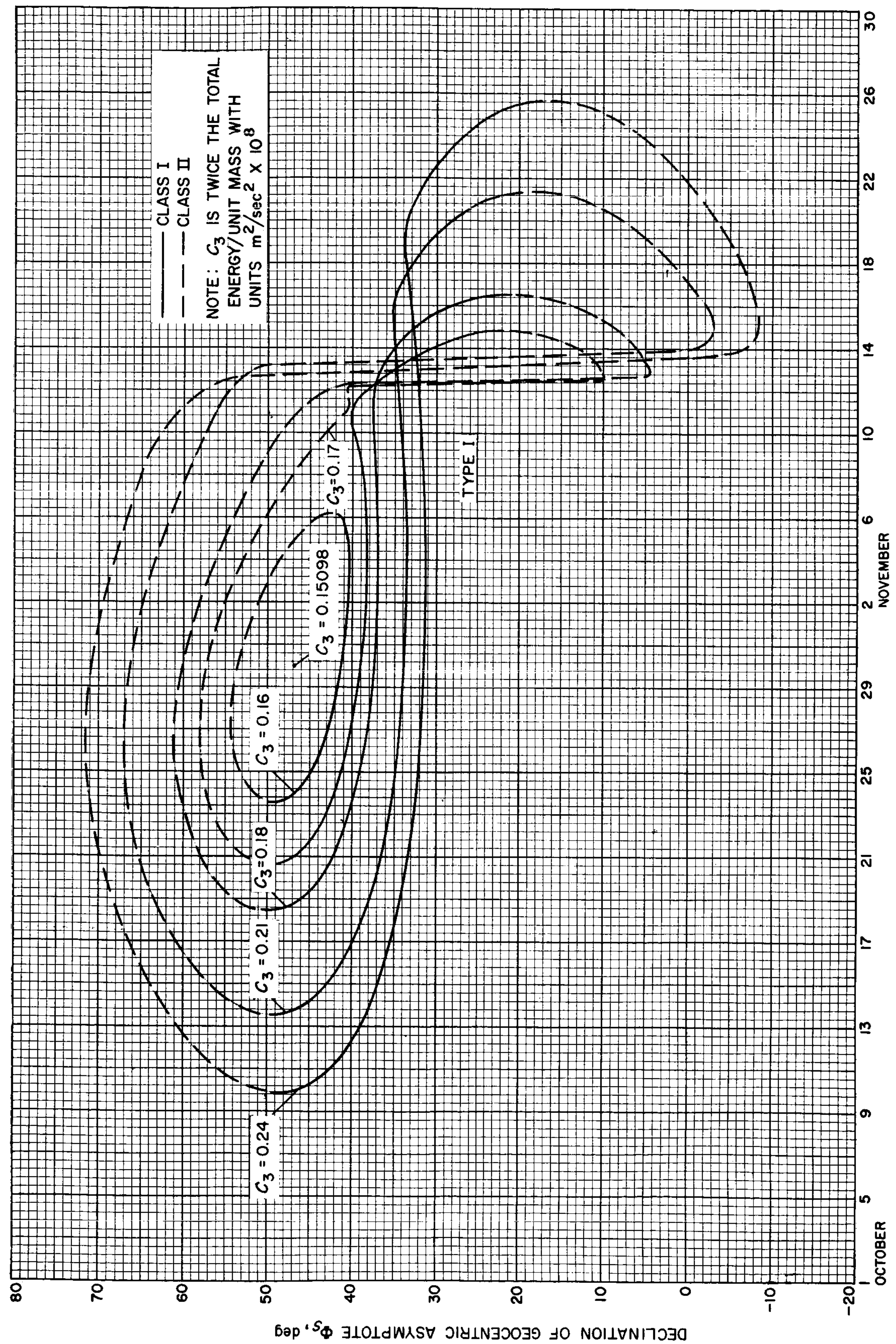

Fig. 11–4. Mars 1962: Declination of geocentric asymptote vs launch date

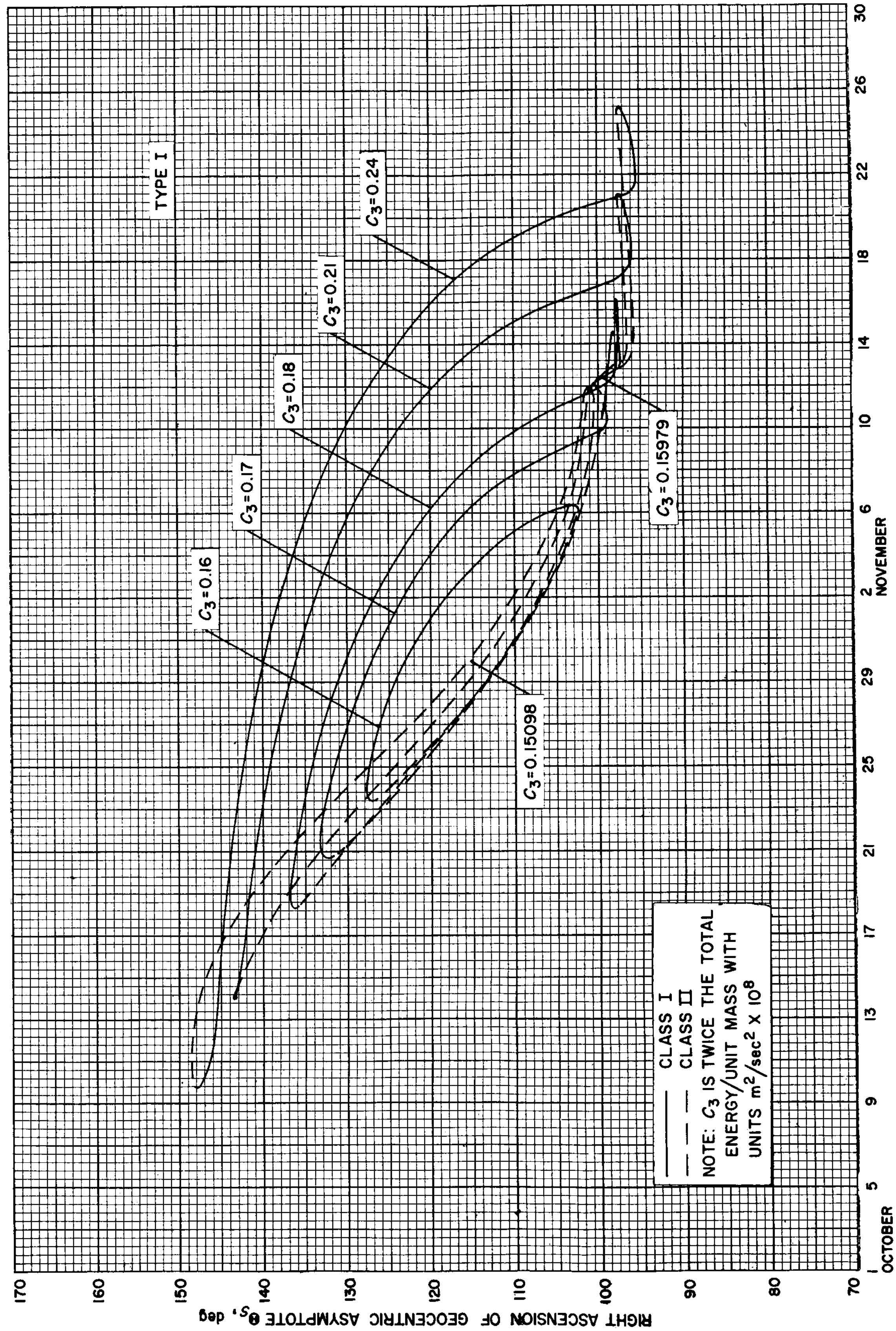

Fig. 11–5. Mars 1962: Right ascension of geocentric asymptote vs launch date

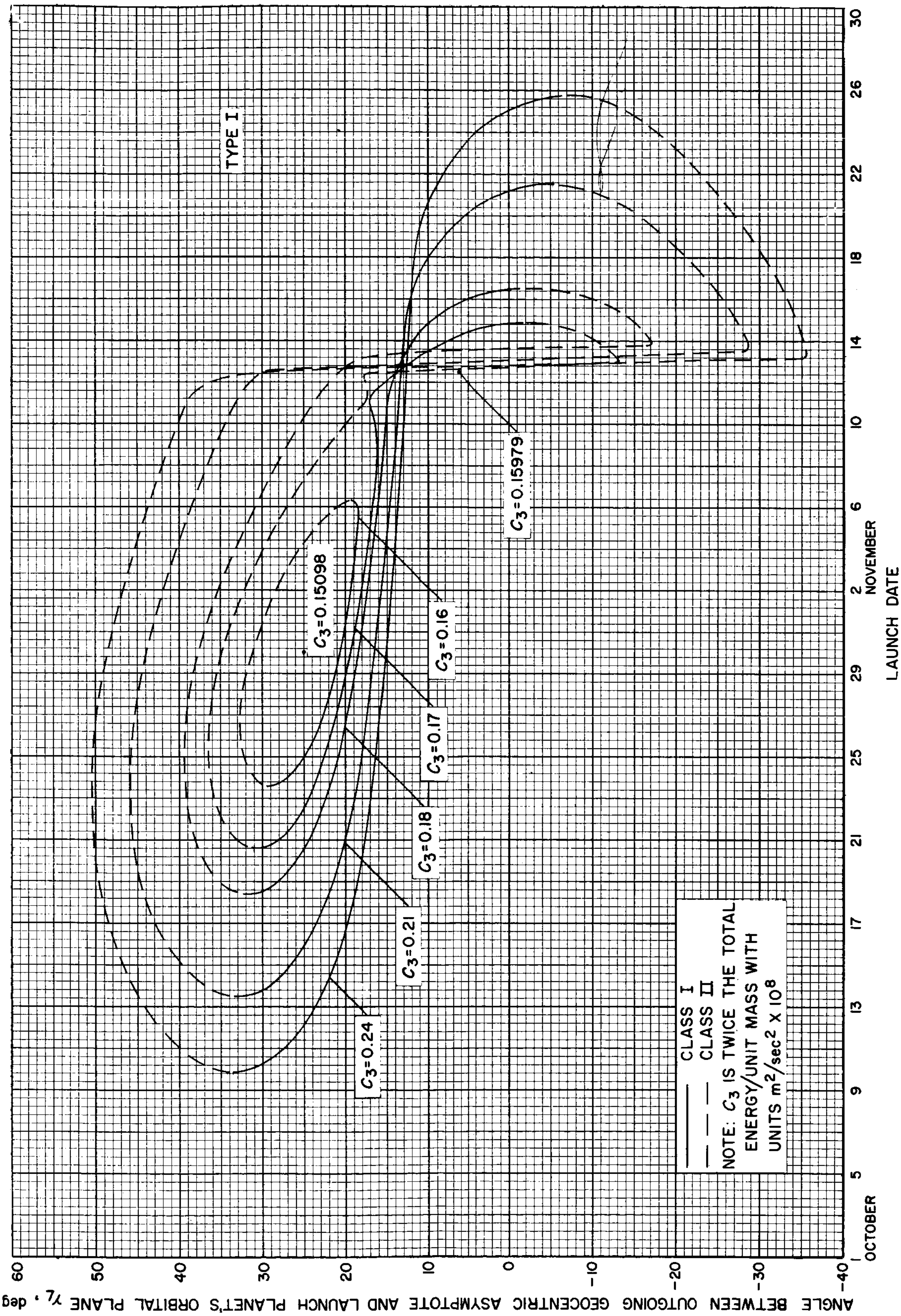

Fig. 11–6. Mars 1962: Angle between outgoing geocentric asymptote and launch planet's orbital plane vs launch date

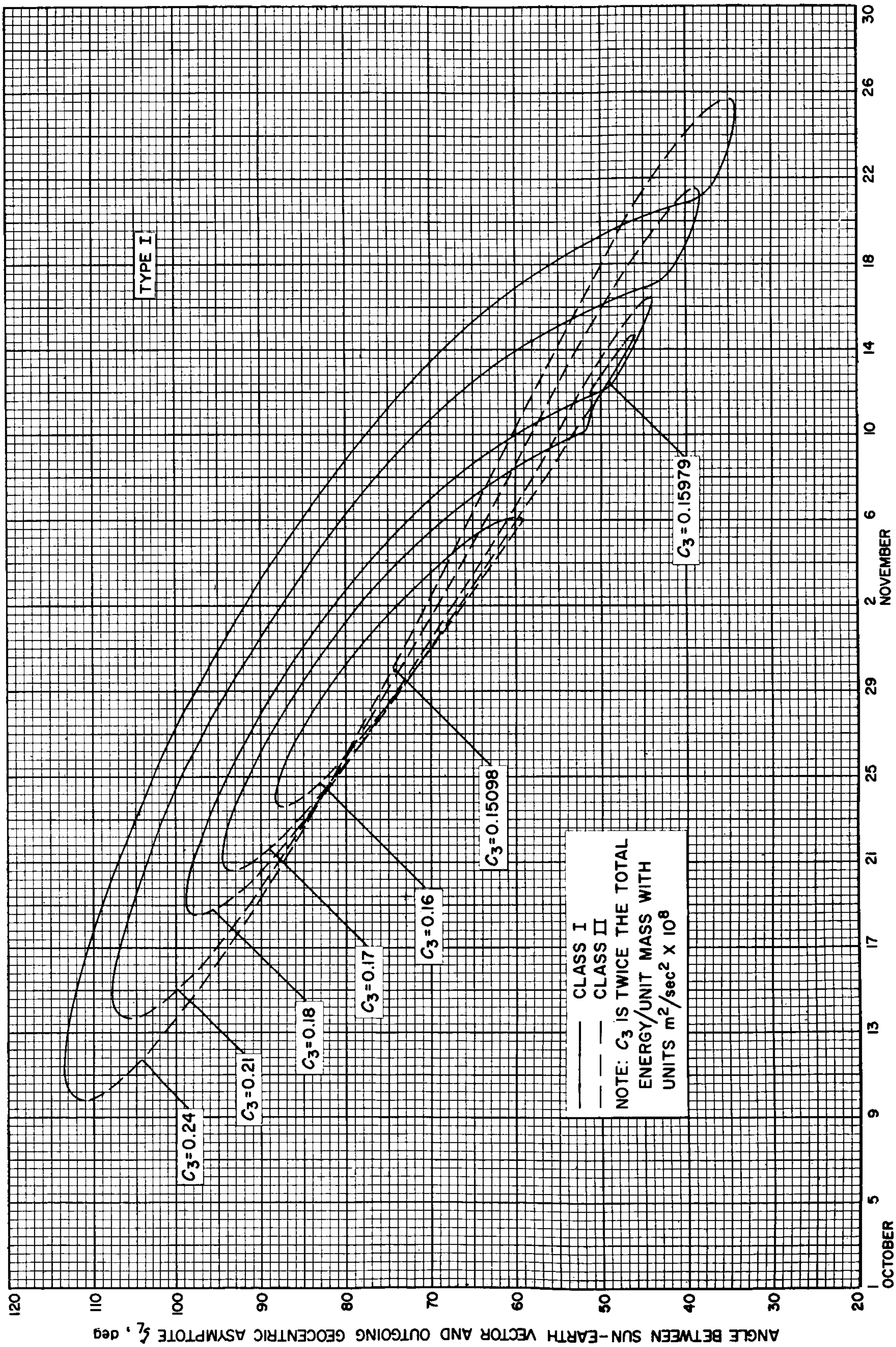

Fig. 11–7. Mars 1962: Angle between Sun–Earth vector and outgoing geocentric asymptote vs launch date

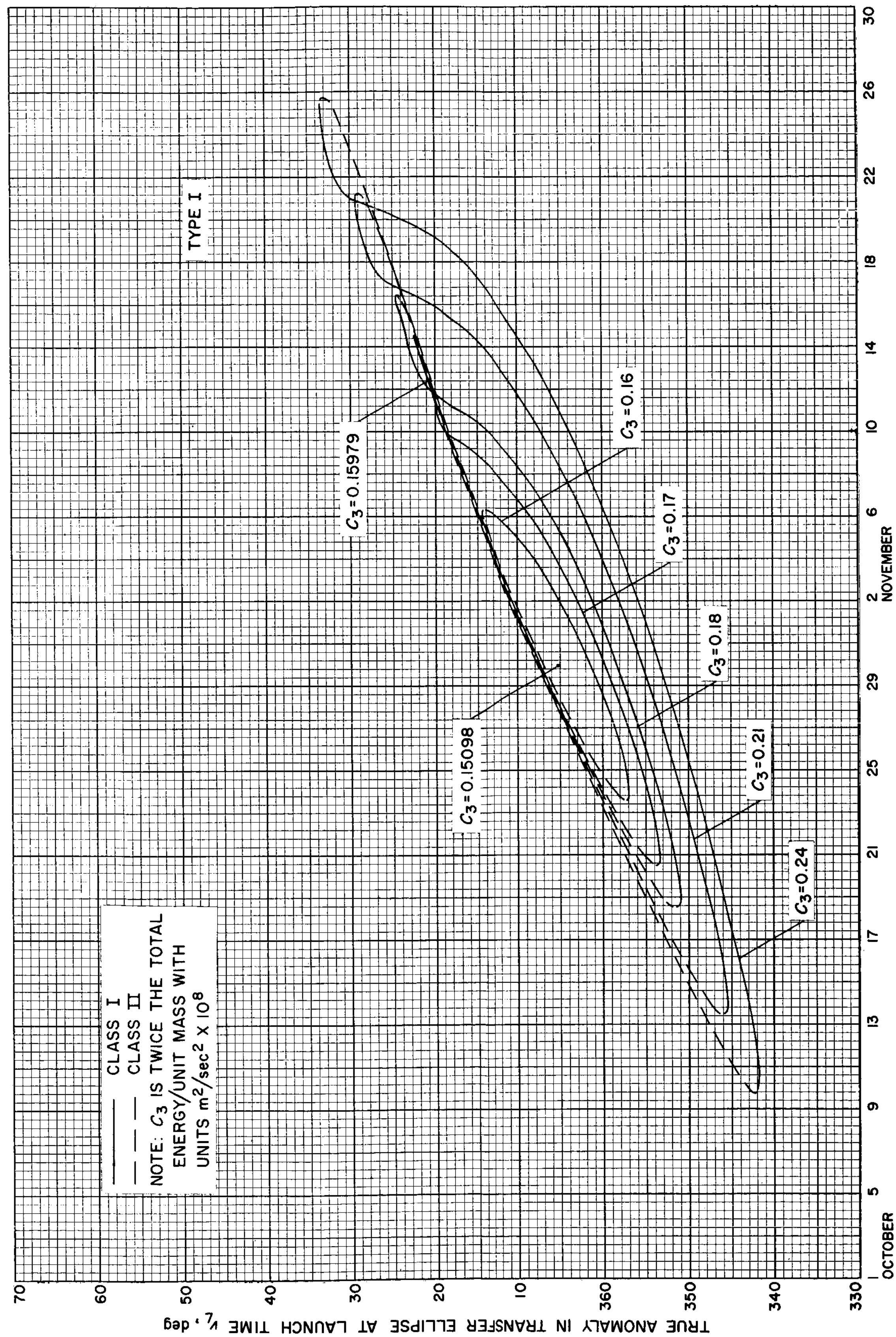

Fig. 11–8. Mars 1962: True anomaly in transfer ellipse at launch time vs launch date

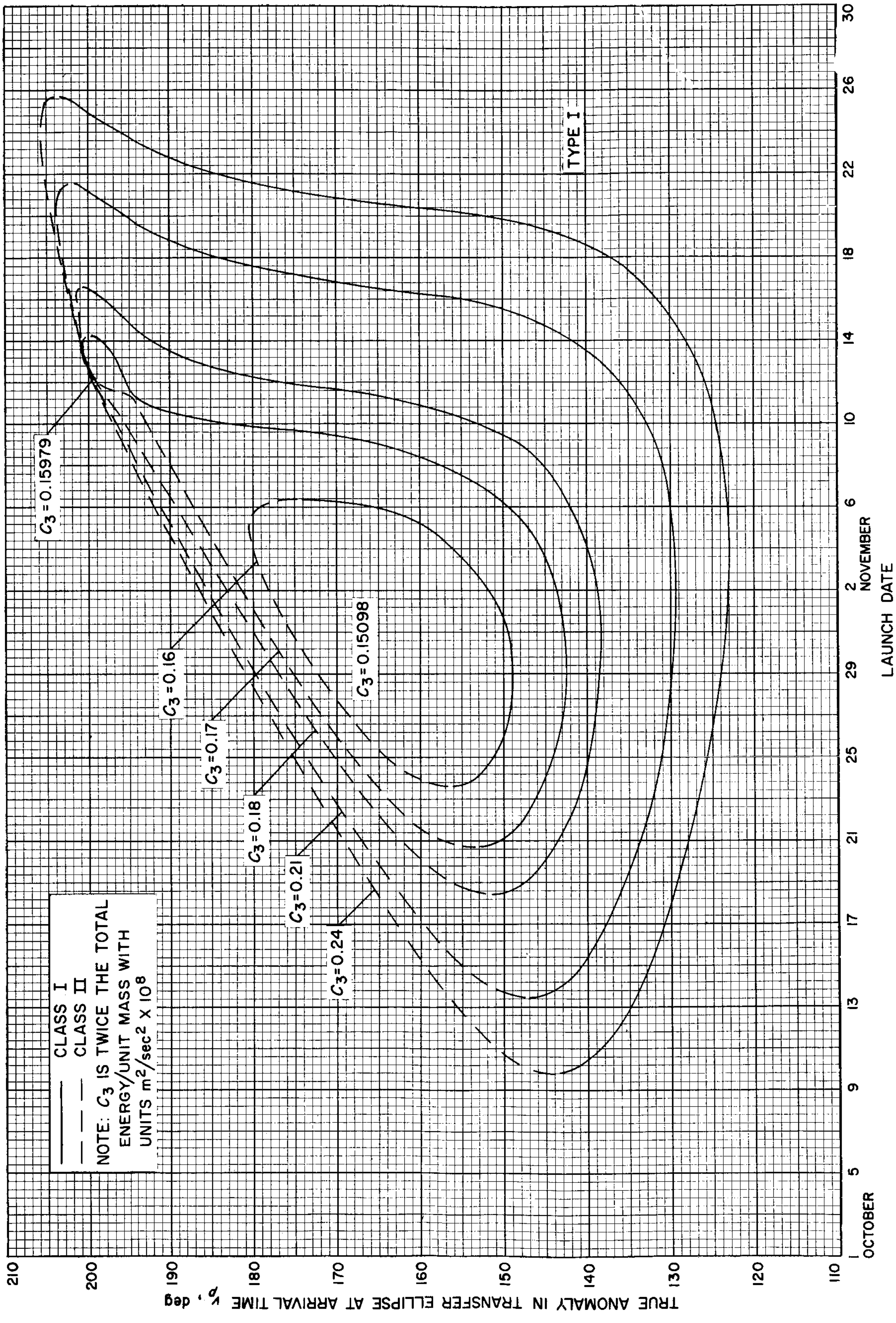

Fig. 11–9. Mars 1962: True anomaly in transfer ellipse at arrival time vs. launch date

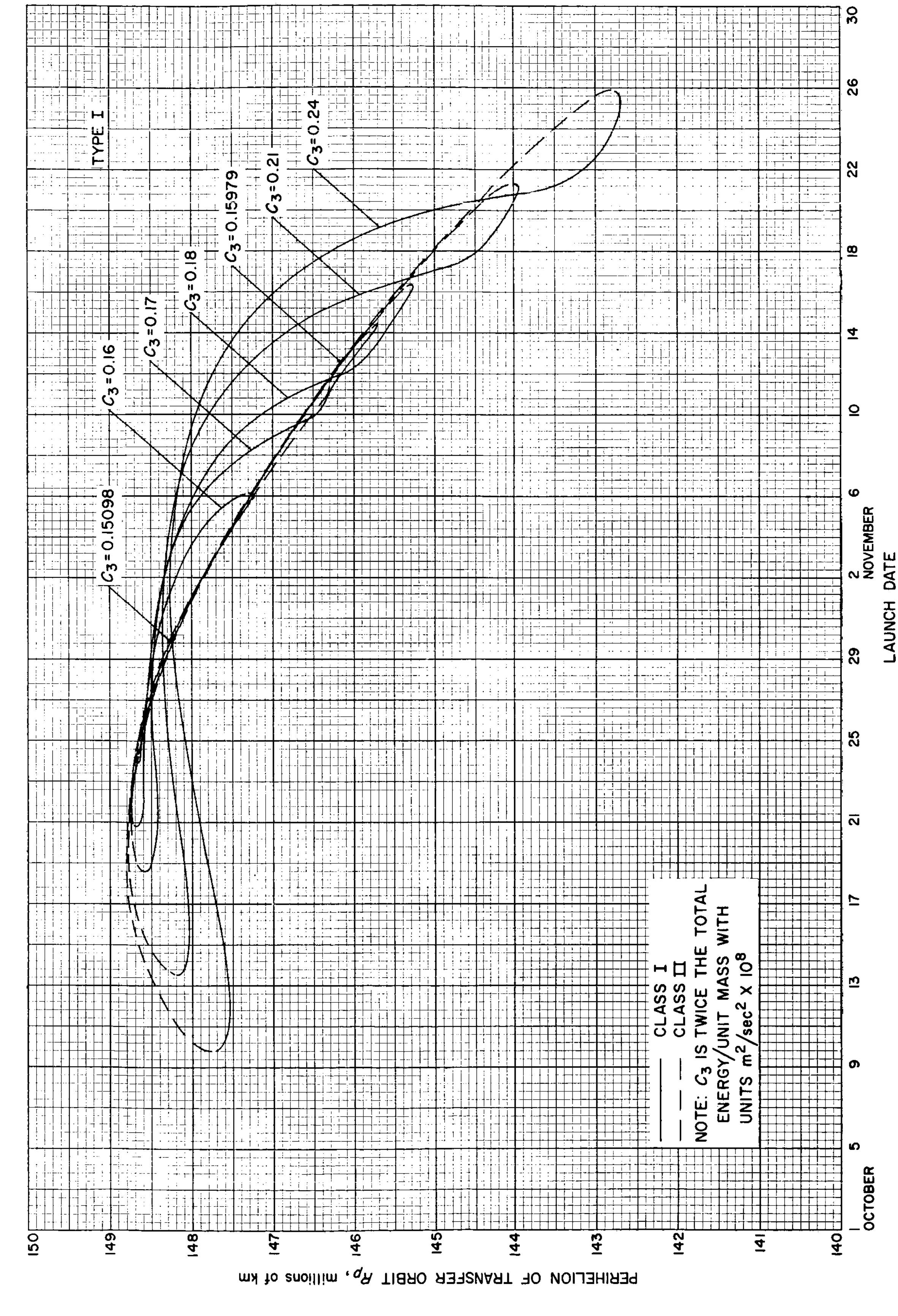

Fig. 11–10. *Mars* 1962: Perihelion of transfer orbit vs launch date

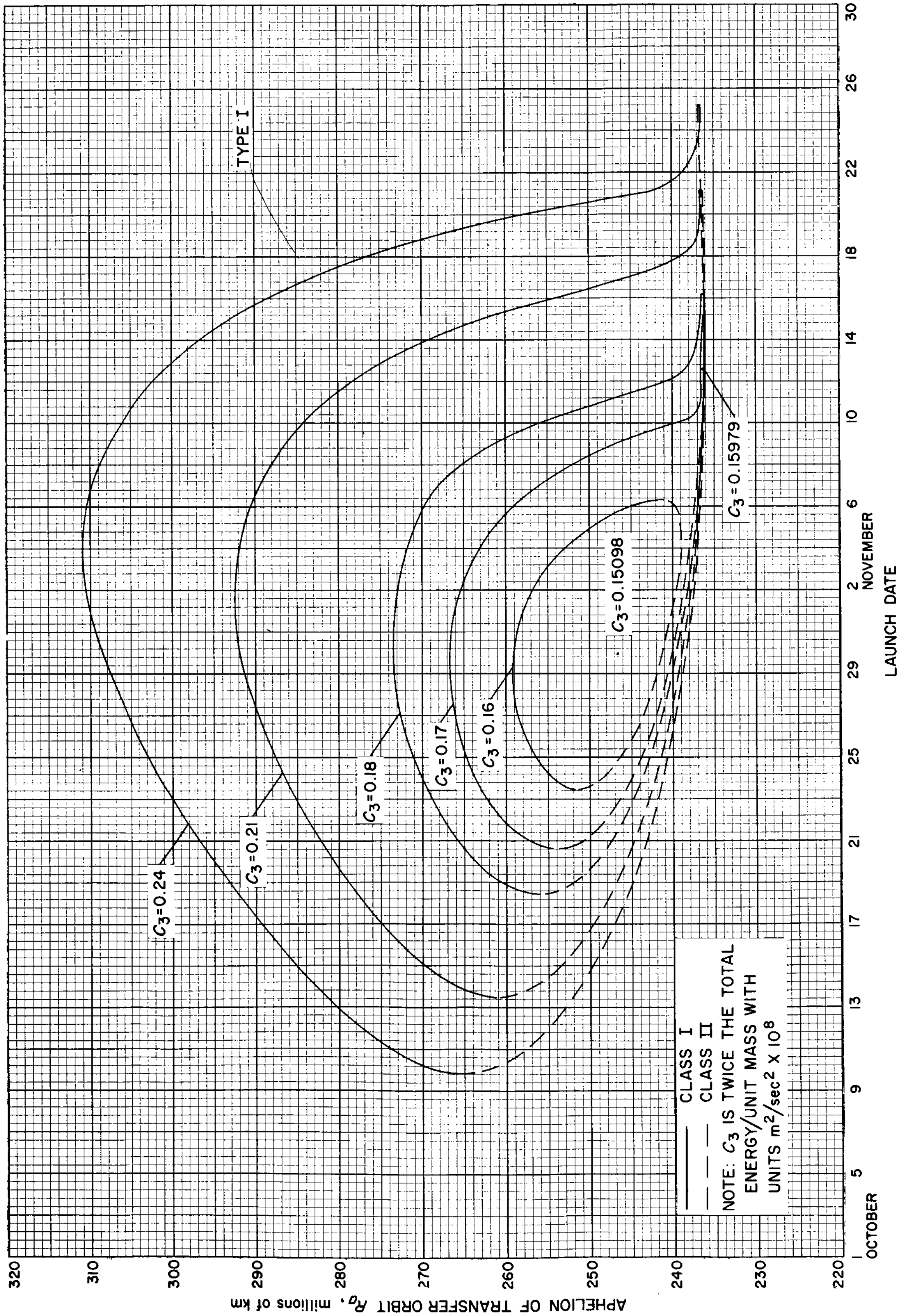

Fig. 11-11. *Mars 1962:* Aphelion of transfer orbit vs launch date

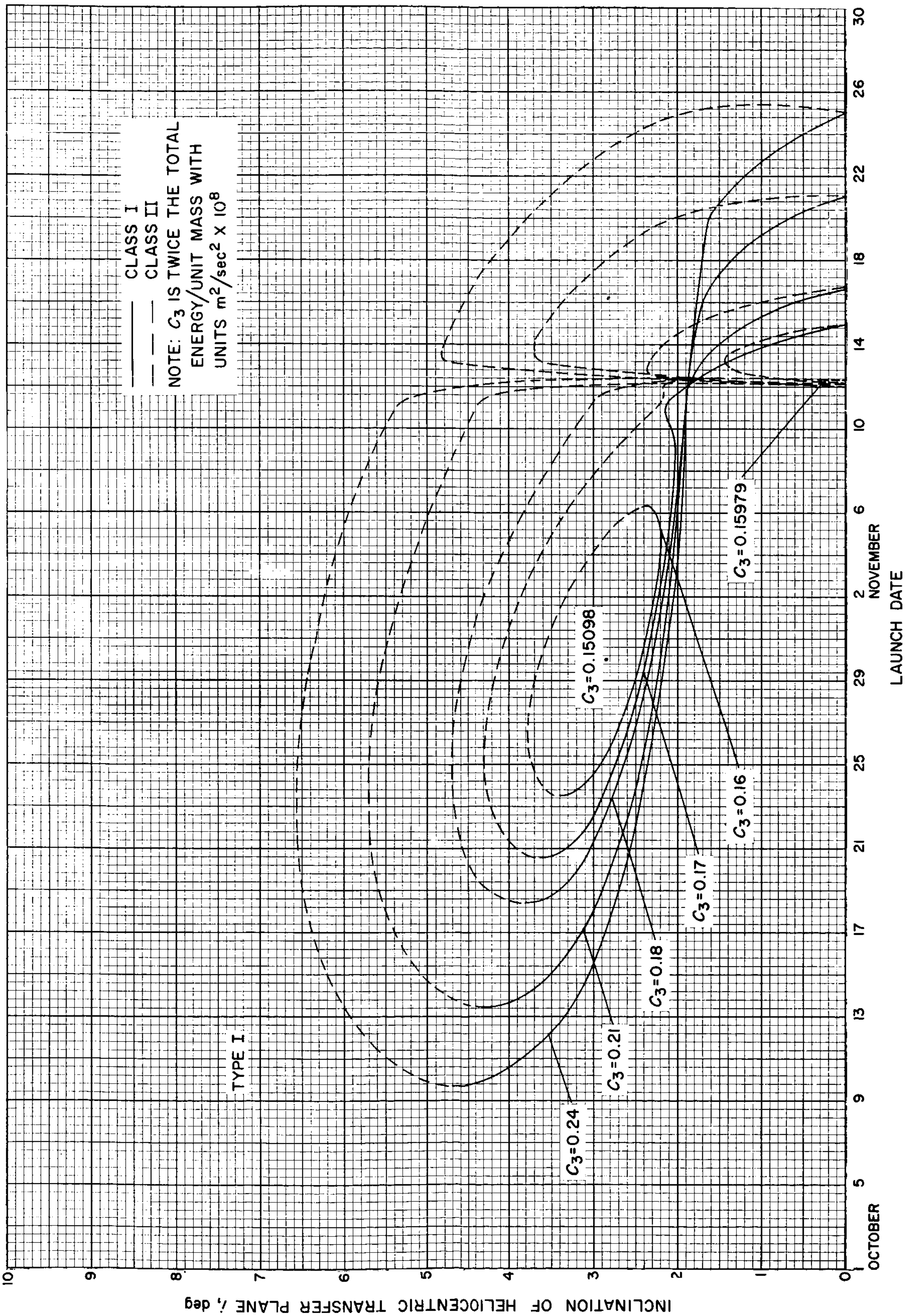

Fig. 11-12. Mars 1962: Inclination of heliocentric-transfer plane vs launch date

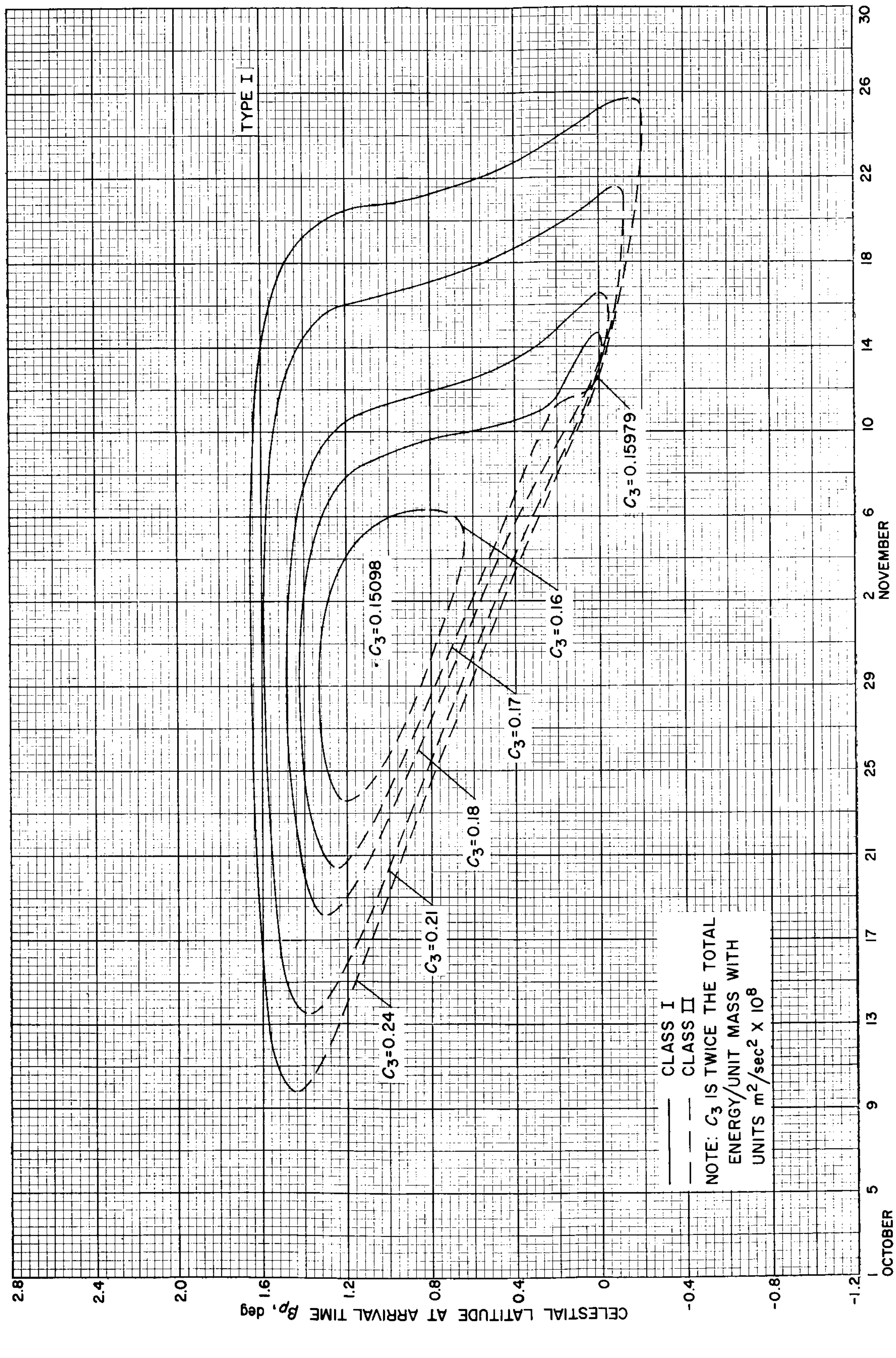

Fig. 11-13. *Mars 1962:* **Celestial latitude at arrival time vs launch date**

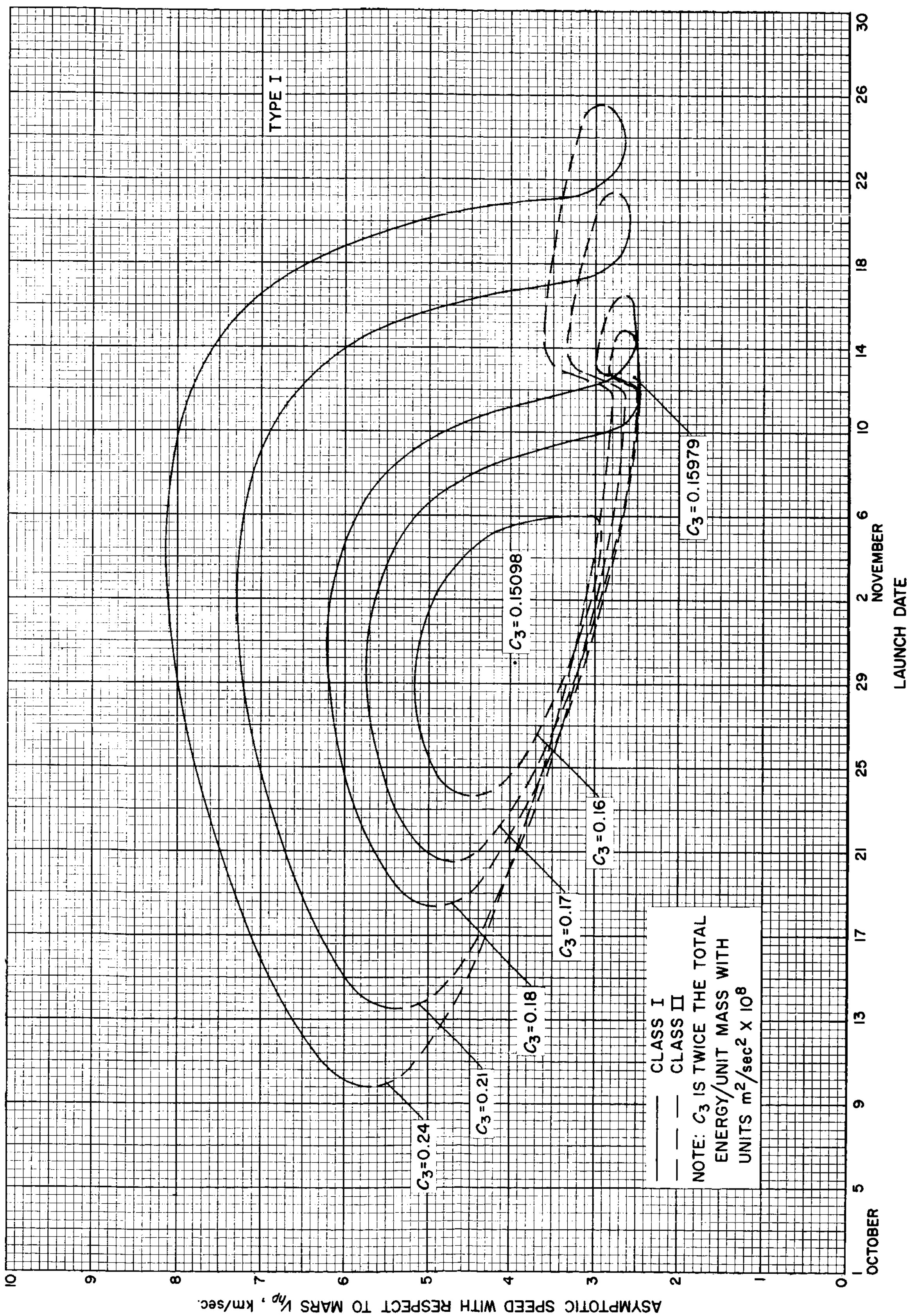

Fig. 11-14. *Mars* 1962: Asymptotic speed with respect to Mars vs launch date

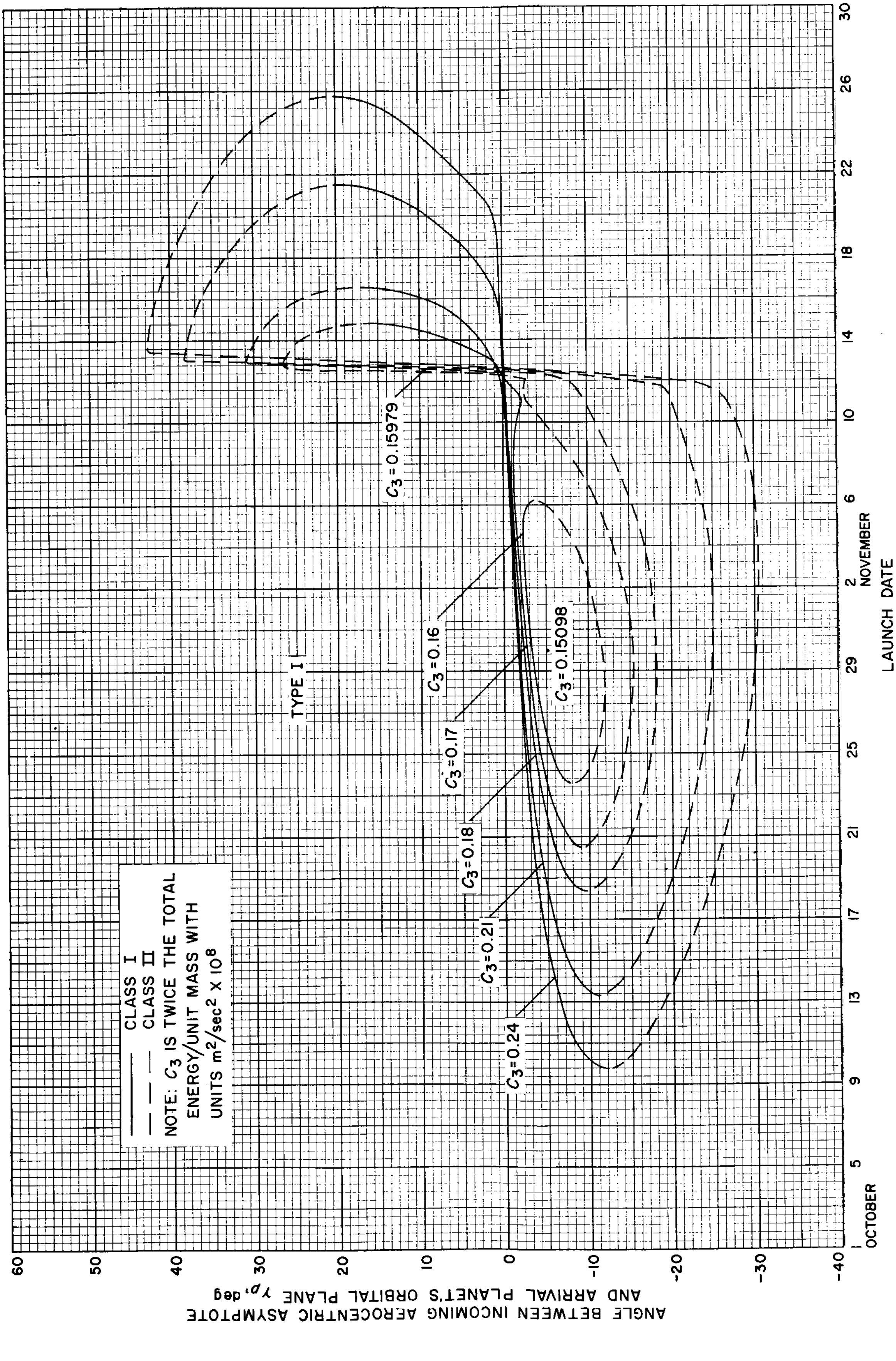

Fig. 11–15. Mars 1962: Angle between incoming aerocentric asymptote and arrival planet's orbital plane vs launch date

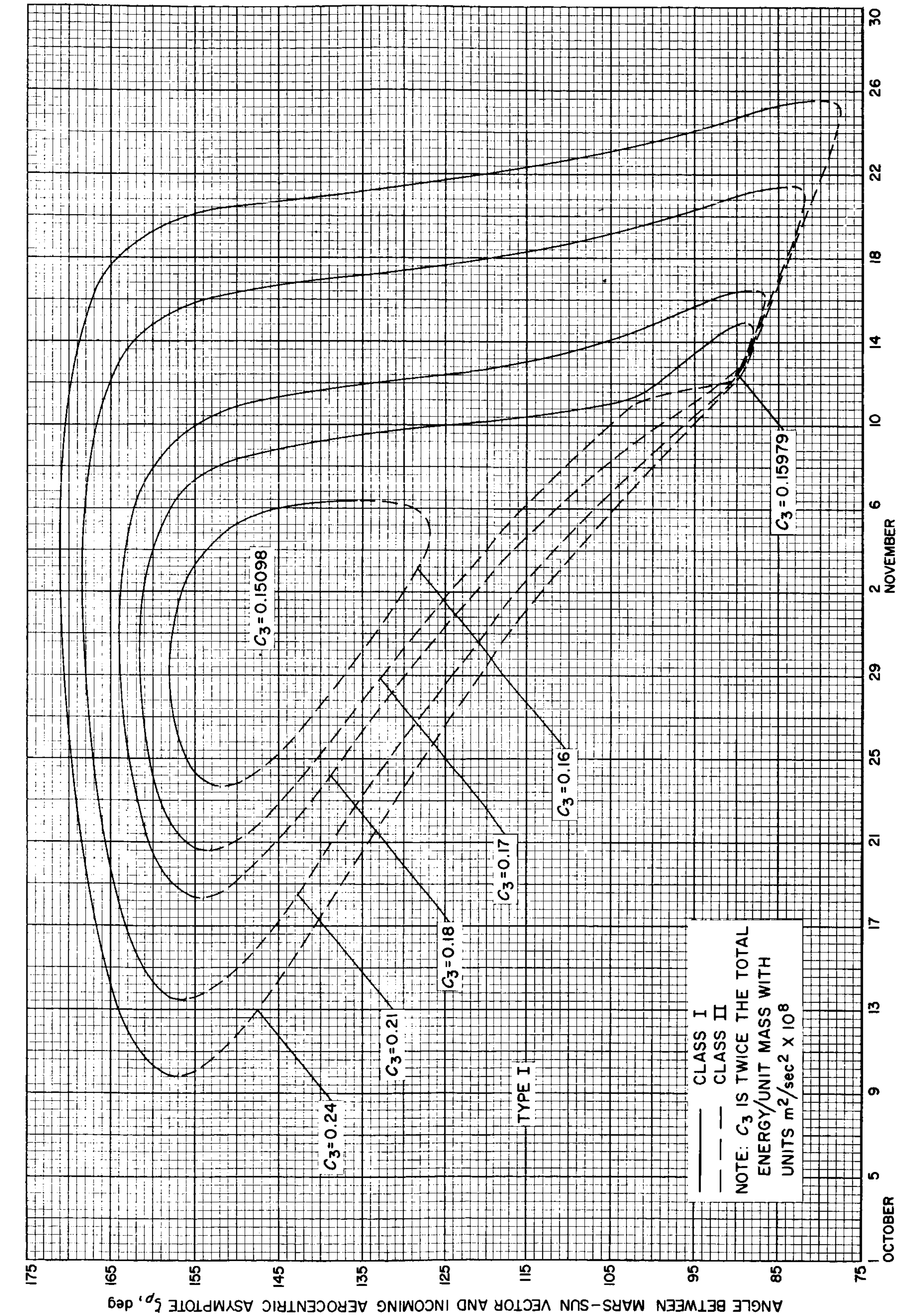

Fig. 11-16. Mars 1962: Angle between Mars–Sun vector and incoming aerocentric asymptote vs launch date

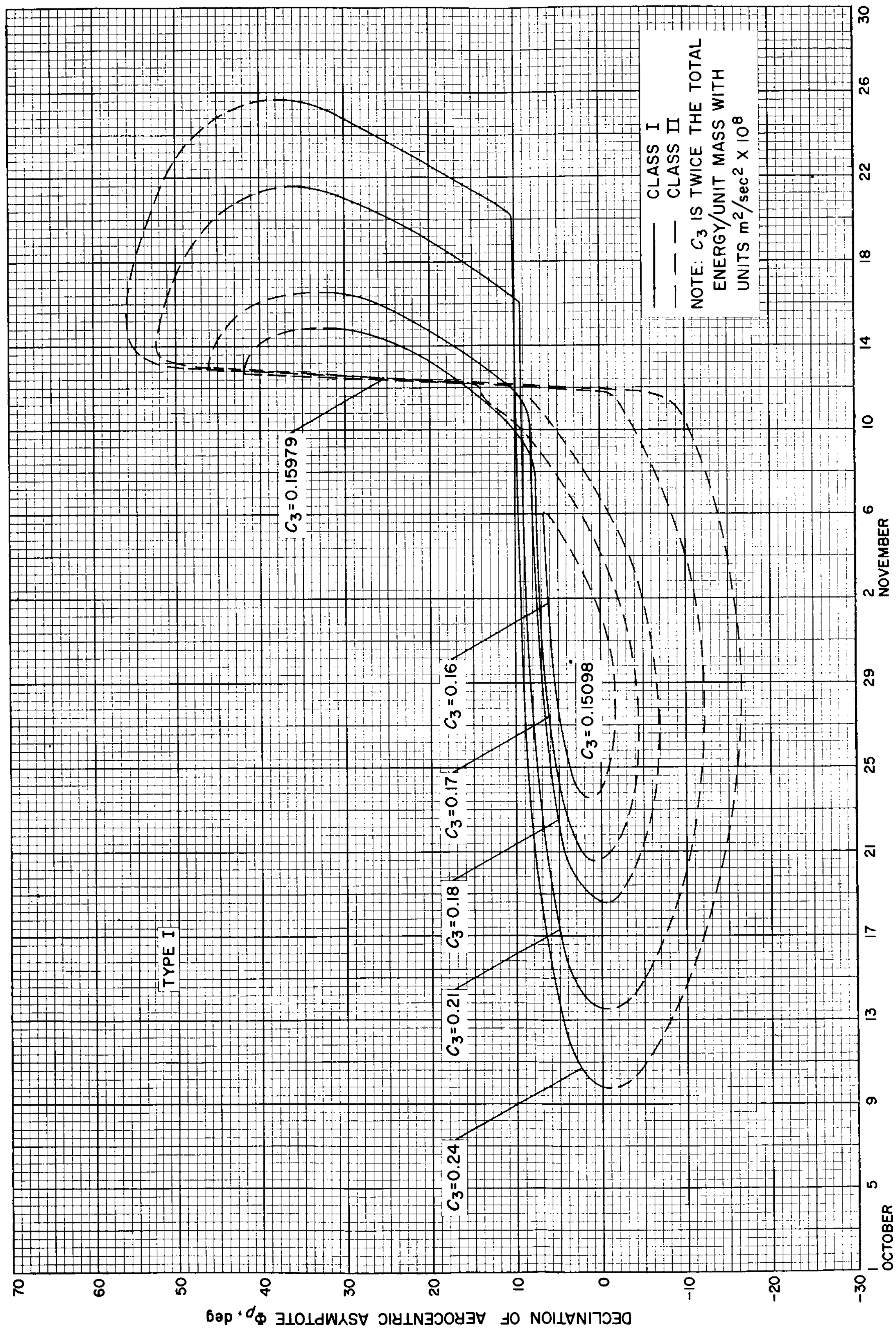

Fig. 11-17. Mars 1962: Declination of aerocentric asymptote vs launch date

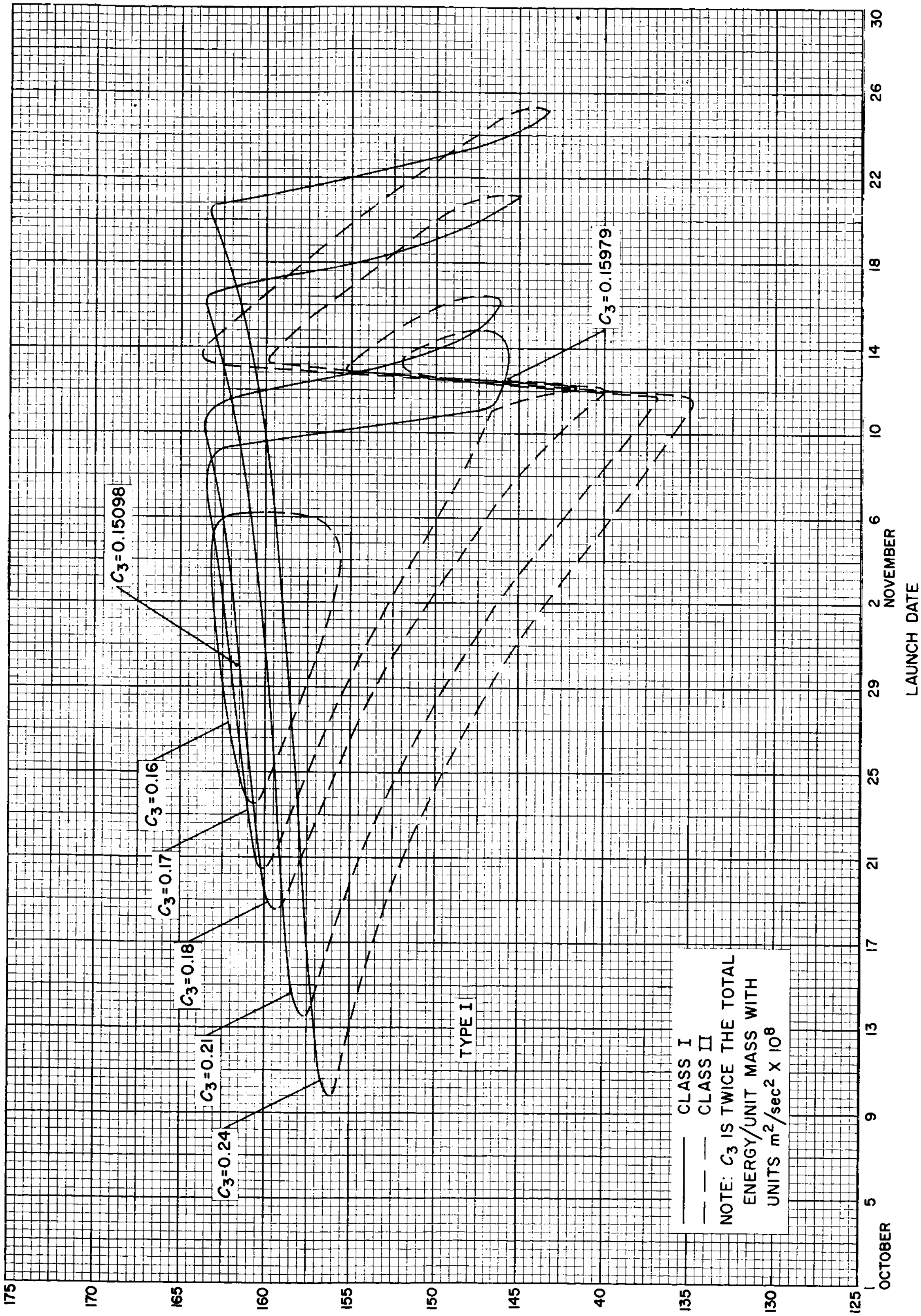

Fig. 11–18. Mars 1962: Right ascension of aerocentric asymptote vs launch date

XII. MARS 1964: TRAJECTORY-PARAMETER GRAPHS

Figure

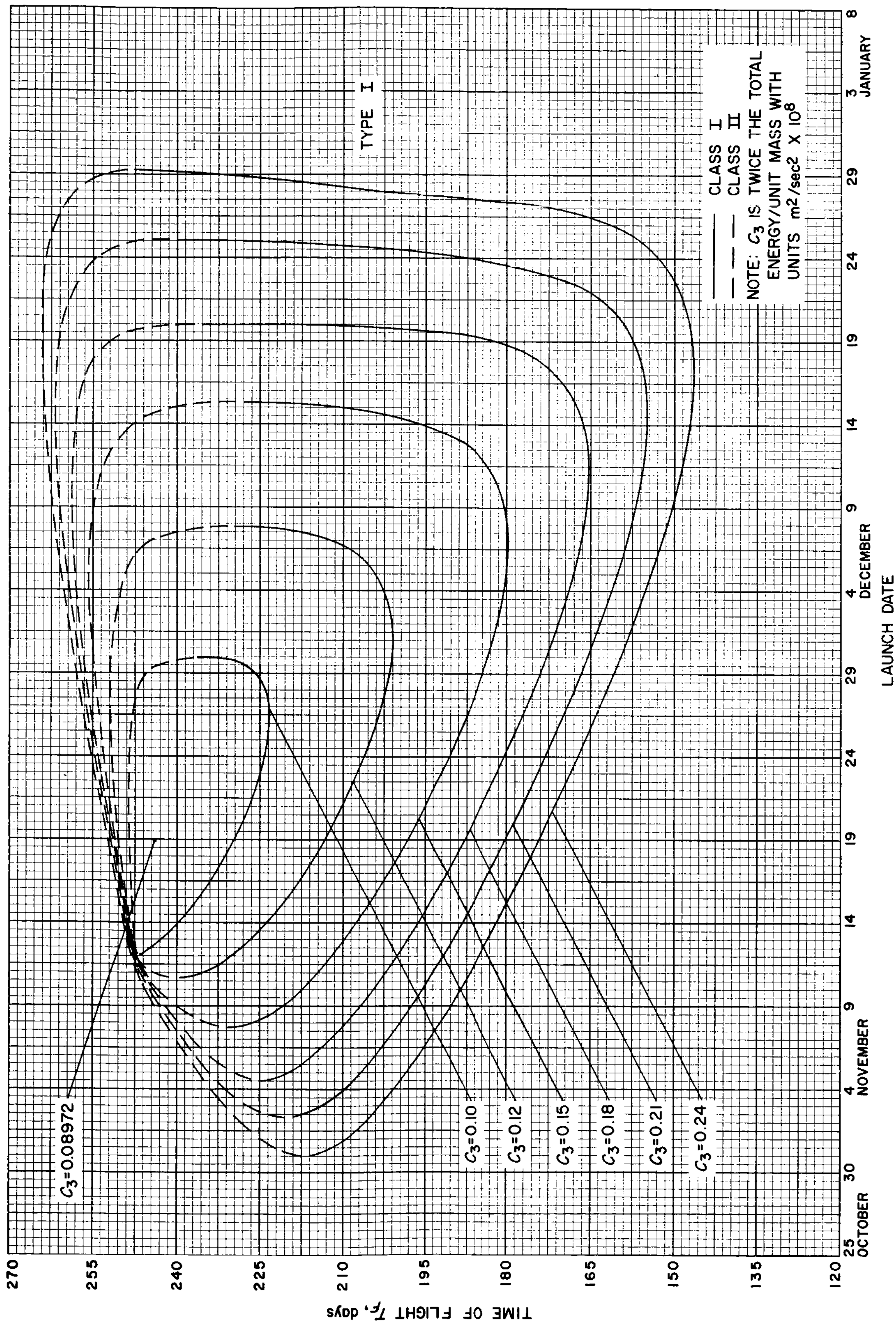

Fig. 12-1. Mars 1964: Time of flight vs launch date

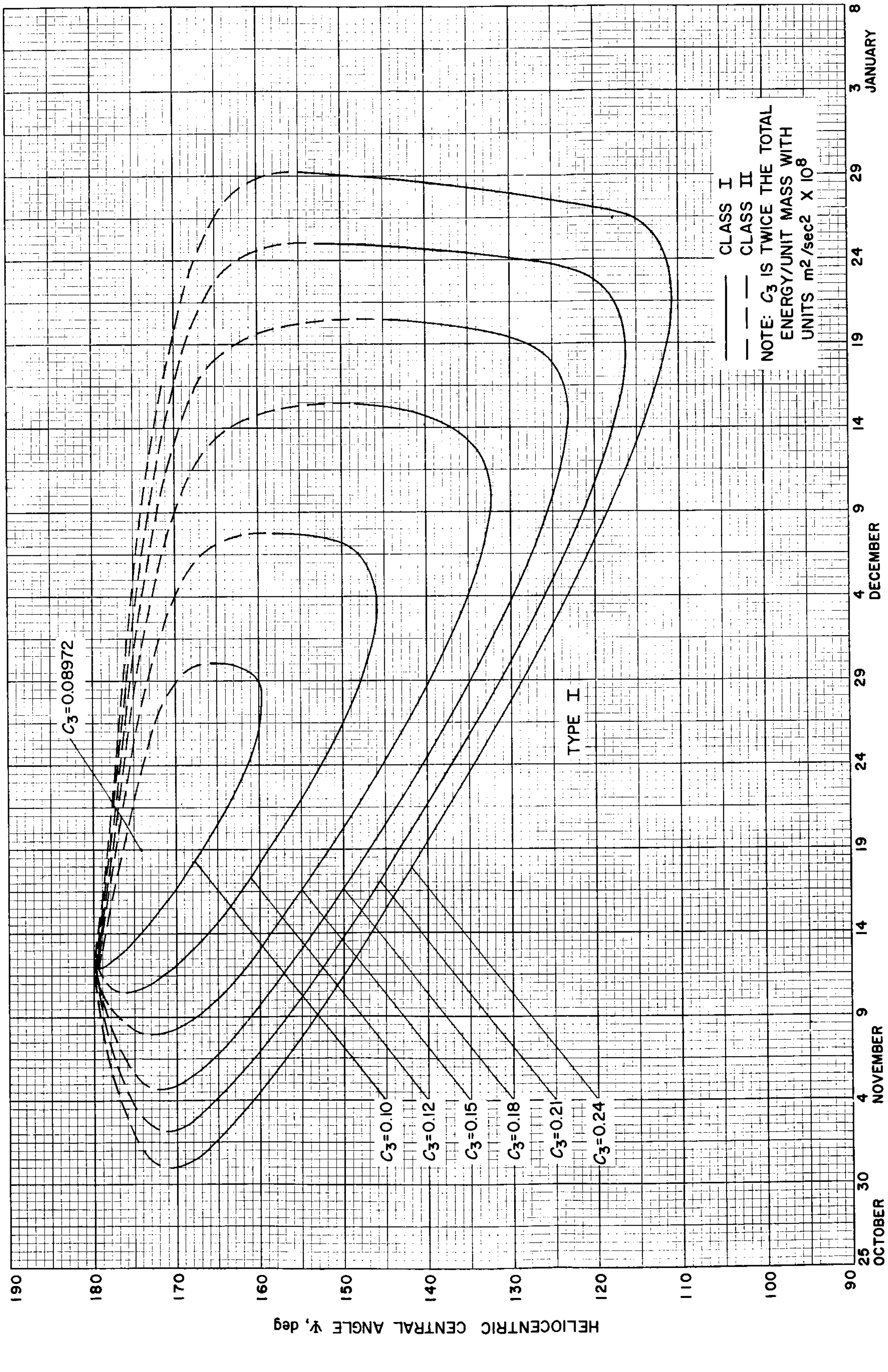

Fig. 12-2. Mars 1964: Heliocentric central angle vs launch date

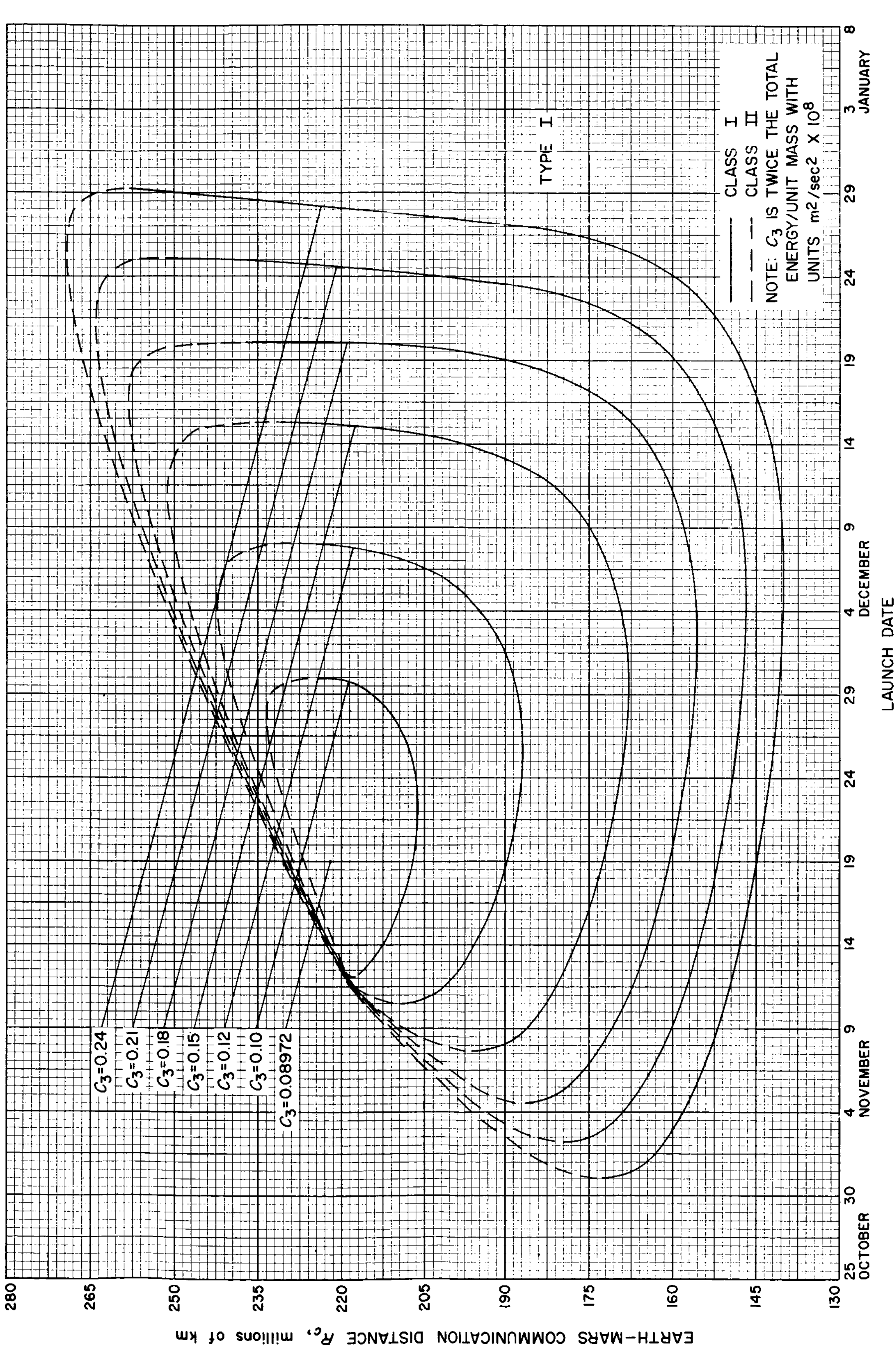

Fig. 12-3. *Mars 1964:* Earth–Mars communication distance vs launch date

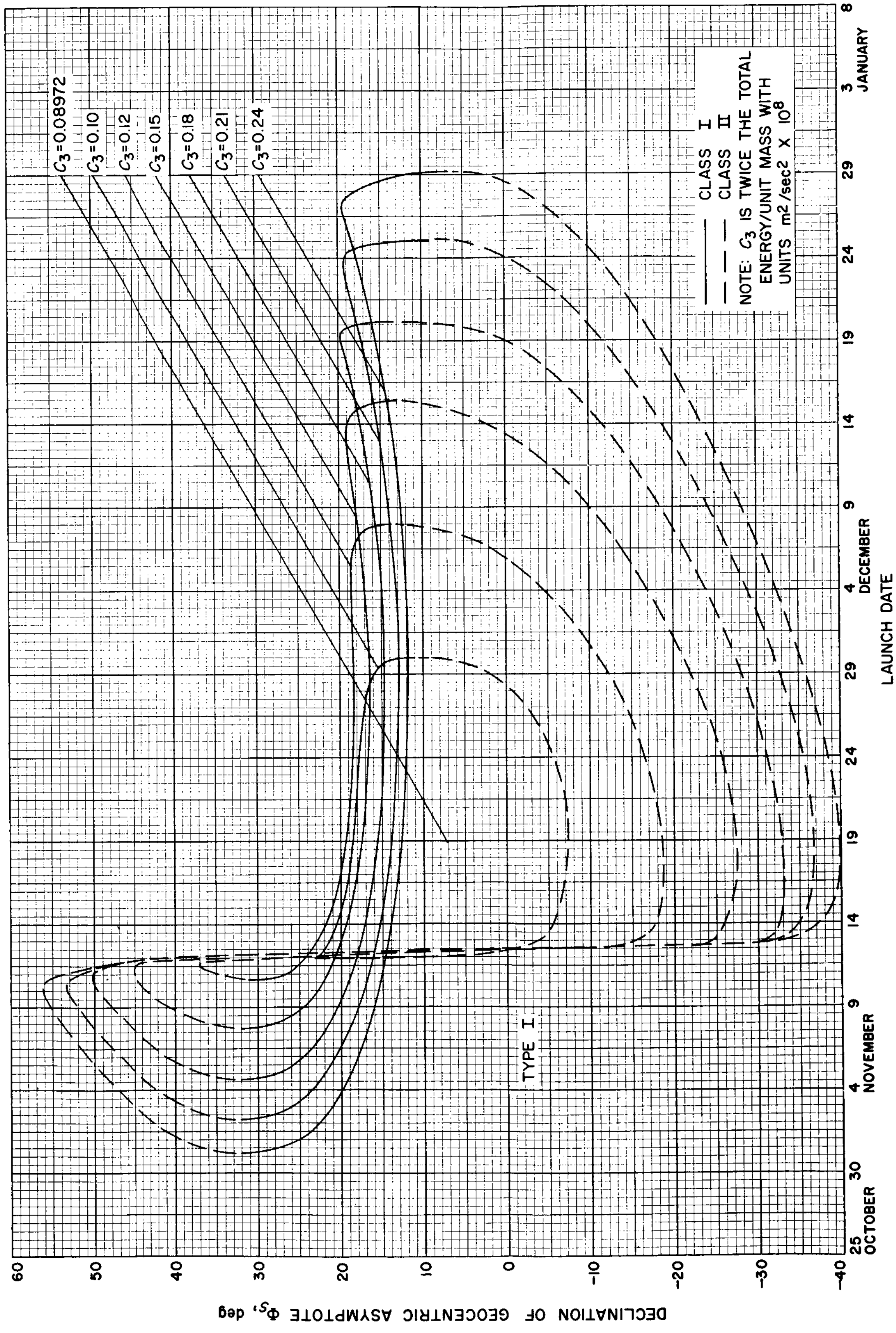

Fig. 12–4. Mars 1964: Declination of geocentric asymptote vs launch date

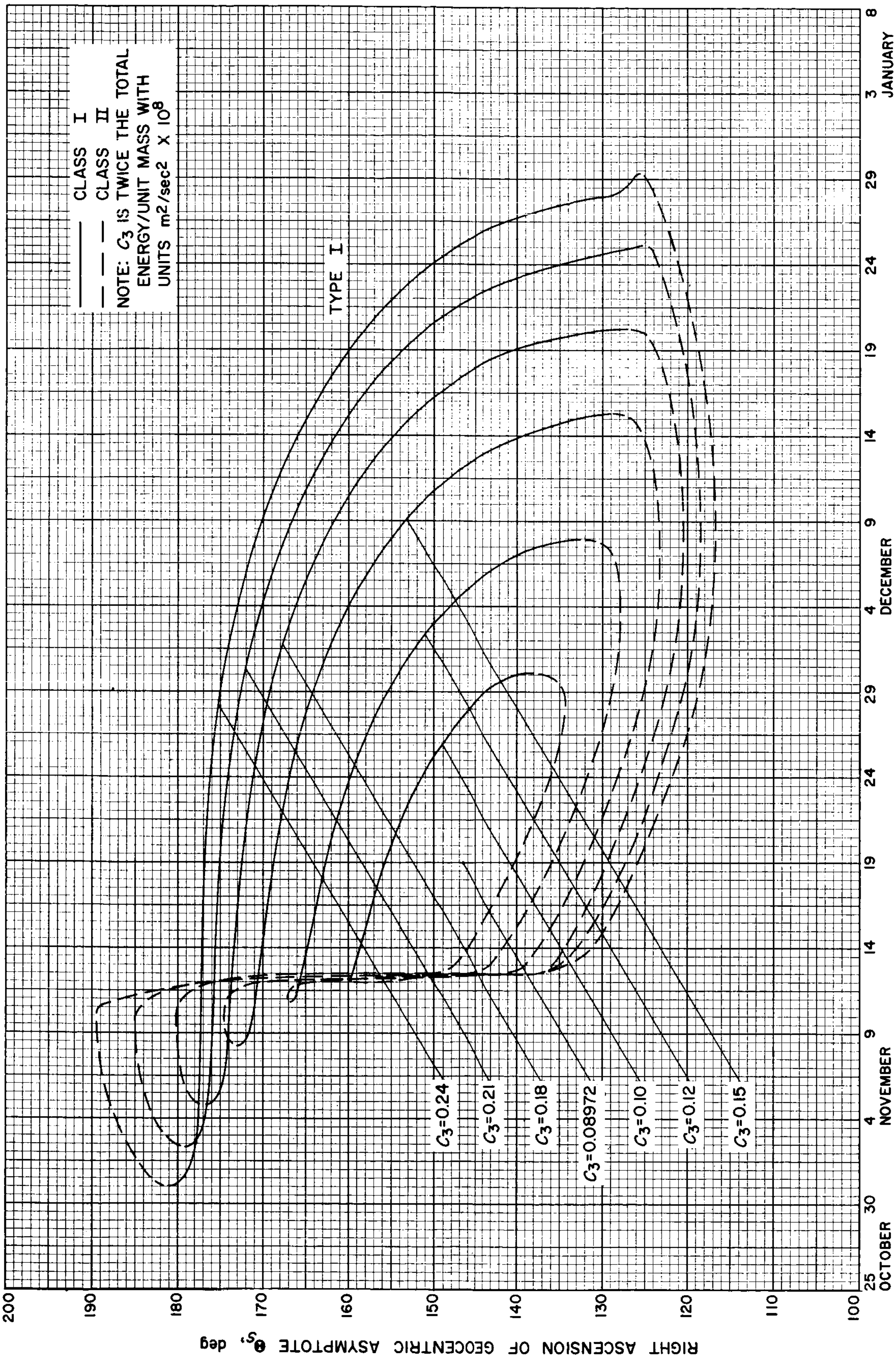

Fig. 12–5. Mars 1964: Right ascension of geocentric asymptote vs launch date

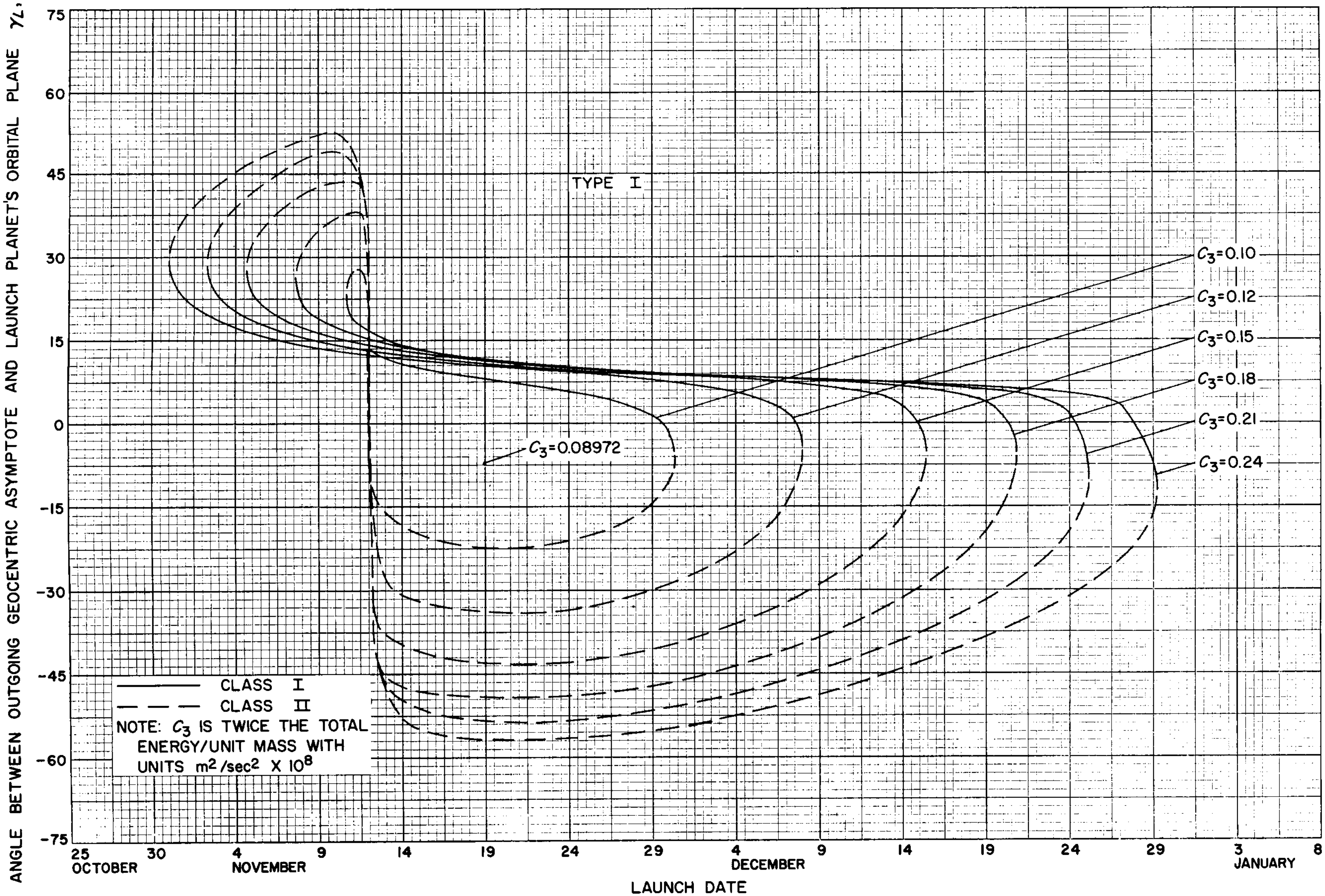

Fig. 12–6. Mars 1964: Angle between outgoing geocentric asymptote and launch planet's orbital plane vs launch date

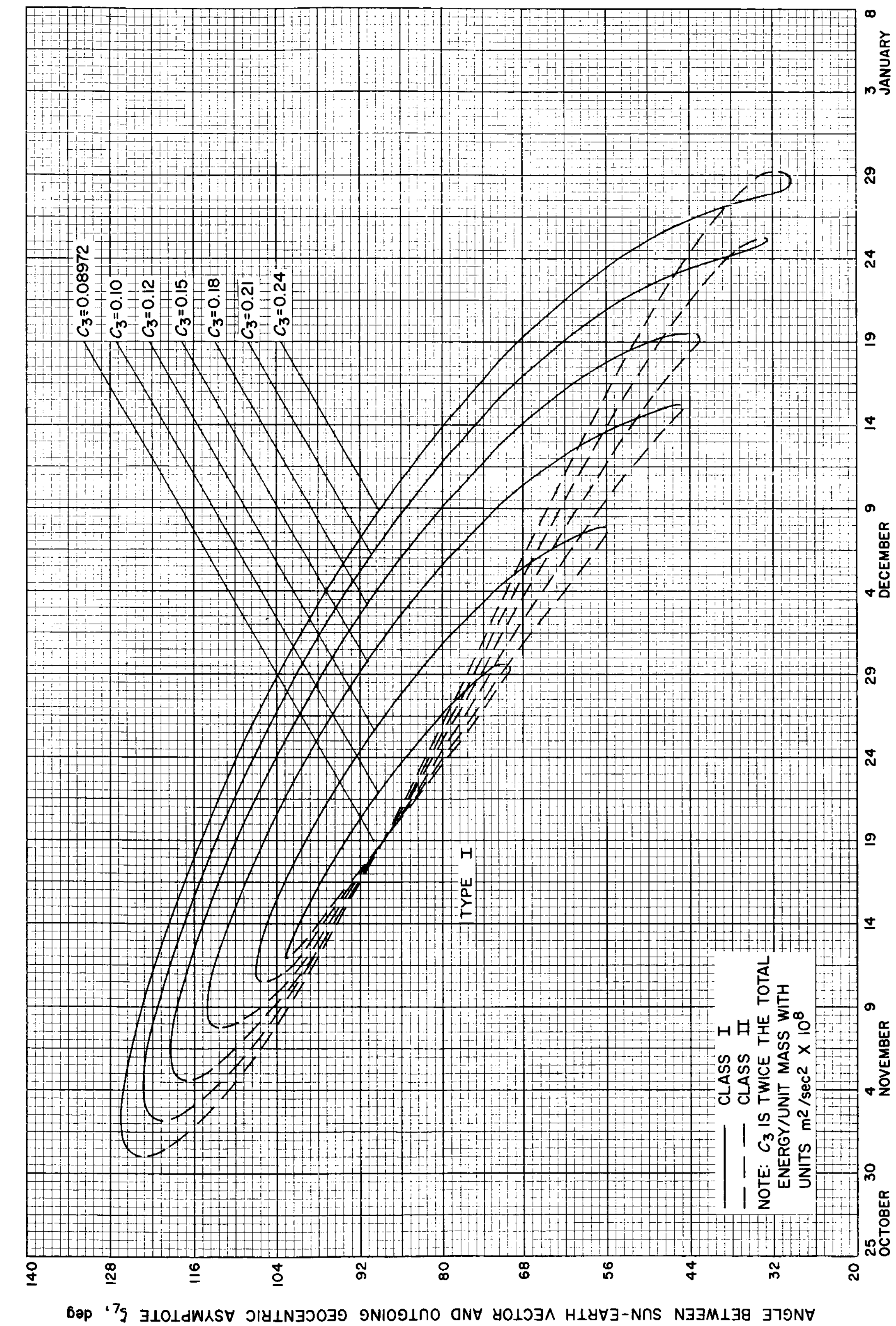

Fig. 12-7. Mars 1964: Angle between Sun-Earth vector and outgoing geocentric asymptote vs launch date

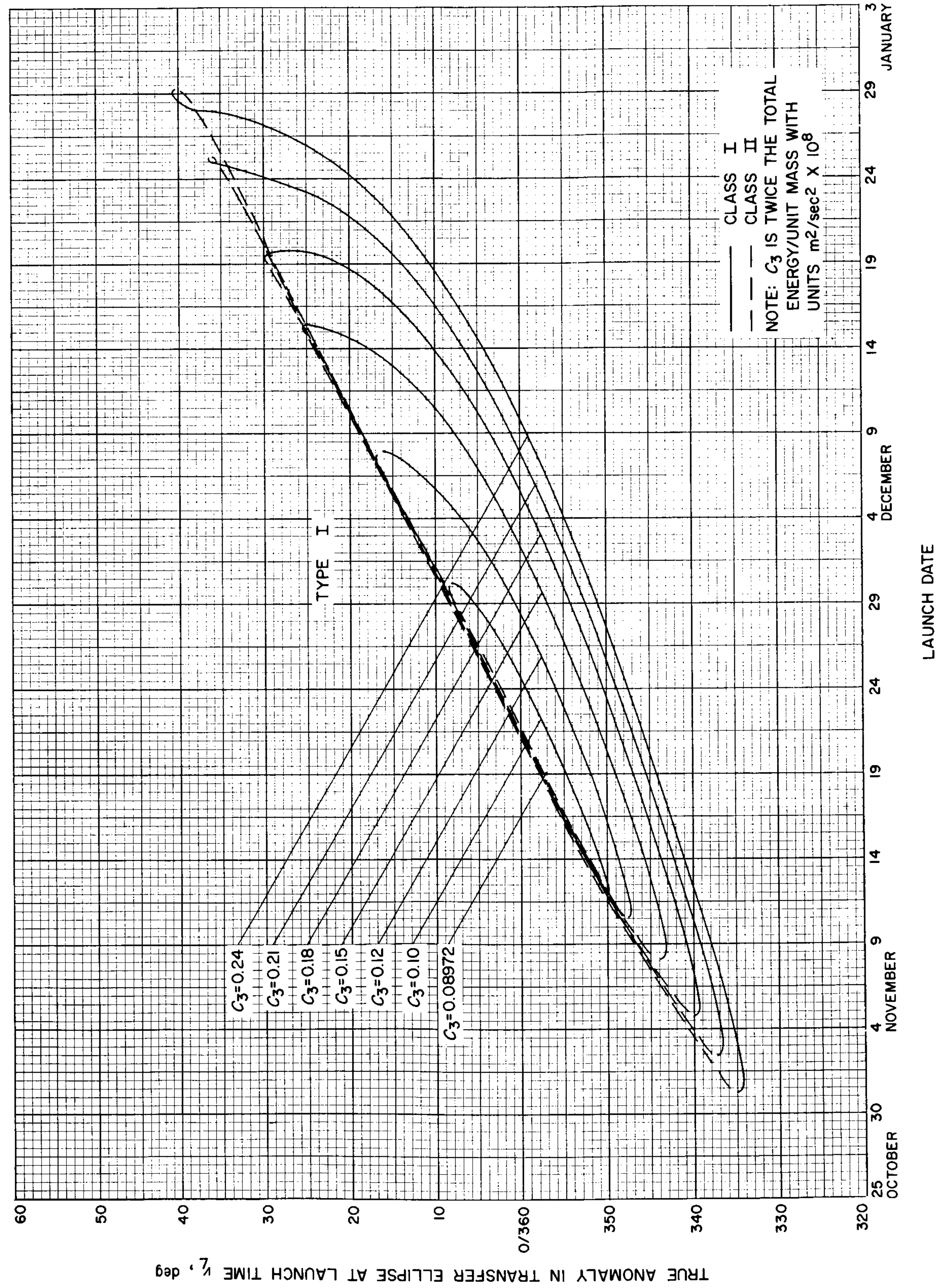

Fig. 12–8. Mars 1964: True anomaly in transfer ellipse at launch time vs launch date

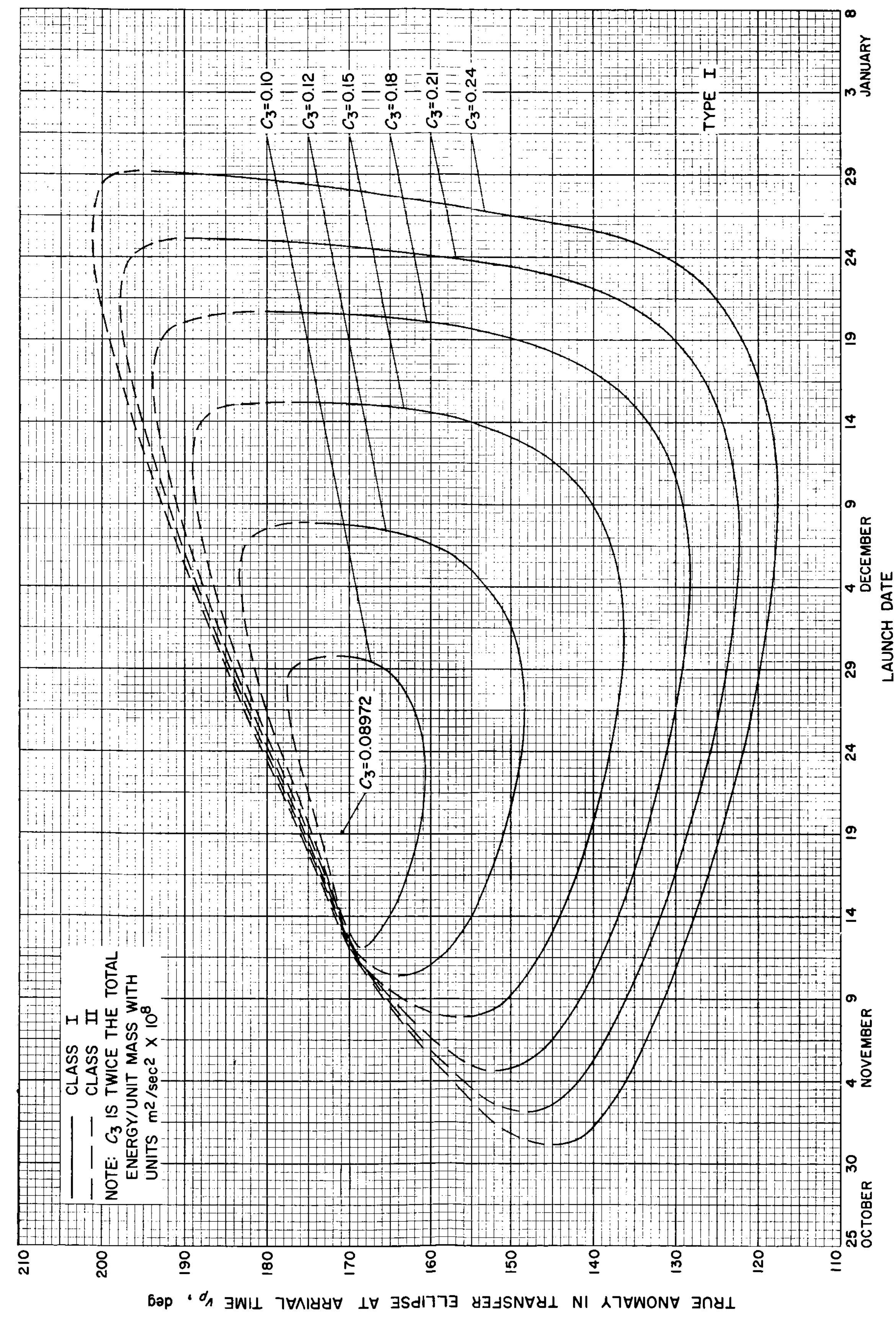

Fig. 12–9. Mars 1964: True anomaly in transfer ellipse at arrival time vs launch date

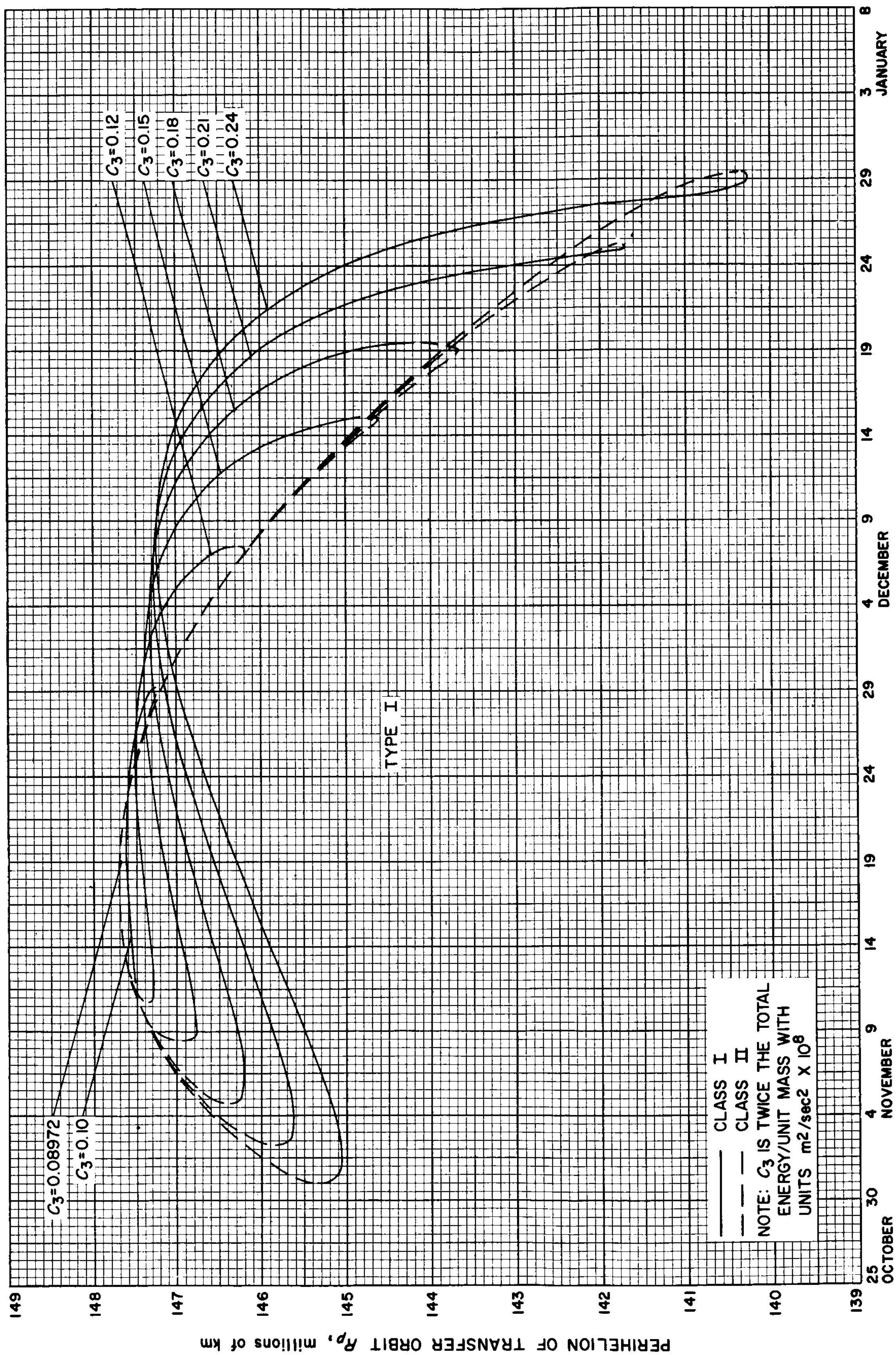

Fig. 12-10. *Mars* 1964: Perihelion of transfer orbit vs launch date

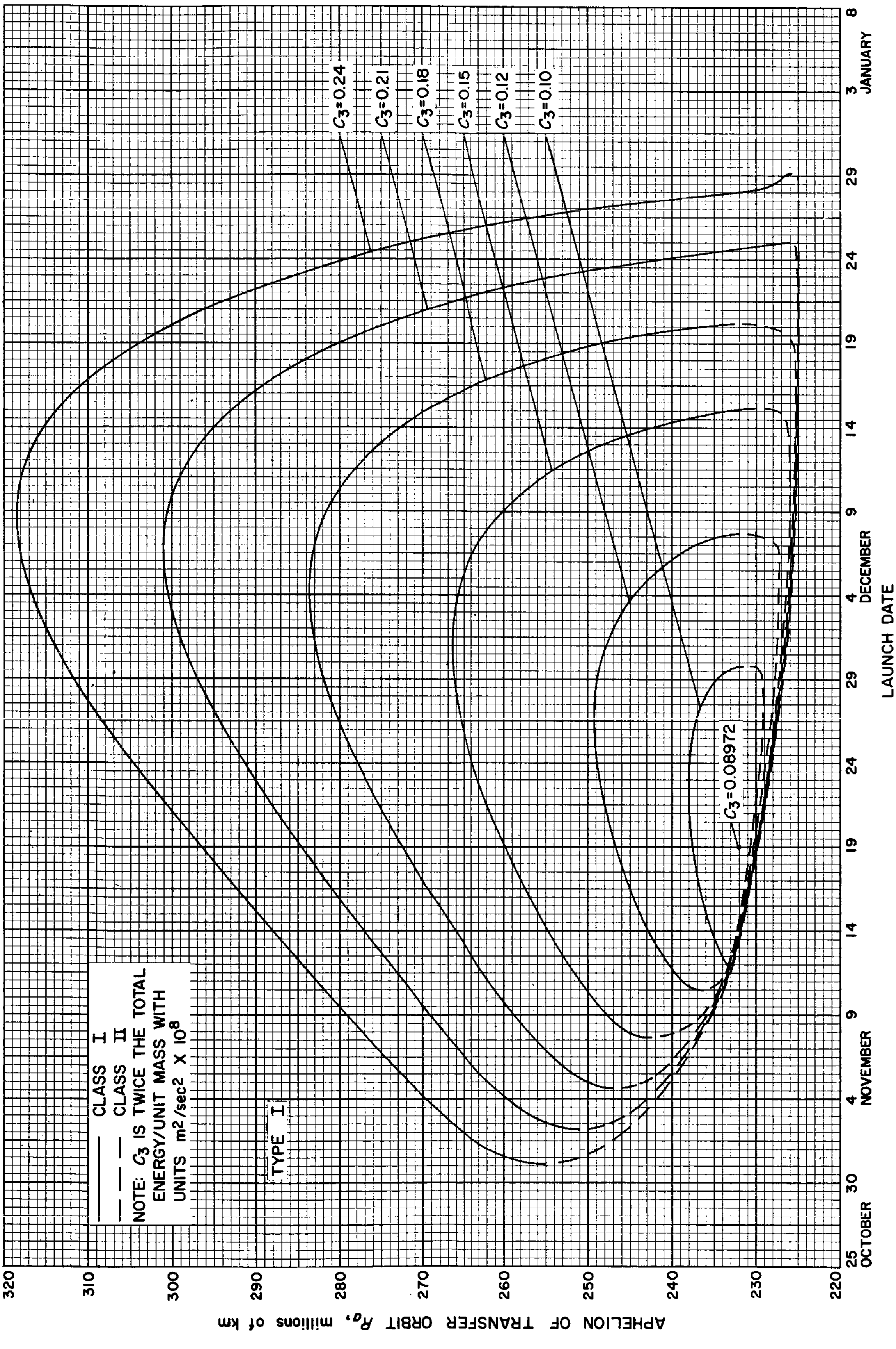

Fig. 12–11. Mars 1964: Aphelion of transfer orbit vs launch date

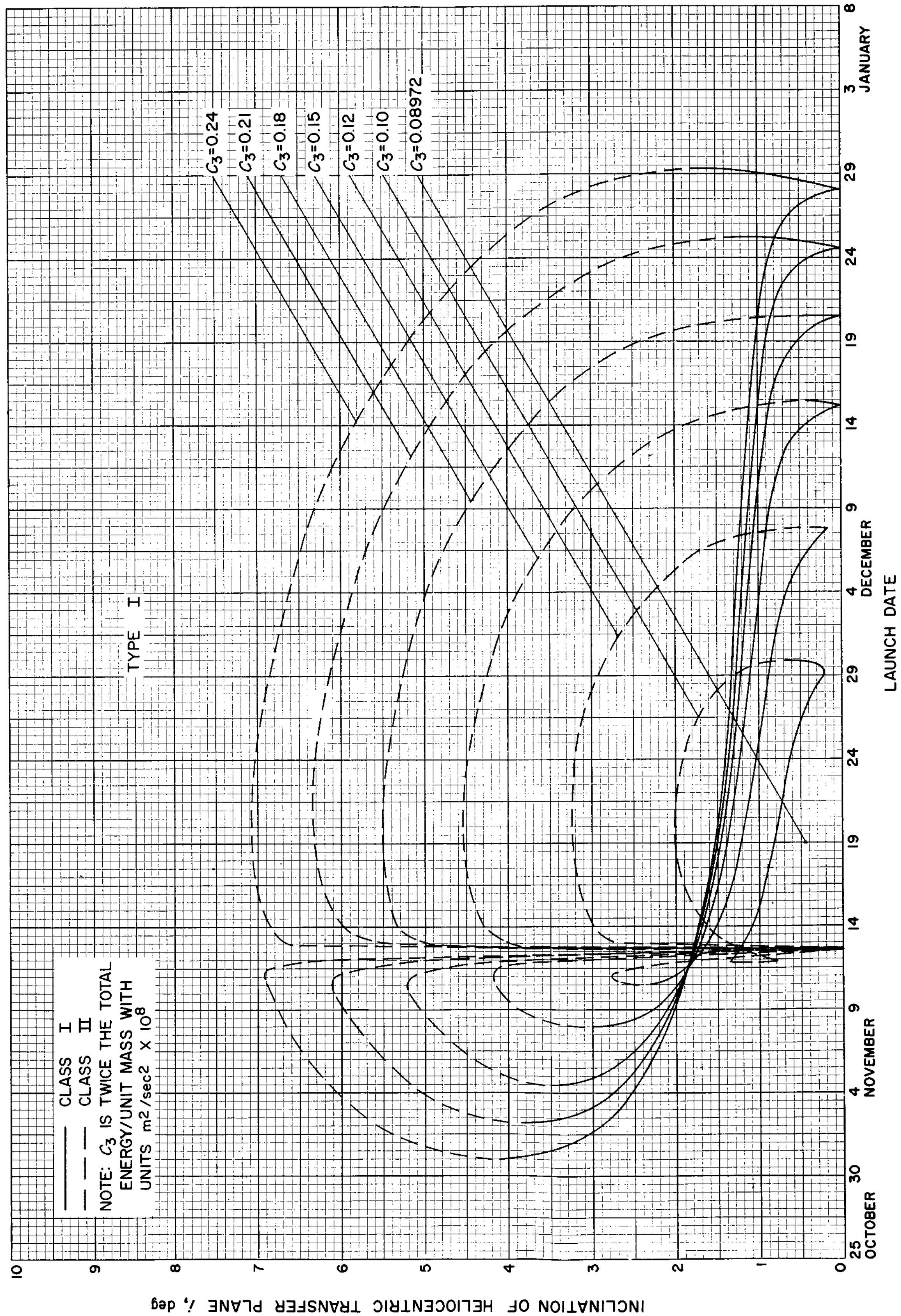

Fig. 12–12. Mars 1964: Inclination of heliocentric-transfer plane vs launch date

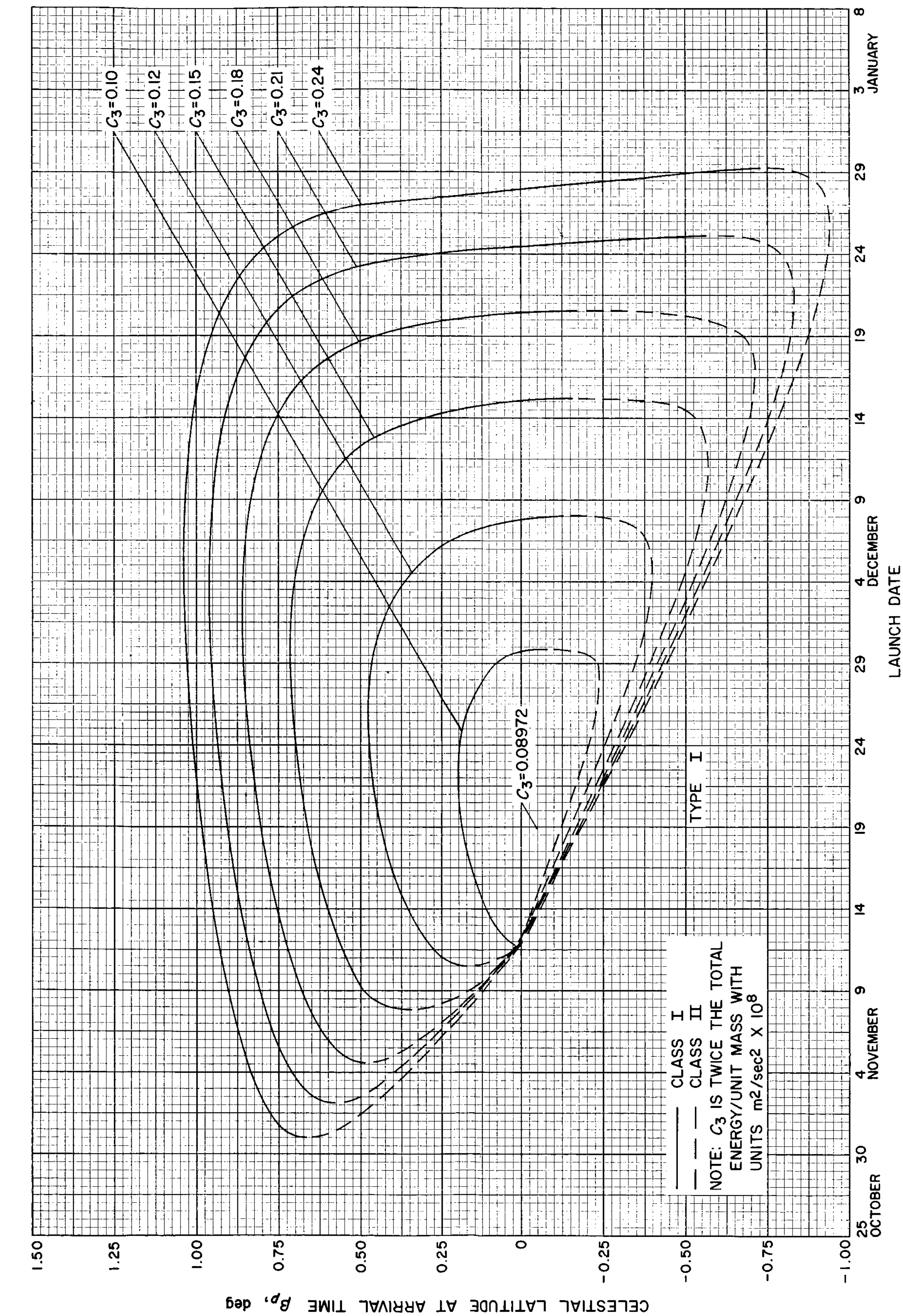

Fig. 12-13. Mars 1964: Celestial latitude at arrival time vs launch date

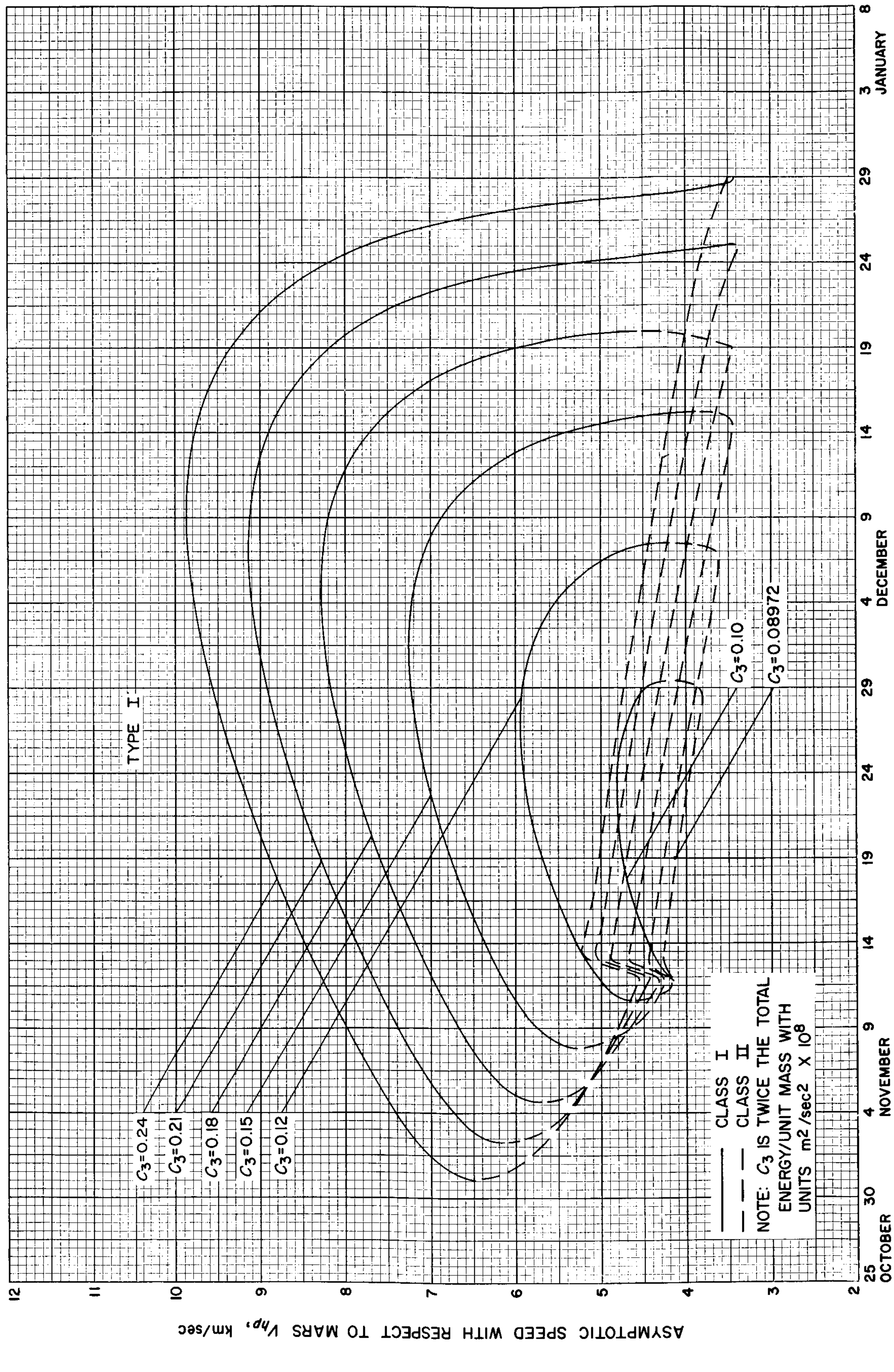

Fig. 12–14. Mars 1964: Asymptotic speed with respect to Mars vs launch date

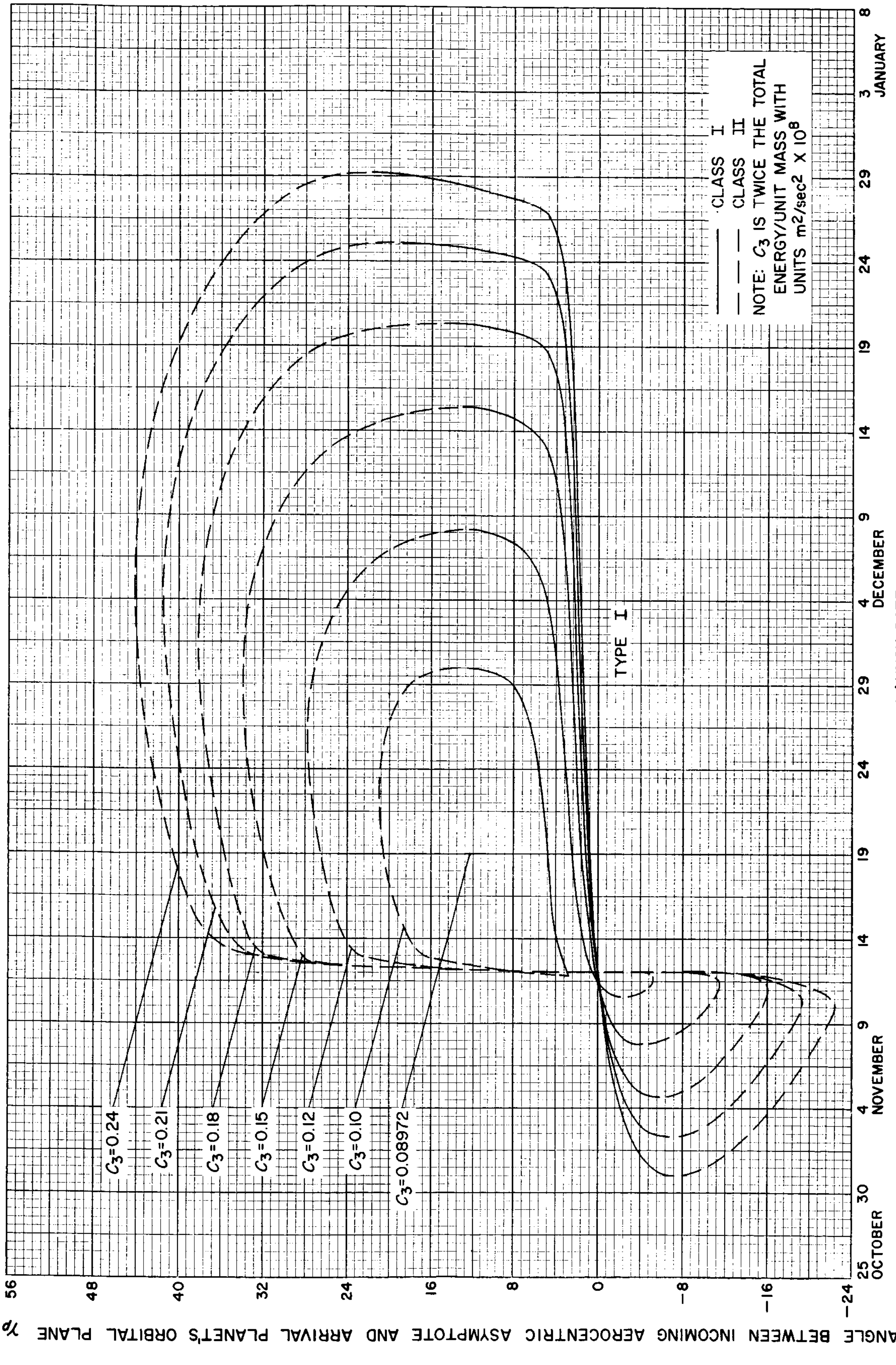

Fig. 12–15. Mars 1964: Angle between incoming aerocentric asymptote and arrival planet's orbital plane vs launch date

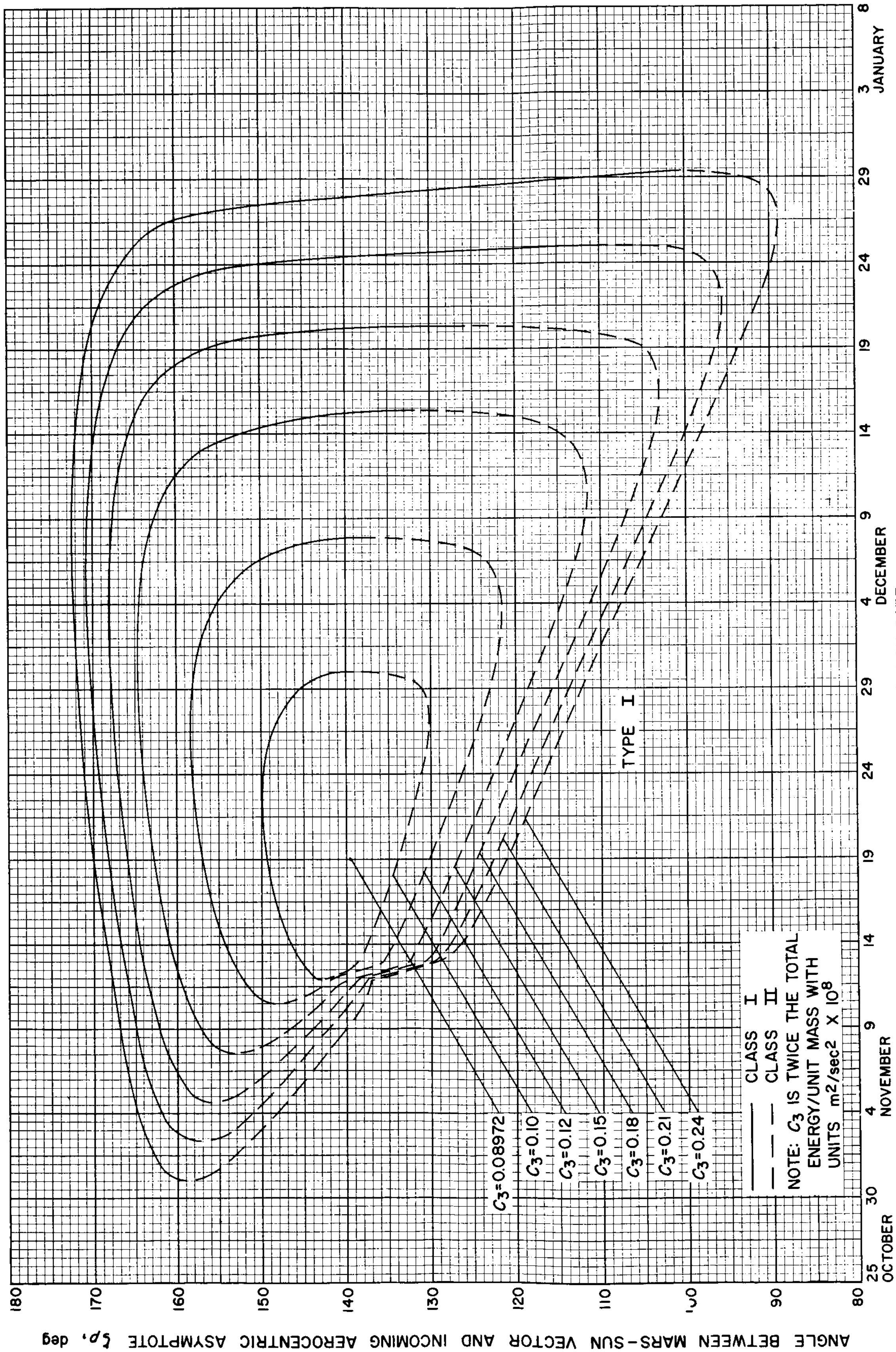

Fig. 12-16. Mars 1964: Angle between Mars–Sun vector and incoming aerocentric asymptote vs launch date

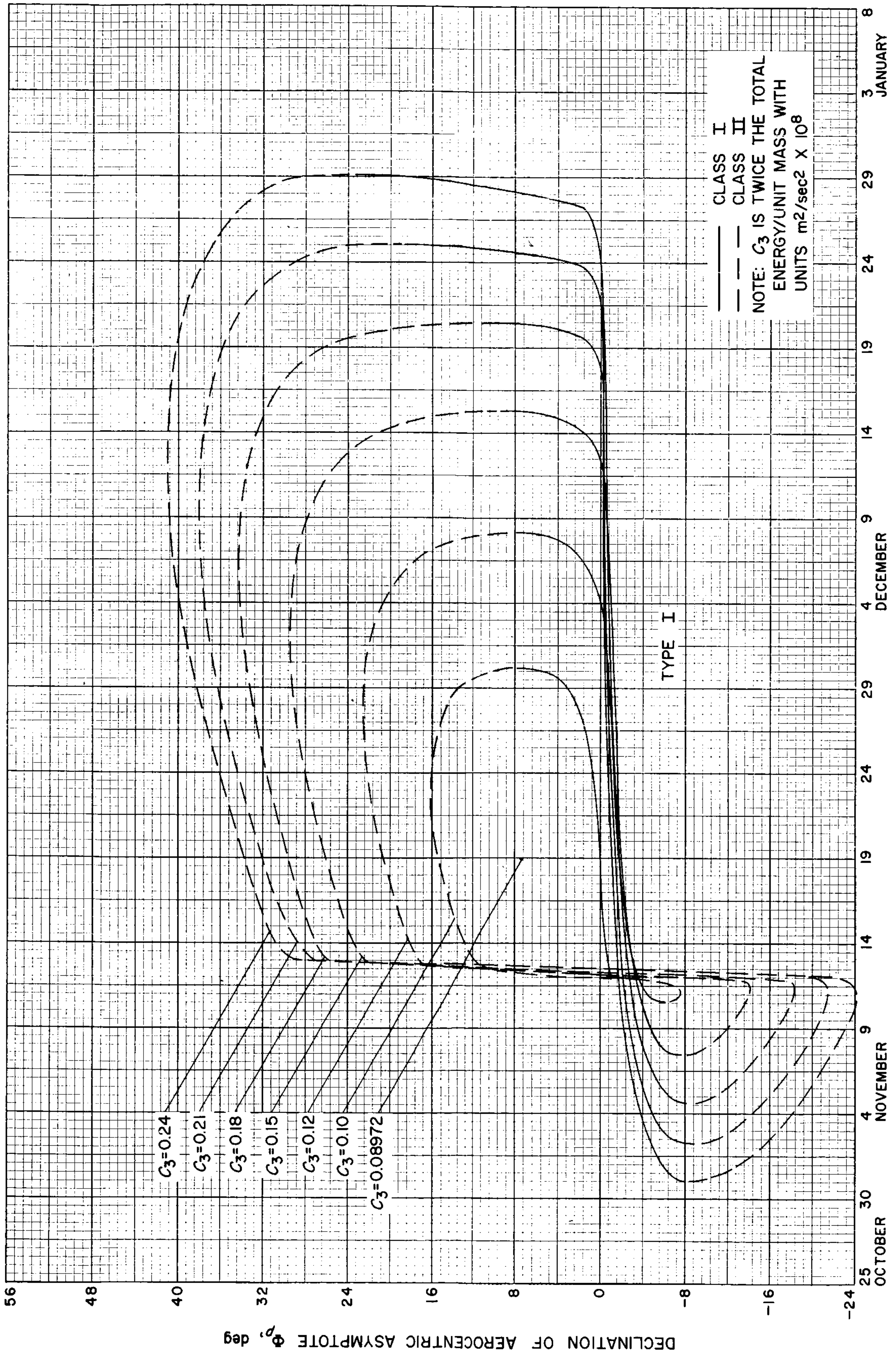

Fig. 12–17. Mars 1964: Declination of aerocentric asymptote vs launch date

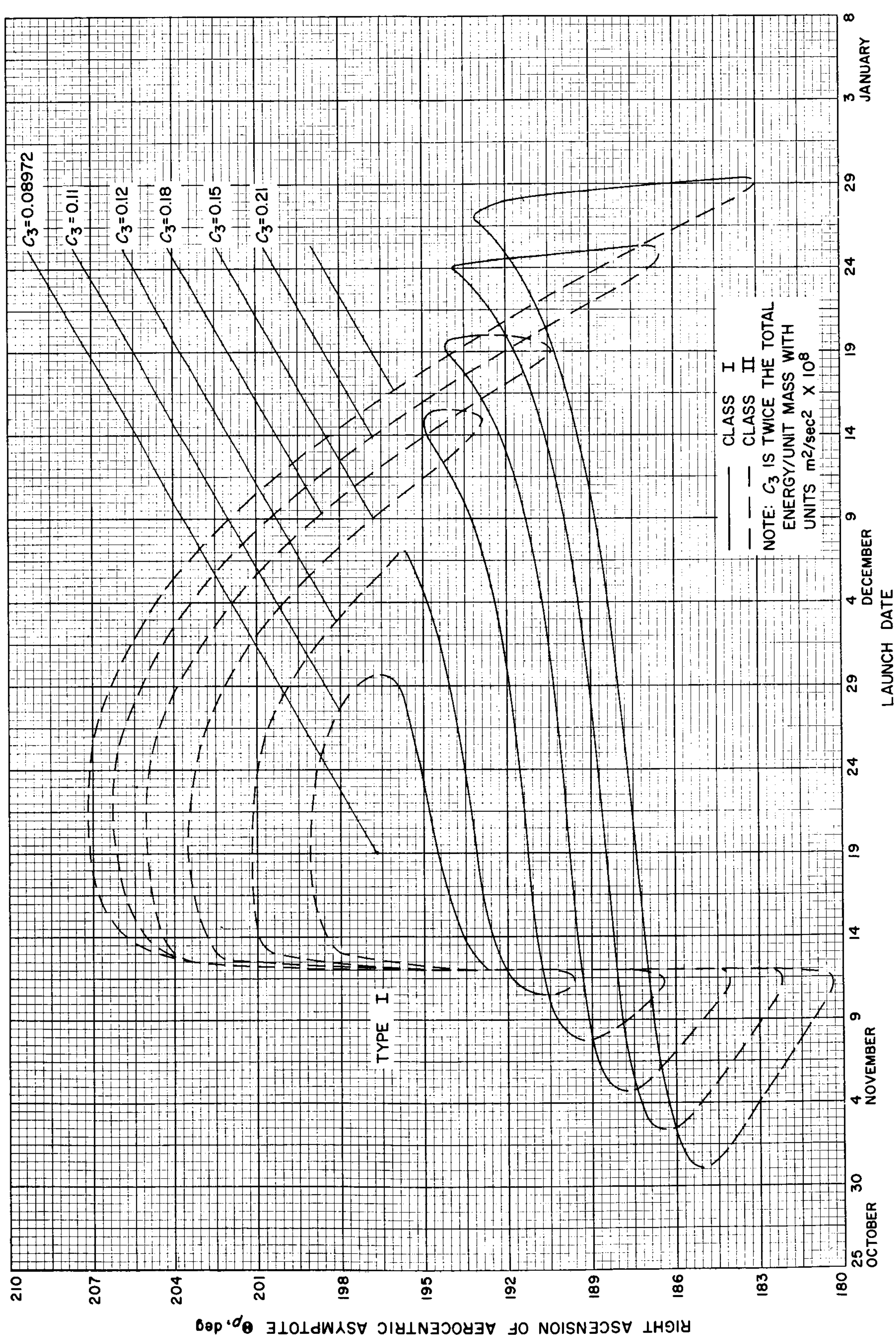

Fig. 12-18. Mars 1964: Right ascension of aerocentric asymptote vs launch date

XIII. MARS 1966: TRAJECTORY-PARAMETER GRAPHS

Figure

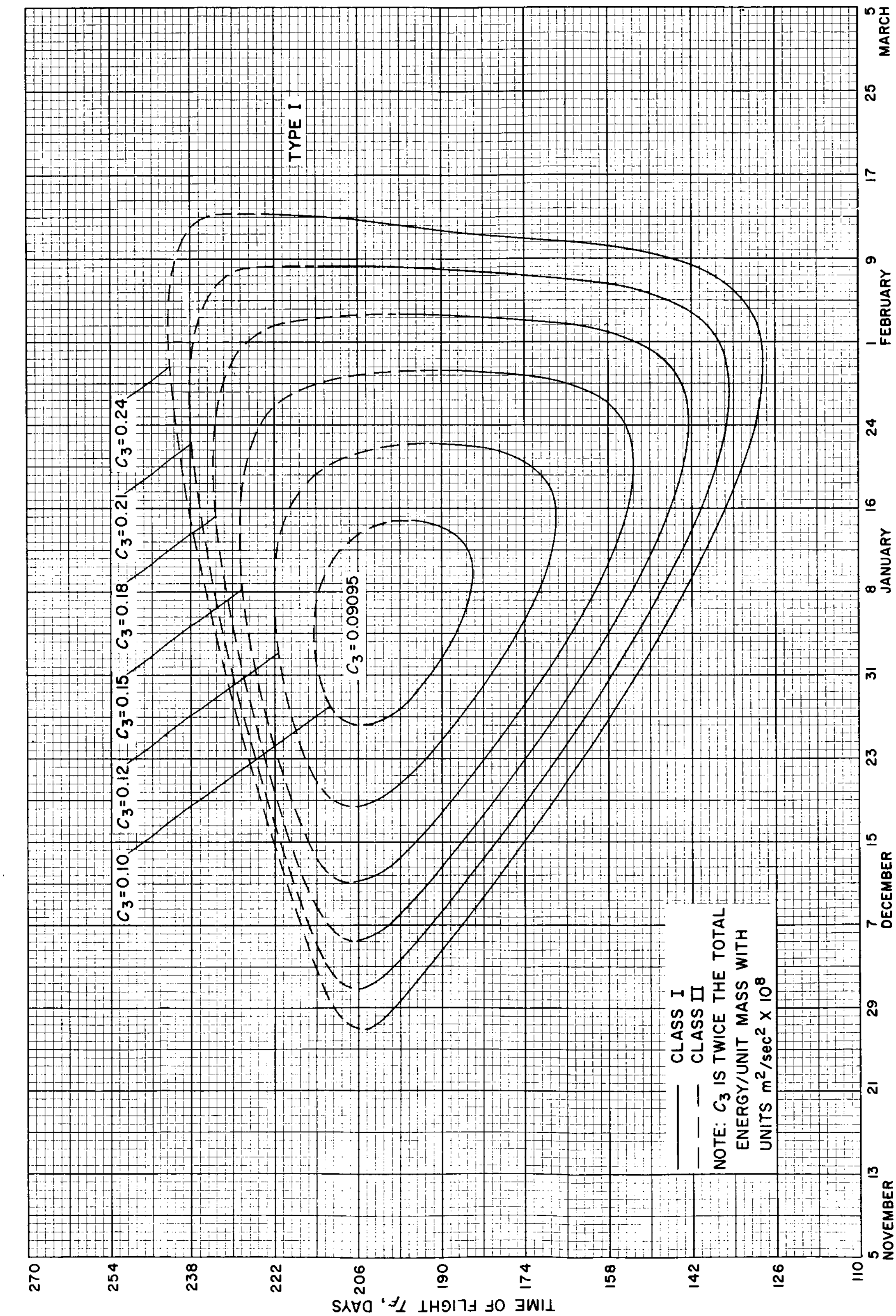

Fig. 13-1. Mars 1966: Time of flight vs launch date

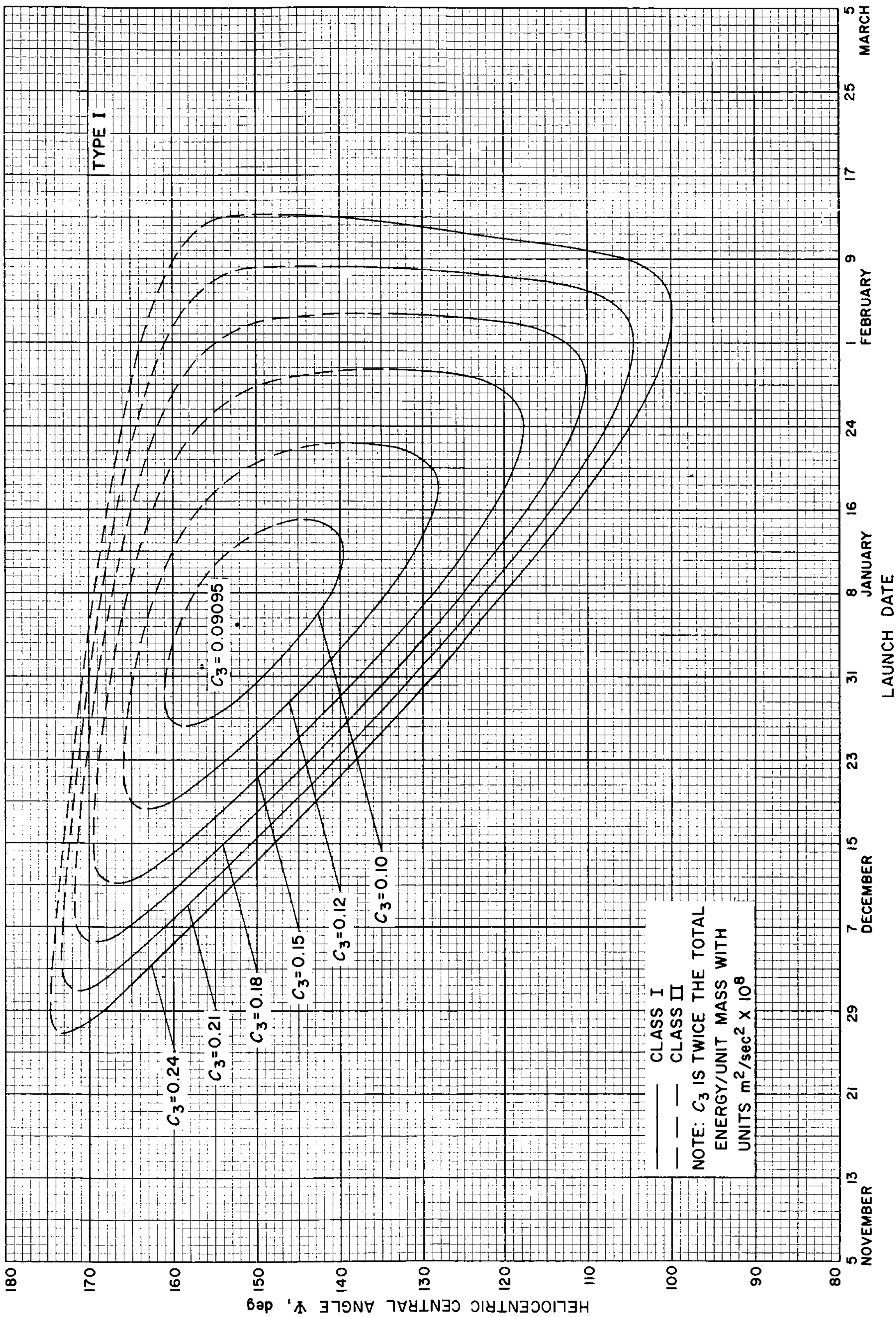

Fig. 13-2. Mars 1966: Heliocentric central angle vs launch date

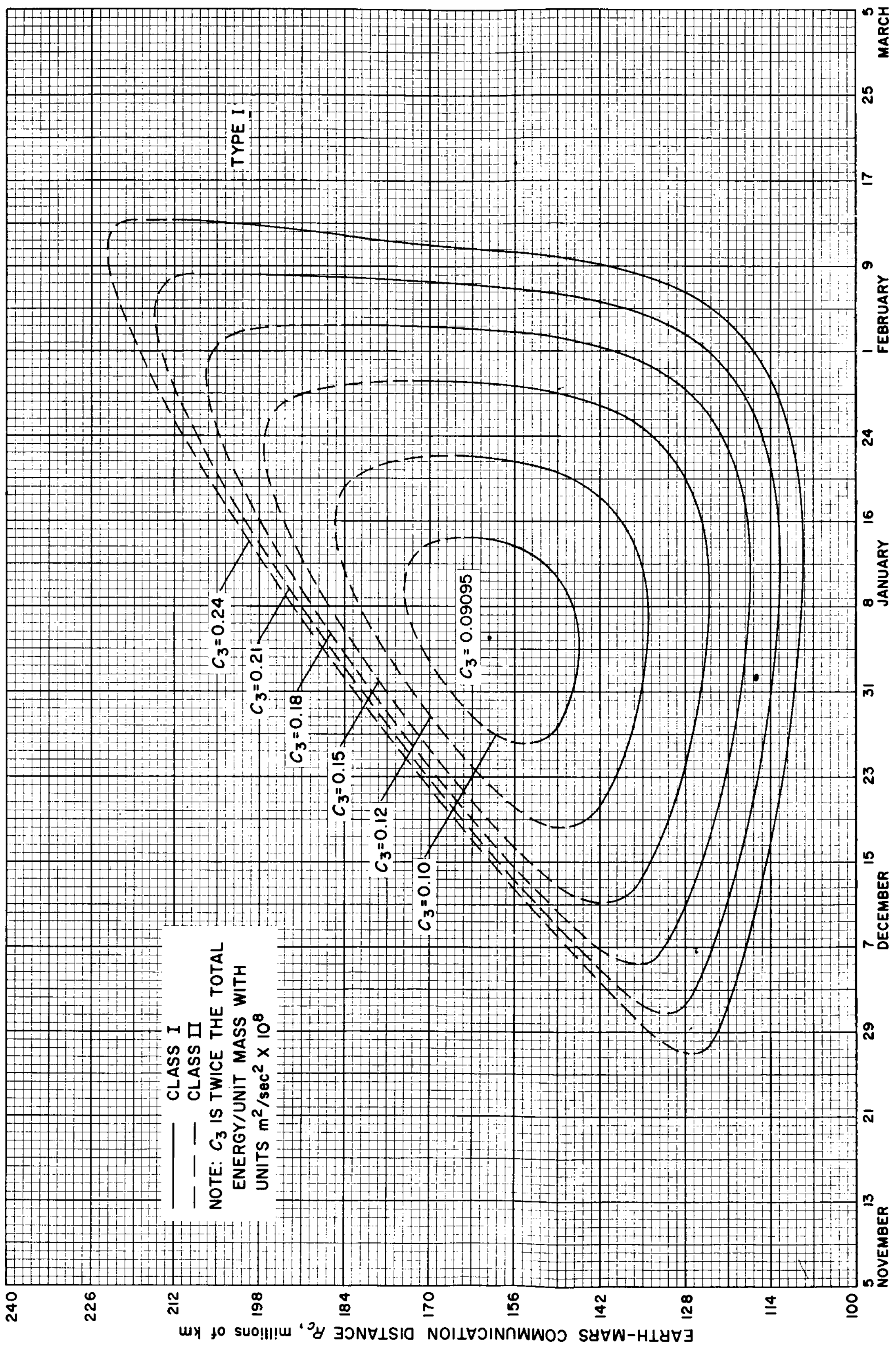

Fig. 13–3. Mars 1966: Earth–Mars communication distance vs launch date

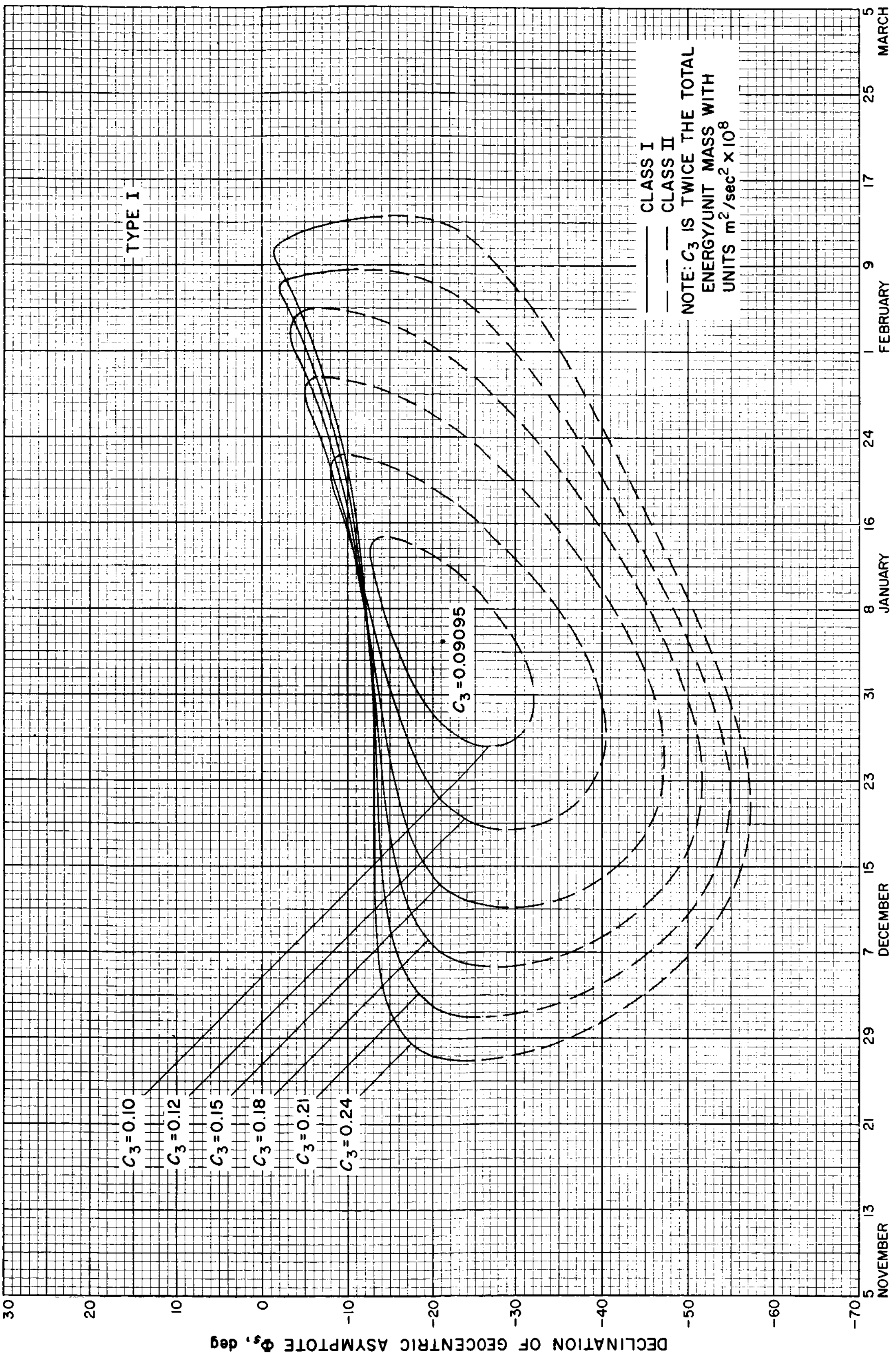

Fig. 13–4. Mars 1966: Declination of geocentric asymptote vs launch date

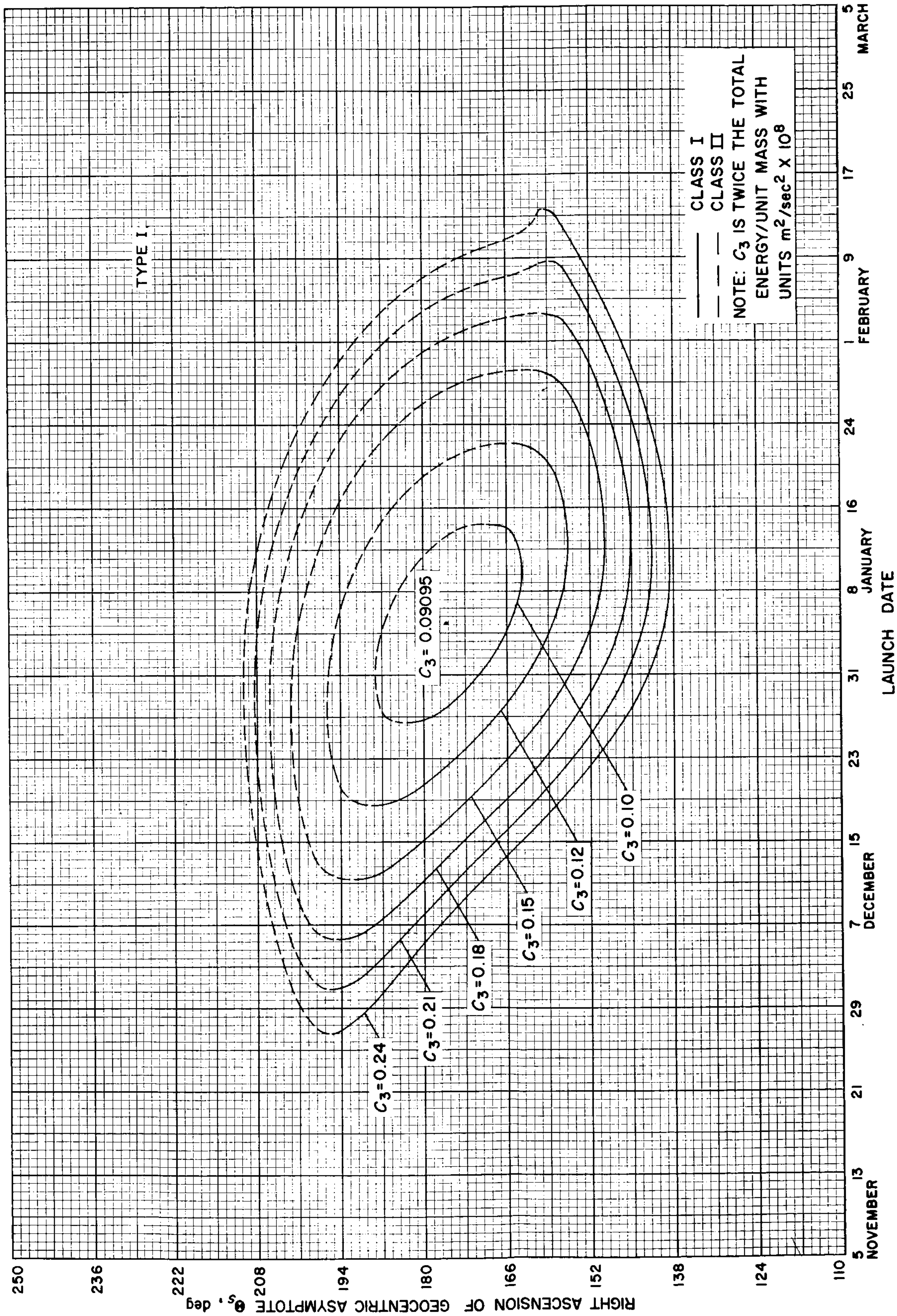

Fig. 13-5. Mars 1966: Right ascension of geocentric asymptote vs launch date

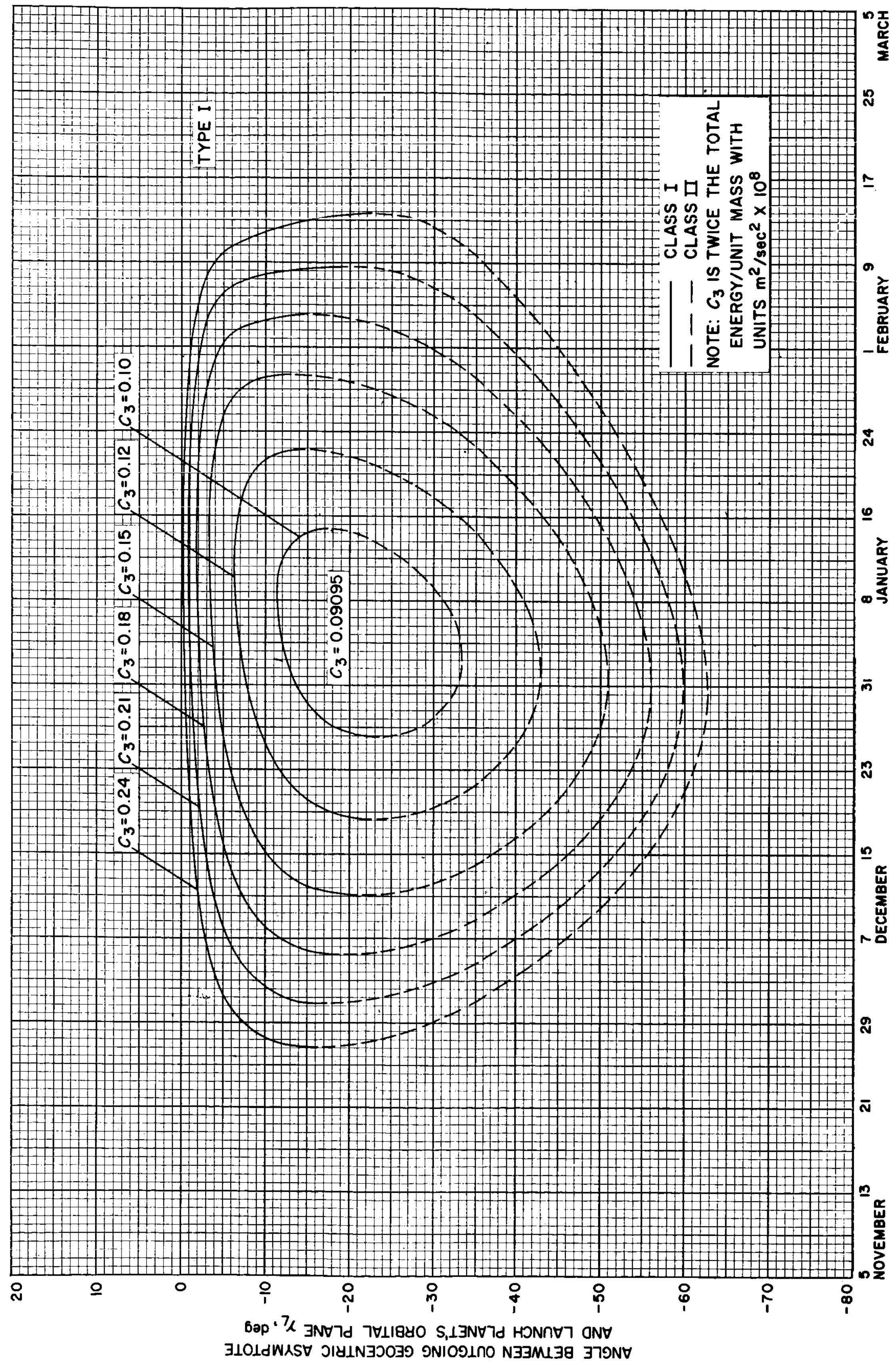

Fig. 13–6. Mars 1966: Angle between outgoing geocentric asymptote and launch planet's orbital plane vs launch date

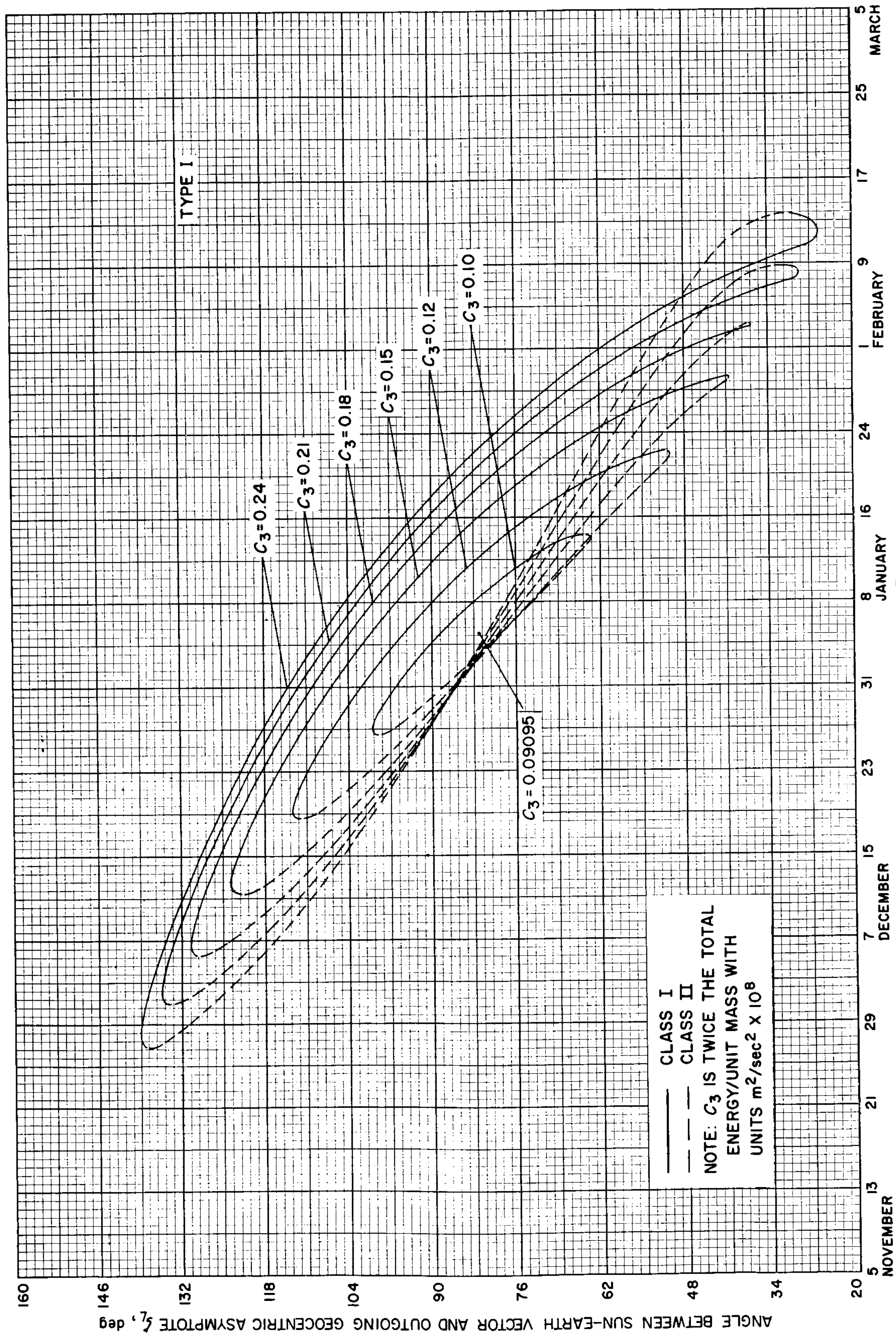

Fig. 13-7. Mars 1966: Angle between Sun-Earth vector and going geocentric asymptote vs launch date

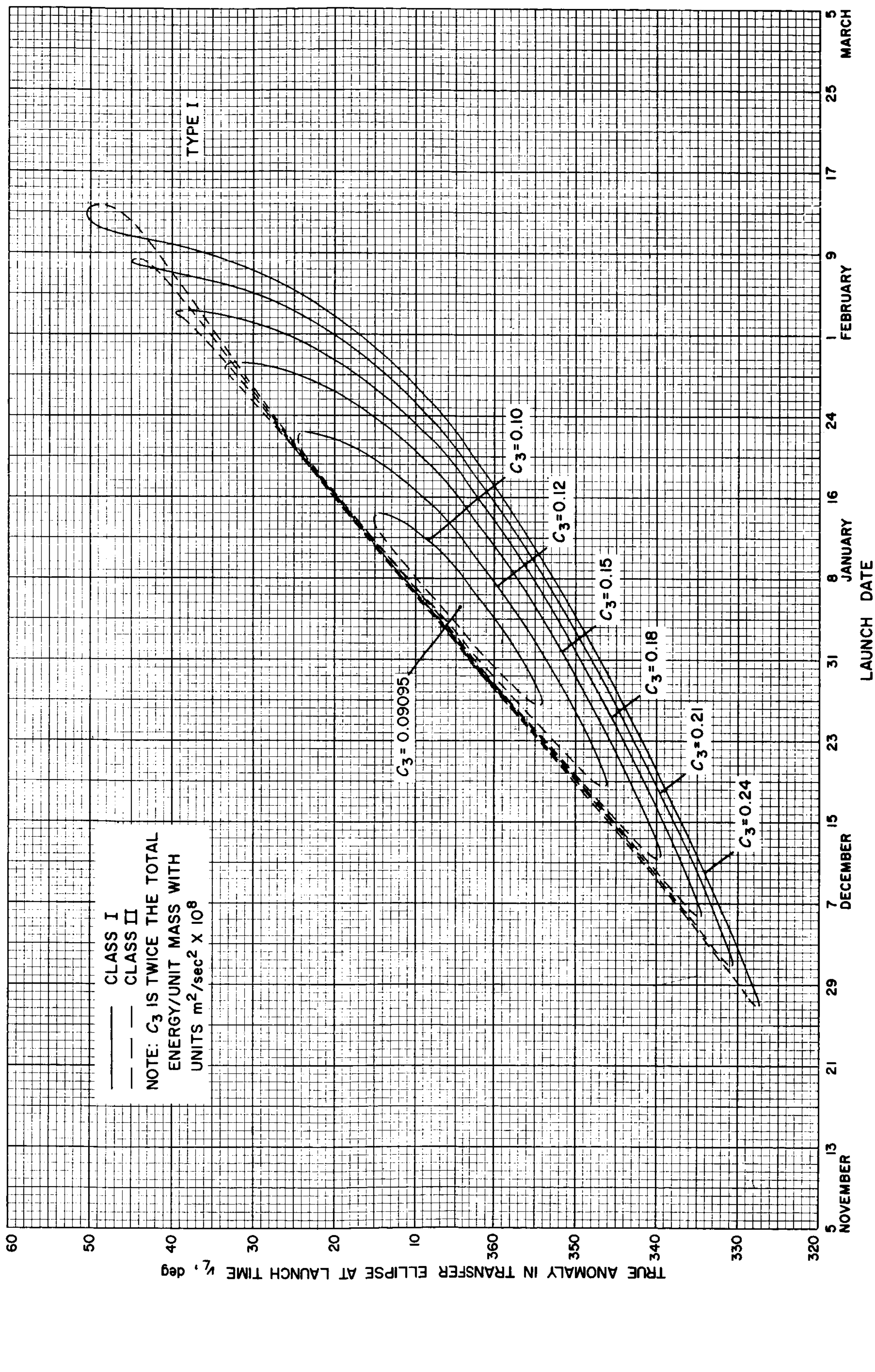

Fig. 13-8. *Mars 1966:* True anomaly in transfer ellipse at launch time vs launch date

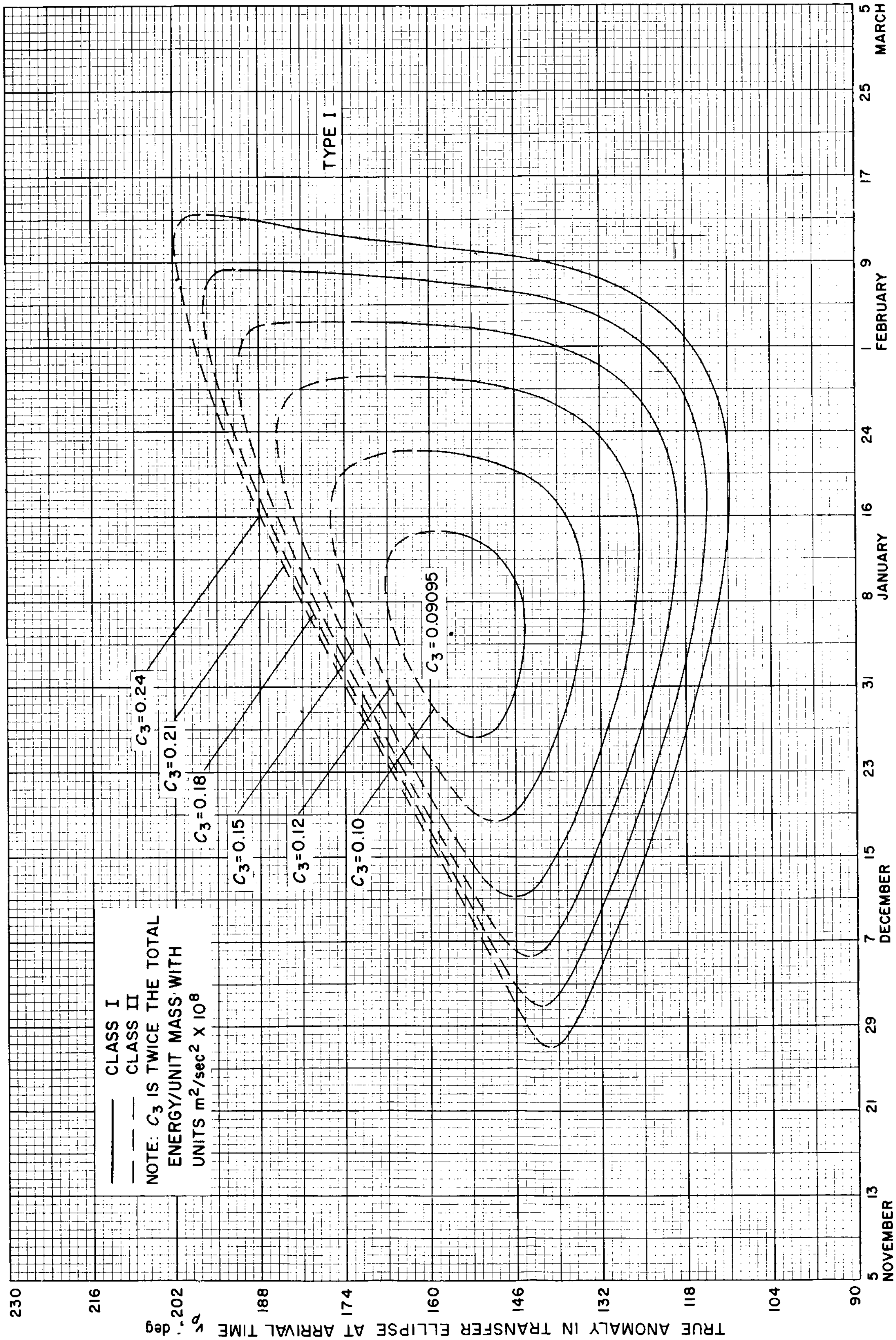

Fig. 13–9. Mars 1966: True anomaly in transfer ellipse at arrival time vs launch date

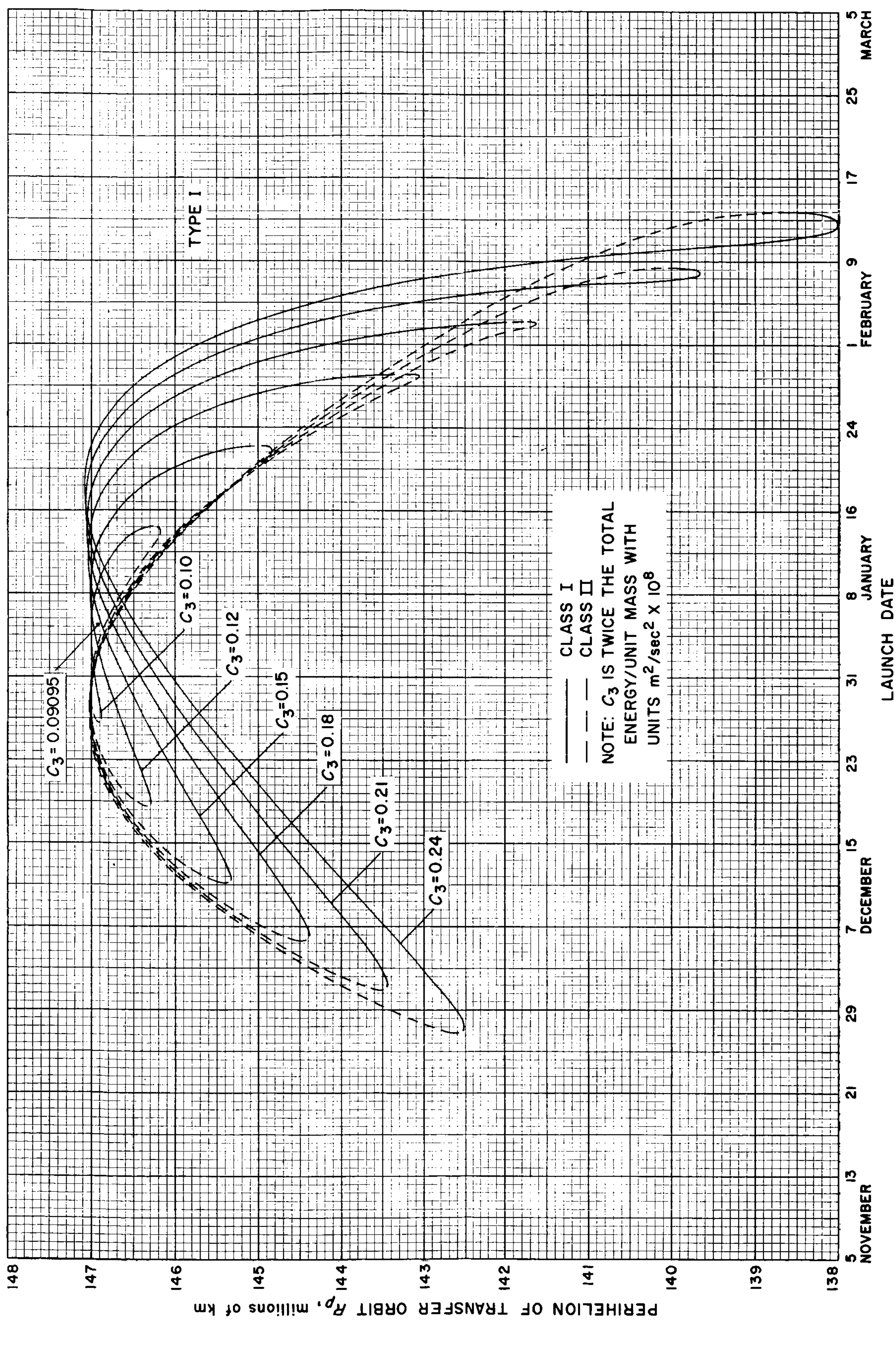

Fig. 13-10. *Mars* 1966: Perihelion of transfer orbit vs launch date

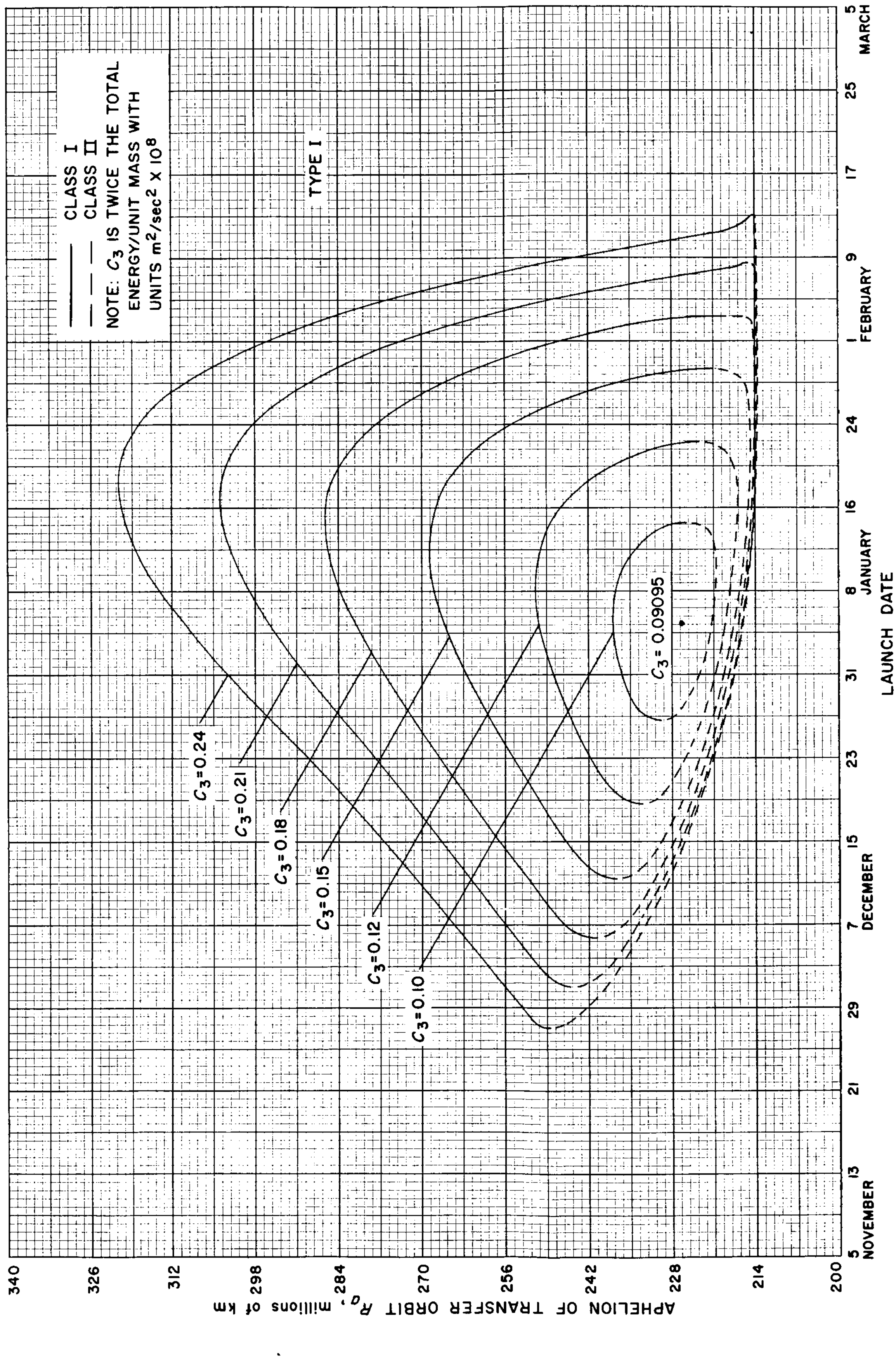

Fig. 13-11. Mars 1966: Aphelion of transfer orbit vs launch date

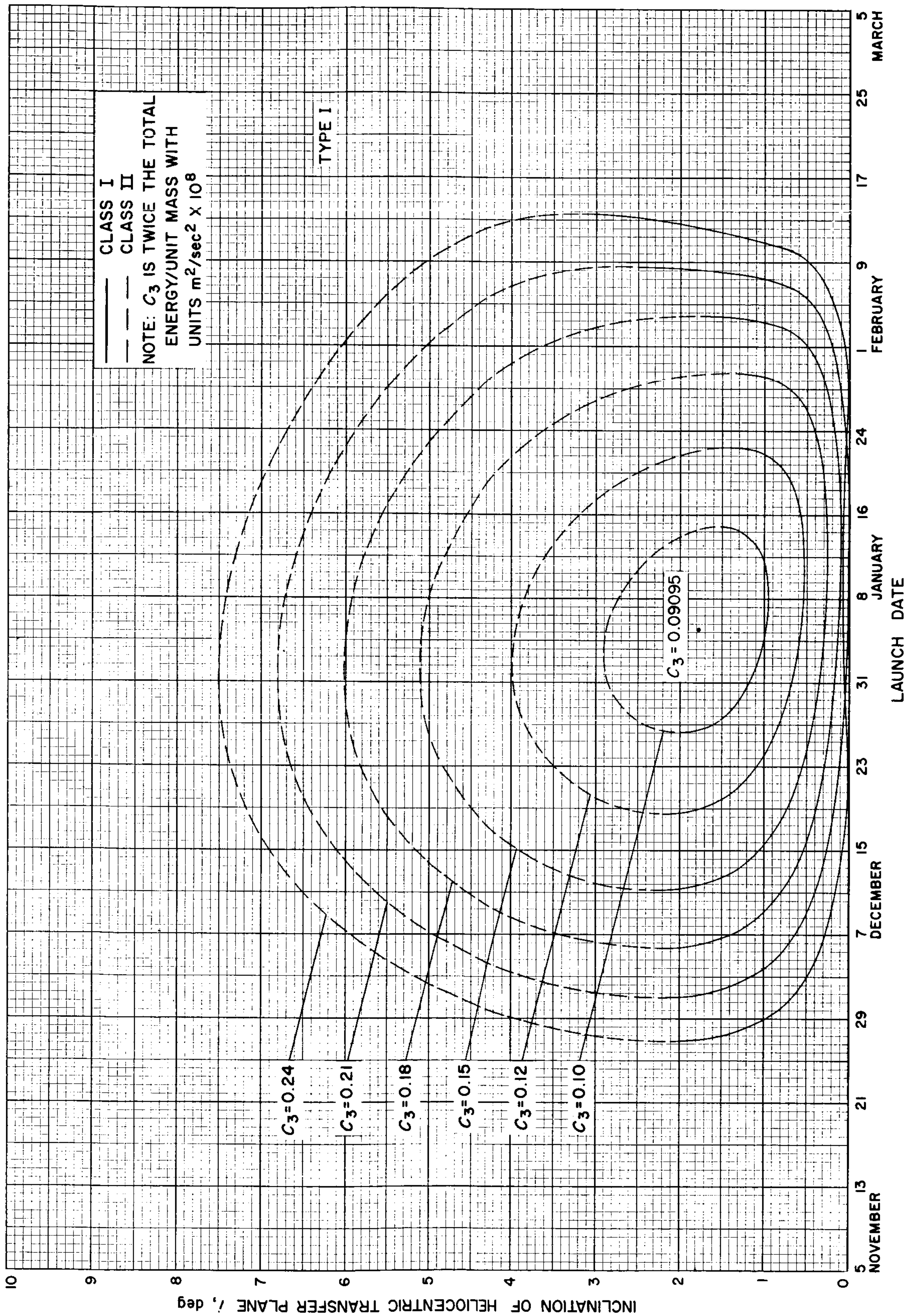

Fig. 13–12. Mars 1966: Inclination of heliocentric-transfer plane vs launch date

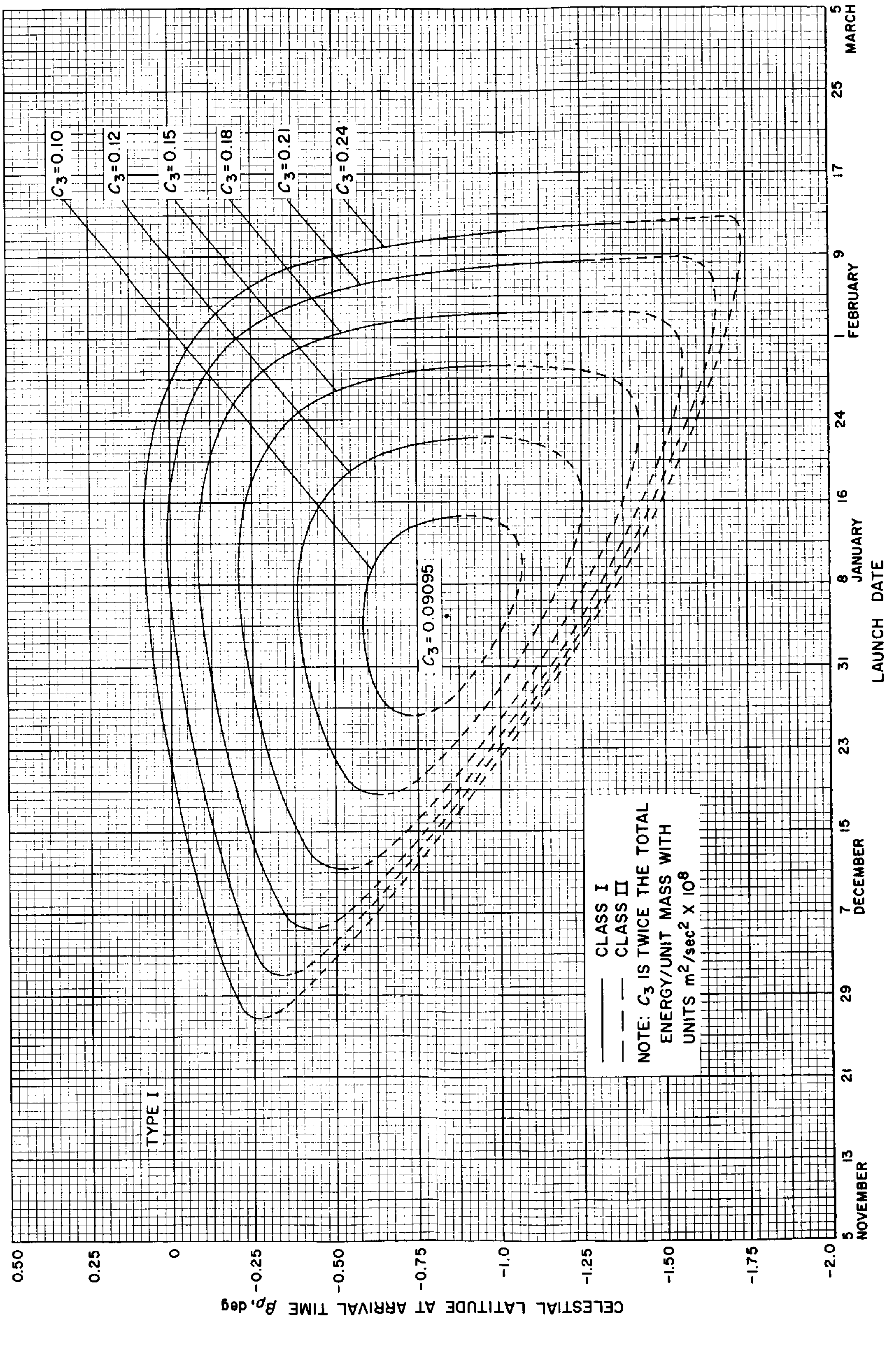

Fig. 13–13. *Mars 1966:* Celestial latitude at arrival time vs launch date

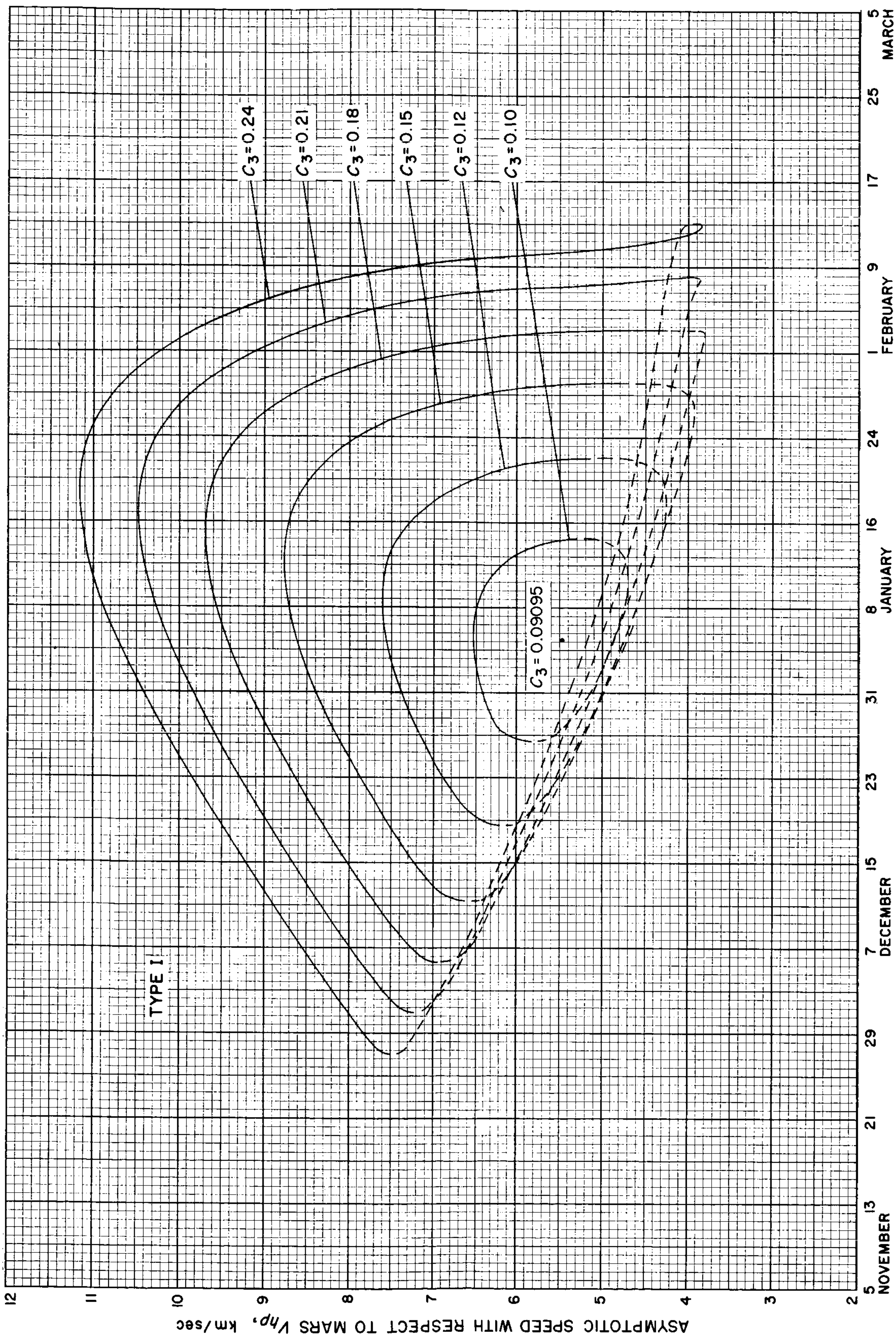

Fig. 13–14. Mars 1966: Asymptotic speed with respect to Mars vs launch date

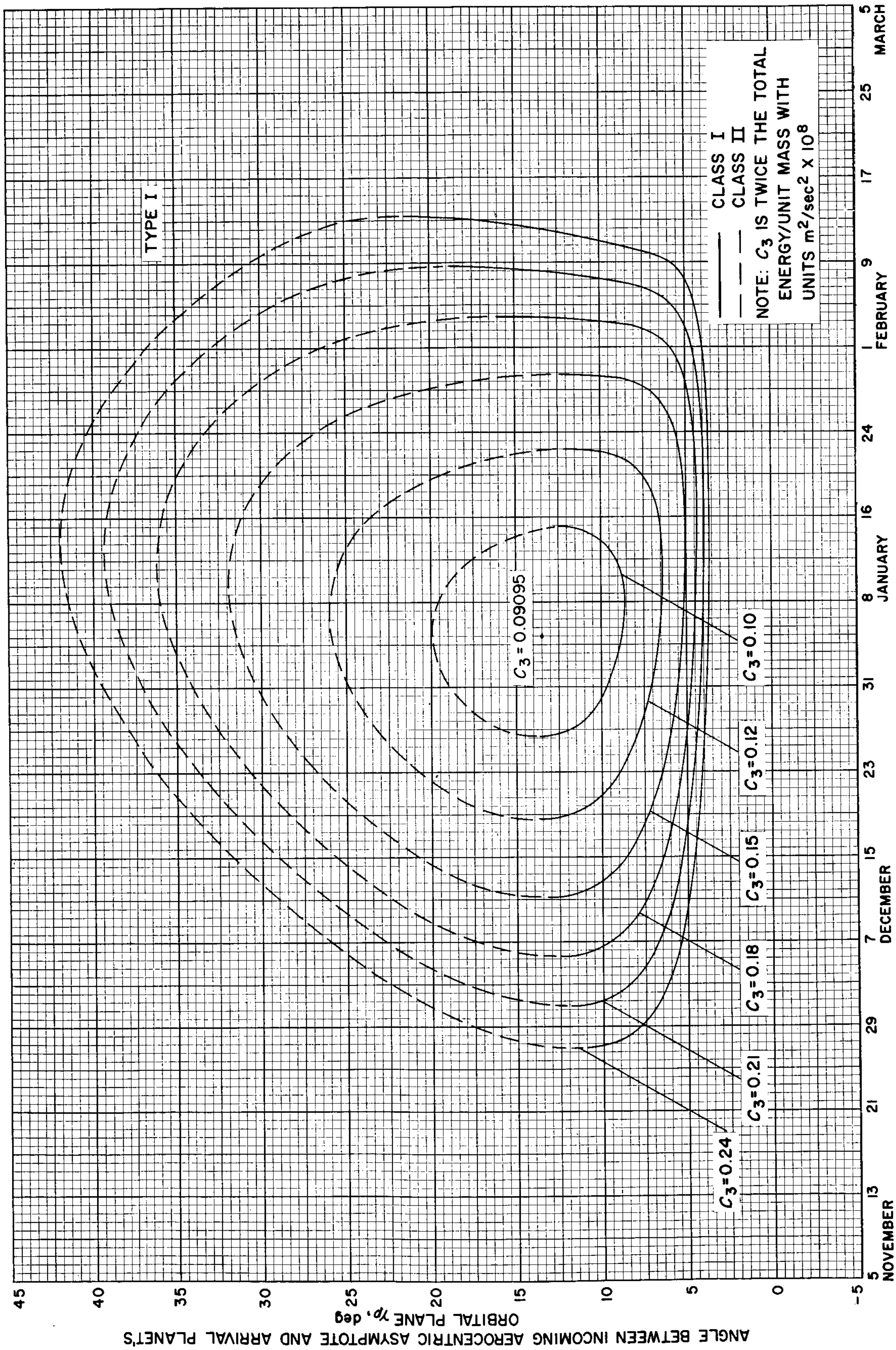

Fig. 13-15. *Mars 1966:* Angle between incoming aerocentric asymptote and arrival planet's orbital plane vs launch date

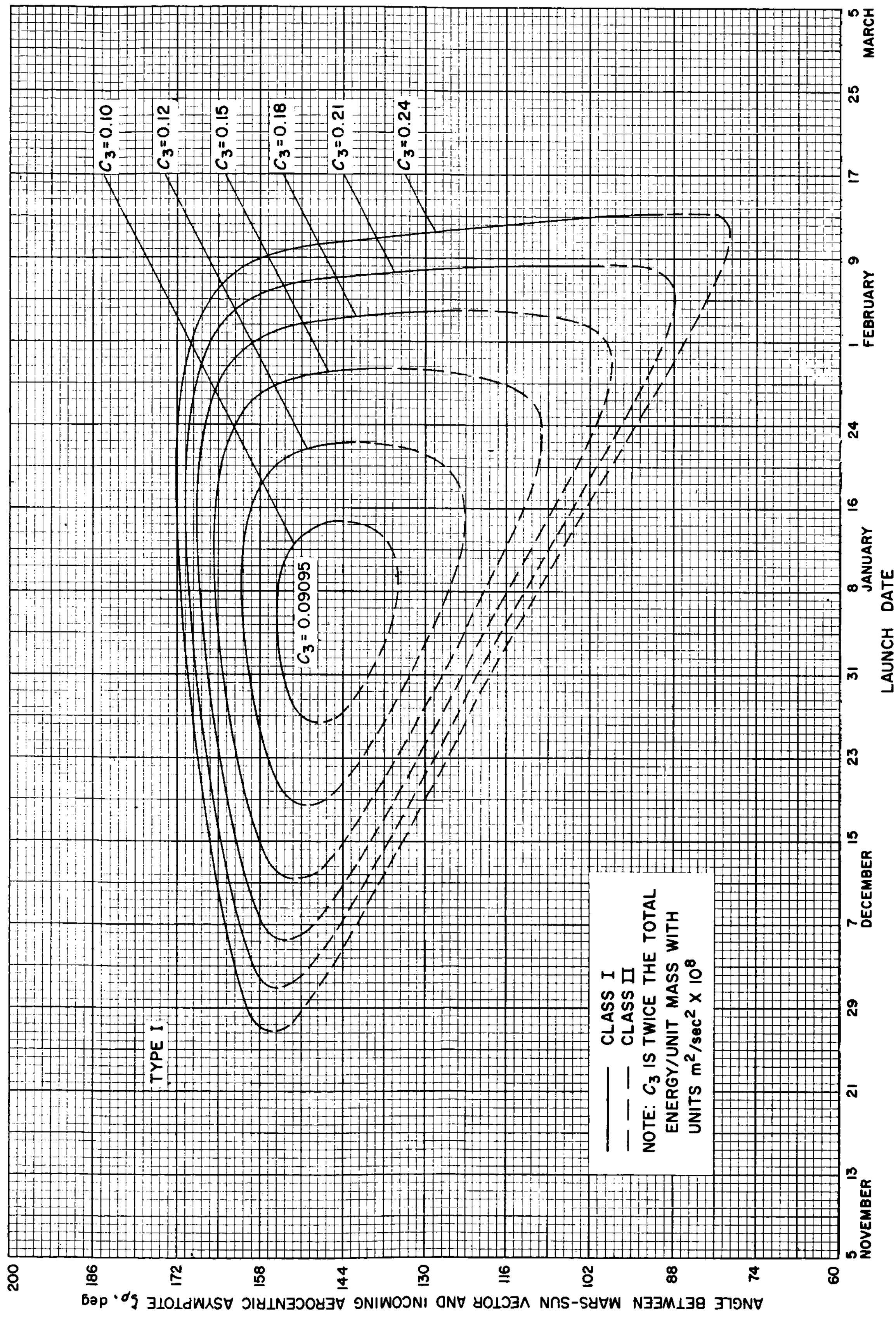

Fig. 13–16. Mars 1966: Angle between Mars–Sun vector and incoming aerocentric asymptote vs launch date

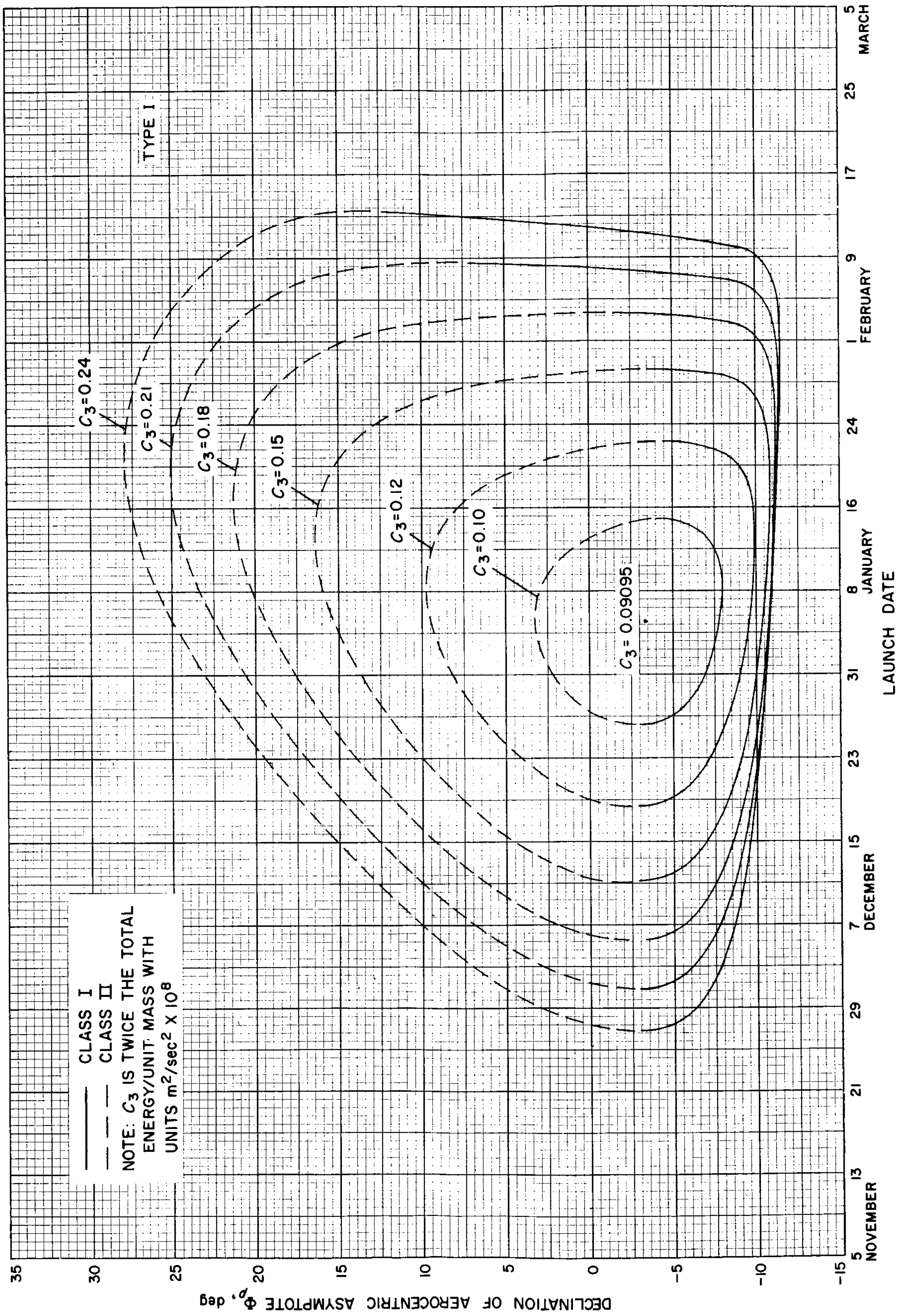

Fig. 13–17. Mars 1966: Declination of aerocentric asymptote vs launch date

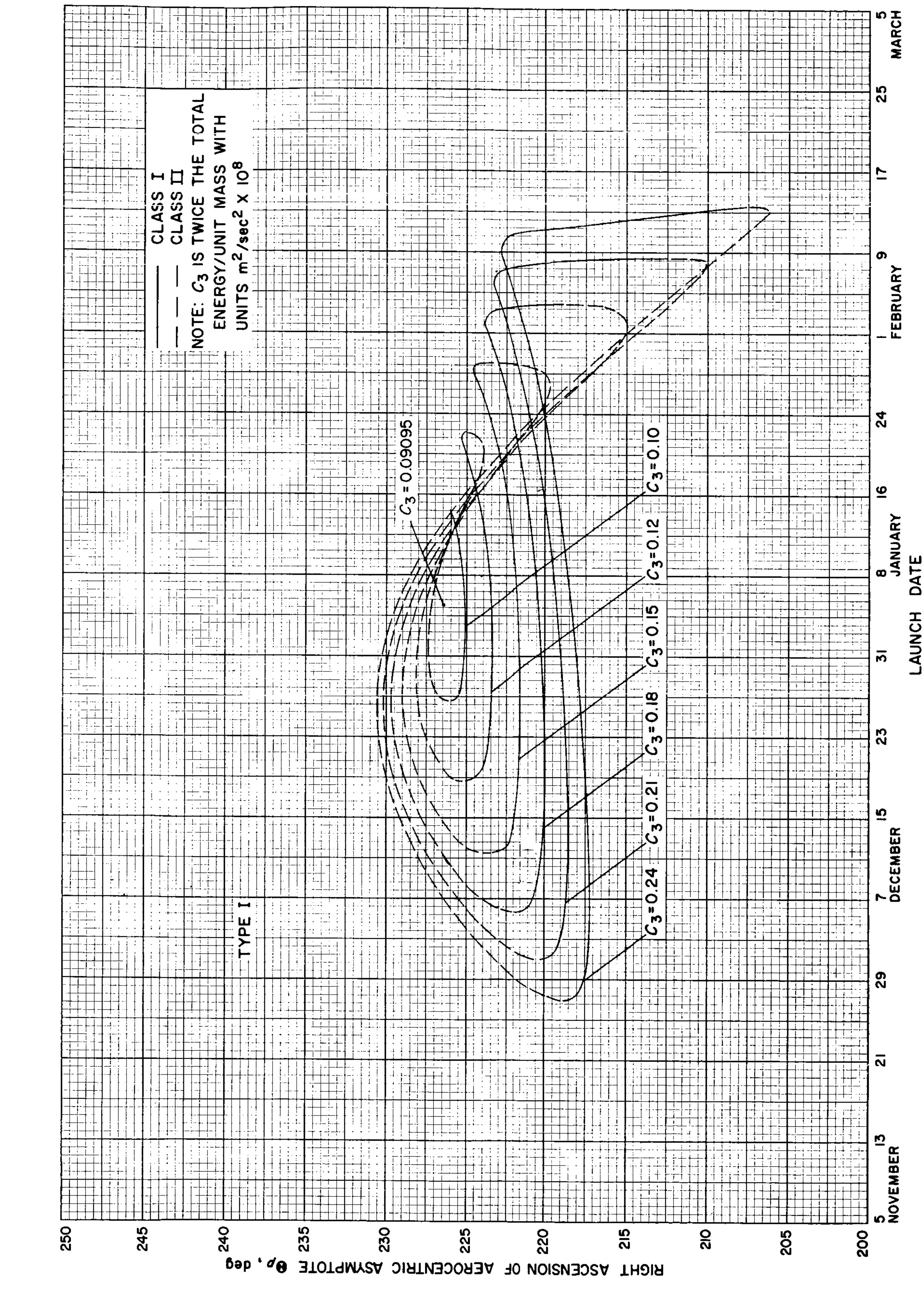

Fig. 13-18. Mars 1966: Right ascension of aerocentric asymptote vs launch date

XIV. MARS 1969: TRAJECTORY-PARAMETER GRAPHS

Figure

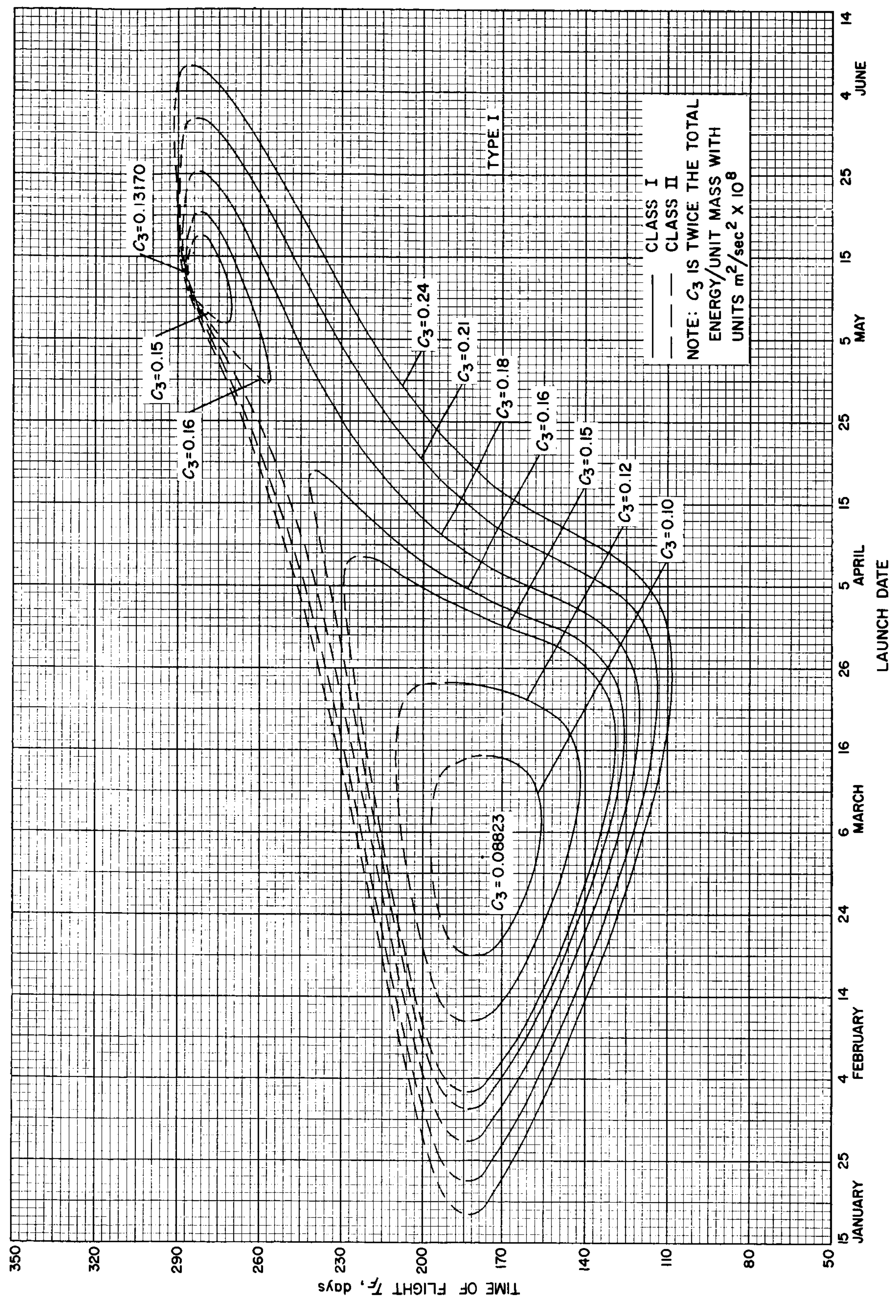

Fig. 14-1. Mars 1969: Time of flight vs launch date

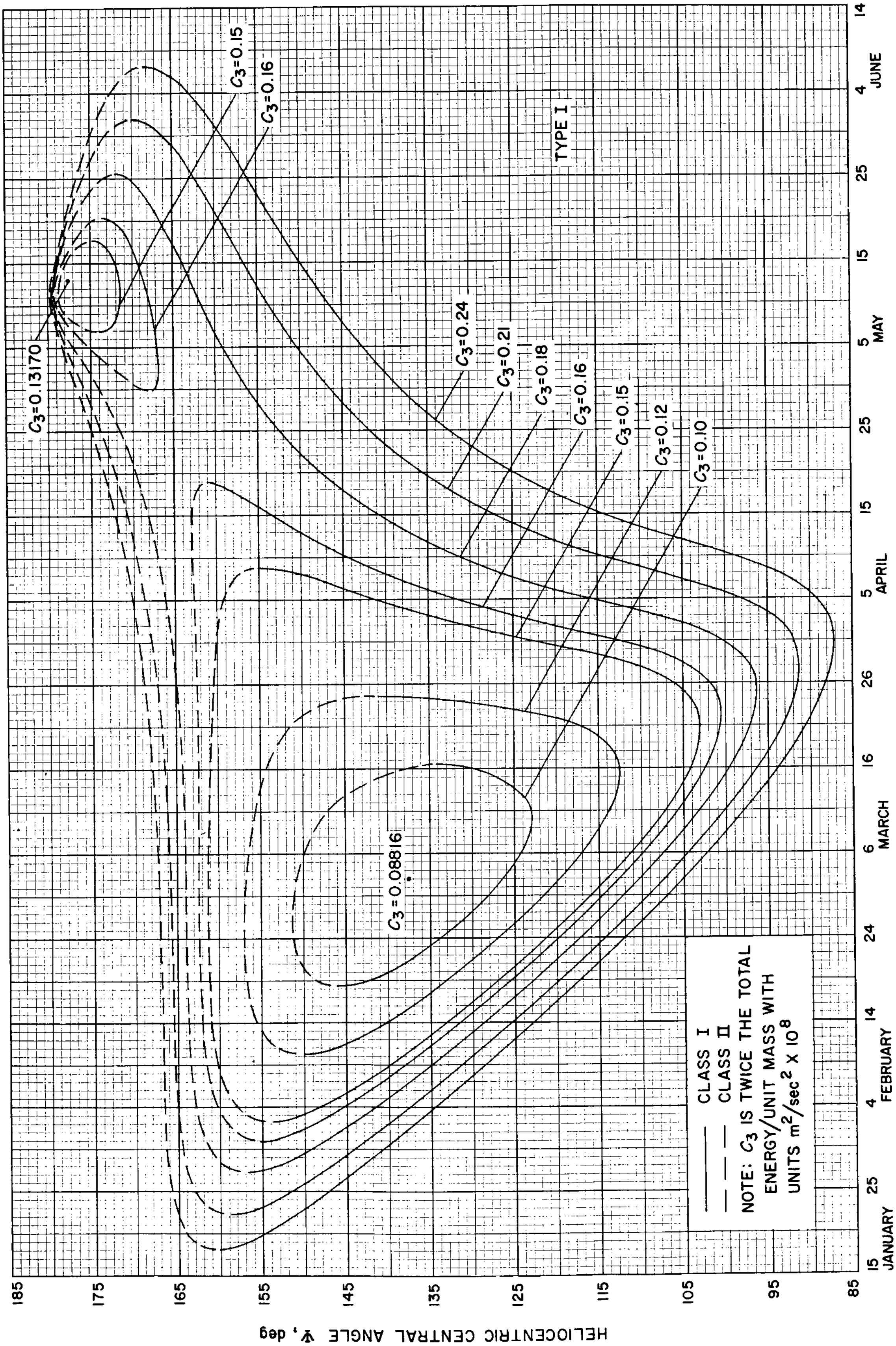

Fig. 14–2. Mars 1969: Heliocentric central angle vs launch date

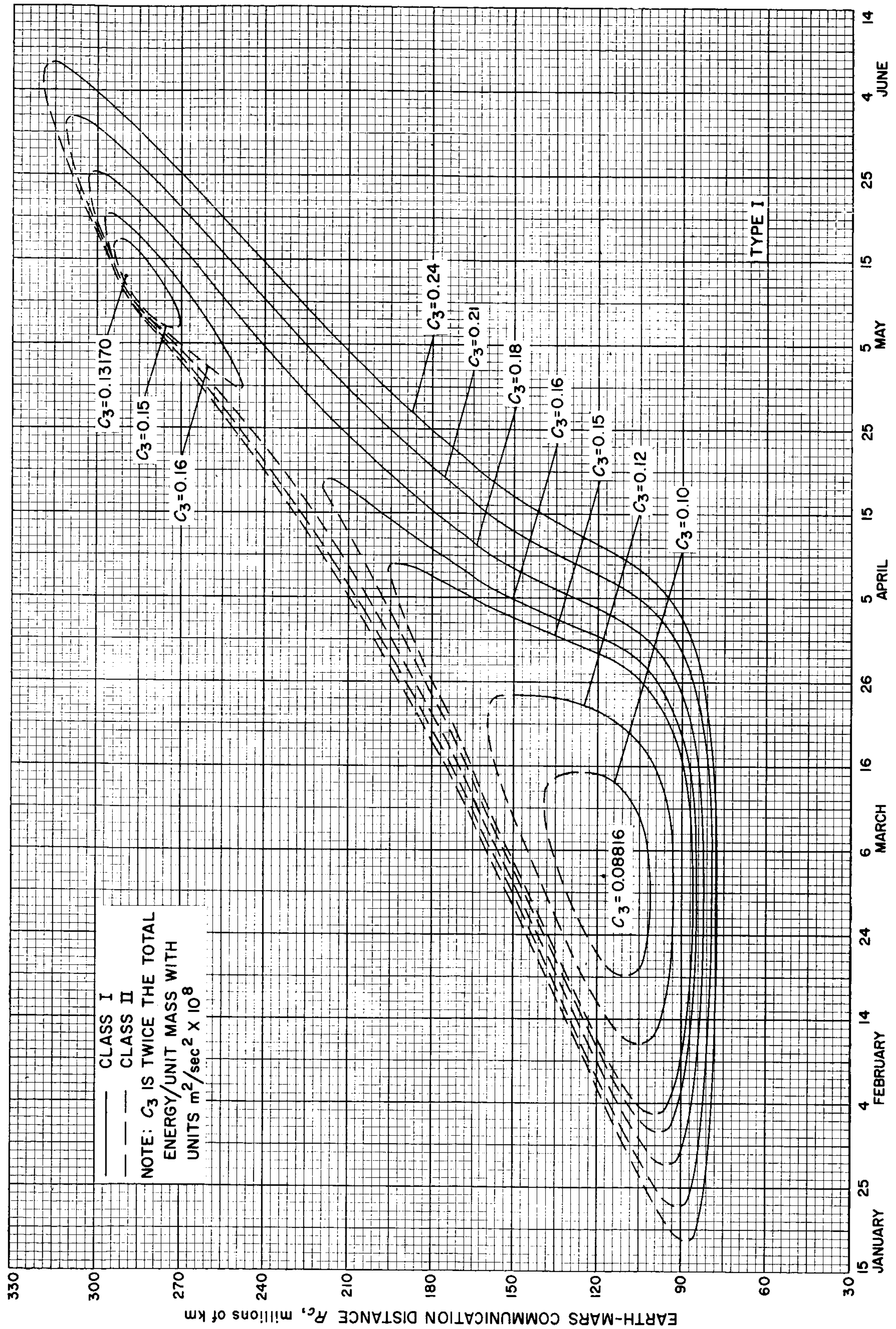

Fig. 14–3. Mars 1969: Earth–Mars communication distance vs launch date

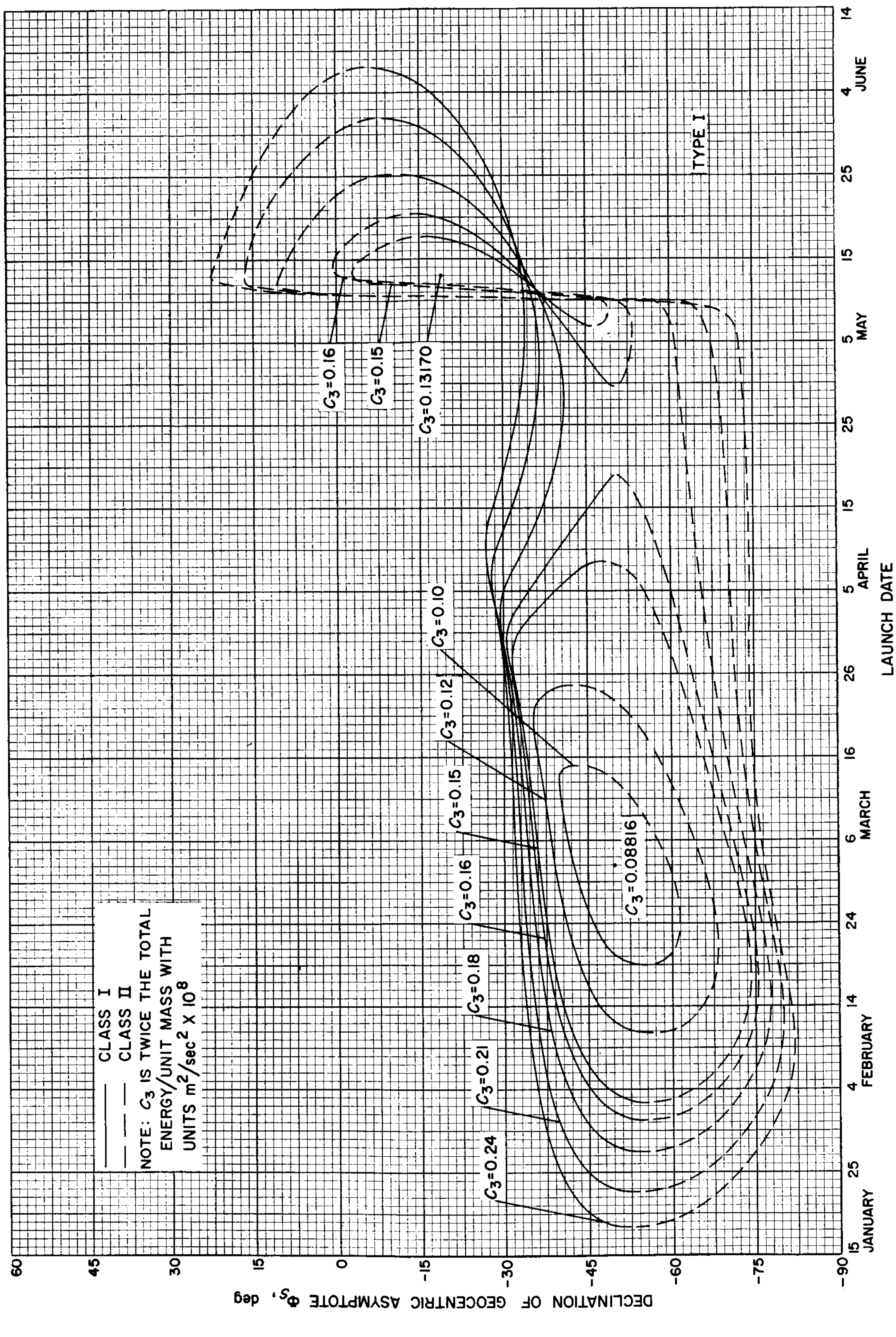

Fig. 14–4. Mars 1969: Declination of geocentric asymptote vs launch date

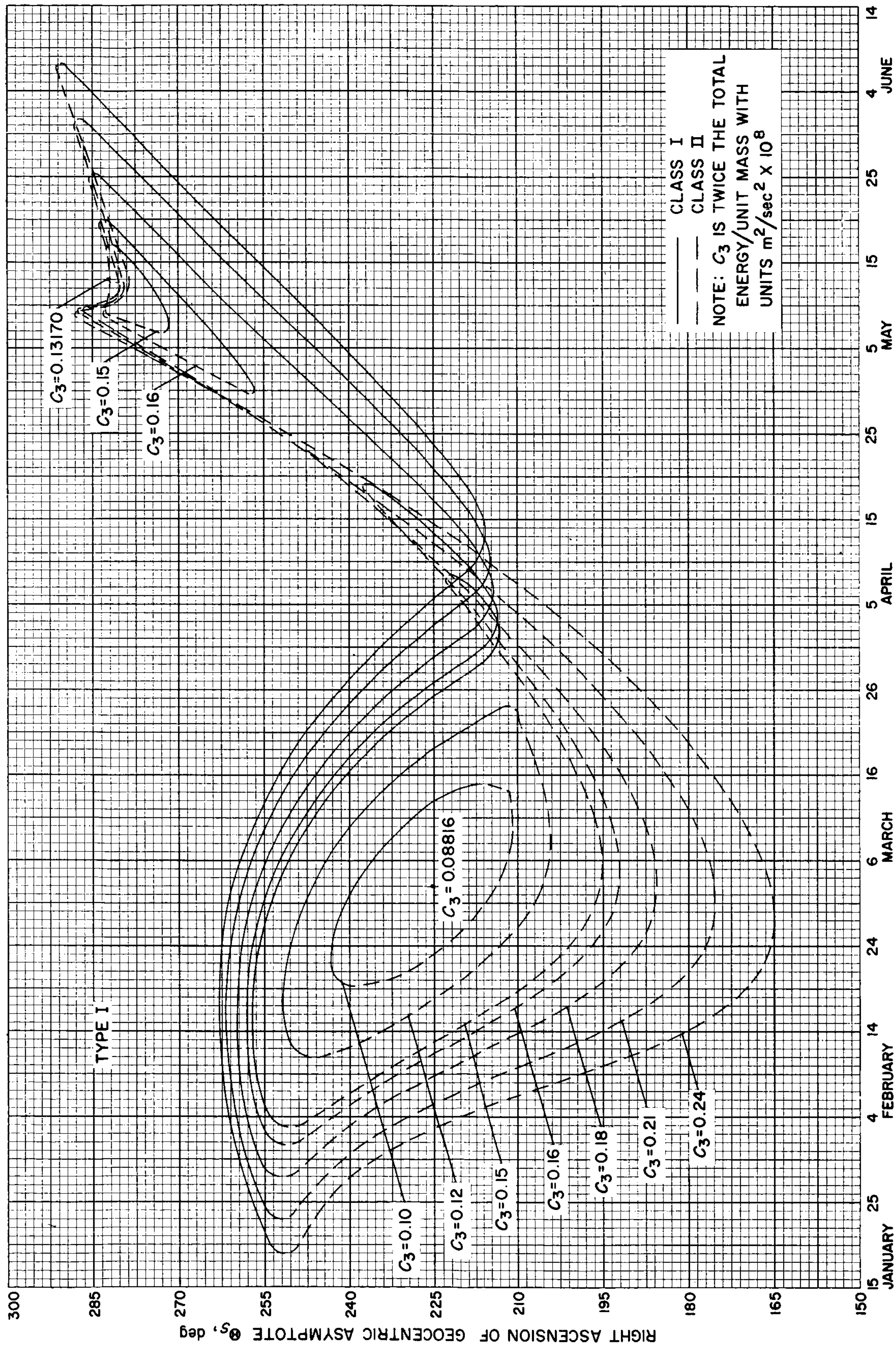

Fig. 14–5. Mars 1969: Right ascension of geocentric asymptote vs launch date

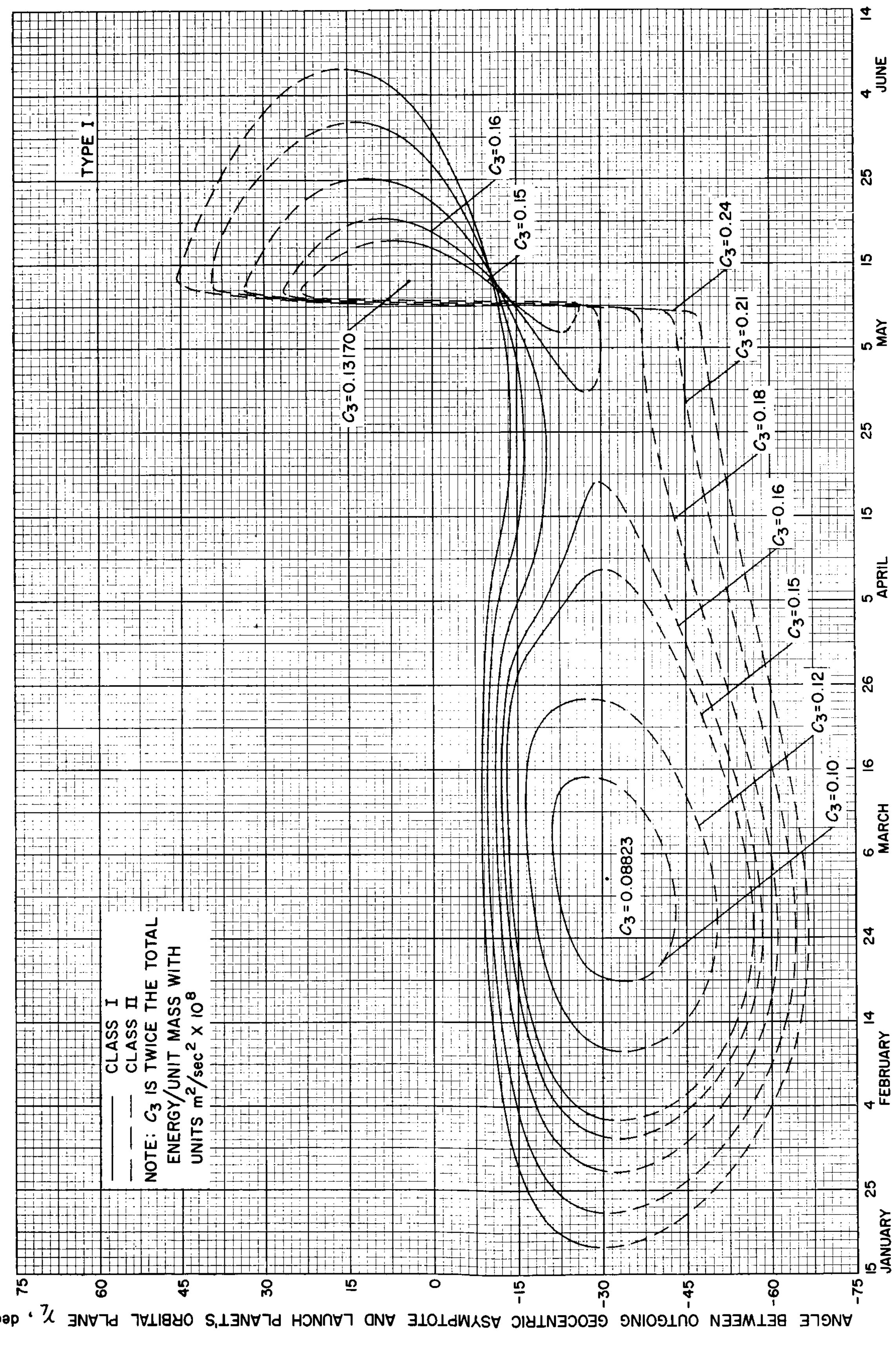

Fig. 14–6. Mars 1969: Angle between outgoing geocentric asymptote and launch planet's orbital plane vs launch date

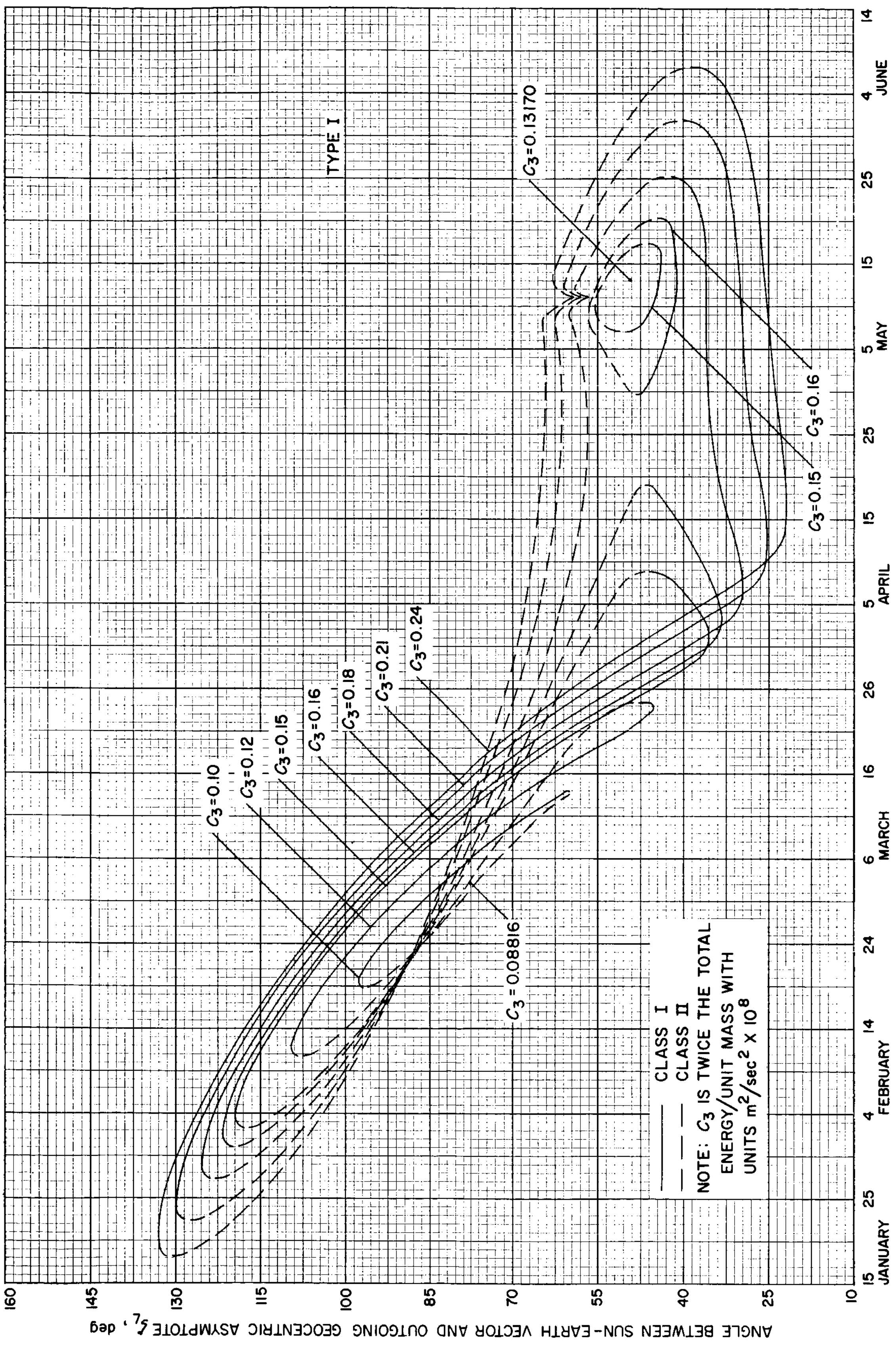

Fig. 14-7. Mars 1969: Angle between Sun–Earth vector and outgoing geocentric asymptote vs launch date

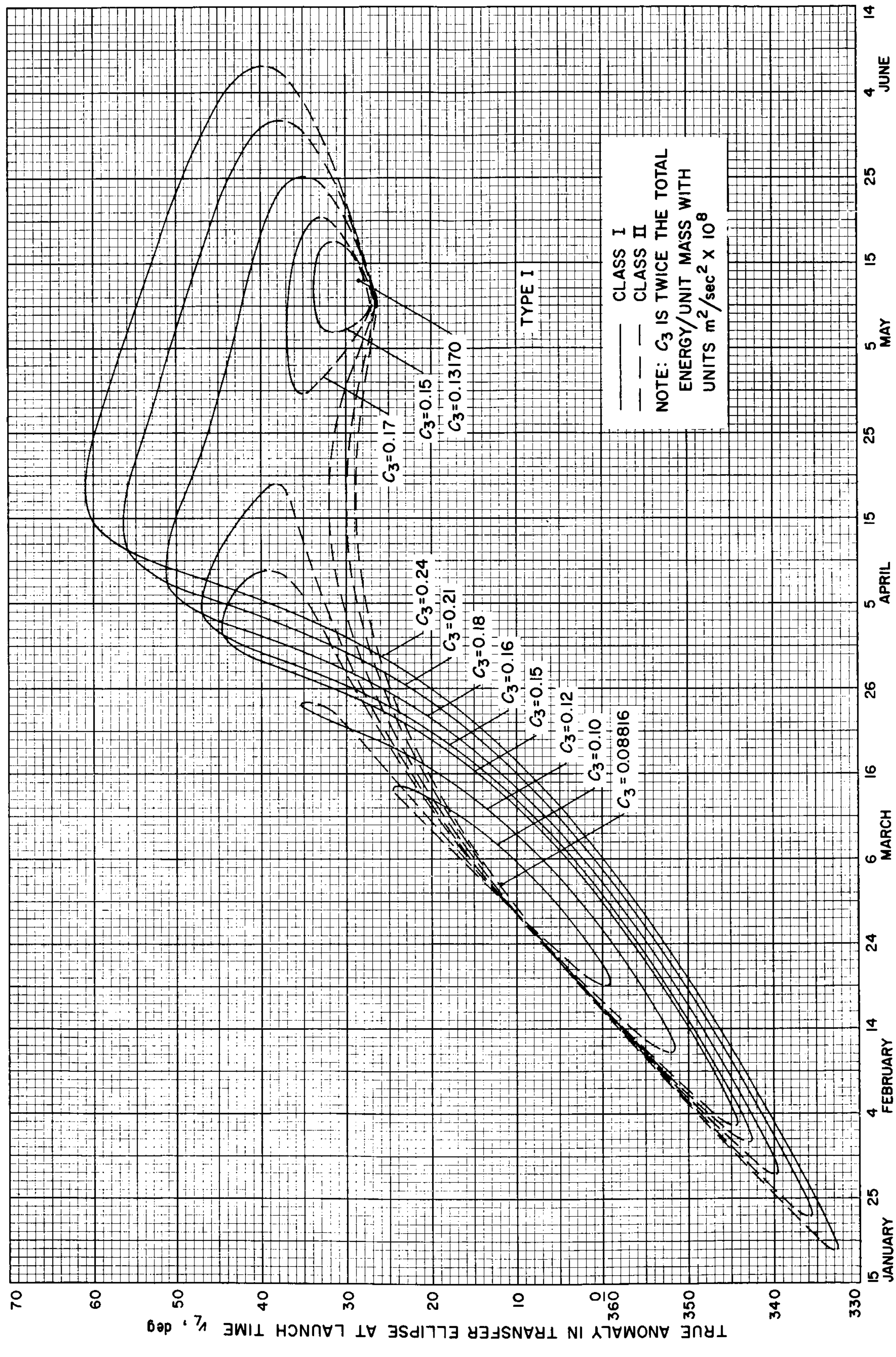

Fig. 14–8. Mars 1969: True anomaly in transfer ellipse at launch time vs launch date

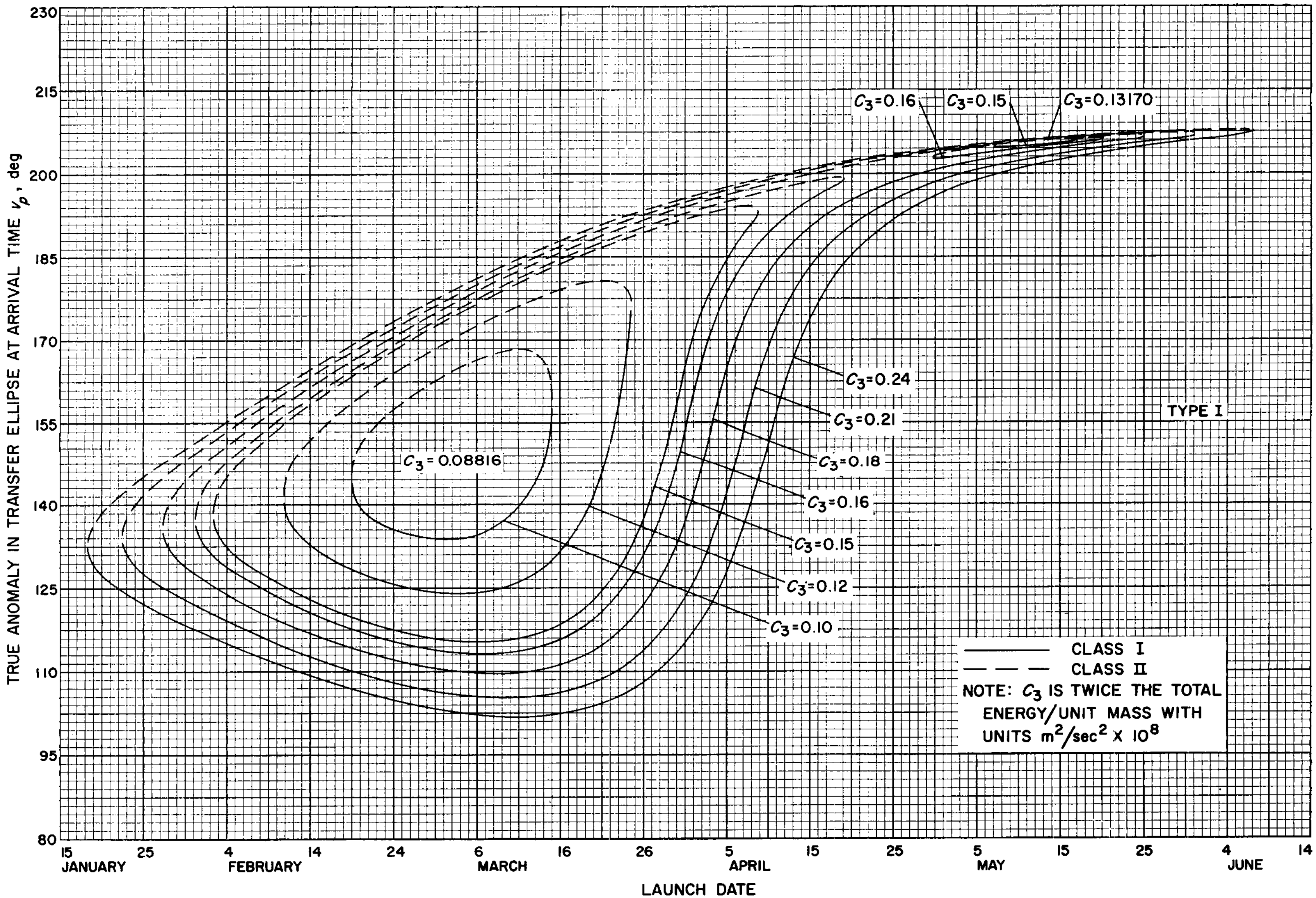

Fig. 14–9. Mars 1969: True anomaly in transfer ellipse at arrival time vs launch date

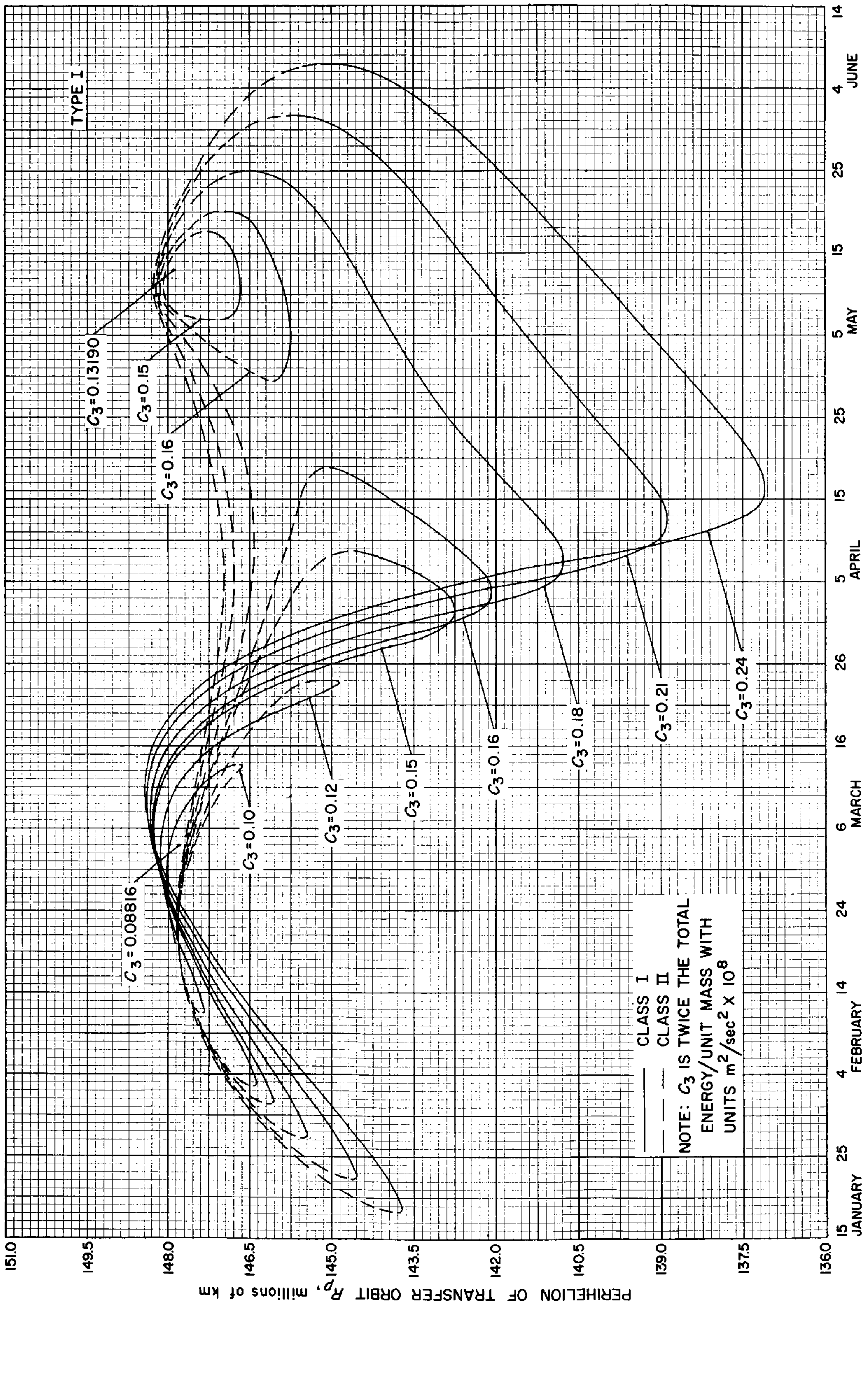

Fig. 14–10. Mars 1969: Perihelion of transfer orbit vs launch date

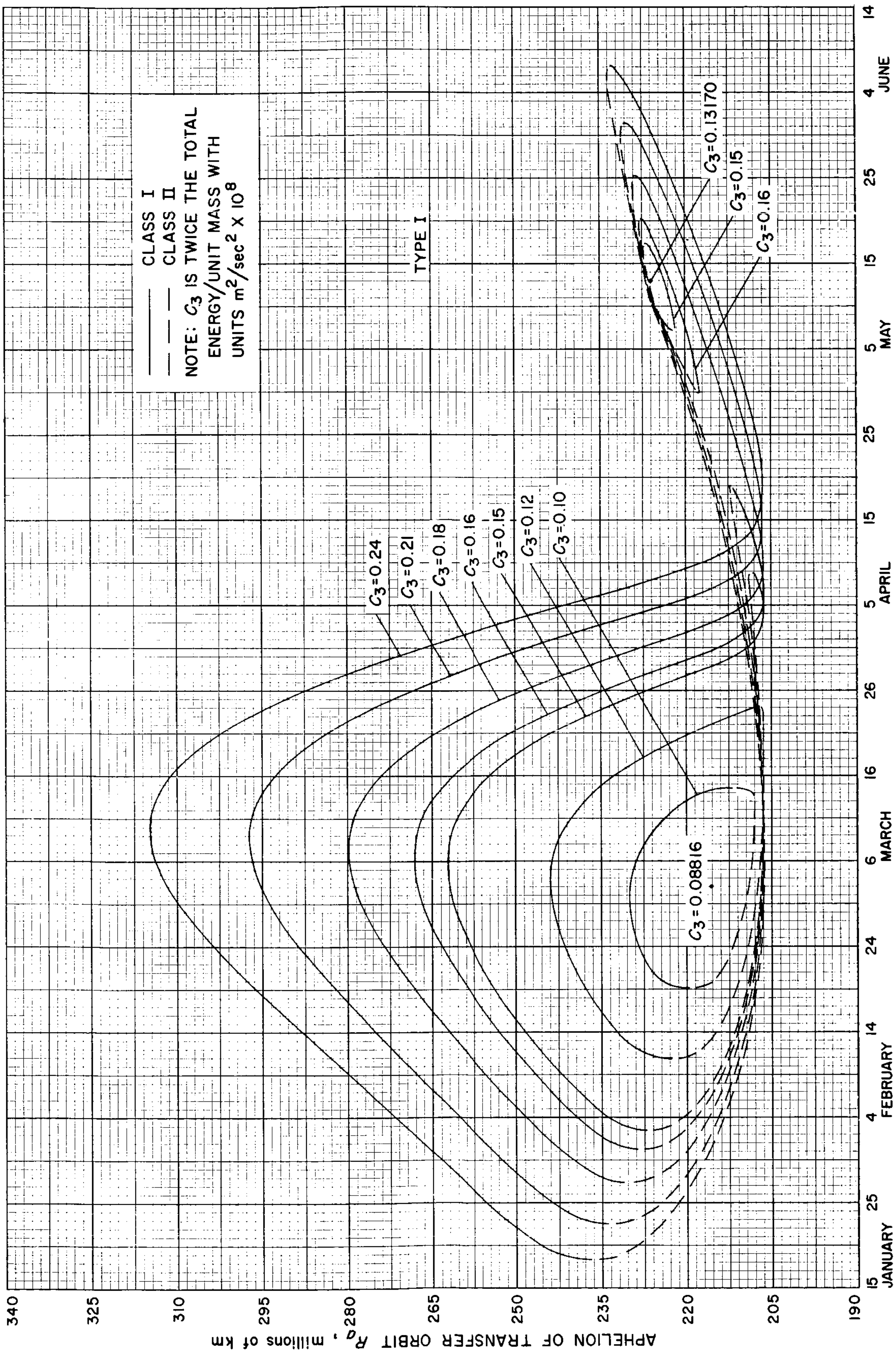

Fig. 14–11. Mars 1969: Aphelion of transfer orbit vs launch date

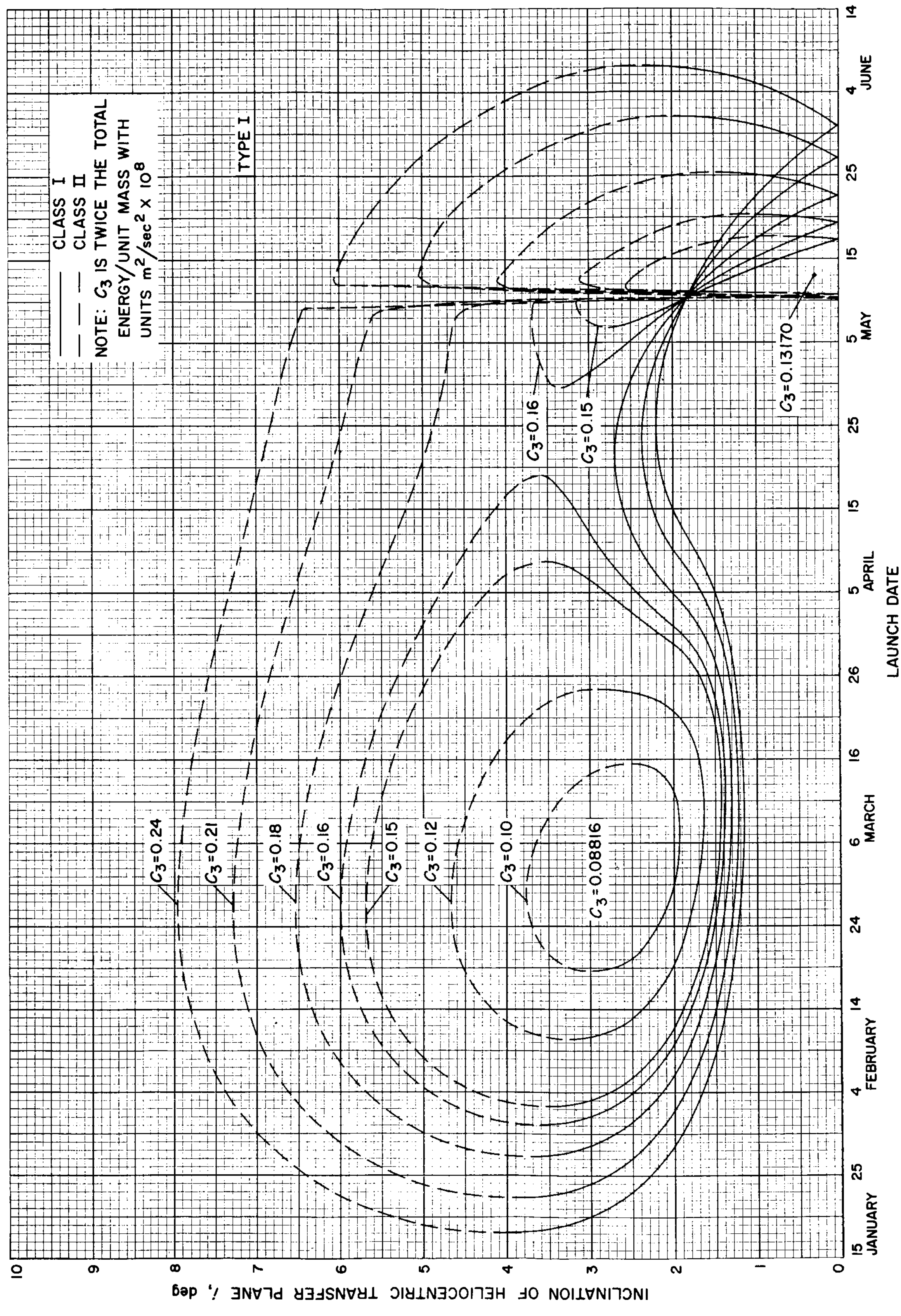

Fig. 14-12. Mars 1969: Inclination of heliocentric-transfer plane vs launch date

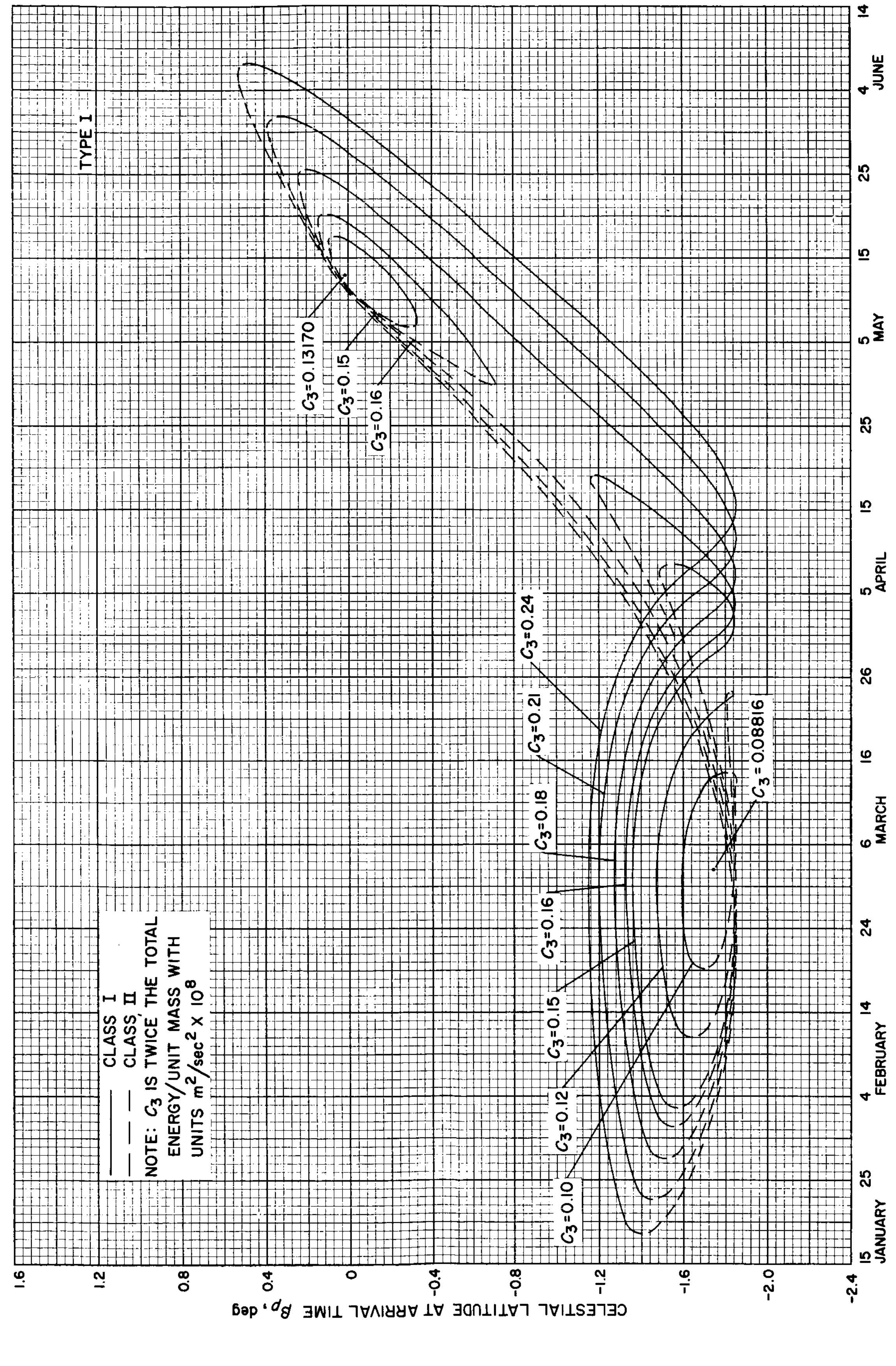

Fig. 14–13. Mars 1969: Celestial latitude at arrival time vs launch date

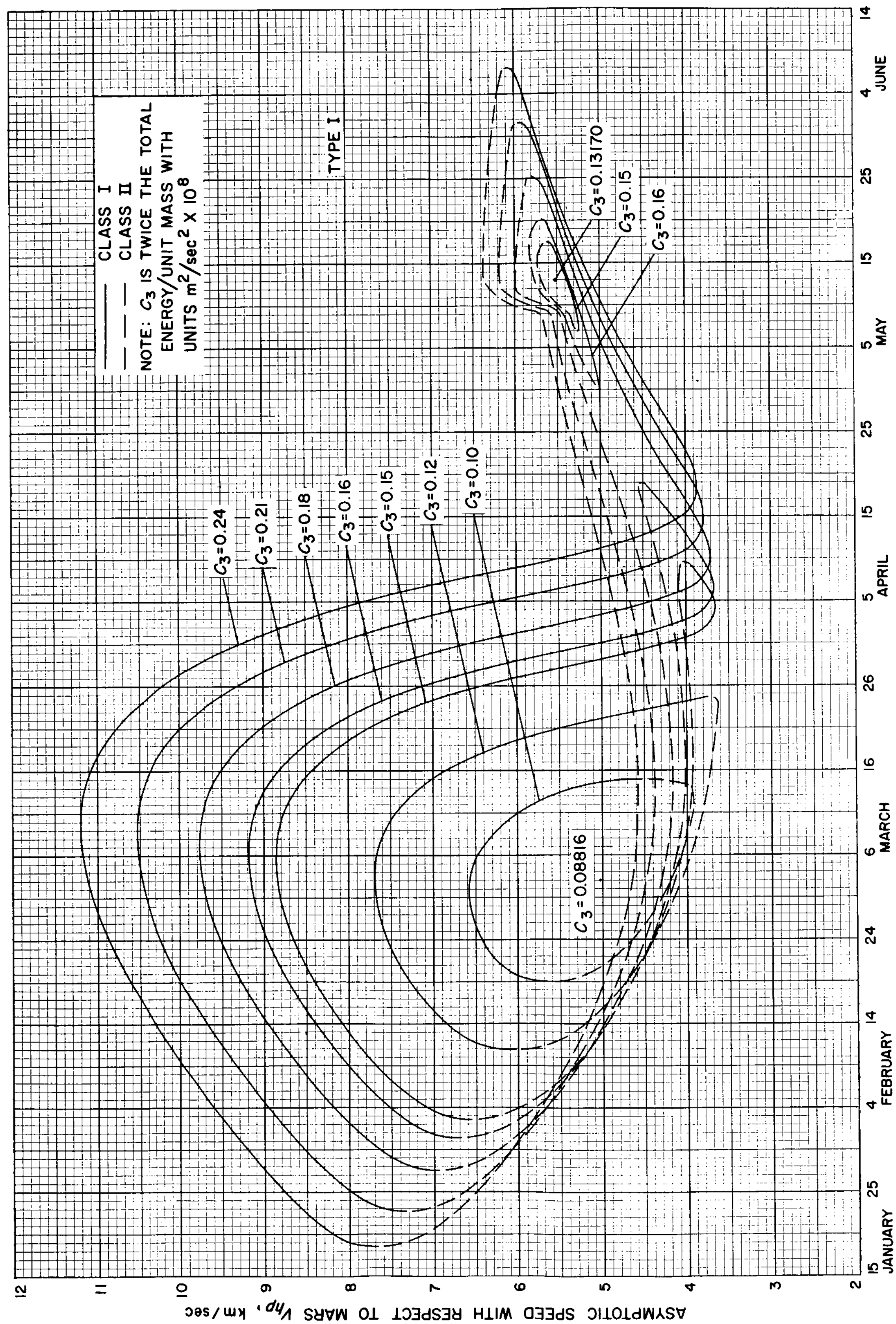

Fig. 14–14. Mars 1969: Asymptotic speed with respect to Mars vs launch date

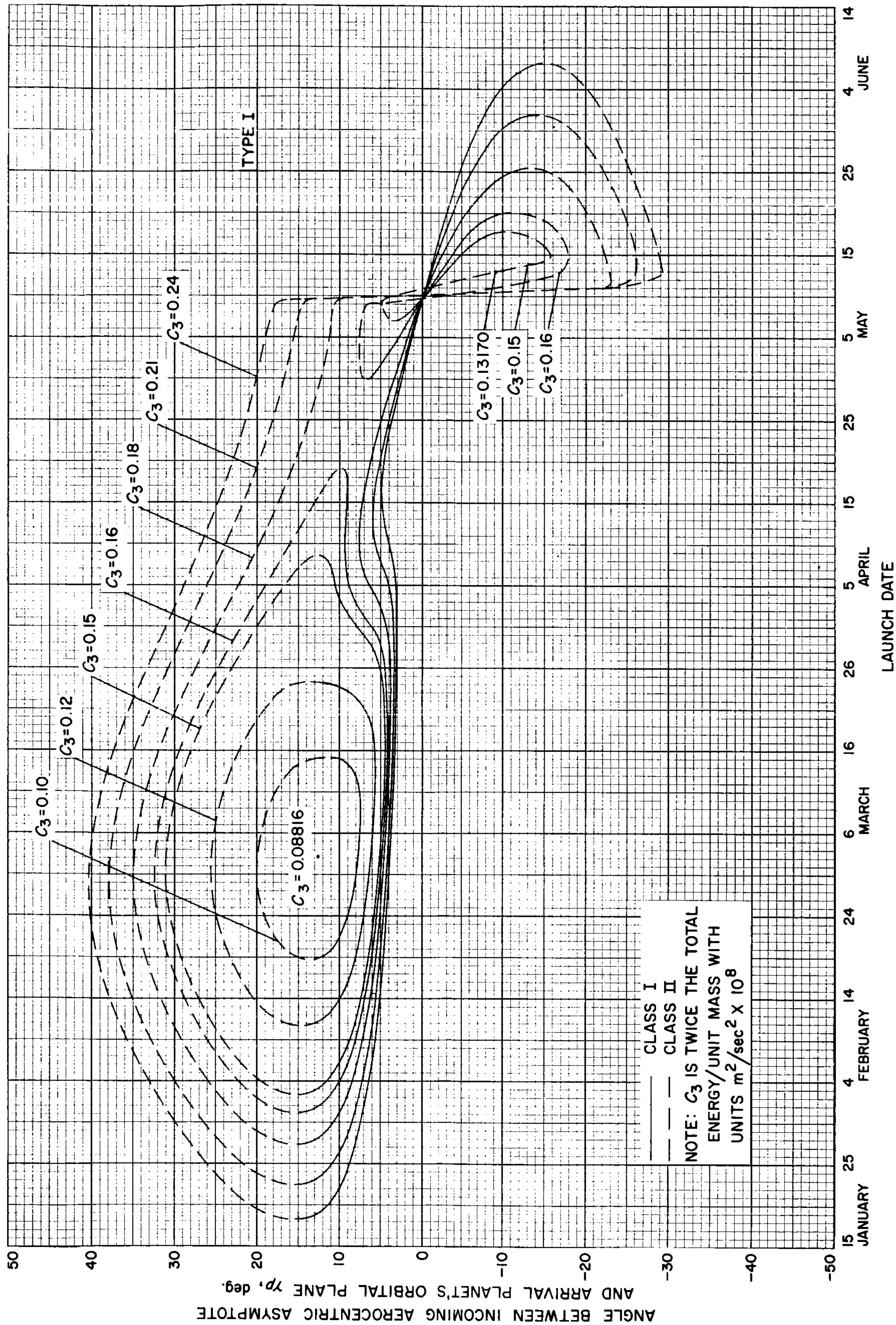

Fig. 14–15. Mars 1969: Angle between incoming aerocentric asymptote and arrival planet's orbital plane vs launch date

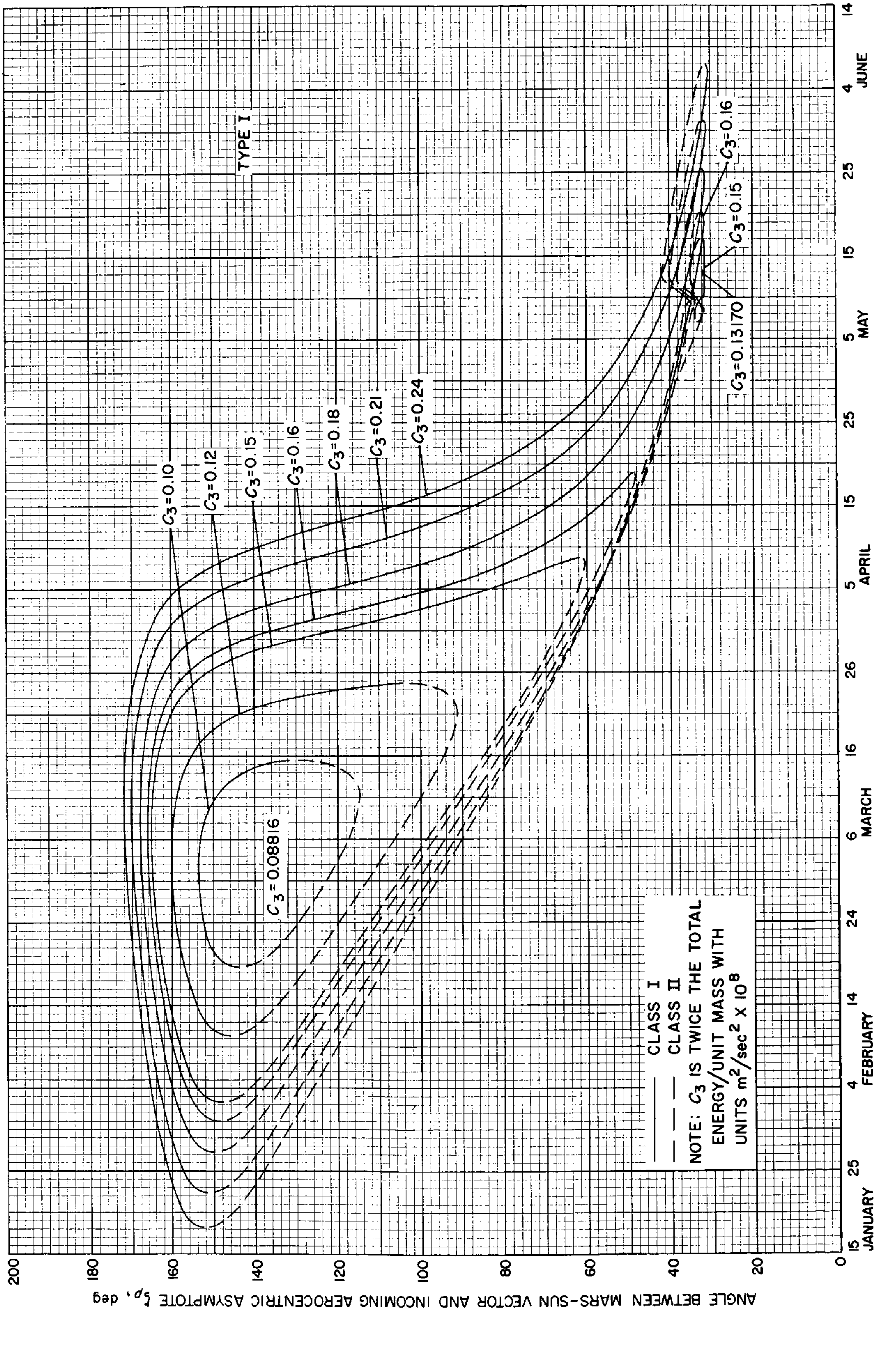

Fig. 14–16. Mars 1969: Angle between Mars–Sun vector and incoming aerocentric asymptote vs launch date

XV. MARS 1971: TRAJECTORY-PARAMETER GRAPHS

Figure

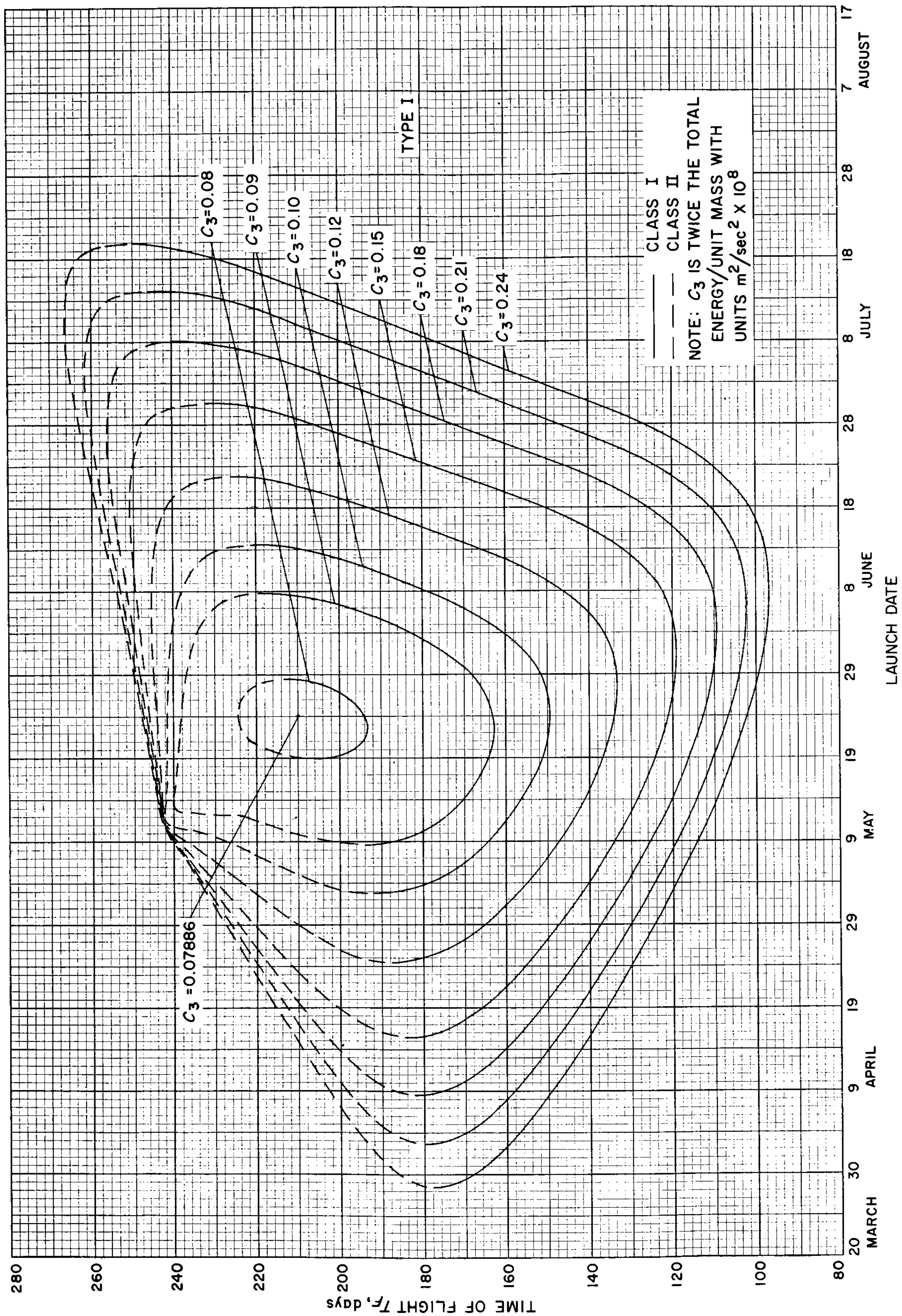

Fig. 15-1. Mars 1971: Time of flight vs launch date

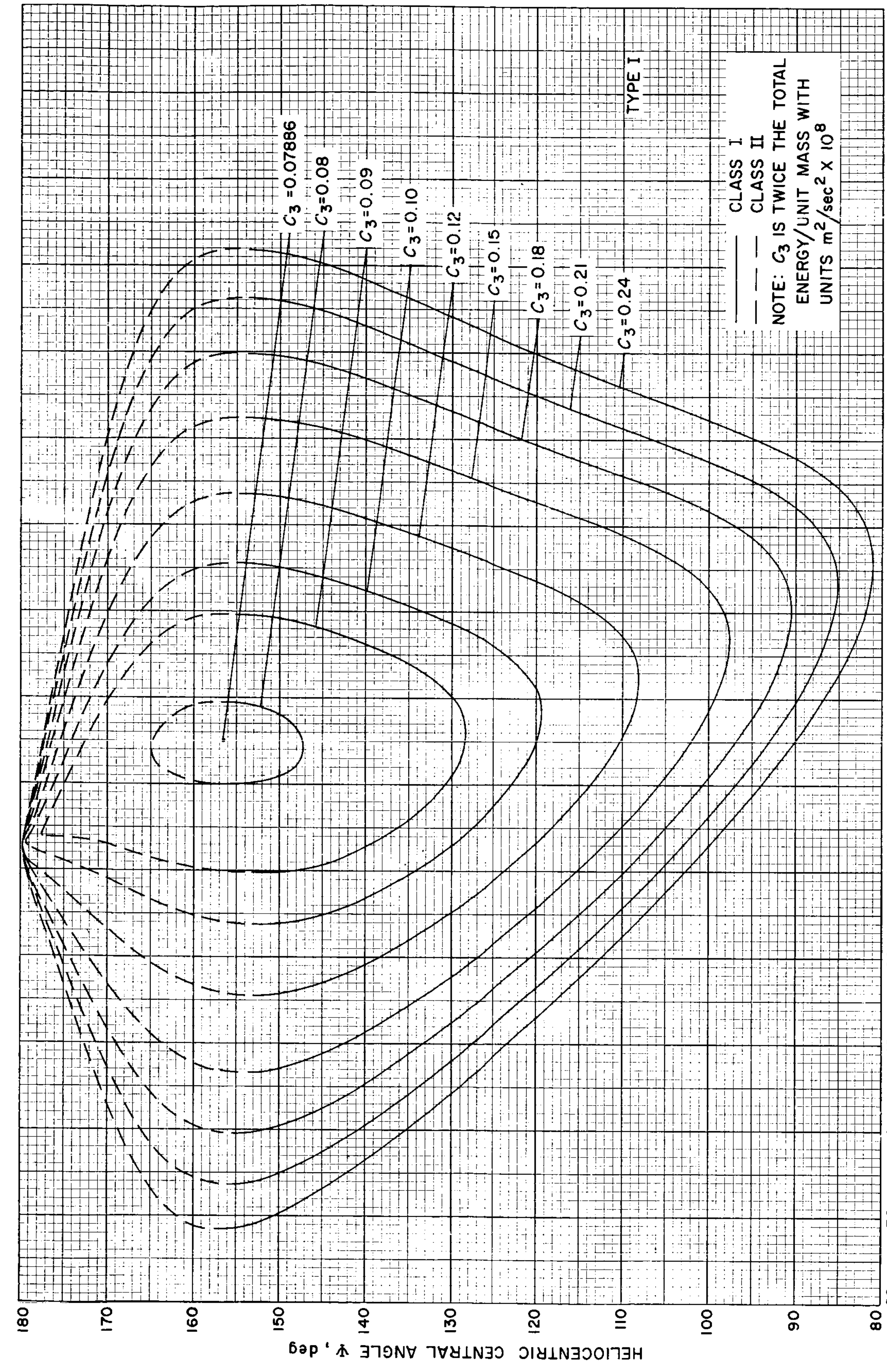

Fig. 15-2. Mars 1971: Heliocentric central angle vs launch date

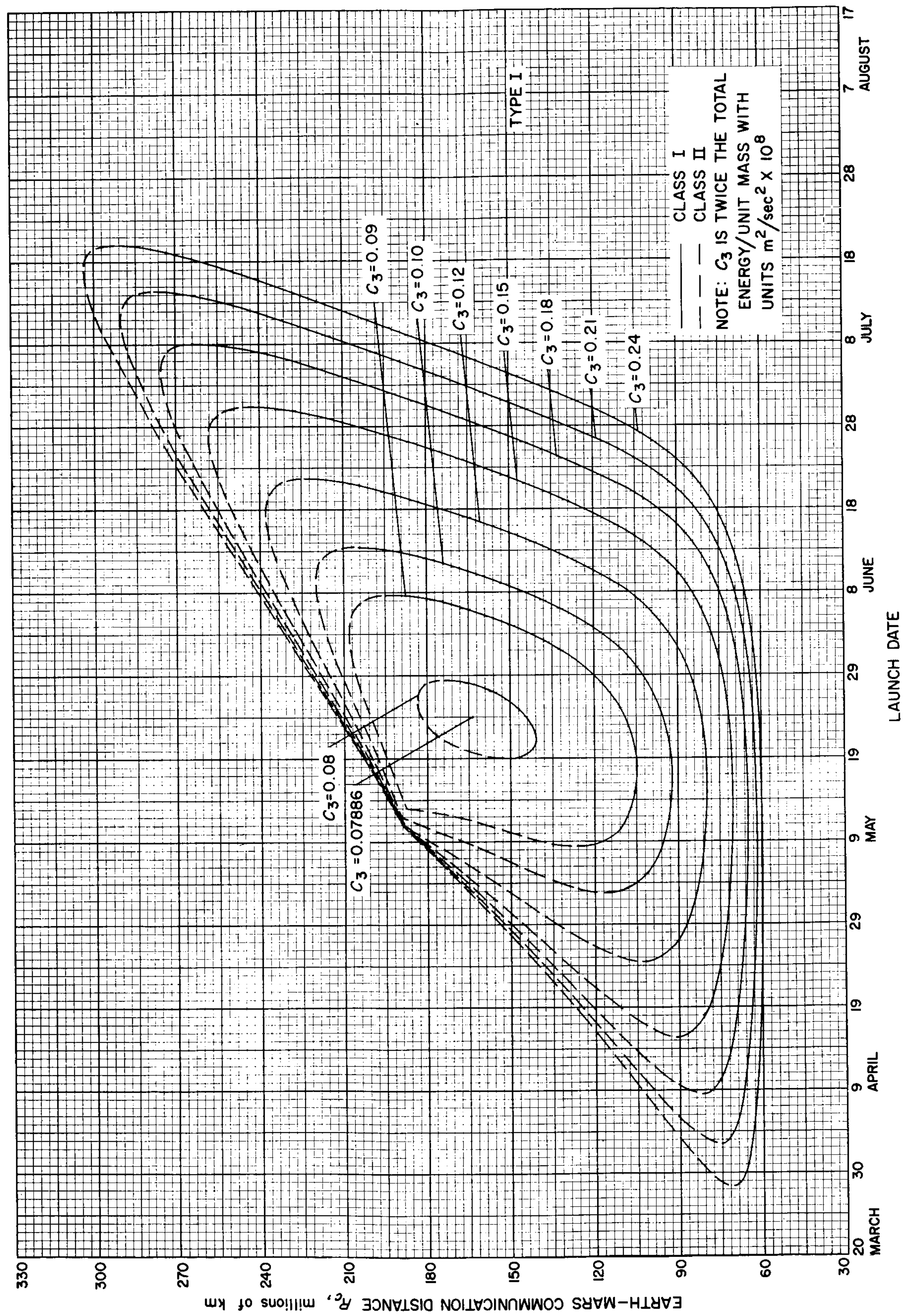

Fig. 15–3. Mars 1971: Earth–Mars communication distance vs launch date

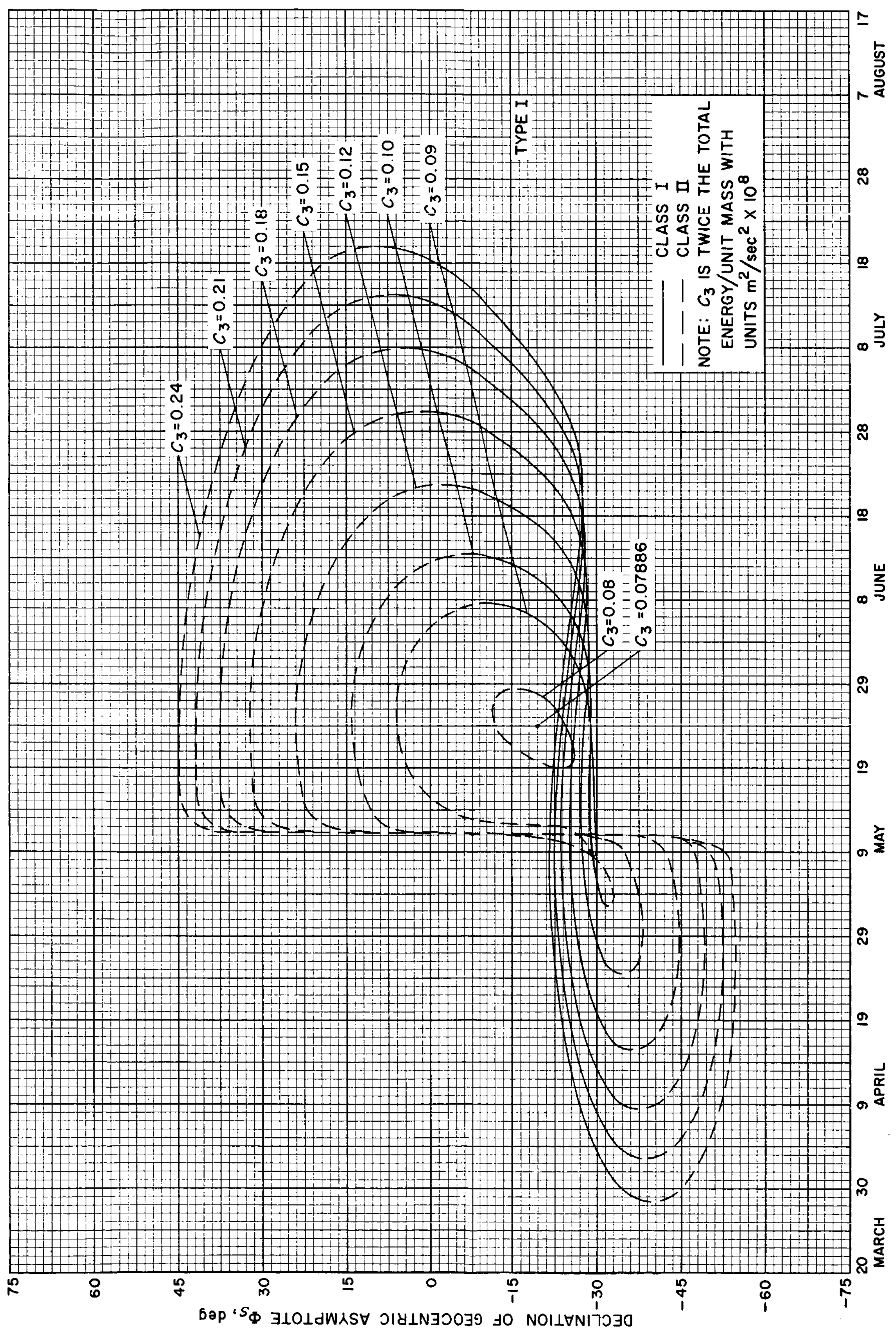

Fig. 15–4. Mars 1971: Declination of geocentric asymptote vs launch date

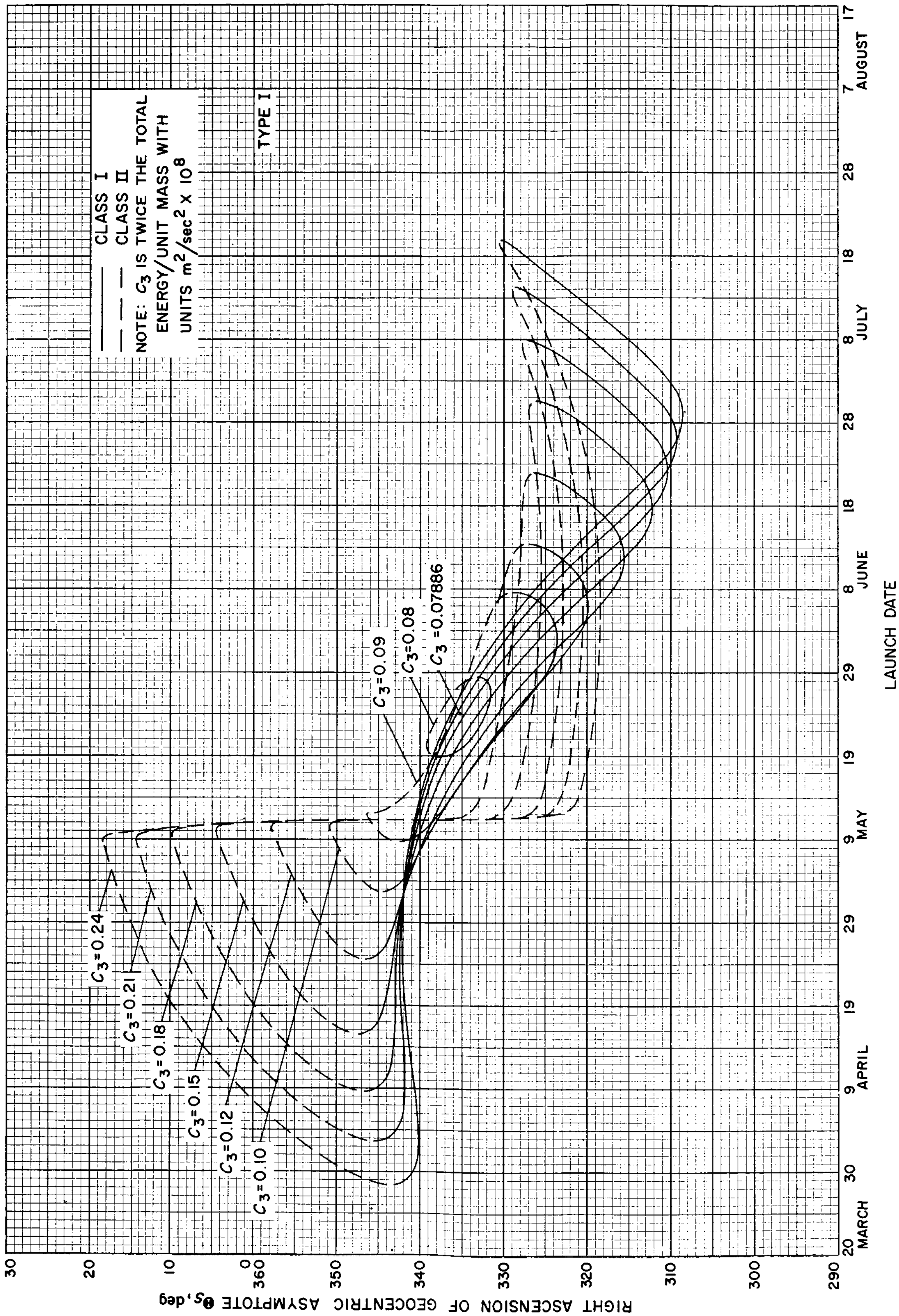

Fig. 15–5. Mars 1971: Right ascension of geocentric asymptote vs launch date

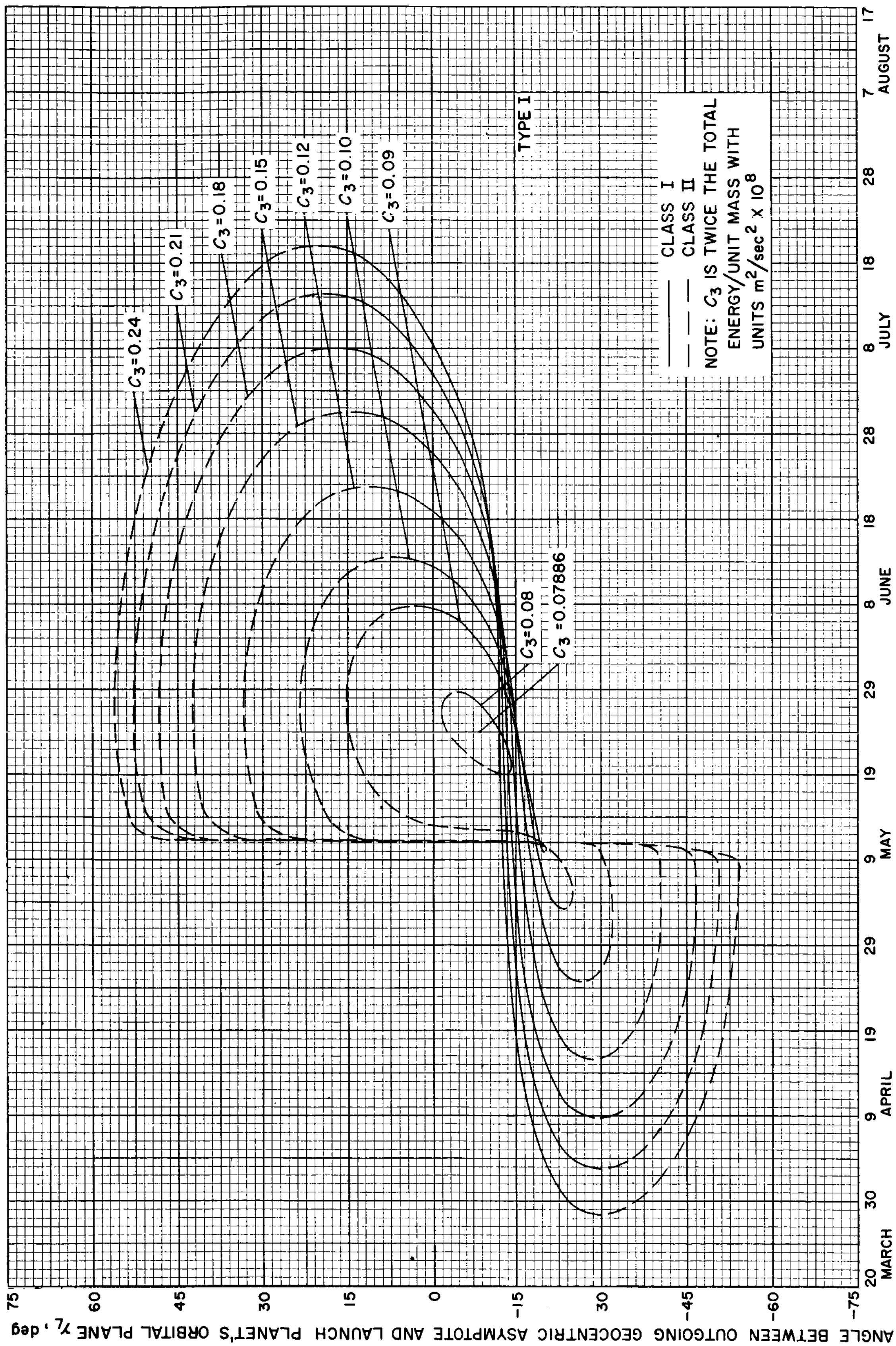

Fig. 15–6. Mars 1971: Angle between outgoing geocentric asymptote and launch planet's orbital plane vs launch date

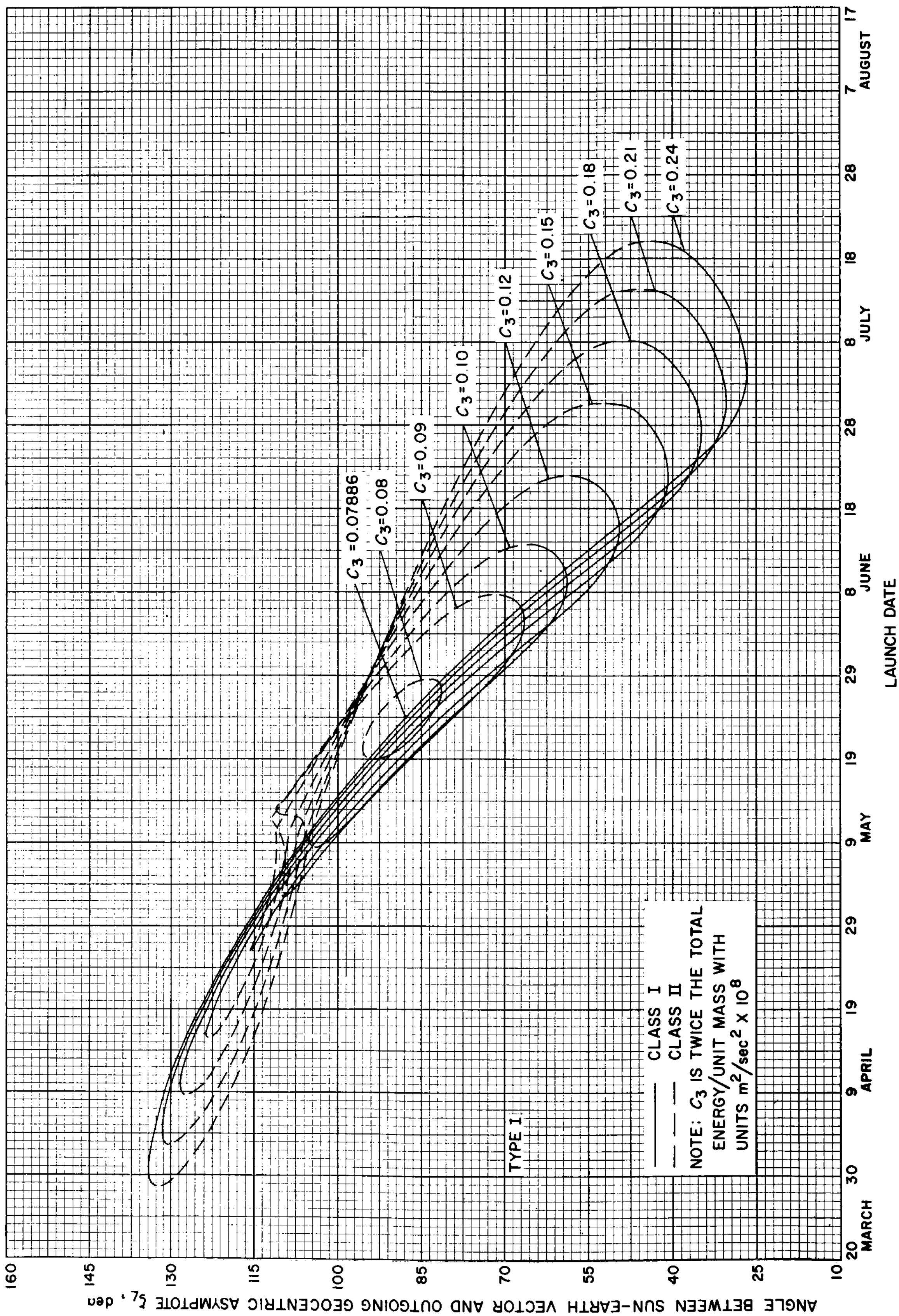

Fig. 15-7. Mars 1971: Angle between Sun–Earth vector and outgoing geocentric asymptote vs launch date

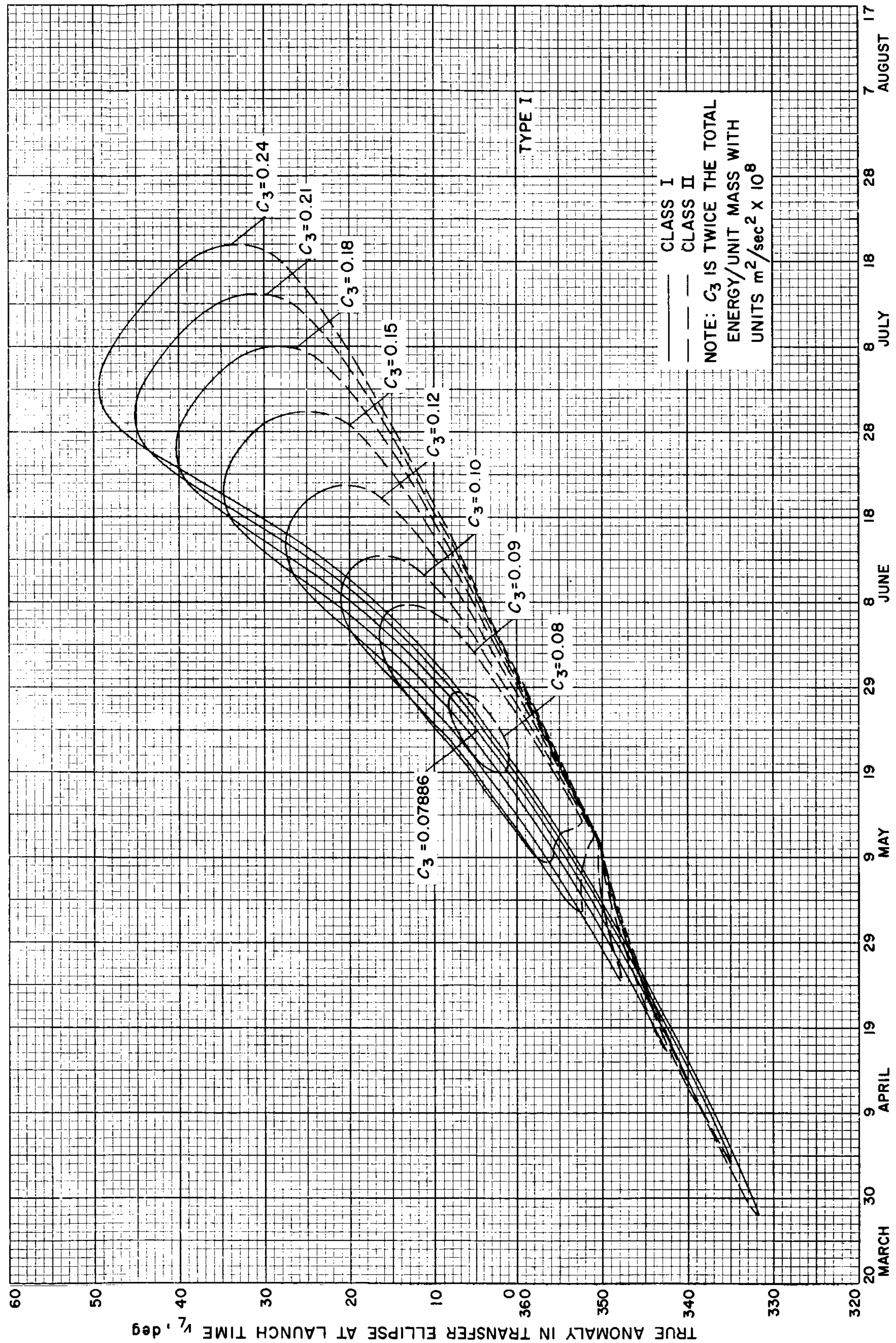

Fig. 15–8. Mars 1971: True anomaly in transfer ellipse at launch time vs launch date

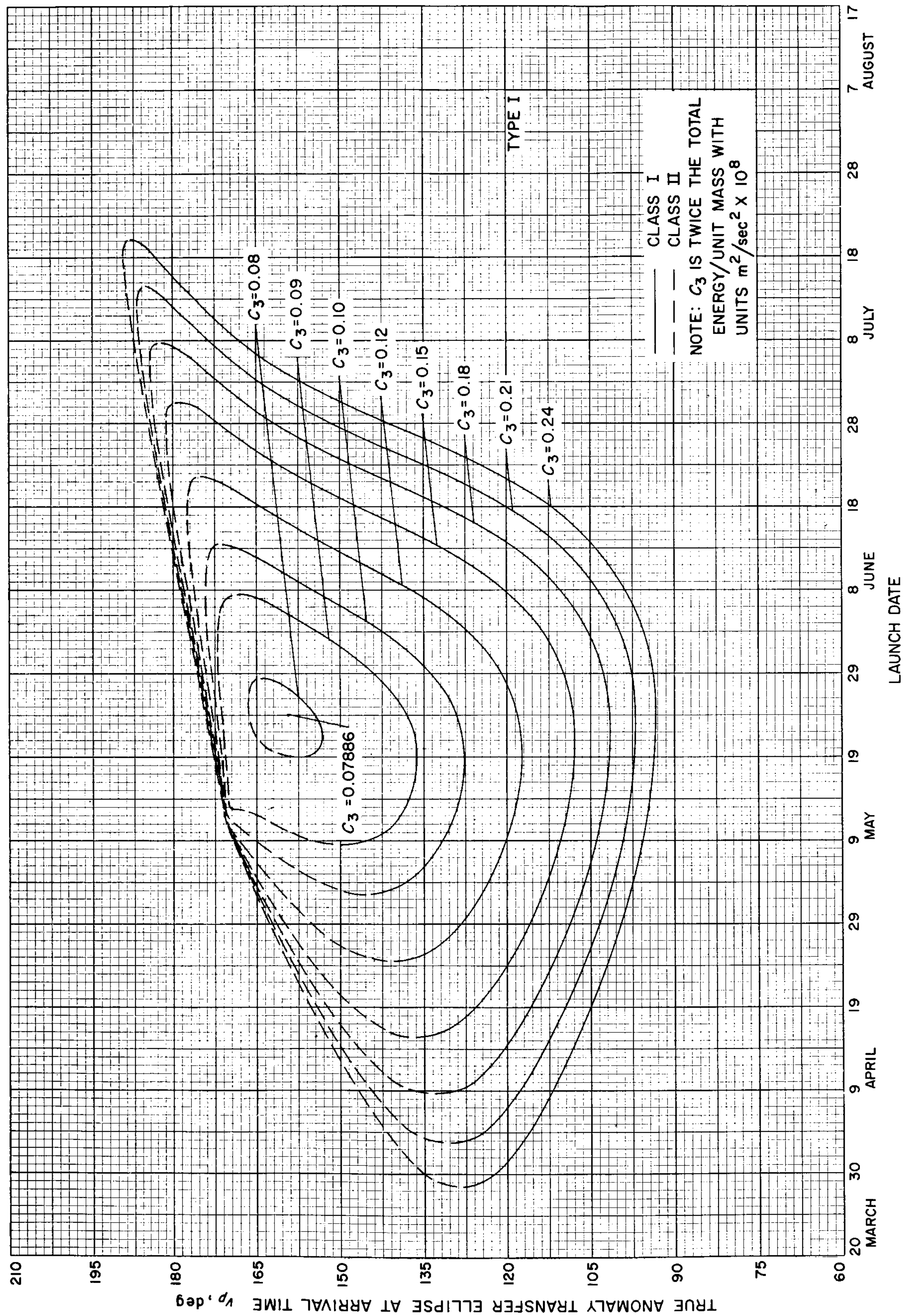

Fig. 15-9. Mars 1971: True anomaly in transfer ellipse at arrival time vs launch date

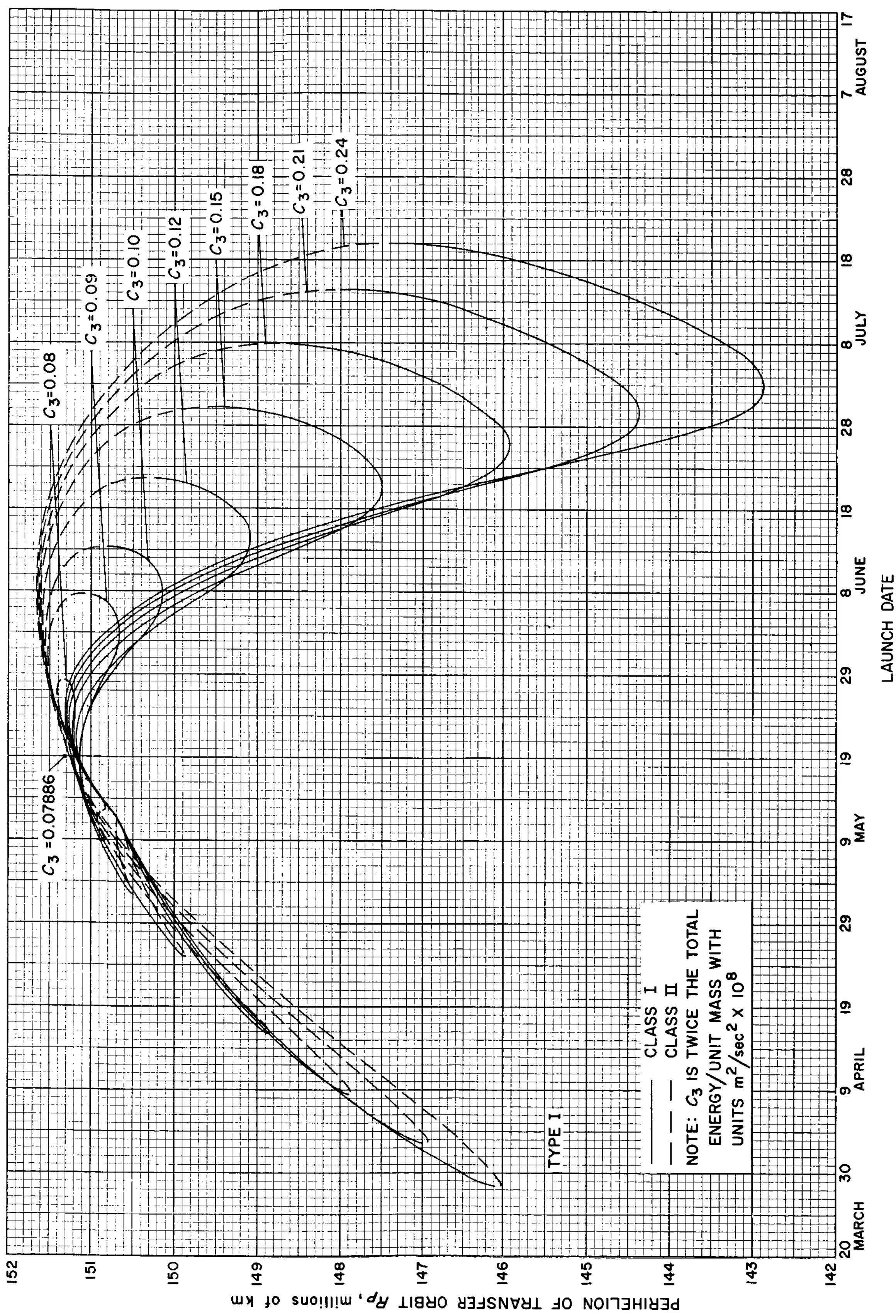

Fig. 15–10. Mars 1971: Perihelion of transfer orbit vs launch date

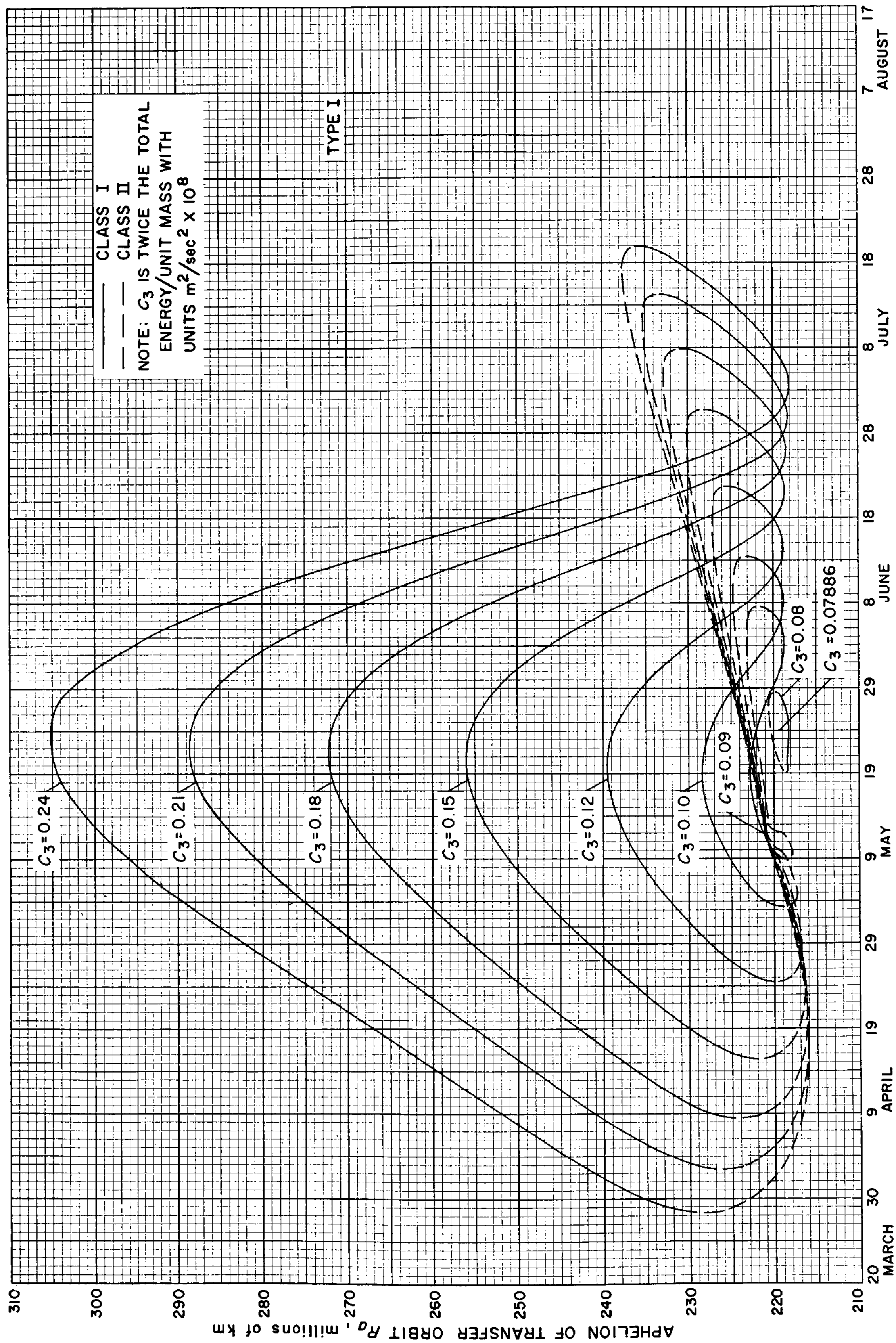

Fig. 15–11. Mars 1971: Aphelion of transfer orbit vs launch date

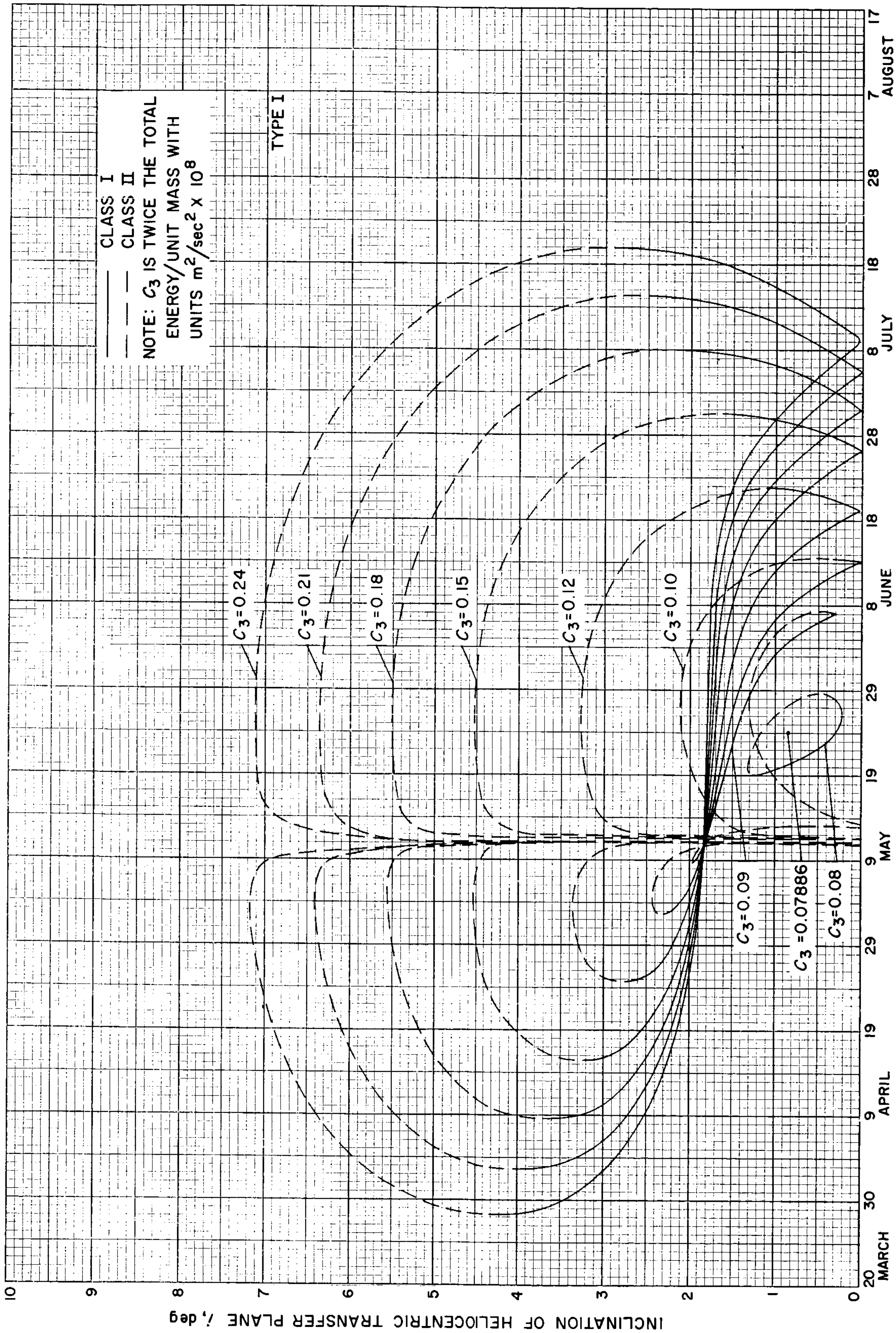

Fig. 15-12. Mars 1971: Inclination of heliocentric-transfer plane vs launch date

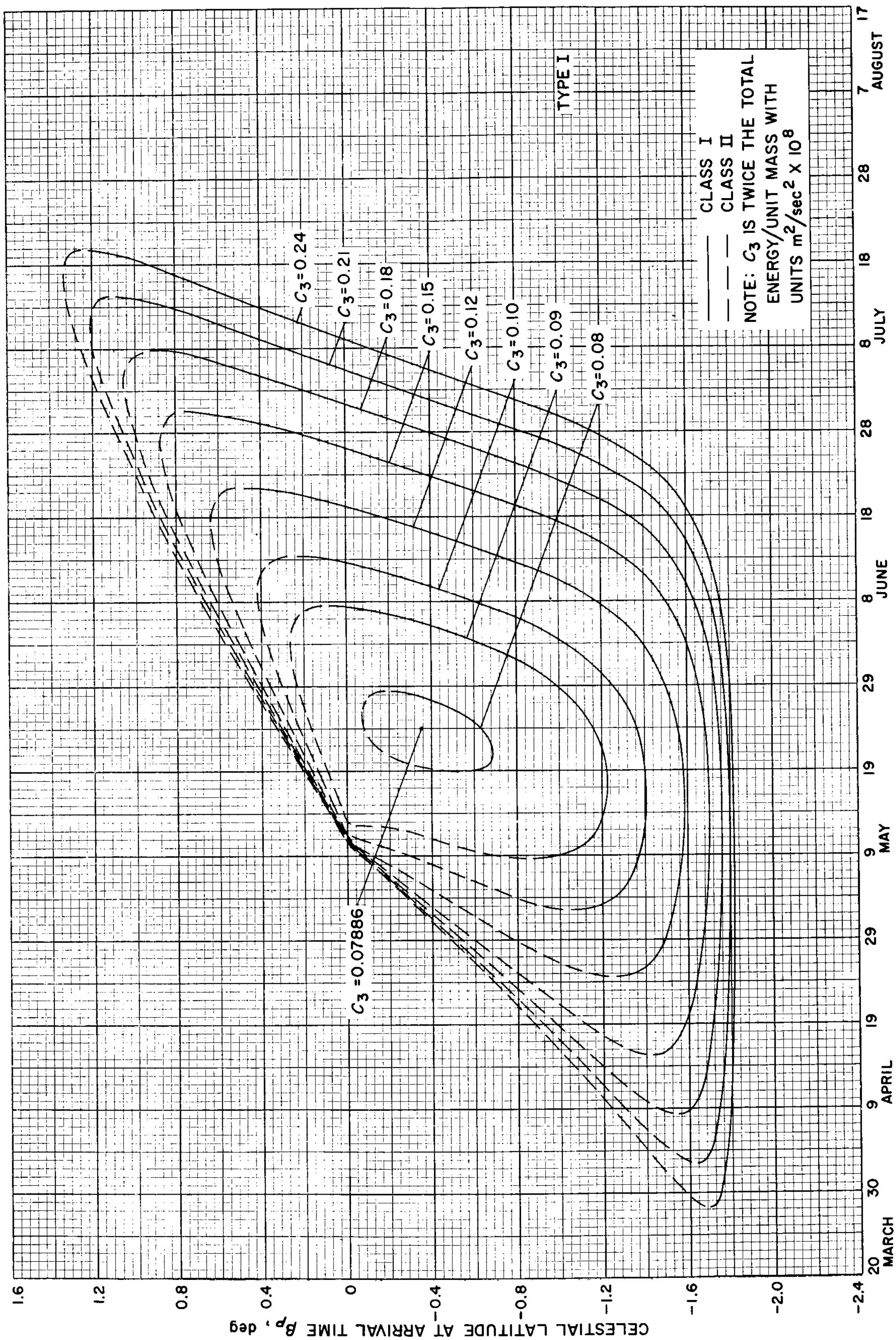

Fig. 15-13. Mars 1971: Celestial latitude at arrival time vs launch date

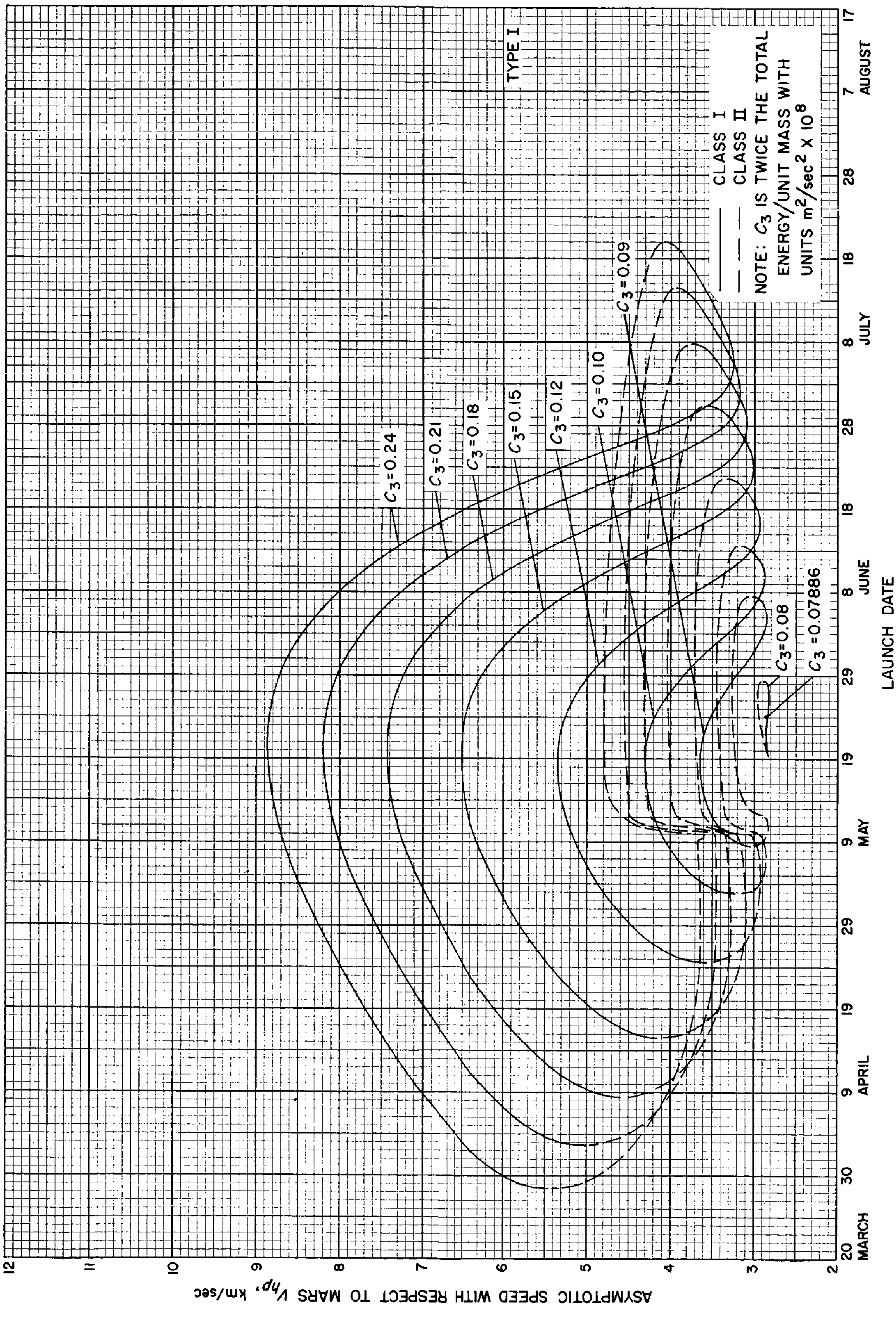

Fig. 15-14. Mars 1971: Asymptotic speed with respect to Mars vs launch date

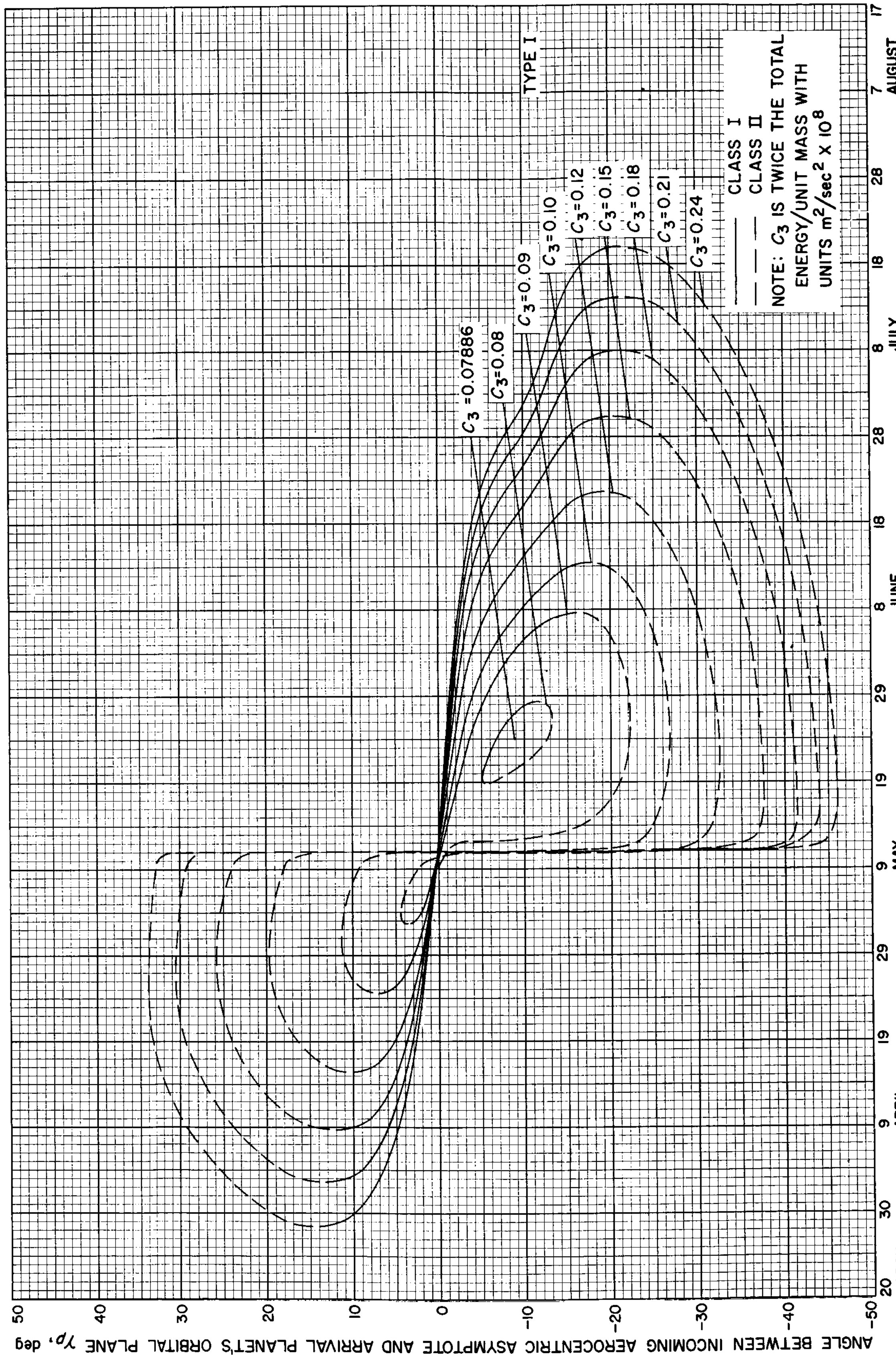

Fig. 15–15. Mars 1971: Angle between incoming aerocentric asymptote and arrival planet's orbital plane vs launch date

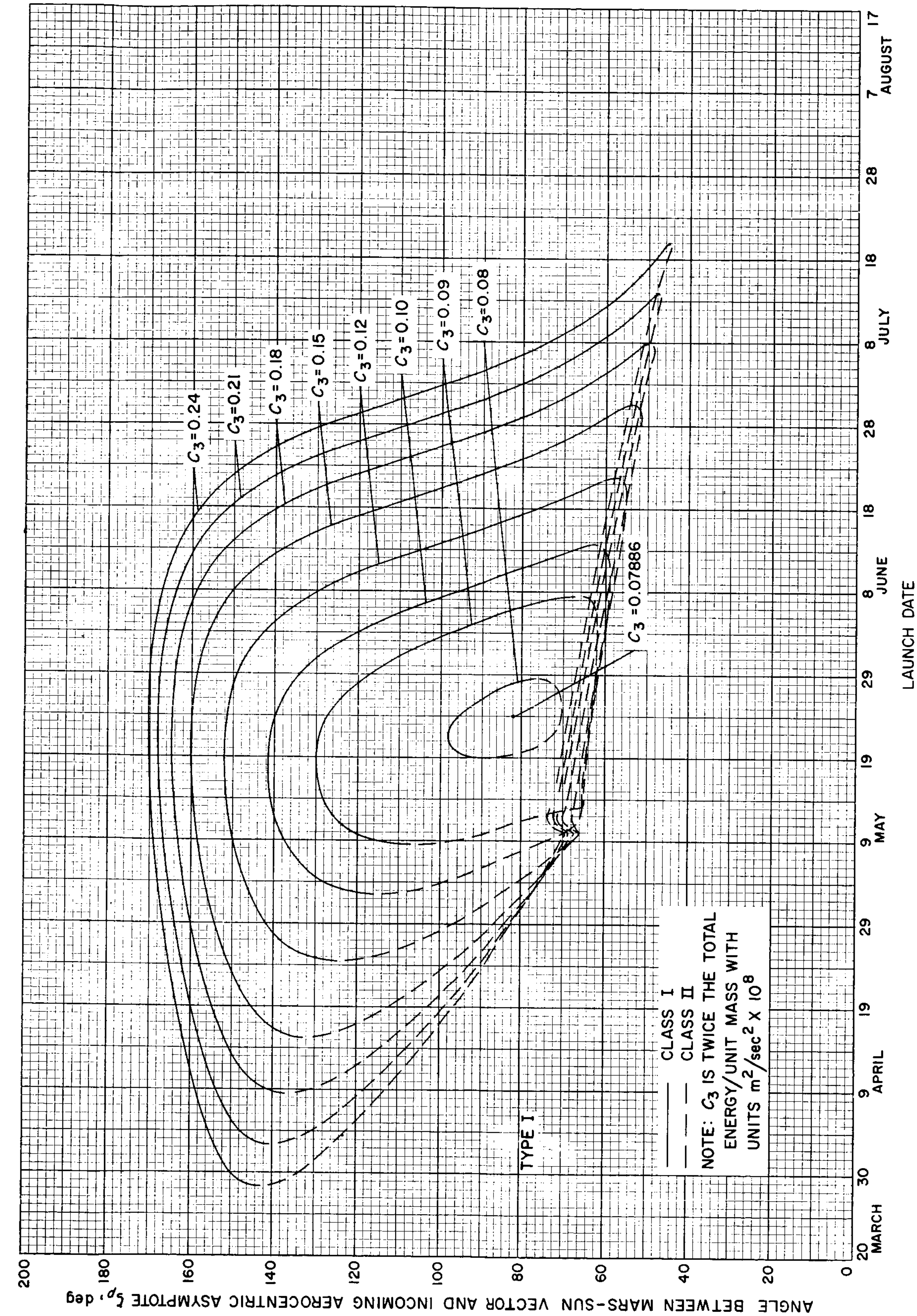

Fig. 15-16. Mars 1971: Angle between Mars–Sun vector and incoming aerocentric asymptote vs launch date

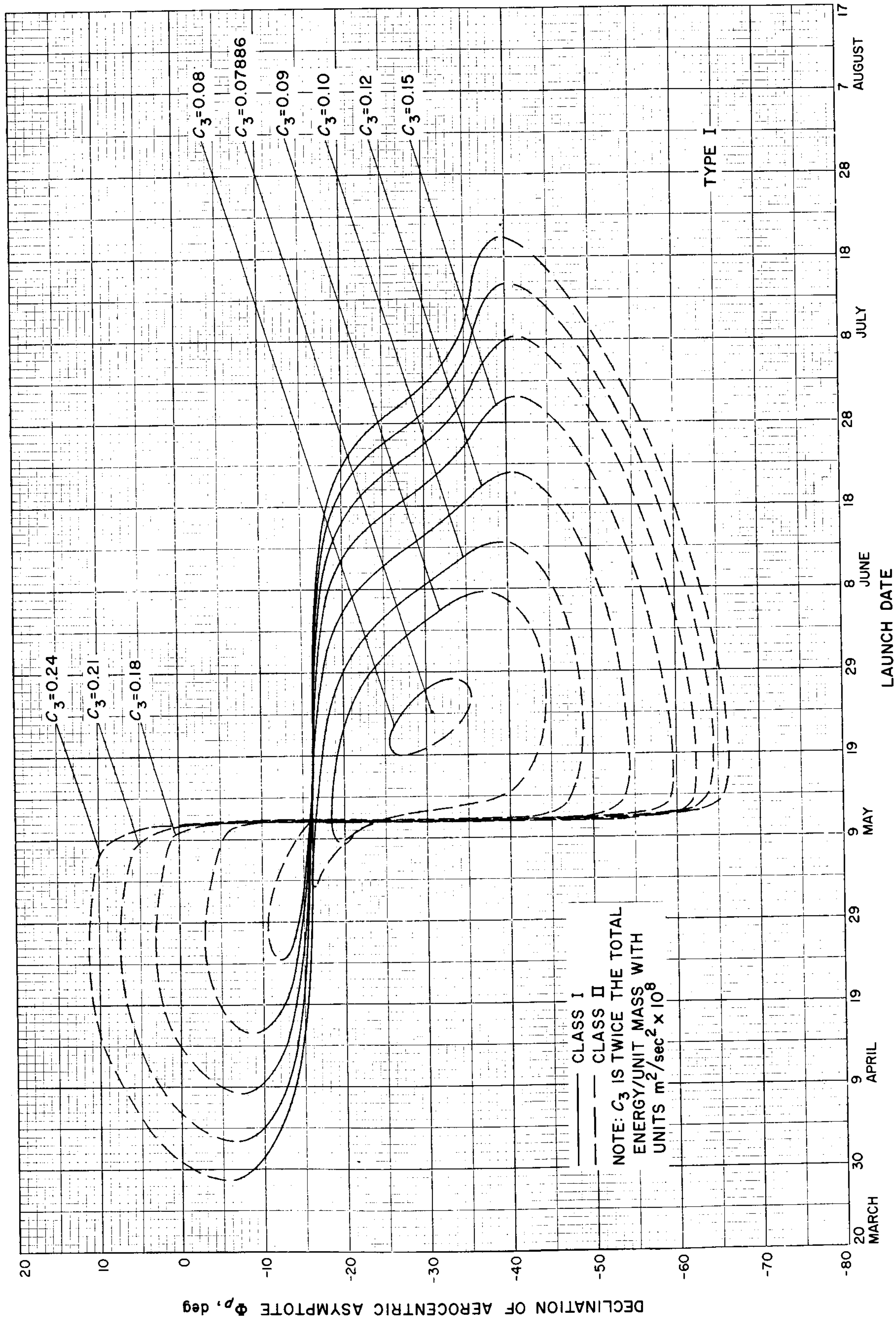

Fig. 15-17. Mars 1971: Declination of aerocentric asymptote vs launch date

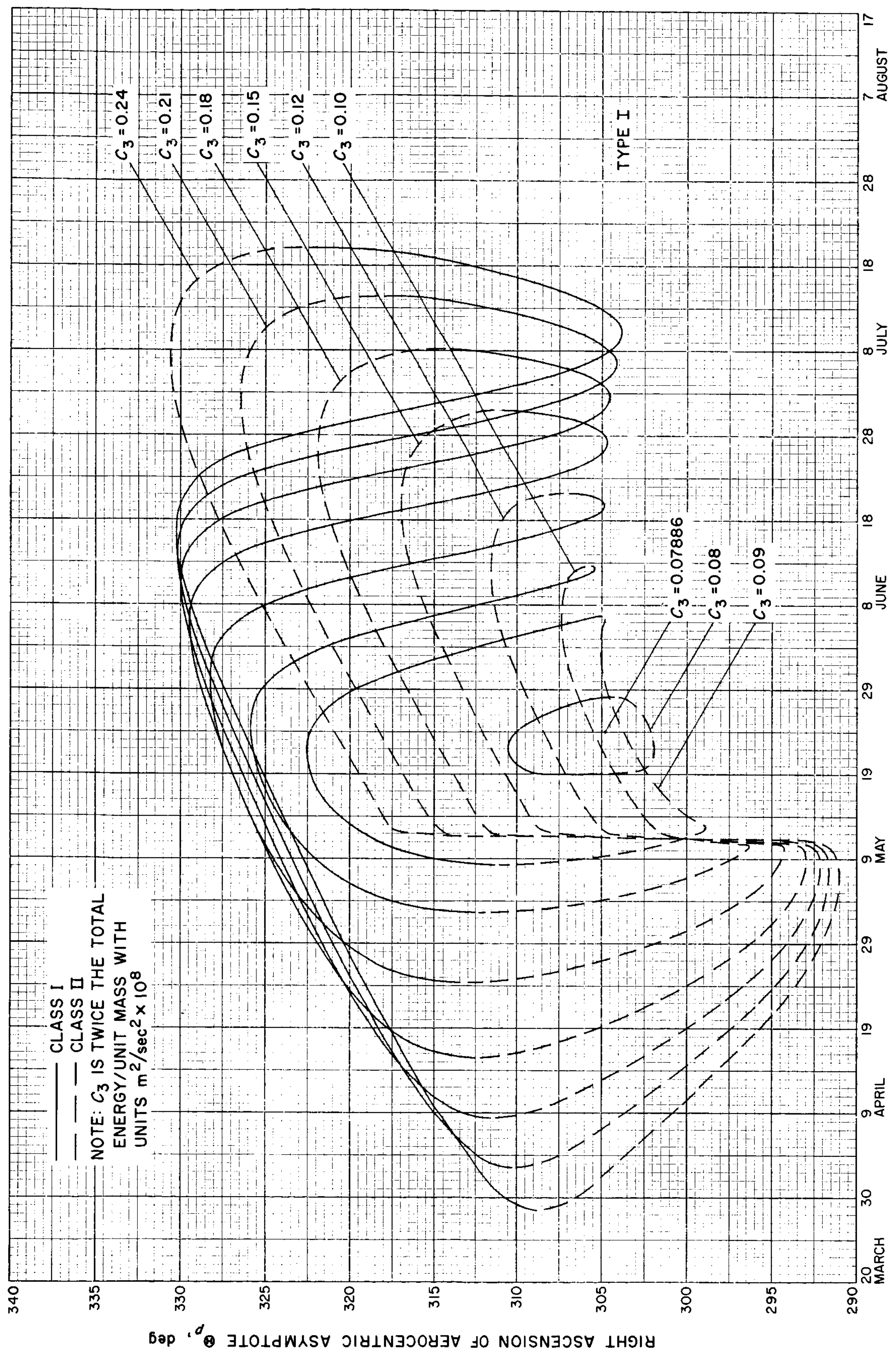

Fig. 15–18. Mars 1971: Right ascension of aerocentric asymptote vs launch date

XVI. MARS 1973: TRAJECTORY-PARAMETER GRAPHS

Figure

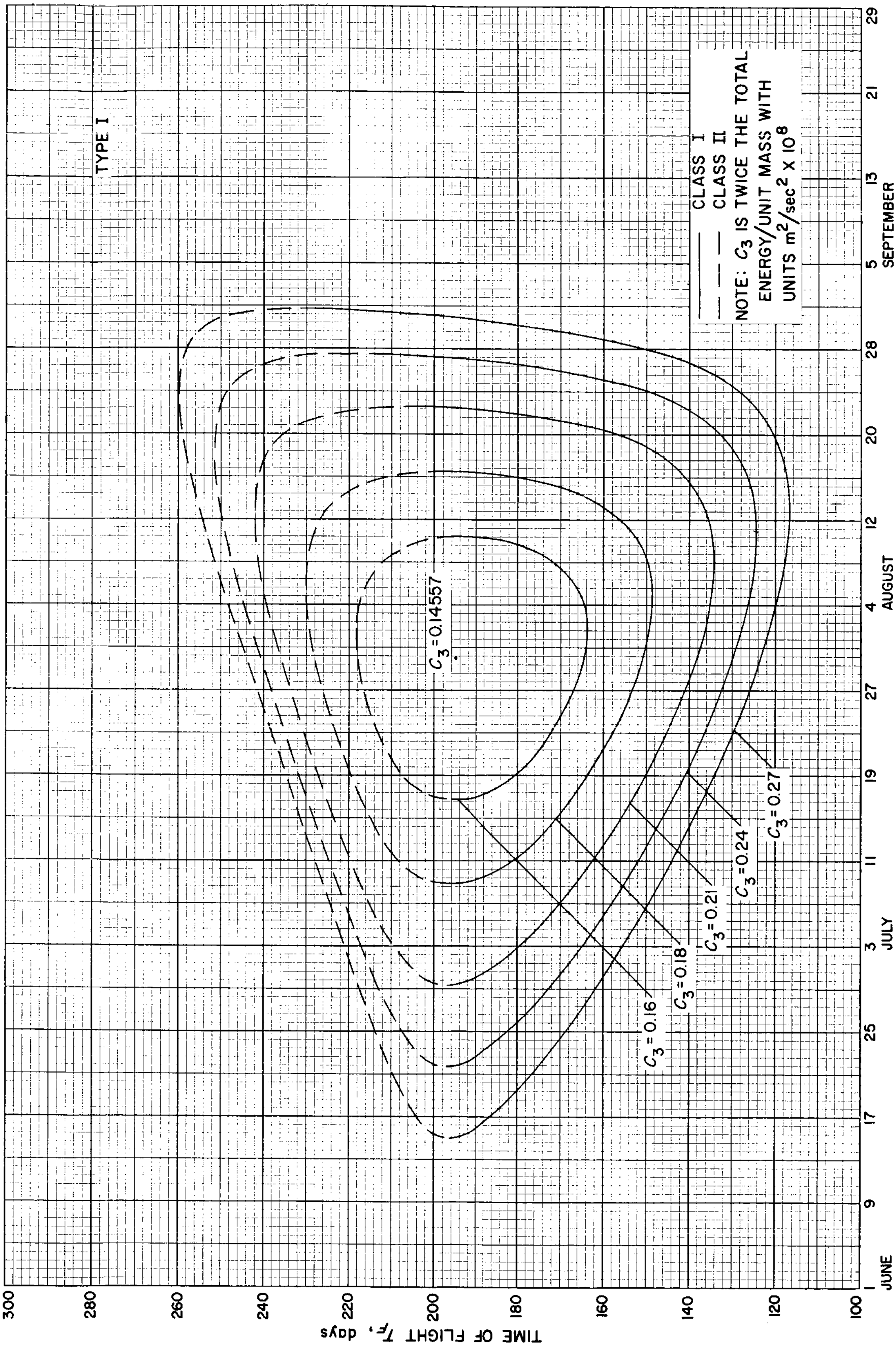

Fig. 16–1. Mars 1973: Time of flight vs launch date

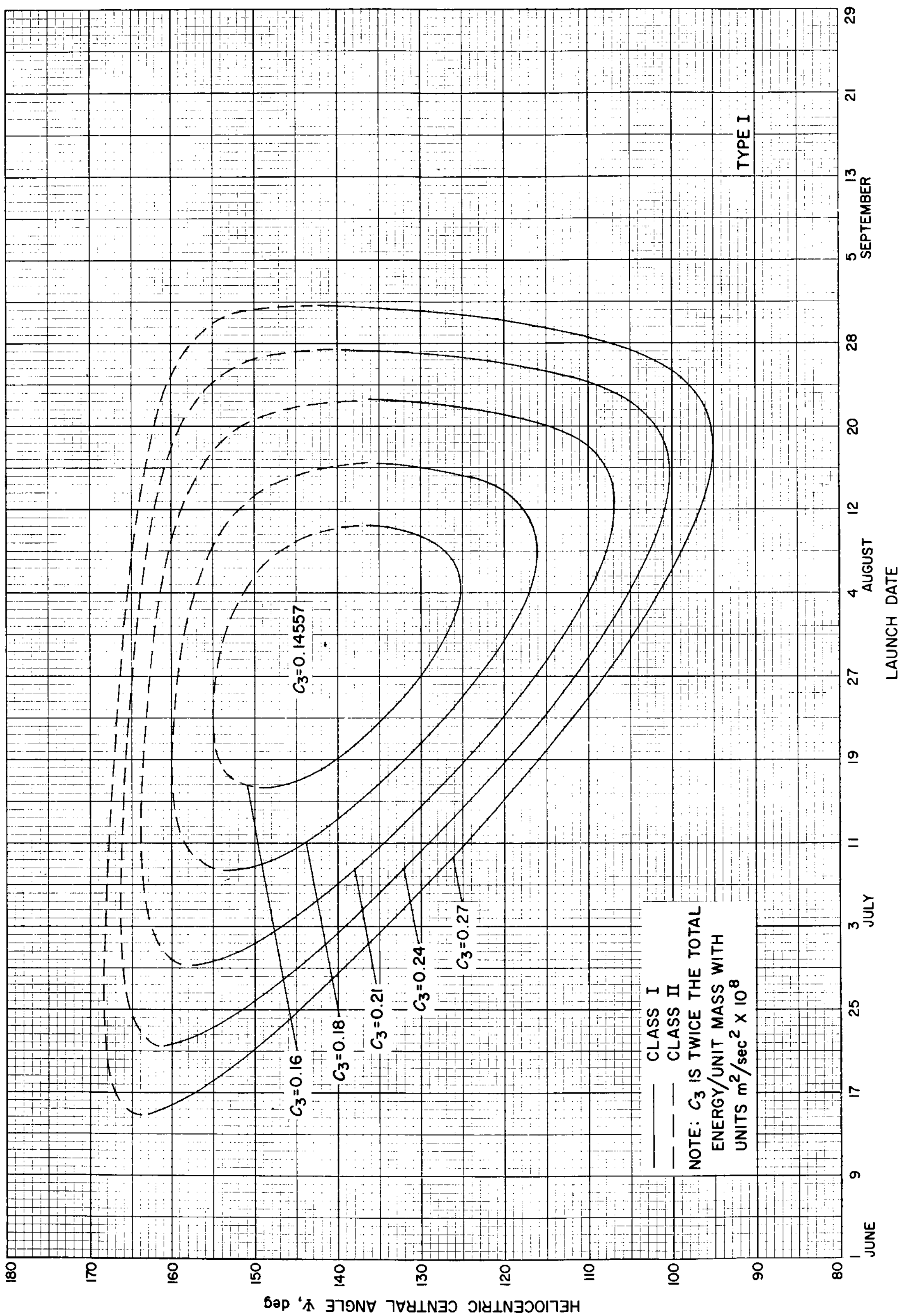

Fig. 16–2. Mars 1973: Heliocentric central angle vs launch date

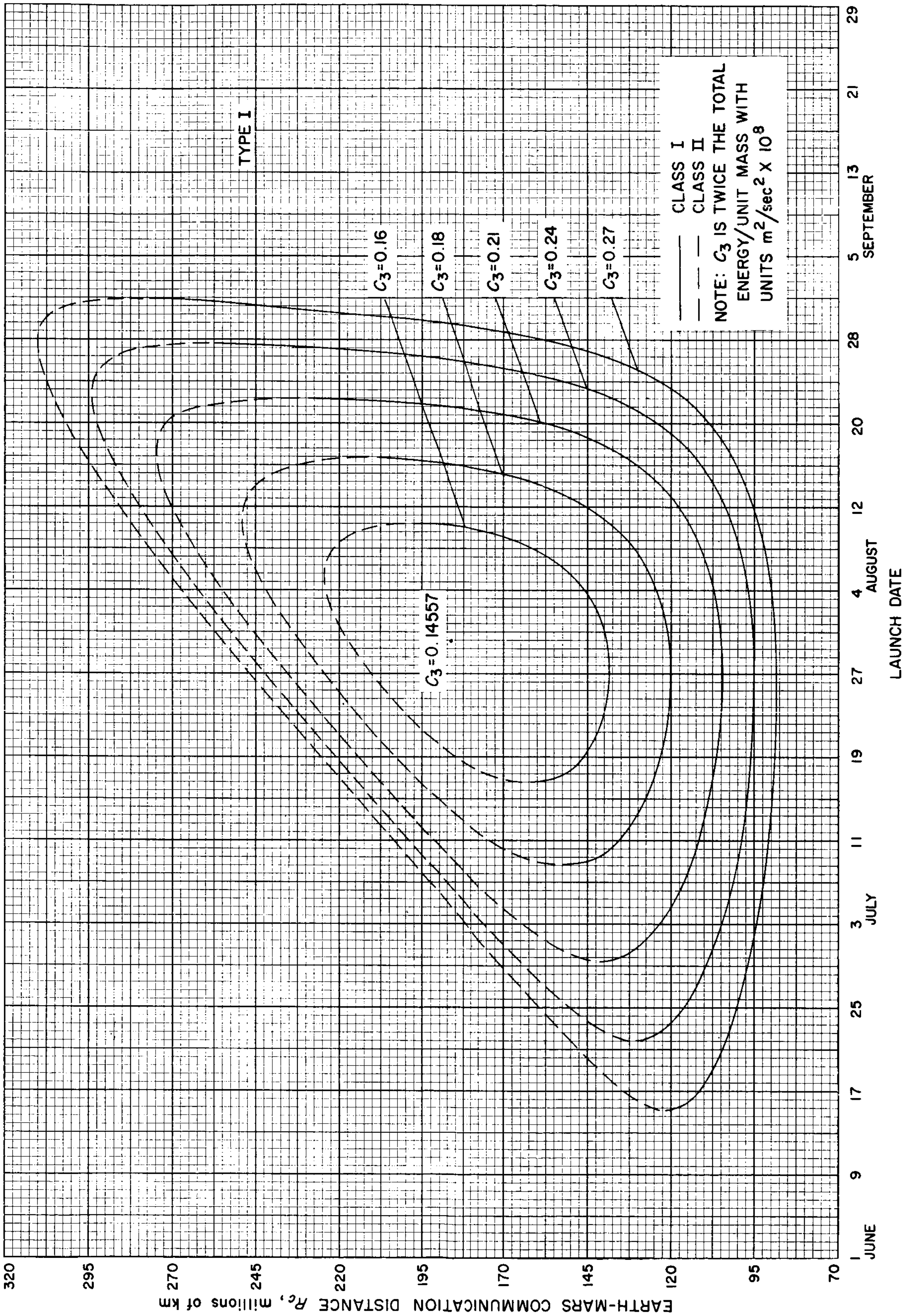

Fig. 16–3. Mars 1973: Earth–Mars communication distance vs launch date

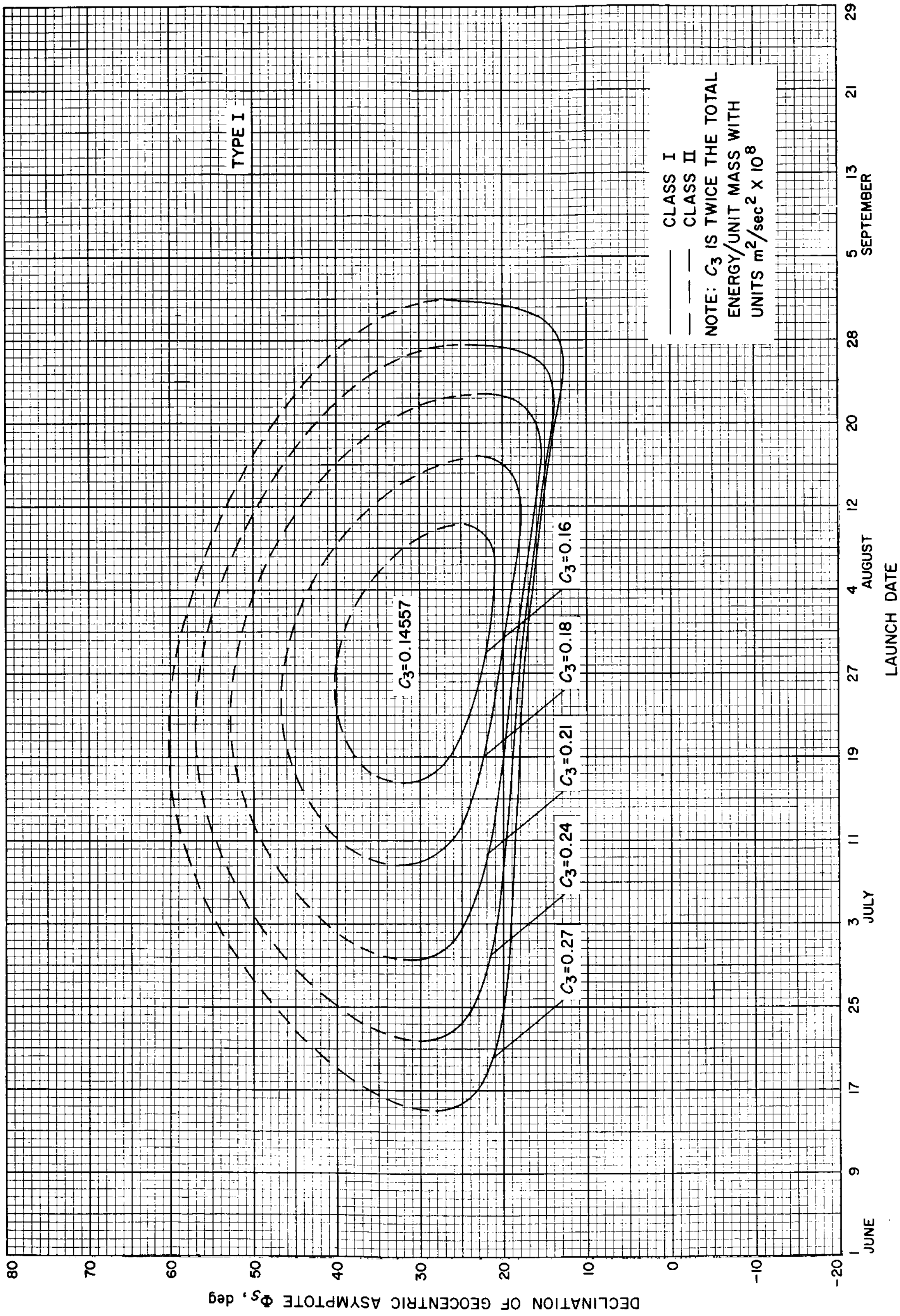

Fig. 16–4. Mars 1973: Declination of geocentric asymptote vs launch date

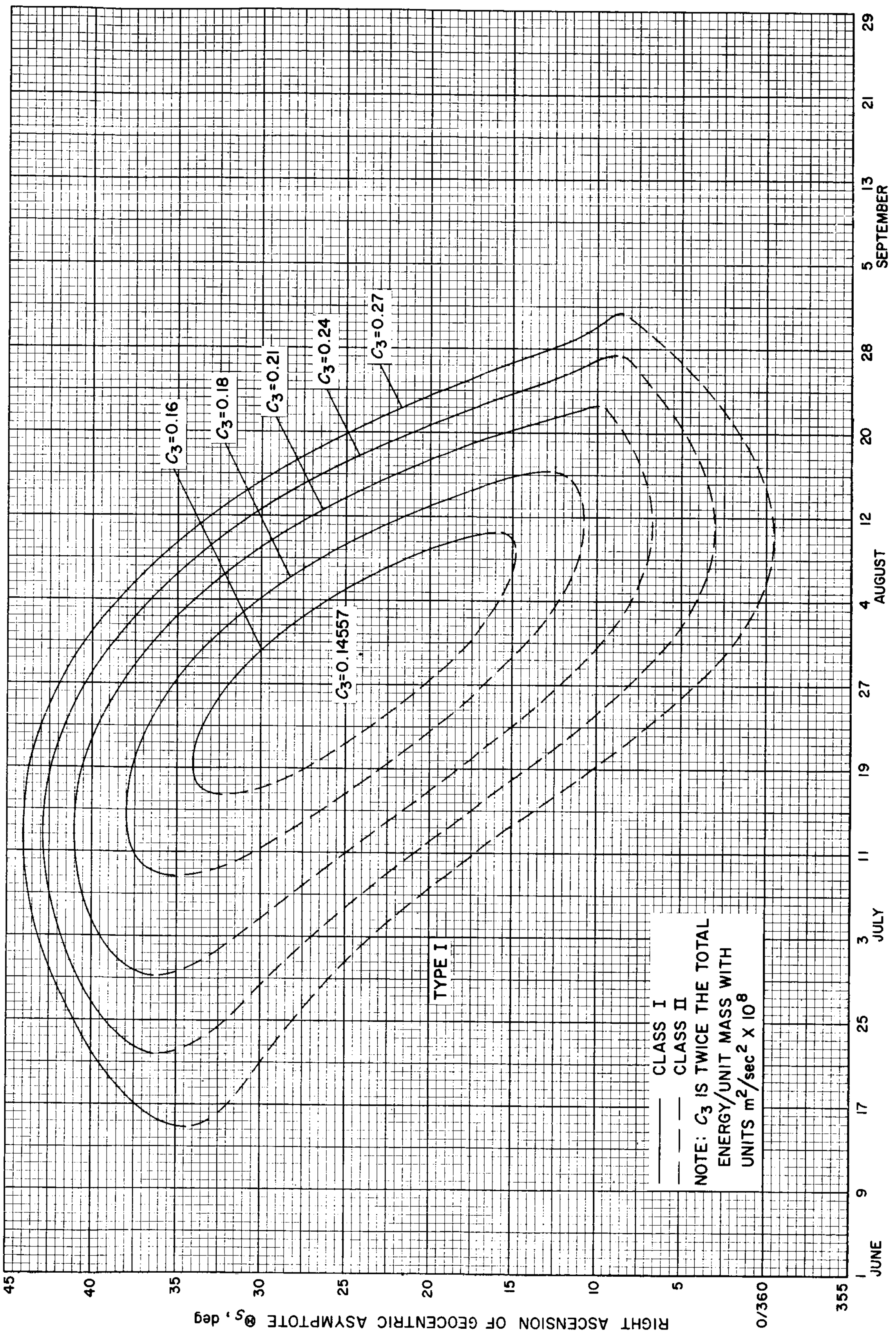

Fig. 16–5. Mars 1973: Right ascension of geocentric asymptote vs launch date

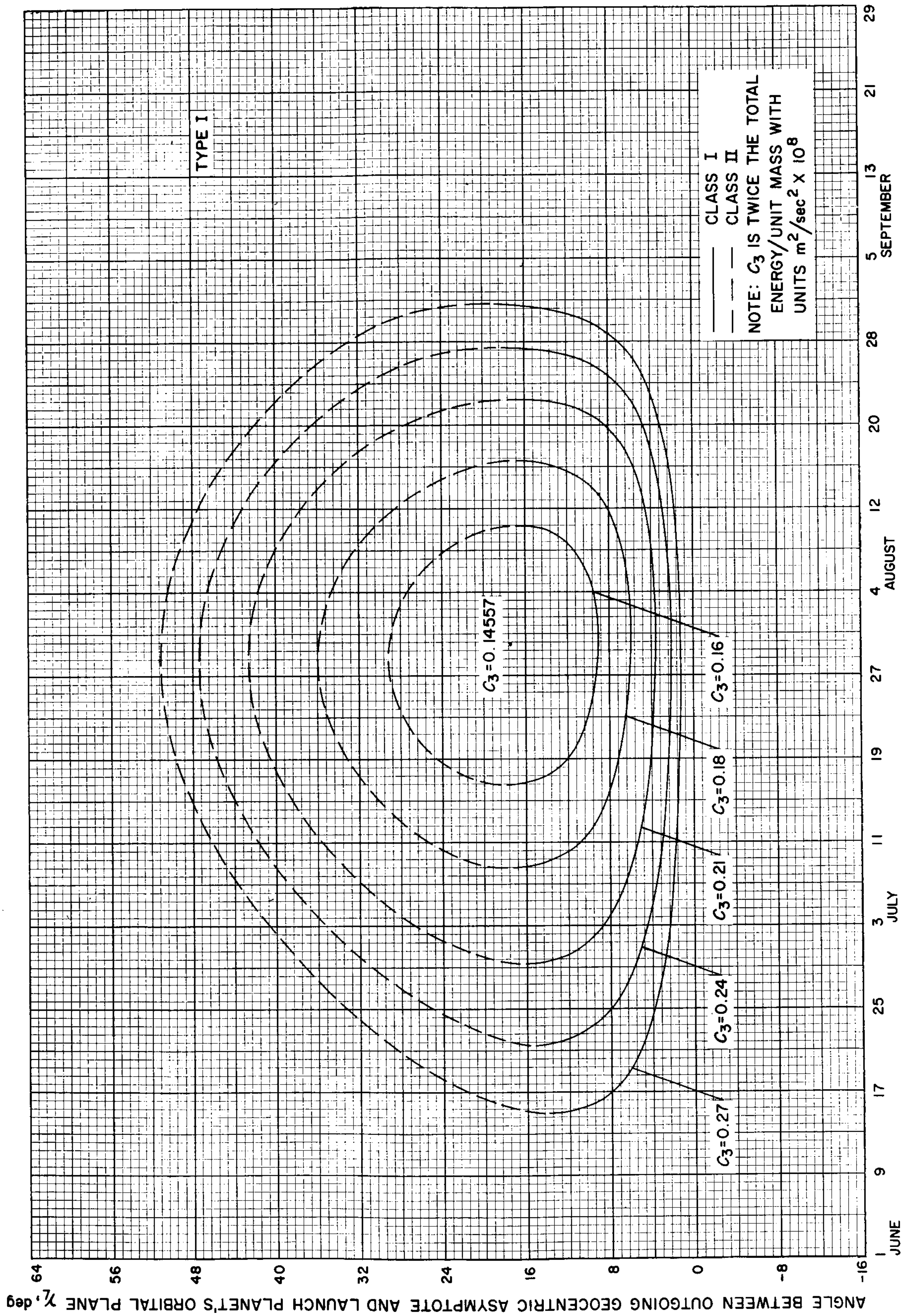

Fig. 16–6. Mars 1973: Angle between outgoing geocentric asymptote and launch planet's orbital plane vs launch date

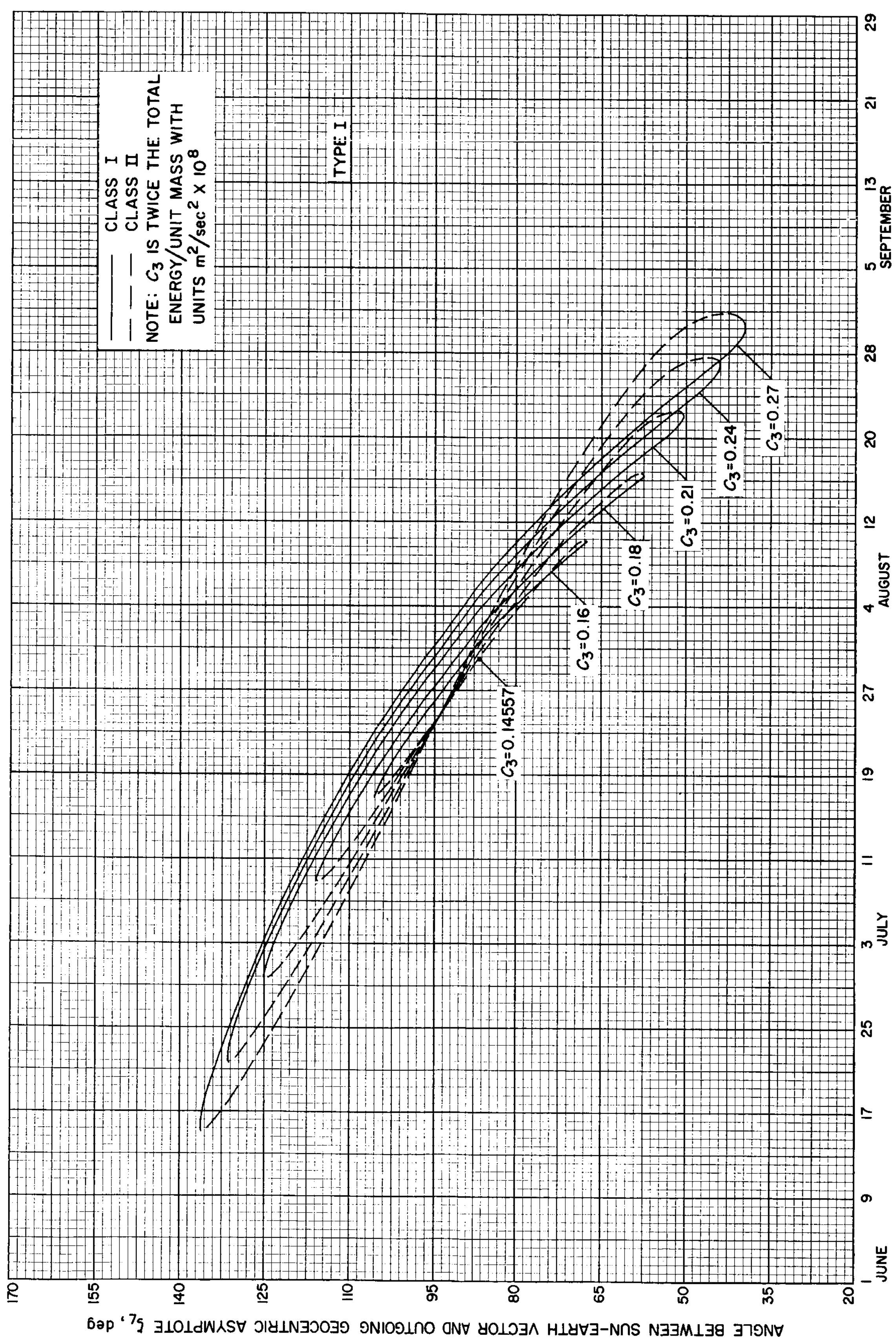

Fig. 16-7. Mars 1973: Angle between Sun–Earth vector and outgoing geocentric asymptote vs launch date

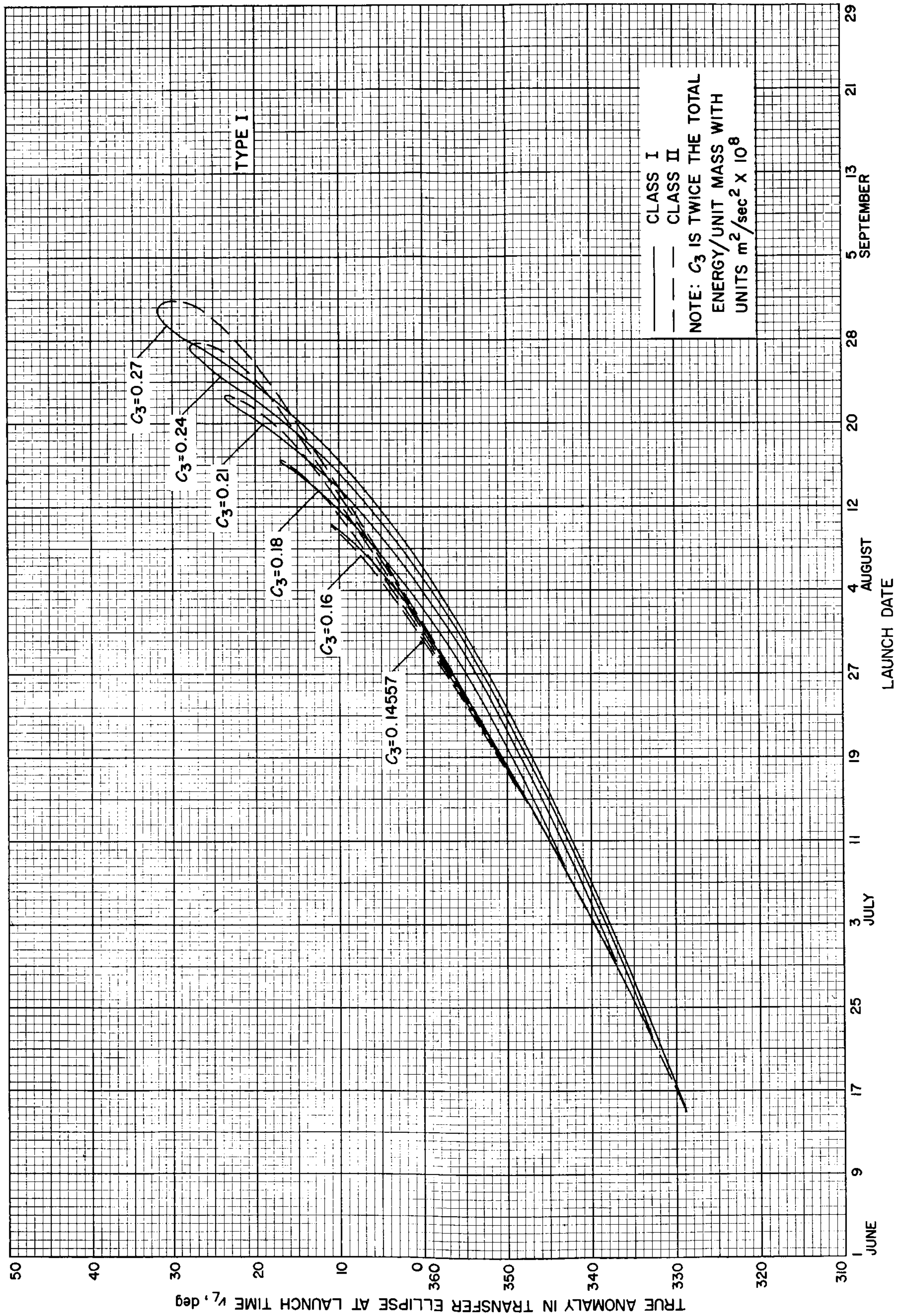

Fig. 16–8. Mars 1973: True anomaly in transfer ellipse at launch time vs launch date

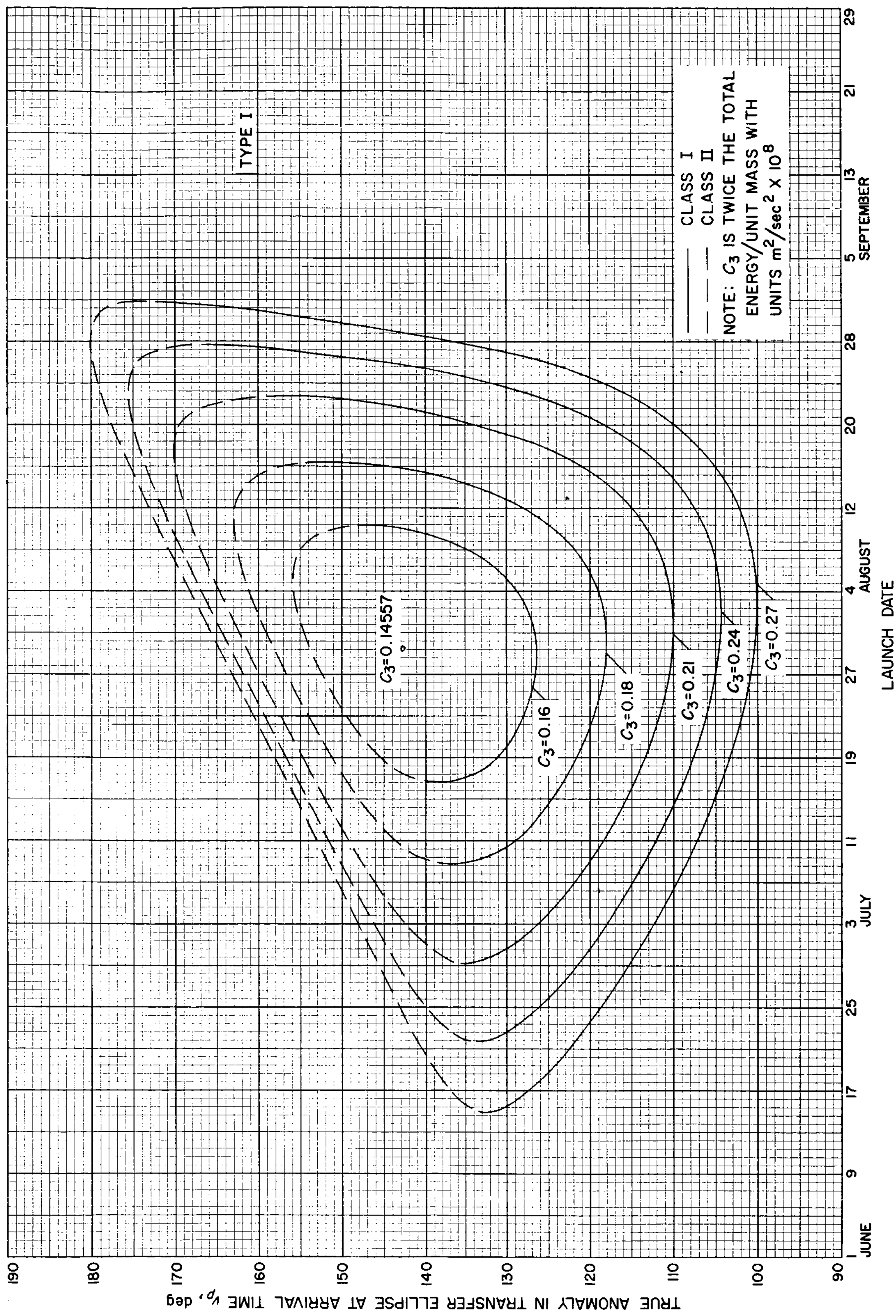

Fig. 16–9. Mars 1973: True anomaly in transfer ellipse at arrival time vs launch date

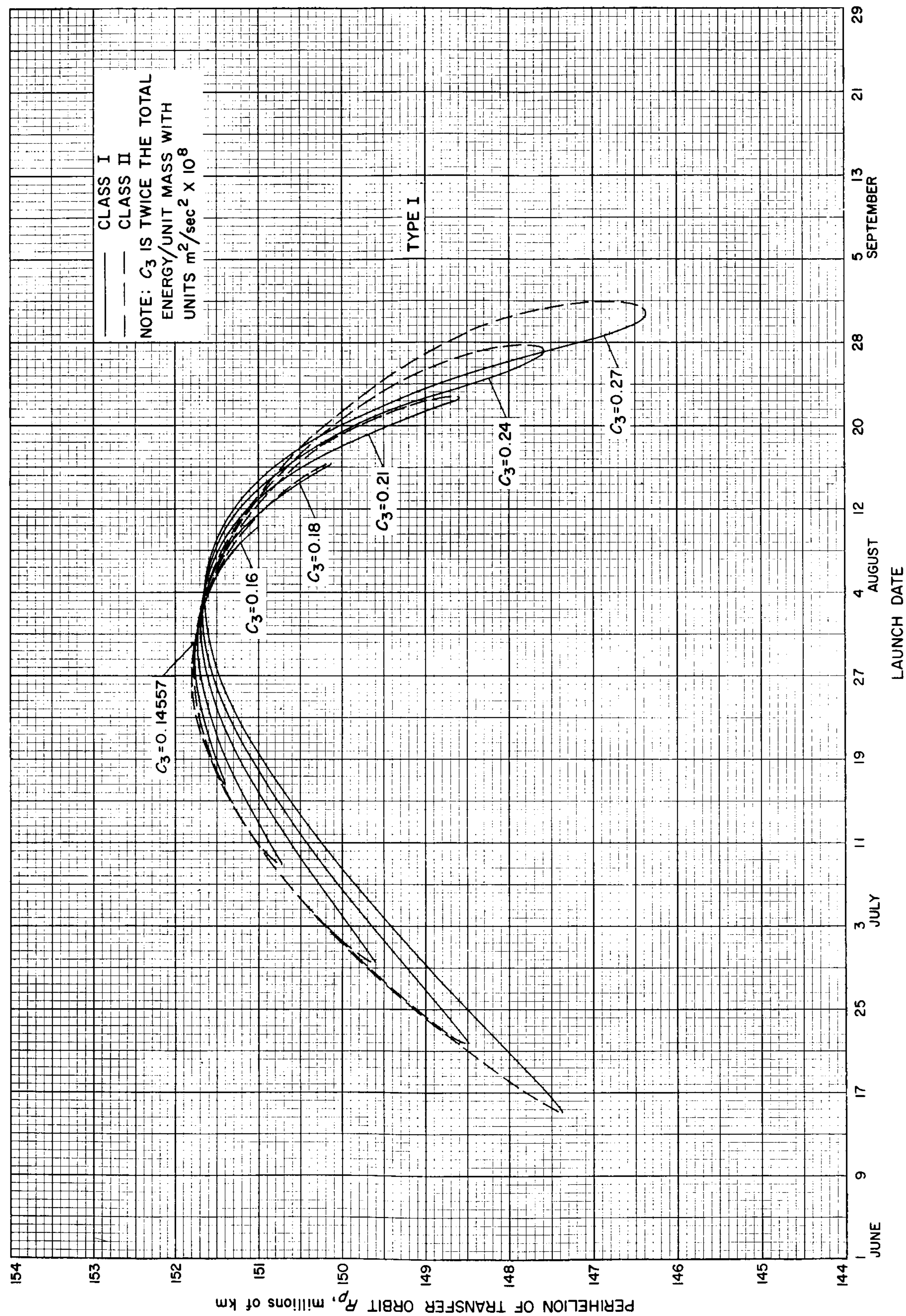

Fig. 16-10. Mars 1973: Perihelion of transfer orbit vs launch date

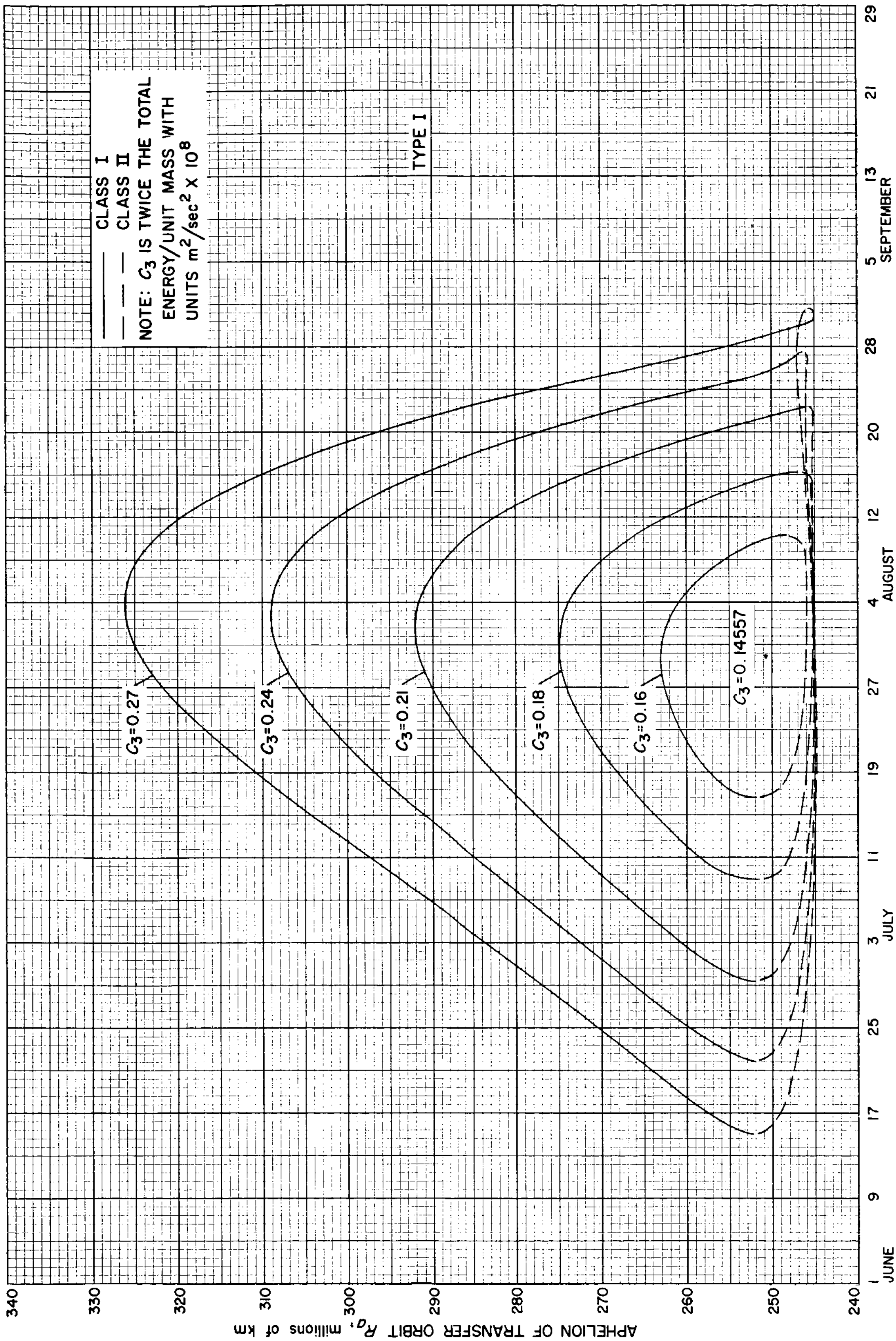

Fig. 16–11. Mars 1973: Aphelion of transfer orbit vs launch date

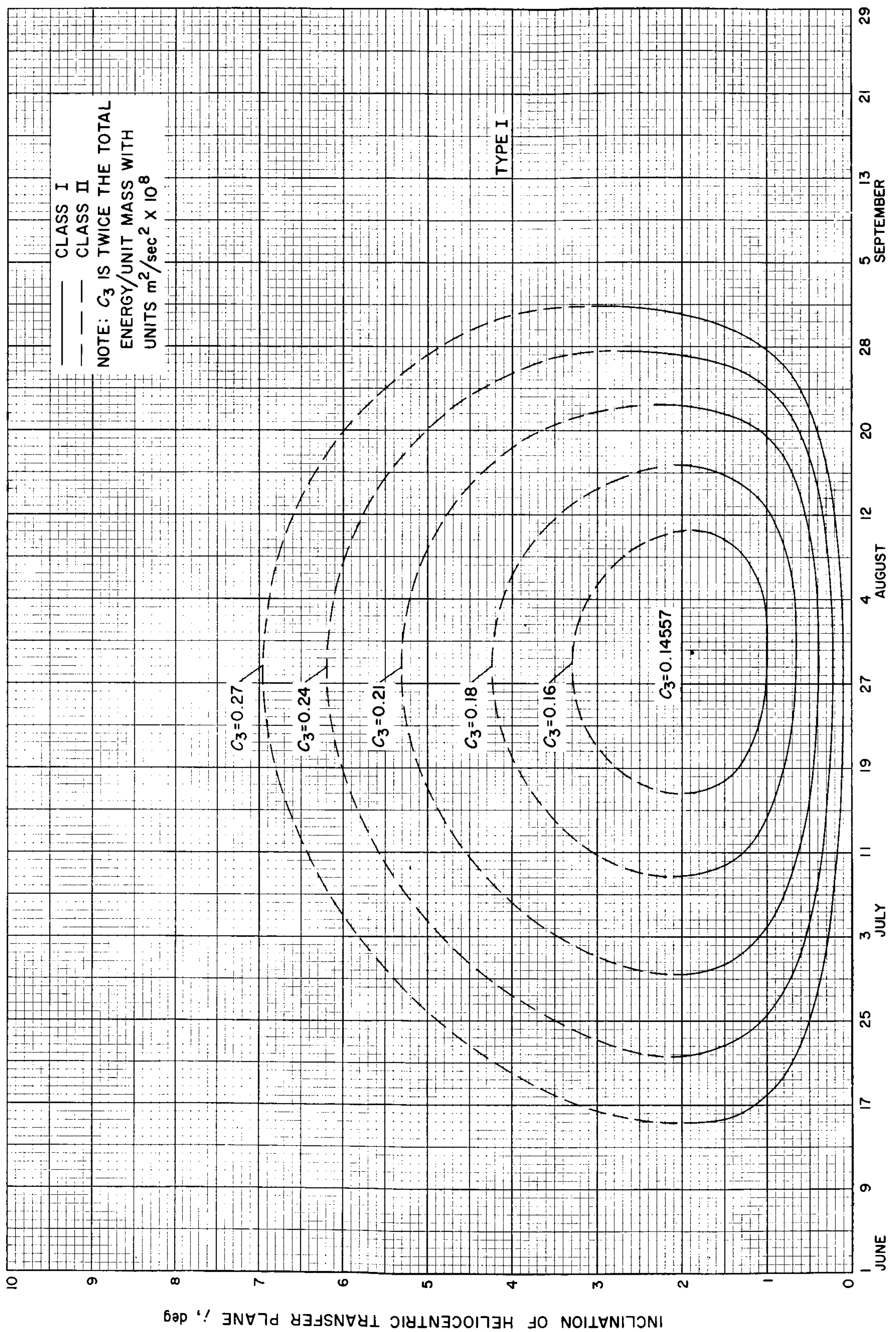

Fig. 16–12. Mars 1973: Inclination of heliocentric-transfer plane vs launch date

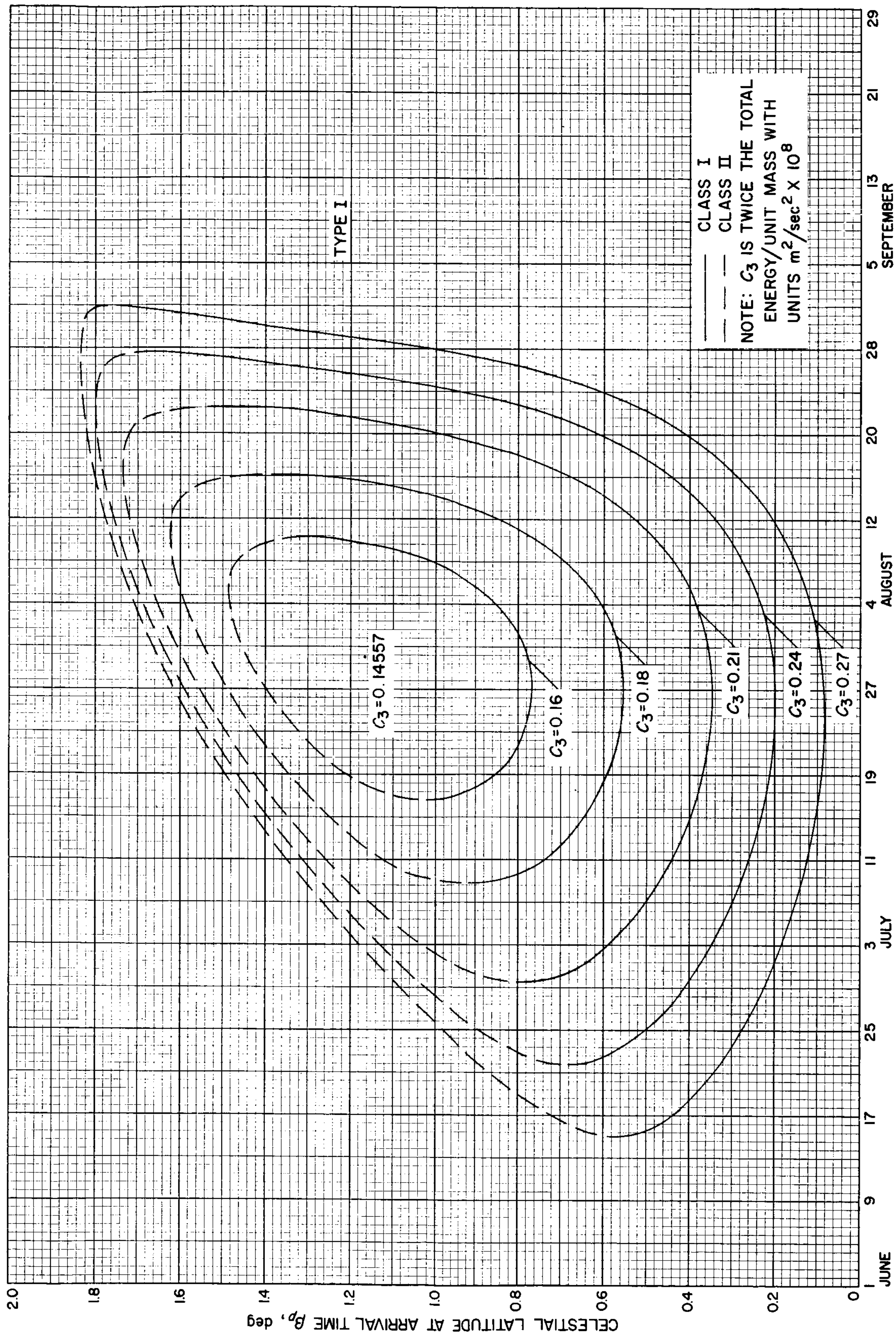

Fig. 16–13. Mars 1973: Celestial latitude at arrival time vs launch date

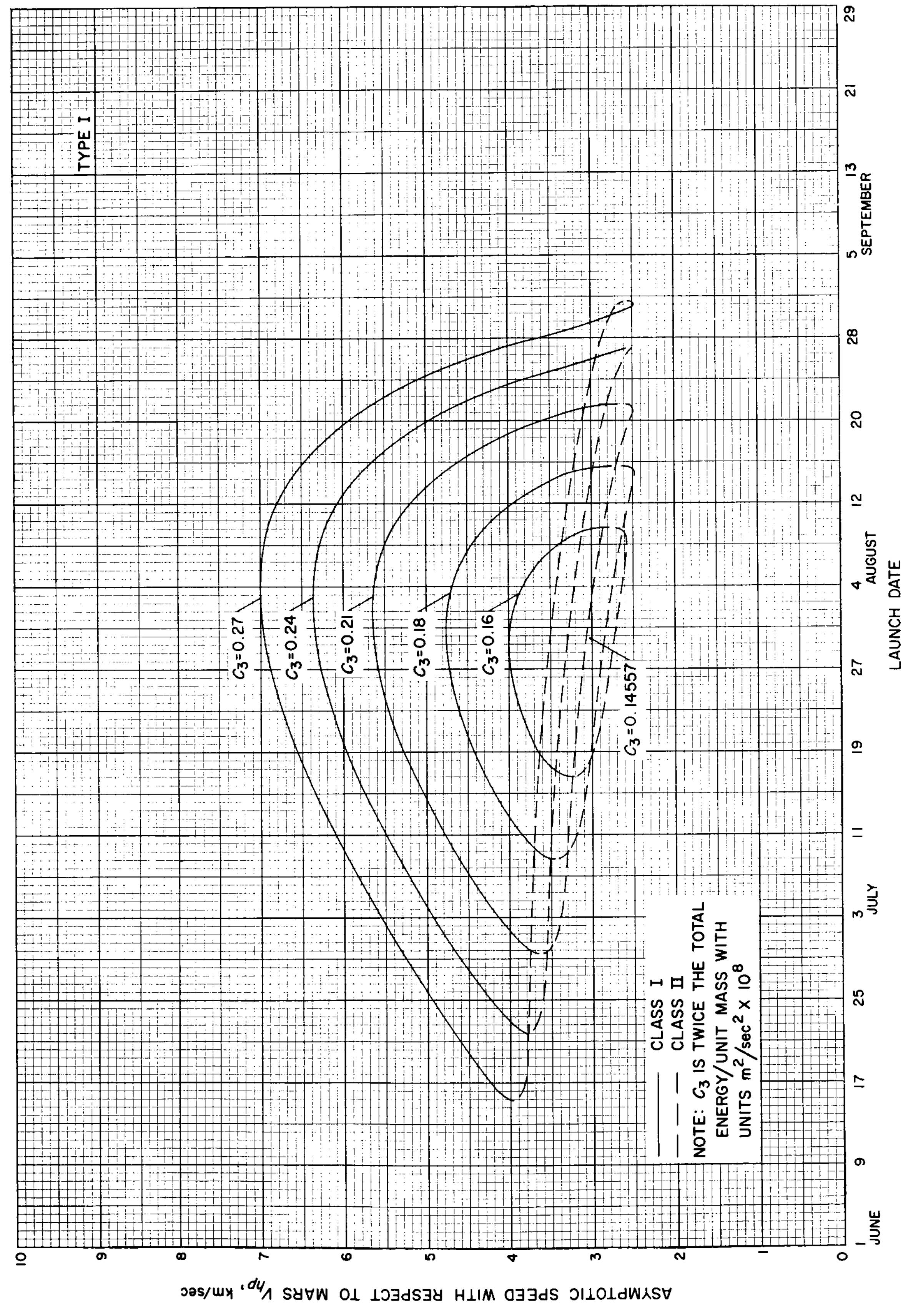

Fig. 16–14. Mars 1973: Asymptotic speed with respect to Mars vs launch date

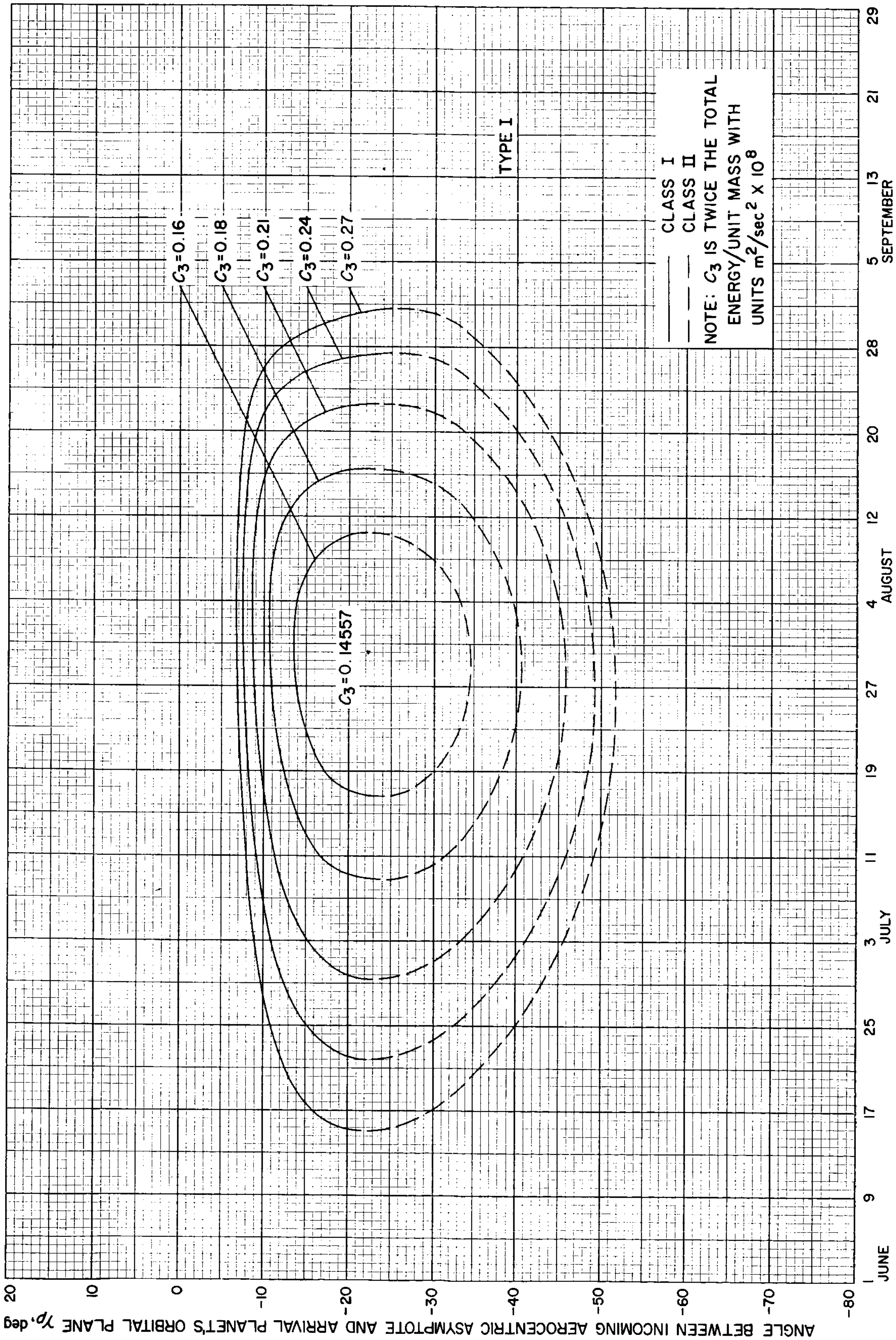

Fig. 16-15. Mars 1973: Angle between incoming aerocentric asymptote and arrival planet's orbital plane vs launch date

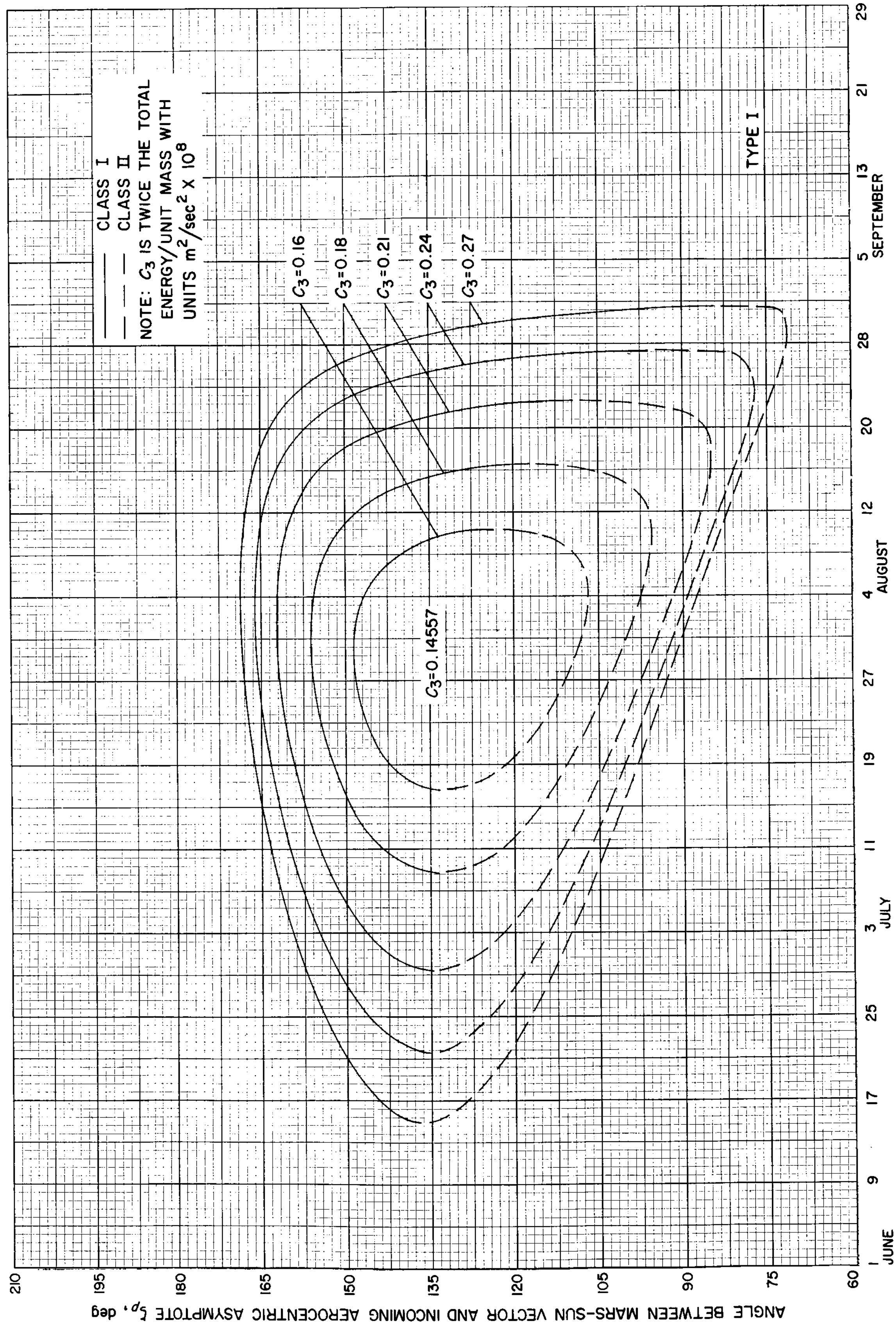

Fig. 16–16. Mars 1973: Angle between Mars–Sun vector and incoming aerocentric asymptote vs launch date

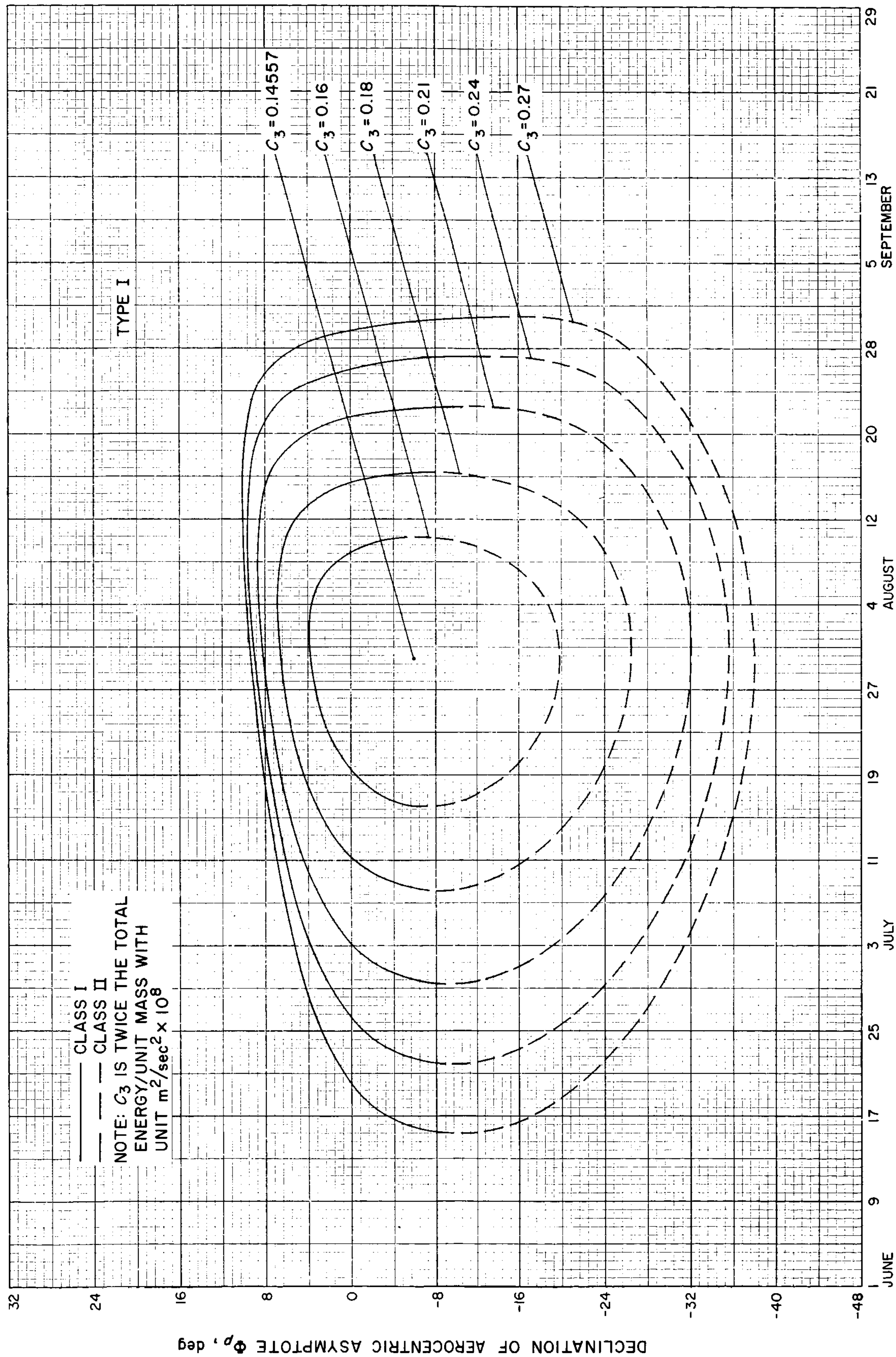

Fig. 16–17. Mars 1973: Declination of aerocentric asymptote vs launch date

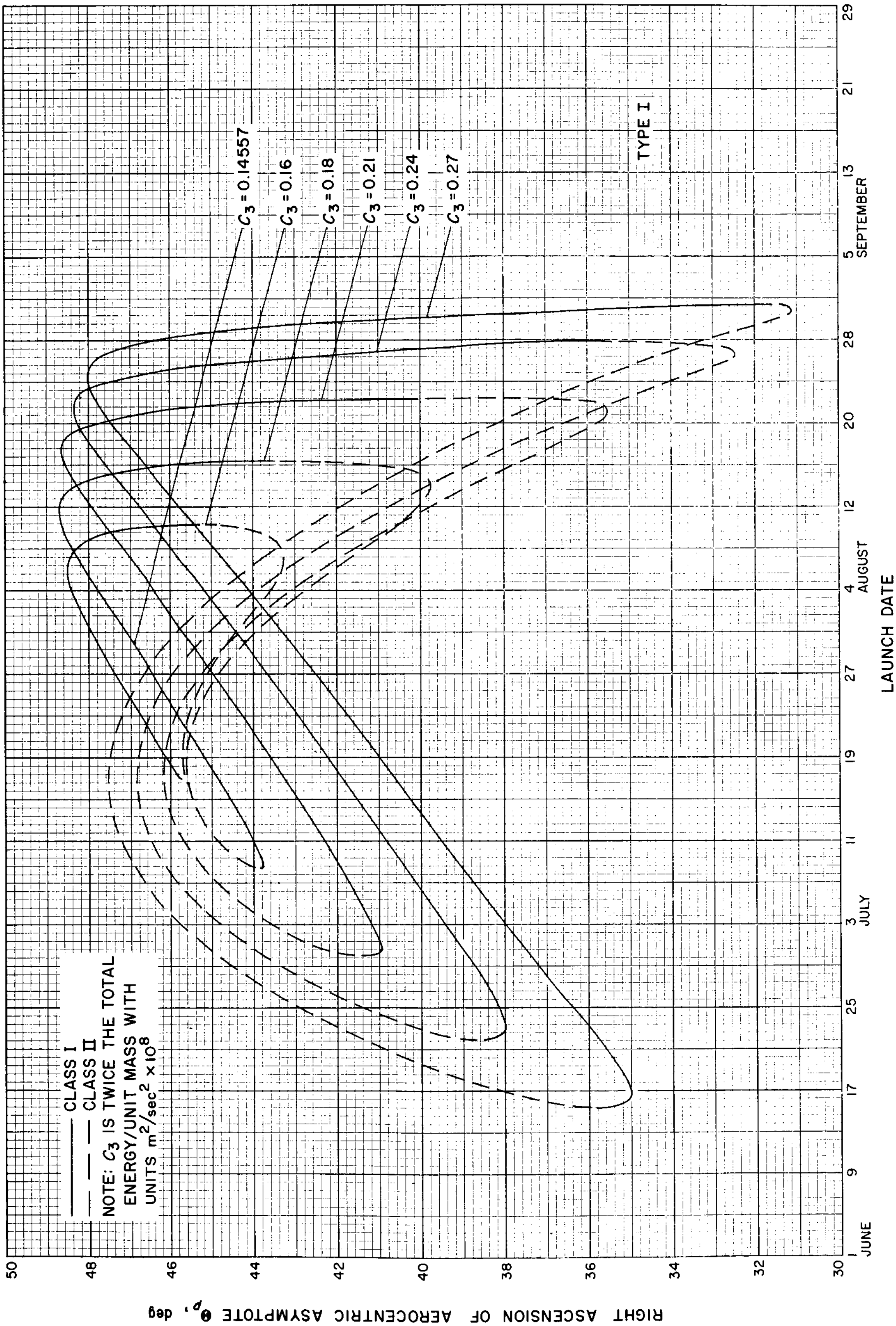

Fig. 16–18. Mars 1973: Right ascension of aerocentric asymptote vs launch date

XVII. MARS 1975: TRAJECTORY-PARAMETER GRAPHS

Figure

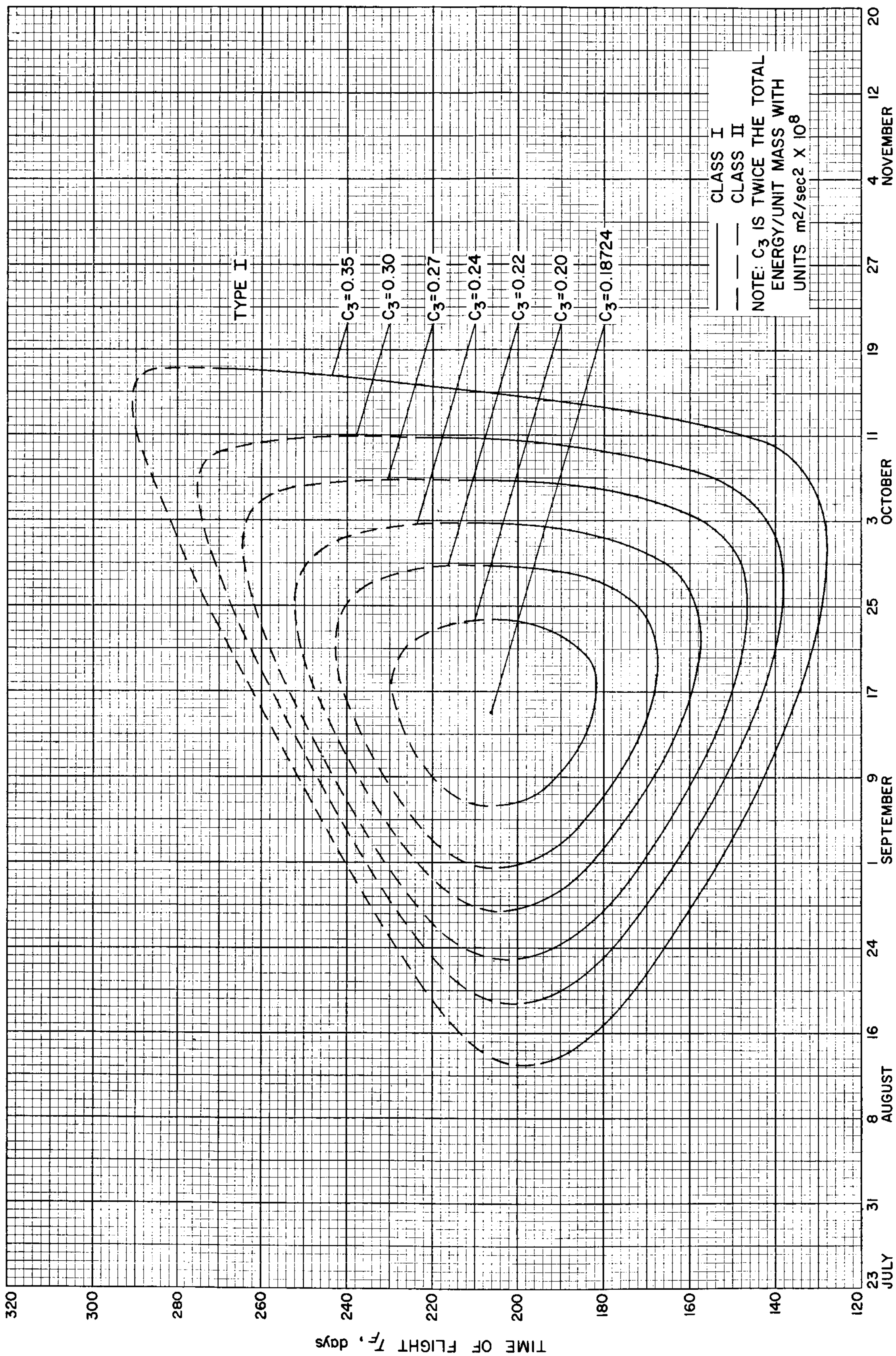

Fig. 17-1. Mars 1975: Time of flight vs launch date

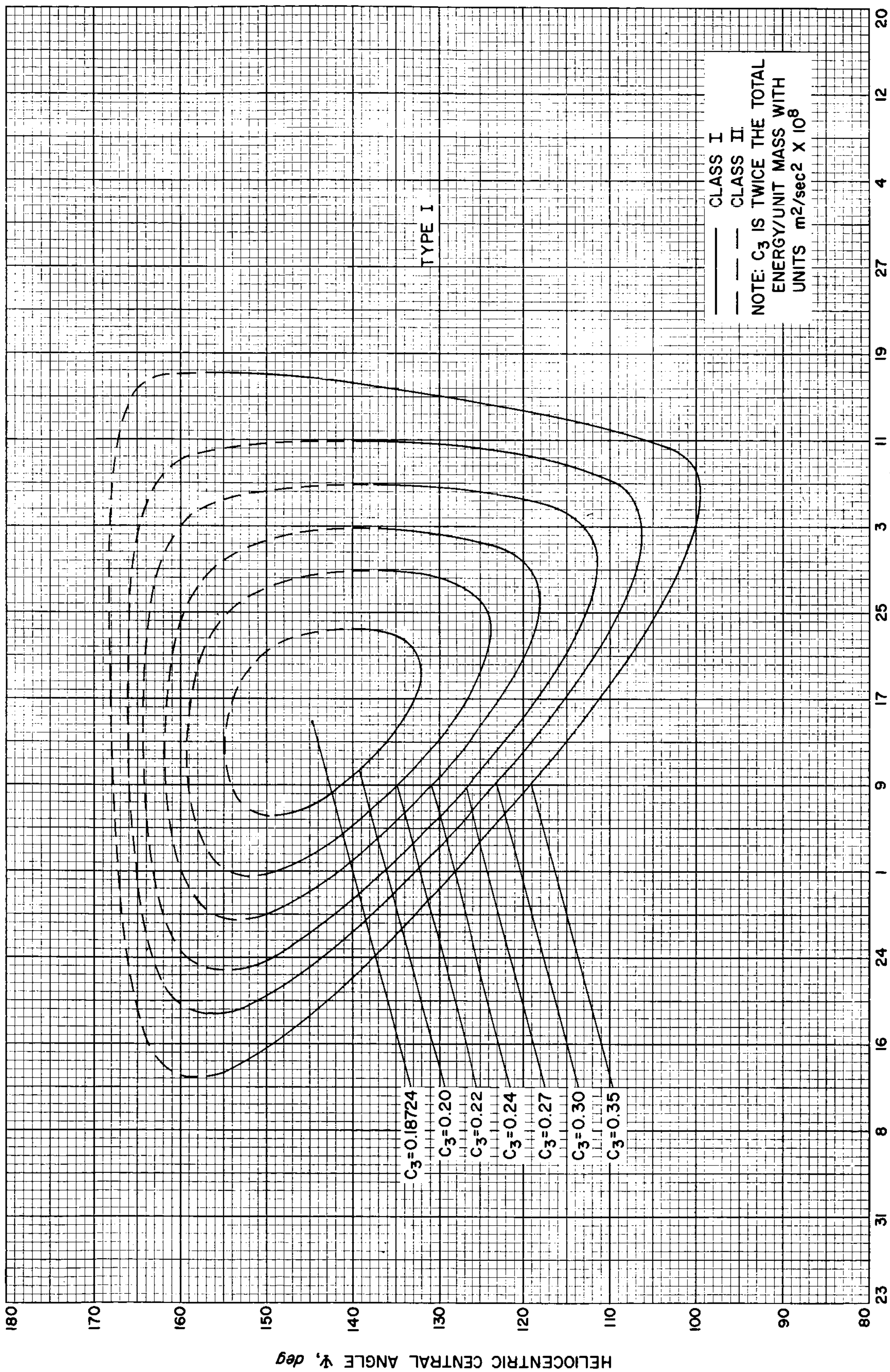

Fig. 17–2. Mars 1975: Heliocentric central angle vs launch date

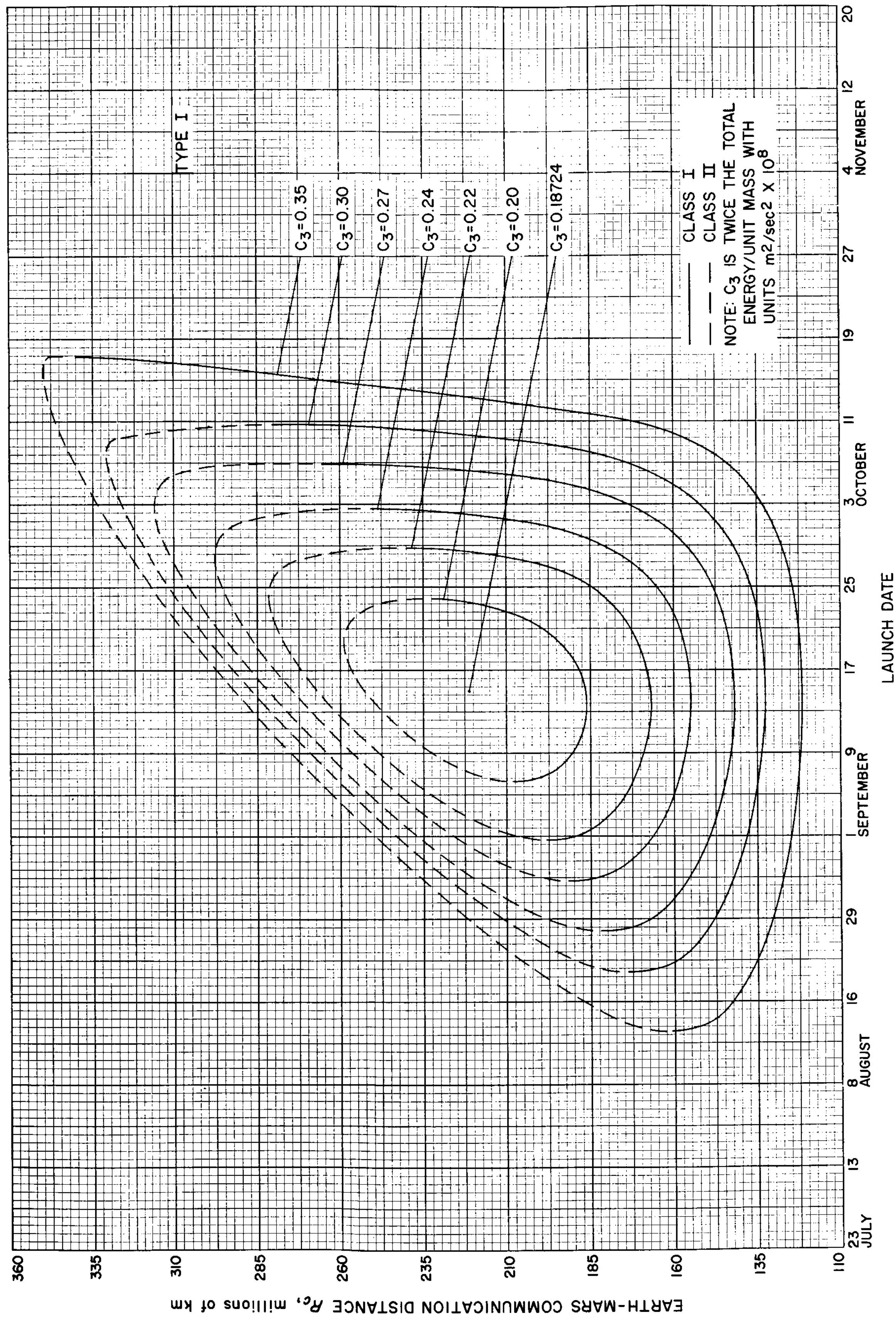

Fig. 17–3. Mars 1975: Earth–Mars communication distance vs launch date

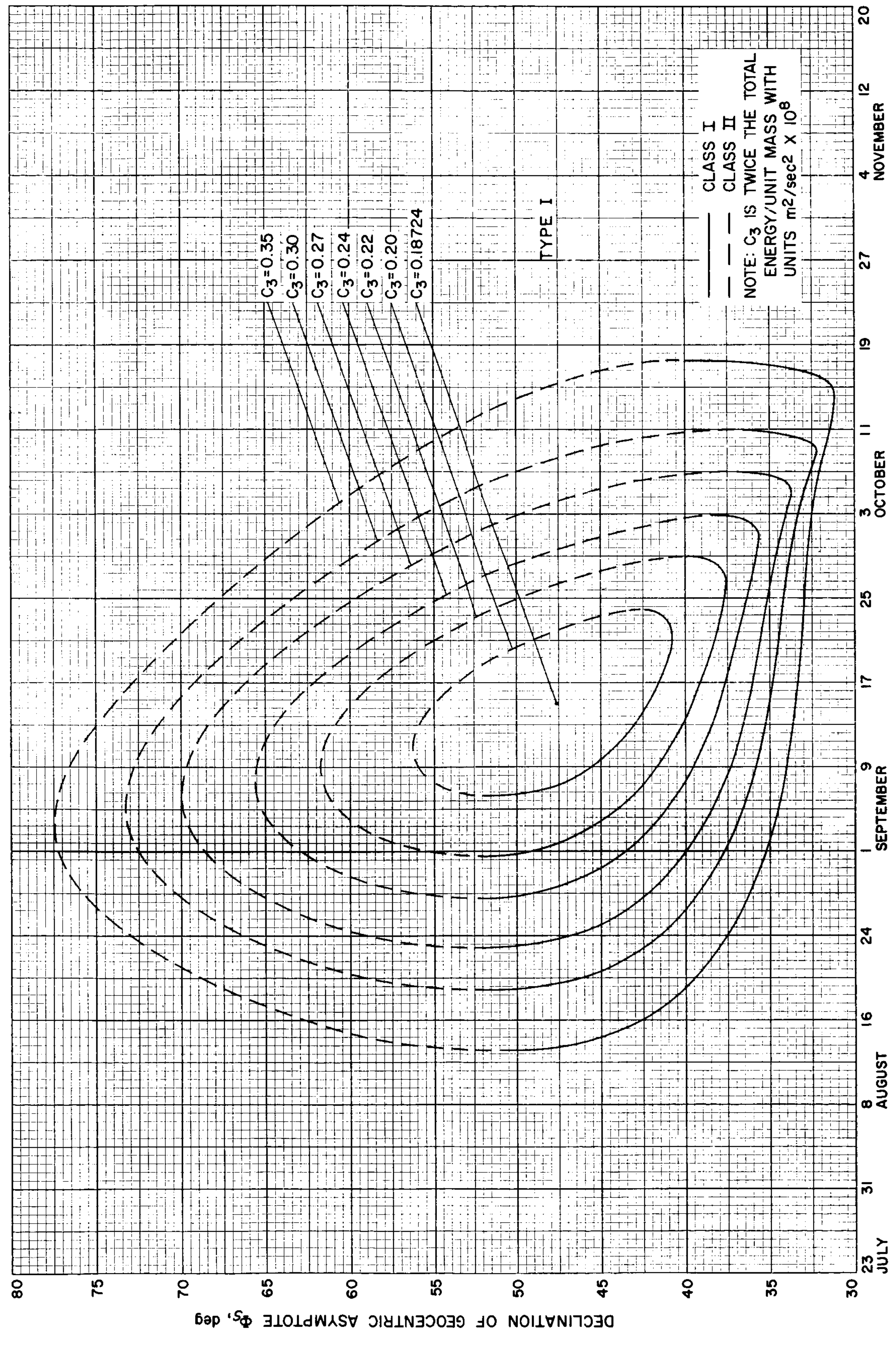

Fig. 17–4. Mars 1975: Declination of geocentric asymptote vs launch date

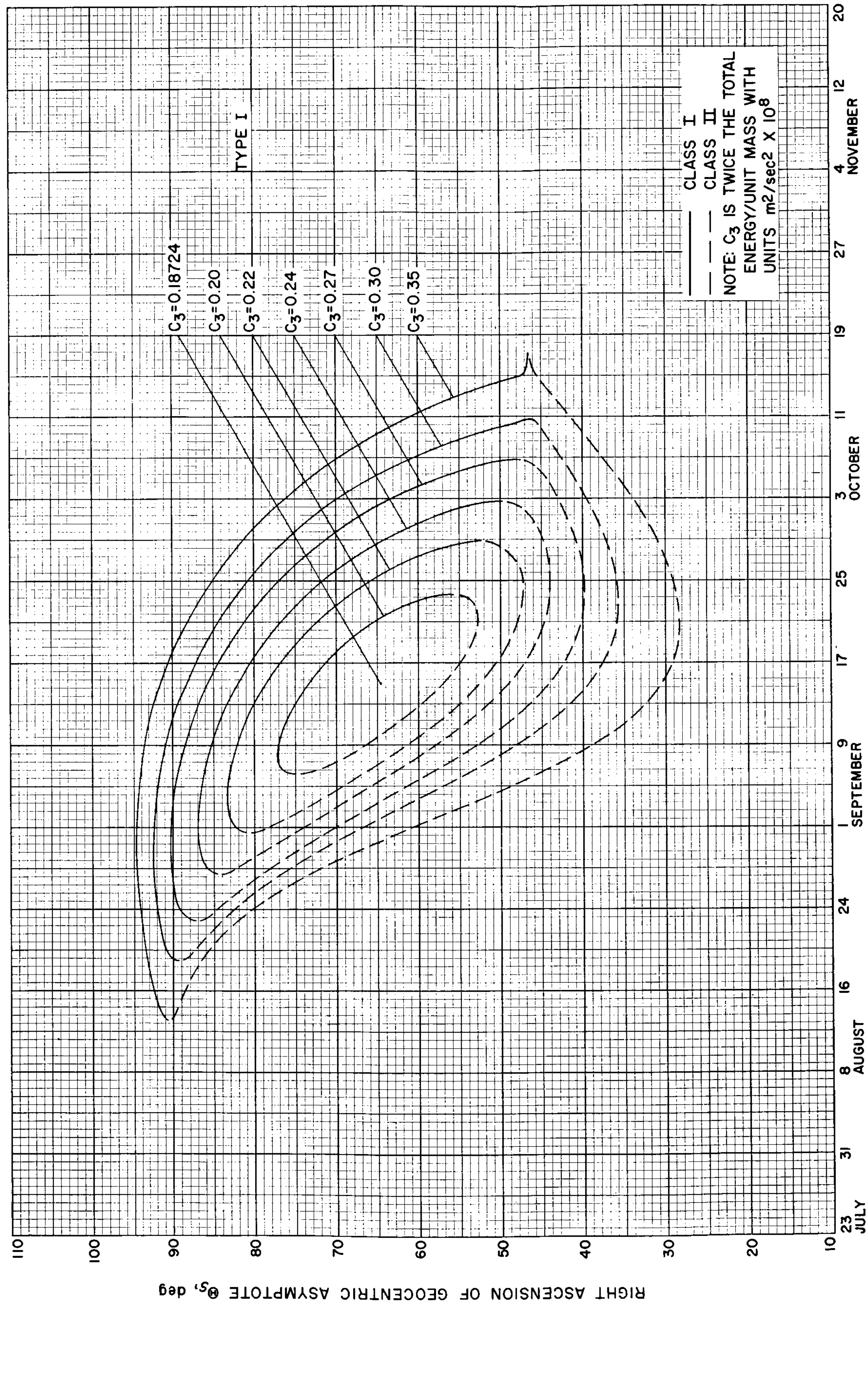

Fig. 17–5. Mars 1975: Right ascension of geocentric asymptote vs launch date

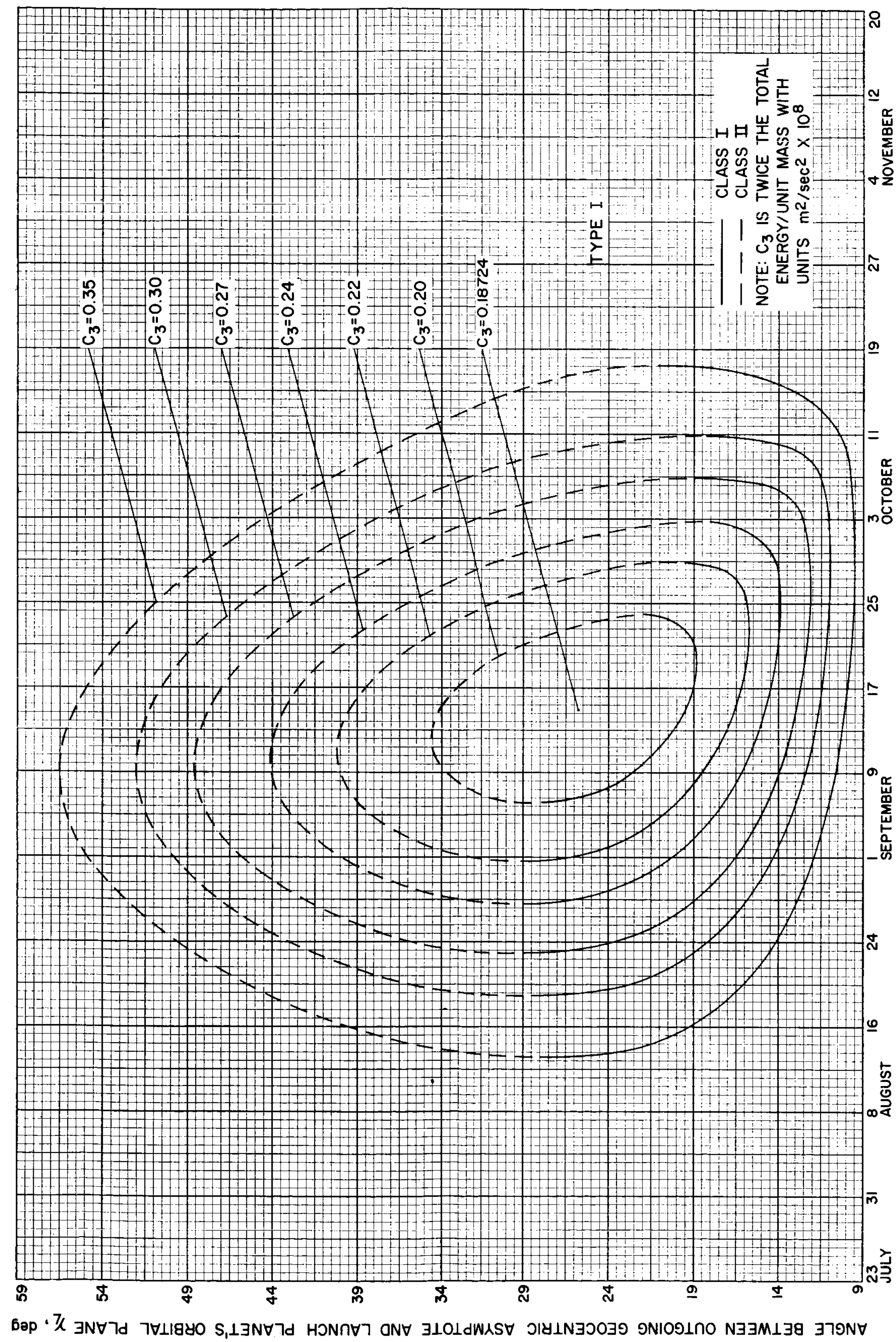

Fig. 17–6. Mars 1975: Angle between outgoing geocentric asymptote and launch planet's orbital plane vs launch date

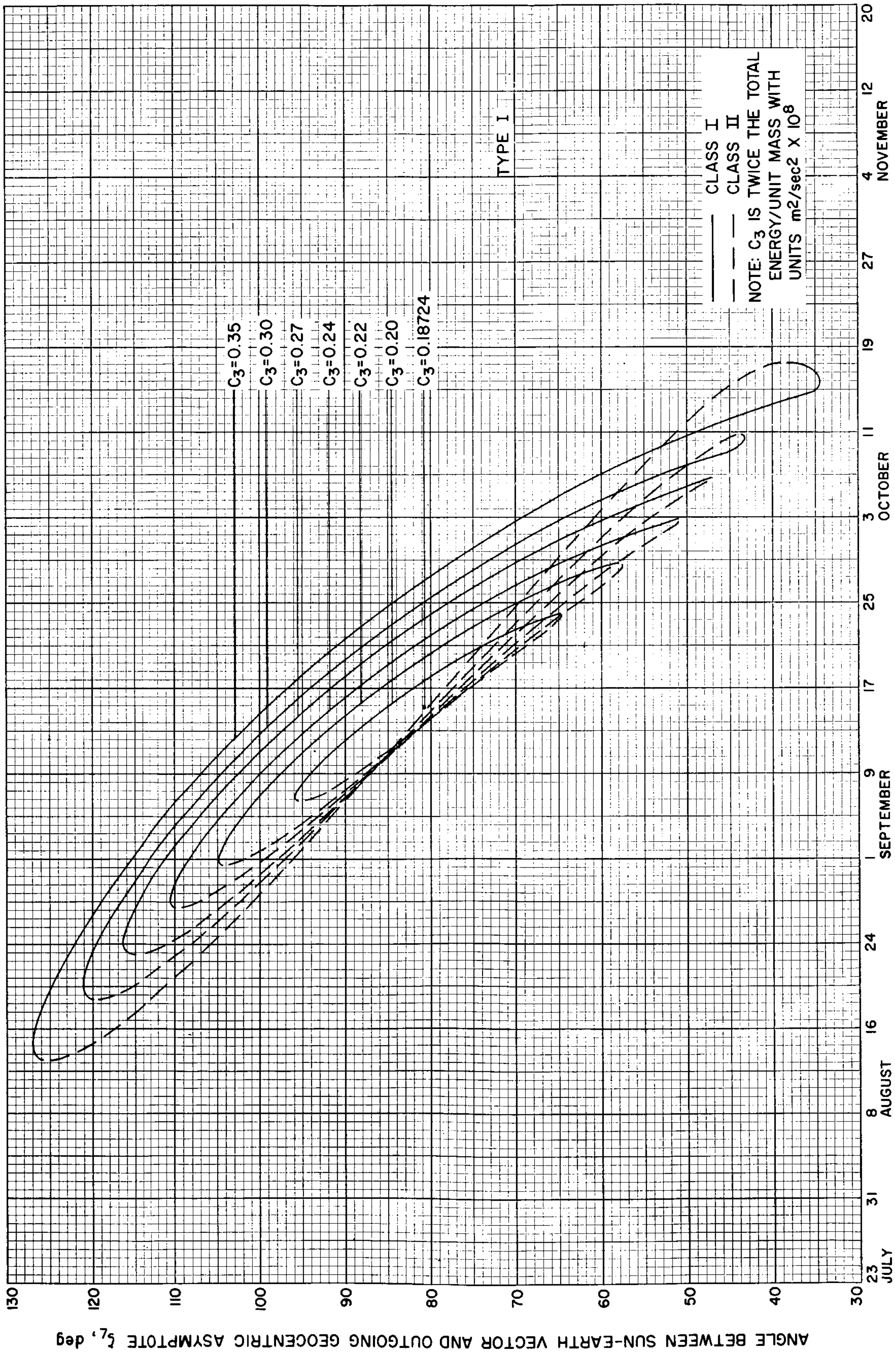

Fig. 17-7. Mars 1975: Angle between Sun–Earth vector and outgoing geocentric asymptote vs launch date

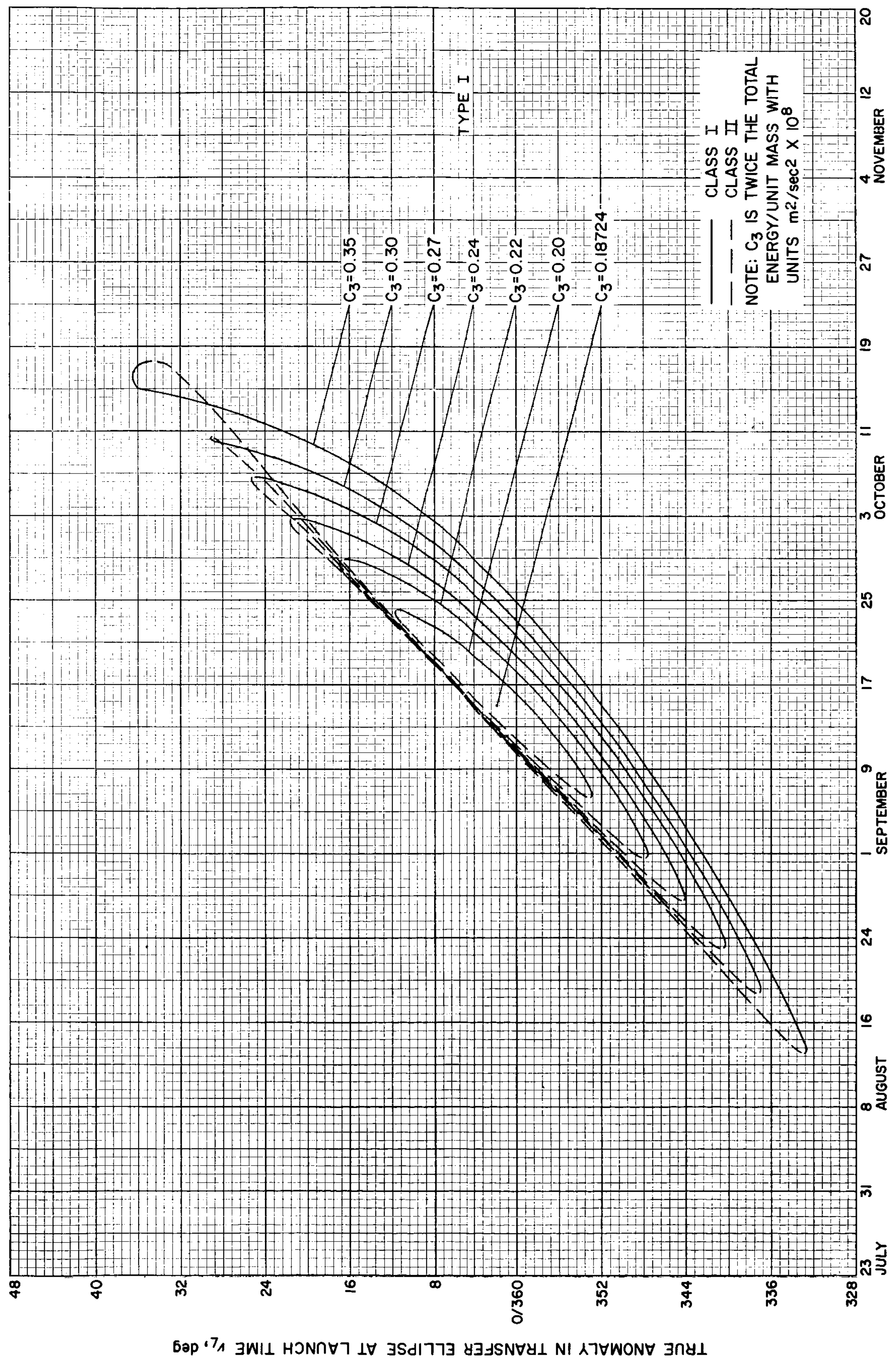

Fig. 17–8. Mars 1975: True anomaly in transfer ellipse at launch time vs launch date

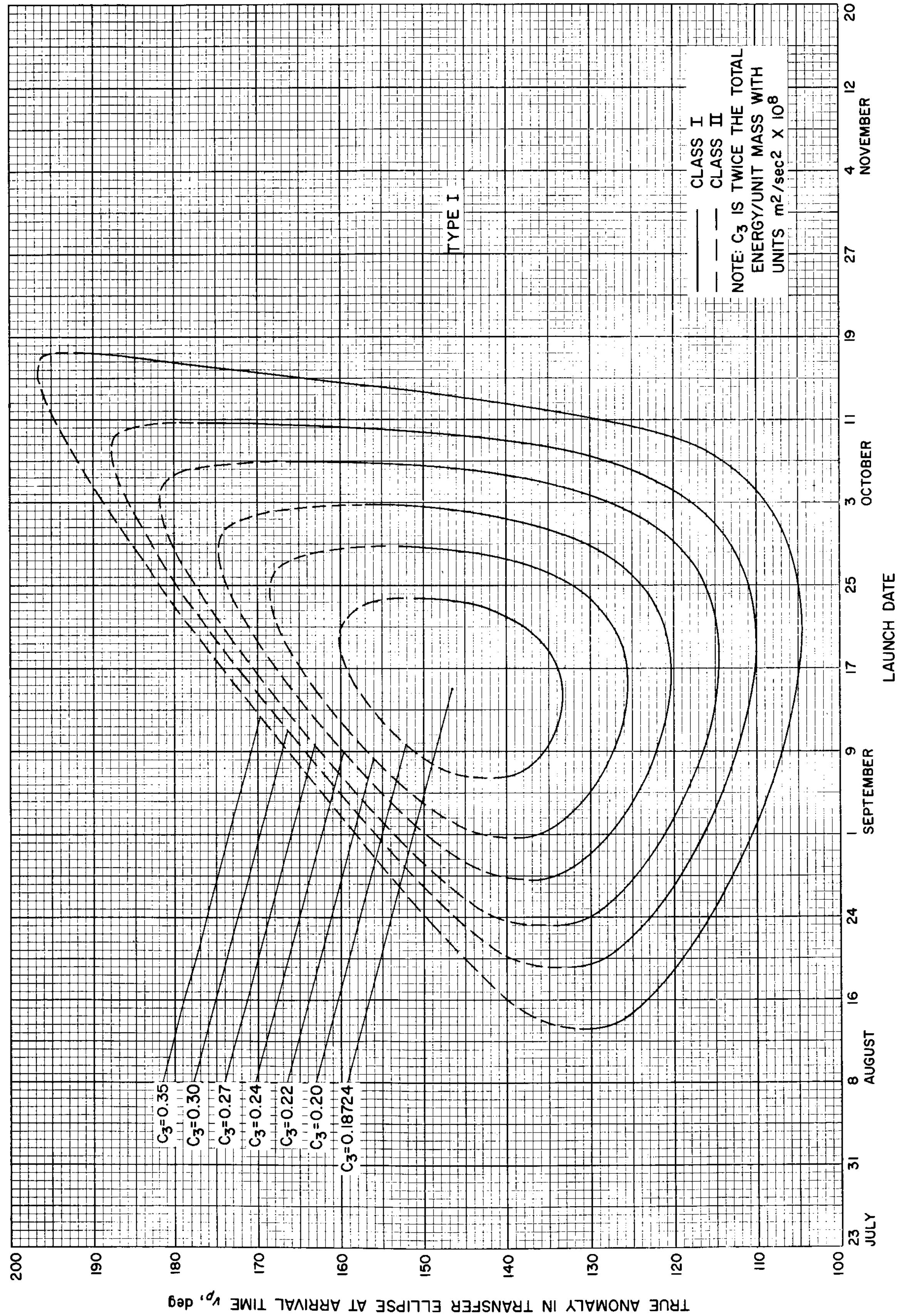

Fig. 17–9. Mars 1975: True anomaly in transfer ellipse at arrival time vs launch date

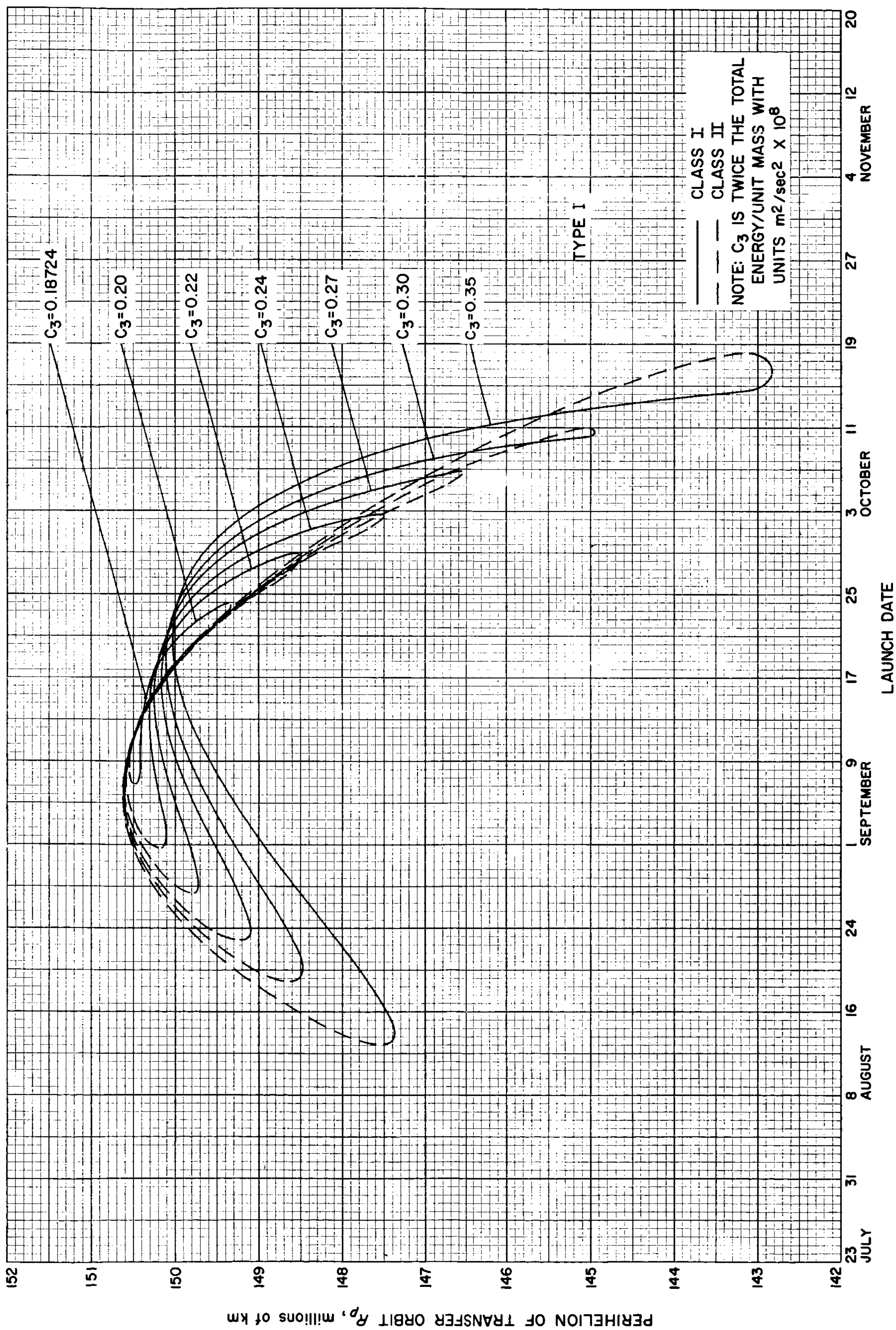

Fig. 17-10. Mars 1975: Perihelion of transfer orbit vs launch date

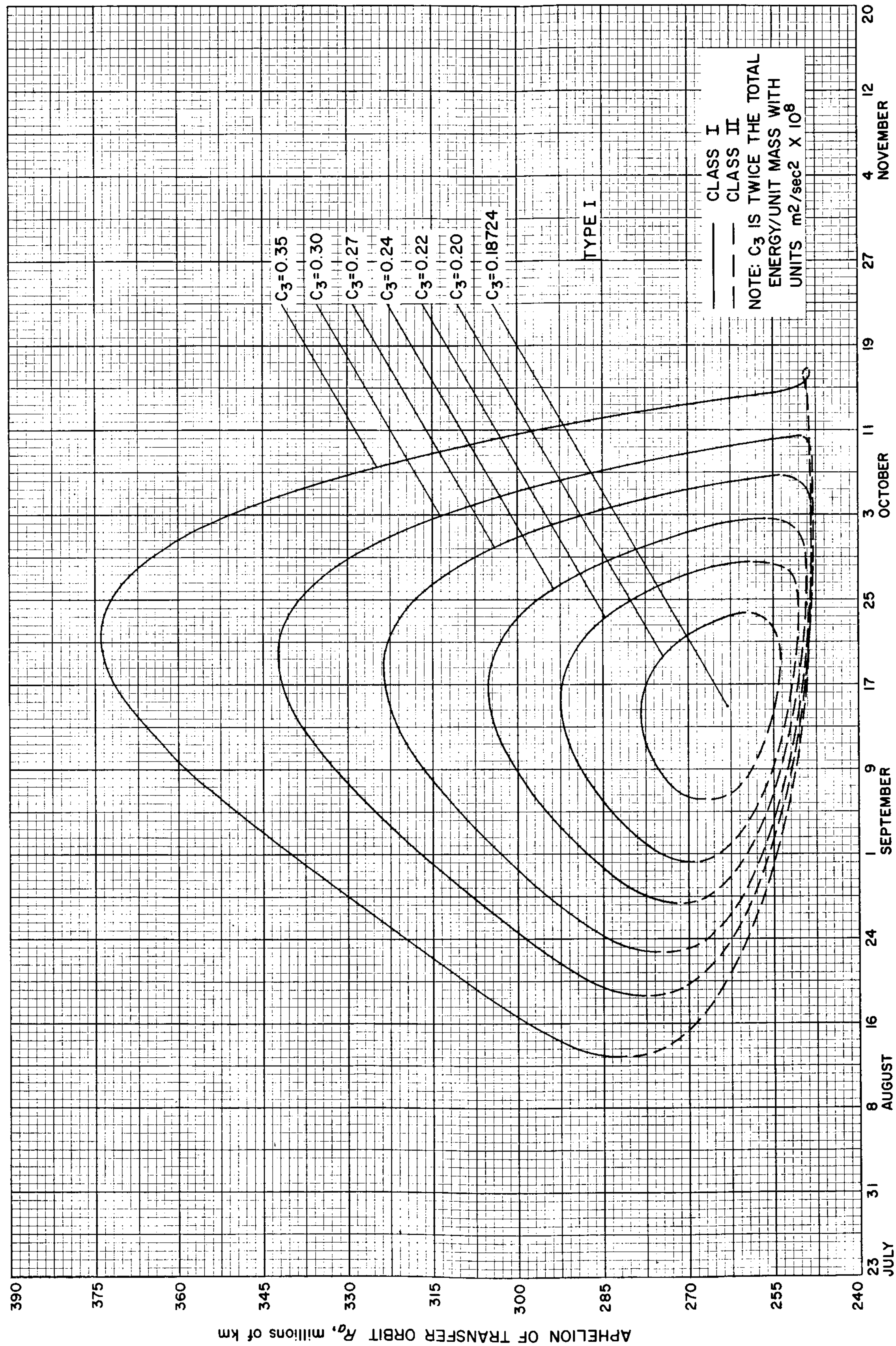

Fig. 17–11. Mars 1975: Aphelion of transfer orbit vs launch date

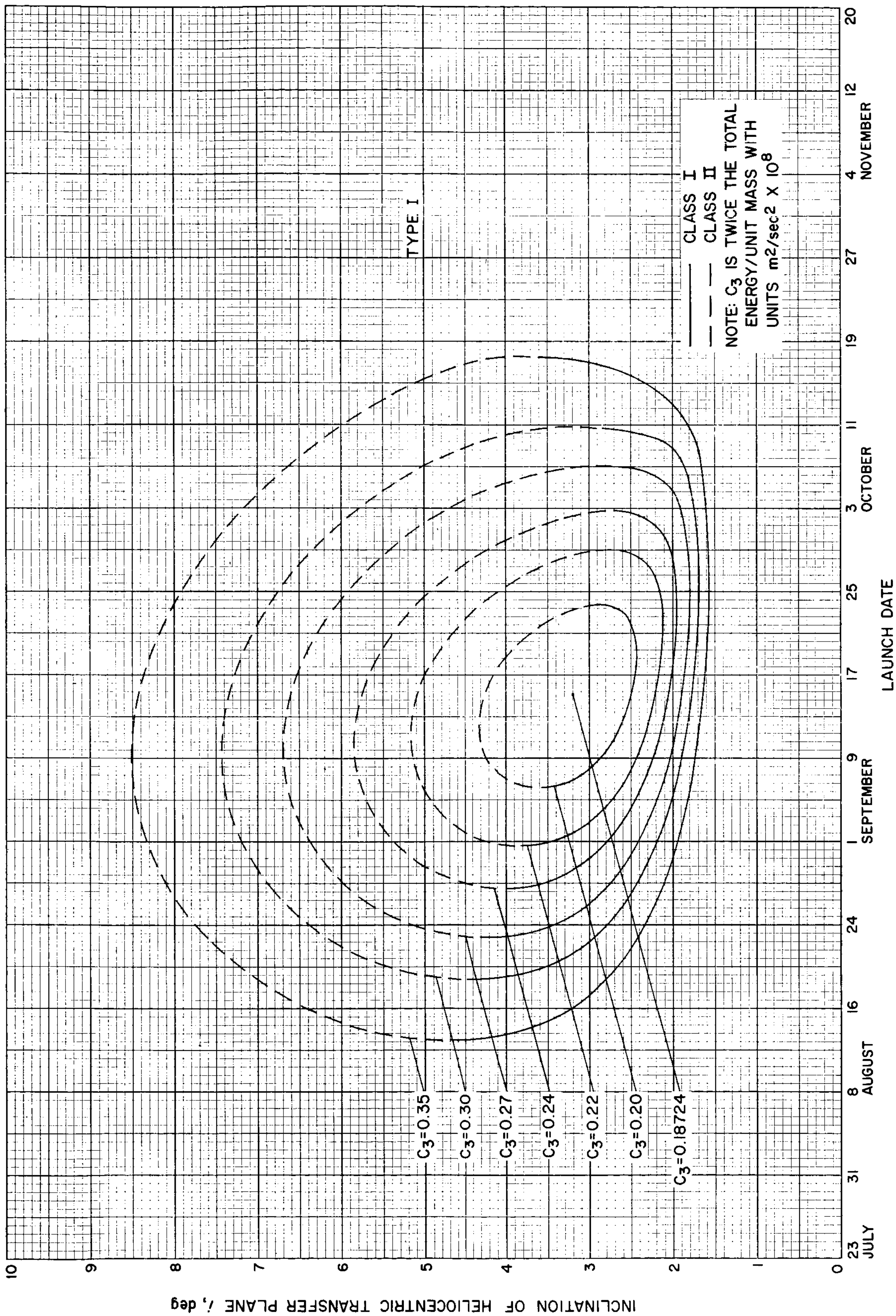

Fig. 17–12. Mars 1975: Inclination of heliocentric-transfer plane vs launch date

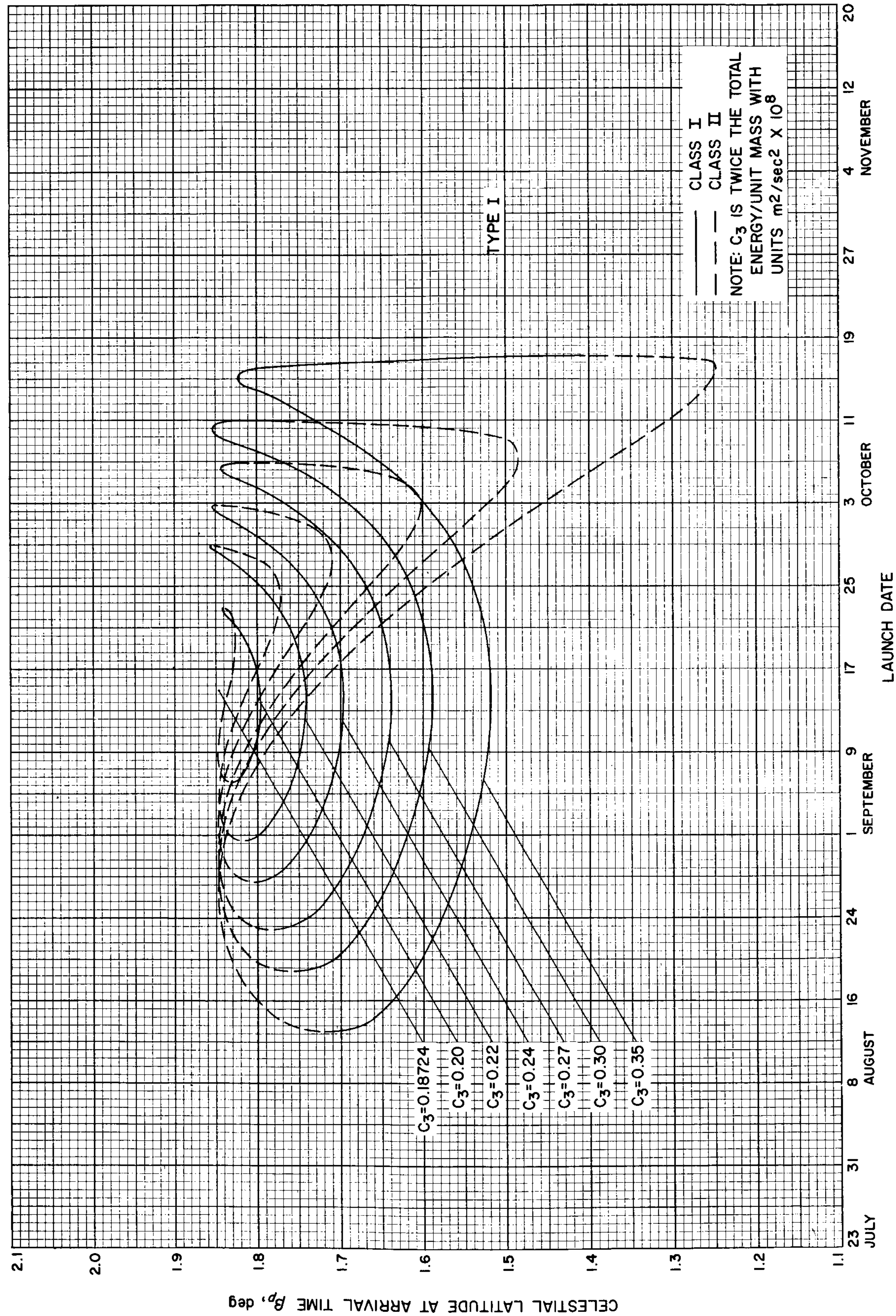

Fig. 17–13. Mars 1975: Celestial latitude at arrival time vs launch date

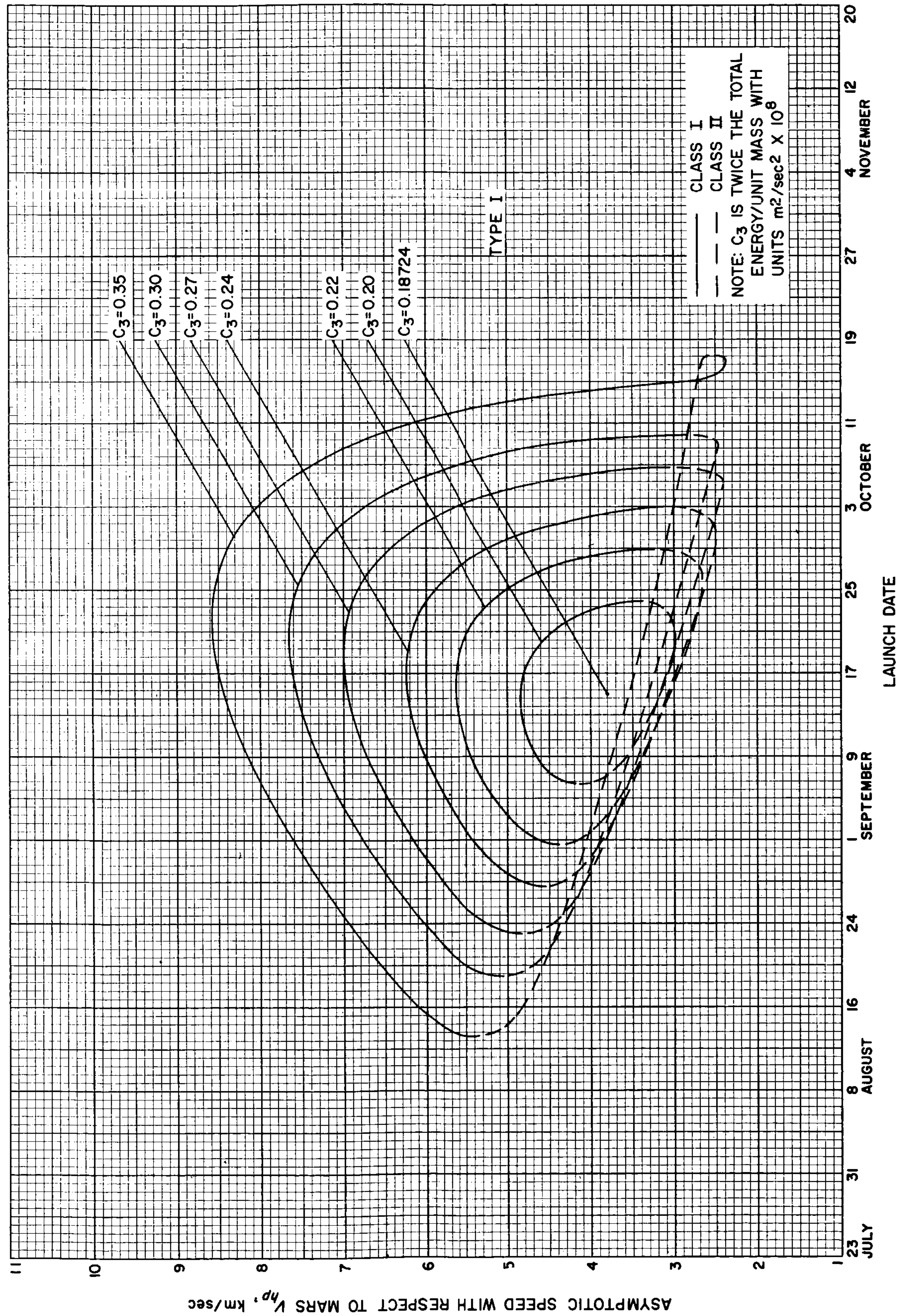

Fig. 17–14. Mars 1975: Asymptotic speed with respect to Mars vs launch date

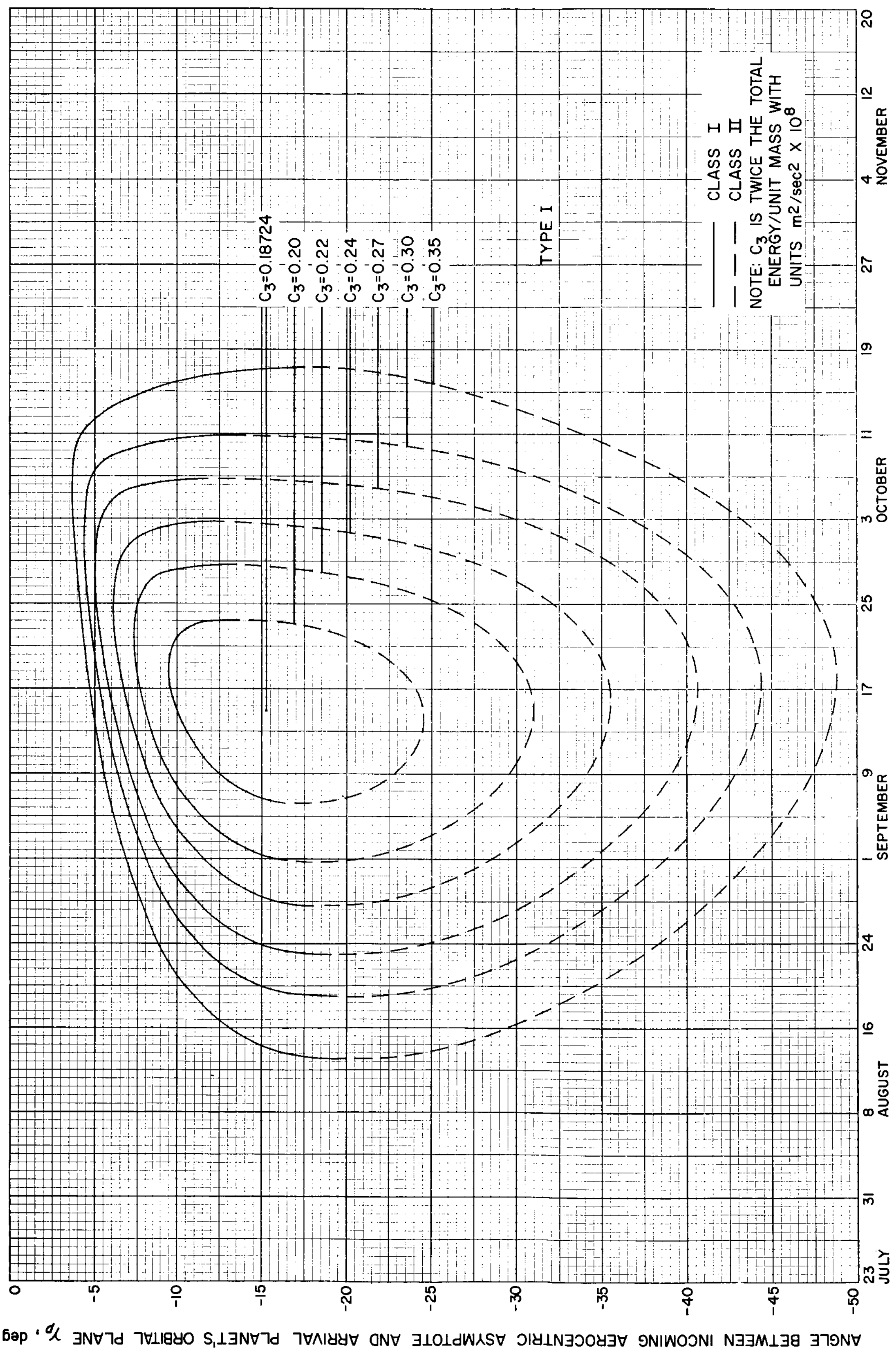

Fig. 17–15. Mars 1975: Angle between incoming aerocentric asymptote and arrival planet's orbital plane vs launch date

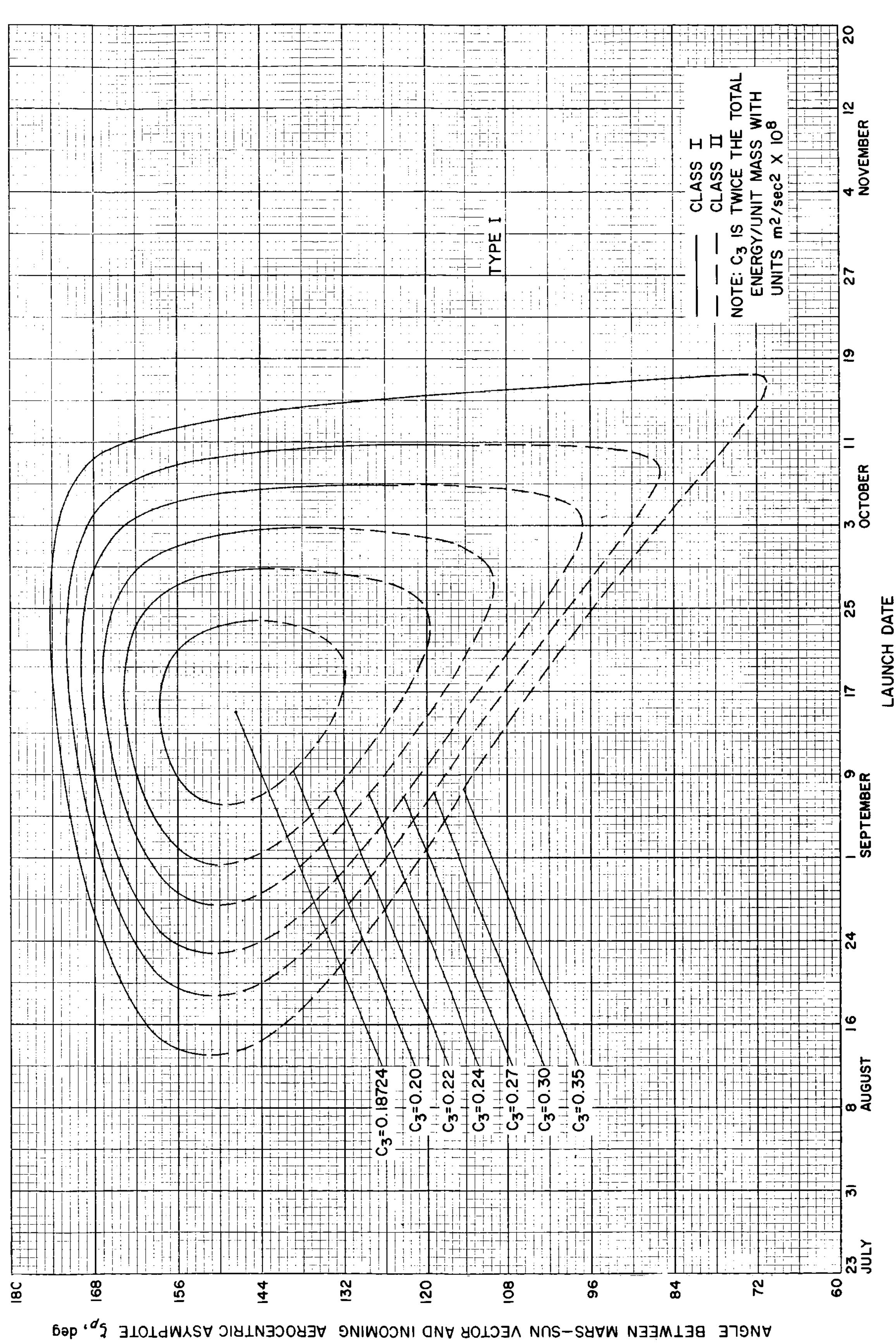

Fig. 17–16. Mars 1975: Angle between Mars–Sun vector and incoming aerocentric asymptote vs launch date

XVIII. MARS 1977: TRAJECTORY-PARAMETER GRAPHS

Figure

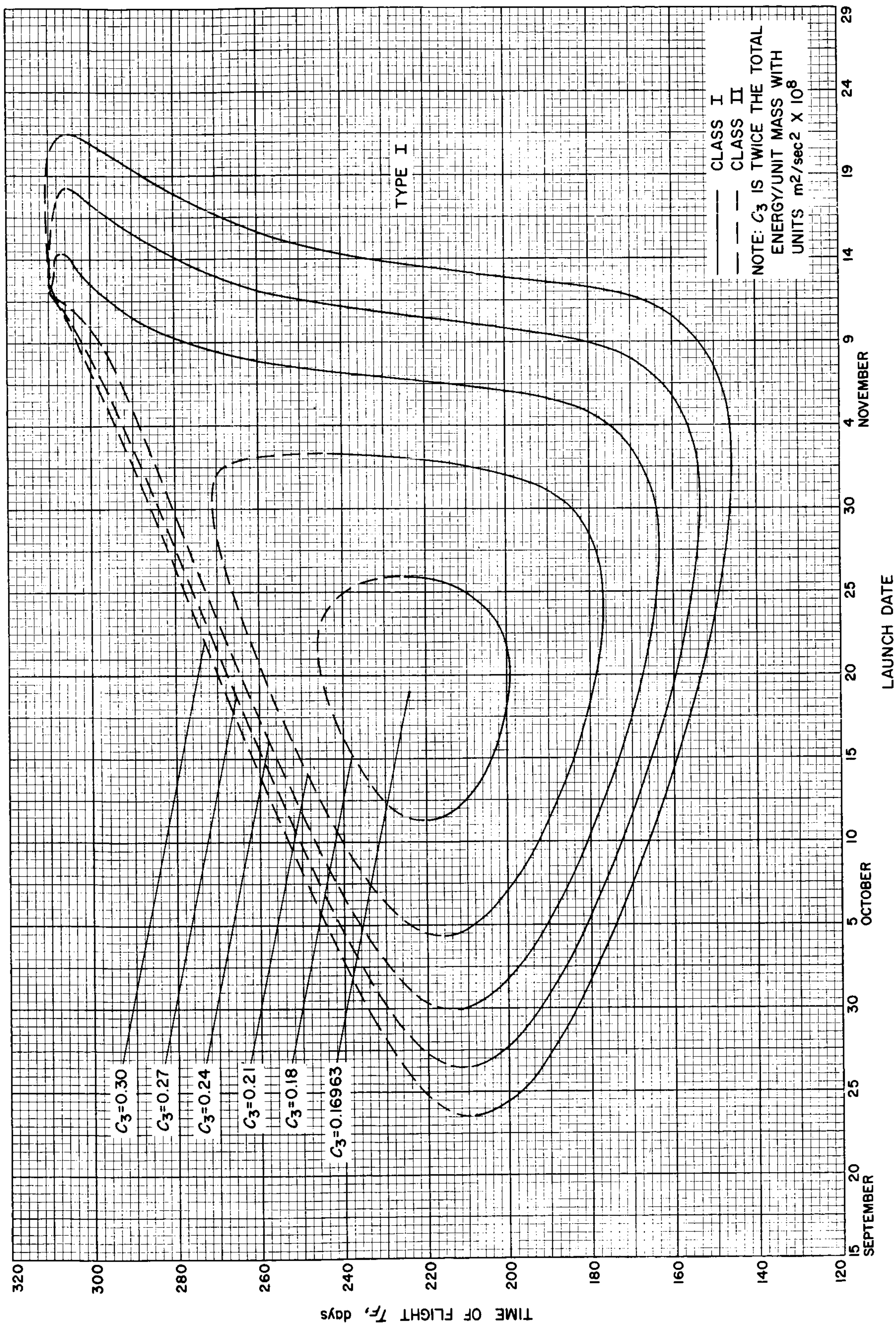

Fig. 18-1. Mars 1977: Time of flight vs launch date

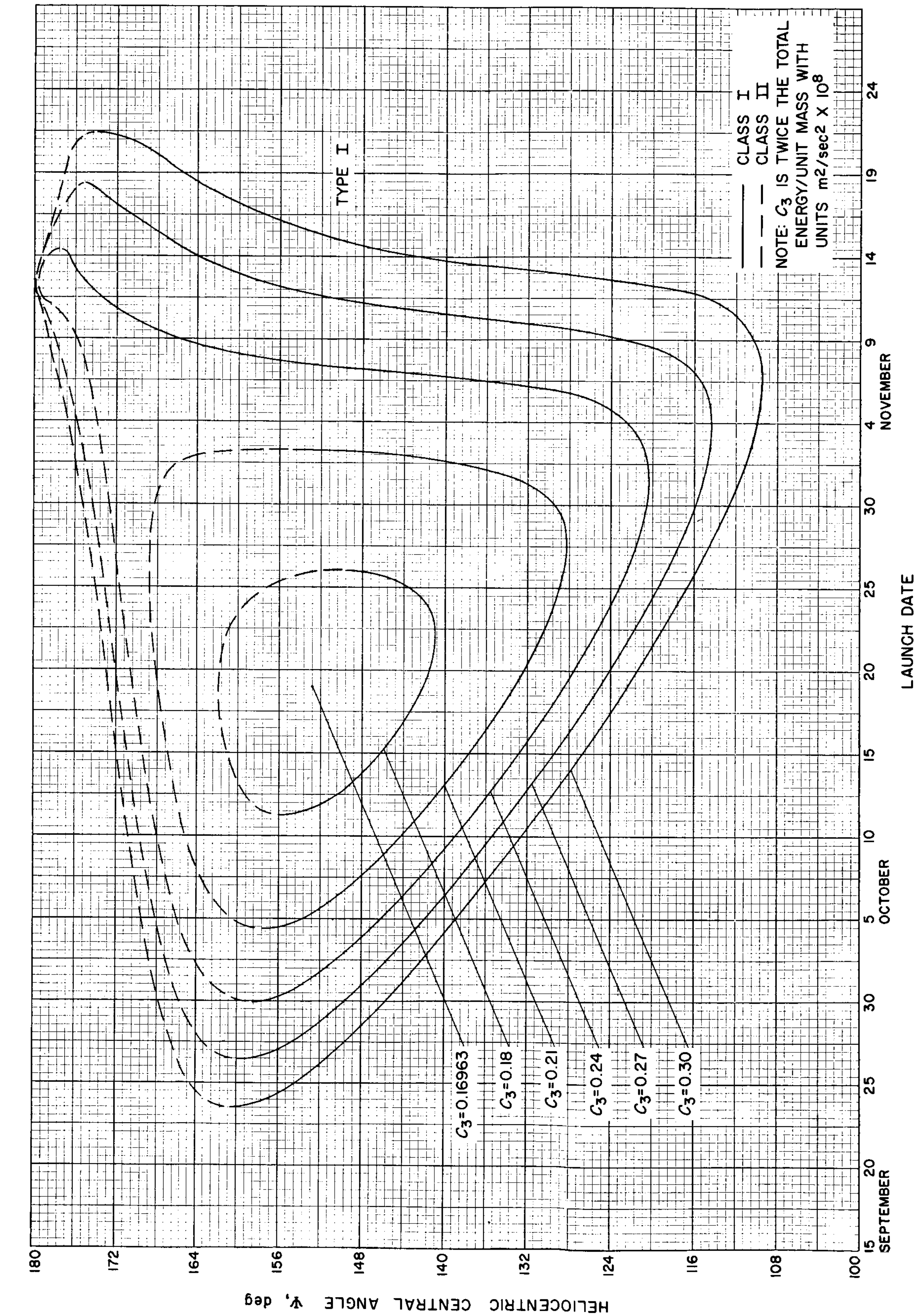

Fig. 18–2. Mars 1977: Heliocentric central angle vs launch date

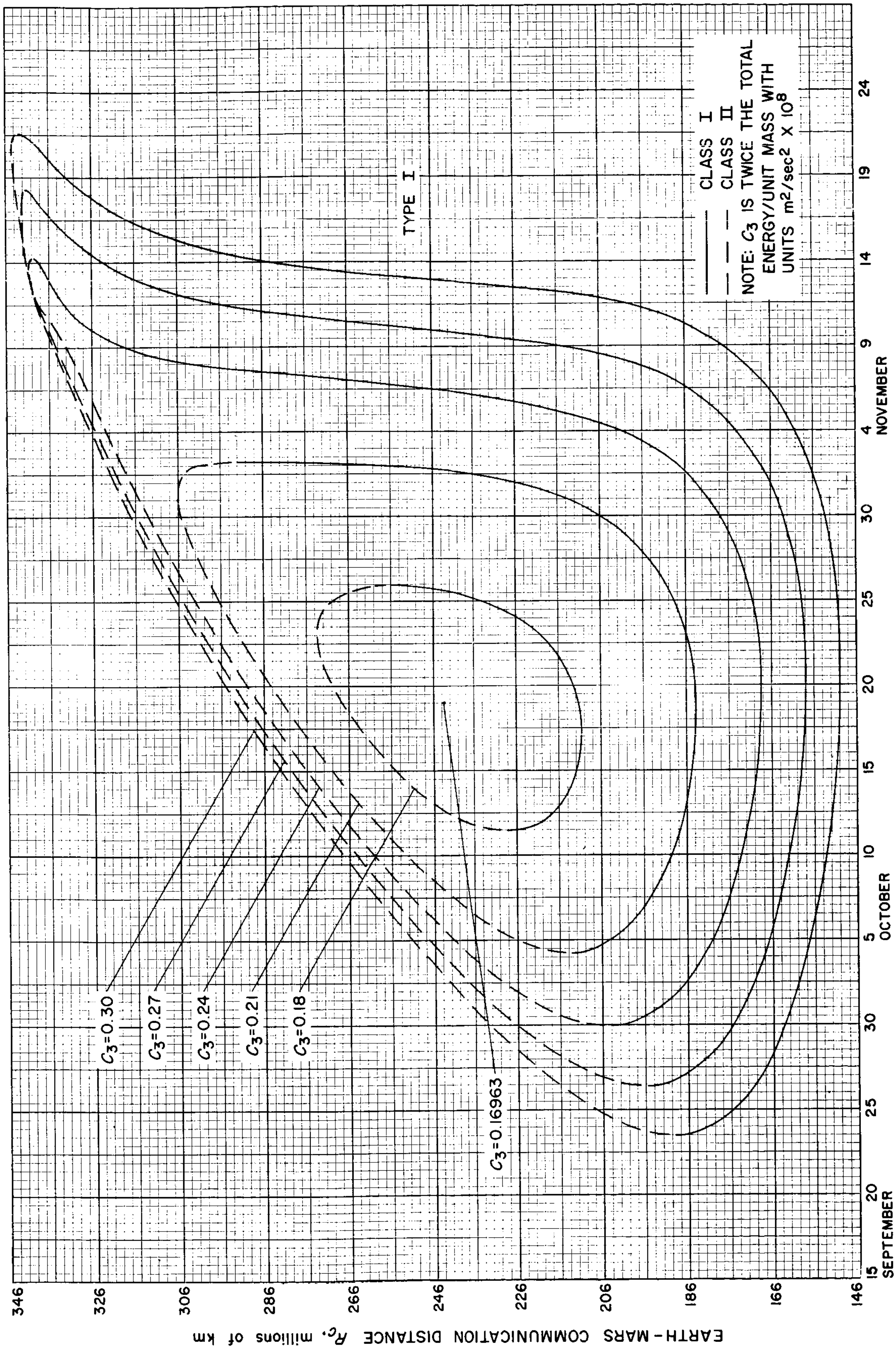

Fig. 18–3. Mars 1977: Earth–Mars communication distance vs launch date

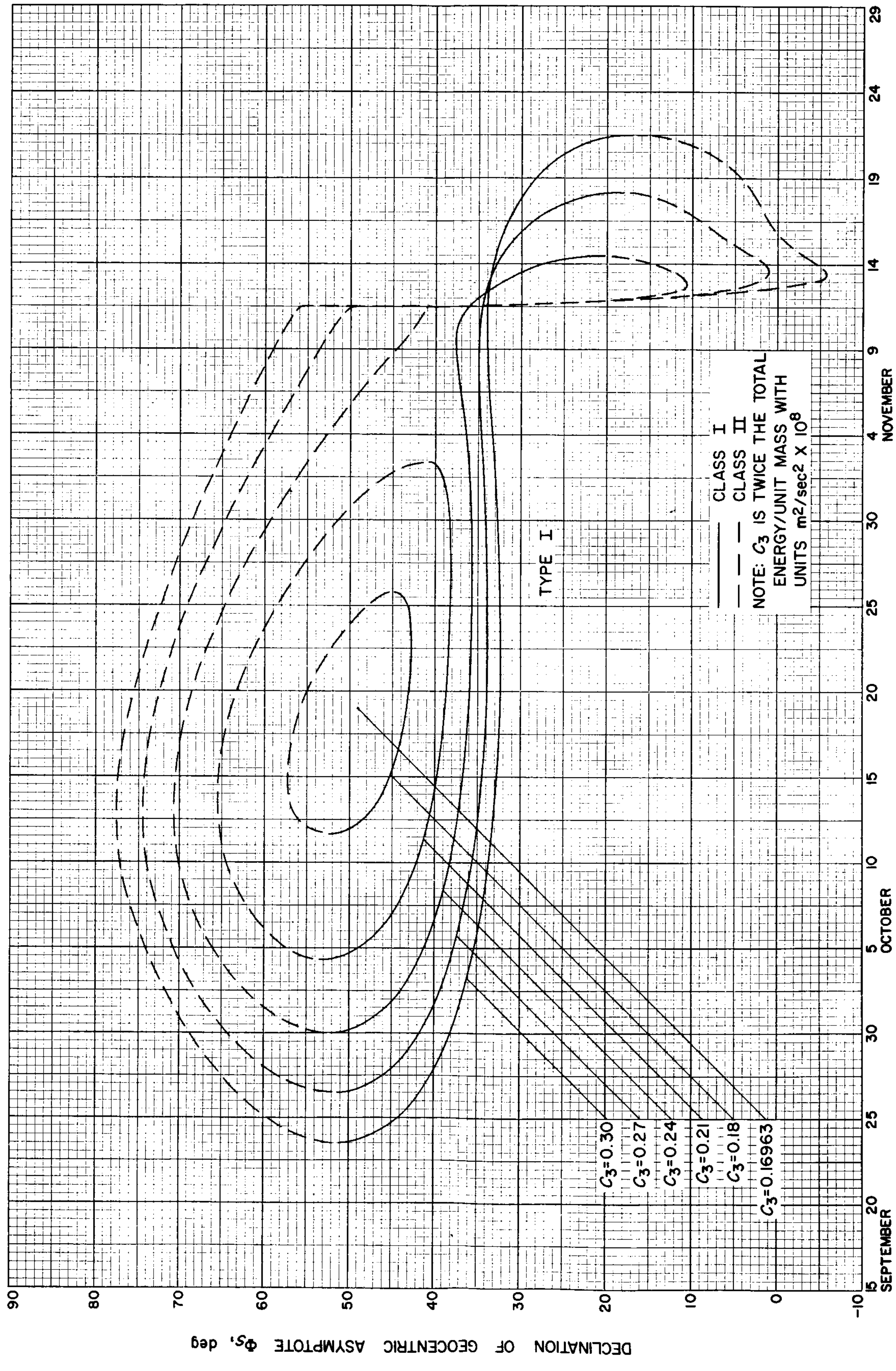

Fig. 18–4. Mars 1977: Declination of geocentric asymptote vs launch date

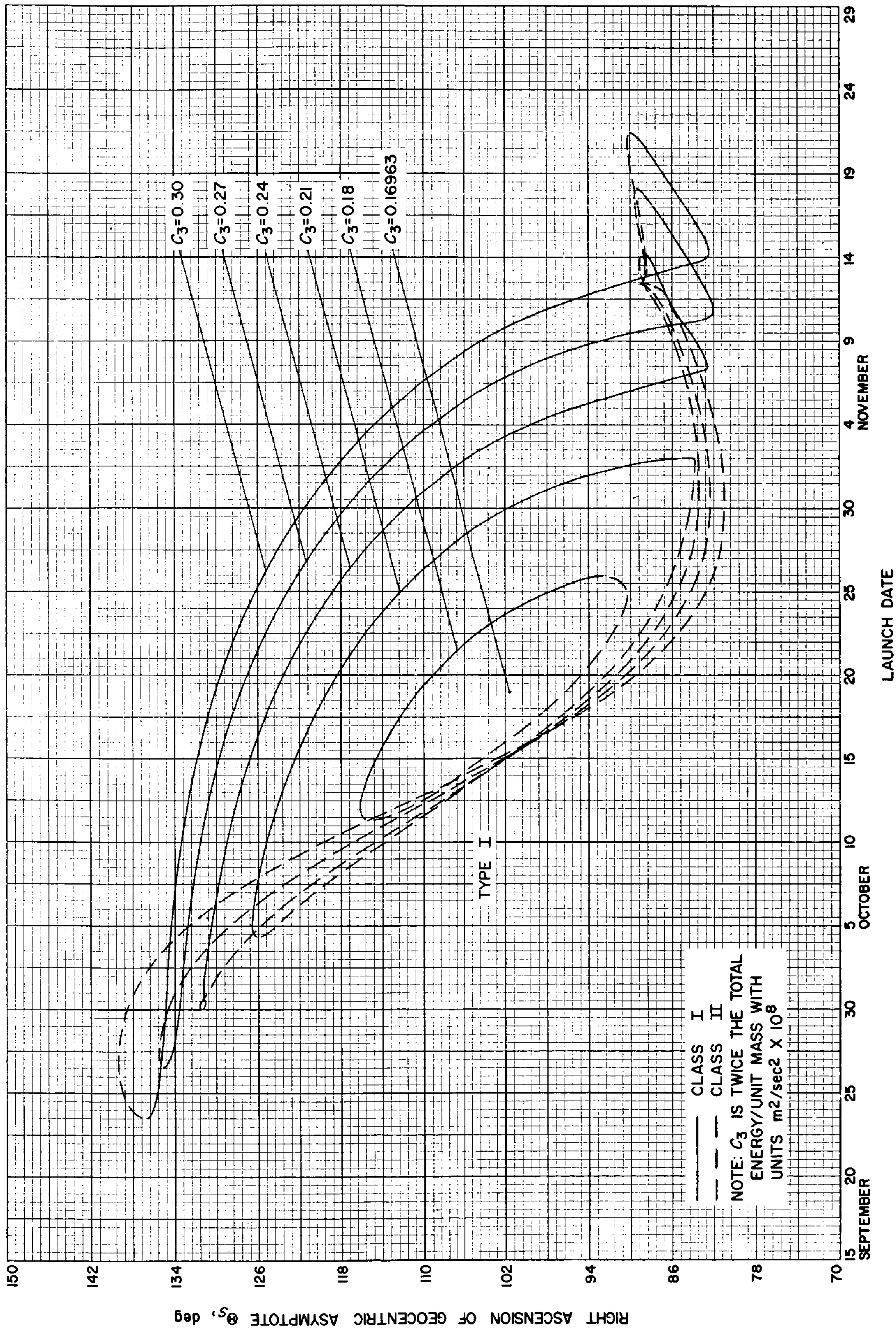

Fig. 18–5. Mars 1977: Right ascension of geocentric asymptote vs launch date

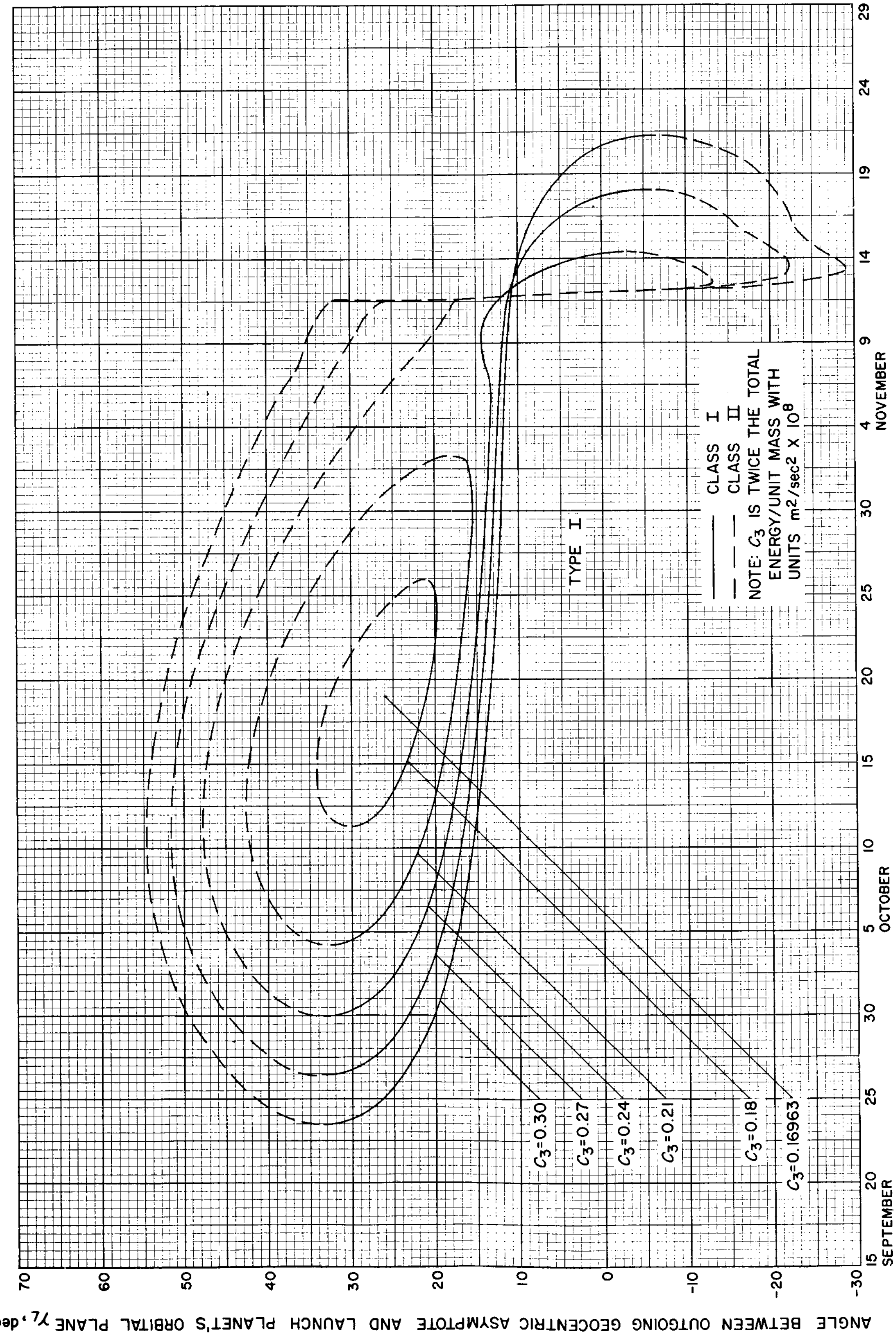

Fig. 18–6. Mars 1977: Angle between outgoing geocentric asymptote and launch planet's orbital plane vs launch date

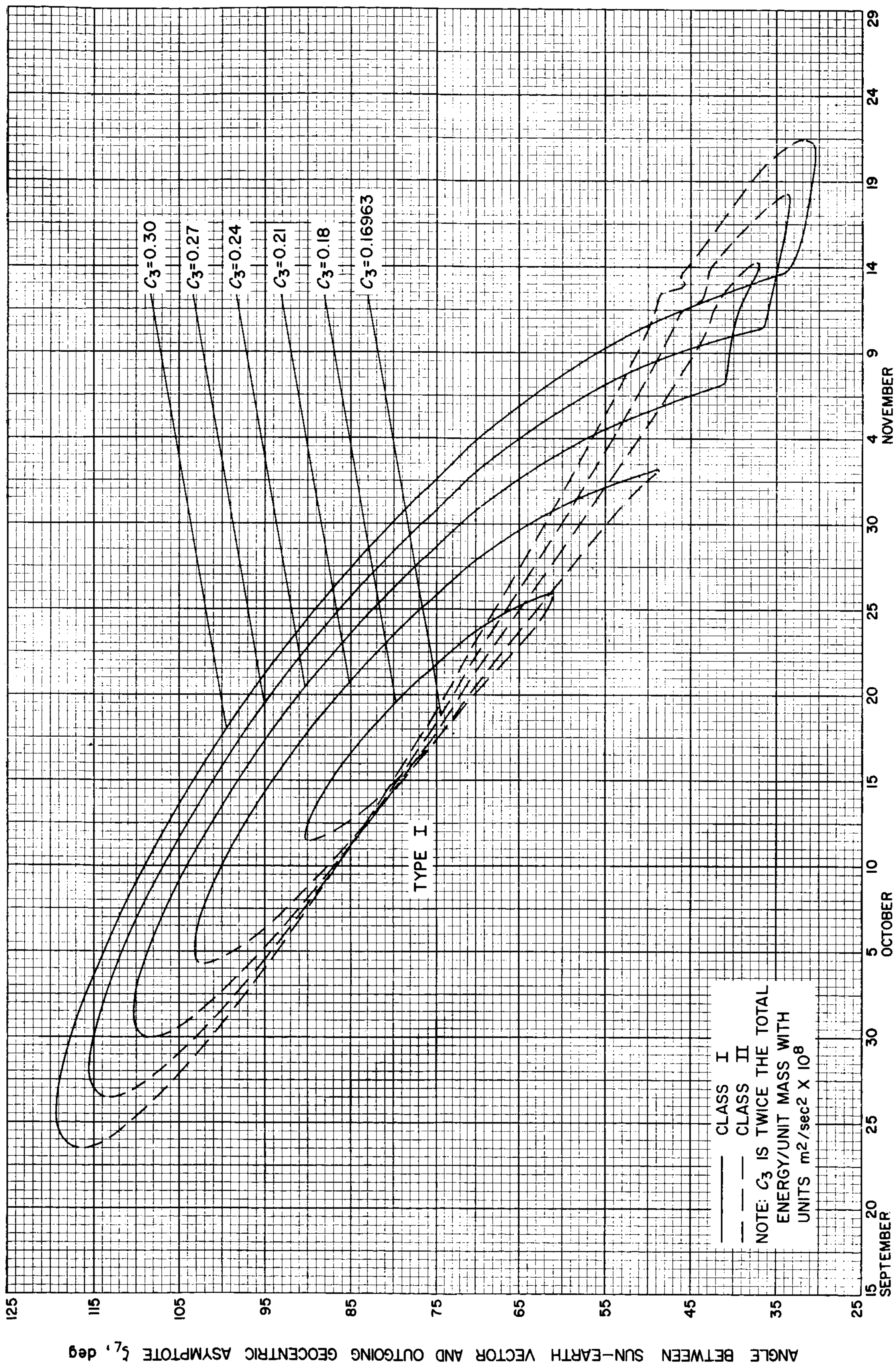

Fig. 18–7. Mars 1977: Angle between Sun–Earth vector and outgoing geocentric asymptote vs launch date

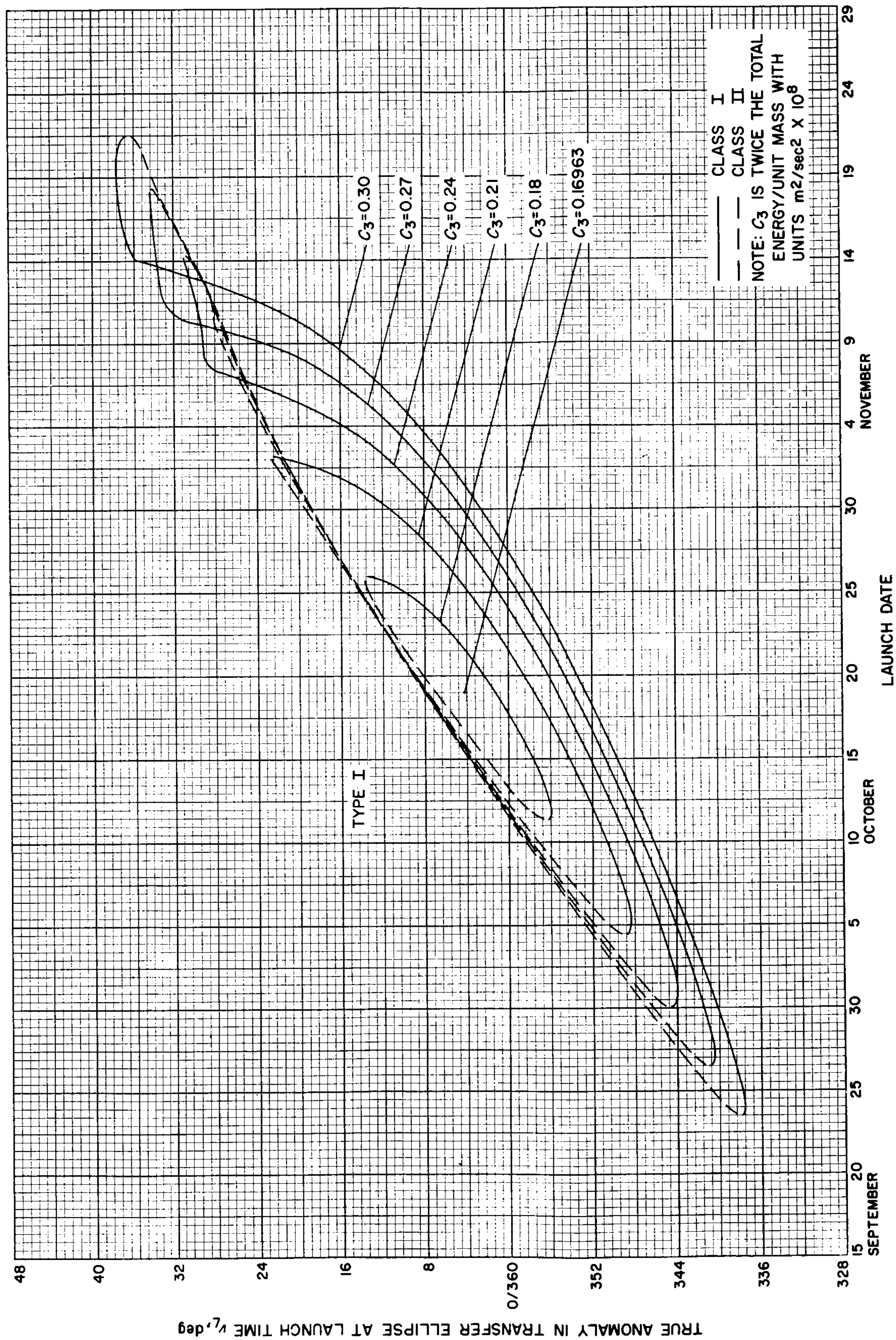

Fig. 18–8. Mars 1977: True anomaly in transfer ellipse at launch time vs launch date

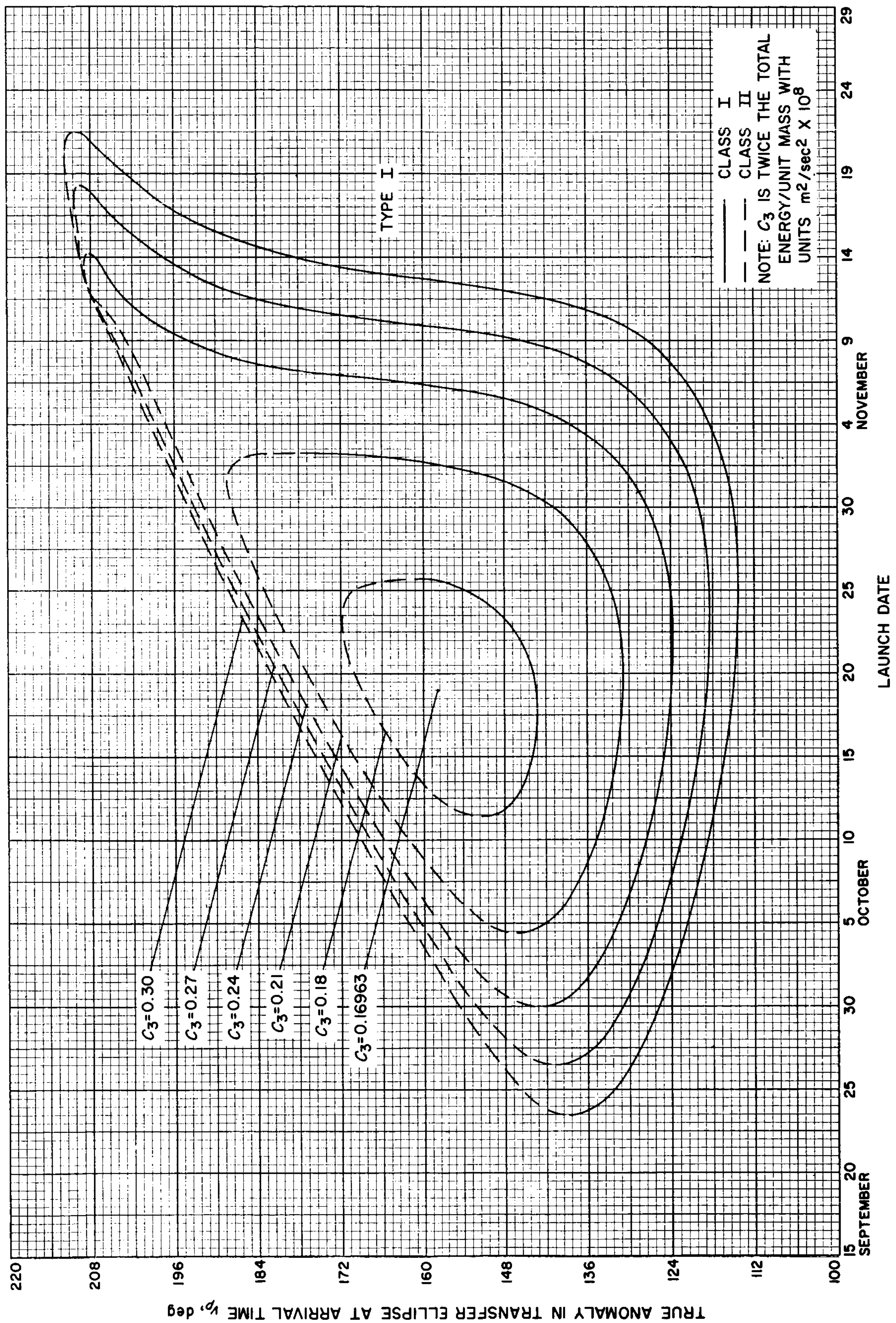

Fig. 18–9. Mars 1977: True anomaly in transfer ellipse at arrival time vs launch date

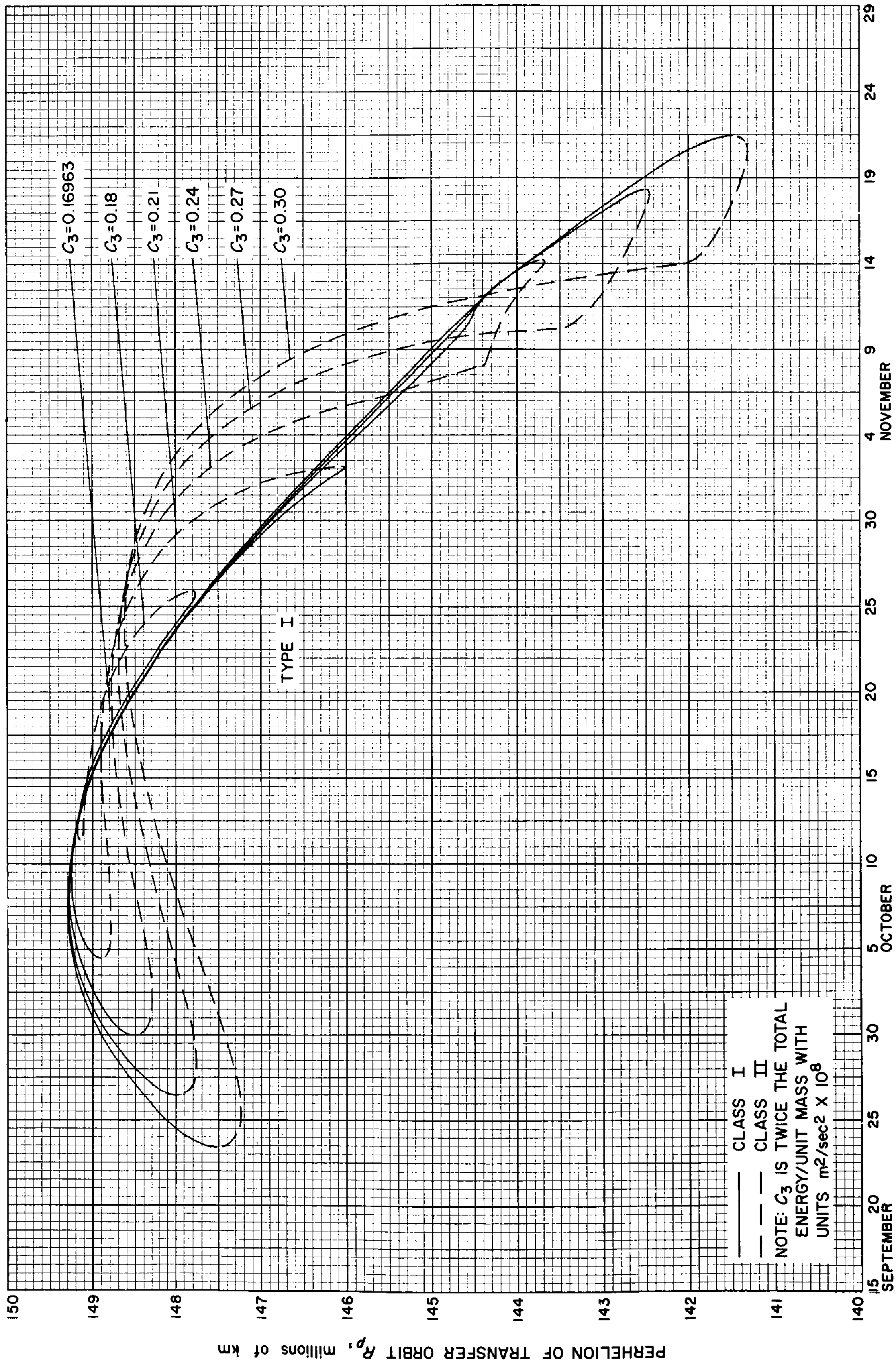

Fig. 18–10. Mars 1977: Perihelion of transfer orbit vs launch date

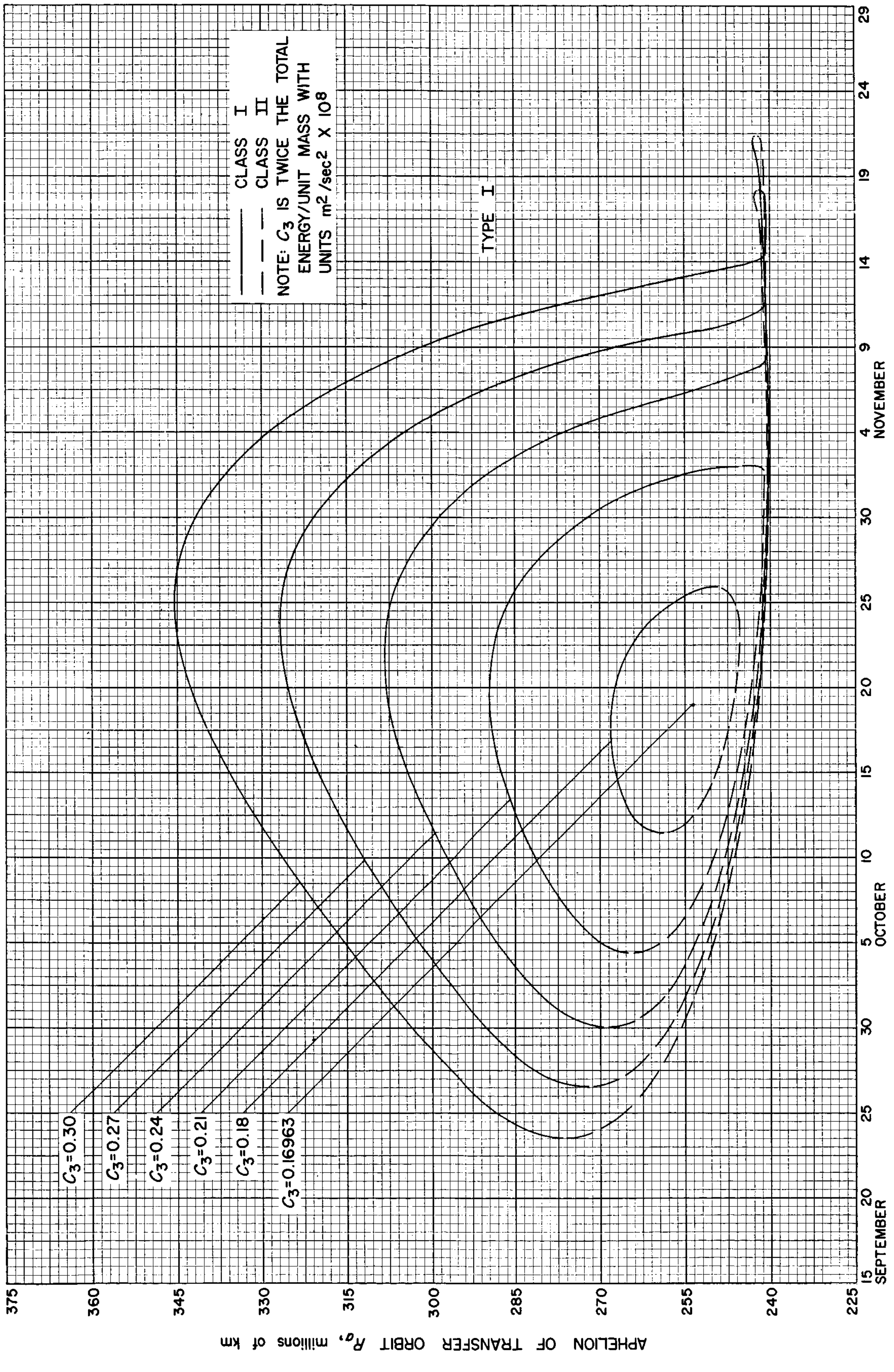

Fig. 18–11. Mars 1977: Aphelion of transfer orbit vs launch date

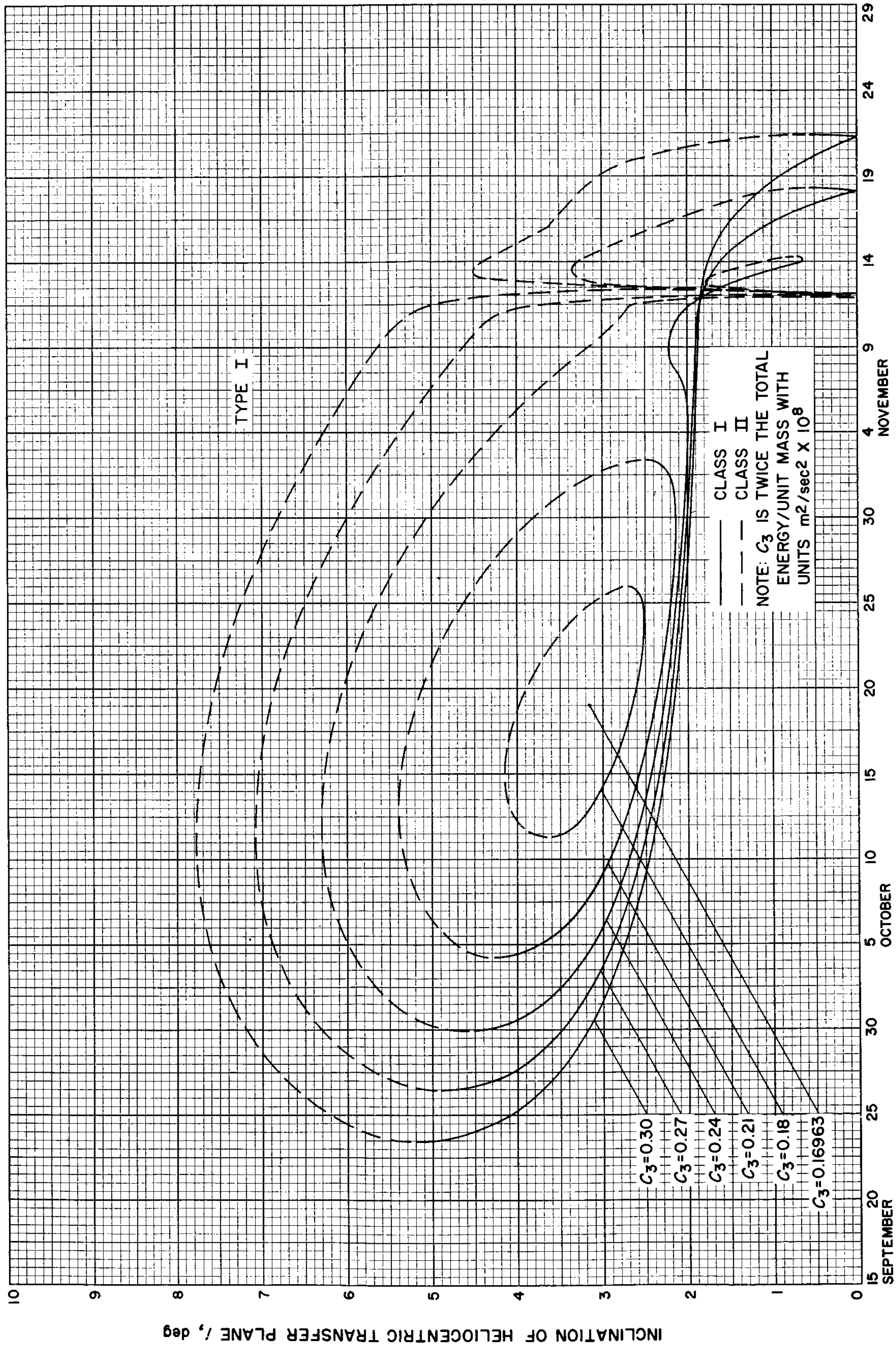

Fig. 18–12. Mars 1977: Inclination of heliocentric-transfer plane vs launch date

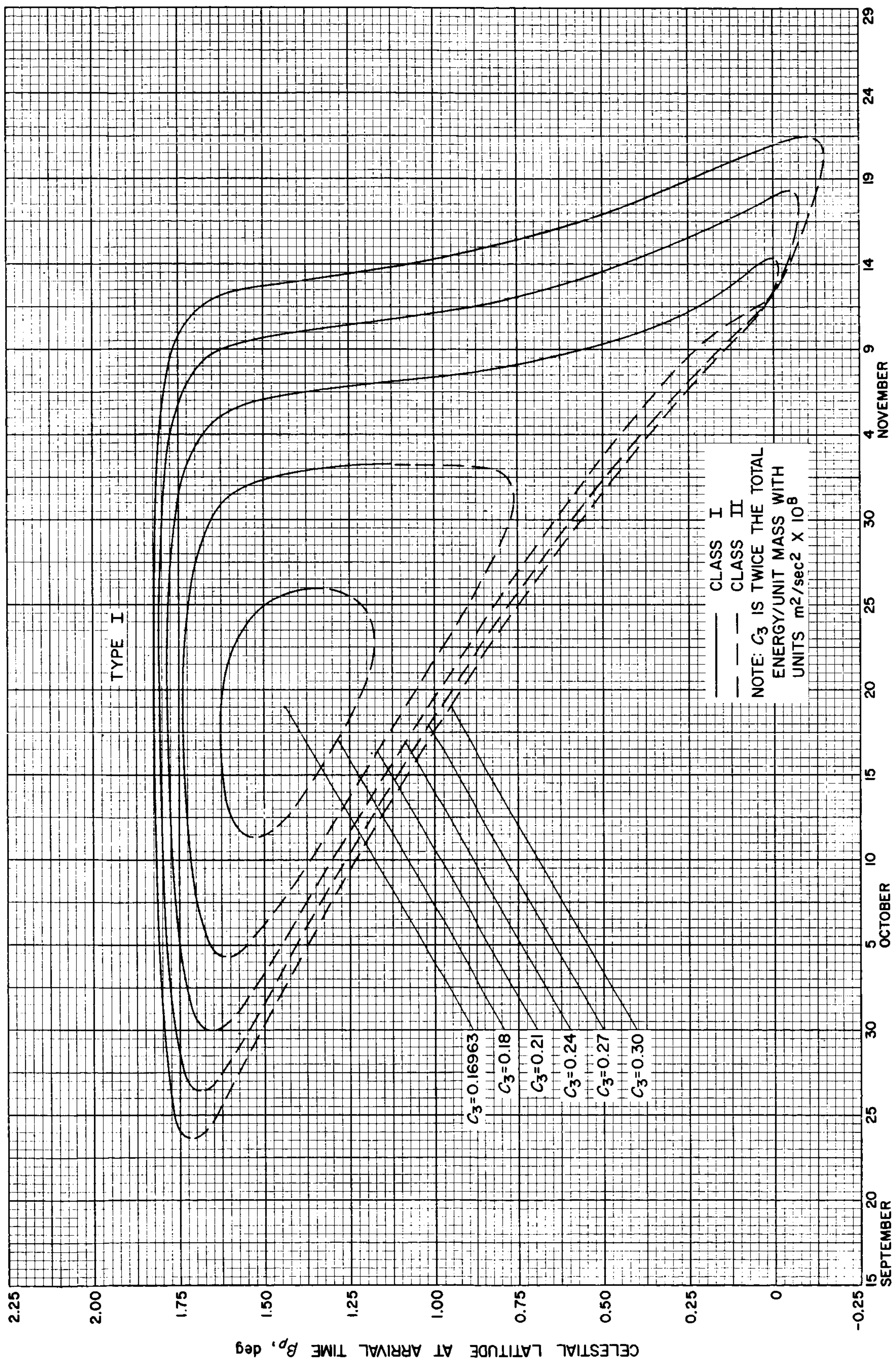

Fig. 18–13. Mars 1977: Celestial latitude at arrival time vs launch date

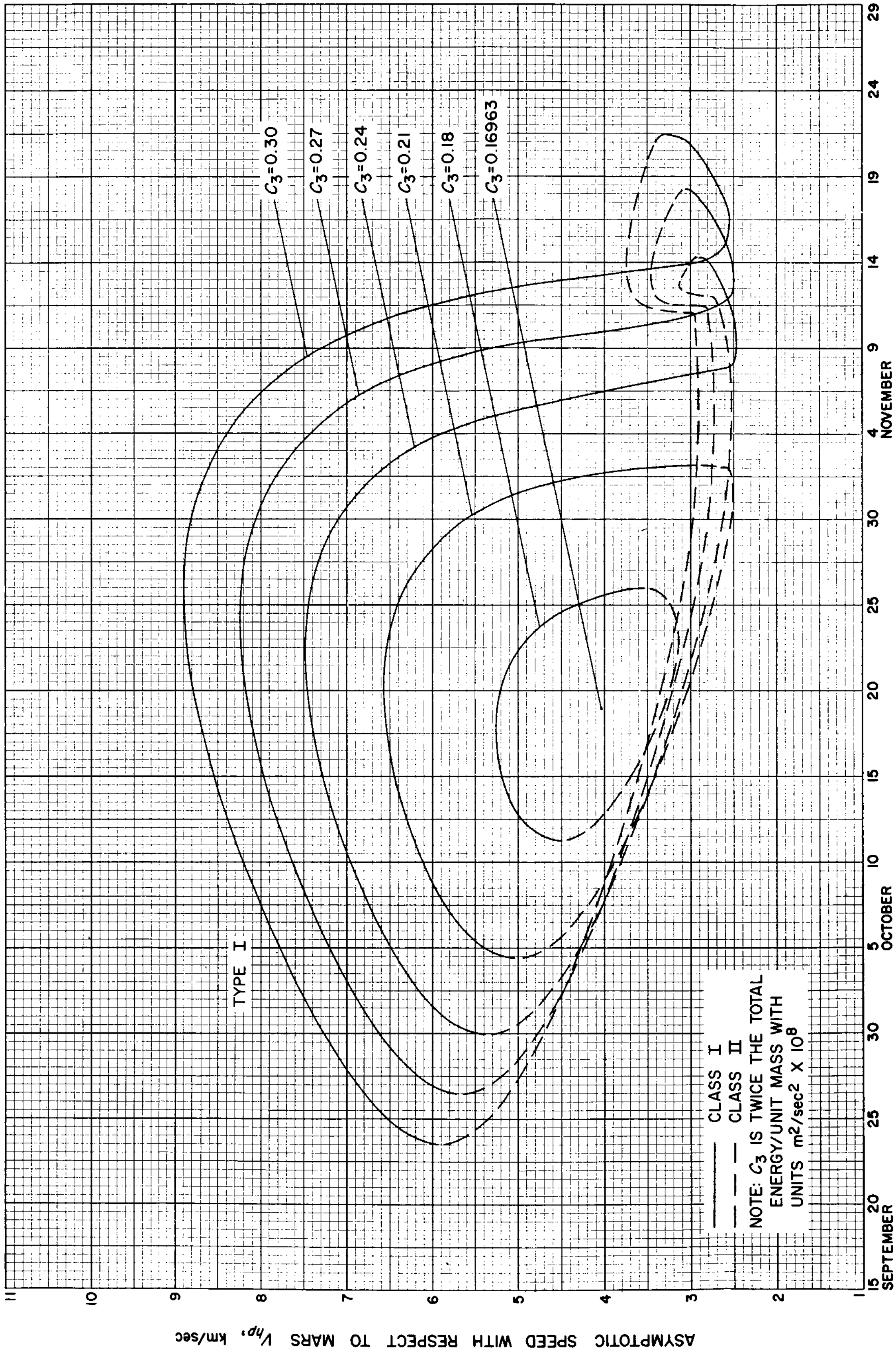

Fig. 18–14. Mars 1977: Asymptotic speed with respect to Mars vs launch date

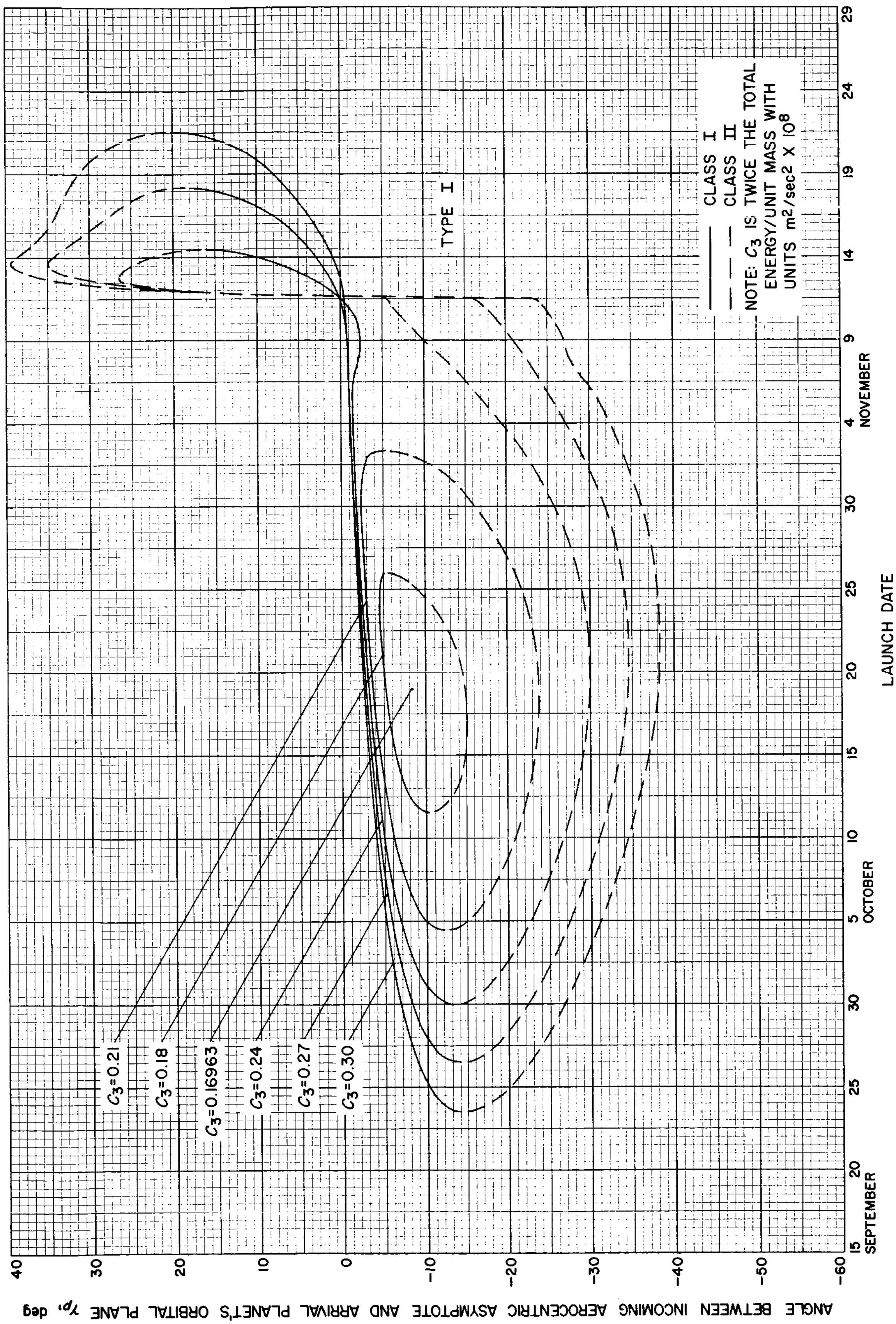

Fig. 18-15. Mars 1977: Angle between incoming aerocentric asymptote and arrival planet's orbital plane vs launch date

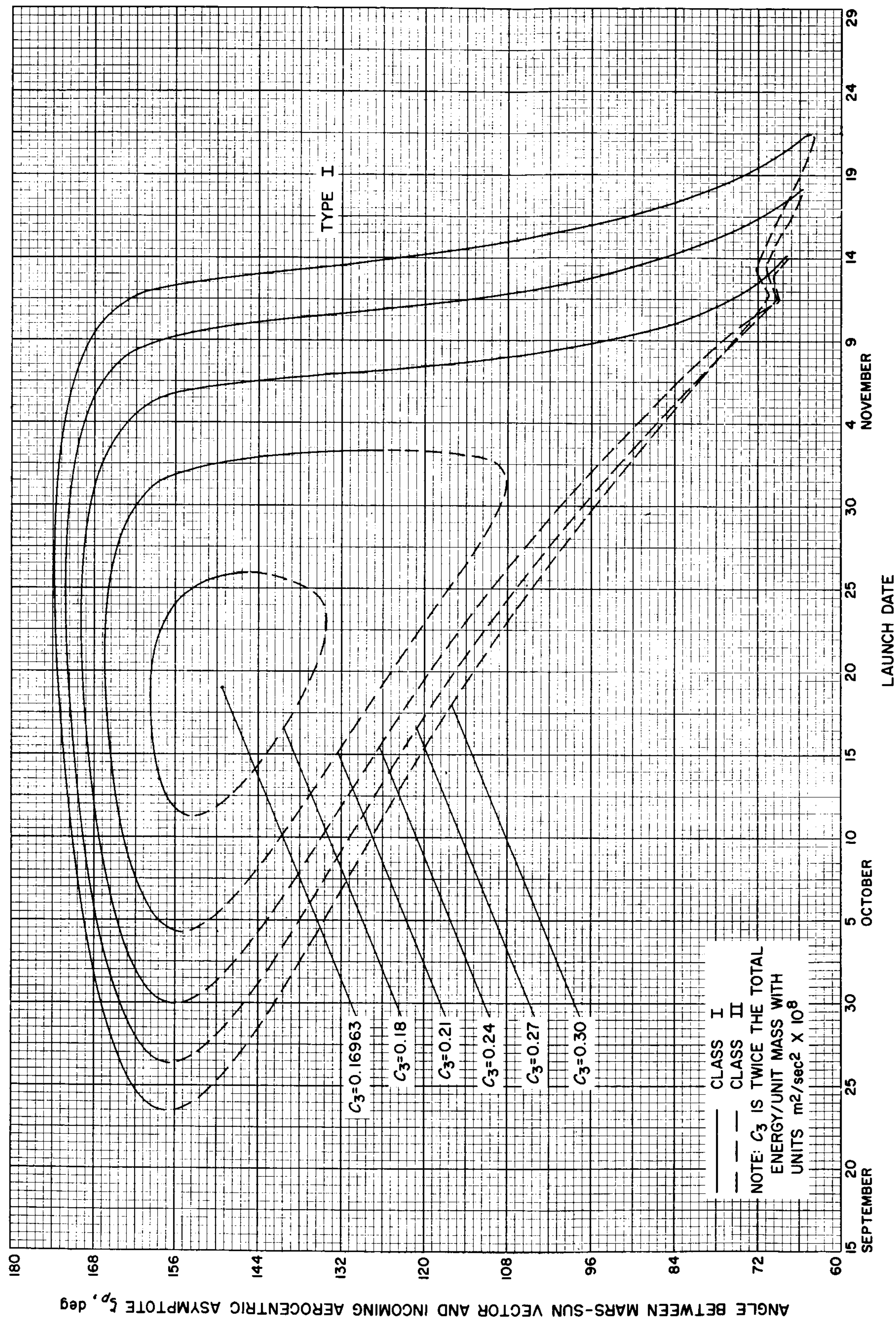

Fig. 18–16. Mars 1977: Angle between Mars–Sun vector and incoming aerocentric asymptote vs launch date

NOMENCLATURE[a]

C_3 *vis viva* energy (injection energy of escape hyperbola)

i inclination of heliocentric transfer orbit, deg

R_a aphelion of transfer orbit, millions of km

R_C Earth–Venus (or –Mars) communication distance, millions of km

R_p perihelion of transfer orbit, millions of km

T_F time of flight, days

v_L true anomaly in transfer ellipse at launch time, deg

v_p true anomaly in transfer ellipse at arrival time, deg

V_{hp} asymptotic speed (or hyperbolic-excess speed) with respect to Venus (or Mars), km/sec

β_p celestial latitude of Venus (or Mars) at arrival time, deg

γ_L angle between outgoing geocentric asymptote and launch planet's orbital plane, deg (also defined as celestial latitude of outgoing asymptote)

γ_p angle between incoming aphrodiocentric[b] or aerocentric[c] asymptote and arrival planet's orbital plane, deg

ζ_L angle between Sun–Earth vector and outgoing geocentric asymptote, deg (also defined as Earth–probe–Sun angle)

ζ_p angle between Venus–Sun (or Mars–Sun) vector and incoming aphrodiocentric (or aerocentric) asymptote, deg (also defined as Sun–probe–target angle)

Θ_p right ascension of aphrodiocentric (or aerocentric) asymptote, deg

Θ_S right ascension of geocentric asymptote, deg

Φ_p declination of aphrodiocentric (or aerocentric asymptote, deg

Φ_S declination of geocentric asymptote, deg

Ψ heliocentric central angle, deg

[a]This table of Nomenclature presents only the notation used in the graphs of Sections IV to XVIII. All other terms are defined at point of first mention in Sections I to III.
[b]Aphrodiocentric refers to Venus.
[c]Aerocentric refers to Mars.

REFERENCES

1. Clarke, V. C., Jr., Roth, R. Y., Bollman, W. E., Hamilton, T. W., and Pfeiffer, C. G., *Earth–Venus Trajectories, 1964-1970,* Vol. 1–5, Technical Memorandum No. 33-99, Jet Propulsion Laboratory, Pasadena, in press.

2. Clarke, V. C., Jr., Roth, R. Y., Bollman, W. E., Hamilton, T.W., and Pfeiffer, C. G., *Earth–Mars Trajectories, 1964-1977,* Vol. 1–7, Technical Memorandum No. 33-100, Jet Propulsion Laboratory, Pasadena, to be published.

3. Battin, R. H., "The Determination of Round-Trip Planetary Reconnaissance Trajectories," *Journal of the Aero/Space Sciences,* Vol. 26, No. 9, September, 1959.

4. Clarke, V. C., Jr., *Design of Lunar and Interplanetary Ascent Trajectories,* Technical Report No. 32-30, Rev. 1, Jet Propulsion Laboratory, Pasadena, March 15, 1962.

5. Holdridge, D. B., *Space Trajectories Program for the IBM 7090 Computer,* Technical Report No. 32-223, Rev. 1, Jet Propulsion Laboratory, Pasadena, September 1, 1962.

6. *The American Ephemeris and Nautical Almanac for the Year 1960,* p. 498, U.S. Government Printing Office, Washington.

7. Allen, C. W., *Astrophysical Quantities,* The Athlone Press, University of London, London, 1955.

ACKNOWLEDGEMENTS

The authors wish to acknowledge the valuable assistance of Mrs. Nancy Evans, who edited and prepared the graphs for the illustrators, and Miss Joan Benson, who carried out the production of the computations and automatic plotting of the graphs.